Low Temperature Difference Alpha-Type Stirling Engine for the Experimental Determination of
Optimal Parameters to Maximize Shaft Power

by

Jason Philip Michaud

A thesis submitted in partial fulfillment of the requirements for the degree of

Master of Science

Department of Mechanical Engineering
University of Alberta

Abstract

An investigation was performed experimentally to determine the combination of parameters that would produce the maximum shaft power for an alpha-type Stirling engine using a thermal source with a temperature below 100 °C. The primary objective of the study was to design and build an alpha-type Stirling engine, using air as the working fluid with a mean pressure near atmospheric pressure, which would turn a crank shaft on its own accord. Parameters would then be varied to measure the corresponding shaft power output of the engine. If the manufactured Stirling engine could not rotate the crankshaft, the engine would be driven to determine the combination of parameters that would minimize the power input required to rotate the engine.

Three different prototype opposed piston alpha (OPA) Stirling engines were designed and assembled to develop the engine to be used as the testing system: the OPA MK I, the OPA MK II, and the OPA MK III. The OPA MK III was chosen as the engine to be used for experiments, and utilized rubber bellows as piston seals, compact radiators for heat exchangers, and a triple Scotch yoke mechanism. The mechanism allowed the stroke length to be set to 50.8 mm or 76.2 mm for the expansion and compression pistons, and it allowed the phase angle to be varied from 90° to 180° in 5° increments.

The engine was instrumented to measure internal pressure, source and sink temperatures, gas temperatures, angular position of the crankshaft, and torque. An experiment plan was developed that manipulated the expansion and compression piston stroke lengths, the phase angle between the pistons, and the engine angular velocity. The phase angle was varied between 120° and 180° in 5° increments, the speed was varied between 30 rpm and 60 rpm in 10 rpm increments, and three engine swept volumes were possible, which resulted in 156 parameter combinations to be tested.

Manual attempts at running the engine with a thermal source temperature of 95 °C and a thermal sink temperature of 2 °C were performed, where the engine failed to run under all tested configurations. As such, significant effort was put into determining the reason it failed to run. To ensure confidence in the results, in-depth studies into the uncertainty of the bellows volume variation, modelling mechanism energy transfer, instrument calibration and uncertainty reduction, and the time required for engine warm-up and steady state operation were performed. Furthermore, the experiment was split into two 156 configuration sets: a baseline experiment with an inactive thermal source and sink, along with a thermal experiment with an active thermal source and sink, so that any performance improvement and thermal effects could be observed.

Results included analyzing and comparing measurements between baseline and thermal experiments for pressure fluctuations, gas temperatures, indicator diagrams, and shaft power input. It was found that compressive heating and expansion cooling had a significant effect at higher compression ratios, such that the measured temperature difference decreased from approximately 90 °C to 75 °C as the phase angle decreased, indicating that the heat exchangers could not sufficiently offset the compressive heating and expansion cooling. Furthermore, comparison of the ideal pressure ratio to the measured pressure ratio at 180° was found to be lower, suggesting the gas temperature was not uniform. The mechanism effectiveness was investigated and found to vary between 0.57 and 0.81. By using the measured shaft work, a mechanism effectiveness above 0.9 would be required for net positive shaft work to appear in the range of 170° to 160° with the current heat exchangers. Therefore, it was concluded that the engine failed to run primarily due to insufficient heat transfer and a low mechanism effectiveness.

Optimal parameter combinations were investigated by comparing the shaft power input of the baseline and thermal experiments. The range of phase angles that contained the optimal value was determined to be between 140° and 160°, with phase angles of 150° and 160° being the most promising. The exact optimal swept volume and phase angle combination that reduced the shaft power input could not be concluded due to uncertainty, but an optimal compression ratio was estimated to lie within the range of approximately 1.12 to 1.24 for a similar engine and operating conditions.

Preface

This thesis is an original work by Jason Michaud. Aspects of the research in Chapter 3, Section 3.5.1, have appeared in the following conference publications:

J. P. Michaud, C. P. Speer, D. A. Miller, and D.S. Nobes, "Empirical Heat Transfer Correlations of Finned-Tube Heat Exchangers in Pulsatile Flow," *World Academy of Science, Engineering and Technology International Journal of Mechanical and Mechatronics Engineering*, vol. 11, no. 6, pp. 1230-1235, 2017.

J. P. Michaud, C. P. Speer, D. A. Miller, and D.S. Nobes, "Empirical heat transfer correlations of finned-tube heat exchangers in oscillating flow for low temperature Stirling engines," *ICFMHTT 2017: 19th International Conference on Fluid Mechanics, Heat Transfer and Thermodynamics*, Venice, Italy, June 21-22, 2017.

J. P. Michaud, D. A. Miller, C. P. Speer, M. Nicol-Seto, and D. S. Nobes, "Dimensionless Heat Transfer Correlations of Finned-Tube Radiators in Fully Reversed Oscillating Flow," *Okanagan Fluid Dynamics Meeting*, Kelowna, British Columbia, Canada, Aug 22-23, 2017.

The author also contributed to the following publications that do not contribute directly to this thesis:

C. P. Speer, D. A. Miller, C. J. A. Stumpf, J. P. Michaud, and D.S. Nobes, "Modification of an ST05G-CNC Stirling Engine to Use a Low Temperature Heat Source," *American Institute of Aeronautics and Astronautics 15th International Energy Conversion Engineering Conference,* AIAA Propulsion Energy Forum, Atlanta, Georgia, USA, July 10-12, 2017.

M. Nicol-Seto, J. P. Michaud, S. Middleton, and D.S. Nobes, "Non-Traditional Drive Mechanism Designs for the Improvement of Heat Transfer in Low Temperature Differential Stirling Engines," *18th ISEC International Stirling Engine Conference*, Tainan, Taiwan, Sept 19-21, 2018

Acknowledgements

Table of Contents

List of Tables

List of Figures

List of Symbols

Roman Character Symbols

Symbol	Description	Units
A_p	Frontal Piston Area	m^3
B_x	Total Systematic Uncertainty	-
b_x	Elemental Systematic Uncertainty	-
CR	Compression Ratio	-
$C_{x_j x_k}$	Correlation Between Parameter x_j and x_k	-
d	Diameter	m
E	Mechanism Effectiveness	-
g	Gravitational Acceleration	m/s^2
h	Water Column Height	m
L_s	Stroke Length	m
m	Mass of Gas	kg
P	Pressure	Pa or psi
P^*	Non-Dimensional Pressure	-
P_{gage}	Gage Pressure	Pa or psi
Q	Heat	J
R	Gas Constant	J / kg·K
R^2	Coefficient of Determination	-
r_1	Horizontal Piston Displacement	m
r_2	Crank Arm Length	m
r_4	Connecting Arm Length	m
S_x	Standard Deviation	-
T	Temperature	°C or K
t	Time	s
TR	Torque Ratio	-
u	Total Uncertainty	-
V	Volume	m^3 or L
V^*	Non-Dimensional Volume	-
V_{cl}	Clearance Volume	m^3 or L
V_{sw}	Swept Volume	m^3 or L
W	Work	J
W_{eff}	Efficacious Work	J
W_f	Forced Work	J
W_s	Shaft Work	J
$\dot{W}_s$	Shaft Power	W
$\dot{W}_\%$	Percent Reduction in Shaft Power	%

Greek and Script Character Symbols

Symbol	Description	Units
α	Phase Angle	° or rad
Γ	Pressure Ratio	-
ΔT	Temperature Difference	°C
η_m	Mechanical Efficiency	-
η_{th}	Thermal Efficiency	-
θ	Crank Angle	° or rad
$\mathcal{P}_x$	Standard Random Uncertainty	-
ρ	Density	kg / m^3
τ	Torque	Nm
Υ	Voltage	V
ω	Angular Speed	rad/s or rpm

Subscripts

Symbol	Description
atm	Atmospheric
$base$	Baseline Experiment
$bellows$	Parameter Pertaining to Bellows
$buffer$	Parameter Pertaining to the Buffer Space
c	Compression (or Compression Space)
cp	Compression Piston
e	Expansion (or Expansion Space)
eng	Parameter Pertaining to Engine
ep	Expansion Piston
gas	Parameter Pertaining to Gas
$H2O$	Parameter Pertaining to Water
h	Heater
h_{in}	Heater Inlet
h_{out}	Heater Outlet
in	Input
ind	Indicated
$indv$	Individual Cycle
k	Cooler
k_{in}	Cooler Inlet
k_{out}	Cooler Outlet
l	Local Parameter
max	Parameter Maximum
$mean$	Mean of Parameter
min	Parameter Minimum
net	Net Value
o	Standard Parameter
out	Output
r	Regenerator
$sink$	Thermal Sink
$source$	Thermal Source
$temp$	Thermal Experiment
$total$	Total of Parameter
$volt$	Raw Voltage

Chapter 1   Introduction

This chapter will consist of a motivation for researching low temperature difference (LTD) Stirling engines, followed by relevant background information about the technology to assist with comprehending the contents of this thesis. After, other advances within the literature will be presented, along with the thesis objectives and structure closing this chapter.

1.1   Motivation

The global drive to diversify into renewable energy systems with a reliable baseload power capacity is ever increasing. Within Canada, 17% of the energy supply is produced from renewable sources, where approximately 67% is generated from hydroelectricity, 23% from biomass, 5% from wind, and remaining from other sources [1]. Currently in Canada, there are no geothermal energy to electricity facilities; however, interest into the conversion of geothermal energy into electricity has been renewed, with projects going forward in western Canada [2]–[4]. Geothermal resources present in Alberta, Canada, are generally below 100 °C, since the majority of the province is part of a sedimentary basin, which although porous and has a relatively low thermal conductivity [5]. Specifically, there are locations in Alberta where low-grade geothermal resources of 100 °C may be found at depths of around 2 km to 3 km [6]. Banks and Harris [7] identified a gross amount of thermal power (MWt) from geothermal resources over a 30-year production period to be approximately 6,100 MWt within the Western Canadian Sedimentary Basin, in Alberta, using oil and gas well data, where the bottom hole temperatures ranged from approximately 60 °C to 150 °C.

The province of Alberta is a large producer of oil and gas, with an estimated 176,000 active wells [8]. Towards the end of the life-cycle of a well, it may become orphaned or abandoned. An orphaned well is one that no longer has a party legally responsible for the closure and reclamation, whereas an abandoned well is one that has been permanently dismantled [8]. The Orphan Well Association reported that 3,406 orphaned wells were to be abandoned in Alberta as of November, 2019 [9]. These wells may provide the opportunity to access the geothermal water, as the bottom hole temperatures may be enough to generate a usable amount of energy.

Low-grade waste heat is another potential source of thermal energy that is abundant in the province of Alberta, which is released from the industrial processes of the oil and gas industry. A study performed on the amount of waste heat available in the Strathcona and Heartland industrial areas near Edmonton, Alberta, Canada reported that approximately 151 MWt of waste heat between 80 °C and 230 °C was being emitted from coolers and compressors in the area [10]. The study also identified that there was an abundance of waste heat released between 20 °C and 80 °C from process coolers, which totaled approximately 565 MWt [10].

A technology that could retrofit orphaned wells to access geothermal resources, or to utilize waste heat from industrial processes, could aid the province to diversify energy generation using renewable energy systems. Suitable thermodynamic cycles to take advantage of these low-grade heat resources do exist, but the technologies that implement them have a varying degree of viability, such as the Organic Rankine cycle (ORC), the Kalina cycle, and the Stirling cycle. Both the ORC and Kalina cycle are closed cycles that utilize a fluid with a low boiling point to produce steam to turn a turbine [11]. The ORC can use a variety of organic fluids, which may be hazardous [12], and the Kalina cycle uses an ammonia-water mixture [11]. Research has been performed into the viability of both the ORC and Kalina cycle with low-grade geothermal resources [11], [12], but both systems require the construction of a large power plant with components such as pumps, turbines, compressors, evaporators, and valves, which reduce the financial viability of the technologies when used with heat sources below 100 °C [11]. There have been attempts to utilize the ORC in waste heat recovery in Alberta, and it has been able to produce electricity, but the reliability of the system must still be tested [13]. The Stirling engine is an externally heated and cooled, closed cycle, regenerative heat engine [14]. Ivo Kolin [15] demonstrated the first low temperature difference (LTD) Stirling engine that could function at a temperature difference of 20 °C. Kolin et al. [16] also proposed that the use of Stirling engines in converting geothermal heat in to mechanical or electrical power was advantageous, but may only be on the scale of a few kW; however, they can be coupled together to form a larger system, and do not require hazardous working fluids nor turbines, compressors, evaporators, and valves. There have been successful commercial Stirling engines, such as the ThermoHeart (Cool Energy, Inc.) [17], that utilize waste heat to produce power.

The research goals established at the inception of this project were to design and manufacture prototype LTD Stirling engines for use with low-grade waste heat or geothermal

resources, with thermal source temperatures below 100 °C, and to determine which Stirling engine configuration would be the most viable. A more in depth introduction into Stirling engines will be discussed in the sections to follow.

1.2   The Stirling Engine

A simplified Stirling engine consists of a sealed working space that allows for changes in volume as a result of the movement of pistons, and inside it contains a working fluid that changes temperature and pressure, and undergoes expansion and compression. The Stirling engine is classified as a heat engine, as it operates between a thermal source where heat is transferred to the engine, and a thermal sink, where heat is rejected from the engine, in order to produce work [18], as illustrated in the schematic of Figure 1-1.
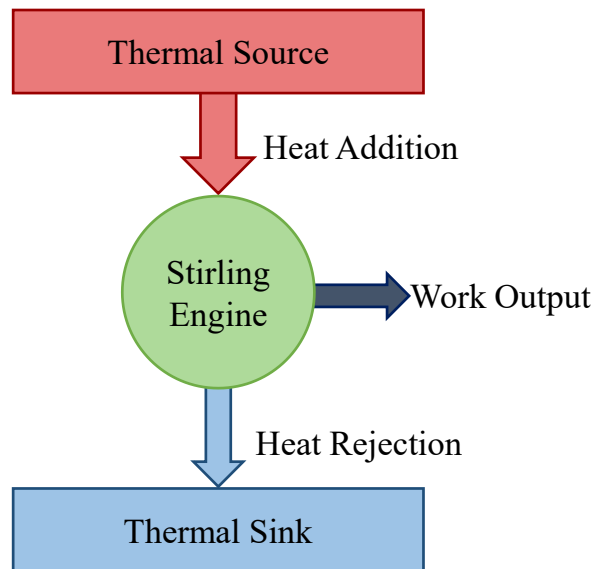
Figure 1-1: Schematic Overview of a Generic Stirling Engine Cycle

Unlike a typical internal combustion engine, which operates on an open-cycle during the intake and exhaust strokes, the Stirling engine operates on a closed cycle, since all the working fluid remains in the engine during all portions of the cycle [19]. The engine is externally heated and cooled, since the thermal source and thermal sink are located outside the engine. The thermal source may provide heat to the engine by means of any energy source, such as fossil fuels, solar radiation, biomass, nuclear sources, waste heat, or geothermal sources [19]. The thermal sink may be anything with a lower temperature than the thermal source such the surrounding ambient air.

A schematic detailing the fundamental components of a simplified Stirling engine for understanding the ideal Stirling cycle is shown in Figure 1-2. From the figure, it can be seen that a Stirling engine requires a working space shown by the expansion and compression spaces, which are maintained at the thermal source and sink temperatures respectively. Furthermore, it requires a way of changing the volume of the working space, shown by the expansion and compression pistons. Moreover, the Stirling cycle is a regenerative cycle where heat is stored inside a regenerator matrix acting as a "thermal battery" to pre-heat and pre-cool the working fluid before it arrives into expansion and compression spaces [18]. Not depicted are the external thermal source and sink.
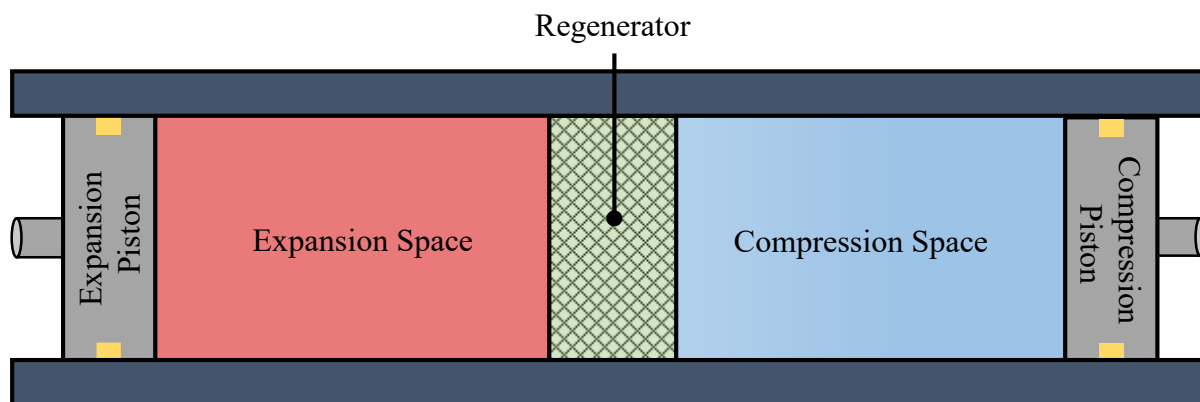
Figure 1-2: Schematic of a Simplified Stirling Engine

1.3   The Ideal Stirling Cycle

The ideal Stirling cycle relies upon a number of assumptions, which are listed as follows:

1. The cycle is reversible [18].
2. The working fluid follows the ideal gas law [20].
3. There are no heat transfer losses between the engine and the source and sink (isothermal processes) [20] .
4. Losses are negligible, including any piston frictional losses, engine leakage, and pressure losses [21].
5. The ends of the regenerator are at the expansion and compression space temperatures, and heat transfer to and from the regenerator is lossless [18].
6. There is no conduction in the longitudinal direction of the regenerator [14].

As assumption 2 states, it is assumed that the gas behaves as an ideal gas following:

$$PV = \text{m}RT \tag{1-1}$$

where P is the gas pressure, V is the gas volume, m is the mass of gas, R is the gas constant, and T is the gas temperature. When comparing the properties of the same gas at two different states in a closed system, state 1 and state 2, the following equation may be used:

$$\frac{P_1 V_1}{T_1} = \frac{P_2 V_2}{T_2} \tag{1-2}$$

One of the advantages of the Stirling cycle over other closed thermodynamic cycles is that it is fully reversible [18]. It has an ideal thermal efficiency, η_{th}, equal to that of the Carnot cycle, which is a function of the maximum, T_{max}, and minimum, T_{min}, temperatures [1-5], as shown:

$$\eta_{th} = \frac{W_{net}}{Q_{in}} = \frac{T_{max} - T_{min}}{T_{max}} \tag{1-3}$$

In the ideal Stirling cycle, there are four fully reversible and discontinuous processes that occur in sequence [14], [18]. The processes (in an arbitrary order) are as follows:

- Process 1→2: Constant Temperature (Isothermal) Expansion
- Process 2→3: Constant Volume (Isochoric) Regenerative Cooling
- Process 3→4: Constant Temperature (Isothermal) Compression
- Process 4→1: Constant Volume (Isochoric) Regenerative Heating

1.3.1 Constant Temperature Expansion

During process 1→2, the majority of the working fluid is in the expansion space, at an elevated temperature, T_e. As a result of the higher temperature, the gas is expanded and produces expansion work, W_e. Heat, Q_e, is transferred to the internal working fluid from an external source to maintain the working fluid at temperature T_e, since the working fluid temperature drops as it expands according to the ideal gas law. This heating of the working fluid maintains an isothermal expansion process [14], [18]. During expansion, the working fluid pressure drops as the working space volume is increased. A snapshot of this process is shown schematically in Figure 1-3.
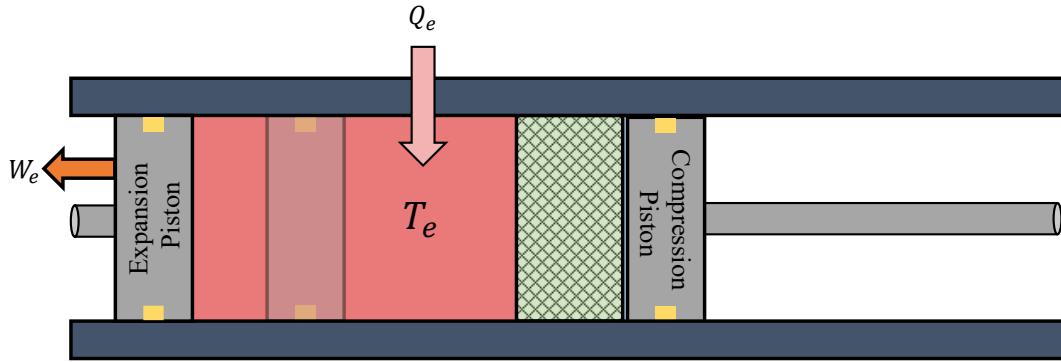
Figure 1-3: Schematic of the Isothermal Expansion Process

1.3.2 Constant Volume Regenerative Cooling

After the isothermal expansion, isochoric regenerative cooling occurs in process 2→3. The working gas is shuttled across the regenerator section, where heat is rejected from the working fluid into the regenerator matrix, $Q_{r_{in}}$, for thermal storage, cooling the gas down to temperature T_c [14], [18]. The majority of the gas is then inside the compression space. The pressure of the working fluid drops due to the reduction in temperature. This process is shown schematically in Figure 1-4.
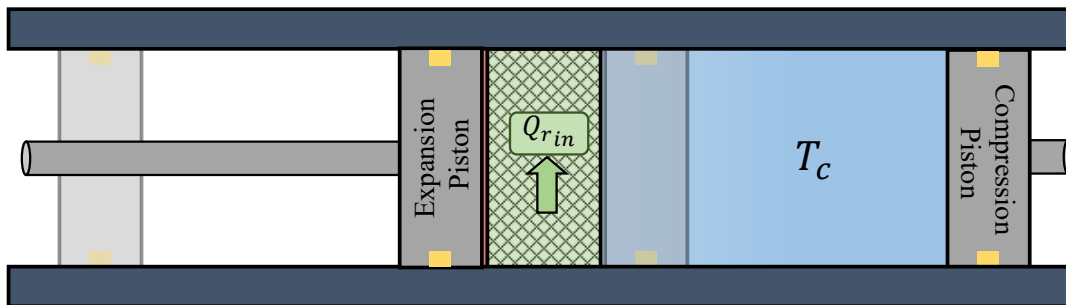
Figure 1-4: Schematic of the Isochoric Regenerative Cooling Process

1.3.3 Constant Temperature Compression

Process 3→4 involves isothermal compression. With the majority of the working fluid inside the compression space at temperature T_c, work, W_c, is applied on the piston to compress the working fluid. As it is compressed, the working fluid temperature and pressure increase as a result of the reduction in working space volume. In order to maintain an isothermal process, heat, Q_c, is rejected from the working fluid to the thermal sink [14], [18]. For illustration, the process is shown in Figure 1-5.

6
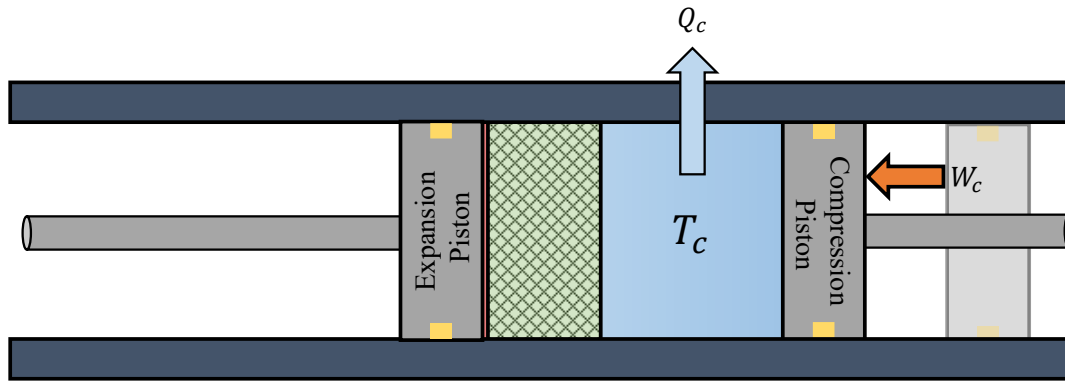
Figure 1-5: Schematic of the Isothermal Compression Process

1.3.4 Constant Volume Regenerative Heating

Following isothermal compression, process 4→1 consists of isochoric regenerative heating. As the working fluid is shuttled across the regenerator once more, heat, $Q_{r_{out}}$, is transferred from the regenerator matrix back into the working fluid, bringing the temperature back to T_e [14], [18]. The majority of the gas is in the expansion space, and the pressure increases due to the temperature increase, according to the ideal gas law at constant volume. The process is shown schematically in Figure 1-6. After process 4→1, the cycle repeats.
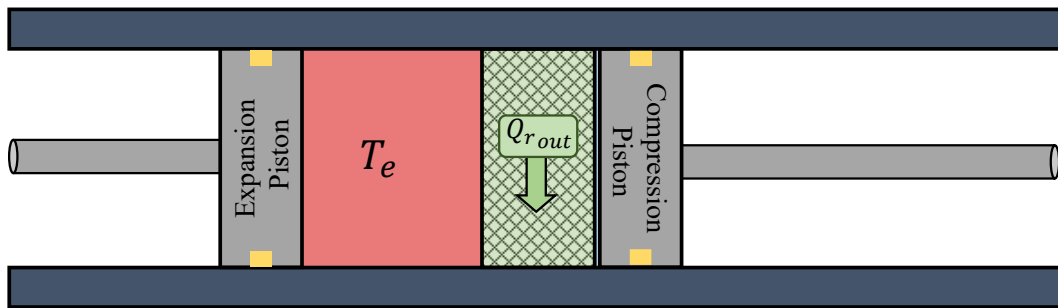
Figure 1-6: Schematic of the Isochoric Regenerative Heating Process

1.3.5 The Ideal Indicator Diagram

By linking the pressure and volume variations from processes 1 through 4 into a closed loop, an ideal indicator diagram for the Stirling cycle is formed. The ideal indicator diagram aids in visualizing when each process occurs, as well as providing the indicated work from the cycle. Figure 1-7 shows a schematic ideal indicator diagram. Since the ideal cycle is discontinuous, each process is interpreted by following the cycle between the corresponding labelled points.

Ideal Stirling Cycle Process
1→2: Isothermal Expansion, Heat Addition
2→3: Isochoric Regenerative Cooling
3→4: Isothermal Compression, Heat Rejection
4→1: Isochoric Regenerative Heating
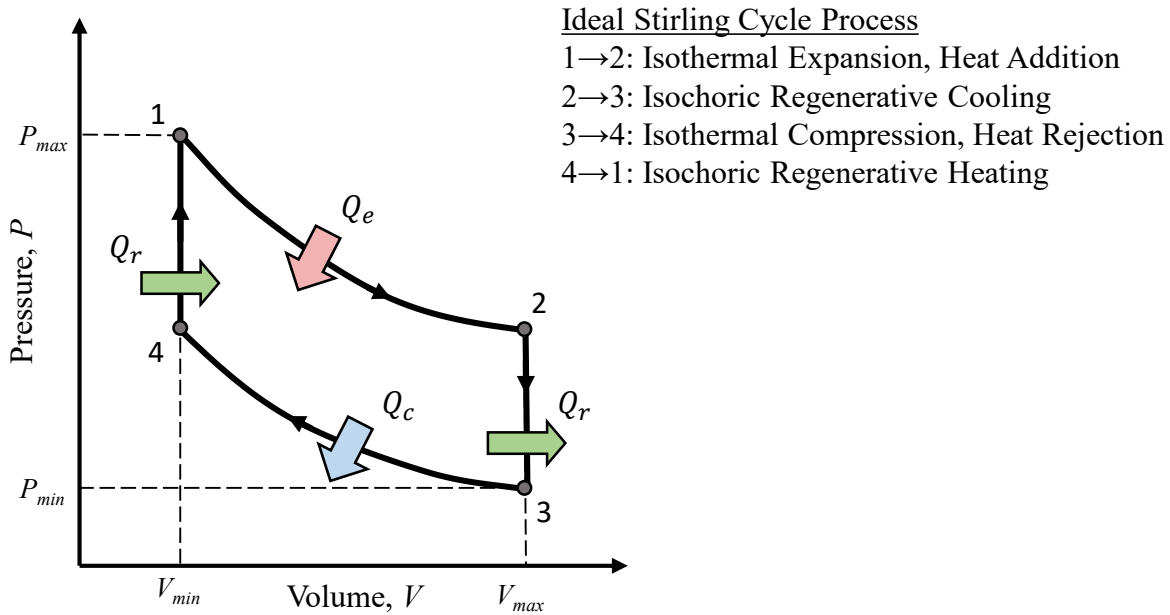
Figure 1-7: Schematic of the Ideal Stirling Cycle Pressure-Volume Diagram

The area enclosed by the indicator diagram represents the indicated work of the cycle. Work is extracted during the expansion process 1→2, and work must be supplied to the engine during the compression process 3→4, therefore the difference in work output and input is equivalent to the net work of the cycle. In a Stirling engine the work is performed by a moving boundary, where the general equation of boundary work [18] is shown as:

$$W_b = \int_1^2 P(V)dV \qquad \text{1-4}$$

where W_b is the boundary work between states 1 and 2, and P is the engine pressure as a function of volume, V. This general equation can be extended to the expansion and compression processes, which occur between the maximum volume, V_{max}, and minimum volume, V_{min}, of the specified workspace shown in Equations 1-5 and 1-6 [22]. Where W_e is the expansion work due to the pressure during expansion, P_e, which varies with volume, and W_c is the compression work required as a result of the pressure during compression, P_c.

$$W_e = \int_{V_{min}}^{V_{max}} P_e(V)\,dV \qquad\qquad 1\text{-}5$$

$$W_c = \int_{V_{min}}^{V_{max}} P_c(V)\,dV \qquad\qquad 1\text{-}6$$

The difference between the expansion work and compression work is equivalent to the ideal indicated work, W_{ind}, as shown :

$$W_{ind} = W_e - W_c \qquad\qquad 1\text{-}7$$

Figure 1-8 illustrates the areas of expansion, compression, and indicated work schematically on an ideal indicator diagram. As mentioned, integrating along the expansion process curve yields the area below the curve, which is the extracted expansion work. Similarly, integrating along the compression process curve yields the area below the curve, which is the required compression work. The difference in areas equates to the area enclosed in the ideal indicator diagram.
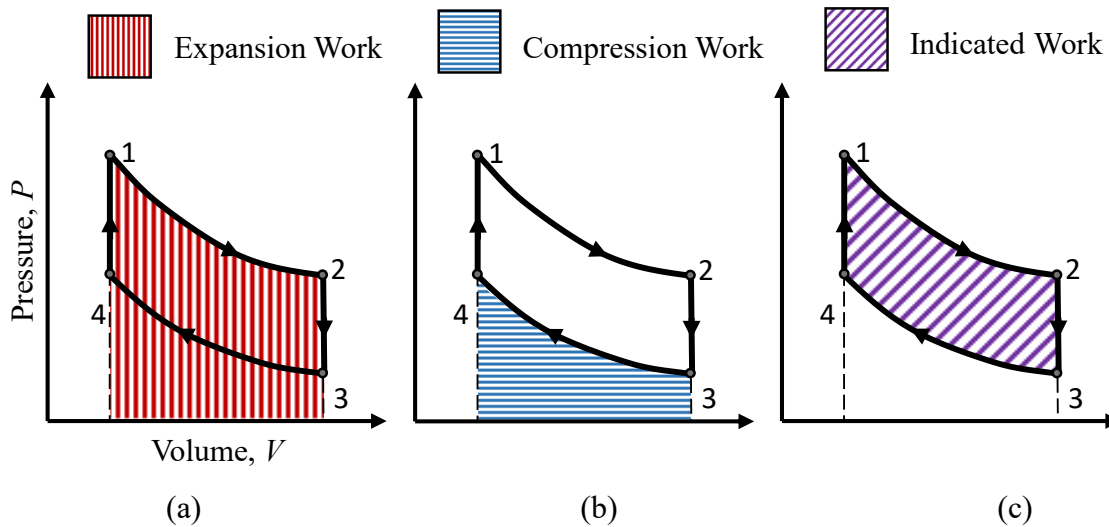
Figure 1-8: Schematic Showing Areas of (a) Expansion Work (b) Compression Work (c) Indicated Work

1.4   The Stirling Engine Cycle in Practice

This section will cover some of the deviations of the practical Stirling cycle, created from a physical heat engine, from the ideal Stirling cycle. There are many factors that influence the cycle, but only an overview of the prominent factors will be discussed here.

1.4.1   The Practical Indicator Diagram

A Stirling engine differs greatly in practice compared to the ideal Stirling cycle. In an ideal Stirling engine, described in Section 1.3, the piston moves discontinuously and sequentially which form the ideal indicator diagram shape. Contrarily, in a practical engine, the piston motion is continuous and usually follows a sinusoidal motion path [23]. As a result, the indicator diagram becomes rounded and portions of the cycle overlap without a clear distinction of the four processes [21]. In addition, expansion and compression does not occur solely in their respective working spaces. Therefore, expansion and compression space indicator diagrams are created, where the area enclosed in the expansion space diagram is the work output from expansion, and the area within the compression space diagram is the work input required to compress the working fluid [21]. The difference in expansion and compression work is equal to the total indicated work, when not considering frictional and flow losses. A schematic representation of generic indicator diagrams for a practical Stirling engine are shown in Figure 1-9, and are created by plotting the workspace volume variations against the pressure variations of an engine.
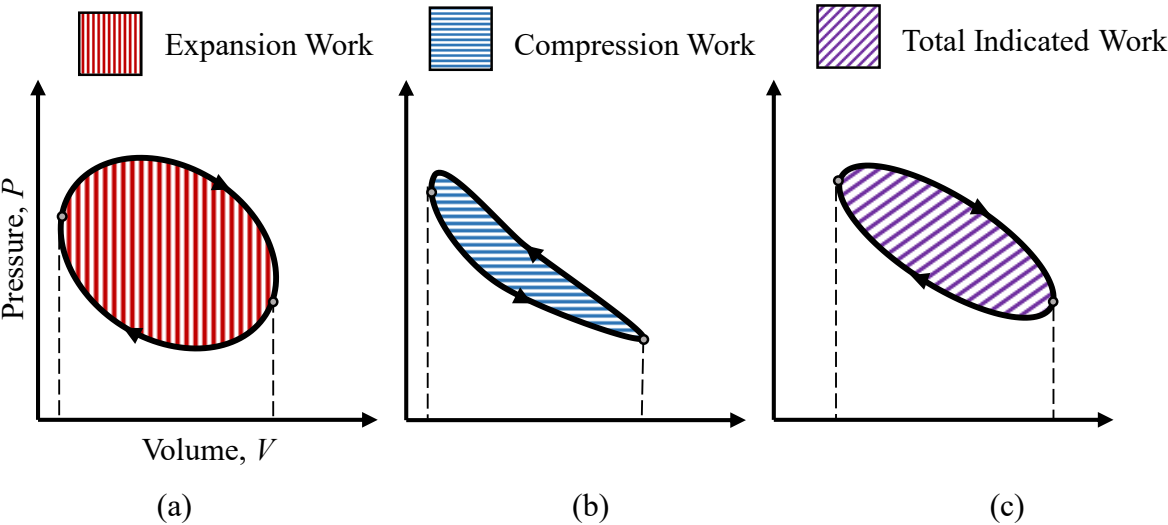
Figure 1-9: Schematic of (a) Expansion, (b) Compression, and (c) Total Indicator Diagrams

10

1.4.2   Parameters that Affect the Practical Stirling Engine Cycle

Many different parameters can be altered to affect the practical Stirling cycle, and there are inherent losses that should be minimized. The identification of the different loss mechanism are especially important when developing a numerical model to predict the performance of an engine design. Well documented overviews of these loss mechanisms can be found in the literature [20], [24]–[26], so only an overview on the geometric parameters that affect the cycle will be provided in this section.

1.4.2.1   Temperature Difference

The temperature difference between the gas in the expansion and compression spaces is one of the parameters that directly influence the amount of indicated work, along with the change in volume, by affecting the pressure during expansion and compression. In the ideal Stirling engine, it is assumed that the temperature in the workspaces are equivalent to that of the thermal source and sink, when in actuality there are losses, such as conduction losses and imperfect heat transfer, that reduce the temperature in the expansion space and increase the temperature in the compression space.

1.4.2.2   Phase Angle

The phase angle, α, is defined as the angle by which the expansion space volume variation leads the compression space volume variation [19]. The phase angle is the primary means of increasing or decreasing the total engine volume variation with set stroke lengths.

Considering that most pistons have a sinusoidal motion in Stirling engines, the volume variations are also approximately sinusoidal. Therefore, for a range of phase angles between 0° and 180°, a 0° phase angle would have the most compression, whereas 180° would have no compression. The optimal phase angle varies depending on the application, and is therefore chosen on a case by case basis depending on if increased power or efficiency is desired [19]. Figure 1-10 shows schematically the difference between a 90° and a 180° phase angle for a generic sinusoidal expansion and compression space volume variation.
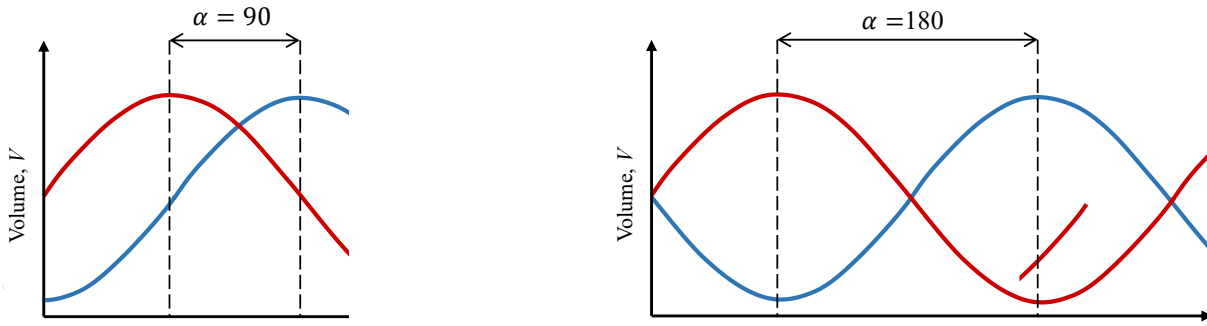
Figure 1-10: Schematic of the Effect of Phase Angle on Volume Variation for 90° and 180° Phase Angles

1.4.2.3 Dead Volume

According to Walker [14], the dead volume is any volume not swept by the pistons, and it includes clearance spaces, regenerator and heat exchanger void volumes, and any volumes associated with ducts and ports. Dead volume is unavoidable in a practical Stirling engine, and during design, effort is spent in finding the balance between reducing dead volume, and increasing heat exchanger area, which in turn will increase heat exchange void volume. The presence of dead volume reduces the power output by reducing the overall pressure variation, since the working fluid cannot be entirely within the expansion or compression space [19]. Therefore, during expansion, the overall temperature is reduced which reduces the pressure, and during compression the overall temperature is increased which increases the pressure. Reader and Hooper [19] presented a useful figure showing the effect of dead volume on the ideal indicator diagram, and it is reproduced in Figure 1-11 to aid the discussion. The ideal indicator diagram 1-2-3-4 is reduced to the resulting indicator diagram 1'-2'-3'-4' from the inclusion of dead volume.
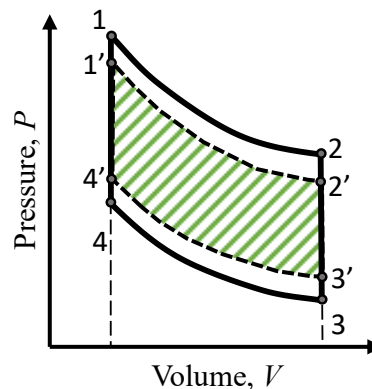
Figure 1-11: Schematic of the Effect of Dead Volume on an Ideal Indicator Diagram
(Adapted from Reader and Hooper)

1.4.2.4   Compression Ratio

The compression ratio, CR, is a non-dimensional parameter used to quantify the change in volume in the engine. The compression ratio is defined as the ratio of the maximum engine volume, V_{max}, to the minimum engine volume, V_{min}, as shown:

$$CR = \frac{V_{max}}{V_{min}} \qquad\qquad 1\text{-}8$$

The compression ratio is dictated by the combination of the phase angle and the stroke lengths of the pistons. A compression ratio equal to unity indicates that there is no volume change in the system. The compression ratio directly influences the difference between maximum and minimum pressure, where a larger value increases the pressure difference.

1.4.3   Stirling Engines and Stirling Heat Pumps

In practice, there are two ways to utilize the Stirling cycle: as a heat engine and as a refrigerator/heat pump. The objective of the Stirling engine is to produce work by absorbing heat from a thermal source and rejecting it to a thermal sink, whereas the objective of the Stirling refrigerator/heat pump is to consume work to remove heat from a cold space and transfer it to a hot space [18]. For a work producing cycle (heat engine), the indicator diagram is followed in the clockwise direction, whereas for a work consuming cycle (refrigerator/heat pump), the diagram is followed in the counterclockwise direction, as shown in Figure 1-12.

(a)   (b)
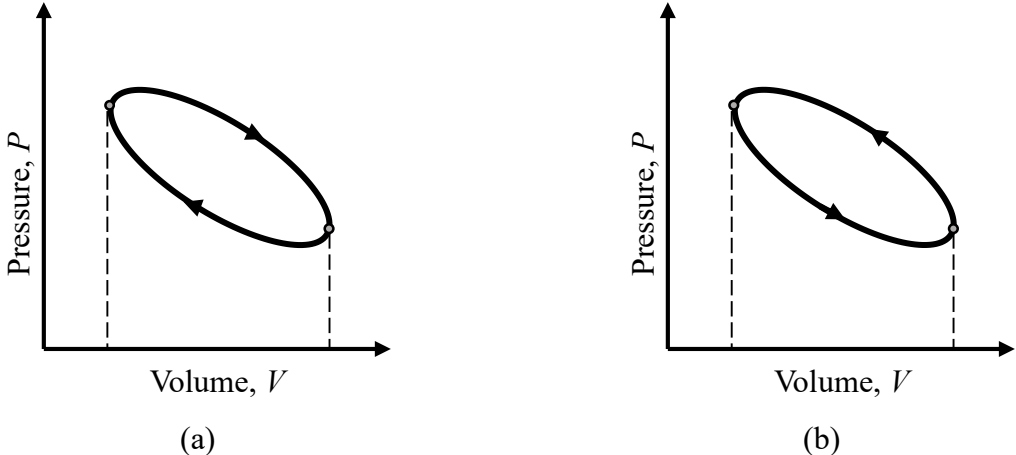
Figure 1-12: Schematic (a) Heat Engine and (b) Refrigerator/Heat Pump Indicator Diagrams

For a Stirling engine, the expansion space indicator diagram should have a larger area than the compression space diagram, and rotate in the clockwise direction, since it is producing work, whereas the compression space diagram should be rotating counterclockwise as it is consuming work. A Stirling heat pump operates in the same way as a Stirling engine; however, the expansion space is at a lower temperature than the compression space [27]. Therefore, the indicated work of the compression space will be larger than the indicated work in the expansion space, which requires work to be supplied to the system [27]. This is shown schematically in Figure 1-13.
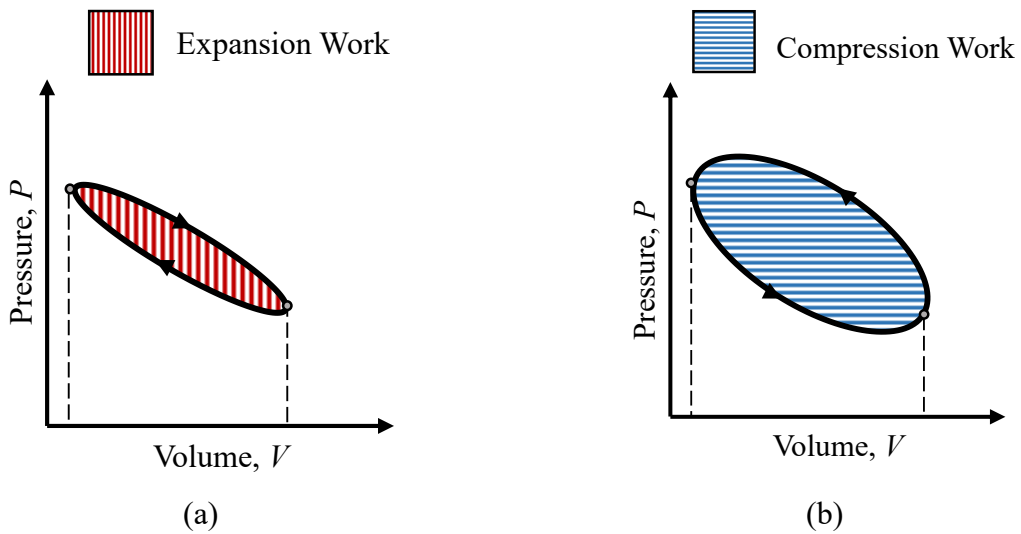
Figure 1-13: Schematic Indicator Diagram for Refrigerator/Heat Pump for (a) Expansion Space and (b) Compression Space

1.5 Types of Stirling Engines

There exist three primary Stirling engine configurations: the alpha, beta, and gamma configurations, with many different variations within those. This thesis will consider single acting engine systems rather than double acting systems, and will focus primarily on alpha-type Stirling engines. The beta and gamma configurations are introduced in this section, as a means of differentiating the alpha configuration.

1.5.1 Alpha Stirling Engines

Alpha Stirling engines are distinguishable from the other primary Stirling engine types as they use two sealed power pistons, and have two distinct cylinders for the expansion and compression of the gas. These pistons perform the function of displacing the gas into either cylinder, as well as compressing and expanding the gas [23]. Despite the disadvantage of more seals, it is usually considered due to the ability to more easily couple engines together to increase the power density [23]. A schematic of the alpha engine is shown in Figure 1-14.
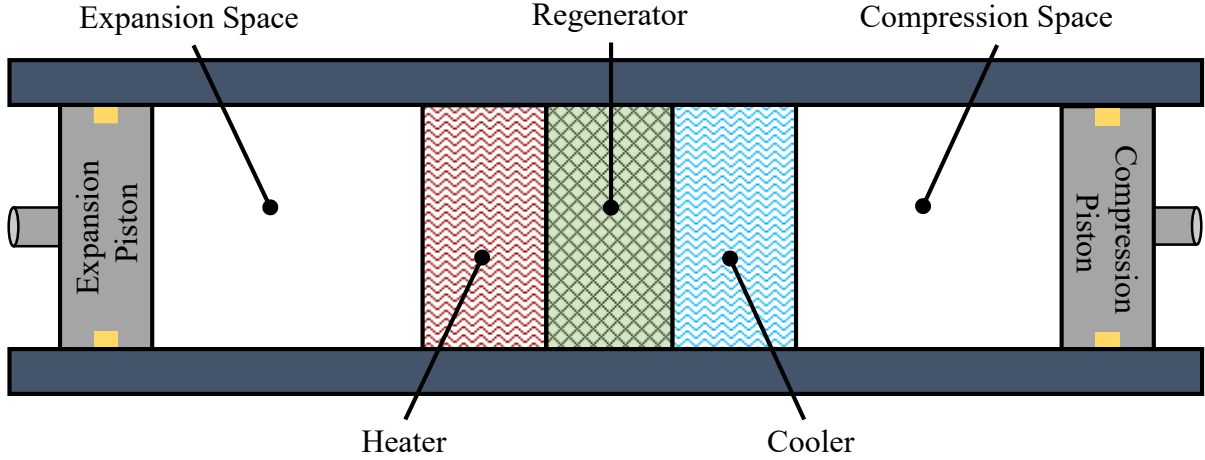
Figure 1-14: Schematic of a Practical Alpha Engine

1.5.2 Beta Stirling Engines

Beta Stirling engines, unlike alpha Stirling engines, have one power piston and one displacer piston, which perform separate functions. The displacer is what shuttles the gas in the engine, and the power piston is what changes the volume of the engine, hence performing the expansion and compression portions of the cycle [23]. Beta engines are unique in that the power

15

piston and displacer piston share the same cylinder. They also have the advantage of being able to have larger compression ratios than the gamma engines [23]. A schematic of the beta engine is shown in Figure 1-15.
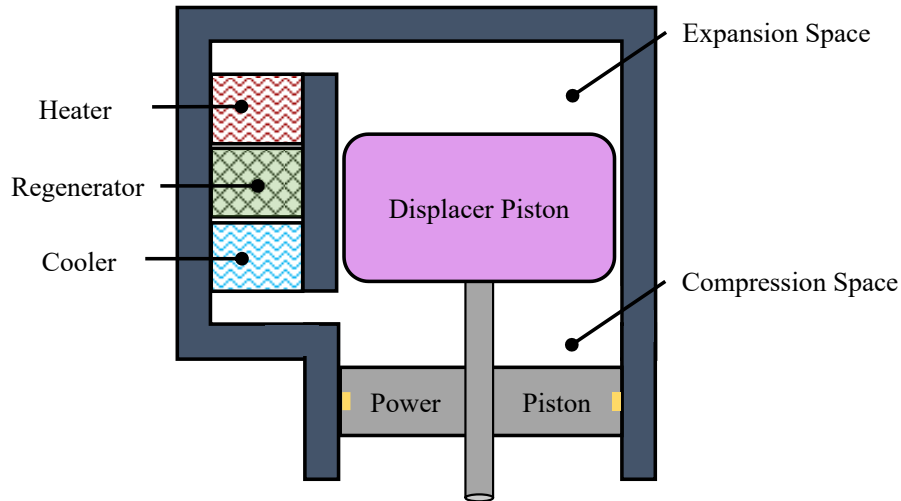
Figure 1-15: Schematic of a Practical Beta Engine

1.5.3 Gamma Stirling Engines

Gamma Stirling engines are more similar to beta engines, as they also contain separate displacer and power pistons; however, they are different in that there are in separate cylinders for the power piston and displacer piston [23]. This design has also been proven to work in many LTD Stirling applications such as using a hot cup of water as a thermal source and ambient temperature as a thermal sink. A schematic of the gamma engine is shown in Figure 1-16.
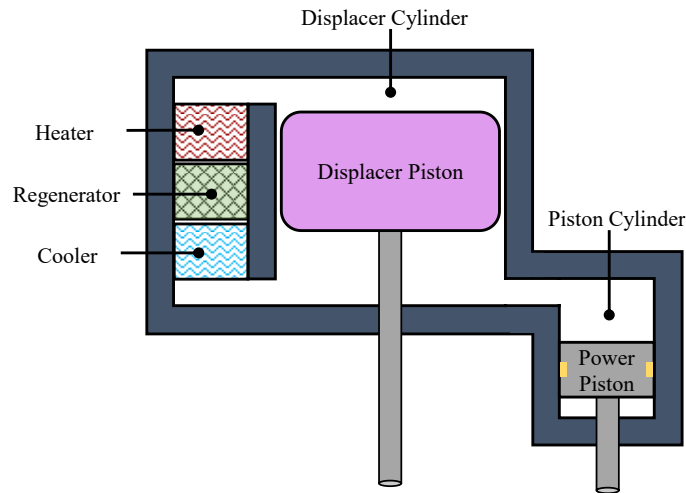
Figure 1-16: Schematic of a Practical Gamma Engine

1.6   Alpha Stirling Engine Components

The basic components of the alpha Stirling engine has already been discussed for an idealized engine. This section will provide a more detailed discussion on the individual components for practical kinematic alpha Stirling engines.

1.6.1   Expansion and Compression Spaces

The expansion space in an alpha-type Stirling engine is the cylinder that contains the expansion piston and is connected to the heater. The working fluid in this space is heated, and during the expansion process, the majority of the working fluid is in this space [23]. Conversely, the compression space contains the majority of the working fluid during the compression process [23]. The compression space is the cylinder connected to the cooler, and it contains the compression piston. The workspaces do not have perfect heat transfer, and are therefore not used intentionally in the heat transfer process.

1.6.2   Heat Exchangers

Dedicated heat exchangers are required in a practical Stirling engine to heat and cool the working fluid. As the fluid passes through the heater, heat is transferred from the thermal source to the working fluid, increasing the temperature and pressure. As it passes through the cooler, heat is transferred from the working fluid to the thermal sink, cooling the fluid and reducing the pressure. One of the assumptions of the ideal Stirling cycle was that the expansion and compression spaces were isothermal, when in practicality they are more closely approximated as being adiabatic [21], [20]. The design of the heat exchangers is a balance between maximizing surface area for heat transfer, and minimizing the dead volume introduced by the heat exchanger void volume.

1.6.3   Regenerator Space

The regenerator space is located between the heater and cooler, and contains a regenerator. A regenerator acts as a thermal storage device. When hot fluid passes through, the fluid transfers heat to the matrix which pre-cools the fluid before entering the cooler; when the cold fluid passes back through the regenerator, it absorbs heat from the regenerator which pre-heats the fluid before entering the heater [21]. The regenerator is generally made of a porous matrix with a high heat

capacity to increase the efficiency of the engine by reducing the load of the heat exchangers to heat and cool the working fluid [23].

1.6.4   Expansion and Compression Pistons

In an alpha Stirling engine, both the expansion and compression pistons displace the working gas and change the engine volume simultaneously [23]. Unlike displacer type engines, both the pistons require a dynamic seal, so that the working fluid does not leak out of the engine. In addition, although both pistons shuttle and change the volume of the working fluid, it is primarily the expansion piston that is moved outward and produces work during expansion, and it is primarily the compression piston that moves inward and must have work done upon it to compress the working fluid during compression [23]. The pistons displace the working fluid throughout the cycle, but the pistons must be out of phase with one another to induce a volume change. The volume variation in the expansion space must lead the volume variation in the compression space for the Stirling cycle to function as an engine [28].

1.6.5   Mechanism

In a practical Stirling engine, to induce a volume change a kinematic mechanism is required. There exist free-piston Stirling engines that do not rely on a kinematic mechanism, but rather the gas or spring forces in the engine [28]. This thesis will focus on kinematic Stirling engines.

The possible choice in mechanisms are numerous and varied, such as Ross-yokes [29], Scotch-yokes, slider-cranks, and swash-plates [30] as examples. The purpose of the mechanism is to constrain the volume variations, maintain a phase angle, and transmit work into and out of the engine.

1.7   Advances in the Literature

The literature pertaining to the research and development of Stirling engines is vast, and has gained some renewed interest for many applications in renewable energy generation and conversion of waste heat to electricity. The focus of the literature review performed was for alpha-type Stirling engines, as that is the configuration being investigated. Literature pertaining to broader LTD Stirling engine studies were referred to as well.

1.7.1   High Temperature Alpha Stirling Engines

Within the literature, many alpha Stirling engines were used in high source temperature applications. These designs provide an experimental insight into the operation of alpha-type Stirling engines, despite their source temperatures. This section will present some high temperature alpha engines used in experiment systems to illustrate the common design choices for these source temperatures.

Kagawa [31] experimented on a 3 kW alpha Stirling engine in a V-configuration, using helium as the working fluid with a gas temperature difference of 379 °C, engine pressures between 3 to 6 MPa, and a phase angle of 100°. The reported thermal efficiency was 31.1% and the mechanical efficiency was 78.9%.

Çinar et al. [32] manufactured a 90° oriented cylinder alpha-type engine that was pressurized between 0.1 MPa to 0.4 MPa with either air or helium as the working fluid. The engine was made to test high thermal source temperature between 800 °C and 1,000 °C. The engine produced 30.7 W at 437 rpm with helium and a phase angle of 90°.

Karabulut et al. [33] also manufactured and tested a high temperature 90° oriented alpha engine, with a thermal source in the range of 600 °C to 1,100 °C at elevated charge pressures using air. The maximum power of this engine was 65 W at 0.25 MPa of pressure and a phase angle of 90°.

Matsuguchi and Kagawa [34] tested a 1 kW alpha Stirling engine (JA-15200-X) in a V-configuration for determining the optimal regenerator type with a heater temperature of 650 °C and a phase angle of 90° using helium as the working fluid at 2 MPa.

From these engines, it can be seen that the optimal configurations yield anywhere from below 100 W to a few kW of shaft power, and it was a common practice at high temperatures to select a phase angle near 90°. Furthermore, the majority of the engines used helium as the working fluid at high charge pressures to increase the amount of power from their systems.

1.7.2   Low Temperature Difference Alpha Stirling Engines

There were very few experimental studies on LTD alpha-type Stirling engines found in the literature, and the definition of "low temperature difference" varied significantly. This section will focus on experiment systems that incorporated alpha-type Stirling engines with temperature differences below 200 °C.

Toda and Matsubara [35] developed an alpha-type Stirling engine with a gas temperature difference of approximately 77 °C using nitrogen as the working fluid. The engine utilized a yoke-type mechanism with 400 mm diameter pistons, 160 mm stroke lengths, and a 150° phase angle. The engine internal pressure was not specified, but the buffer space pressure was as high as 0.8 MPa. At a buffer pressure of 0.5 MPa, the maximum shaft power was reported to be approximately 506 W at a speed of 176 rpm.

Tveit et al. [36] designed a prototype alpha Stirling engine for low temperature waste heat recovery from steam with a temperature of approximately 180 °C. The purpose of the engine was to test different parameters to find the optimal values for the operating conditions. The engine was to use pressurized helium at 6 MPa, where the stroke could be changed to allow for a swept volume between 1.6 L to 2.7 L and phase angles between 127° to 163° in 6° increments. The results from testing system have not been found in the literature.

From these designs, it appears that high internal gas pressures, working fluids other than air, and higher phase angles were common design features for LTD alpha Stirling engines.

1.7.3   Parameter Optimization

The majority of the work on parameter optimization was done using numerical methods and simulations. The parameters that were often optimized were phase angle, engine frequency, dead volume, and compression ratio; however, the majority of the numerical models presented for alpha Stirling engines studied high temperature differences [37]–[42], which are not necessarily

valid for low temperature differences. The following section presents information that has been found on low temperature difference parameter optimization, with a focus on alpha-type engines.

1.7.3.1 Phase Angle Optimization

Hoegel et al. [43] utilized a commercial Stirling engine simulation software, Sage (Sage, Gedeon Associates), to determine optimal parameters for a double-acting alpha Stirling engine with source temperature of 150 °C with a 5 MPa mean pressure. The optimal phase angle from the simulation was between 30° and 45° in a Siemens arrangement. The working fluid was varied between hydrogen, helium, and nitrogen, where hydrogen produced the most amount of power, and helium produced twice as much as nitrogen. In 2014, Hoegel et al. [44] performed another simulation for single-acting alpha Stirling engines using helium as the working fluid, with a thermal source of 150 °C or 750 °C and a thermal sink of 40 °C. The phase angle and frequency were varied to optimize the power output, where at 150 °C a phase angle of 160° was optimal, and at 750 °C a phase angle of 120° was optimal. For frequency, the optimum was 25 Hz at 150 °C and 100 Hz at 750 °C. The study also showed a porosity above 0.85 for the regenerator was best for the 160° phase angle at 150 °C. The simulation did not consider mechanical losses.

1.7.3.2 Dead Volume Distribution

When designing a Stirling engine, it is common practice to minimize dead volume, as it can have adverse effects on the temperature of the working gas that reduce the engine pressure fluctuations [19]. Nevertheless, there has been some research into how to best distribute the dead volume present in the engine. Bauwens [45] determined through an adiabatic Stirling engine model that distributing the dead volume to the compression space and minimizing it in the expansion space increases the coefficient of performance of a Stirling refrigerator using helium.

Gschwendtner and Bell [46] utilized a 3rd order Sage simulation to determine if the dead volume outside of the heat exchangers or regenerator would be beneficial to power and efficiency of an opposed alpha-type Stirling engine. The simulation had a thermal sink temperature of 20 °C and a variable source temperature of 100 °C, 400 °C, or 700 °C and a phase angle of 90°. Although the amount of "optimized" dead volume was not stated, nor where it was distributed, they found that the inclusion of dead volume would marginally increase power output and would have a more significant effect on increasing the thermal efficiency, especially at lower source temperatures.

1.7.3.3 Compression Ratio

Egas and Clucas [47] presented a relation for the "ideal" compression ratio, CR_{ideal}, for LTD engines being equal to the temperature ratio defined as the ratio of the thermal source temperature , T_{source}, over the thermal sink temperature, T_{sink}, shown in:

$$CR_{ideal} = \frac{T_{source}}{T_{sink}}$$

1-9

Equation 1-9 is not necessarily an optimal value, as it uses ideal Stirling cycle equations without losses in the formulation, but rather an upper limit for the compression ratio. Egas came to the conclusion that gamma-type Stirling engines are most suited for LTD applications.

Stumpf [48] designed and manufactured gamma-type Stirling engines to experimentally optimize parameters for maximum shaft power at thermal sources below 100 °C, and developed an expression to estimate the optimum compression ratio for maximum shaft power, CR_{SP}, for LTD Stirling engines using air and that have a buffer pressure equal to atmospheric pressure. The expression was developed empirically using data from similar LTD gamma-type Stirling engines. The equation was essentially the mean value between Egas' ideal compression ratio and Kolin's [49] empirical correlation compression ratio, and uses only information about the thermal source temperature, T_{source}, and sink temperature, T_{sink}, as shown in:

$$CR_{SP} = 0.624 \times \frac{T_{source}}{T_{sink}} + 0.376$$

1-10

1.7.3.4 Other Optimized Parameters

El-Ehwany et al. [50] designed a parallel cylinder alpha-type Stirling engine with several configurations of tube heat exchangers that were situated in elbow-bends. The engine parameters were optimized for each heat exchanger design using a Schmidt model and trial and error, where equal and non-equal stroke lengths were considered. Nitrogen was the working fluid and pressure of up to 4 MPa were considered. It appeared that the non-equal stroke lengths provided slightly higher predicted power than equal stroke lengths for a given heat exchanger.

Iwabuchi and Kanzaka [51] suggested that under periodically reversing flow, the heat transfer coefficients may be influenced by the piston phase angle. He tested phase angles of 90°

and 180° and suggested that the heat transfer coefficient for 180° was higher, and that for reversing flow conditions it is also higher than steady flow conditions for both phase angles tested.

Homutescu and Balanescu [52] researched the optimum diameter ratio for the expansion and compression piston for maximum work using the isothermal model and adiabatic model with losses for an alpha-type Stirling engine with a temperature difference of 190 °C and hydrogen as the working fluid, and determined that a value between 1 and 1.1 was optimal.

1.7.3.5   Numerical Model Validation for LTD Engines

Speer [25] utilized a gamma-type Stirling engine (ST05G-CNC) and modified the piston diameter, crankcase volume, and workspace dead volume to reduce the minimum thermal source that the engine could operate at. He managed to reduce the minimum source temperature from 242 °C to 145 °C by reducing the piston diameter and increasing the crankcase volume. The results were then compared to a first order isothermal numerical model and a second order adiabatic model, and found that the models overestimated the performance of the engine at low source temperatures.

Miller [26] performed experiments on the same engine as Speer (a modified ST05G-CNC) to compare experimental measurements with a second order adiabatic numerical model. Several source temperatures between 242°C and 418 °C were tested and compared to the model, which showed that the model inaccurately predicted performance, but more so for reduced source temperatures. Miller also investigated the effect of flywheel size and found that an increased polar moment of inertia increased the engine speed settling time and decreased the overshoot during the transient period, and decreased the speed fluctuations during steady-state operation.

1.8 Thesis Objectives and Structure

The goal of the research project that this thesis contributes towards was to experimentally determine the optimum configuration for a LTD Stirling engine operating with a thermal source temperature below 100 °C. For this thesis, thorough research into the viability of an alpha-type Stirling engine at low thermal source temperatures was performed. The specific research objectives to be addressed are as follows:

1. Investigate the viability and evaluate the performance of a lab scale alpha-type Stirling engine with a thermal source temperature below 100 °C and a thermal sink temperature above 0 °C that can rotate a crankshaft on its own accord.

2. Experimentally determine which configuration of stroke length and phase angle would produce the maximum shaft power for an alpha-type Stirling engine using air as the working fluid, a mean pressure close to atmospheric pressure, and a temperature difference no greater than 100 °C.

3. If the manufactured engine cannot rotate the crankshaft on its own accord, evaluate different configurations of stroke length and phase angles to determine experimentally which design parameters need to be improved to increase the likelihood of a functioning low thermal source temperature alpha-type Stirling engine by driving the engine.

Chapter 2 will introduce some of the first order numerical models from the literature which were used to predict the performance early in the design cycle and understand the effect of changing the operating parameters of the prototype Stirling engine. It will then introduce a model from the literature used for understanding the energy transfer through the mechanism and estimate the shaft work and the effectiveness of the mechanism.

Chapter 3 will provide the design objective and constraints for the prototype engine, and provide information about the 3D printing technology that was leveraged to manufacture complex components for the engine. The three prototypes of the opposed piston alpha engine will be presented, along with an in-depth description of their design and properties. The issues of each iteration, as well as the insights learned and improvements implemented into future iterations will be discussed.

Chapter 4 will explain the experiment setup, including the instrumentation and data acquisition devices used. The procedure for calibrating the instruments will then be discussed. An experiment plan and procedure will be established, listing the number of tests and which variables were manipulated, controlled, or responding. Two experiments will be performed, one while driving the engine with a motor with an inactive thermal source and sink, and one with an active thermal source and sink. Some of the techniques used for data processing will be explained, along with expressions for important variables in the results. Finally, an uncertainty analysis will be performed, and the uncertainty of the instruments and output variables will be provided.

Chapter 5 will discuss the results obtained from the experiment, and provide an insight into the workings of the engine. The results for the experiment with an inactive thermal source and sink will first be discussed, followed by the experiment where the engine was heated and cooled. Then a comparison between the results will be made to provide an insight into the engine performance.

Chapter 6 will provide conclusions about the experiment, as well as recommend future work to be performed.

Chapter 2   Stirling Engine Modeling

For Stirling engine analysis, there exist various numerical models to analyze and predict thermodynamic performance. Within the field, the models are generally referred to as first order, second order, or third order [24]. A first order model is one that considers no losses in the system, and may or may not have a closed form solution [24]. A second order model starts with a first order model, but calculates decoupled losses to subtract from the first order results [24]. A third order model solves differential conservation equations of an engine that is broken up into cells or nodes, where the losses are not decoupled like in the second order model [24]. Basic first order models were used in the initial design process to understand the effect of changing parameters. This section will provide an overview of the basic isothermal thermodynamic model used (from the works of Urieli and Berchowitz [20]), and will then present a model used to understand the energy transfer throughout a Stirling engine (from the collection of works of Senft [53]).

2.1   Isothermal Model

The isothermal model is a first order model that is built upon the approximation that the temperature of the working fluid in the expansion space is at the same constant temperature as the heater, and the temperature of the working fluid in the compression space is at the same constant temperature as the cooler [20]. The benefit of this model is the relatively straight forward manner in which an expression for the working fluid pressure as a function of volume can be obtained [20]. In addition, different drive mechanisms can be utilized in the model if an expression for the volume variations as a function of crank angle is known. The assumptions for the model are as follows [20]:

- The engine does not leak, so the working fluid mass is constant.
- The working fluid is an ideal gas.
- The engine has a constant angular velocity.
- The kinetic and potential energy of the working fluid are negligible.
- The expansion and compression spaces are isothermal.
- There are no thermal losses in the heater, cooler, and regenerator.
- There are no frictional losses or pressure drops in the system.
- The regenerator is assumed to have a linear temperature distribution.

A schematic adapted from Urieli and Berchowitz [20] is shown in Figure 2-1, where an opposed piston alpha-type Stirling engine is broken into five regions: the compression space, cooler, regenerator, heater, and expansion space with corresponding subscripts c, k, r, h, and e.
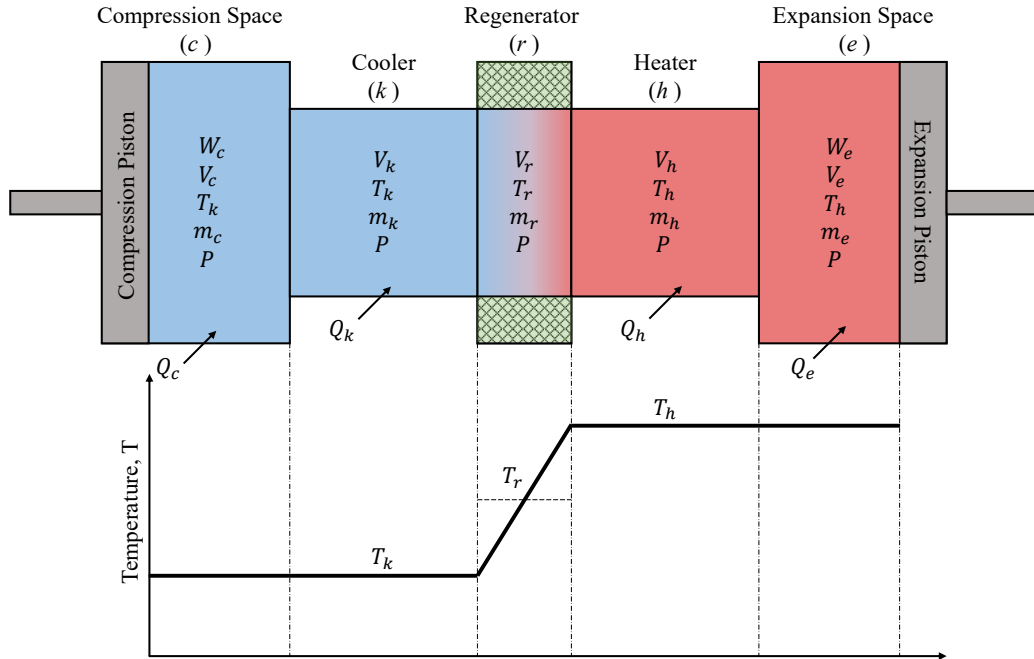
Figure 2-1: Schematic of the Isothermal Model (Adapted from Urieli and Berchowitz)

From the schematic, the isothermal conditions in the expansion and compression space can be visualized, where the compression space is at the temperature of the cooler, T_k, and the expansion space is at the temperature of the heater, T_h. The end of the regenerator in contact with the cooler is also at temperature T_k, and the end in contact with the heater is at T_h. The temperature distribution is assumed to be linear throughout the regenerator.

The formulation of the equations for this model are presented in the works of Urieli and Berchowitz [20], and an overview will be presented here. The model relies on the knowledge of the total mass of the working fluid in the engine, m_{total}, which can be calculated by knowing the charge pressure of the engine. The mass is assumed to be distributed into each of the five sections as shown in Figure 2-1 and described by Equation 2-1, where the mass in each section is represented by m.

$$m_{total} = m_c + m_k + m_r + m_h + m_e \qquad \text{2-1}$$

Applying the ideal gas law to Equation 2-1 and rearranging yields the expression in Equation 2-2, where P is the engine pressure, V is the volume of each section, R is the gas constant, and T is the temperature in each section.

$$P(\theta) = m_{total} \times R \times \left[\frac{V_c(\theta)}{T_k} + \frac{V_k}{T_k} + \frac{V_r \cdot \ln\left(\frac{T_h}{T_k}\right)}{T_h - T_k} + \frac{V_h}{T_h} + \frac{V_e(\theta)}{T_h} \right]^{-1} \qquad \text{2-2}$$

The indicated work is equal to the sum of the work done by the expansion space and compression space over a cycle, as shown:

$$W_{ind} = W_c + W_e = \oint P(\theta) \left(\frac{dV_c}{d\theta} + \frac{dV_e}{d\theta} \right) d\theta \qquad \text{2-3}$$

With the assumptions that the cycle has reached steady state, and the mass in the system remains the same, performing an energy balance on a control volume around the expansion space results in the heat transferred to the expansion space, Q_e, being equal to the work produced by the expansion space, W_e, as summarized in Equation 2-4. Performing a similar analysis on the compression space shows that the heat transferred out of the compression space, Q_c, is equal to the work done on the compression space, W_c, as summarized in Equation 2-5. Since the heat exchangers do not perform work and the workspaces are assumed to have heat transfer losses in this model, the heat exchangers have no effect on heat transfer in the system.

$$Q_e = W_e \qquad \text{2-4}$$

$$Q_c = W_c \qquad \text{2-5}$$

2.2   Model for Energy Transfer in Cyclic Heat Engines

Senft [22] developed a mechanical model, which provided a limit on mechanical efficiency for all kinematic engines. The theory presented the flow of energy transfer throughout a cycle, and the effect that the mechanism friction and the pressure on the backside of the piston (buffer pressure) had on reducing the shaft work of the engine [22]. The amount by which the indicated work is reduced depends on how the work is transferred through the components of the engine, which in practice depends on the specific engine geometry. This model was established primarily for single workspace and single acting engines [22], [53]; however, the analysis was generalized enough to extend it to alpha-type Stirling engines. This section will summarize the pertinent aspects of the model.

2.2.1   Buffer Pressure Effects

The buffer pressure is the pressure that acts on the backside of the piston, and may be considered constant or variable [53]. Constant buffer space engines are normally exposed to atmosphere. Variable buffer space engines are those that have an enclosed space behind the piston, where the piston motion would change the volume and pressure in the buffer space [22]. The buffer space acts as an energy reservoir much like a flywheel, but since it acts directly on the piston, the energy transfer path is essentially lossless for large buffer spaces such as the atmosphere [22]. For a finite buffer space, losses may be present which would reduce the indicated work before it is transferred to the mechanism.

2.2.2   Efficacious and Forced Work

Senft [53] established additional definitions termed efficacious work, W_{eff}, and forced work, W_f. Efficacious work is the work transmitted from the piston to the mechanism. Contrarily, forced work is work transmitted from the mechanism to the piston, so that it can move in opposition to the pressure difference across it [53]. Efficacious and forced work are illustrated schematically for the expansion and compression processes in Figure 2-2.
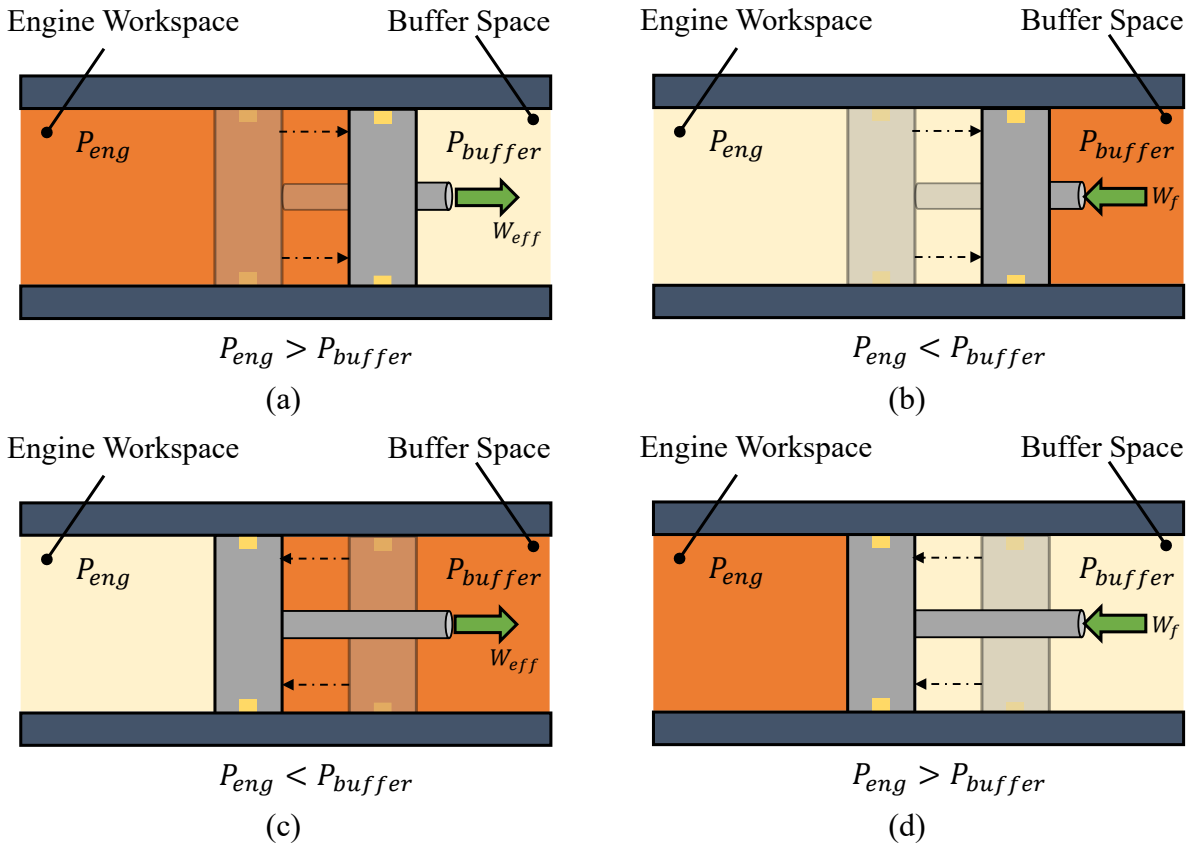
Figure 2-2: Schematic Representations of Expansion Process (a) Efficacious Work and (b) Forced work, and Compression Process (c) Efficacious Work and (d) Forced work
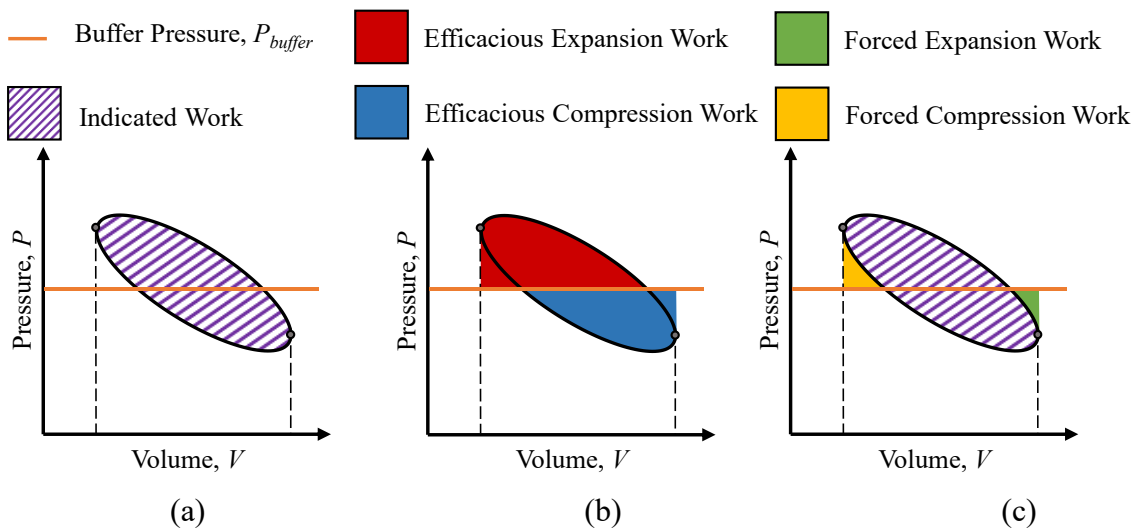
Figure 2-3: Schematic Illustrating the Locations of (a) Indicated Work (b) Efficacious Work and (c) Forced Work for a Generic Buffer Pressure and Indicator Diagram

A schematic of the areas of efficacious and forced work on an indicator diagram are shown in Figure 2-3, which was adapted from a figure created by Stumpf [48]. The efficacious expansion work occurs when the engine pressure is above the buffer pressure during expansion. Efficacious compression work occurs when the engine pressure is below the buffer pressure during compression. During both these portions of the cycle, the piston will move with the pressure difference, not requiring work input. The expansion forced work occurs when the engine pressure is below the buffer pressure during expansion, so the piston would have to move against this pressure difference, which would require a work input. Likewise, compression forced work occurs when the engine pressure is above the buffer pressure during compression, which would be more difficult to compress and require additional work input.

If the buffer pressure is assumed constant, the indicated work is equal to the difference in efficacious work and forced work as shown [53]:

$$W_{ind} = W_e - W_c = W_{eff} - W_f \qquad\qquad 2\text{-}6$$

The choice of buffer pressure can directly influence the amount of efficacious and forced work in the cycle. As the buffer pressure line is changed, the area between the buffer pressure line and the compression or expansion process curve is changed as well. Figure 2-4 demonstrates three scenarios: if the buffer pressure was less than the minimum cycle pressure, equal to the cycle pressure at the maximum engine volume, and equal to the cycle pressure at the minimum engine volume. Figure 2-4(a) shows that there would be efficacious expansion work and forced compression work only. Figure 2-4(b) reduces the forced compression work in comparison to Figure 2-4(a), and adds efficacious compression work without adding forced expansion work. Figure 2-4(c) demonstrates the opposite, where forced expansion work is added to the system while eliminating forced compression work. The amount of efficacious expansion and compression work is reversed. There are many possible values for buffer pressure, but if atmosphere is used as the buffer space then the buffer pressure is limited to the local atmospheric pressure.
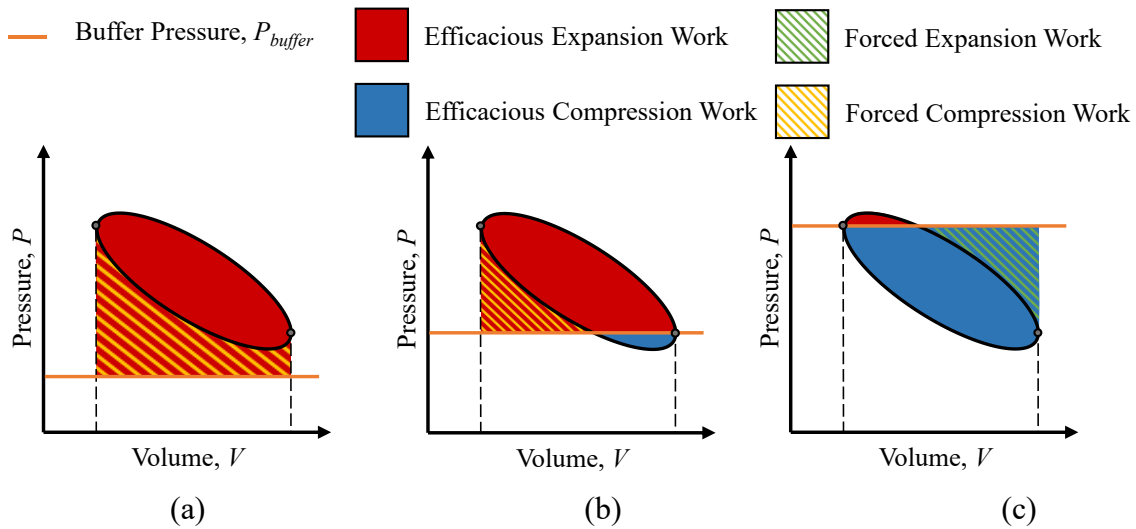
Figure 2-4: Schematic of the Effect of Buffer Pressure on the Efficacious and Forced Work Distribution for (a) Buffer Pressure Below Minimum Cycle Pressure (b) Buffer Pressure Crossing Point of Maximum Volume and (c) Buffer Pressure Crossing Point of Minimum Volume

2.2.3 Shaft Work

The indicated work must be transmitted to an output shaft to be utilized as shaft work, which requires a mechanism. As work is transferred to the flywheel for storage, the mechanism causes frictional losses that reduce the efficacious work to a value, W_{out}, which becomes the work out of the system reduced by friction [53]. Contrarily, when the cycle requires work input from the flywheel, the work input, W_{in}, must be larger than the forced work required, because it will be reduced by friction [53]. The actual shaft work out of the engine, W_s, is the difference between the work output of the system and the work input to the system, shown in Equation 2-7. If the work output is greater than the work input, the engine will function; if the opposite is true, the engine will not function.

$$W_s = W_{out} - W_{in} \qquad\qquad 2\text{-}7$$

Senft [53] introduced a parameter to describe how effective a mechanism is at transferring work across it, called the mechanism effectiveness, E. The mechanism effectiveness is defined as the ratio of the actual torque applied to the shaft to the ideal torque if no friction were present, and has a value between 0 and 1. Equations for the work output and work input for the system can be

expressed as functions of the efficacious work, forced work, and mechanism effectiveness as shown in Equations 2-8 and 2-9.

$$W_{out} = E \times W_{eff} \qquad \text{2-8}$$

$$W_{in} = \frac{1}{E} \times W_f \qquad \text{2-9}$$

2.2.4 Fundamental Efficiency Theorem

The mechanical efficiency of a heat engine, η_m, is defined as the ratio of shaft work to indicated work as shown [53]:

$$\eta_m = \frac{W_s}{W_{ind}} \qquad \text{2-10}$$

Senft [53] then derived an expression to estimate the upper bound on mechanical efficiency, called the Fundamental Efficiency Theorem, defined as:

$$\eta_m \leq E - \left(\frac{1}{E} - E\right) \times \frac{W_f}{W_{ind}} \qquad \text{2-11}$$

By assuming a constant mechanism effectiveness, the inequality in Equation 2-11 becomes an equality, and the equation can be used to estimate the shaft work of the engine by substituting Equation 2-10 into Equation 2-11, as shown in Equation 2-12 [53]. The indicated work is reduced by the mechanism effectiveness, and the more forced work there is in the cycle, the more the shaft work is reduced.

$$W_s = E \times W_{ind} - \left(\frac{1}{E} - E\right) \times W_f \qquad \text{2-12}$$

Usually the mechanism effectiveness is unknown, and an estimate can be used to calculate the approximate shaft work expected using knowledge of the indicated and forced work present in the system; however, if the shaft work is measured, the mechanism effectiveness can be calculated by rearranging Equation 2-12.

2.2.5 Extension to Alpha-Type Engines

The previous analysis has been done with displacer type engines in mind; however, the analysis can still be extended to dual workspace engines, such as the alpha Stirling engine, with some modifications. For alpha Stirling engines, both the expansion and compression spaces contribute efficacious and forced work because there are two pistons with pressure differences across them, which are subject to losses from the mechanism. Figure 2-5 shows a schematic of how work is transmitted through an alpha-type engine with opposed pistons.
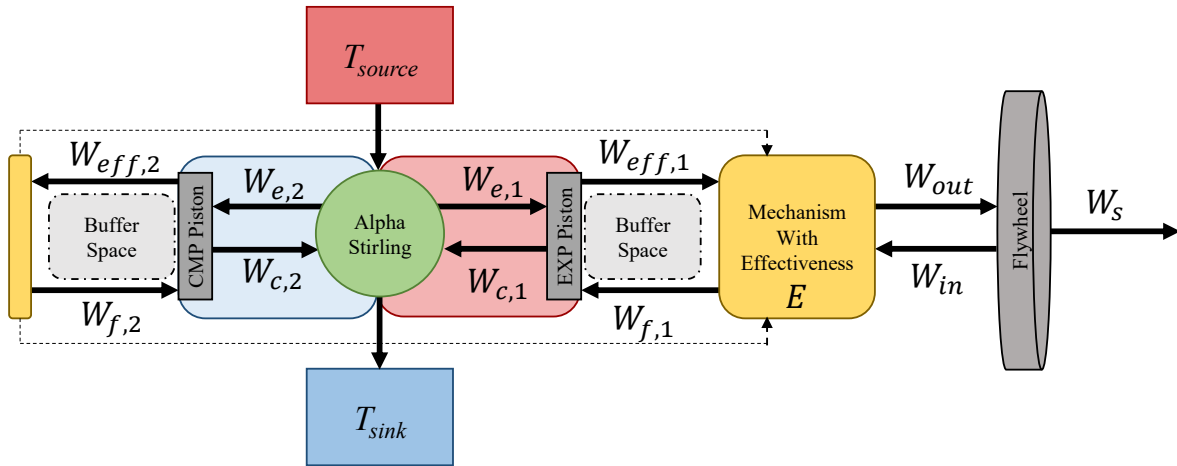
Figure 2-5: Schematic of the Work Transmission in an Opposed Piston Alpha-Type Stirling Engine

The compression and expansion spaces both undergo a volume change to form their respective workspace indicator diagrams. Depending on the buffer space pressure, efficacious work and forced work are present in each workspace indicator diagram. If the buffer pressure is assumed constant, Equation 2-6 holds, and the total efficacious work is the summation of the expansion space efficacious work, $W_{eff,1}$, and the compression space efficacious work, $W_{eff,2}$, shown in Equation 2-13. Likewise, the total forced work is the summation of the expansion space forced work, $W_{f,1}$, and the compression space forced work, $W_{f,2}$, shown in Equation 2-14. Substituting back into Equation 2-6 yields Equation 2-15.

$$W_{eff} = W_{eff,1} + W_{eff,2} \qquad \text{2-13}$$

$$W_f = W_{f,1} + W_{f,2} \qquad \text{2-14}$$

$$W_{ind} = \left(W_{eff,1} + W_{eff,2}\right) - \left(W_{f,1} + W_{f,2}\right) \qquad \text{2-15}$$

The mechanism reduces each efficacious work component, and increases the amount of work required to overcome forced work. Assuming that the mechanism effectiveness is the same for the expansion and compression spaces, substituting the above equations into Equation 2-12, yields the fundamental efficiency theorem for dual work space engines, defined as:

$$W_s = E\left(W_{eff,1} + W_{eff,2}\right) - \frac{1}{E}\left(W_{f,1} + W_{f,2}\right) \qquad \text{2-16}$$

If the shaft work is measured, rearranging Equation 2-16, and solving the quadratic yields a solution to the assumed constant mechanism effectiveness, as shown:

$$E = \frac{W_s \pm \sqrt{W_s^2 + 4\left(W_{eff,1}\right)\left(W_{f,1} + W_{f,2}\right) + 4\left(W_{eff,2}\right)\left(W_{f,1} + W_{f,2}\right)}}{2\left(W_{eff,1} + W_{eff,2}\right)} \qquad \text{2-17}$$

Senft [54] did demonstrate that for dual workspace engines, that even with a mechanism effectiveness of 0.9, the mechanical efficiency of the engine would not be able to exceed 73%. Cheng and Yang [55] utilized a numerical model to optimize geometric parameters for maximum shaft work that considered the effects of forced work and mechanism effectiveness for alpha, beta, and gamma engines. The result for the alpha engine indicated that increasing the mechanism effectiveness from 0.7 to 0.8 would result in nearly double the amount of shaft work (in dimensionless form). The study also indicated that the optimal phase angle for low temperature difference alpha engines would be between 130° and 180° with a mechanism effectiveness of 0.8.

2.3   Chapter 2 Summary

This chapter presented overviews of the isothermal model and the model used for energy transfer in cyclic heat engines. The models presented were used together to provide estimates of performance early in the prototype development. The heat engine energy transfer model developed by Senft was also adapted to alpha-type Stirling engines to determine the effect of the dual workspaces and pistons have on the expression of mechanism effectiveness.

Chapter 3   Engine Development

This chapter will introduce the three alpha-type Stirling engine prototypes that were designed and manufactured. The design objective and constraints will first be presented, followed by a brief introduction into the additive manufacturing technologies used to create the complex components of the engines. The prototypes will then be discussed in order of creation, where the design process and decisions will be presented, as well as the outcomes after the engines were built.

3.1   Design Objective

The objective of designing a LTD alpha-type Stirling engine was to manufacture an engine that could be used as a test system to satisfy the goals of this thesis. Specifically, to be able to experimentally determine which stroke length and phase angles were best suited for maximum shaft power for an LTD alpha-type Stirling engine. In addition, the test engine did not necessarily need to produce a net positive amount of power to be deemed successful; however, all effort was made to design and build an engine that would turn a crankshaft without external input.

3.2   Design Constraints and Criteria

At the start of the project, it was established that the alpha Stirling engine design needed to satisfy a number of design constraints. There were six major constraints, as well as some other design decisions chosen early in the project that were perpetuated in all the alpha Stirling engine designs. The six major constraints are listed in Table 3-1.

Table 3-1: Stirling Engine Initial Design Constraints

Design Constraint	Constrained Value
Thermal Source Temperature	Below 100 °C
Thermal Sink Temperature	Above 0 °C
Thermal Exchange Fluid	Liquid
Engine Working Fluid	Air
Working Fluid Charge Pressure	Atmospheric Pressure
External Buffer Pressure	Atmospheric Pressure

As discussed in Chapter 1, the initial goal of the development of a low temperature alpha Stirling engine was to convert the low-grade thermal energy from local geothermal resources or waste heat in Alberta, Canada into usable mechanical energy. Many geothermal resources in

Alberta that were identified by geologists have a temperature below 100 °C [5]. Therefore, the thermal source temperature was chosen to be below 100 °C to emulate the local conditions. For the thermal sink, the temperature was chosen to be above 0 °C, since the annual average air temperature in Edmonton, Alberta, Canada was calculated to be approximately 2.6 °C according to climate normal data sampled at the Edmonton International Airport [56]. To approximate a liquid to liquid exchange of heat from geothermal brine to some other thermal exchange fluid, it was decided that a liquid that could handle the thermal source and sink temperatures should be used.

Although there are several possible working fluids for Stirling engines, such as air, nitrogen, helium, and hydrogen [14], [19], the engine working fluid was chosen to be air, as it is readily available from the surrounding atmosphere, it has no cost to acquire, sealing challenges are reduced, and it presents little to no danger compared to helium or hydrogen if there was a leak in the system. In addition, the engine was to be charged with atmospheric air, so that the buffer space of the engine would not be enclosed in a pressurized environment.

When further considering the design intent of the engine, a modular design was desired, so that components being tested could be easily replaced or improved without a complete engine redesign. The ability to change parameters, such as the piston stroke length and phase angle, was an important feature for experimentation. In addition, since the engine was to be designed for lab scale testing, it was decided that the design should incorporate the ability to couple multiple engines together to increase the power output in the event that the engine functioned.

Considering that the engine was designed for use with a low temperature source, unconventional materials and means of manufacturing were possible, such as the use of plastics and 3D printing. Therefore, where possible, plastic was used to reduce cost, although the size of the components were limited to the build volume of the 3D printers. Another benefit of manufacturing with plastic would be that it could be used for components that need to be insulated to decrease conduction losses.

3.3   3D Printing Technology

This section details the 3D printing technology, the materials used, as well as how parts were post-processed into useable components.

3.3.1   3D Printing Methods

Two additive manufacturing methods were used to create plastic components and prototypes: Fused Filament Fabrication (FFF) and Stereolithography (SLA). FFF printing is a method by which material is extruded through a heated nozzle and deposited onto a build plate, building up the part layer by layer [57]. Conversely, SLA printing directs a set of mirrors that reflect a laser to precise points in a tray of photoactive resin, and cures the resin while also building the part up layer by layer [57]. Both methods were used in the manufacturing of the alpha-type Stirling engines. The 3D printers used throughout the prototype development were several Ultimaker FFF printers (Ultimaker 2 / 2+ / 3, Ultimaker BV), as well as a Form 2 SLA printer (Form 2, Formlabs).

The FFF printers were used to manufacture the majority of the larger plastic components for the Stirling engine, since the build volume of the Ultimaker printers were larger than the SLA printer. The parts were constrained to the size of the build volumes of the printers, which are shown in Table 3-2. Moreover, the components printed on these machines were often more cost effective, and had a relatively quick printing time compared to SLA printing. This was due to the parts not being printed solid on the FFF machines, but rather with a 20 to 30 % density for the infill structure. The materials commonly used for the FFF printers were acrylonitrile butadiene styrene (ABS) and polylactic acid (PLA). ABS was used for parts that required heat resistance, as it has a glass transition temperature of approximately 108 °C [58], where it is approximately 60 °C for PLA [59]. ABS was also used for parts that required more post-processing, as it was more difficult to post-process PLA parts.

Table 3-2: 3D Printer Build Plate Dimensions

3D Printer	Length (*X*-Axis) [mm]	Width (*Y*-Axis) [mm]	Height (*Z*-Axis) [mm]	Reference
Ultimaker 2	223	223	205	[60]
Ultimaker 2+	223	223	205	[61]
Ultimaker 3	215	215	200	[62]
Form 2	145	145	175	[63]

In contrast, SLA printing was used primarily for parts that required certain mechanical properties, that required a fine resolution and dimensional accuracy, or solid parts that were required to hold pressure. The build volume of the Form 2 printer was considerably smaller than the FFF printers in the *X*- and *Y*-axes, shown in Table 3-2. To improve print speed at the expense of print quality, the layer thickness primarily used was 0.1 mm. Resins used were generally the Standard Clear, Black, or Grey resins, which have similar properties [64]. Occasionally, components would be printed in a high temperature resin or a tough resin. The high temperature resin was used for components that required to withstand high temperatures due to the increased heat deflection properties [65]. Tough resin was used if components needed greater impact resistance [66].

3.3.2   3D Printing Post-Processing

Often, the 3D printed parts had defects and needed to be post-processed for the components to be functional. Some of the issues inherent with FFF components were warping, dimensional inaccuracy, layer gaps, and the porous infill. After the print was completed, both FFF and SLA parts needed to be sanded to a smooth surface, to mitigate the dimensional inaccuracies. In addition, components inside the engine were subjected to pressurized environments and were required to hold up against pressure fluctuations. Also, they needed to be sealed so that they did not contribute to the engine dead volume. This was especially difficult since the parts often had a porous infill and gaps between layers as shown in Figure 3-1.
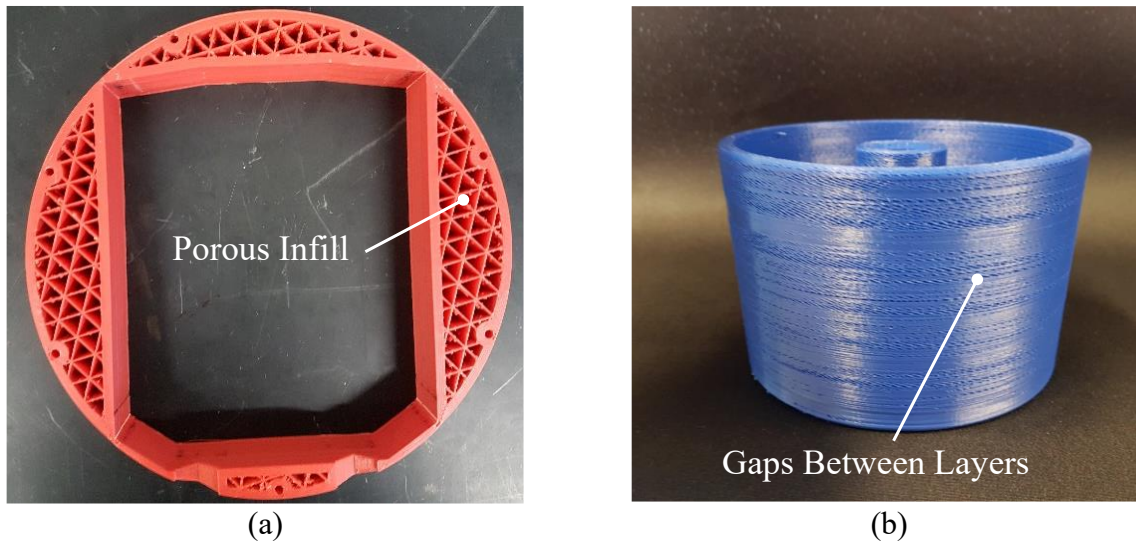
Figure 3-1: Prints Requiring Sealing Due to (a) Porous Infill and (b) Gaps Between Layers

To combat this, different methods of sealing were researched. Two of the most common methods were acetone smoothing and using epoxy coatings. Acetone smoothing was a relatively quick method for fusing the layers together, and it resulted in a glossy finish without much geometric change; however, the process often reduced the strength of the parts [67]. Conversely, epoxy coating had the benefit of increasing part strength as well as sealing effectively, but required multiple coats for sealing to be effective, and changed the dimensions of the part. Salata [68] showed that the epoxy coated samples had increased sealing performance compared to uncoated and spray painted samples, as well as an increased tensile strength. The SLA parts often only required sanding due to the imperfections that the support material left behind.

3.4   Opposed Piston Alpha: Mk I

The first prototype alpha Stirling engine was designed to be a small scale concept engine, and created as an exercise in additive manufacturing of Stirling engines. When the design of the prototype began, it was known that future iterations would be larger in scale and may require multiple engines coupled together to produce a useful amount of power from the low temperature difference. Therefore, a configuration that could be scaled and mechanically coupled was designed. This section will provide an overview of the components of the Opposed Piston Alpha (OPA) MK I, as well as the design process behind the prototype.

3.4.1 MK I Engine Components and Properties

The geometric limit for the scale of the engine was chosen such that it would be portable and fit on a benchtop. Inspiration for the design of this engine came from the abundant LTD gamma-type hobby engines available, for which there was a lack of similar products for alpha-type engines. Recent examples of small-scale 3D printed gamma-type Stirling engines that utilize thermal sources below 100 °C have been developed by Clucas and Gutschmidt [69] for educational purposes. The prototype was chosen to have opposed power pistons, as this allowed for simple geometries to be manufactured, with reduced flow losses from additional bends and tubing. The engine consisted of an expansion and compression space, a heater and cooler, a regenerator, power pistons, and a mechanism to transfer the energy to and from the flywheel. An image of the solid model showing the different components of the OPA MK I engine can be seen in Figure 3-2.
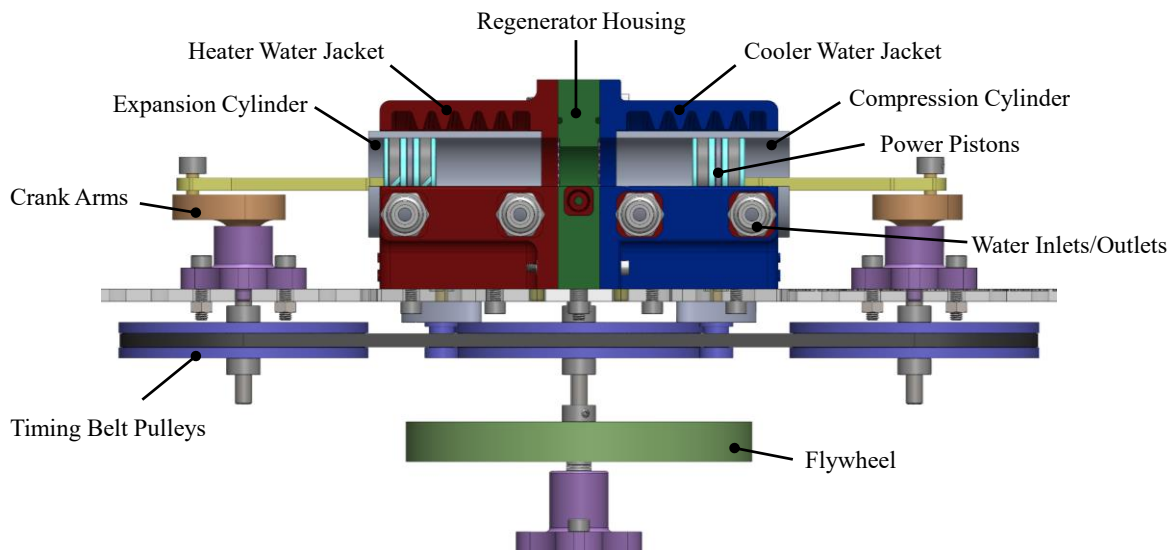
Figure 3-2: Solid Model Section View of the OPA MK I Stirling Engine

The OPA MK I was designed to be modular, so the engine body consisted of three modules: an expansion space housing, regenerator space housing, and a compression space housing. The expansion space housing consisted of the heater water jacket and expansion cylinder. Similarly, the compression space housing contained the cooler water jacket and compression cylinder. The regenerator space housing was the component that held the regenerator matrix, which was chosen to be fine gauge steel wool. Each module was 3D printed using ABS, and then acetone smoothed to ensure the layers were sealed. The modules connected together using bolts, with an O-ring sealing between each module.

41

Expansion and compression cylinders with an inner diameter of 44.45 mm and a length of 82.55 mm were chosen as a basis for the scale of the engine. Power pistons with a diameter of 44 mm were 3D printed from ABS, and utilized a greased O-ring to seal against the cylinder walls. The water jackets were designed to circulate hot and cold water between 5 °C and 95 °C. For this preliminary design, it was decided to heat and cool the cylinder walls directly, so as to minimize the size of the engine. Helical channels that led from the water inlet to the water outlet were designed, so that contact was ensured around the cylinders rather than the water following the shortest flow path. The cylinders were made from stock aluminum tubing, chosen for its increased heat conduction compared to steel tubing, and the exposed surface area within the engine was approximately 107.8 cm^2.

The mechanism for the engine consisted of a slider-crank mechanism for each power piston, connected to timing belt pulleys which would transmit work to the output shaft. A solid model representation of the mechanism can be seen in Figure 3-3. Crank arms were 3D printed out of resin, with a crank arm length of 25.4 mm, which resulted in a 50.8 mm stroke length. With 44 mm diameter power pistons and a 50.8 mm stroke length, the piston swept volume was approximately 0.137 L. The connecting rods were made from acrylic sheet, and were selected to be 103.9 mm long, 2.4 times greater than the piston diameter, to reduce the side forces.
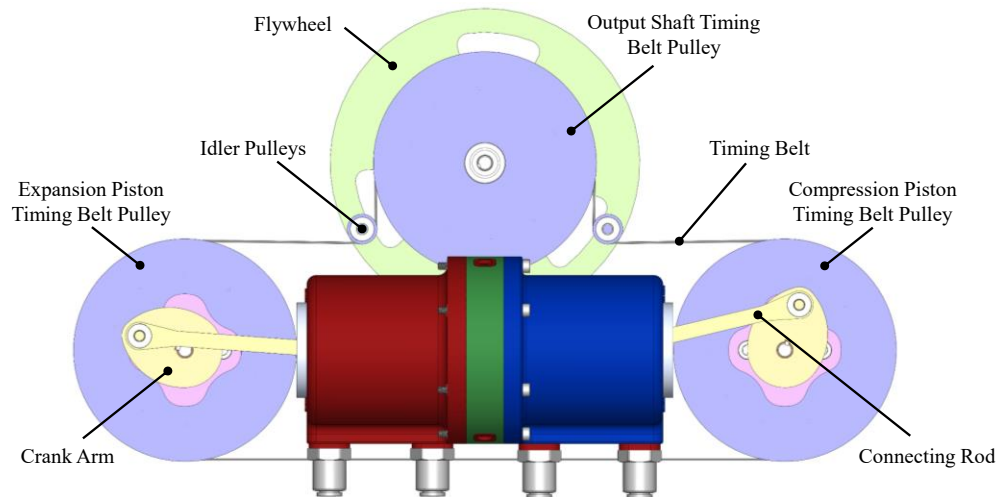
Figure 3-3: Top View of the OPA MK I Solid Model Showing the Mechanism

Each timing belt pulley had 180 teeth, so that the phase angle between the pistons could be adjusted between 0° and 360°, in 2° increments. There were three 3D printed timing belt pulleys, one connected to the expansion piston, compression piston, and output shaft. The flywheel was

connected to the output shaft, and was made from a generic 5 lb weight. An MXL sized timing belt connected each pulley, and was tensioned with idler pulleys. The timing belt length was not a standard size, so the ends of the belt had to be fastened together to create a custom timing belt. The phase angle was able to be adjusted by rotating one timing pulley relative to the other.

3.4.2 MK I Design Outcomes

Once the engine was manufactured, as shown in Figure 3-4, it was tested by circulating water at 5 °C in the cooler, and water at 95 °C in the heater, but the engine did not function. A number of issues were identified to have contributed to the engine not working, including engine leakage, timing belt construction, and insufficient heat transfer.
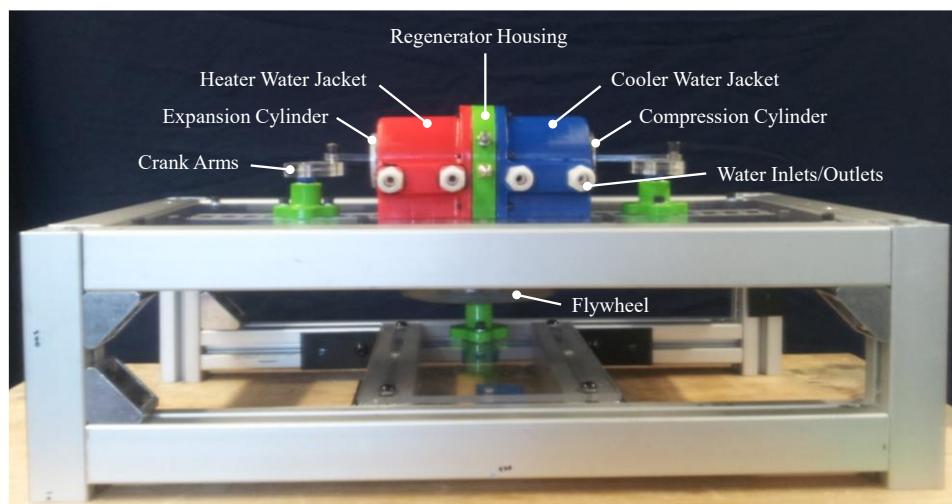
Figure 3-4: Annotated Image of the OPA MK I

Engine leakage was difficult to overcome with this design, as it occurred primarily around the piston seal. Installing the piston seal was a compromise between sealing capability and sliding friction. The greased O-ring was not an elegant solution to these opposing constraints, as it was difficult to obtain an even seal around the cylinder. Also, the leakage occurred between the modules was a result of warping in the ABS prints, which at the time of construction was not fully resolved. As mentioned, the timing belt was not a standard size, so it needed to be attached manually. Different methods were attempted such as using superglue, vulcanizing tape, and sewing the ends together. None of these methods worked long term, and the joint would fail when driving the engine since the belt teeth were not properly aligned. Relying on heat conducting through the cylinder walls was ineffective at heating the working fluid to the desired temperatures. The surface

area was relatively low, and could be improved with the use of dedicated heat exchangers. These areas were identified as key areas for improvement in the next design iteration. A table summarizing the OPA MK I properties is shown in Table 3-3.

Table 3-3: OPA MK I Engine Properties

Properties	OPA MK I
Working Fluid	Air
Piston Seal	Greased O-ring
Effective Piston Diameter	44 mm
Stroke Length	50.8 mm
Engine Swept Volume	0.274 L
Bore Diameter	44.45 mm
Phase Angle Range	0° - 360°
Phase Angle Increment	2°
Mechanism Type	Slider-Crank + MXL Timing Belts
Flywheel Construction	5 lb Weight Plate
Flywheel Moment of Inertia	Not Calculated
Regenerator Material	Steel Wool
Regenerator Dead Volume	0.055 L
Heat Exchanger Type	Cylinder Walls
Heat Exchanger Material	Aluminum
Heat Exchanger Surface Area	107.8 cm^2
Heat Exchanger Dead Volume	0 L
Thermal Source Temperature	95 °C
Thermal Sink Temperature	5 °C
Compression Space Clearance Volume	-
Expansion Space Clearance Volume	-

3.5   Opposed Piston Alpha: Mk II

The Opposed Piston Alpha MK II was designed to address the issues and problems from the initial build of the small scale OPA MK I. The major modifications were:

1. Dedicated heat exchangers were incorporated into the design.
2. Increased engine volume to increase the potential power output.
3. Redesigned piston seals to enhance sealing and reduce friction.
4. Redesigned mechanism to utilize standard components rather than custom 3D printed parts.
5. Larger Flywheel required for increased moment of inertia.

The following section will provide an overview of the OPA MK II, as well as the decisions and outcomes of the design.

3.5.1   MK II Heat Exchanger Selection

An early step in the design of the OPA MK II was to determine an alternate method for transferring the heat from the thermal source and sink that was compact, yet had a large surface area for heat transfer. A computer water-cooling radiator was determined to have the desired form factor and a high surface area for increased heat transfer. Several sizes existed for the radiators, so Michaud et al. [70], [71] performed separate experiments to test which would perform best under oscillating flow conditions. First, a brief overview of the experiment and the results pertinent to the selection of the radiator will be provided. A discussion on the implementation of the chosen radiator into the design of the OPA MK II will then follow.

3.5.1.1   Heat Exchanger Testing System

A radiator testing system was created which consisted of a flow duct, a piston and cylinder connected to a slider-crank mechanism, a hot and cold radiator, and a servo-motor for driving the piston. An annotated image of the experiment setup can be seen in Figure 3-5.
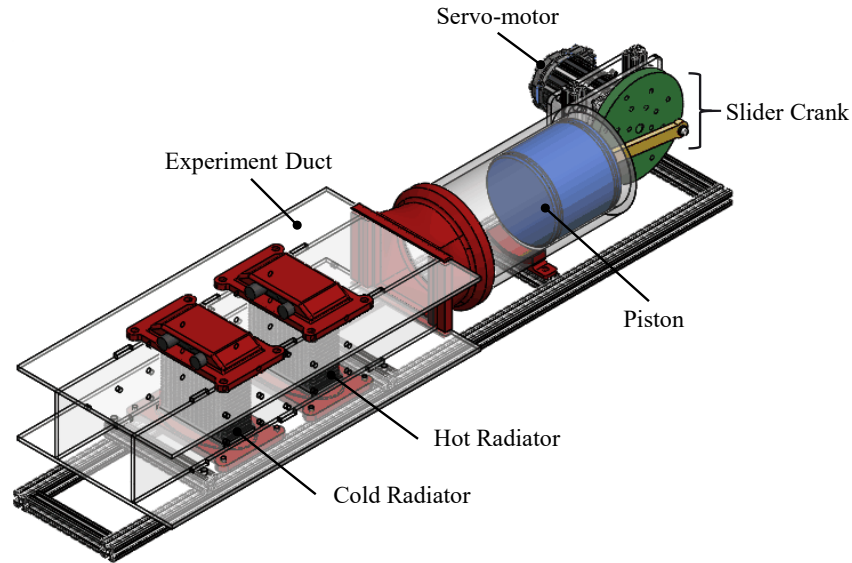
Figure 3-5: Annotated Solid Model Representation of the Radiator Testing System

The experiment consisted of an acrylic duct with a 144 mm by 113.7 mm cross section, and a length of 610 mm. One end of the duct was connected to a cylinder with 114 mm diameter piston connected to a slider-crank mechanism and servo-motor (ClearPath CPM-MCVC-3441S-RLN, Teknic Inc.) to generate oscillatory air flow at specified speeds of 50 rpm to 200 rpm in 50 rpm increments. A flexible plastic membrane was connected to the other exposed end, to contain the air, but avoid compressibility effects. The stroke length was able to be varied between 50.8 mm and 152.4 mm in 25.4 mm increments.

Three radiators with different thicknesses were tested, a 16 mm thick radiator (EK-CoolStream SE 120, EKWB), a 22 mm thick radiator (EK-CoolStream PE 120, EKWB), and a 46 mm thick radiator (EK-CoolStream SE 120, EKWB). The radiators consisted of flat tube water channels with brazed copper fins that formed triangular flow passages for air. Table 3-4 lists the radiator dimensions and approximate surface area determined from the creation of a solid model in SolidWorks.

Table 3-4: Tested Radiator Properties and Dimensions

Radiator	Width [mm]	Height [mm]	Depth [mm]	Approximate Fin Surface Area [cm^2]
XE 120	120	125	46	9319
PE 120	127	114	22	5961
SE 120	114	120	16	3511

Two radiators of the same size were inserted into the duct, and water was circulated at 60 °C in one, and at 5 °C in the other. A maximum of 60 °C was chosen so as not to go above the temperature rating of the acrylic used [72]. The radiators were 106 mm apart, and 29 exposed junction Type-T thermocouples (TJFT72, Omega Engineering Inc.) were used to measure the temperature distribution in the duct. The temperature was sampled at a rate of 50 Hz for 10 s, which was more than twice the frequency of the fastest speed tested. These measurements were averaged, because the thermocouple response time was estimated to be slower than the cycle period [73]. Figure 3-6 shows the dimensions for the locations of the thermocouples in the experiment system.

(a)   (b)
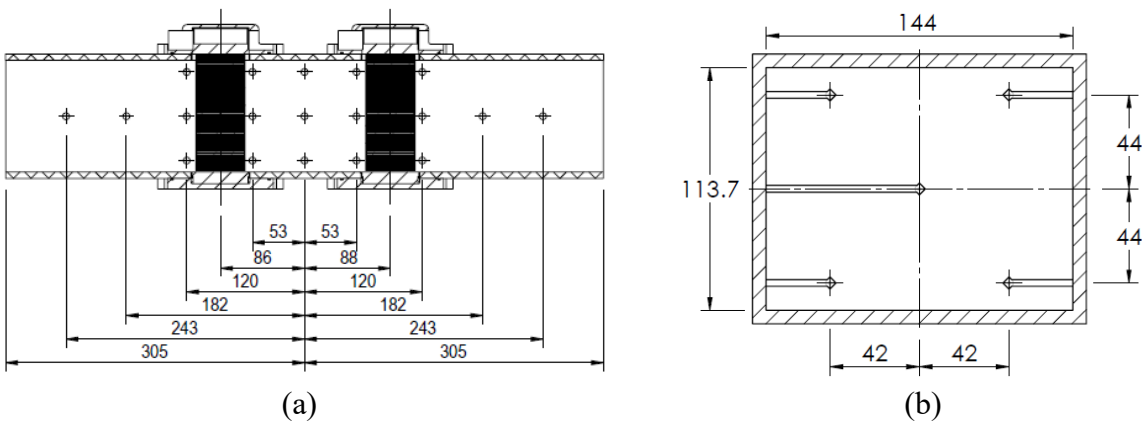
Figure 3-6: Schematic of the Thermocouple Locations for (a) the Lengthwise Dimensions and (b) the In-Plane Dimensions (Dimensions in mm)

The uncertainty in the temperature measurements were too large to distinguish exactly which radiator performed the best. Despite the inconclusive data on the radiator performance, the experiment was not without insight. The mean temperature measurements for stroke lengths of 50.8 mm, 76.2 mm, and 101.6 mm at a servo-motor speed of 50 rpm with the SE and XE radiators installed are shown in the 3D plot in Figure 3-7 and Figure 3-8 respectively.
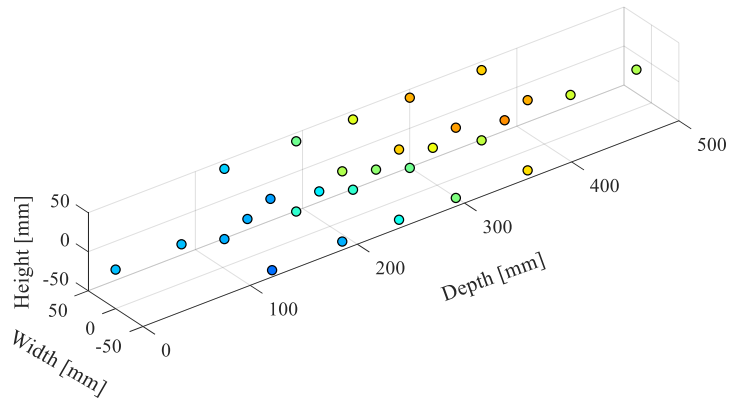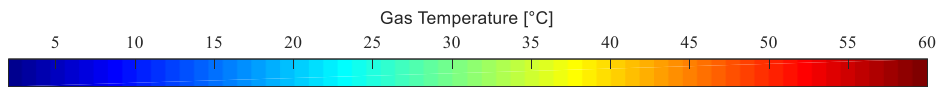
(a)
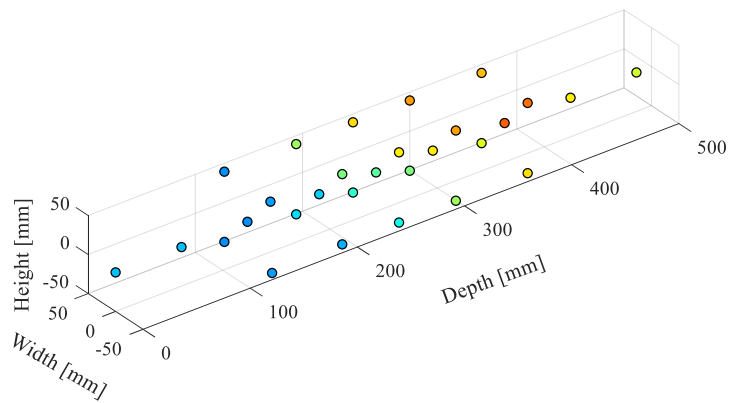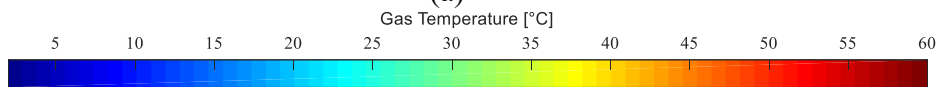
(b)
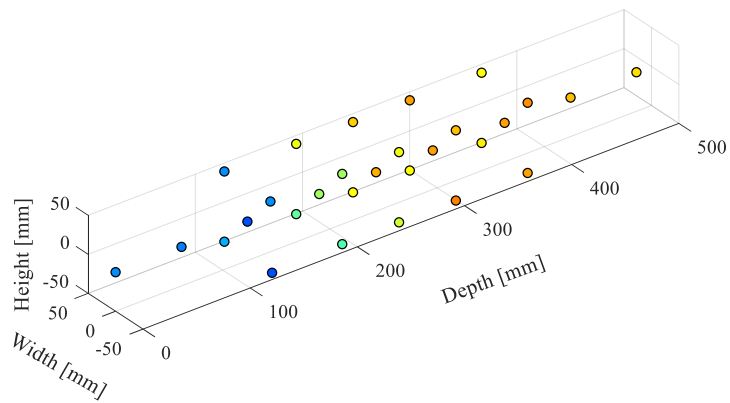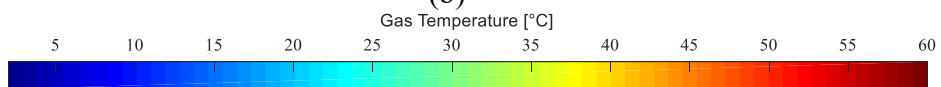
(c)

Figure 3-7:Gas Temperature Measurements with the SE Radiators Installed and Driven at 50 rpm for a Stroke Length of (a) 50.8 mm (b) 76.2 mm and (c) 101.6 mm
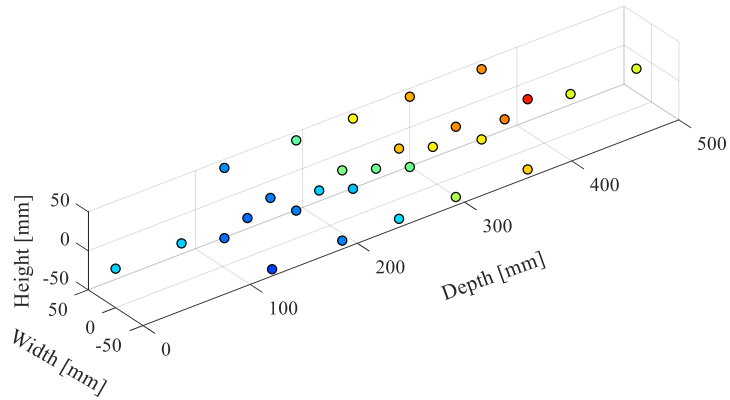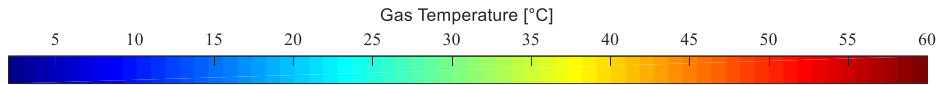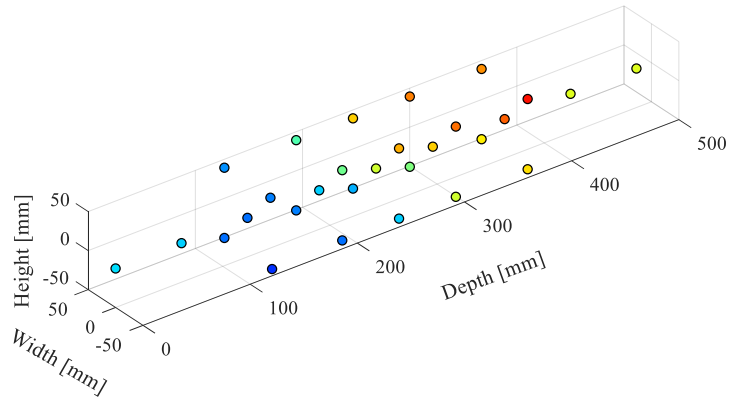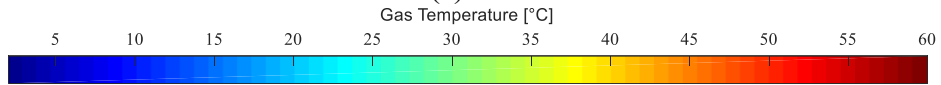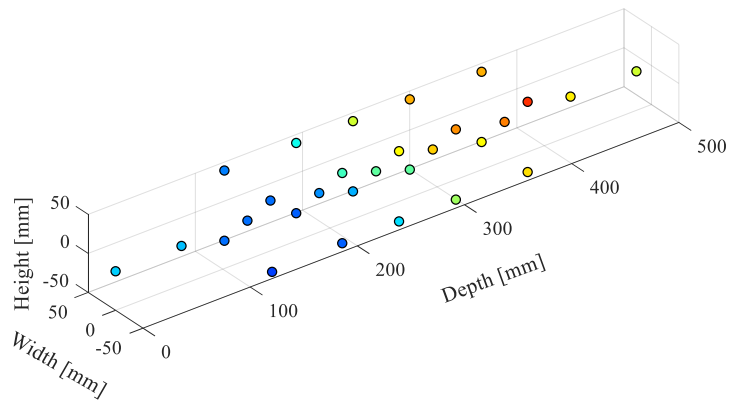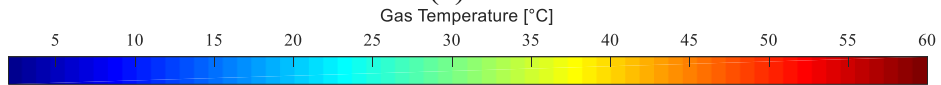
Figure 3-8:Gas Temperature Measurements with the XE Radiators Installed and Driven at 50 rpm for a Stroke Length of (a) 50.8 mm (b) 76.2 mm and (c) 101.6 mm

When comparing the temperature distributions between the SE and XE radiators, the XE radiator was able to attain higher temperature differences, but the upstream and downstream temperatures differences were larger for the SE radiators. The temperature upstream and downstream of the radiators did not attain near the set point temperatures, which was attributed to the excess dead volume. It should be noted that the uncertainty in temperature was approximately ±2 °C, which will be explained further in Chapter 4.

The larger stroke lengths also increased the difference in the measured hot and cold air temperatures, which would naturally increase the amount of fluid flushed through the radiators. Therefore, it was decided that the stroke length was to be increased from the 50.8 mm stroke in the OPA MK I, and the dead space was to be minimized further in the design of the OPA MK II so that the fluid could be properly flushed through the radiators.

Also, it was found that within a plane of thermocouples, the air temperature was warmer near the top of the test system than towards the bottom, in some cases with a difference of 10 °C, due to density differences between the hot and cold air. This was also indicative of insufficient flushing of the air through the radiators as a result of the large dead spaces before, after, and between the radiators.

Although this experiment did not provide a conclusive answer for which radiator performed the best under oscillating flow conditions, this experiment ended up being an important exercise into the nuances of experiment design, the importance of uncertainty, and the data collection process. Many of the lessons learned were used to improve future experiments. Examples of what was learned were:

- How to build and instrument an experiment that allows for testing of a wide range of conditions, such as radiator type, stroke length, and frequency of oscillation.
- How to effectively create an experiment plan, collect data, and process the results into useful information.
- How to 3D print larger components and anticipate post processing.
- The amount of fluid flushed through the radiator was important in maximizing the temperature difference.
- Clearance volumes between the piston and the heat exchangers as well as between heat exchangers should be minimized to aid in engaging the working fluid with the radiators.

3.5.1.2 MK II Heat Exchanger Implementation

The 46 mm thick radiator was chosen to be implemented into the OPA MK II out of the radiators considered due to the higher surface area. Heat exchanger housings were designed to locate the rectangular heat exchangers within the cylindrical bore of the engine, and can be seen in Figure 3-9. Each heat exchanger housing had 16 ports for thermocouples to be inserted, so that a similar temperature distribution to the radiator testing system could be obtained.
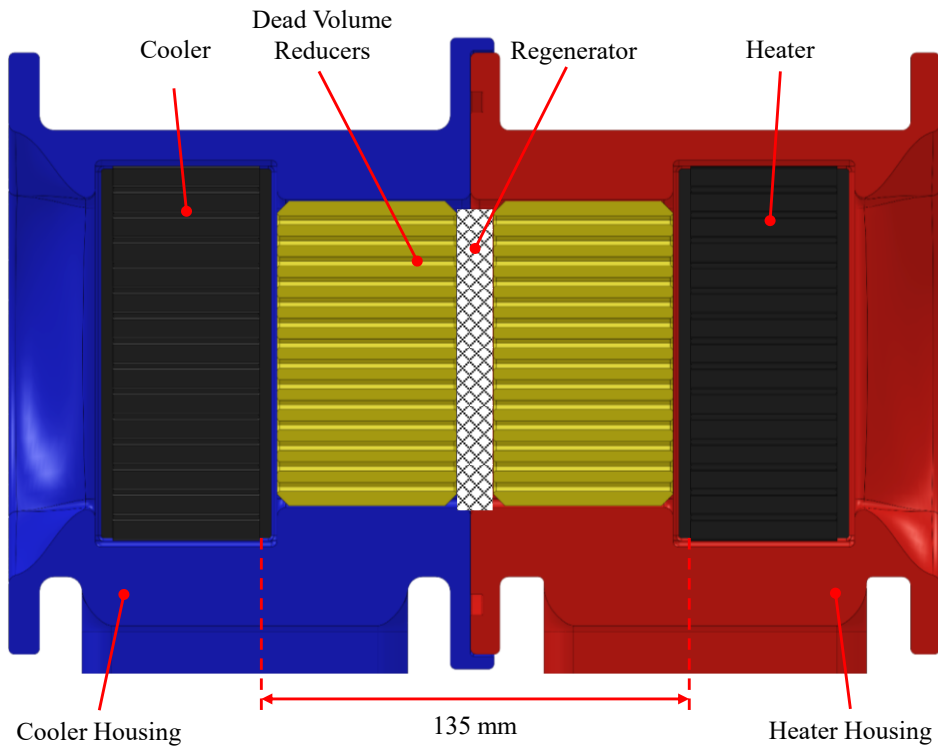
Figure 3-9: OPA MK II Heat Exchanger Assembly Section View

Due to the inlet and outlet ports for the radiators being located on the side rather than the bottom of the manifold, as shown in Figure 3-10, the shortest distance possible between them was 135 mm. This was not as compact as desired, so dead volume reducing components (DVRCs) were inserted in between the radiators to reduce the dead volume in that section from 1.3 L to 0.196 L.
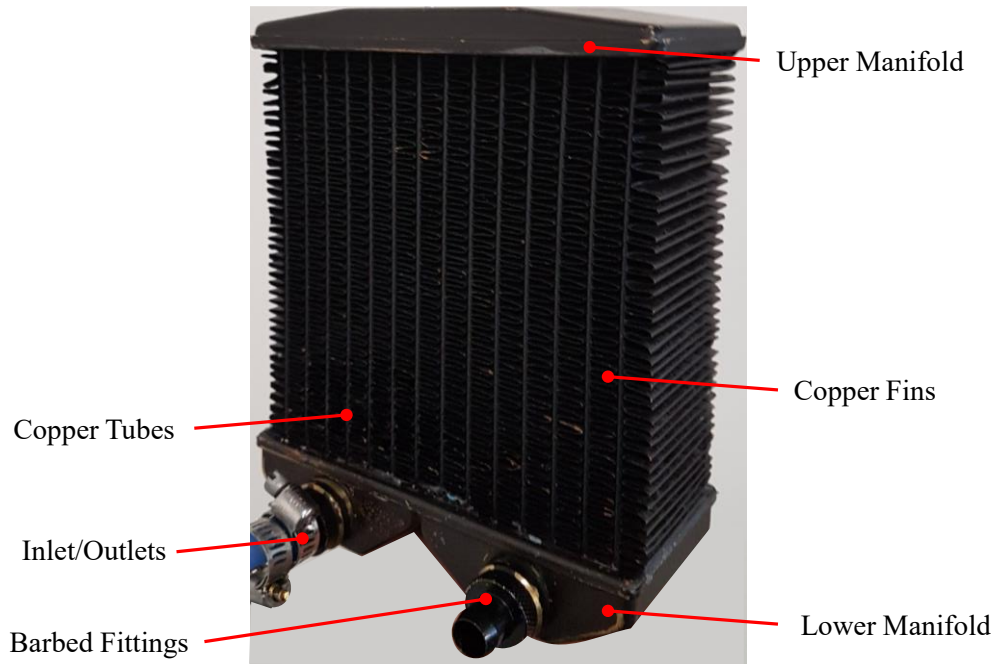
Figure 3-10: Annotated Image of the 46 mm Thick Radiator

No dedicated regenerator was inserted between the DVRCs, but the DVRCs themselves would act as a regenerator to some extent by storing the thermal energy of the fluid that passed through it. According to Martini [24], a well-designed regenerator is required to attain high efficiencies, but it is not required; however, with an inefficient regenerator, the heat transfer required for the cycle will be greater. In addition, no regenerator material was inserted because other gamma-type engines in the same research group were working without a regenerator [48], so it was assumed that they were not crucial for the engine to function, but rather would increase the efficiency of the engine at the cost of increased pressure drop.

3.5.2 MK II Engine Body

Although the OPA MK II was still an opposed piston alpha-type Stirling engine, the overall design of the OPA MK II differed from the MK I. The engine was still designed to be modular, and have the ability to couple multiple engines, but the engine body became more complex as a result of the dedicated heat exchangers and different piston sealing method. The expansion and compression cylinders were separated into three components due to the different sealing method employed: the buffer space, the rear cylinder, and the forward cylinder. There were also separate housings for the dedicated heater and cooler, as can be seen in Figure 3-11.
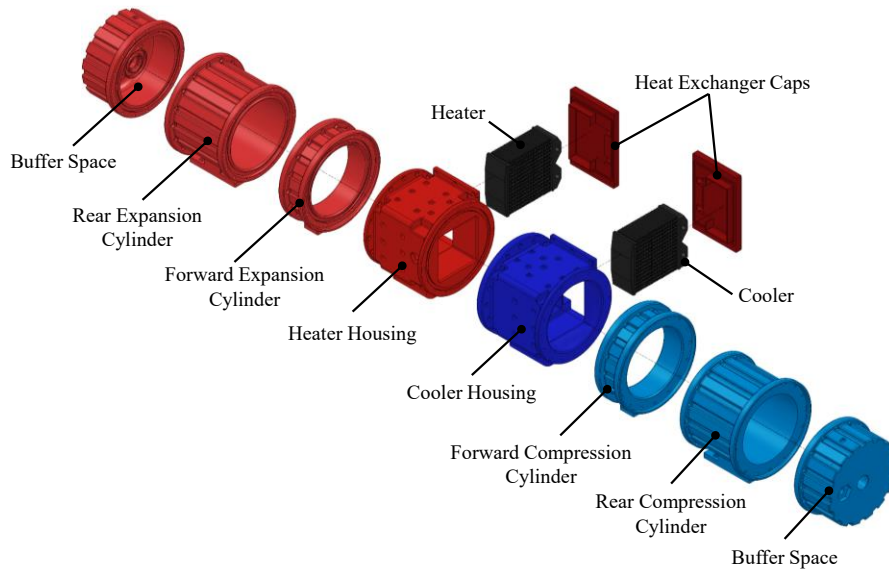
Figure 3-11: Exploded View of the OPA MK II Engine Body

All these components were 3D printed using ABS and acetone smoothed. The size of this iteration was governed by the 3D printer build volume. The engine body components were made to maximize the print volume, which allowed for an inner bore diameter of 152.4 mm. The length of the engine body when assembled was 899 mm, and it had an outer diameter of 216 mm.

3.5.3 MK II Piston Seal

Rather than utilizing an O-ring seal where the friction was large, and proper sealing was difficult, a rolling diaphragm seal (3-600-362-FCJFW, Bellofram Corp.) was implemented. The piston and cylinder assembly can be seen in Figure 3-12.
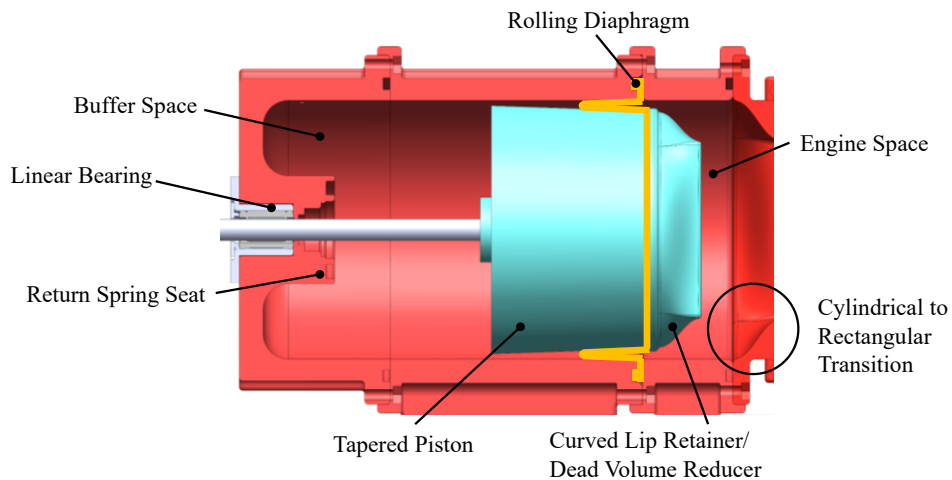
Figure 3-12: Schematic of the Rolling Diaphragm Piston Seal

The benefits of the rolling diaphragm were the negligible sliding friction and the negligible seal leakage. The convolution rolls rather than sliding against the bore, and the internal pressure seals the diaphragm against the piston and cylinder walls [74]. To utilize the diaphragm, the expansion and compression space cylinders needed to be separated into forward and rear components, so the diaphragm could be clamped. A tapered piston and curved-lip retainer were designed and 3D printed to support the shape of the diaphragm following the guidelines suggested by the manufacturer [75]. The taper on the piston started at a diameter of 140 mm and went to a diameter of 146 mm, giving an effective diameter of 146 mm. The curved-lip retainer was printed to have a clearance volume reducing component that flushed the volume of the transition between cylindrical bore to rectangular radiator housing.

One of the requirements for this seal was that a pressure difference was maintained across it, such that the pressure inside the engine was always higher than the buffer space pressure. If the buffer space pressure exceeded the pressure on the inside of the engine, the diaphragm would collapse, and friction would be present that would damage the diaphragm [74]. Two methods were incorporated into the design of the engine to address this challenge: a port to pressurize the engine, and a return spring that would return the diaphragm to the mid-stroke position [75], [76]. A port in the buffer space was also incorporated to allow the pressure in the buffer space to equalize with atmosphere.

3.5.4 MK II Mechanism Design

For the drive mechanism, it was decided to continue using timing belts and pulleys with a slider-crank mechanism, but rather than 3D printing the pulleys and crank mechanism, standard components were implemented. The timing belt size was increased from an MXL belt to an HTD belt with a 5 mm pitch and 2.1 m closed length. The timing pulleys had 72 teeth and were made of aluminum. The reduction in the amount of teeth reduced the possible phase angles to between 0° and 360° in 5° increments. Two belts were used for each crank mechanism, which led to a single output shaft, as can be seen in Figure 3-13.
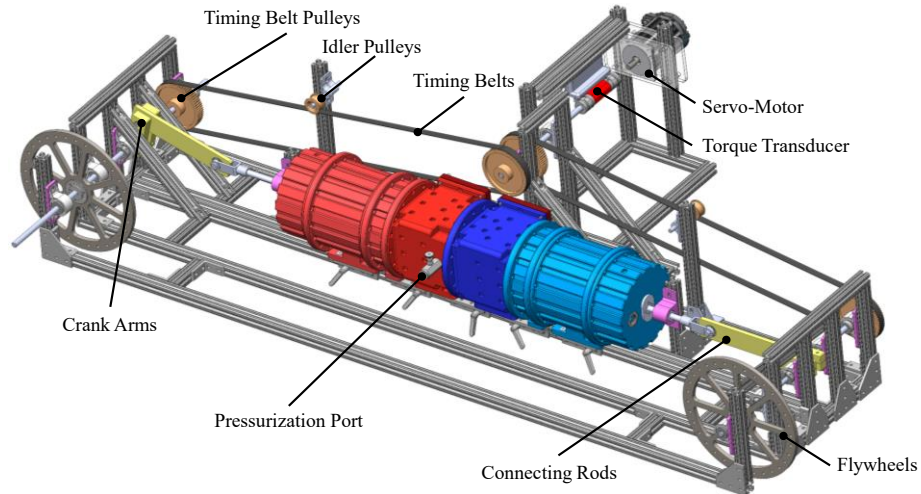
Figure 3-13: Annotated OPA MK II Solid Model Showing the Mechanism

The crank arms and connecting rods were made from steel, and were CNC milled to specification. The crank arms were designed for a stroke length of 101.6 mm, which was one of the tested stroke lengths in the radiator testing system that corresponded to an allowable stroke of the rolling diaphragm. The crank arms were 193.8 mm in length. With the chosen piston diameter and stroke length, the total engine swept volume was approximately 3.4 L. The rods connected to the connecting rod and piston were made of 12.6 mm diameter steel and translated through linear ball bearings. Sealed ball bearings for 12.6 mm shaft were used to support all the rotating shafts.

On each crank mechanism, flywheels were attached. The required moment of inertia was unknown, since the speed and torque fluctuations for the engine were unknown. In an attempt to oversize the flywheel, a 292.1 mm diameter steel disk with a thickness of 9.53 mm were waterjet cut. Spokes were cut out of the flywheels to the decrease the mass, and create additional weights that could be attached around the outside diameter to further increase the moment of inertia. The moment of inertia without the weights was estimated to be 0.016 kg/m^2 within SolidWorks.

3.5.5 MK II Design Outcomes

Once again, after testing the engine with a thermal source and sink of 95°C and 5 °C the engine did not function. At this larger scale, many more issues arose that would need to be addressed. A servo-motor was connected to the system to attempt to drive the engine and collect data that could further troubleshoot the issues, but the servo-motor had difficulty overcoming the friction in the system. The two most significant issues were engine leakage and mechanical

friction. An image of the manufactured engine compared to the solid model during the design phase can be seen in Figure 3-14.

(a)

(b)
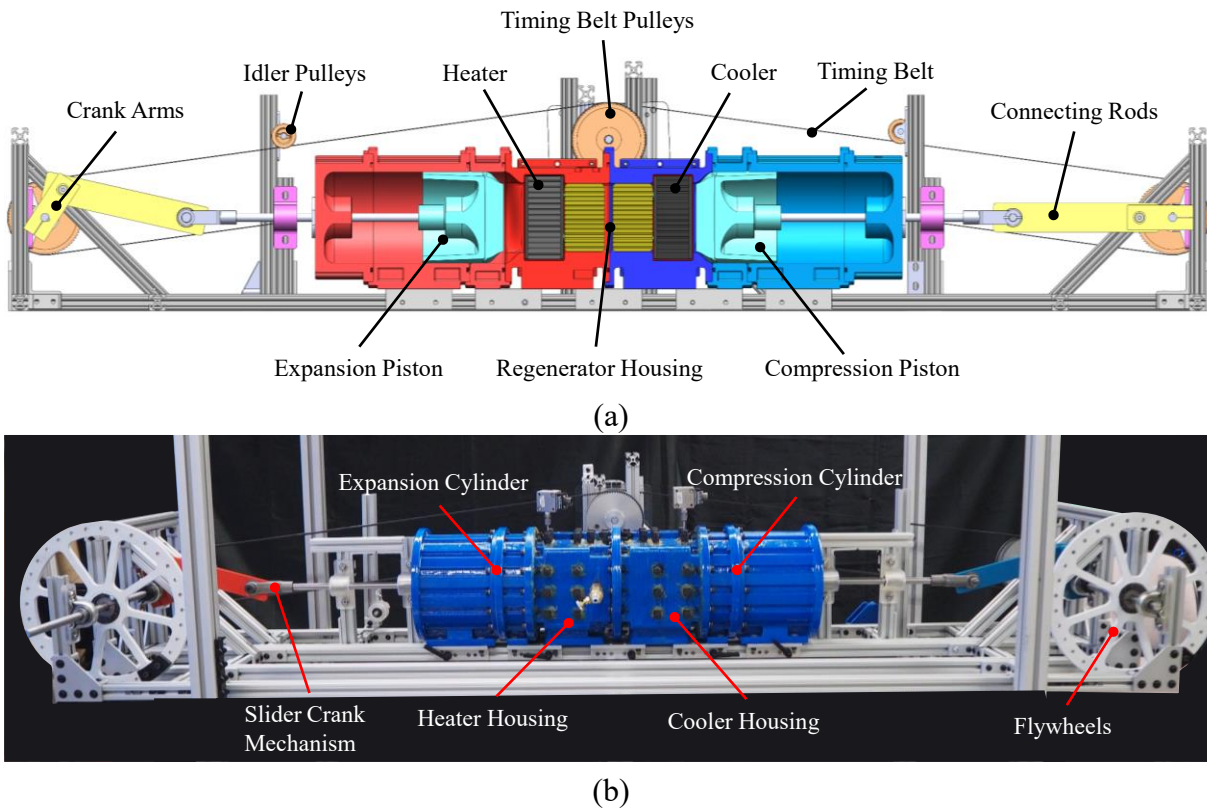
Figure 3-14: Comparison Between the OPA MK II (a) Solid Model Section View and (b) Physical Prototype

The engine leaks were a result of relying on 3D printing the entire engine body. Warping and layer separation were exaggerated at this scale due to the non-uniform printing environment temperature. This occurred due to the temperature gradient between the build-plate and the top of the print, where the ambient air caused the material to contract which could delaminate the print from the build-plate, or create cracks in the print. It was found that the majority of leaks occurred through cracked layers, around instrument ports, between module flanges, and around fasteners. With significant leaks, the engine pressure would be reduced, which would reduce the amount of indicated work.

The engine leaks also prevented the rolling diaphragm from working properly. The leaks prevented the engine from being pressurized above the buffer space pressure which lead to the diaphragm collapsing due to pressure reversals, and increased the seal friction. Also, the return spring did not function as intended, since it required the semi-enclosed buffer space to support it.

56

The buffer space vent hole caused too much flow friction, such that the air would compress and the pressure would increase, which caused the diaphragm convolution to collapse further. At the time of the design and construction of the OPA MK II, the theory of forced work and buffer pressure effects was not well understood, which would have influenced the design of this engine. Relying on the engine pressure to be greater than the buffer pressure at all times would increase the amount of forced work in the system, as illustrated in Figure 2-4(a), which would decrease the indicated work as well as the mechanism effectiveness.

Friction in the mechanism also impacted the engine. Sealed ball bearings were selected to support rotating shafts, which were filled with viscous grease that increased bearing friction and inhibited the rotation of the mechanism. The alignment of the linear bearings and the timing belt pulleys were also crucial, yet difficult to accomplish due to the degrees of freedom of the aluminum t-slot framing. Two linear ball bearings were used to support the piston shaft, which needed to be aligned, such that the piston was concentric in the bore and shaft was concentric between both bearings. Misalignment of the pulleys caused the timing belt to slide and contact the side of the pulley, increasing friction and wear. With all these factors increasing the mechanism friction, the flywheels also needed to be larger.

This build of the engine provided many additional insights to improve the next design iteration of the engine, so that proper experiments could be conducted such as:

- Warping and layer separation needed to be addressed by enclosing the 3D printer within an insulated enclosure to increase the air temperature uniformity in the chamber.
- Acetone smoothing the parts did not effectively fuse the layers together, so using an epoxy to coat the 3D printed parts was considered, which would fill any gaps in the part.
- The amount of instrument ports and flange connections needed to be reduced to decrease the amount of leak points.
- Enclosing the 3D printed engine body within an impermeable outer shell would decrease leaks.
- Rolling diaphragm seals were difficult to implement into the engine with the current design constraints and operating conditions, so another solution was investigated.
- Misalignment of the pulleys increased mechanism friction, and the belt backlash was larger than desired.

- The lubricant within the bearing elements needed to be less viscous to reduce mechanism friction.

A summary of the engine properties compared to the MK I can be seen in Table 3-5.

Table 3-5: OPA MK II Engine Properties

Properties	OPA MK I	OPA MK II
Working Fluid	Air	Air
Piston Seal	Greased O-ring	Rolling Diaphragm
Effective Piston Diameter	44 mm	146 mm
Stroke Length	50.8 mm	101.6 mm
Engine Swept Volume	0.274 L	3.4 L
Bore Diameter	44.45 mm	152.4 mm
Phase Angle Range	0° - 360°	0° - 360°
Phase Angle Increment	2°	5°
Mechanism Type	Slider-Crank + MXL Timing Belts	Slider-Crank + HTD Timing Belts
Flywheel Construction	5 lb Weight Plate	Two Steel Disks With Spokes
Flywheel Moment of Inertia	Not Calculated	0.016 kg/m^2 (each)
Regenerator Material	Steel Wool	Plastic Channels
Regenerator Dead Volume	0.055 L	0.479 L
Heat Exchanger Type	Cylinder Walls	46 mm Radiators
Heat Exchanger Material	Aluminum	Copper
Heat Exchanger Surface Area	107.8 cm^2	9319 cm^2
Heat Exchanger Dead Volume	0 L	0.868 L (each)
Thermal Source Temperature	95 °C	95 °C
Thermal Sink Temperature	5 °C	5 °C
Compression Space Clearance Volume	-	0.169 L
Expansion Space Clearance Volume	-	0.169 L

3.6 Opposed Piston Alpha: MK III

Through the experience of manufacturing the OPA MK I and MK II, it was clear that the quality and accuracy of the components in the system needed to be improved, so that experiment measurements could be made with confidence. An updated iteration of the engine was designed and manufactured to address the issues of the first two prototypes. The primary improvements to be incorporated into the design were as follows:

- Reduce the amount of leaks in the engine by using an impermeable housing over a 3D printed engine core.
- Create a more compact engine with reduced dead volume by reducing the spacing between heat exchangers.
- Reduce the amount of critical 3D printed components by using machined parts.
- Utilize a low friction piston seal that does not rely on a pressure differential across it to function properly.
- Develop an alternate mechanism that does not rely on belts, yet can rapidly change phase angles within a range similar to what was possible with timing belts.
- Reduce piston side loads as a result of a slider-crank mechanism, and have the ability to vary the stroke length.
- Improve the mechanism by using open face bearings lubricated with oil rather than grease.
- Increase flywheel moment of inertia further.
- Design to allow direct coupling of a second engine on the same mechanism for balancing and increased power.

The following section will provide an overview of the OPA MK III engine, as well as the decisions and outcomes of the design.

3.6.1 MK III Engine Body

The engine body was improved to address the issue of workspace leakage and excessive dead volume, while maintaining a similar bore size to the MK II. An exploded view of the engine body components is shown in Figure 3-15.
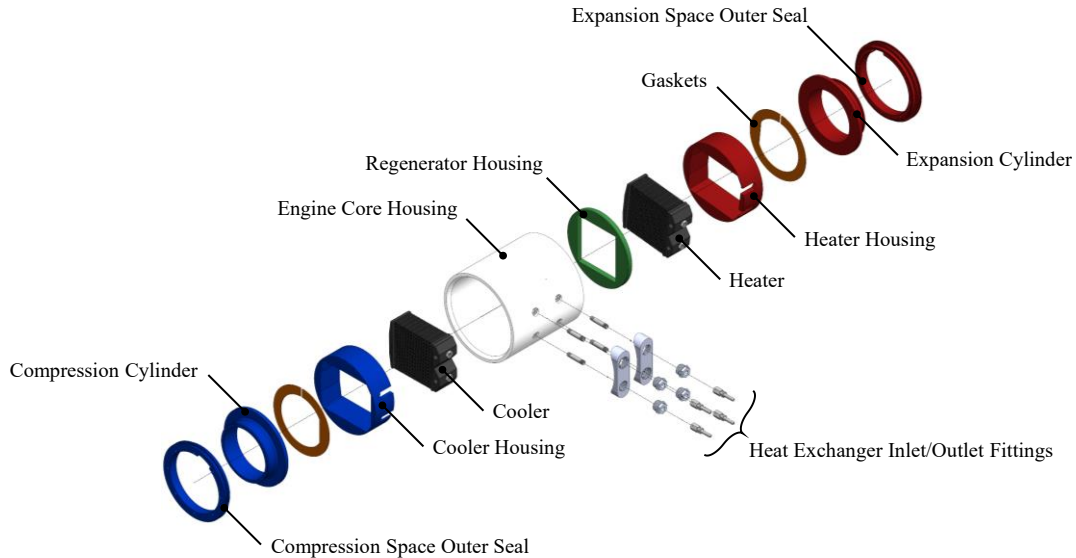
Figure 3-15: Exploded View of the OPA MK III Engine Body Solid Model

The engine body can be split between an engine core and an engine core housing. The engine core consisted of the 3D printed components that make up the expansion cylinder, regenerator housing, compression cylinder, and the heater and cooler housings. The engine core 3D printed parts were epoxy coated to prevent the infill voids from contributing to the dead volume, and threaded rods were used to connect each component together. An engine core housing was made to encase the engine core and prevent the working fluid from leaking. It was made of a 220 mm length of CPVC pipe with an outer diameter of 219 mm and an inner diameter of 193.7 mm. It should be noted that the engine body only contained a portion of the expansion and compression spaces, with the remainder built into the piston seal that will be explained further.

3.6.2 MK III Heat Exchangers

The heat exchangers used in the OPA MK III were the same as those in the MK II, except inlet and outlet ports were drilled into the bottom of the manifold, and coupling nuts were soldered to the bottom to allow the barbed fittings to attach. This was done so that the location of the barbed fittings did not dictate the spacing between radiators. This eliminated the need for DVRCs in the regenerator space, which were a source of pressure drop and flow losses in the system. The spacing between the radiators was reduced from 135 mm to 22.45 mm with this modification. The radiators were inserted into radiator housings that filled the gaps between the rectangular radiator and the cylindrical bore of the engine core housing, as seen in Figure 3-16. The triangular gap near the manifold was filled with another 3D printed part to take up dead volume.
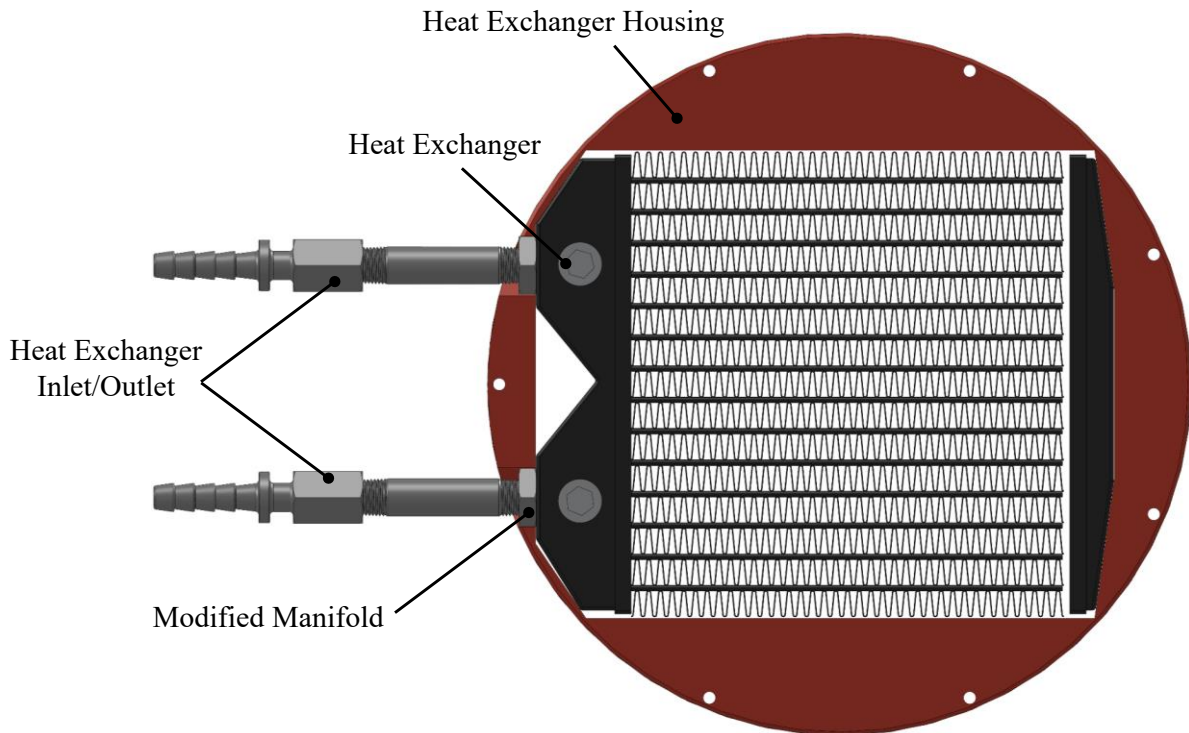
Figure 3-16: Solid Model of Heat Exchanger Assembly and Housing

As with the MK II, no regenerator was inserted in the regenerator housing, so as to reduce the pressure drop at the expense of thermal efficiency. As stated, other engines built within the research group were able to turn a crankshaft first without a regenerator, and once proven that the engine would run, the regenerator was inserted. The regenerator housing volume was 0.187 L.

3.6.3 MK III Piston Seal

From previous experience designing the seals for the other engines, it was decided that effort should be made into a new solution to piston sealing that had low friction, and did not rely on a pressure difference across the seal. The bellows seal was a more unconventional method for sealing a piston-cylinder, but has been demonstrated in Stirling engine literature in the form of metal bellows [77] and rubber bellows [48],[78]. By implementing rubber bellows, the contact between the piston and cylinder was eliminated, hence greatly reducing mechanism friction. The bellows used were multi-convoluted nitrile bellows (BC-2100, TheRubberStore.com). The bellows had a maximum extended length of 120 mm, a compressed length of 19 mm, an inner diameter of 140 mm, and an outer convolution diameter of 173 mm [79]. The bellows thickness was measured to be approximately 1.3 mm. The dimensions of the bellows are shown on a solid model representation in Figure 3-17.
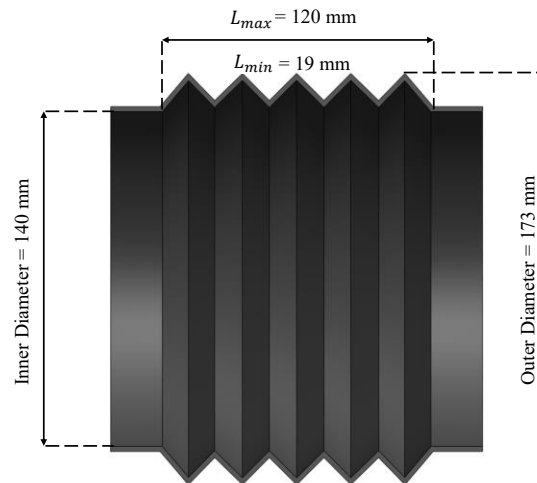
Figure 3-17: Schematic of the Bellows with Overall Dimensions

The bellows were attached to the 3D printed engine cylinder components semi-permanently using a large diameter hose clamp and silicone, and were attached to the pistons using a duplicate hose clamp to compress a layer of gasket material between the bellows and the piston for improved sealing. When tightened, the amount of leakage past the pistons was negligible. The connection of one end of the bellows to the power piston and the other end to the engine core formed the remaining portion of the expansion and compression spaces. A schematic of a power piston is shown in Figure 3-18.
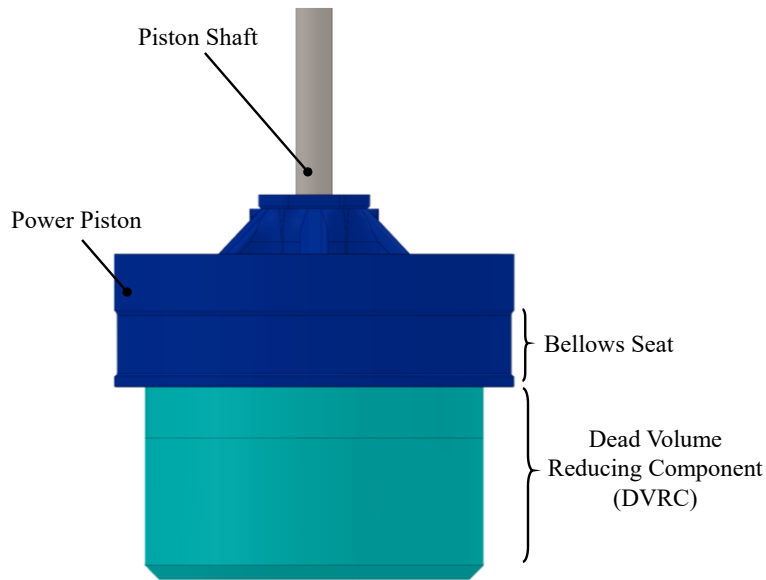
Figure 3-18: Schematic of the OPA MK III Piston

The 141 mm diameter power pistons were 3D printed on the SLA printer to ensure they had a 100% infill, so that the working gas could not leak through the piston. The piston had a built in bellows seat that secured the bellow from slipping off the piston during operation. As a result of the bellows having a minimum compression length of 19 mm, the piston face would not be flush against the radiator. Therefore, piston face dead volume reducing components (DVRCs) were created to flush into the engine cylinder bore. The diameter of the DVRCs were 120 mm so as to be able to fit within the 130 mm inner bore diameter of the 3D printed compression and expansion cylinders with room for alignment. Depending on the stroke length selected, DVRCs could be added or removed to increase or decrease dead volume. The pistons were also designed to have up to three embedded thermocouples inserted through channels to measure the temperature near the piston face.

Although the rubber bellows solved the problem of leakage past the piston and excessive mechanical friction due to dynamic seals, additional challenges were introduced such as determining what the volume variation of a bellows would be, and constraining the geometry so that the bellows did not collapse under negative engine pressure, or over expand as a result of positive engine pressure. Therefore, retaining rings were required to prevent excessive geometric changes in the bellows to keep a constant convolution maximum and minimum height.

The first attempt at creating retaining rings consisted of physically twisting the ends of a 0.8 mmm diameter steel wire for the outer retaining rings, and taping an overlapping section of a 1.6 mm diameter steel wire for the inner retaining rings. A photo of the outer wire retaining ring with a close up view of the coupling method can be seen in Figure 3-19(a). This worked well for the outer retaining as they were mechanically secured to prevent slipping. Although, it did not work for the inner retaining rings, since the taped ends would consistently break apart. It was difficult to get the exact same shape and diameter for all the rings using this method.

| (a) | (b) |
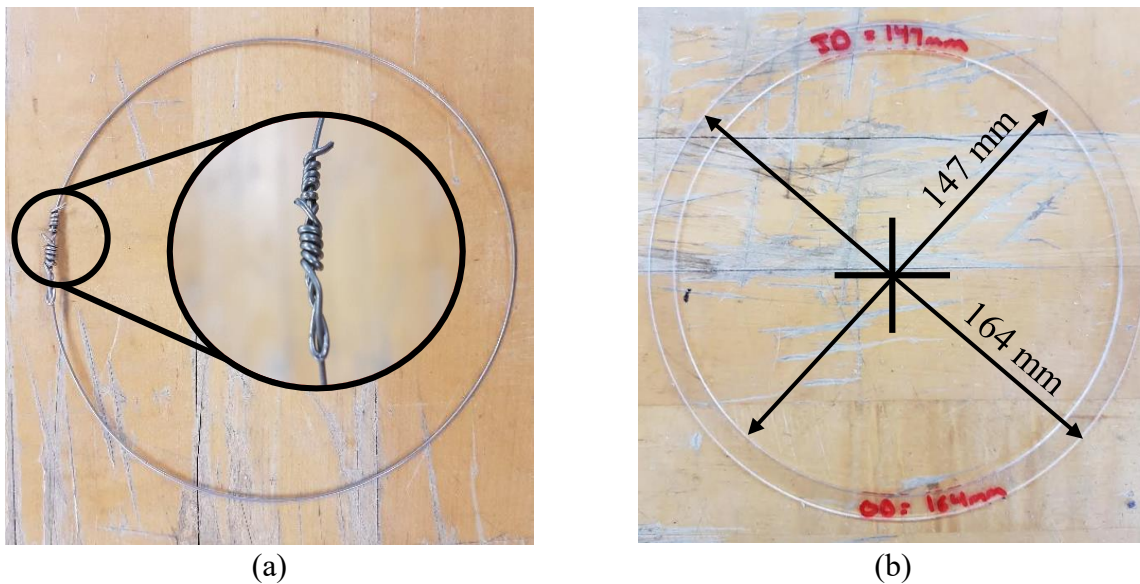
Figure 3-19: Annotated Image of the (a) Wire Retaining Ring (b) Acrylic Retaining Ring

To address these issues, identical rings were cut using a laser cutter out of 1.6 mm acrylic sheets. The rings were designed so that the inner diameter would constrain the inner convolutions when the ring was placed on the outside of the bellows, and the outer diameter would constrain the outer convolutions from collapsing when the ring was placed inside the bellows. An image of the acrylic retaining ring with dimensions can be seen in Figure 3-19(b). The outer diameter of the ring was 164 mm with an inner diameter of 147 mm. These dimensions ensured that the outer convolution diameter (from the inside) was between approximately 164 mm and 171 mm, and the inner convolution diameter (from the inside) was between approximately 140 mm and 145 mm.

3.6.4   MK III Mechanism Design

The crank arms used in the OPA MK III were modified from the MK II to allow for more stroke variations. The MK II only allowed for a 101.6 mm stroke length, which was the maximum

length the bellows could be extended. Two additional stroke lengths were machined on the same crank arm, equivalent to 50.8 mm and 76.2 mm stroke lengths. A schematic of the crank arms can be seen in Figure 3-18. The 101.6 mm stroke length would not be used due to the minimum extended length of the bellows seals.
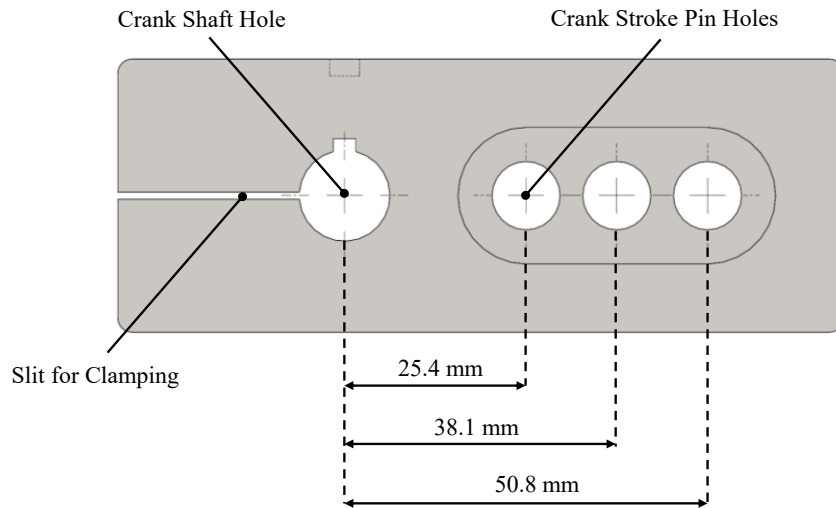
Figure 3-20: Schematic of the OPA MK III Crank Arms

The crank arms were connected to the expansion piston, using a Scotch yoke mechanism, with a roller bearing and slot. This mechanism was chosen instead of the slider-crank because the mechanism converts rotational motion directly into linear motion with minimal side loads. The piston motion became truly sinusoidal, and had a direct analytical solution for the equations of motion [80]. A schematic of the entire mechanism (without the frame) can be seen in Figure 3-21.
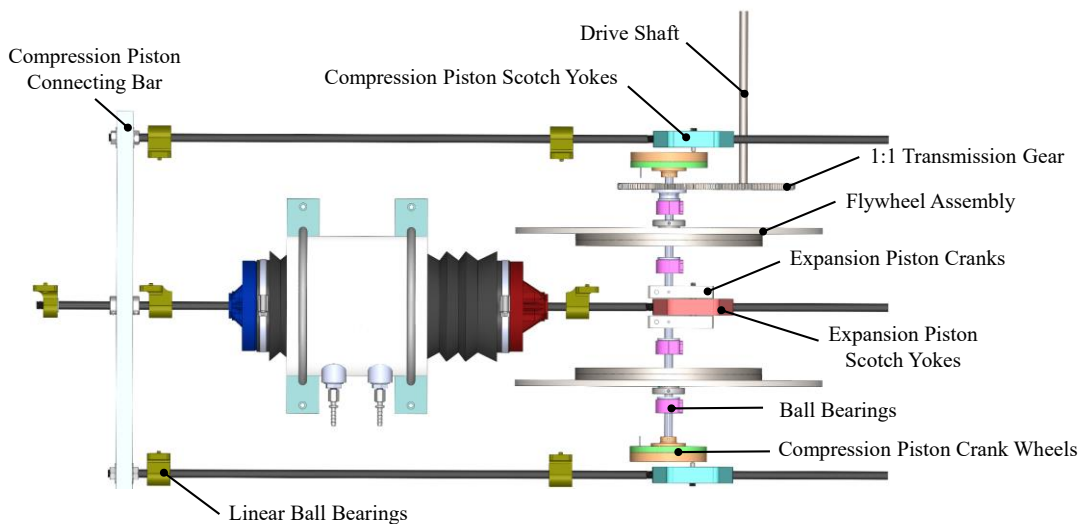
Figure 3-21: Top View of the OPA MK III Mechanism

The mechanism design had three Scotch yokes, two for the compression piston and one for the expansion piston, which were connected to the same crank shaft as the expansion piston. The yoke slots had linear rods extending from each side to reach the pistons. A connecting bar was required to connect both the compression piston yokes together. The rods were supported using linear ball bearings, and it should be noted that the placement of linear bearings was mirrored to support the yokes such that they were not cantilevered (not pictured in Figure 3-21). Open face ball bearings were used instead of the sealed ball bearings to reduce the mechanism friction, and they were lubricated with oil instead of grease. By using the Scotch yoke mechanism, the kinematic and thermodynamic phase angles became equivalent, where they were only approximately the same for the slider-crank mechanism [81]. To change the phase angle, custom 3D printed compression piston crank wheels were created as shown in Figure 3-22.
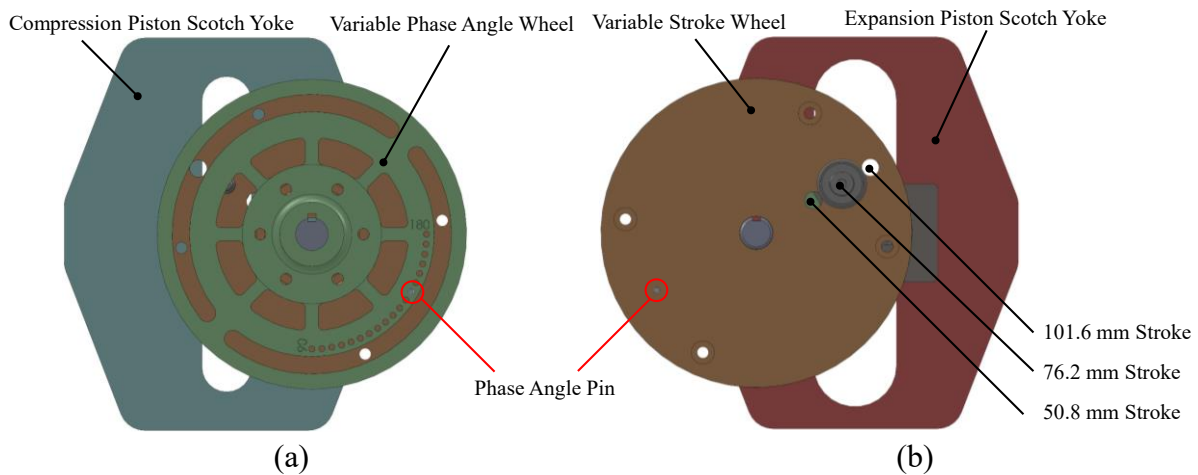
Figure 3-22:Compression Piston Cranks (a) Variable Phase Angle Wheel (b) Variable Stroke Wheel

The cranks were made of two components, a variable phase angle wheel and a variable stroke wheel. Both wheels were mounted to the same shaft and could rotate relative to each other, until secured by tightening four bolts that ran through slots in the variable phase angle wheel. The variable phase angle wheel had holes that corresponded to phase angles between 90° and 180° in 5° increments relative to the expansion piston. The variable stroke wheel had a single hole to insert a pin through both wheels to select the desired phase angle. This changed the angular position of the yoke roller. The yoke roller was connected to a bolt that could be positioned in one of three compression piston stroke holes, corresponding to a stroke of 50.8 mm, 76.2 mm, or 101.6 mm. Both the compression piston crank wheels needed to be configured the same for the mechanism to

function properly. Figure 3-23 illustrates how the phase angle was changed between the expansion and compression pistons. When at 180° phase angle, no volume change occurred and the working fluid was shuttled back and forth in the engine. Figure 3-23(a) shows both the expansion and compression yokes aligned at 180°, where the expansion space would be at maximum volume, and the compression space would be at minimum volume. Figure 3-23(b) and (c) show the configuration at a phase angle of 150° and 90°.

| 180 Phase Angle | 150 Phase Angle | 90 Phase Angle |
| (a) | (b) | (c) |
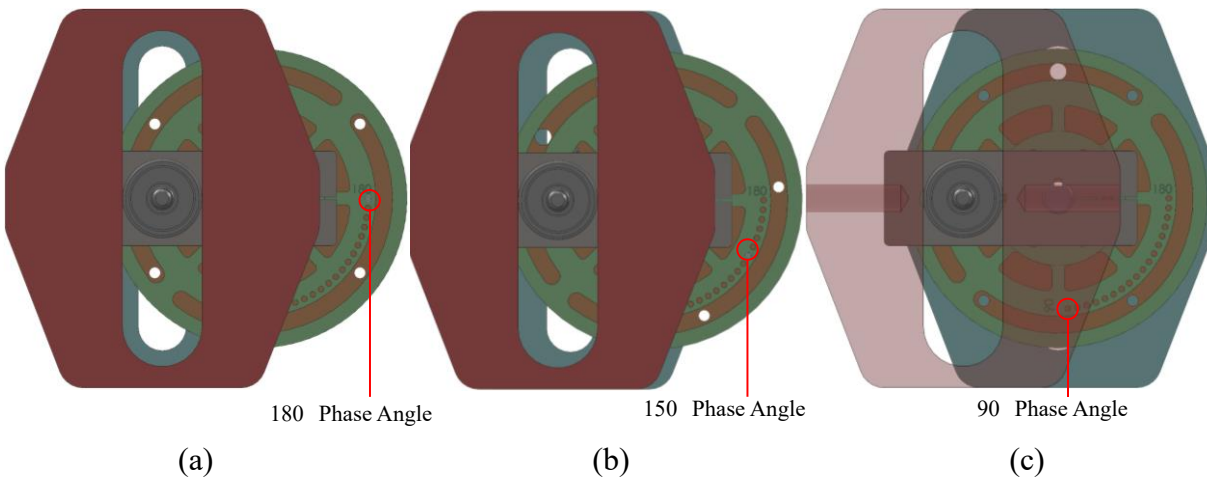
Figure 3-23: Schematic of Varying Phase Angle Between Expansion and Compression Pistons
(a) 180°, (b) 150°, and (c) 90°

With the ability to change the stroke length for the expansion and compression pistons independently, the number of swept volume and compression ratio configurations for testing increased. Depending on the stroke length combinations and DVRCs used, the clearance space dead volume between the pistons and the heat exchangers changed as well. For stroke lengths of 50.8 mm and 76.2 mm using the DVRC for minimum dead volume at a stroke of 76.2 mm, a schematic representation of the amount of clearance space dead volume is shown in Figure 3-24. For the compression space, the clearance volume was either 0.476 L or 0.284 L if a 50.8 mm or 76.2 mm stroke was used, respectively. Whereas for the expansion space, the clearance volume was either 0.539 L or 0.344 L if a 50.8 mm or 76.2 mm stroke was used, respectively. The dead volume values were measured after the engine was assembled, so assembly tolerances were the cause for unequal amount of dead volumes in the expansion and compression spaces.

Compression Space Clearance Volume

(a)

Expansion Space Clearance Volume

(b)
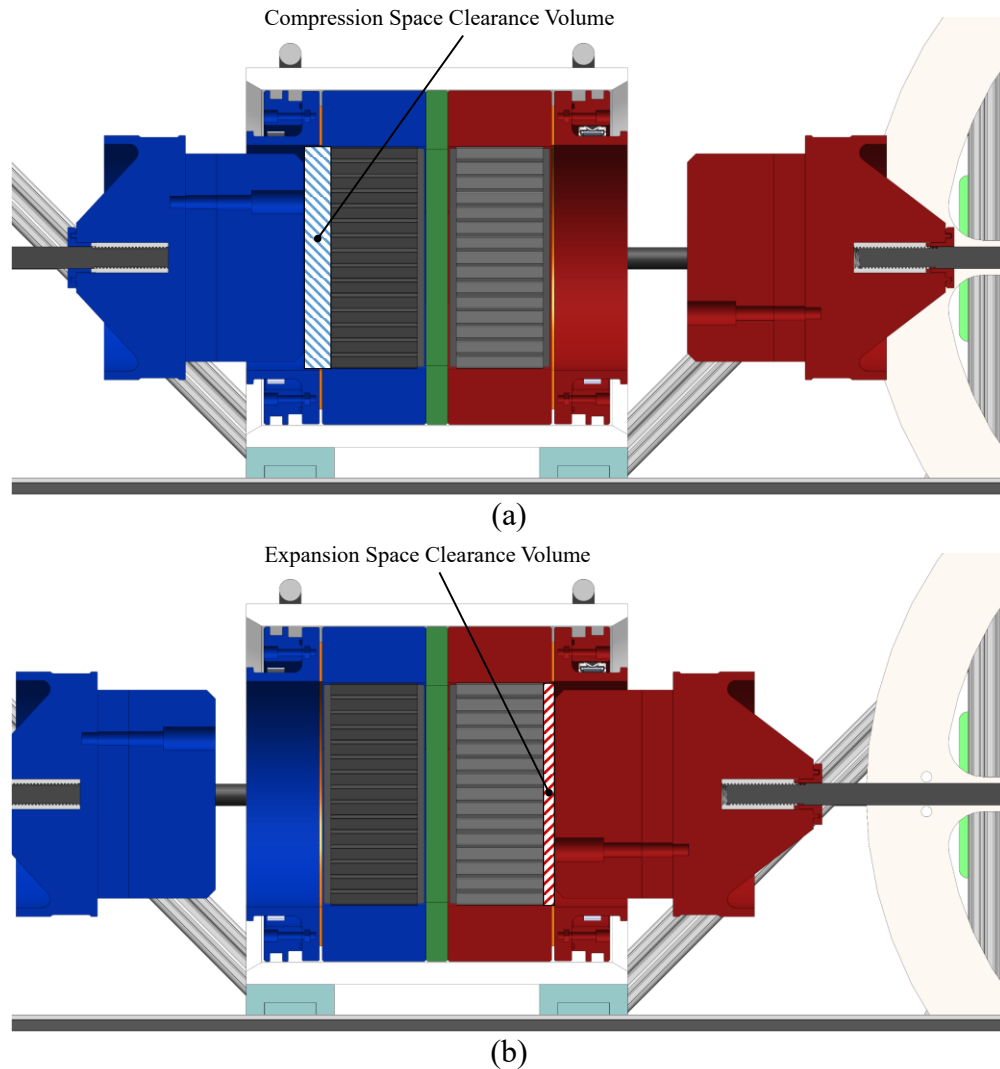
Figure 3-24: Schematic of the Clearance Space Dead Volume at (a) 50.8 mm and (b)76.2 mm Strokes Using a DVRC to Minimize Dead Volume for a 76.2 mm Stroke

The moment of inertia of the flywheels was also increased by combining the previous flywheels from the OPA MK II, with another extended 480 mm diameter flywheel ring that connected to the outside of the flywheel, as shown in Figure 3-25. As with the OPA MK II, two flywheel were used in the mechanism. The moment of inertia increased to 0.53 kg/m^2 for each flywheel assembly, as determined in SolidWorks.
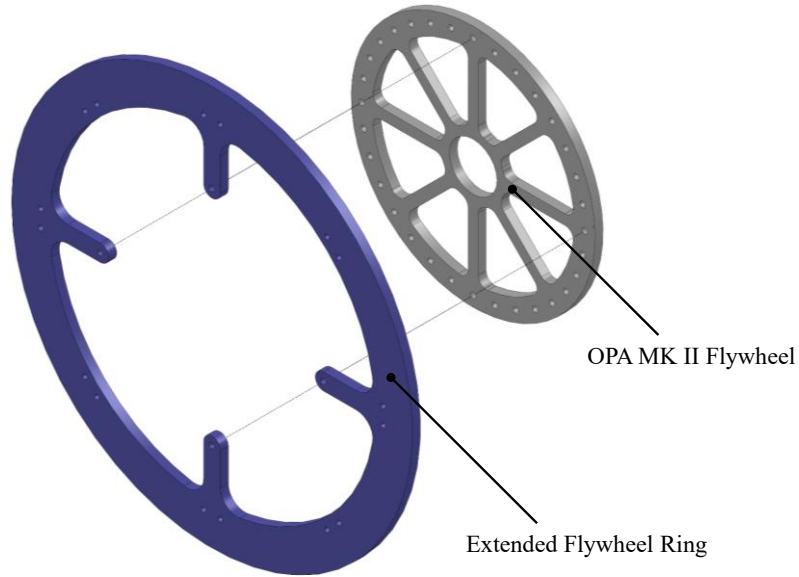
Figure 3-25: Exploded View of the OPA MK III Flywheel Assembly

3.6.5 MK III Design Outcomes

The isothermal model and fundamental efficiency theorem, detailed in Chapter 2, were used in conjunction to estimate the range of phase angles for experimentation. Figure 3-26 illustrates the estimated shaft work output for various phase angles of the OPA MK III with a 76.2 mm stroke length for both pistons, assuming the expansion space temperature was 90 °C and the compression space temperature was 7 °C, and a constant mechanism effectiveness of 0.9, with a buffer space pressure equal to atmospheric pressure.
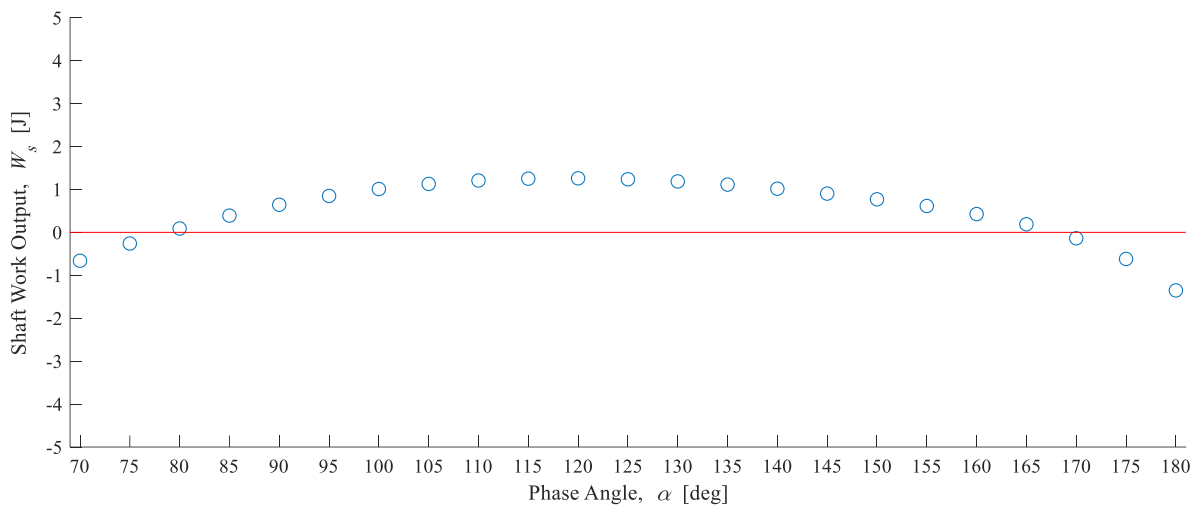
Figure 3-26: Initial Shaft Work Prediction from Isothermal and Fundamental Efficiency Models

The gas temperatures were given a 5 °C penalty from the thermal source and sink temperatures. It was not possible to know or estimate the mechanism effectiveness without first building an engine, so it was selected to be 0.9 for the initial prediction. From the figure, a phase angle of 90° was not optimal at these conditions, as was the chosen phase angle for many high temperature alpha engines as discussed in Section 1.7. Phase angles below 90° were plotted to illustrate that the shaft power output would continue to decrease beyond 90°. The optimal estimate seemed to be near 120°. With these initial estimates showing the potential for the engine to function, the OPA MK III was manufactured and assembled as shown in Figure 3-27.
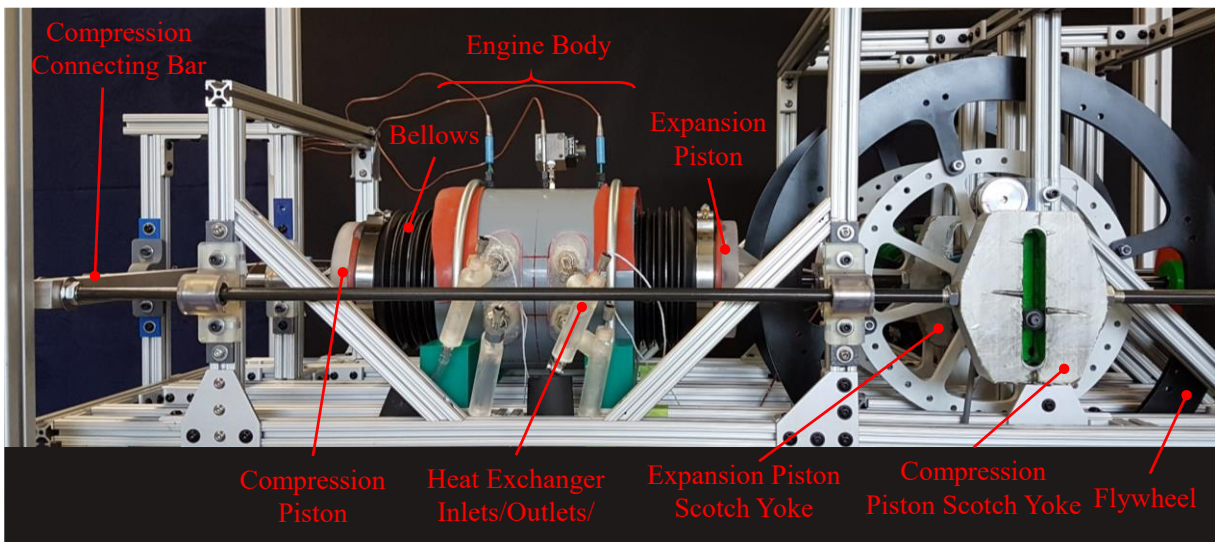
Figure 3-27: Annotated Image of the Assembled OPA MK III

The mechanism had much less friction compared to the previous prototypes, and could remain rotating for several minutes. The engine did not leak noticeably, and leak points that did exist were easily addressed with silicone. The method of changing the phase angle was a success and became relatively simple with practice. It was decided that this iteration of the engine was to be used for experiments, which will be discussed in Chapter 4 and Chapter 5. Recall that one of the design goals for this iteration was to be able to couple a second engine on the same mechanism; however, due to financial and time constraints, a second engine was not built for the experiments. As such, the remainder of this thesis will focus on a single engine configuration for the experiments.

3.7   Chapter 3 Summary

An opposed piston alpha-type Stirling engine prototype was designed according to the initial design objectives and constraints. The engine was to operate below a thermal source temperature of 100 °C, using air as the working fluid with a mean pressure approximately equal to atmospheric. The engine was then to be used as an experimental system to be able to experimentally determine which stroke length and phase angles were best suited for maximum shaft power for an LTD alpha-type Stirling engine. Due to the low thermal source temperature, plastics were used to reduce the cost, insulate components, and manufacture complex parts using 3D printing.

The design cycle consisted of designing and manufacturing three prototype alpha Stirling engines. The first iteration was a small scale concept engine that did not function due to the limited size, insufficient heat transfer, seal friction and leakage, and a mechanism that would fail. The second iteration was a larger engine with dedicated heat exchangers, a low friction diaphragm seal, and a more rigid mechanism using standard components rather than custom 3D printed parts. This engine also did not function, since the 3D printed engine components were much larger and more prone to cracks and warping. As a result, engine leakage could not be managed, which made the rolling diaphragm seals unable to function properly and increased the mechanism friction.

These two prototypes were not suitable for any experiments, so a third iteration was created that could be used as an experiment platform. The engine was inserted into an impermeable plastic pipe to reduce leakage, and a flexible bellows seal was utilized that had low friction and did not require a pressure differential across it. The mechanism was greatly enhanced over previous iterations, and it utilized a triple scotch yoke mechanism that could vary the stroke lengths of the expansion and compression piston independently, and test phase angles between 90° and 180° in 5° increments. A table comparing the properties and dimensions of the three prototype engines is shown in Table 3-6.

Table 3-6: Opposed Piston Alpha Prototype Dimensions and Properties Comparison

Properties	OPA MK I	OPA MK II	OPA MK III
Working Fluid	Air	Air	Air
Piston Seal	Greased O-ring	Rolling Diaphragm	Bellows
Effective Piston Diameter	44 mm	146 mm	140 mm (Bellows ID)
Stroke Length	50.8 mm	101.6 mm	50.8 mm or 76.2 mm
Engine Swept Volume	0.274 L	3.4 L	1.564 L, 1.955 L, 2.346 L
Bore Diameter	44.45 mm	152.4 mm	130 mm
Phase Angle Range	0° - 360°	0° - 360°	0° - 180°
Phase Angle Increment	2°	5°	5°
Mechanism Type	Slider-Crank + MXL Timing Belts	Slider-Crank + HTD Timing Belts	Triple Scotch Yoke
Flywheel Construction	5 lb Weight Plate	Two Steel Disks With Spokes	OPA MK II Flywheels + Extension Ring
Flywheel Moment of Inertia	Not Calculated	0.016 kg/m^2 (each)	0.53 kg/m^2 (each)
Regenerator Material	Steel Wool	Plastic Channels	None
Regenerator Dead Volume	0.055 L	0.479 L	0.187 L
Heat Exchanger Type	Cylinder Walls	46 mm Radiators	46 mm Radiators
Heat Exchanger Material	Aluminum	Copper	Copper
Heat Exchanger Surface Area	107.8 cm^2	9319 cm^2	9319 cm^2
Heat Exchanger Dead Volume	0 L	0.868 L (each)	0.868 L (each)
Thermal Source Temperature	95 °C	95 °C	95 °C
Thermal Sink Temperature	5 °C	5 °C	2 °C
Compression Space Clearance Volume	-	0.169 L	0.476 L or 0.284 L
Expansion Space Clearance Volume	-	0.169 L	0.539 L or 0.344 L

Chapter 4   Experiment Setup and Methodology

Within this chapter, the methodology of the experiment to test the effect of changing piston stroke length, phase angles, and engine speed will be presented and discussed. Initially, the experiment setup will be discussed, which includes the engine system and instrumentation for measuring pressure, temperature, torque, and speed. The experiment procedure will be described, including the selected manipulated, controlled, and uncontrolled variables. Pertinent information about the procedure for data processing will be introduced, and the uncertainty analysis procedure will be described.

4.1   Experiment Setup

The experiment setup was comprised of multiple systems, as seen in the process instrumentation diagram (PID) for the experiment, shown in Figure 4-1. The systems included the heating and cooling loops, the Stirling engine system, the temperature measurement system, the pressure measurement system, the power measurement system, the motoring system, and the data acquisition (DAQ) system.
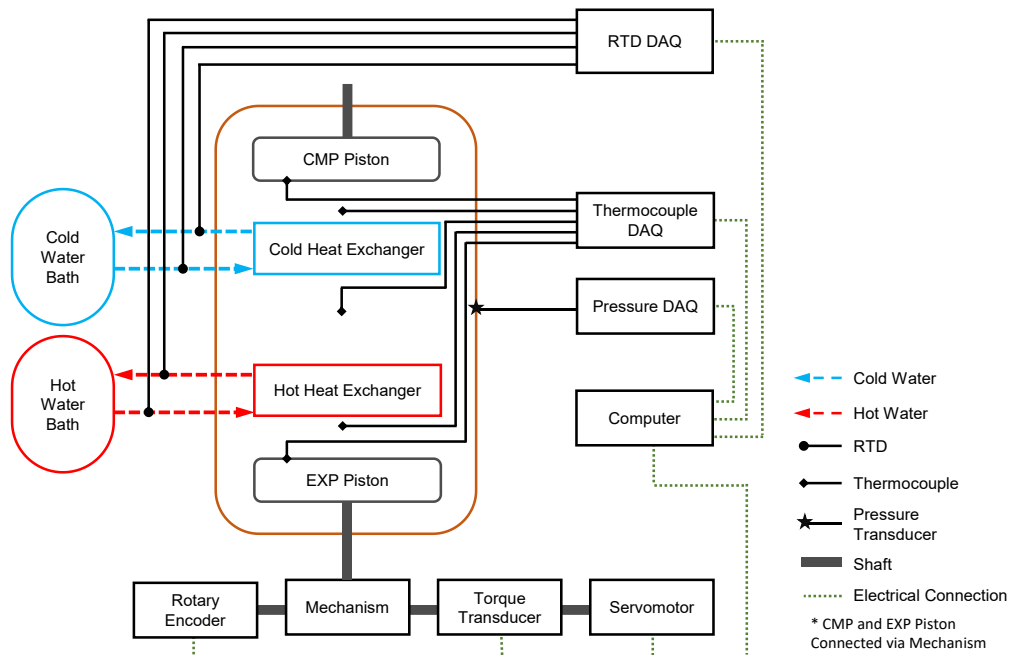
Figure 4-1: PID of the Opposed Piston Alpha Stirling Engine Experiment

The heating and cooling loops consisted of hot and cold circulating baths as the thermal source and sink, which circulated the fluid to the heat exchangers in the engine. The Opposed Piston Alpha (OPA) Mk III was the engine used for experiments. The temperature measurement system was comprised of five thermocouples, and four resistance temperature detectors (RTDs). The pressure measurement system included one differential pressure transducer. The power measurement system consisted of a torque transducer to determine the dynamic torque, and a rotary encoder to measure the engine crank angle. The motoring system utilized a servo-motor to drive the engine at specified speeds. Within the DAQ system, devices for measuring and digitizing the output of the RTDs, thermocouples, and pressure transducer were connected to the data collection computer. This section will provide an overview of the system, with a more detailed discussion about the individual measurement devices provided in Section 4.2.

4.1.1   Heating and Cooling Loop Systems

The heating and cooling loops consisted of two temperature controlled circulating baths: a 13 L bath (12101-41, Cole-Parmer Canada Company) and a 28 L bath (12111-21, Cole-Parmer Canada Company). The 13 L bath was used as the thermal source, because it required less time to heat the smaller volume of liquid, and the 28 L bath was used as the thermal sink. Water circulated through the heating and cooling loops to emulate a Stirling engine connected to a low-grade heat geothermal source below 100 °C.

To more accurately control the flow rate of the water baths, a peristaltic pump (MasterFlex L/S 7523-80, Cole-Parmer Canada Company) with two pump heads (one for each bath) was used, which was calibrated following the calibration procedure in the manual [82]. The water bath outlet lines ran through the peristaltic pump and continued into heat exchangers. Figure 4-2 shows an image of how the heating and cooling system was connected to the engine. Tubing with foam insulation was used to reduce the amount of heat transferred to the environment as the fluid passed through the tubes.
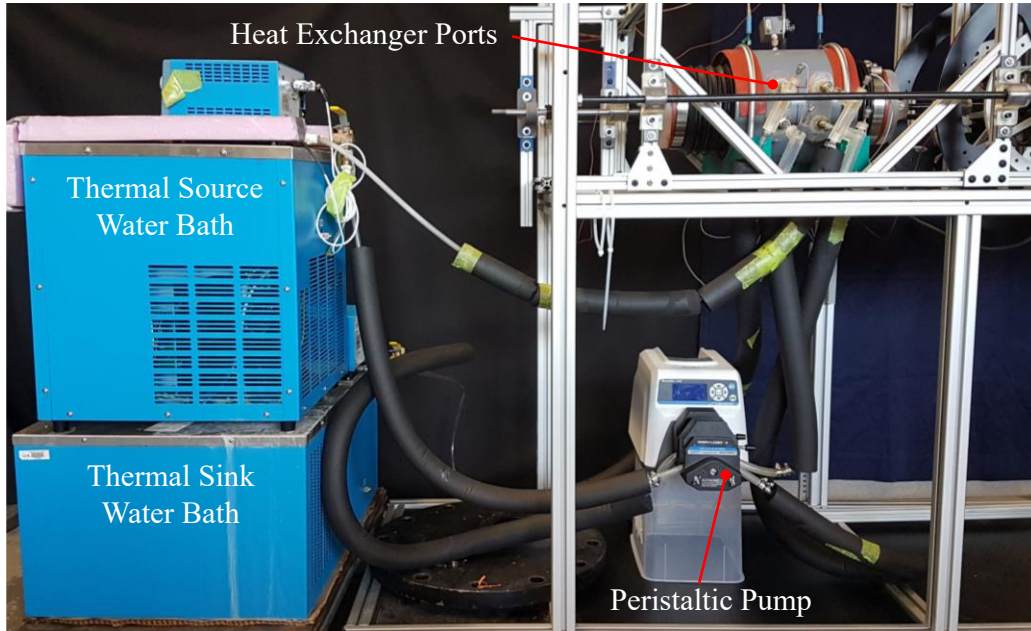
Figure 4-2: Photograph of the Experiment Heating and Cooling Loop

4.1.2 Engine Motoring System

The engine motoring system was connected to the engine in the event that the engine would not produce a net positive amount of power. Figure 4-3 shows an image of the engine motoring system, which included a torque transducer (TRS600, FUTEK Advanced Sensor Technology Inc.), coupled to a 1.2 Nm torque limiting coupler (MAGTORK MTL10-1/2, Magnetic Technologies LTD), with a servo-motor (ClearPath CPM-MCVC-3441S-RLN, Teknic Inc.) coupled to the other side.
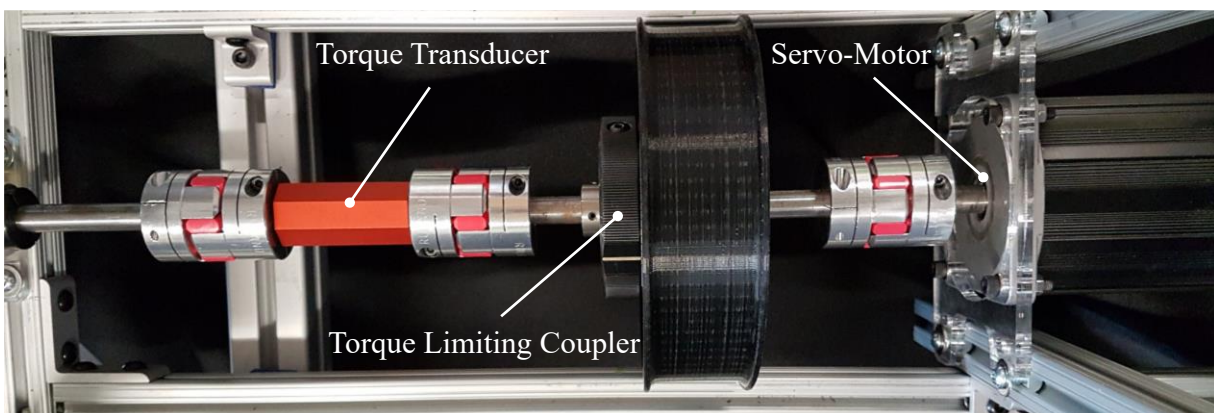
Figure 4-3: Image of the Engine Motoring System Instrumentation

A 1 Nm torque transducer was installed with the torque limiting coupler; however, if more than 1 Nm was required to drive the engine, a 10 Nm transducer could also be installed with the torque limiting coupler removed from the system. The engine motoring system could not be coupled directly to the engine output shaft as a result of the two Scotch yoke mechanisms on either side of the engine, so two 3D printed spur gears with a 1:1 gear ratio were used to connect the two parallel shafts.

4.2   Data Acquisition System

The data acquisition system consisted of instruments to measure the working fluid temperature and pressure, heater and cooler water temperatures, engine crank angle position, and engine torque. The instruments consisted of thermocouples, RTDs, a differential pressure transducer, rotary encoder, and torque transducer. These instruments were connected to the DAQ hardware, which digitized the sensor signals. The following section explains the individual measurement devices and DAQ system in further detail.

4.2.1   Thermocouple Measurements

Within the OPA MK III engine, five exposed junction type-T thermocouples (TTSS-116E-6, Omega Engineering Inc.) measured the internal gas temperature. The thermocouples had a range of 0 °C to 260 °C, and a bead diameter of approximately 1.575 mm (0.062 in), with a probe length of 152.4 mm (6.0 in). Figure 4-4 shows the approximate location and depth of the thermocouples inside the engine.
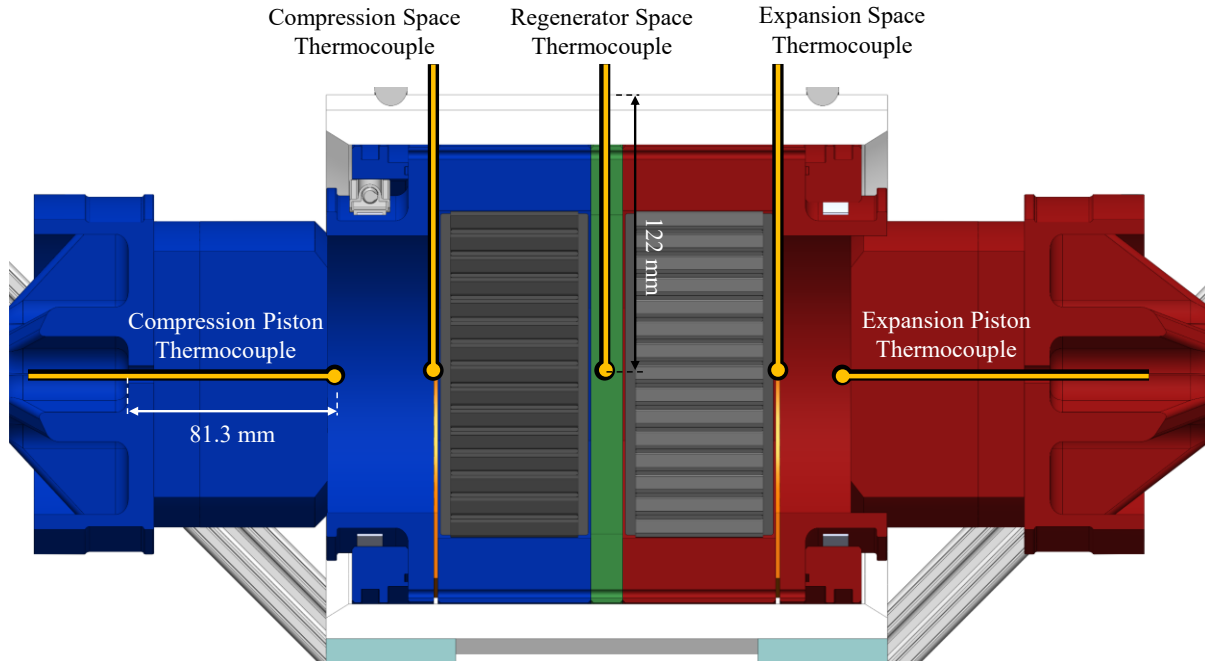
Figure 4-4: Schematic of the Thermocouple Locations and Insertion Depth

The thermocouples were located in the compression space near the cold radiator, in the regenerator space, and in the expansion space near the hot radiator. In addition, one thermocouple was embedded in the compression piston face, and another in the expansion piston face. The thermocouples located in the compression, expansion, and regenerator spaces were inserted radially into the engine body at depth of approximately 122 mm, measured from outer engine body, to be near the center of the engine. The thermocouples inside the piston faces were inserted a depth of approximately 81.3 mm, measured from the back face of the piston, such that the bead was beyond the face of the DVRCs, yet within the clearance space. An annotated drawing with the dimensions pertaining to the piston face and the location of the thermocouples is shown in Figure 4-5. As shown, the thermocouple was offset from the center by 35.25 mm, due to the piston shaft interference. Three thermocouple ports were incorporated into the design; however only one was used. The expansion and compression piston face thermocouples were positioned so that they were approximately collinear.
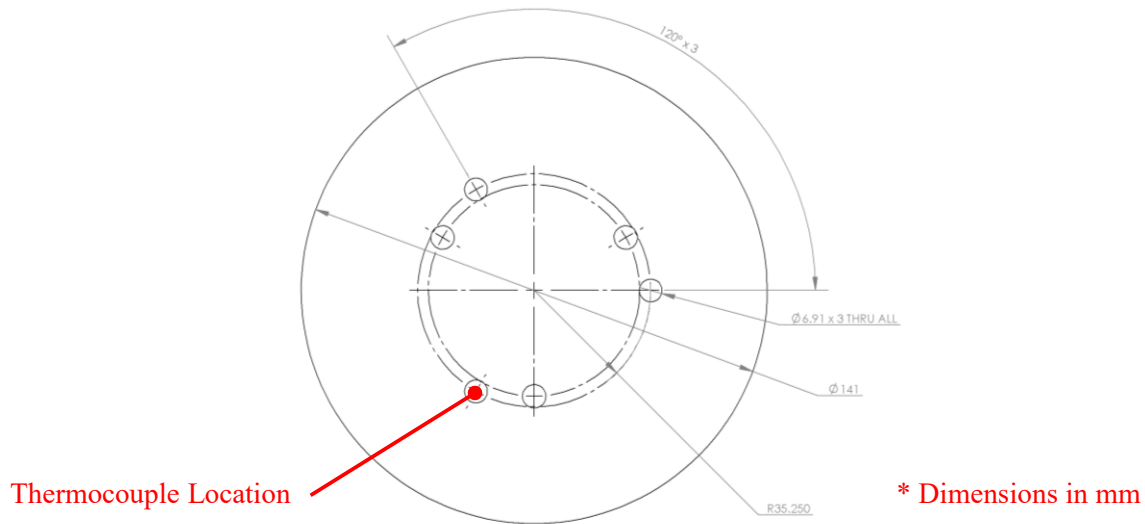
Figure 4-5: Annotated Drawing of the Piston Face Thermocouple Locations

The thermocouples were connected to a thermocouple terminal block (TC 2095, National Instruments Inc.), which transferred the signals to a low-noise chassis (SCXI 1000, National Instruments Inc.), with a data acquisition module (SCXI 1600, National Instruments Inc.) and a digitization module (SCXI 1102B, National Instruments Inc.) equipped. The signals were then passed to the data collection computer. The thermocouples were sampled at a rate of 5,000 Hz, which was more than twice the maximum engine frequency of 1 Hz, as per the sampling rate theorem [83]. The thermocouple response time was estimated to be slower than the cycle period, so only the mean temperature values were used. Due to the nature of oscillating flow, flow properties required for the calculation of the time response were not available.

4.2.2 RTD Measurements

Within the heating and cooling loop, four 3-wire RTDs (RTD-810, Omega Engineering Inc.) were located at the inlets and outlets of the hot and cold radiators. The RTD probe locations are shown in Figure 4-6. The RTDs were inserted into 3D printed 90° elbows, so that the water flowed along the length of the RTDs, which minimized the stem losses associated with conduction along the RTD sheath [84]. The RTDs were connected to a RTD temperature input module (NI-9217, National Instruments Inc.), which was connected directly to the data collection computer. The sampling rate for the water temperature readings was set to 100 Hz, since this was the maximum sampling rate of the input module with four RTDs simultaneously sampling [85].
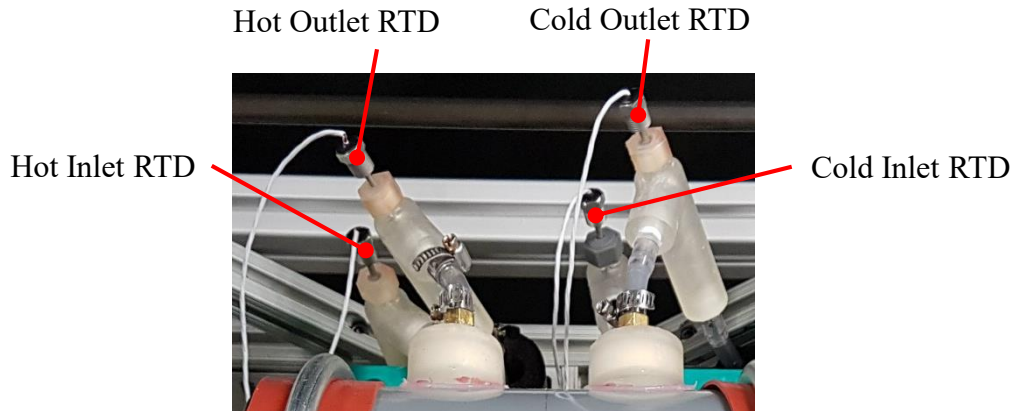
Figure 4-6: Image of the RTD Probe Locations in 3D Printed Elbow

4.2.3 Crank Angle Measurement

The angular position of the drive shaft was measured using a 500 pulse rotary encoder (15S-19M1-0500NV1ROC-F03-S1, Encoder Products Company). The encoder was connected to the drive shaft via a timing belt and a 60 tooth timing belt pulley. This arrangement can be seen in Figure 4-7. The encoder was aligned with the Z-pulse occurring when the expansion space was at the minimum volume.
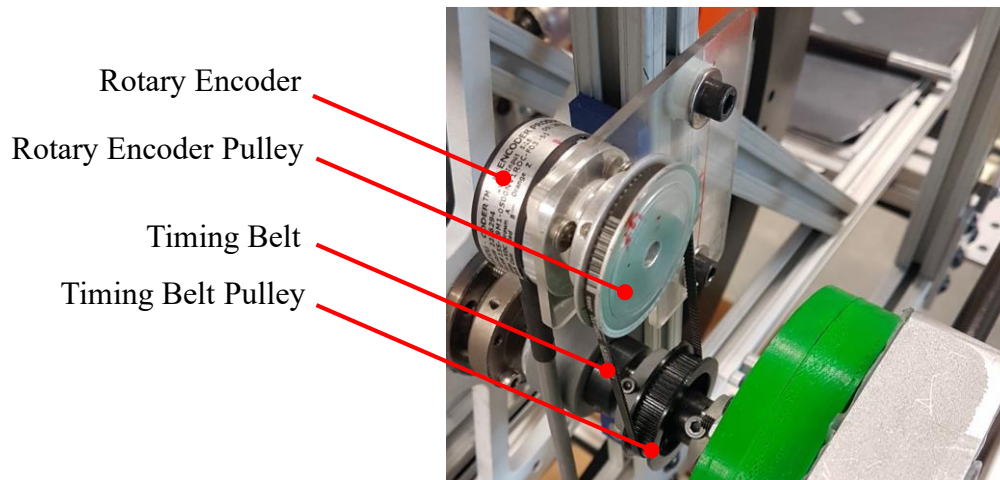
Figure 4-7: Image of the Crank Angle Measurement System

The encoder output three types of pulses, an A-pulse, a B-pulse, and a Z-pulse. Only the A- and Z-pulses were utilized, with the A-pulse having 500 pulses per revolution, and the Z-pulse having a single pulse per revolution. A power supply (GPD-3303S, GW Instek) was used to power the rotary encoder, and the supplied voltage was 5 V DC. Since the pulses were binary, the output

voltage was measured as either 0 V or 5 V depending on if the pulse was on or off. The voltages were sampled by a USB multifunction I/O device (USB-6211, National Instruments Inc.) which was connected to the data acquisition computer. At the fastest engine speed being tested, the rotary encoder would output 500 pulses/s. The voltage sampling rate was set to 10,000 Hz, which was sufficient to capture the pulses, since 20 samples were taken before a single pulse from the rotary encoder occurred.

4.2.4 Pressure Measurement

To measure the cyclic pressure variations, a differential pressure transducer (DP15-50, Validyne Engineering), with a diaphragm rated for 5 psi (DP15 3-36, Validyne Engineering), was positioned above the regenerator housing in the center of the engine body. The pressure transducer was connected to one channel in a multi-channel carrier demodulator (CD280-DUAL, Validyne Engineering). The pressure transducer was also connected to the same USB multifunction I/O device as the rotary encoder, and therefore had the same sampling rate of 10,000 Hz.

Since the Validyne pressure transducer measured differential pressure, one side of the transducer was connected to the engine via compression tube fittings, while the other end was exposed to atmospheric pressure. The atmospheric pressure during testing was also measured, as it was not constant between experiments. The atmospheric pressure was measured using the built-in pressure sensor in a mobile device (Galaxy S7, SAMSUNG) running the Science Journal application (Version 2.1.803, Google LLC), which was itself calibrated to the University of Alberta Mechanical Engineering Building's barometer calibration standard (Model not present) on different days. The atmospheric pressure measured on the mobile device on average measured the pressure 0.3 kPa below the barometer.

4.2.5 Torque Measurement

Within the engine motoring system, a non-contact rotary torque sensor (TRS600, FUTEK Advanced Sensor Technology Inc.) was used to measure the torque fluctuations. Either a 1 Nm or 10 Nm version of the same torque transducer was used depending on the requirements to drive the engine system at a designated speed. The torque measurement was sampled at 10,000 Hz, since it was sampled using the same USB multifunction I/O device as the pressure transducer and rotary encoder. In order to function, the transducer required an external power supply (GPD-3303S, GW

Instek) which provided an input of 20 V DC into the transducer. The transducer provided an output of ±5 V [86], depending on the direction of rotation, with 5 V being equivalent to the maximum rated torque of the transducer used (either 1 Nm or 10 Nm). Each transducer was factory calibrated, with the calibration certificates shown in Appendix A.

4.3   Instrumentation Calibration

The collected data needed to be an accurate representation of the measured quantities, so calibration of the instruments to a known standard was performed. This section explores the methods and procedures of the calibration process for the temperature and pressure instruments.

4.3.1   Thermocouple and RTD Calibration

Calibration was performed on the thermocouples and RTDs in the system. The compression space, regenerator space, and expansion space thermocouples were calibrated before the compression and expansion piston face thermocouple, since the piston face thermocouples were added after initial trial runs of the engine. The procedure for calibration was the same for both batches. Initially, the thermocouples and RTDs were placed next to a mercury filled thermometer (Ertco 1005-3S, Thermo Fisher Scientific), so that the effect of spatial temperature variation was minimized, as shown in Figure 4-8.

Figure 4-8: Image of the Thermocouple and RTD Bundle

The bundle was then submerged into either the 13 L temperature controlled water bath (12101-41, Cole-Parmer Canada Company), or the 28 L temperature controlled water bath (12111-21, Cole-Parmer Canada Company). The 28 L water bath was used to cool the water to temperatures below room temperature, while the 13 L water bath heated the water to temperatures above room temperature. This was done so that there was a dedicated heating and cooling unit, which reduced

the amount of time for the water baths to reach their set point temperature for the calibration procedure.

Temperature measurements were taken at 5 °C, 20 °C, 40 °C, 60 °C, 80 °C, and 95 °C, which were within the tested temperature range of the engine. The water baths were left at the set point for five minutes before inserting the thermocouple bundle, and then another five minutes surpassed before collecting any temperature data. The water bath temperature was recorded from both the water bath itself, and from the mercury filled thermometer. Then, data was collected for 10 seconds at 5000 Hz for the thermocouples, and at 100 Hz for the RTDs. A summary of recorded temperatures can be seen in Table 4-1 and Table 4-2.

Table 4-1: Workspace Thermocouple and RTD Calibration Readings

Set point [˚C]	Water Bath Reading [˚C]	Mercury Thermometer Reading [˚C]	Water Bath Used
5.00	5.00	4.40 ± 0.05	Cole-Parmer 12111-21
20.00	20.00	19.50 ± 0.05	Cole-Parmer 12111-21
40.00	40.00	39.70 ± 0.05	Cole-Parmer 12101-41
60.00	60.00	59.90± 0.05	Cole-Parmer 12101-41
80.00	80.00	80.70 ± 0.05	Cole-Parmer 12101-41
95.00	95.00	95.60 ± 0.05	Cole-Parmer 12101-41

Table 4-2: Piston Face Thermocouple and RTD Calibration Readings

Set point [˚C]	Water Bath Reading [˚C]	Mercury Thermometer Reading [˚C]	Water Bath Used
5.00	5.00	4.40 ± 0.05	Cole-Parmer 12111-21
20.00	20.00	19.70 ± 0.05	Cole-Parmer 12111-21
40.00	40.00	39.60± 0.05	Cole-Parmer 12101-41
60.00	60.00	60.00 ± 0.05	Cole-Parmer 12101-41
80.00	80.00	80.70 ± 0.05	Cole-Parmer 12101-41
95.00	94.80	97.40 ± 0.05	Cole-Parmer 12101-41

Five separate calibration curves were created, one for each of the thermocouples. They were created by plotting the non-calibrated thermocouple temperature measurement against the mercury thermometer temperature measurement. A linear fit was applied to each data set, resulting in a separate equation that was used to obtain the corrected value of temperature for each thermocouple. The linear fit equations and the coefficient of determination values, R^2, for each fit can be seen in Table 4-3. The thermocouples seemed to be under predicting the temperature by approximately

5 °C for the workspace measurements, and by approximately 3 °C for the piston face measurements. The thermocouple calibration curves are shown in Figure 4-9.

Table 4-3: Table of Thermocouple Fits and R^2 Values

Thermocouple Location	Linear Fit Equation [°C]	R^2 value
CMP Space, T_c	$T_{gas} = 1.005 \times T_c + 5.036$	0.9997
RGN Space, T_r	$T_{gas} = 1.005 \times T_r + 5.122$	0.9997
EXP Space, T_e	$T_{gas} = 1.007 \times T_e + 5.100$	0.9998
EXP Piston, T_{ep}	$T_{gas} = 1.027 \times T_{ep} + 3.144$	0.9990
CMP Piston, T_{cp}	$T_{gas} = 1.028 \times T_{cp} + 3.144$	1.0
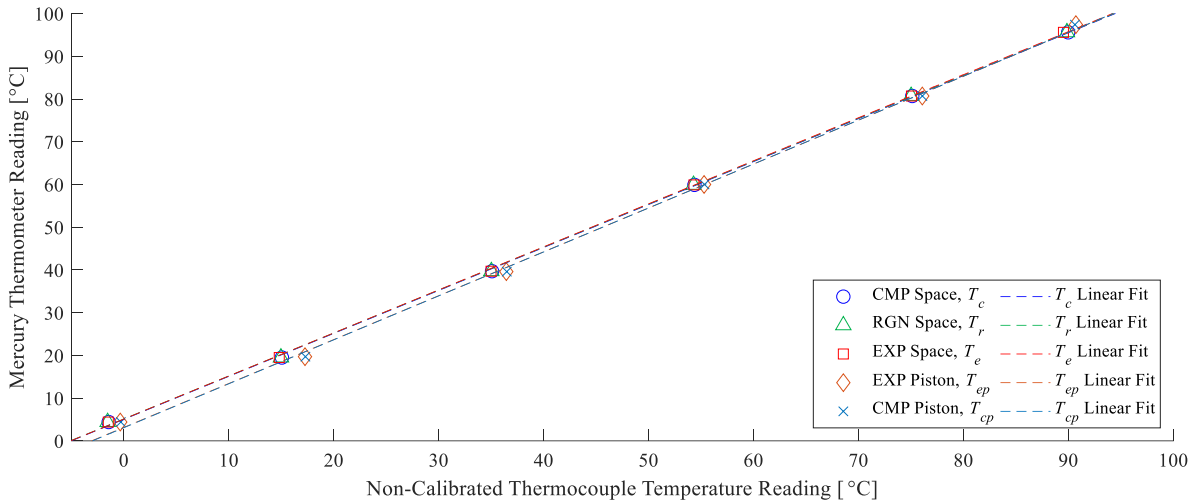
Figure 4-9: Calibration Curves for Thermocouple Probes

The same calibration procedure was applied to the four RTDs. A linear fit was applied to each data set, resulting in a separate equation that could be used to obtain the corrected value of temperature for each RTD. The linear fit equations and R^2 values for each RTD can be seen in Table 4-4. The RTD calibration curve is shown in Figure 4-10.

Table 4-4: Table of RTD Fits and R^2 Values

Thermocouple Location	Linear Fit Equation [°C]	R^2 value
Heater Inlet, $T_{h_{in}}$	$T_{H2O} = 0.9912 \times T_{h_{in}} - 1.218$	1.0
Heater Outlet, $T_{h_{out}}$	$T_{H2O} = 0.9884 \times T_{h_{out}} - 0.9127$	1.0
Cooler Inlet, $T_{k_{in}}$	$T_{H2O} = 0.9873 \times T_{k_{in}} - 0.3534$	1.0
Cooler Outlet, $T_{k_{out}}$	$T_{H2O} = 0.9888 \times T_{k_{out}} - 1.151$	1.0
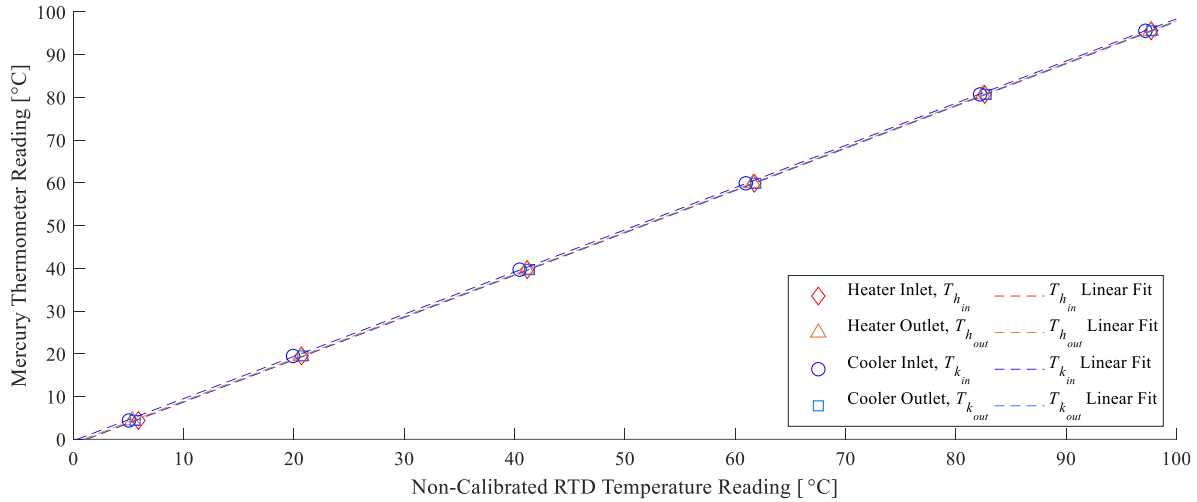
Figure 4-10: Calibration Curves for RTD Probes

4.3.2 Pressure Transducer Calibration

To calibrate the differential pressure transducer, a pressure transducer calibrator (DPI 603, GE Druck) was used to subject the transducer to specified pressures. Since the transducer was equipped with a diaphragm rated for 5 psi, it was decided that a pressure of 5 psi would equate to an output voltage of 10 V, making conversion between output voltage and pressure 0.5 psi/V. This was achieved by adjusting the zero control on the demodulator until the voltage was measured to be 0 V. Then, the span on the demodulator, was adjusted until the voltage reading was 10 V when subjected to a pressure of 5 psi. Units of psi were used instead of the SI equivalent units due to the specifications of both the pressure transducer and calibration device being expressed in units of psi. The span was checked by subjecting the transducer to pressures between 0 and 5 psi in 0.5 psi increments. As the calibration pressures were increased in this range, samples were collected for 5 seconds at 10,000 Hz. The results were averaged, and used to create a calibration/conversion curve that was applied to future pressure measurements. The data was fitted with a linear polynomial, since the relationship between pressure, P, and the pressure voltage reading , P_{volt} , was expected to be linear. The equation of the fit is shown in Equation 4-1 with an R^2 value of 1.

$$P = 0.4984 \times P_{volt} + 0.0089$$
<div align="right">4-1</div>

The pressure transducer was then post-calibrated once the experiments were complete, to reduce the calibration uncertainty, which was approximately 0.225 psi with the Druck. The

original calibration procedure was performed again, so the transducer was subjected to approximately the same pressures with the Druck calibrator, to ensure that the transducer readings did not shift significantly.

For the post-calibration, a manometer was built to calibrate the transducer [87]. A plastic tube partially filled with distilled water was suspended such that a water column height of 3.52 m was possible. One end of the tube had a free surface exposed to atmosphere and the other end was attached to the transducer, with a u-bend in between. The free-surface end of the manometer was raised and lowered to subject the transducer to different pressures between 0 psi and 5 psi in 0.5 psi increments. The pressure was first increased to the 5 psi, then decreased back to atmospheric pressure. At each increment, the height between the two menisci was measured, and samples were taken at 10,000 Hz for 5 s. The manometer pressure was calculated using the fundamental pressure relationship shown in Equation 4-2, which is valid at standard conditions. The gage pressure, P_{gage}, is dependent on the density of the fluid, ρ, gravity, g, and the height of the water column, h.

$$P_{gage} = \rho g h \qquad\qquad 4\text{-}2$$

Since the measurements were not taken at standard conditions, the measured water column height was corrected by applying correction factors for the density and gravity, so that Equation 4-2 could be used with standard values for density and gravity [88]. The corrected height was calculated using Equation 4-3 [88], where the subscripts o and l represent the standard conditions and local conditions respectively.

$$\rho_l g_l h_l = \rho_o g_o h_o \qquad\qquad 4\text{-}3$$

An updated calibration curve was then created. The resulting calibration equation is shown in Equation 4-4, with an R^2 value of 1. Figure 4-11 shows the three calibration curves, with the manometer curve being used for post calibration, where it can be seen that the fits line up closely.

$$P = 0.5021 \times P_{volt} - 0.0249 \qquad\qquad 4\text{-}4$$
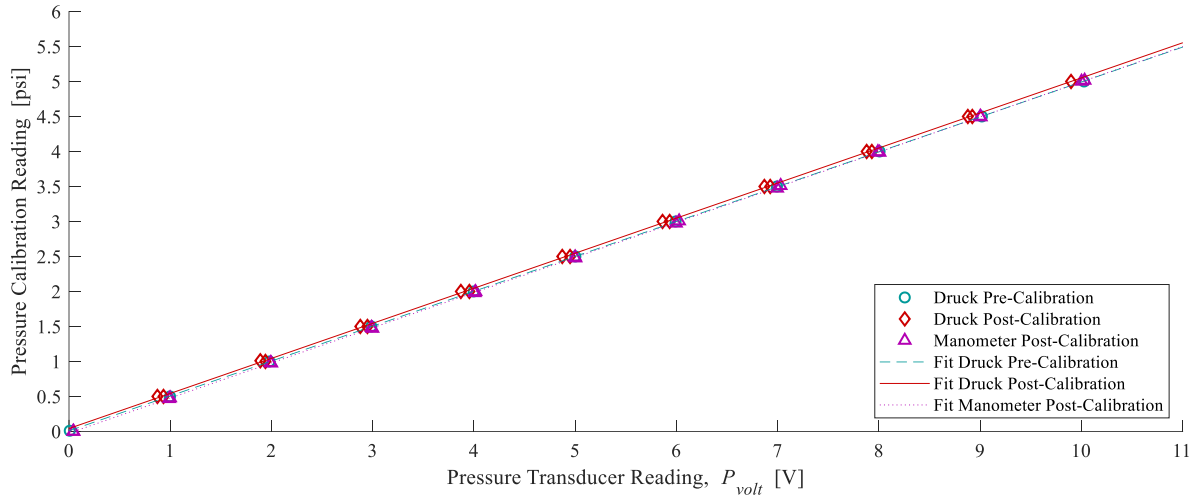
Figure 4-11: Calibration Curves for the Differential Pressure Transducer

A sample pressure curve showing the uncertainty bounds on pressure for the initial Druck calibration procedure compared to the manometer post-calibration can be seen in Figure 4-12. By using the manometer post-calibration, the uncertainty in pressure was reduced by an order of magnitude.
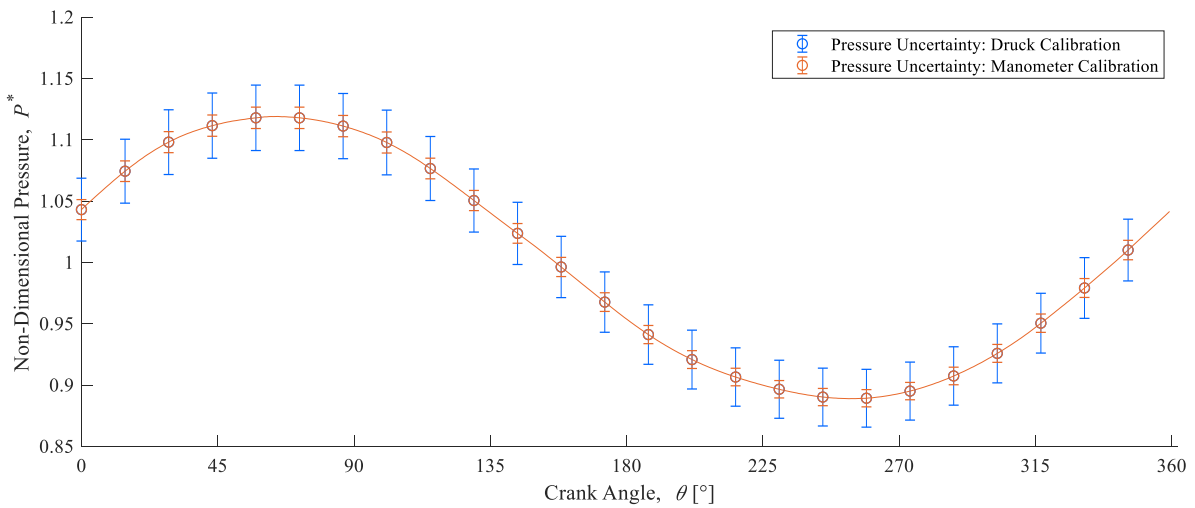
Figure 4-12: Plot Comparing the Reduction in Uncertainty Bounds for Pressure when Post-Calibrating with a Manometer

4.4 Experiment Procedure

An experiment procedure was developed to ensure the collected data was consistent and repeatable between tests, which were often performed on different days for a few weeks due to the time required for testing. An experiment plan was created to thoroughly document the amount of tests performed, and which variables were manipulated or controlled in the experiment. Then an engine warm-up period and a time to steady state were established, so that the engine reached a consistent state for testing based on the temperature, pressure, and torque fluctuations in the engine. After the engine was warmed-up, an established procedure was followed.

4.4.1 Experiment Plan

To properly plan the experiment procedure, the manipulated, controlled, and responding variables were selected. The manipulated variables were the expansion (EXP) piston stroke length, the compression (CMP) piston stroke length, the phase angle that the expansion piston leads the compression piston, and the average angular velocity of the engine when driven with an electric motor. The stroke length was varied between three different configurations, as shown in Table 4-5.

Table 4-5: Manipulated Stroke Length Combinations

Configuration Number	Compression Stroke [mm]	Expansion Stroke [mm]	Engine Swept Volume [L]
1	50.8	50.8	1.564
2	50.8	76.2	1.955
3	76.2	76.2	2.346

The combination of a 76.2 mm compression stroke and a 50.8 mm expansion stroke was not performed since more work would be required to compress the gas than would be extracted from expansion. These stroke combinations directly change the amount of volume swept in the engine, as shown in Table 4-5. The phase angle was varied between 120° and 180° in 5° increments to find an experimental optimum for an LTD alpha Stirling engine, which has been suggested within the chosen range in the literature using numerical simulations [55], [89], as well as from the initial first order estimate of the OPA MK III in Section 3.6.5. The rotational velocity was manipulated using the Teknic motor, and was varied between 30 rpm and 60 rpm in 10 rpm increments. This range was chosen, since at 30 rpm, the engine was close to the stall point when no thermal input was present, and 60 rpm was selected as it was near the loaded operating speed for a LTD gamma-type engine built in the same research group with the similar operating

conditions [48]. The stroke lengths were varied, as there were no clear studies found on the effect of changing the stroke length, or having differing stroke lengths in a LTD alpha Stirling engine. The engine speed was also manipulated to see if a slower speed would noticeably increase the heat transfer by increasing the time for heat transfer. Table 4-6 provides a summary of the manipulated variables, and shows the amount of levels (combinations) each variable has.

Table 4-6: Summary of Manipulated Variables

Parameter	Units	Min Value	Max Value	Increments	Levels
EXP Stroke	mm	50.8	76.2	25.4	2
CMP Stroke	mm	50.8	76.2	25.4	2
Angular Velocity	rpm	30	60	10	4
Phase Angle	°	120	180	5	13

The controlled variables were the thermal source and sink temperatures, and the water volume flow rate. The set point temperature of the cold water bath was selected to be 2 °C, whereas the set point temperature of the hot water bath was selected to be 95 °C. These temperatures were selected since water boils at 97.8 °C and freezes at 0 °C at the elevation of the city of Edmonton, Alberta, Canada [90], therefore, to remain at the liquid phase yet maximize the temperature difference, a few degrees above the freezing point and below the boiling point of water was selected. To more accurately control the flow rate, the peristaltic pumps were used and set to 1.983 LPM after calibration, which was the auto calibration value for 2 LPM that appeared after following the calibration procedure in the manual [82]. A summary of the controlled variables may be seen in Table 4-7.

Table 4-7: Summary of Controlled Variables

Parameter	Value	Units
Thermal Source Temperature	95.0	°C
Thermal Sink Temperature	2.0	°C
Water Volume Flow Rate	1.983	LPM

The responding variables that were measured were the crank angle position, the engine pressure, the engine gas temperature, the heater and cooler inlet and outlet temperatures, and the torque input. With these variables, it was possible to calculate parameters such as the shaft power, engine volume variation, and indicated work, which were used to quantify the engine performance at different operating conditions.

The uncontrolled variables included the daily uncorrected atmospheric pressure at the elevation of the city of Edmonton, Alberta, Canada, as well as the room humidity and temperature.

The local uncorrected atmospheric pressure was recorded before each experiment for future use in data processing.

With the manipulated, controlled, and responding variables known, it was possible to construct an experiment plan using a full factorial experiment, which allows for the testing of all possible combinations of manipulated variables [91]. Since there were 3 levels tested for the piston stroke combination, 4 levels for the angular velocity, and 13 levels for the phase angle, this equated to an experiment with 156 runs. No additional replicates were performed for the exact same test, since it was difficult to obtain comparable results over a long period of time, and the instrumentation needed to be dismantled from the engine and DAQ system for other experiments; however, multiple engine cycles were recorded.

Complete randomization between each individual run was not performed, since the time to complete the experiment would greatly increase if the phase angle and stroke had to be changed between each run, as it took approximately 10 minutes to change them. Therefore, each phase angle was assigned a value, and then a random number generator created in Microsoft Excel was used to sort the order of the phase angle experiments. The stroke length combination was not completely randomized, since that would require the stroke to be changed between tested angular velocities, which would also greatly increase the time to run the 156 experiments. Therefore, each stroke combination was selected at random, but would stay the same until all the angular velocity tests were completed at random using a random number generator. The experiment plan is shown in Appendix B.

4.4.2 Warm-up Period and Cyclic Steady State Justification

To develop a consistent experiment procedure, it was necessary to determine the time required for the engine to initially become thermally stable, and to know the time taken for the engine to attain a cyclic steady state. First, the water baths were set to their set point of 2 °C and 95 °C. Once the baths reached the set point temperatures, the water was circulated through the engine for approximately 15 minutes, after which the peristaltic pump was engaged at 1.983 LPM. After this initial cycling of water, the warm-up period and the time to reach cyclic steady state were found.

4.4.2.1   Warm-Up Period Justification

The warm-up period was defined as the point in time that the average internal gas temperature measurements reached a steady state, neglecting the expected cyclic oscillations in temperature. To determine this, the engine was driven at a speed of 50 rpm, with 76.2 mm stroke lengths for both pistons, and set to a phase angle of 180°, such that the air in the engine was being shuttled through the radiators without compression or expansion. The thermocouple embedded in the face of the expansion piston was used to determine the warm-up time, since at the location it was measuring, the temperature took the longest to converge to a steady average temperature. The temperature was sampled for 20 s at 10 minute intervals until the 40 minute mark, after which samples were taken every 5 minutes until an hour was reached. The graph shown in Figure 4-13 was produced to determine the warm-up period. It should be noted that the data points are connected for visual aid, and not because the data is implied to be continuous.
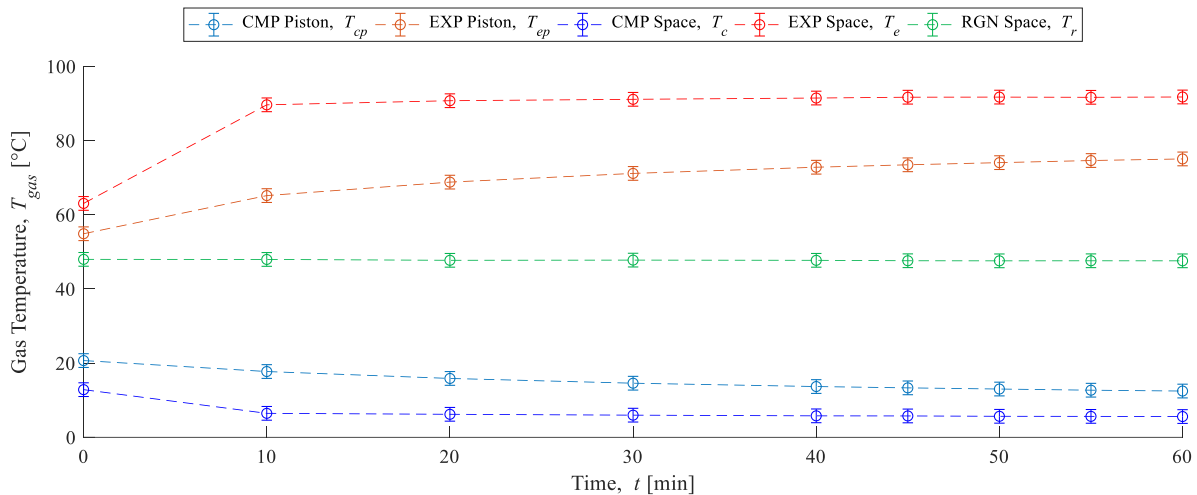
Figure 4-13: Measured Gas Temperatures During Warm-Up Period

After the 15 minute water bath circulation period, the measured gas temperatures did not reach their settled value. The live data stream of gas temperatures continued to change noticeably at the data acquisition computer when performing the experiment (where the uncertainty was not displayed) until approximately 40 minutes, when the gas temperatures began to converge. Therefore, to be conservative, the warm-up period was selected to be 45 minutes after the 15 minute water bath circulation. The rate of change in temperature with respect to time of the expansion piston thermocouple and compression piston thermocouple, between 45 and 50 minutes, were approximately $+ 0.116$ °C/min and $- 0.063$ °C/min, respectively. The error bars in Figure

4-13 were added post collection and will be explained further in Section 4.6. From them, it can be seen that after approximately 20 minutes, the change in temperature was not significant, therefore, the 45 minute warm-up period was deemed a sufficient length.

4.4.2.2   Cyclic Steady-State Justification

After the warm-up period was determined, the time required for the engine to reach a cyclic steady state between tests was examined. It was decided to test the time required to reach steady state at a phase angle of 150°, and at an engine speed of 60 rpm. Each stroke length combination was tested, since this would change the amount of volume that was swept through the heat exchangers. The phase angle of 150° was chosen as there was enough compression to observe when the pressure fluctuations become steady, yet not so much that the engine could be damaged over the length of the test. An engine speed of 60 rpm was selected so as to be conservative, since it gave the least amount of time for heat transfer out of the speeds that were tested.

The engine was first driven open to atmosphere. When the mean engine pressure was at a point where the oscillations were approximately symmetric, the valve to the engine was closed, and the test commenced for a duration of 300 seconds. This initial priming of the engine was going to be performed before all future experiments, and was therefore included during this experiment. After the data was collected, a period of approximately 10 minutes elapsed between subsequent tests, so that the air inside the engine could cool down before the next test was initiated.

The steady state justification experiment was performed before and after the warm-up period discussed in Section 4.4.2.1, so as to highlight the importance of the warm-up period before collecting data. Figure 4-14 shows the internal gas temperatures collected by the thermocouples before the warm-up procedure, for the swept volume of 2.346 L. From the plot, it appears that within 300 seconds, the temperatures reached a cyclic steady state, except the temperature measured by the thermocouple embedded into the expansion piston. This appears to indicate that 300 seconds was not sufficient for the gas further away in the workspace to approach a steady temperature.
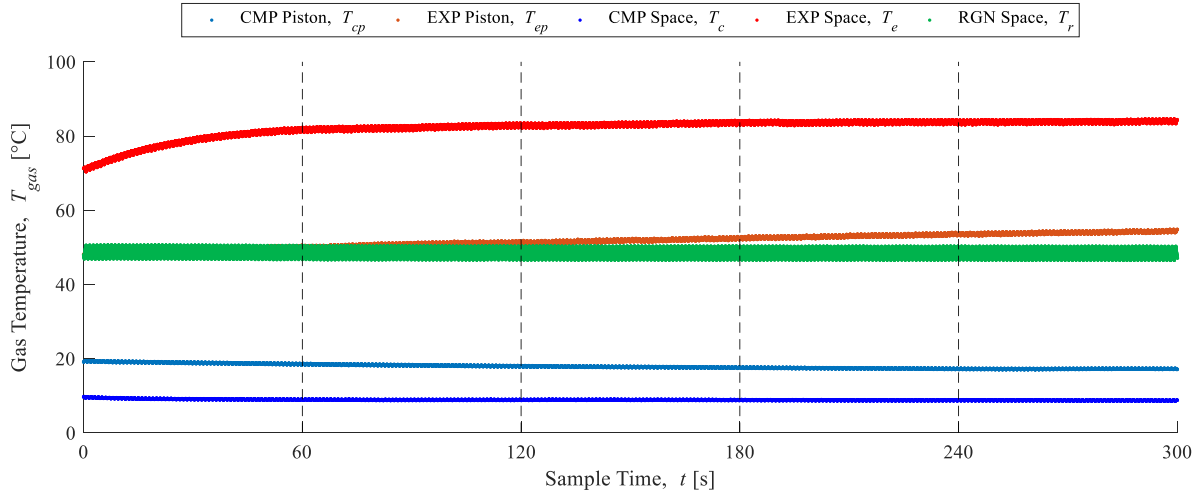
Figure 4-14: Thermocouple Gas Temperature Readings, Before Warm-Up Procedure

After the warm-up period, the same test was performed. Figure 4-15 shows the thermocouple gas temperature readings after the warm-up period for an engine swept volume of 2.346 L. It can be seen that the expansion and compression space temperatures have almost reached their peak after the warm-up period, and the temperature measured at the expansion piston face has increased significantly. From this data, a cyclic steady state time was selected to be 180 seconds after the mean engine pressure was stabilized to be conservative, since after approximately 120 seconds there was an insignificant change in temperature. The plots for the other swept volume configurations showed the same trends, and are shown in Appendix C. Torque and pressure plots for each swept volume configuration during the final 60 s of the test are shown in Appendix C.
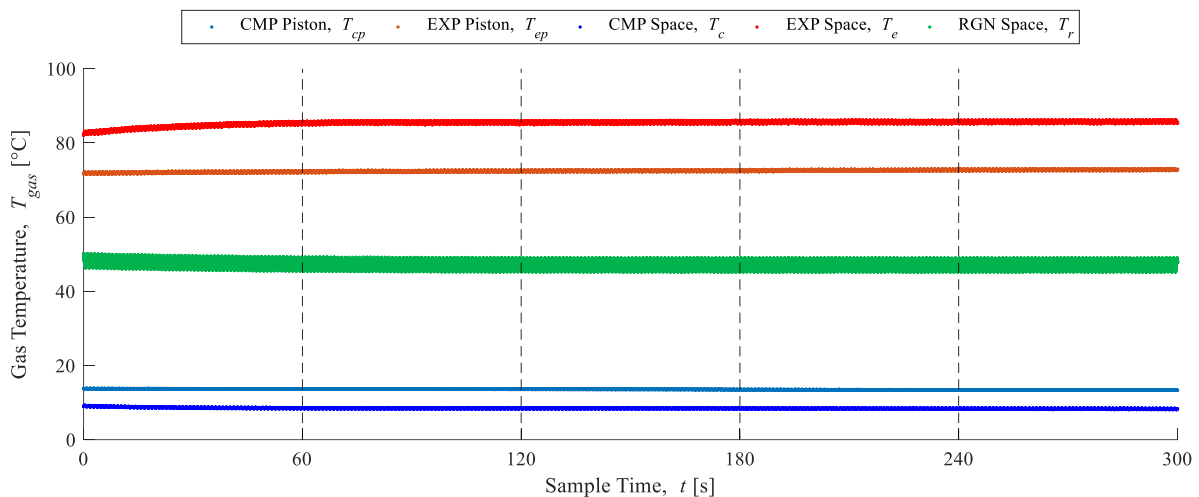
Figure 4-15: Thermocouple Gas Temperature Readings, After-Warm Up Procedure

4.4.3   Baseline Experiment Procedure

In order to confirm any performance improvement as a result of selected combinations of manipulated variables, baseline experiments for the OPA were performed without any thermal input into the system. The engine was driven with the Teknic servo-motor with the goal of calculating the power required to drive the engine at specified speeds, phase angles, and strokes. These results would then be compared with the thermal experiments. The procedure used to perform the baseline tests is listed as follows:

1. The desired phase angle and strokes for the expansion and compression pistons were set.
2. The engine pressure port was open so that the internal pressure was equal to the atmospheric pressure. The engine was then driven with the Teknic servo-motor at the desired speed, and the valve was closed gradually until the pressure oscillations were approximately symmetric.
3. The engine was then motored for approximately 3 minutes. This was sufficient time for the temperature readings inside the engine to settle as well as the torque fluctuations.
4. Voltage data was collected at a sampling rate of 10,000 Hz for a sample time of 20 s.
5. Thermocouple measurements were collected at a sampling rate of 5,000 Hz for a sample time of 20 s.
6. RTD measurements were collected at a sampling rate of 100 Hz for a sample time of 20 s.
7. The other speeds being tested were cycled through based on the random testing order.
8. After the data was collected, the engine was stopped, and the stroke lengths were changed depending on the test order shown in Appendix B.
9. The procedure was repeated until all stroke and speed combinations were tested for the specified phase angle.
10. The phase angle was changed based on the testing order and the process was repeated.

4.4.4   Thermal Experiment Procedure

After the baseline experiments were completed, a new set of experiments was performed in which hot and cold water was circulated in the heat exchangers, creating a thermal source and thermal sink. The thermal procedure was similar to the baseline procedure, with some exceptions, and is listed as follows:

1. The hot water bath was set to 95 °C and the cold water bath was set to 2 °C. The water baths reached the set temperatures in approximately 40 minutes.
2. Once at temperature, the water was circulated into the engine using the internal water bath pumps for 15 minutes for an initial heat exchanger warm up.
3. The warm-up period was performed. The engine was cycled at a phase angle of 180° with a 76.2 mm stroke on both the compression and expansion piston at 50 rpm for approximately 45 minutes, until the expansion piston thermocouple read approximately 70 °C.
4. The desired phase angle being tested was set.
5. The stroke lengths were changed to obtain the desired engine swept volume.
6. The peristaltic pumps were powered on to control the water volume flow rate at 1.983 LPM.
7. The engine was open to atmosphere and then driven with the servo-motor at the desired speed. The valve was closed gradually until the mean pressure stabilized and the pressure fluctuations were approximately symmetric.
8. With the servo-motor was disconnected, a manual attempt was given, where the engine was cycled by spinning the flywheel for a few minutes to see if the engine would run without being driven.
9. The experiment commenced by driving the engine for the cyclic steady state time of 3 minutes.
10. Voltage data was collected at a sampling rate of 10,000 Hz for a sample time of 20 s.
11. Thermocouple measurements were collected at a sampling rate of 5,000 Hz for a sample time of 20 s.
12. RTD measurements were collected at a sampling rate of 100 Hz for a sample time of 20 s.
13. The other speeds being tested were cycled through based on the random testing order.

14. After the data was collected, the engine was stopped and the stroke lengths were changed depending on the test order.

15. The procedure was repeated until all stroke and speed combinations were tested for the specified phase angle.

16. The phase angle was changed based on the testing order, and the process was repeated.

4.5   Data Processing

MATLAB was used to import, process, and present the raw data. This section presents samples of the raw data, introduces some of the techniques used to process the data into useful information, explains some of the non-dimensional parameters used, and shows how the engine volume variations, dead volumes, and bellows volume variations were quantified.

4.5.1   Raw Data

After data collection, the raw data needed to be processed so that it could be interpreted. The data files contained information about the voltage readings of the rotary encoder, pressure transducer, and torque transducer. A sample of the raw voltage for pressure and torque is shown in Figure 4-16. It can be seen that the pressure and torque measurements were consistent during the course of the sample time.
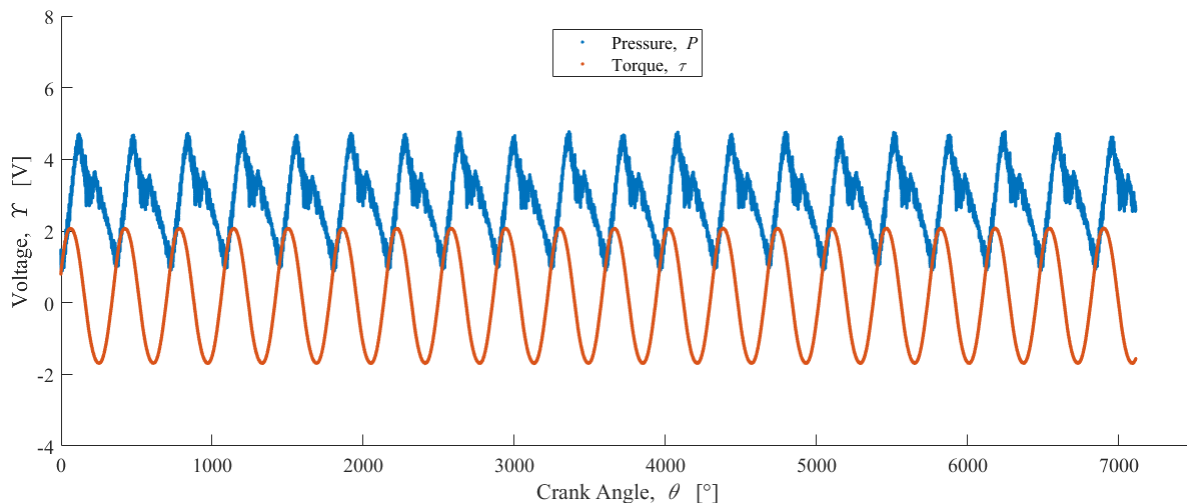
Figure 4-16: Sample Raw Voltage Plot, Excluding Rotary Encoder Pulses

In addition to the voltage readings, thermocouple and RTD measurements were taken with their respective DAQ devices. Sample raw temperature readings for the thermocouples are shown in Figure 4-17, and in Figure 4-18 for the RTDs. Fluctuations can be seen in the sample thermocouple data; however as discussed in Section 4.2.1, the time response of the thermocouples was slow and only mean temperature measurements were used. For the RTD measurements, the difference between inlet and outlet temperatures can be seen where the outlet of the heater had a

reduced temperature compared to the inlet, and the outlet of the cooler had increased in temperature.
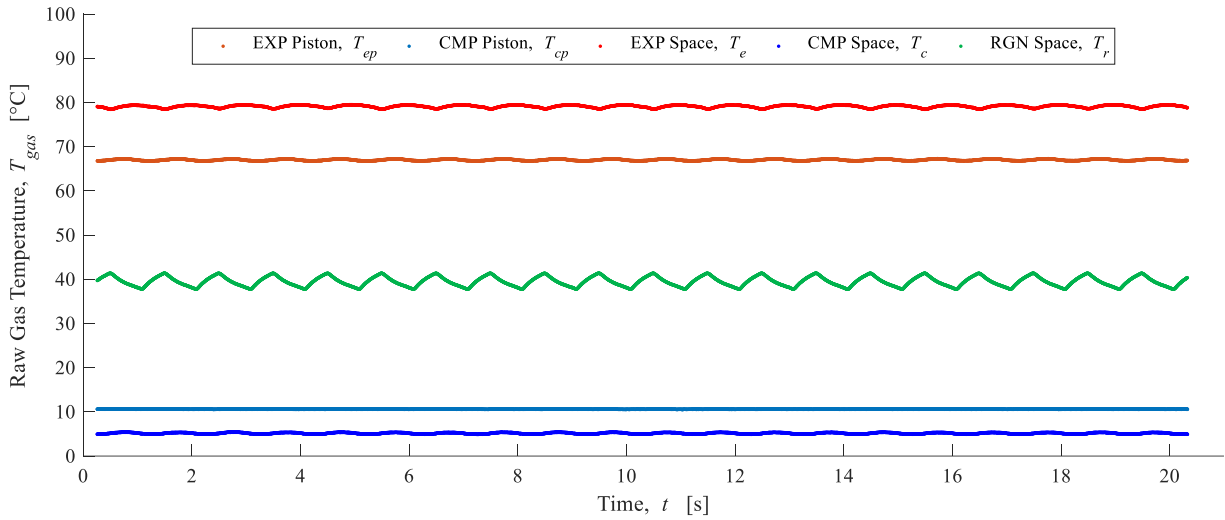
Figure 4-17: Sample Raw Thermocouple Gas Temperature Measurements
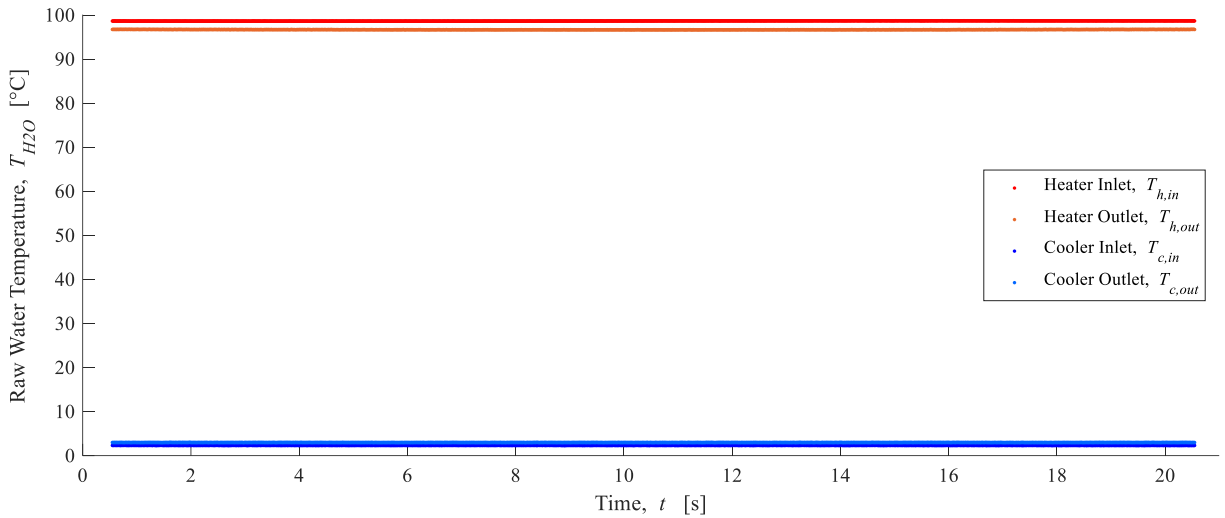
Figure 4-18: Sample Raw RTD Water Temperature Measurements

4.5.2 Torque Filtering

During testing, the engine was driven by a servo-motor maintaining the engine velocity. While the velocity fluctuated about the set-point, the applied torque fluctuated as well in response. When viewing a sample plot of the torque fluctuations for one cycle, noise can be seen in the

signal. This noise could be attributed to the servo-motor response, background electrical noise from DAQ devices and other sources, or backlash in the gearing system.

A built-in smoothing algorithm in MATLAB was applied to the torque signal, so that the random noise present in the signal was attenuated. A zero-phase, 10-point moving average filter was used to suppress the effect of noise using the *filtfilt* function in MATLAB [92]. The *filtfilt* function countered the phase lag associated with moving average filters [92], and with a lower number of neighboring points used the peaks were not attenuated as much, but still filtered out the noise. The moving average filter was well suited for reducing random noise while also being simple to implement, but it has poor frequency filtering [93]. A sample plot comparing the raw signal for one cycle and the filtered signal is shown in Figure 4-19, where the noise reducing effect of the filter can be seen.
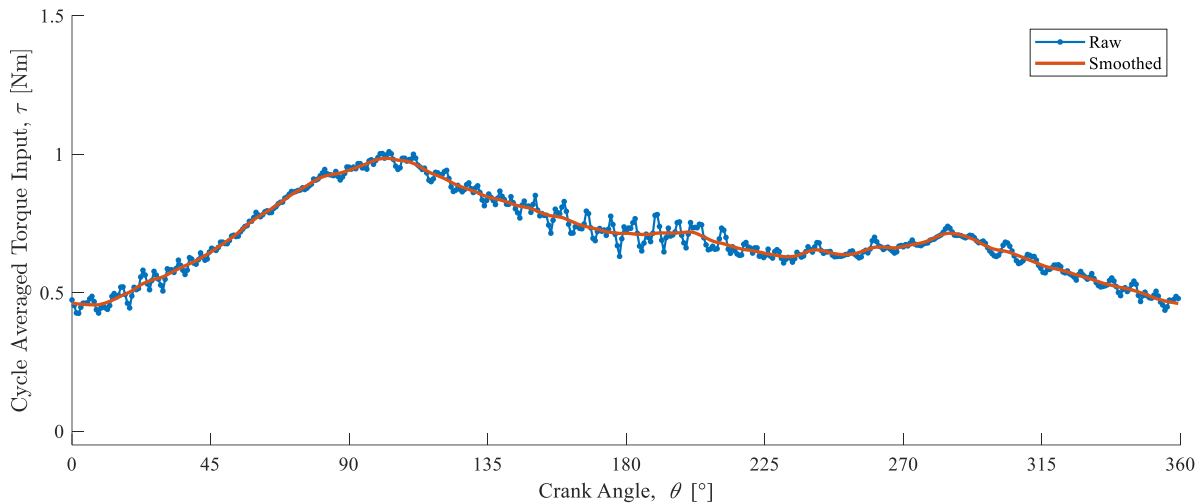
Figure 4-19: Moving Average Filter Applied to Cycle Averaged Torque

Since the torque data was used to calculate the average power input, the effect of filtering was investigated by calculating the power input using both the filtered and non-filtered torque data. It was found that the smoothing resulted in at most an average difference in power input of 0.03 W. Therefore, for the purposes of visualizing the torque fluctuations and calculating the power input, the smoothing was considered to have a negligible effect.

4.5.3 Cycle Averaging Data

After the raw data was processed, it was separated into individual cycle data sets. The consistency of the data was checked, and the number of captured cycles, after trimming the incomplete cycles, was recorded. The incomplete cycles were trimmed by removing the data before the first *Z*-pulse and after the last *Z*-pulse of the rotary encoder. The data was then cycle averaged, so that conclusions about the overall cycle performance of the engine could be determined. Cycle averaging was performed by taking the mean value of the data across each cycle at the same encoder increment. Once completed, the output was a single vector of cycle averaged data for one cycle. This was performed for pressure, torque, and angular velocity measurements. Figure 4-20 shows a sample of the individual cyclic pressure fluctuations of the engine for 18 cycles. The individual data sets overlap with each other with negligible deviation from cycle to cycle, justifying the cyclic averaging process. Figure 4-21 also shows a sample of 18 cycles of the smoothed torque fluctuations, which were also cycle averaged. Both figures consist of individual plotted data points.
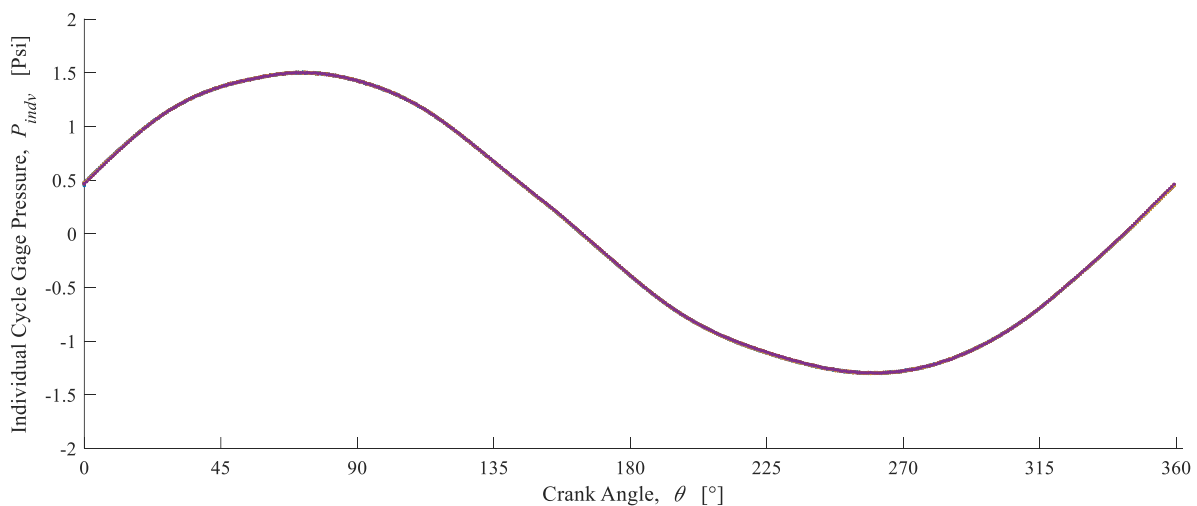
Figure 4-20: Individual Cycle Gage Pressure Fluctuations for Cycle Averaging
(18 Curves Plotted)
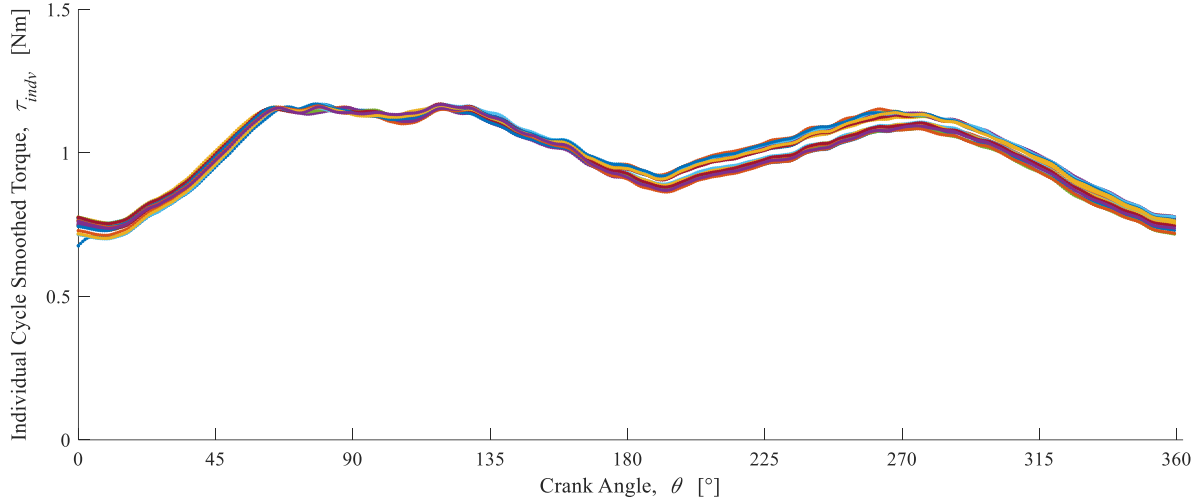
Figure 4-21: Individual Cycle Smoothed Torque Fluctuations for Cycle Averaging
(18 Curves Plotted)

4.5.4 Non-Dimensional Parameters

Throughout the analysis, a number of non-dimensional parameters were used to either quantify performance, or to facilitate comparisons between experiments. A non-dimensional pressure, P^*, was used to compare pressure fluctuations, P, between experiments. The pressure fluctuations were divided by the mean pressure of the cycle, P_{mean}. Thus, when comparing pressures, the mean cycle pressure will always be located at a value of 1. The expression for non-dimensional pressure is shown in Equation 4-5. The non-dimensional buffer pressure, P^*_{buffer}, was formulated the same way, using the measured atmospheric pressure, P_{atm}, as shown in Equation 4-6.

$$P^* = \frac{P}{P_{mean}}$$
4-5

$$P^*_{buffer} = \frac{P_{atm}}{P_{mean}}$$
4-6

A non-dimensional volume, V^*_{eng}, was used to differentiate between the configurations tested by dividing the volume fluctuation, V_{eng}, by the engine swept volume, $V_{sw_{eng}}$, as shown by:

$$V^*_{eng} = \frac{V_{eng}}{V_{sw_{eng}}}$$
4-7

By doing so, the amount of dead volume in the system could be visualized when comparing engine volume.

Similar definitions were used for the non-dimensional expansion space volume, V_e^*, and compression space volume, V_c^*, shown in Equations 4-8 and 4-9. The respective volume fluctuations and swept volumes for the workspace were used in the equations.

$$V_e^* = \frac{V_e}{V_{swe}} \tag{4-8}$$

$$V_c^* = \frac{V_c}{V_{swc}} \tag{4-9}$$

The ratio between the cycle pressure maximum, P_{max}, and minimum, P_{min}, was used as a non-dimensional pressure ratio, Γ, expressed as:

$$\Gamma = \frac{P_{max}}{P_{min}} \tag{4-10}$$

This ratio was used to quantify the pressure amplitudes in each experiment.

The compression ratio, CR, expressed as:

$$CR = \frac{V_{max}}{V_{min}} \tag{4-11}$$

was calculated for each engine configuration as the ratio of the maximum volume, V_{max}, to the minimum volume, V_{min}. This expression provided an understanding of the amount of compression in each configuration, which varied with phase angle and stroke combination.

4.5.5 Engine Volume Variations

The total engine volume variation, V_{eng}, was separated into five individual volumes: the expansion space, V_e, the compression space, V_c, the heater gas volume, V_h, the regenerator space, V_r, and the cooler gas volume, V_k. By adding the individual volumes of the engine, it was possible to calculate the total engine volume as:

$$V_{eng} = V_e + V_c + V_h + V_r + V_k \tag{4-12}$$

The heater, cooler, and regenerator volumes were considered dead volumes, as they were not volumes directly swept by the power pistons [14], and they did not vary throughout the cycle

as a function of crank angle, θ. The expansion space and compression space did vary throughout the cycle, and it was necessary to determine an analytical solution for the volume variation of these spaces. The engine mechanism consisted of a Scotch yoke mechanism, which had known equations describing the horizontal displacement [80]. The engine being considered had opposed pistons, so the equations of motion were modified slightly due to the phase difference between the pistons. The derivation of the volume variation equations for the expansion and compression space may be seen in Appendix D.

Expressions for the expansion space and compression space volume variations are shown in Equations 4-13 and 4-14, respectively. Variables within the expansion space volume variation equation include the expansion space clearance volume, V_{cle}, the expansion piston swept volume, V_{swe}, and the crank angle. For the compression space expression, the variables are the compression space clearance volume, V_{clc}, the compression piston swept volume, V_{swc}, the crank angle, as well as the phase angle, α.

$$V_e = V_{cle} + \frac{1}{2}V_{swe}(1 - \cos(\theta)) \qquad\qquad 4\text{-}13$$

$$V_c = V_{clc} + \frac{1}{2}V_{swc}(1 - \cos(\theta - \alpha)) \qquad\qquad 4\text{-}14$$

The volumes of the heater, cooler, and regenerator space depend on the physical geometry of the engine being studied, and therefore do not have explicit equations related to their volume.

4.5.5.1 Determining Dead Volume

To determine the dead volume in the engine, it was first necessary to determine where it occurred. The locations that were identified to contain dead volume were the clearance volume between the pistons and the radiators when the distance between them was at a minimum, the un-swept volume in the gaps between radiator fins, and within the regenerator housing. It was assumed that the 3D printed parts inside the engine were not leaking, or had negligible leakage, since the parts were epoxy coated before installation into the engine.

The solid model of the engine, as well as measurements of the components and their position, were used to determine estimates for the clearance volumes of the expansion and compression spaces. Since the pistons had DVRCs, discussed in Section 3.6.3, it was possible for

the dead volume to vary with stroke length, depending on which dead volume reducer was installed. For the baseline and thermal experiments, the dead volume reducer for the 76.2 mm stroke lengths were used for all cases, since it would not collide with the heat exchangers when a 50.8 mm stroke was used and the engine did not have to be disassembled. The clearance volumes were slightly different for the compression and expansion spaces, due to assembly tolerances.

The regenerator housing was sized to have a void volume of 0.187 L when no regenerator was inserted. The entire regenerator housing volume was considered dead volume, since no regenerator was inserted in the engine during the experiments. A regenerator was not inserted since the flow friction associated with it was more of a concern than the increase in efficiency at the early design stages.

To determine the volume of the heat exchangers, a tank with a width of 146 mm, a length of 301 mm, and a wall thickness of 2 mm was filled with 2.7 L of water. The water depth before inserting the radiator was measured to be 67.75 mm. After the radiator was inserted into the tank, the depth rose to 75.10 mm, which was a difference of 7.35 mm and equated to a volume change of 0.323 L. This value was considered the solid volume of the radiator. The radiator dead volume was determined by knowing the void volume inside the 3D printed heat exchanger housing, which was 1.19 L. The difference in volume between the 3D printed housing and the solid volume of the radiator was equivalent to the radiator dead volume, and was calculated to be 0.868 L, which was the same for the heater and cooler. The dead volumes considered in the engine are tabulated in Table 4-8.

Table 4-8: Dead Volume Distribution in the Engine

Dead Volume Contribution	Volume [L]
Expansion Piston Clearance, V_{cle} (76.2 mm Stroke with Reducer)	0.344
Compression Piston Clearance, V_{clc} (76.2 mm Stroke with Reducer)	0.284
Expansion Piston Clearance, V_{cle} (50.8 mm Stroke with Reducer)	0.539
Compression Piston Clearance, V_{clc} (50.8 mm Stroke with Reducer)	0.479
Heater Air Flow, V_h	0.868
Regenerator Space, V_r	0.187
Cooler Air Flow, V_k	0.868

4.5.5.2   Determining Bellows Convolution Volume

Since the pistons used a set of bellows for sealing, it introduced additional convolution volumes that needed to be considered in the volume variation equations shown in Equations 4-13 and 4-14. The additional $V_{bellows}$ terms in Equations 4-15 and 4-16 represent the convolution volume.

$$V_e = V_{cle} + \frac{1}{2}V_{swe}(1 - \cos(\theta)) + V_{bellows} \qquad\qquad 4\text{-}15$$

$$V_c = V_{clc} + \frac{1}{2}V_{swc}(1 - \cos(\theta - \alpha)) + V_{bellows} \qquad\qquad 4\text{-}16$$

To determine the bellows convolution volume, it was necessary to perform some supplementary experiments to develop a solid model of the bellows at different crank positions to then develop an equation describing the estimated bellows convolution volume at any crank angle. To estimate the bellows convolution volume, measurements were taken from the bellows on the expansion side when the crank angle was varied from 0° to 360°, in 15° increments. The extended length from peak to peak, the extended length from trough to trough, as well as the distance between peaks were measured using digital calipers to assist in creating a solid model in SolidWorks for each crank position. These measurements are shown schematically in Figure 4-22.
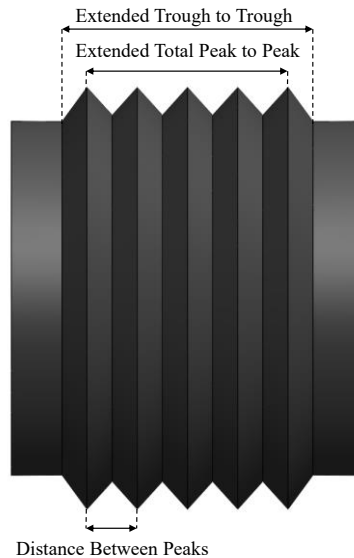

Figure 4-22: Schematic of the Measurement Locations on the Bellows

To obtain the measurements at the desired crank angle increments, the Teknic servo-motor was used in a position control mode to rotate the engine to specified crank angles. The rotary encoder was used to ensure that the engine was at a crank angle of 0° when the expansion piston volume was minimum. The phase angle of the engine was set to 180°, and the stroke length was set to 76.2 mm, and then 50.8 mm, on both pistons. The 50.8 mm stroke did not fully compress the bellows. The servo-motor was set to the home position of 0 counts, and was attached to the engine so it aligned with the crank angle reading of 0° ± 1° from the rotary encoder. Each count on the servo-motor was equivalent to 0.45°. The Teknic was set to hold the engine at each of the 25 specified crank angles while measurements of the bellows geometry were taken. Two repeats for each stroke length were taken, and then the measurements were averaged. The measured dimensions were tabulated in Appendix E.

The bellows convolution shape itself was difficult to predict at any point in the cycle. Although, there were four conceptual cases which could describe the approximate shape of the bellows. The ideal linear convolution profile is illustrated in Figure 4-23 (a), where no deviation in the bellows convolution exits between the peak and trough. One extreme case occurred when the bellows was collapsed resulting from the pressure outside of the bellows being greater than inside the bellows, so the convolution deflects inward, as shown in Figure 4-23 (b). Another case occurred when the bellows was over pressurized internally, resulting in the convolution deflecting outward, as shown in Figure 4-23 (c). The observed case that occurred most frequently at different crank angles is demonstrated in Figure 4-23 (d). As illustrated, there was an inflection point along the bellows convolution, resulting in an approximately equal bellows deflection inward and outward, and was a result of the bellows geometry being constrained by the inserted retaining rings, discussed in Section 3.6.3.
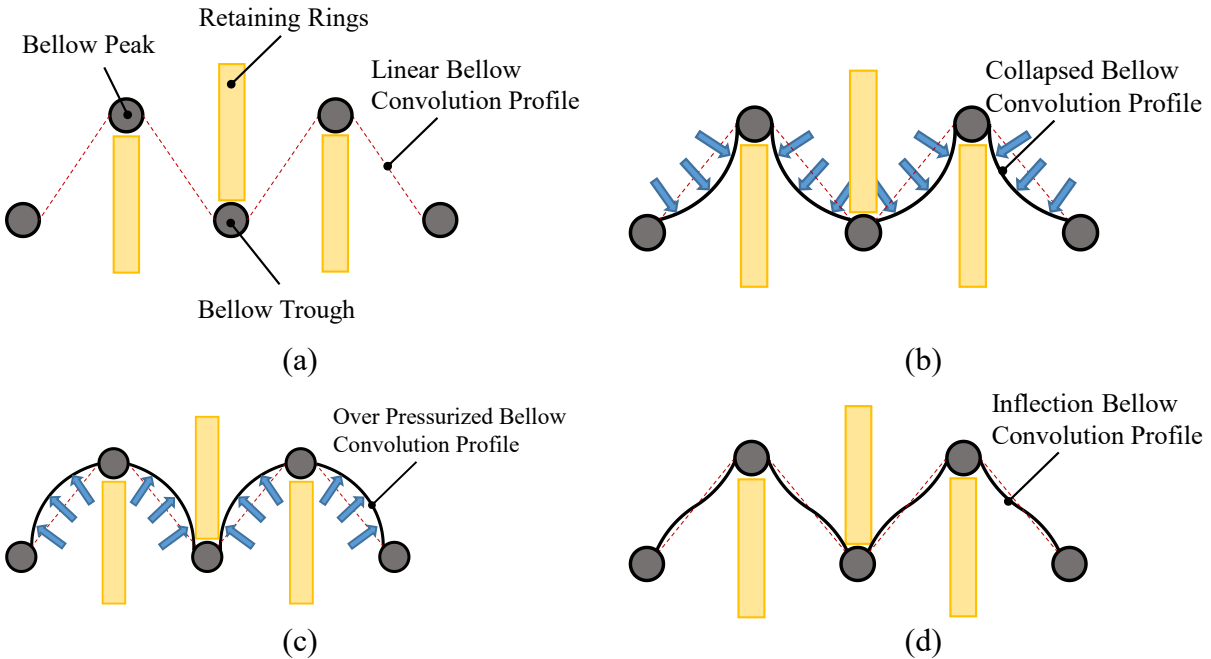
Figure 4-23: Conceptual Profiles of the Bellows Convolutions (a) Linear Bellows, (b) Collapsed Bellows, (c) Expanded Bellows, (d) Bellows with an Inflection Profile

To determine the volume of the bellows under these conditions, a solid model was created; however, to complete the solid model some simplification assumptions were required:

1. The geometric profile of the convolutions was assumed to resemble Figure 4-23 (d) throughout the cycle (as observed), such that the deflection profile on either side of the inflection was assumed to be equal and opposite.

2. The material profile between the peaks and troughs of the folds was assumed to be linear for the solid model, since the above assumption was made.

3. The bellows convolutions were assumed to be symmetric.

4. The expansion and compression cylinder bellows were assumed to have the same convolution variations for 76.2 mm and 50.8 mm strokes.

The solid model was created using the measurements and the above assumptions, as seen by the example sketch of the bellows profile in Figure 4-24.
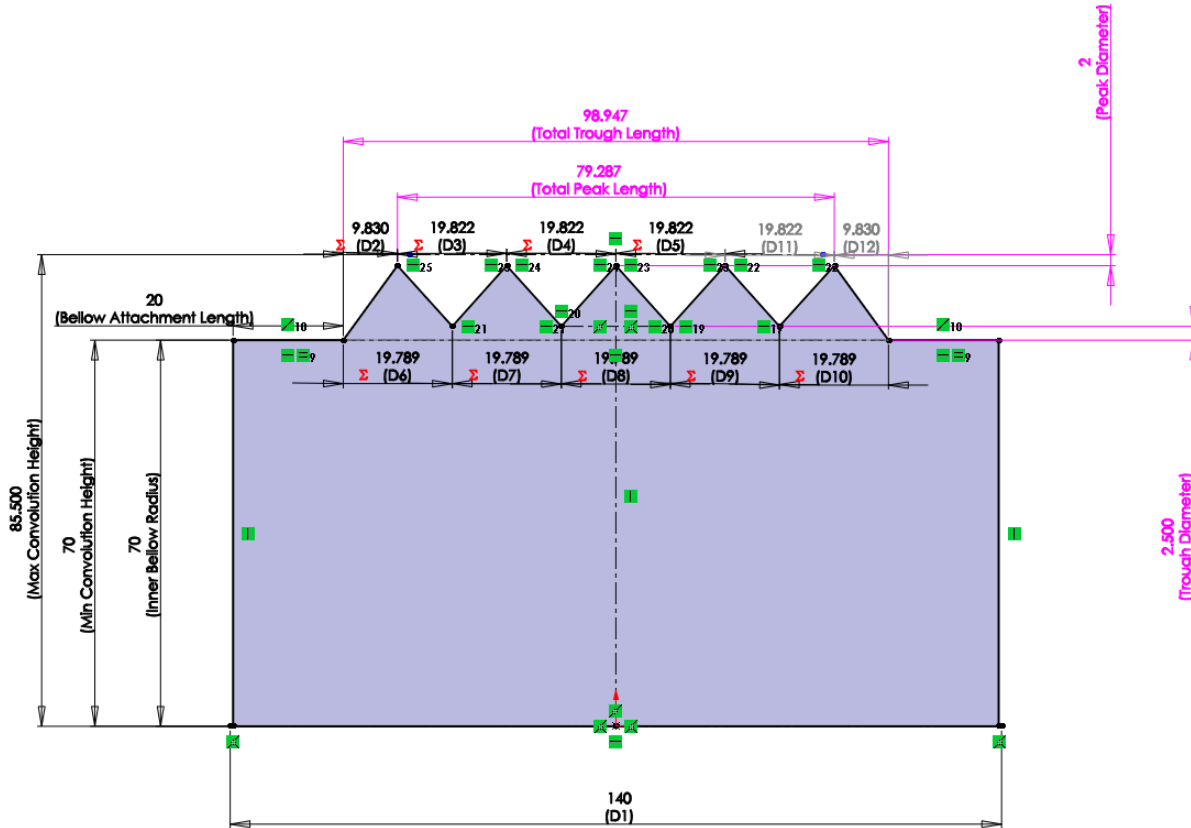
Figure 4-24: Example Sketch of the Bellows Profile in the Solid Model

The distance between inner troughs (D6, D7, D8, D9, and D10) was governed by the total trough length divided by the number of troughs, shown in Equation 4-17. The outside peak half distance (D2, and D12) was governed by the total trough length subtracted by the total peak length divided by two, shown in Equation 4-18. The inner peaks (D3, D4, D5, and D11) were governed by the total peak length divided by the number of peaks, shown in Equation 4-19.

$$\text{inner trough width} = \frac{\text{total trough length}}{5} \qquad \text{4-17}$$

$$\text{outer peak half width} = \frac{\text{total trough length} - \text{total peak length}}{2} \qquad \text{4-18}$$

$$\text{inner peak width} = \frac{\text{total peak length}}{4} \qquad \text{4-19}$$

This process was repeated for each crank angle and stroke length, to obtain the approximate bellows convolution volumes from the solid model. Table E–3 and Table E–4 in Appendix E

records the volume data obtained from the solid models for both 76.2 mm and 50.8 mm strokes respectively.

Using the volumes obtained from the experimental measurements of the bellows and the resulting solid model, a functional expression for the data was determined using a three-term ($n = 3$) Fourier fit in MATLAB. A Fourier fit was selected since the piston motion was harmonic with a Scotch yoke mechanism, so the volume variations would be as well. The expression for the bellows convolution volume with coefficients is shown in Equation 4-20 with an R^2 value of 0.9994.

$$V_{bellows} = a_0 + a_1 \cos(w\theta) + b_1 \sin(w\theta) + a_2 \cos(2w\theta) + b_2 \sin(2w\theta) + a_3 \cos(3w\theta) + b_3 \sin(3w\theta)$$

4-20

The coefficients for the bellows convolution volume are shown in Table 4-9 for both a 76.2 mm and 50.8 mm stroke length.

Table 4-9: Table of Fourier Fit Coefficients for the Bellows Convolution Volume Expression

Fourier Fit Coefficients	76.2 mm Stroke Length	50.8 mm Stroke Length
a_0	2.2161×10^{-4}	2.2085×10^{-4}
a_1	-1.4990×10^{-4}	-1.1189×10^{-4}
b_1	-9.2396×10^{-7}	5.9000×10^{-6}
a_2	4.9283×10^{-7}	-5.9390×10^{-6}
b_2	6.0354×10^{-7}	-1.1482×10^{-6}
a_3	3.6966×10^{-6}	8.8745×10^{-7}
b_3	-7.1501×10^{-7}	-5.7690×10^{-7}
w	1	1

A comparison between the calculated engine volume neglecting the bellows convolution volume and considering the convolution volume is shown in Figure 4-25. It is obvious that when considering convolution volume, the overall engine volume increases. The increase was significant, so the bellows convolution volume was not neglected.
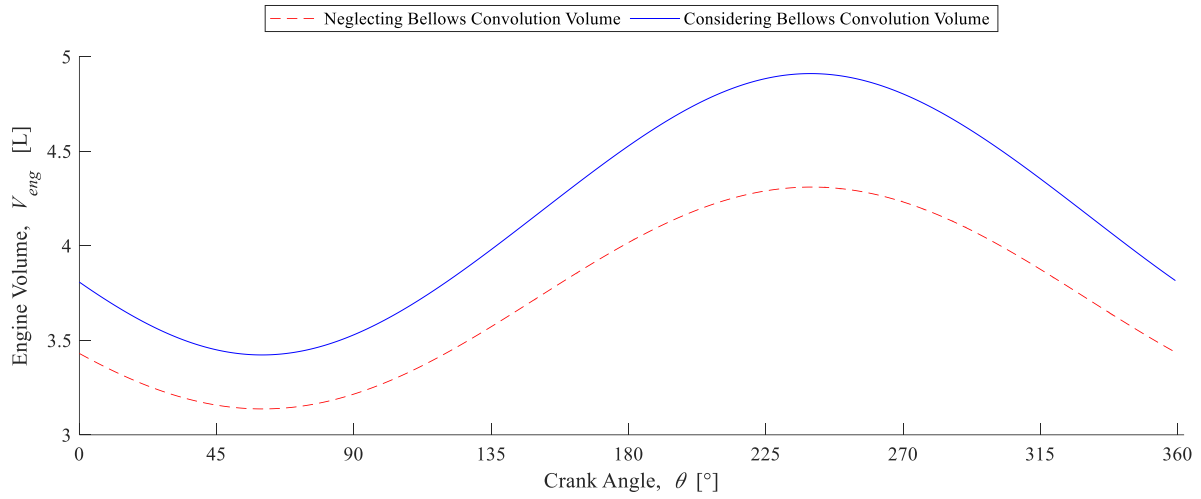
Figure 4-25: Engine Volume Comparison Between Neglecting and Considering Bellows Convolution Volume

4.6 Experiment Uncertainty Analysis

The standard uncertainty was calculated for all the output measurements considering the built-in errors of the devices used to collect data, errors due to calibration, errors due to data acquisition, and errors due to measurement methods. The elemental standard uncertainties of the directly measured parameters were then propagated into the equations that were dependent on those measurements. This section will present the pertinent information on the uncertainty analysis that was completed. Procedures followed for the uncertainty analysis have been drawn primarily from the works of Wheeler and Ganji [83], as well as from Coleman and Steele [94]. Appendix F will show detailed samples of the uncertainty analysis performed.

4.6.1 Random Uncertainty

The random uncertainty associated with a measurement is one that that has varied within the measurement period [94]. Random uncertainties for the instruments used to collect data were reported as a combined manufacturer's accuracy, or else as temperature shifts, repeatability errors, resolution errors, or noise. The general equation for the standard random uncertainty [83], $\mathcal{P}_x$, is given as:

$$\mathcal{P}_x = t_{0.025}S_x \qquad\qquad 4\text{-}21$$

where $t_{0.025}$ is the student's t-score for a 95% confidence interval, and S_x is the standard deviation of the measurement. A confidence interval of 95% was used in the determination of the t-value since large samples (>30) were taken when acquiring the data. Therefore, the t-value was assumed to have a value of 2 [83].

To calculate the standard random uncertainty for a given measurement, the elemental errors of each instrument used in the measurement was first combined using the root sum of squares (RSS). The elemental sources of error are the individual sources of error for a given instrument [83]. Specifically, as shown in Equation 4-22 [83], the individual standard deviations for each elemental source of error, S_i, needed to be combined for the RSS, where S_x is the combined standard deviation of a measurement considering the elemental sources of error, and q is the number of elemental sources of error. Since the instrumentation manufacturers specified the

standard uncertainties, in order to combine the individual standard deviations, the provided random uncertainty needed to be divided by the student's t-score before RSS was performed.

$$S_x^2 = \sum_{i=1}^{q} S_i^2 \qquad\qquad 4\text{-}22$$

If the standard deviation of a mean value was being determined, Equation 4-23 [94] was used where $S_{\bar{x}}$ is the mean standard deviation over N independent measurements.

$$S_{\bar{x}} = \frac{S_x}{\sqrt{N}} \qquad\qquad 4\text{-}23$$

4.6.2 Systematic Uncertainty

Systematic uncertainty is defined as an uncertainty that remains consistent throughout the measurement [83]. The systematic uncertainty was often given as part of the combined manufacturer's accuracy. Other common systematic uncertainties that were reported or considered were linearity errors, calibration errors, readability errors, and hysteresis errors. As with random uncertainties, the elemental systematic uncertainties must be combined using RSS [83]:

$$b_x^2 = \sum_{i=1}^{q} b_i^2 \qquad\qquad 4\text{-}24$$

where b_x is the combined systematic uncertainty of a measurement considering sources of elemental errors, and b_i is the systematic uncertainty of individual sources of elemental errors.

4.6.3 Total Standard Uncertainty

In order to calculate the total standard uncertainty of a measurement, u_F, the total random uncertainty, $\mathcal{P}_F$, and total systematic uncertainty, B_F, were combined using RSS [83]:

$$u_F = \sqrt{B_F^2 + \mathcal{P}_F^2} = \sqrt{B_F^2 + (t_{0.025}S_F)^2} \qquad\qquad 4\text{-}25$$

When the uncertainty of a direct measurement was calculated, S_F was treated the same as S_x in Equation 4-22, and B_F was treated the same as b_x in Equation 4-24.

4.6.4   Propagation of Uncertainties

In the case when a useful parameter could not be measured directly, and was instead calculated using a governing equation, F, which is a function of variables x_i, like that shown in Equation 4-26, the uncertainty of each variable x_i needed to be propagated into the uncertainty of the desired parameter.

$$F = f(x_1, x_2, \dots, x_N) \qquad \text{4-26}$$

If the variables within the governing equation were independent of each other, then a simplified propagation of uncertainty equation was used [83]:

$$u_F = \left(\sum_{i=1}^{N} \left[u_{x_i} \frac{\partial F}{\partial x_i} \right]^2 \right)^{\frac{1}{2}} \qquad \text{4-27}$$

where u_{x_i} is the combined uncertainty of variable x_i. If the governing equation was a product of variables in the form of Equation 4-28 [83] then the simplification shown in Equation 4-29 [83] was used to calculate the total uncertainty.

$$F = \text{Const} \times \left(x_1^a \cdot x_2^b \cdot \dots \cdot x_n^N \right) \qquad \text{4-28}$$

$$\frac{u_F}{F} = \sqrt{ \left(a \frac{u_{x_1}}{x_1} \right)^2 + \left(b \frac{u_{x_2}}{x_2} \right)^2 + \dots } \qquad \text{4-29}$$

In certain governing equations, some of the variables were not independent. One of the restrictions in the use of Equation 4-27 was that errors between variables must not correlate [83], which has occurred in some measurements that use the same data acquisition devices or calibration standards. The pressure ratio and temperature difference are examples of parameters that were identified to have correlations between variables. In such cases, a correlation effects term was added to the propagation of uncertainty [94]. The correlation effects term could be applied within the random or systematic uncertainty equations, depending on the type of correlated error.

Equations 4-30, 4-31, and 4-32 [94] were used to include the correlation effects, $C_{x_j x_k}$, into the systematic uncertainty of a parameter, where $b_{x_j x_k}$ denotes the summation of the product of each uncertainty due to the correlation between parameters x_j and x_k. The term L indicates the number of correlations between parameters x_j and x_k.

$$B_F^2 = \sum_{i=1}^{N} b_{x_i}^2 \left(\frac{\partial F}{\partial x_i}\right)^2 + C_{x_j x_k} \qquad \text{4-30}$$

$$C_{x_j x_k} = 2 \left(\frac{\partial F}{\partial x_j}\right) \left(\frac{\partial F}{\partial x_k}\right) b_{x_j x_k} \qquad \text{4-31}$$

$$b_{x_j x_k} = \sum_{z=1}^{L} \left(b_{x_j}\right)_z \left(b_{x_k}\right)_z \qquad \text{4-32}$$

Equations 4-33, 4-34, and 4-35 [94] describe the correlation effects as in Equations 4-30 to 4-32, but applied to the random uncertainty standard deviation instead, where $S_{x_j x_k}$ denotes the summation of the product of each correlated standard deviation between parameters x_j and x_k.

$$S_F^2 = \sum_{i=1}^{N} S_{x_i}^2 \left(\frac{\partial F}{\partial x_i}\right)^2 + C_{x_j x_k} \qquad \text{4-33}$$

$$C_{x_j x_k} = 2 \left(\frac{\partial F}{\partial x_j}\right) \left(\frac{\partial F}{\partial x_k}\right) S_{x_j x_k} \qquad \text{4-34}$$

$$S_{x_j x_k} = \sum_{z=1}^{L} \left(S_{x_j}\right)_z \left(S_{x_k}\right)_z \qquad \text{4-35}$$

4.6.5 Bellows Convolution Volume Uncertainty

To determine the uncertainty in the bellows convolution volume, image processing was used. Image processing was employed to determine the relative difference in volume when the bellows was unpressurized versus pressurized, which represented the pressure fluctuations throughout a cycle. The expansion piston was maintained at a crank angle of 180°, and a mobile camera was used in a remote capture mode to obtain photographs of the bellows at different pressures, for both 76.2 mm and 50.8 mm strokes. The pressure was varied from 0 psi to 4 psi in 0.25 psi increments, covering a range of engine pressures possible depending on phase angle. A sample photograph for 2 psi is shown in Figure 4-26, with a box showing the area of image processing interest.
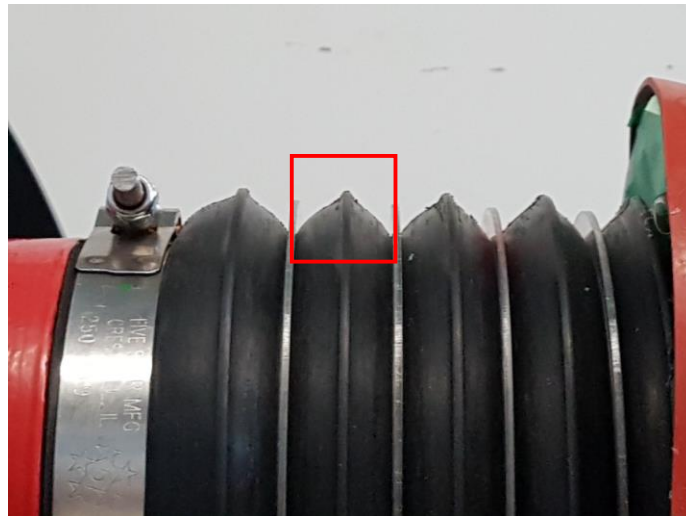
Figure 4-26: Image of the Bellows for Image Processing at 2 psi

The photographs were changed to binary images for processing. Figure 4-27(a) demonstrates a sample of the binary images, with a window size slightly larger than the bellows convolution of interest, since the convolution moves about in the frame as the pressure increases. Figure 4-27(b) shows the same binary image manually cropped to a fixed aspect ratio around the fold of interest. The peak of the bellows was still in the image since there was a distinct point on all images for cropping.
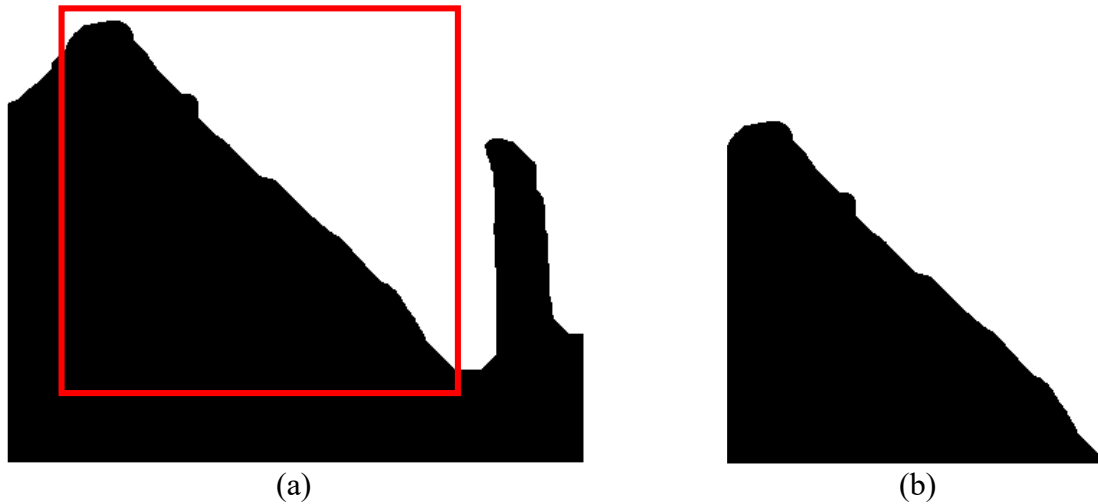
Figure 4-27: Sample Binary Images of (a) Convolution of Interest (b) Manual Crop of Area of Interest

With all the images processed as shown in Figure 4-27(b), the change in area of the bellows was determined relative to the area of the unpressurized bellows. This was used to estimate the uncertainty in the volume variation of the bellows convolutions throughout the cycle. Once the area of the bellows convolution in the image was determined, a ratio was calculated, and it was assumed that the change in area corresponded to the same change in volume. Additional assumptions were as follows:

1. The bellows convolutions were assumed symmetric, therefore only half of the convolution was analyzed.

2. The bellows convolutions were assumed to deform equally. Since some convolutions were more deformed than others, when considering the entire bellows, the volume was assumed to be equally distributed in the five convolutions.

3. A percent change in projected area of the bellows was assumed to correspond to a direct and proportional change in volume.

The resulting ratio was applied to an estimated unpressurized half convolution volume of 28.92 mL from the solid model, and the results are tabulated for the 50.8 mm and 76.2 mm stroke in Appendix G. Figure 4-28 depicts the estimated uncertainties for each charge pressure tested. The line connecting the uncertainty data is for visualization only.
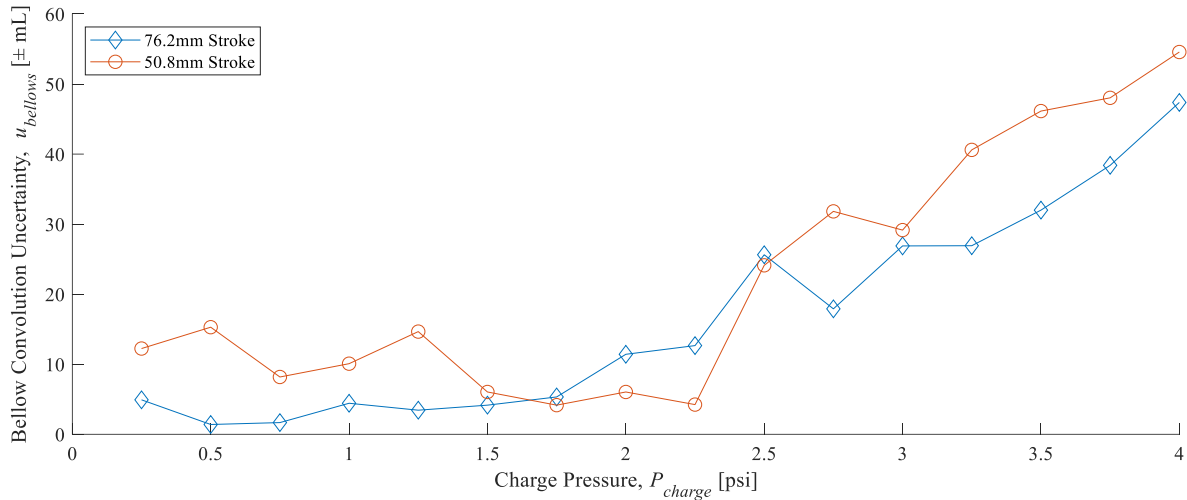
Figure 4-28: Graphical Representation of the Estimated Bellows Convolution Uncertainty for Each Charge Pressure from Image Processing

To have a more conservative estimate of the convolution volume uncertainty, intervals were chosen for each 1 psi increment. The highest value of uncertainty within those intervals was chosen as the upper uncertainty limit for pressures contained within the interval. The uncertainty intervals are shown graphically in Figure 4-29.
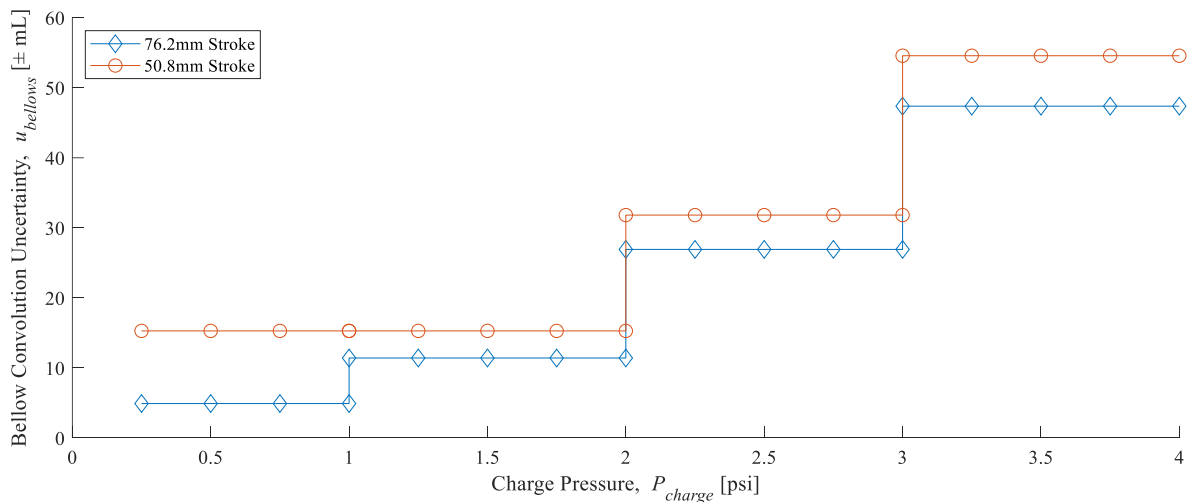

Figure 4-29: Graphical Representation of the Chosen Bellows Convolution Uncertainty Intervals for Each Charge Pressure from Image Processing

In Figure 4-29, there are now step values for the uncertainty, and it can be seen that the uncertainty in the bellows convolution volume for a 50.8 mm stroke is higher than for a 76.2 mm stroke. This is due to the bellows not being fully collapsed at the smaller stroke, and there is more volume contained in the bellows convolution. For a 76.2 mm stroke, the uncertainty intervals were

± 4.9 mL, ± 11.4 mL, ± 26.9 mL, and ± 47.4 mL, for between 0 and 1 psi, 1 and 2 psi, 2 and 3 psi, and between 3 and 4 psi. Similarly, for a 50.8 mm stroke, the uncertainty intervals were ± 15.3 mL, ± 15.3 mL, ± 31.8 mL, and ± 54.6 mL. Depending on where the maximum pressure in the cycle fell within these set intervals, the value for the convolution volume uncertainty was used in the propagation of uncertainty equation for the determination of the engine volume uncertainty.

4.6.6 Indicated Work and Mechanism Effectiveness Uncertainties

To determine the uncertainty in the expansion space and compression space indicated work, the uncertainty in pressure and volume was added or subtracted from the original data, so that the maximum work indicator diagram would envelop the measured indicator diagram, as shown in Figure 4-3. This was considered as the maximum uncertainty in indicated work for the expansion and compression spaces for each configuration. The difference between the maximum indicated work and the measured indicated work was taken to obtain the uncertainty in indicated expansion and compression work.
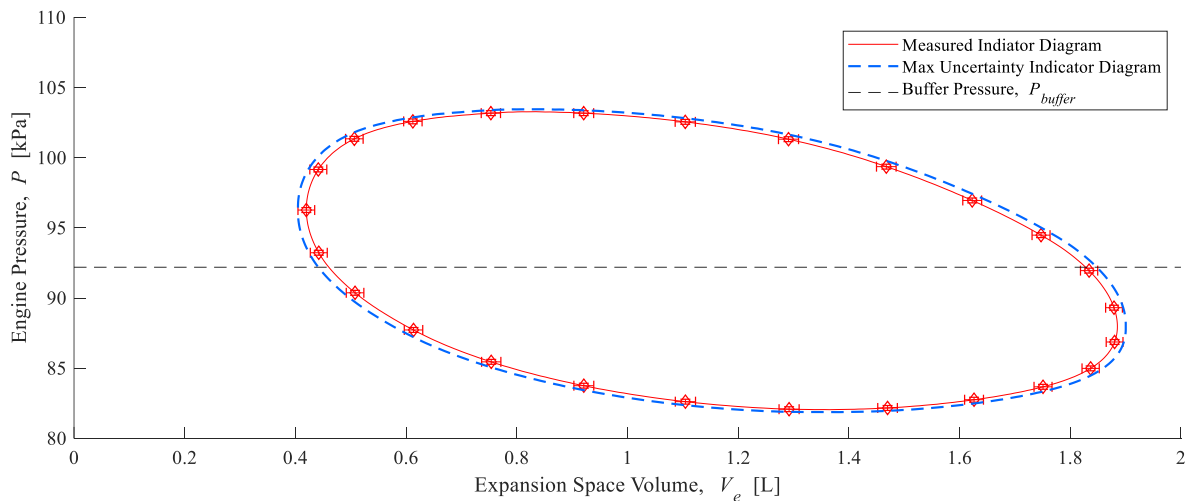
Figure 4-30: Max Uncertainty in Indicated Expansion Work for Phase Angle of 120° and Swept Volume of 2.346 L

For the efficacious and forced work uncertainties, the efficacious and forced work was calculated for the new maximum indicator diagrams for each configuration. The difference between the measured values and the maximum values were taken for both the efficacious and forced work, resulting in defined uncertainty bounds for each configuration.

These uncertainties were then propagated using Equation 4-27 with the governing equation shown in Equations 2-13, 2-14, and 2-15 to determine the total efficacious work, forced work, and indicated work uncertainties for each configuration. Tables for the calculated uncertainties for the expansion efficacious and forced work, compression efficacious and forced work, expansion space indicated work, and compression space indicated work are shown in Appendix H. The engine indicated work uncertainty for each configuration is shown in Table 4-10.

Table 4-10: Table of Indicated Work Uncertainty

Phase Angle, α [°]	Indicated Work Uncertainty, $u_{W_{ind}}$ [J]		
	V_{sw} =1.564 L	V_{sw} =1.955 L	V_{sw} =2.346 L
180	± 0.50	± 0.62	± 0.69
175	± 0.46	± 0.59	± 0.65
170	± 0.48	± 0.64	± 0.69
165	± 0.54	± 0.71	± 0.77
160	± 0.62	± 0.77	± 0.87
155	± 0.72	± 0.87	± 0.98
150	± 0.72	± 0.88	± 0.98
145	± 0.77	± 0.93	± 1.03
140	± 0.83	± 0.99	± 1.09
135	± 0.87	± 1.11	± 1.26
130	± 0.92	± 1.17	± 1.34
125	± 0.98	± 1.24	± 1.42
120	± 1.06	± 1.31	± 1.49

The uncertainty in the mechanism effectiveness was determined by using the propagation of uncertainty, with Equation 2-17 as the governing equation. Due to the complexity of the equation and the resulting partial derivatives, a commercial solver (WolframAlpha, Wolfram Alpha LLC) was used to calculate the partial derivatives with respect to each variable. The uncertainty was calculated for each configuration and is shown in Table 4-11.

Table 4-11: Table of Mechanism Effectiveness Uncertainty

Phase Angle, α [°]	Mechanism Effectiveness Uncertainty, u_E [J]		
	V_{sw} =1.564 L	V_{sw} =1.955 L	V_{sw} =2.346 L
180	± 0.09	± 0.08	± 0.05
175	± 0.10	± 0.08	± 0.05
170	± 0.09	± 0.06	± 0.06
165	± 0.08	± 0.05	± 0.05
160	± 0.08	± 0.05	± 0.05
155	± 0.05	± 0.04	± 0.03
150	± 0.06	± 0.04	± 0.03
145	± 0.05	± 0.04	± 0.03
140	± 0.05	± 0.03	± 0.03
135	± 0.04	± 0.03	± 0.03
130	± 0.04	± 0.03	± 0.02
125	± 0.04	± 0.03	± 0.02
120	± 0.03	± 0.03	± 0.02

4.6.7 Instrumentation and Output Uncertainties

The instruments used in the experiment each had a standard uncertainty that was calculated from the random and systematic elemental errors associated with the instrument, calibration procedures, measurement methods, and the data acquisition equipment. The calculated standard uncertainties are reported in Table 4-12. If the standard uncertainty varied with the measurement reading, the maximum and minimum uncertainties were tabulated instead.

Table 4-12: Instrument Standard Uncertainties

Instrumentation	Total Standard Uncertainty	Min Standard Uncertainty	Max Standard Uncertainty
Pressure Transducer (DP15-50, Validyne Engineering)	% RO	± 0.0252 psi	± 0.0254 psi
Torque Transducer (TRS600, FUTEK Advanced Sensor Technology Inc.)	% RO	± 2.69 × 10^{-4} Nm	± 7.27 × 10^{-3} Nm
Rotary Encoder (15S-19M1-0500NV1ROC-F03-S1, Encoder Products Company)	± 1.00 °	-	-
RTD Probe (RTD-810, Omega Engineering Inc.)	± 0.62 °C	-	-
Type-T Thermocouple (TTSS-116E-6, Omega Engineering Inc.)	± 1.85 °C	-	-

Similarly, the standard uncertainties were calculated for any output variable used, by applying the appropriate propagation of uncertainty equations. Table 4-13 showcases the calculated uncertainties. The sources of error that contributed towards the instrumentation uncertainty as well as sample propagation equations for the output variable uncertainties are shown in Appendix F.

Table 4-13: Standard Uncertainties of Output Variables

Output Variable	Total Standard Uncertainty	Min Standard Uncertainty	Max Standard Uncertainty
Mean Pressure	-	± 0.027 psi	± 0.102 psi
Crank Angle	± 1.0 °	-	-
Phase Angle	± 1.0 °	-	-
Expansion Space Volume	-	± 11.0 mL	± 19.5 mL
Compression Space Volume	-	± 11.1 mL	± 21.0 mL
Engine Volume	-	± 17.3 mL	± 29.3 mL
Non-dimensional Pressure	-	± 0.0027	± 0.0087
Non-dimensional Expansion Space Volume	-	± 0.0094	± 0.0249
Non-dimensional Compression Space Volume	-	± 0.0095	± 0.0264
Non-dimensional Engine Volume	-	± 0.0074	± 0.0187
Pressure Difference	± 0.0422 psi	-	-
Mean Gas Temperature Difference	± 1.45 °C	-	-
Mean RTD Temperature Difference	± 0.48 °C	-	-
Compression Ratio	-	± 0.0073	± 0.014
Pressure Ratio	-	± 0.00066	± 0.00098
Shaft Power	-	± 7.11 × 10^{-4} W	± 0.28 W
Shaft Work	-	± 0.0033 J	± 0.0272 J
Indicated Work	-	± 0.456 J	± 1.49 J
Mechanism Effectiveness	-	± 0.02	± 0.1

4.7　Chapter 4 Summary

Within this chapter, experiment setup and methodology were presented. An experiment apparatus that could address the research questions posed by this thesis was created. The experiment procedure was created to manipulate the piston stroke lengths, phase angle, and engine speed for two separate experiments. In total, there were 156 individual configurations that needed to be tested in a baseline and thermal experiment. By doing so, the effect of differing stroke lengths, the optimal phase angle, and the effect of engine speed could be investigated experimentally for LTD alpha-type Stirling engines. The procedure for data processing was also introduced, as well as the methods for calibrating and determining the uncertainty in the instrumentation.

Chapter 5 Engine Experiment Results

Chapter 5 will first present the analysis and interpretation of the data collected from the baseline experiments without any water flowing through the heat exchangers. Following the baseline experiments, a similar analysis for the thermal experiments will be conducted to observe the effect of hot and cold fluid through the heat exchangers. A comparative discussion between the baseline and thermal results will follow. The results presented for discussion within this chapter will focus largely on a phase angle of 120°, unless a comparison between phase angles is warranted. This method of presenting the results was chosen due to the large number of configurations tested. By selecting one phase angle to highlight results that were found to be consistent throughout the phase angles tested, the discussion will be presented in a more logical and concise manner. The complete set of figures for all the conditions tested will appear in the Appendices.

As discussed in Section 4.4.4, manual starting attempts were made by spinning the flywheel to see if the engine could run unassisted. In all the configurations tested, the engine did not produce a net positive amount of power. As such, the results presented for the thermal experiments were obtained by driving the engine with a servo-motor.

In regards to figures in this chapter:

- Unless otherwise specified, if data markers appear with a line connecting them, the data density was so great that the individual data points were undistinguishable, and only every 20th data point was plotted for the curve along with the uncertainty bounds.

- Figure axes were chosen to allow the comparison between the baseline and thermal experiments. As such, there may be unused areas on the figures.

- The uncertainty bounds may not be shown if they lie within the data markers. In such a case, it will be specified.

5.1　Engine Leak Rate

The first experiment conducted before running the engine was to determine the rate at which the engine leaked air. If the leak rate was significant, it would result in a reduction of power output as it would reduce the overall mean pressure, if the engine mean pressure was pressurized above atmospheric, and the engine may then require an external compressor to maintain the engine mean pressure [19], [25]. In an engine with a mean pressure equal atmospheric, leakage would reduce the pressure during expansion, and increase the pressure during compression, as the pressure would try to equalize with the environment, which would result in a loss of power. In the case of the engine being driven by a servo-motor, a reduction in engine pressure would decrease the amount of work extracted during the expansion phase, which would in turn increase the amount of power input required from the servo-motor. Therefore, effort was made to reduce the amount of leakage to the external environment.

To test the leak rate, the engine was pressurized with an external air compressor. Once the engine pressure reached approximately 2 psi, the valve was closed, and pressure data was collected for 60 s. The resulting data can be seen in Figure 5-1, where every 20,000[th] data point is plotted with uncertainty bounds. The maximum pressure reached was 2.27 psi at a time of 1.9 s, and the minimum pressure reached was 1.90 psi after 58.1 s. The leak rate was then found to be 0.0063 psi/s, which was deemed sufficiently low as the minimum speed being tested was equivalent to half a cycle per second, resulting in a leak rate of 0.0126 psi/cycle. From this data, it was assumed that the leak rate had a negligible contribution to the engine not functioning.
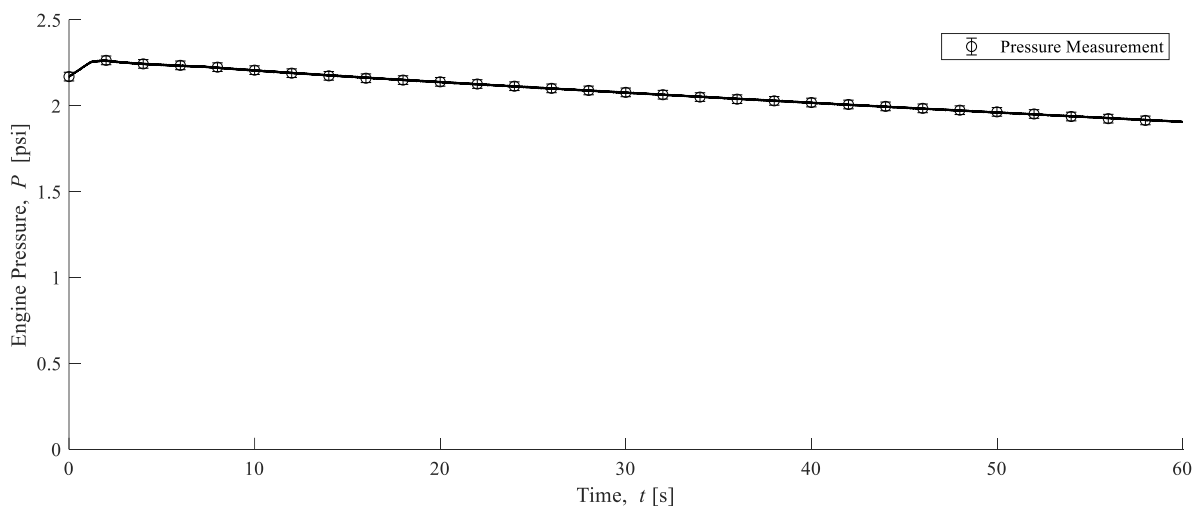
Figure 5-1: Engine Leak Rate Test at 2 psi over 60 s

5.2   Baseline Experiments

The baseline experiments were conducted so that significance could be given to the experiments performed with the heater and cooler transferring heat. The experiment outcomes were twofold: first, the volume, pressure, and torque fluctuations could be analyzed without the influence of the thermal source and sink, and second, the baseline experiments provided an estimate in the power required to drive the engine and overcome losses for each configuration.

5.2.1   Engine Volume Variations

To visualize the different engine volume variations in each configuration, the volume variations during one cycle for each swept volume and phase angle tested were plotted. The full set of figures can be seen in Appendix I. Shown in Figure 5-2 are the volume variations of the expansion and compression spaces, as well as the total engine volume for the swept volume of 1.564 L. This swept volume corresponds to when both the expansion and compression piston strokes are 50.8 mm. Since the data density was so great, the individual data points were omitted from plotting, and only every 20th data marker with uncertainty bounds was plotted.

The volume variations in Figure 5-2(a) have a phase angle of 180°. At this phase angle, the working fluid was shuttled from the compression space to the expansion space without any expansion or compression, as can be seen by the near horizontal line for the total engine volume. The total engine volume may not have been completely horizontal due to the flexible bellows seal; however, the total engine volume was within uncertainty. In Figure 5-2(b), the phase angle was 120°, and it can be seen that the points of maximum and minimum engine volume occur at the intersection of the expansion and compression space curves. As the phase angle was decreased from 180° to 120°, the amplitude of the total engine volume increased. Since a crank angle of 0° was defined to be the minimum expansion space volume, the compression space curve translates relative to the expansion space curve with decreasing phase angle.
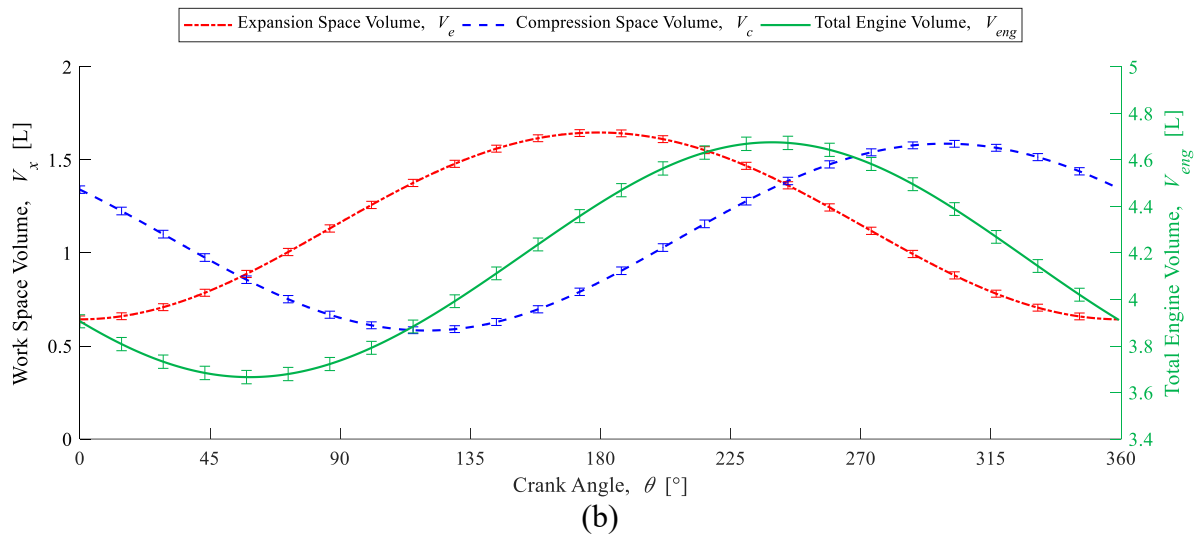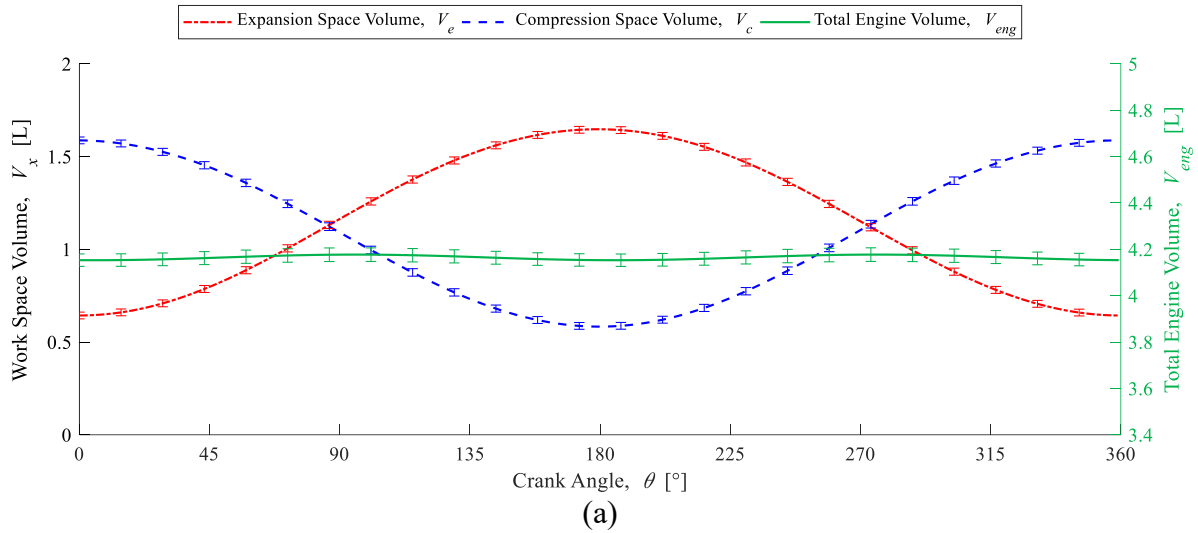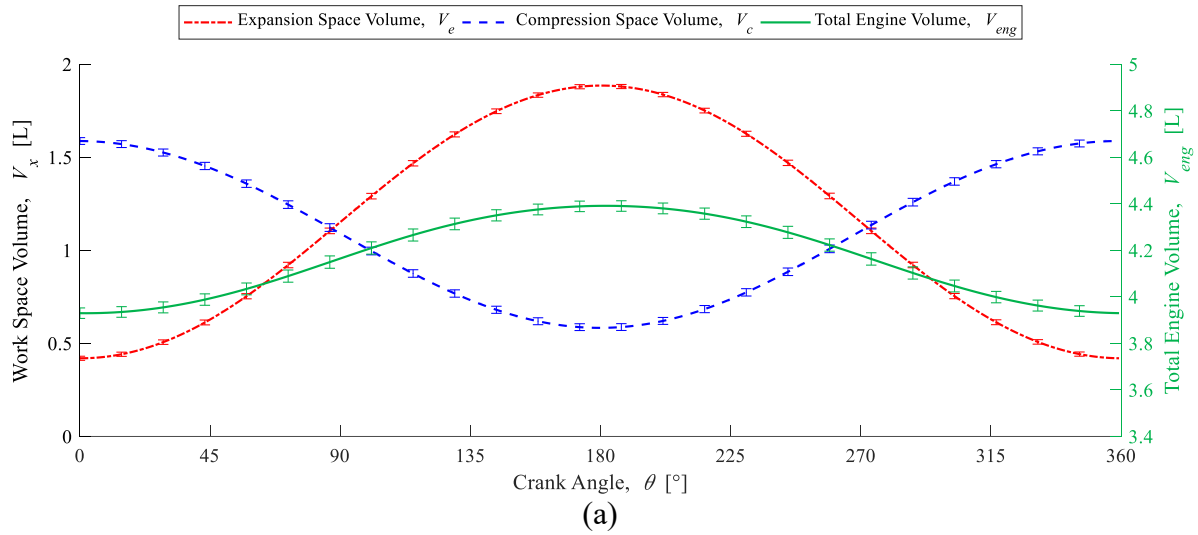
Figure 5-2: Volume Variations During One Cycle with a Swept Volume of 1.564 L with (a) 180° and (b) 120° Phase Angles (Every 20th Data Marker Plotted)

Similarly, Figure 5-3(a) and Figure 5-3(b) show the work space volume variations for an engine swept volume of 2.346 L, which corresponds to 76.2 mm piston strokes, for a phase angle of 180° and 120° respectively. The main difference between Figure 5-2 and Figure 5-3 were the larger amplitudes of the volume variations. When comparing the 1.564 L and 2.346 L swept volumes, the minimum engine volume was lower for the 2.346 L case. This was due to the construction of the engine. Without an extended DVRC for the 1.564 L configurations, the clearance between the heat exchangers and the piston faces was not minimized and more dead volume was present in both the expansion and compression spaces.
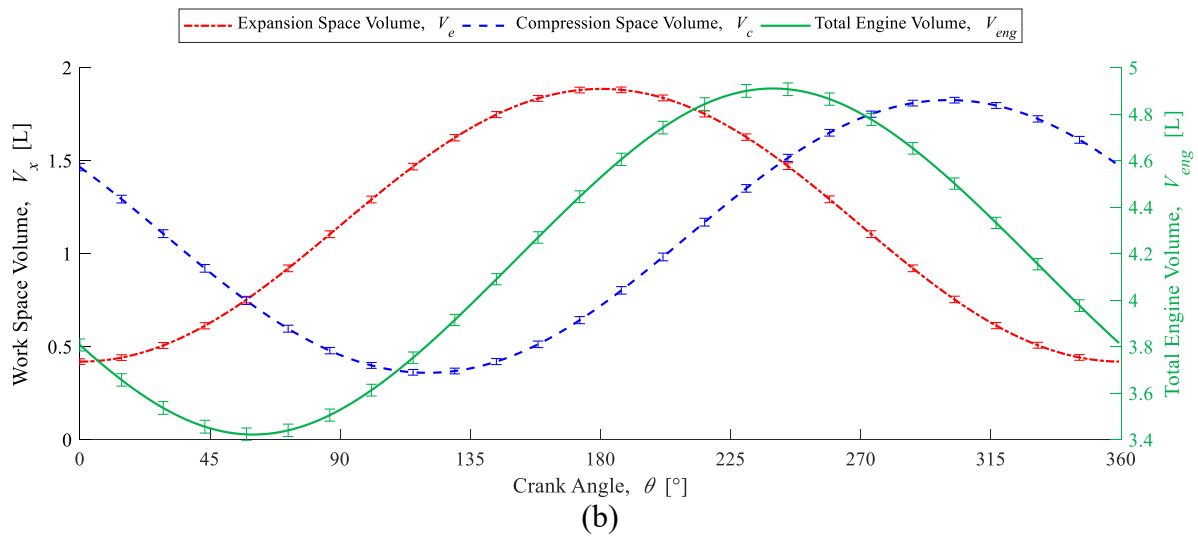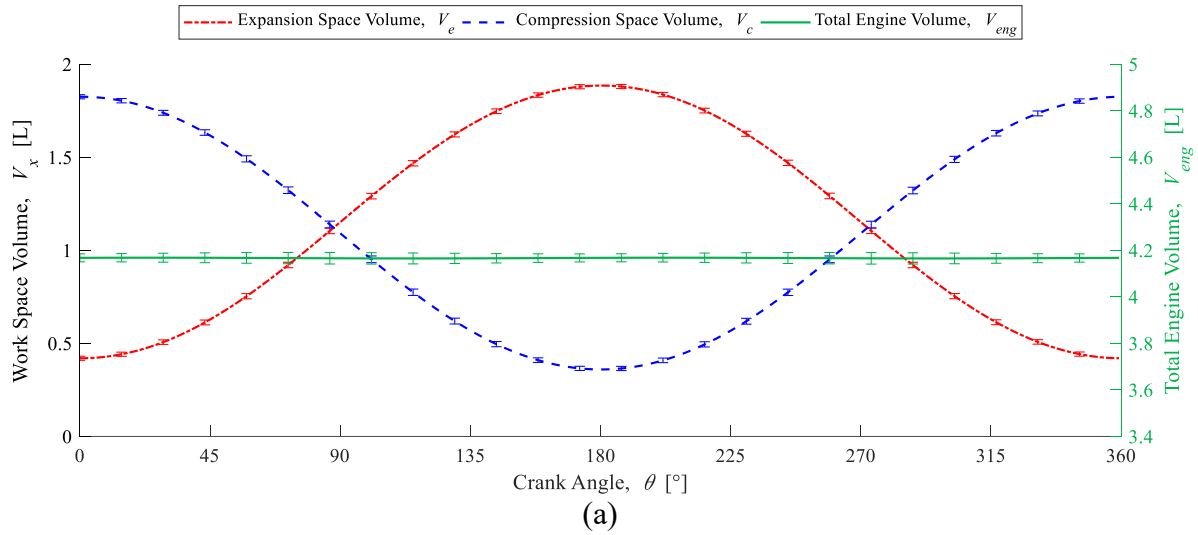
Figure 5-3: Volume Variations During One Cycle with a Swept Volume of 2.346 L with (a) 180° and (b) 120° Phase Angles (Every 20th Data Marker Plotted)

For the case of differing stroke lengths of 50.8 mm for the compression piston and 76.2 mm for the expansion piston, Figure 5-4 presents the volume variations with an engine swept volume of 1.955 L. From Figure 5-4(a) it was immediately apparent that the volume varied with a phase angle of 180°. In addition, it can be seen in Figure 5-4(b) that the points of maximum and minimum engine volume no longer occur at the intersection points of the expansion and compression space curves. The minimum compression space volume was larger than the expansion space volume, indicating that there was more dead volume in the compression space.
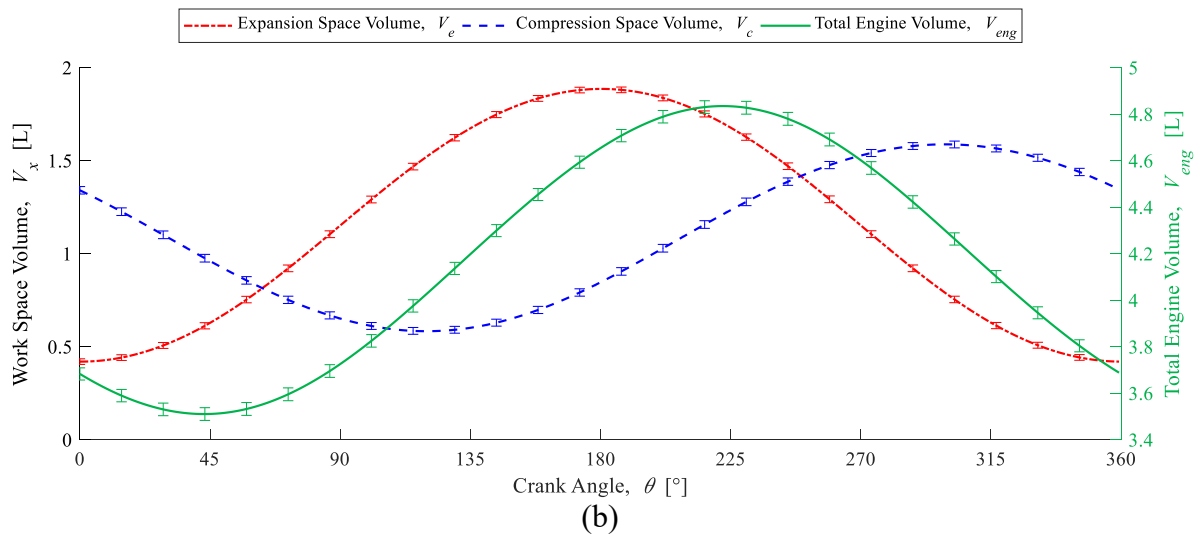
Figure 5-4: Volume Variations During One Cycle with a Swept Volume of 1.955 L with (a) 180° and (b) 120° Phase Angles (Every 20th Data Marker Plotted)

To further illustrate the volume variation present at 180° with a 1.955 L swept volume, Figure 5-5 was created by plotting the expansion space volume variations when both a 50.8 mm and 76.2 mm stroke was used, as well as the volume variation of the compression space when a 50.8 mm stroke was used. When both the expansion and compression piston strokes were the same, the workspace volume variation were approximately the same when the clearance space volume was neglected. When the strokes were not equal, the dashed expansion space curve had a different shape than the solid expansion space curve. When the dashed curve was above the solid curve, the gas was expanded. When the dashed curve was below the solid curve, the gas was compressed. Therefore, the volume was not shuttled at a constant volume with a phase angle of 180°.
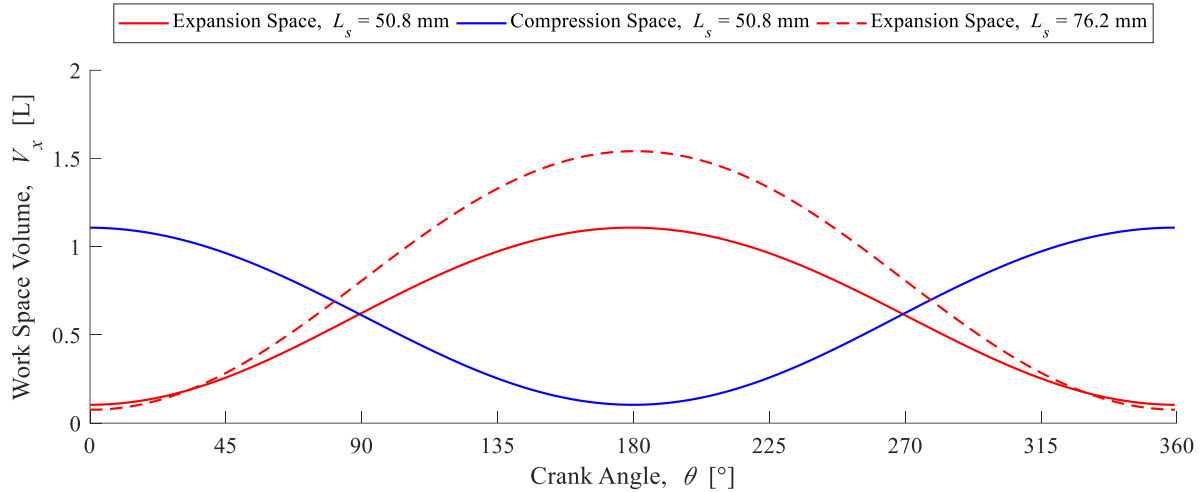
Figure 5-5: Expansion Space Volume Variation Comparison Between Stroke Lengths of 50.8 mm and 76.2 mm

5.2.1.1   Compression Ratio

The compression ratios for each engine configuration were calculated and are documented in Table 5-1. As the phase angle decreases, the compression ratio increases, and in general increases with the increasing swept volume configurations. The compression ratio at 180° was close to unity for swept volumes of 1.564 L and 2.346 L. When the expansion and compression strokes were different at 1.955 L, the compression ratio was higher between 150° and 180° than for the other two configurations due to the larger volume variations at higher phase angles.

Table 5-1: Calculated Compression Ratios for Each Configuration Tested

Phase Angle, α [°]	Compression Ratio, CR		
	$V_{sw} = 1.564$ L	$V_{sw} = 1.955$ L	$V_{sw} = 2.346$ L
180	1.006	1.117	1.001
175	1.022	1.122	1.032
170	1.043	1.132	1.065
165	1.065	1.148	1.098
160	1.088	1.167	1.133
155	1.111	1.189	1.168
150	1.134	1.212	1.204
145	1.157	1.238	1.241
140	1.181	1.264	1.279
135	1.204	1.292	1.317
130	1.228	1.320	1.356
125	1.252	1.348	1.395
120	1.275	1.377	1.435

5.2.2 Pressure Fluctuations – Baseline Experiment

With the absence of external heating and cooling in the baseline experiments, the pressure fluctuation in the engine was due in large part to the volume change in the engine. Thermal effects from the cooling during expansion and heating during compression of the working fluid would also affect the pressure, but to a lesser degree. By analyzing the pressure fluctuations in the baseline tests, the change as a result of external heating and cooling will be more apparent.
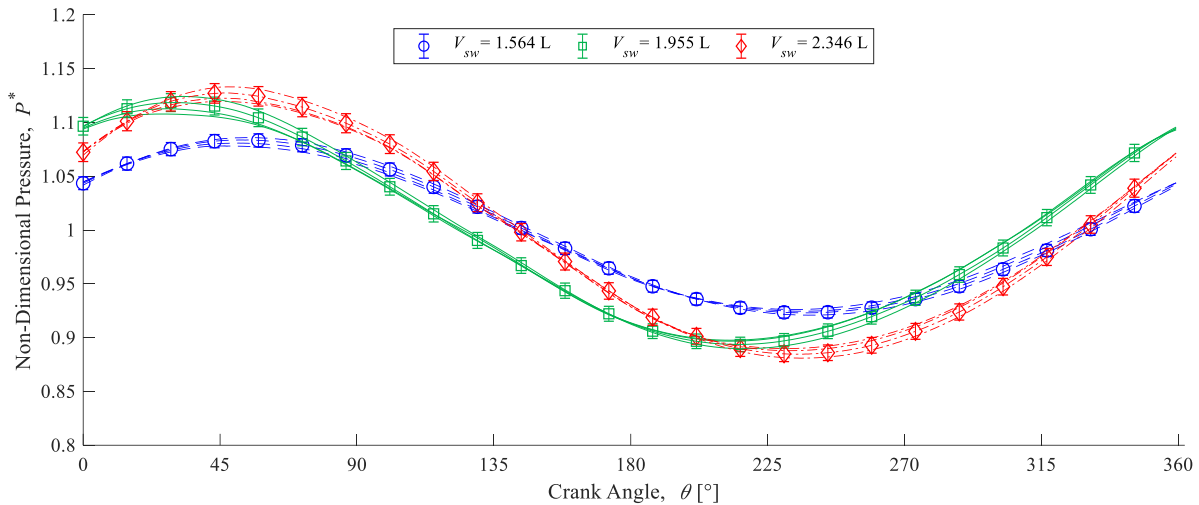
Figure 5-6: Pressure Fluctuation for All Swept Volumes and Speeds Tested for the Baseline Experiment at 120° (Every 20th Data Marker Plotted)

The dependency of pressure on engine speed was investigated to determine if the shape of the pressure fluctuation changed notably between speeds. During the experiment, the engine speed was changed from 30 rpm to 60 rpm in 10 rpm increments. The pressure fluctuation for each engine swept volume at each engine speed tested is shown in Figure 5-6. A non-dimensional pressure, defined in Section 4.5.4, was used for ease of comparison since the experiments were not all conducted at the same mean pressure due to atmospheric conditions. In the figure, for each swept volume there are four lines representing each speed. Every 20th data point was plotted for the 50 rpm curve along with the uncertainty bounds. The uncertainty bounds for the crank angle are not shown, since they lie within the data markers. It is apparent that if the uncertainty in each curve was plotted, all the curves for a specified swept volume would lie within uncertainty, so a speed dependency was not distinguished. As a result, pressure fluctuation plots will be presented for an engine speed of 60 rpm, rather than for each tested speed unless otherwise specified. The remaining baseline pressure plots for each speed and phase angle can be seen in Appendix J.

(a) 1.564 L
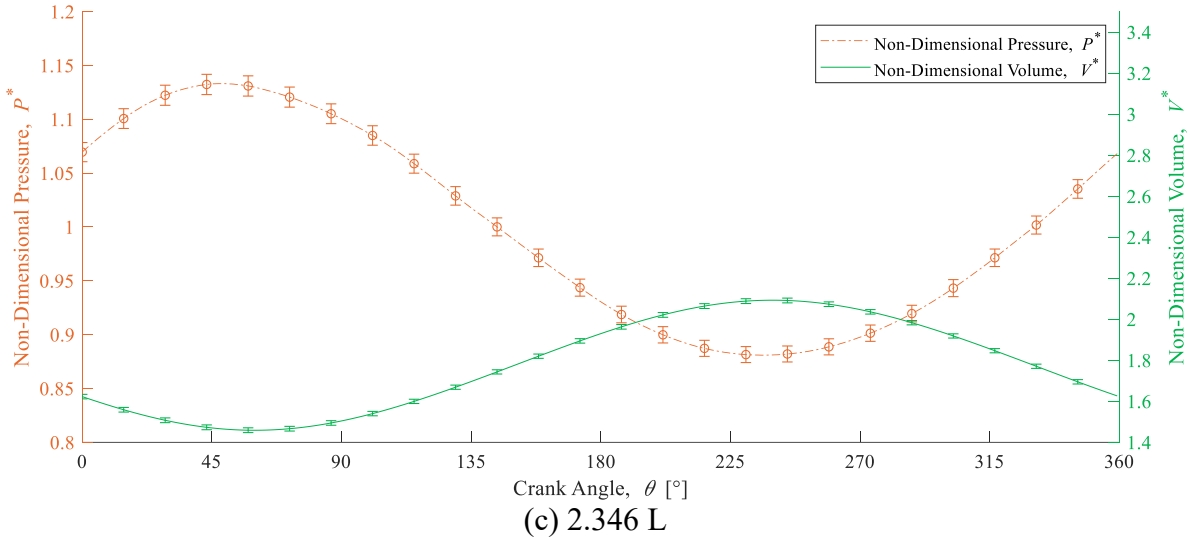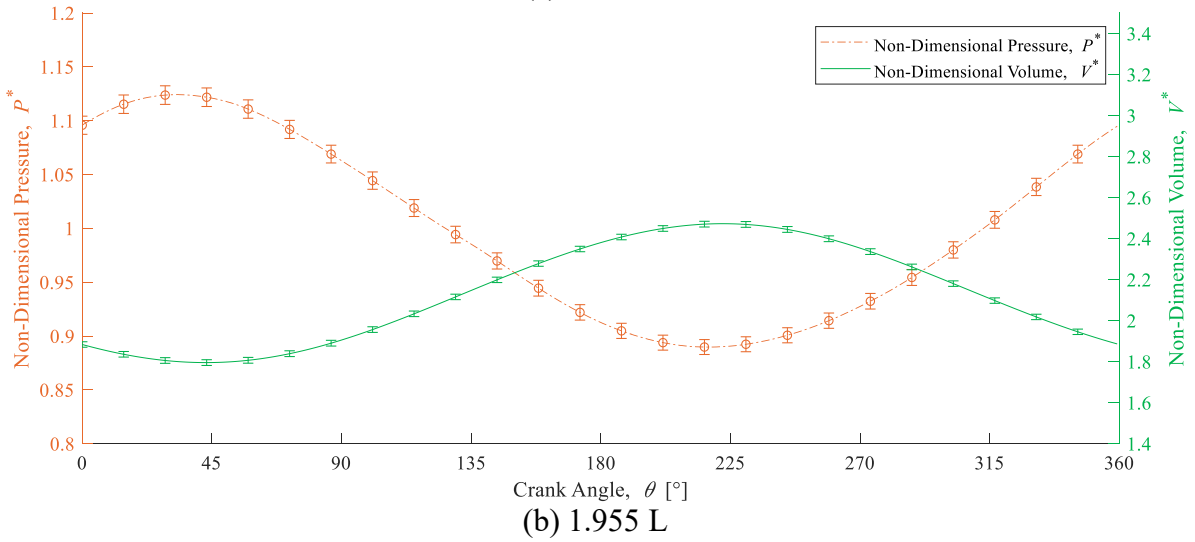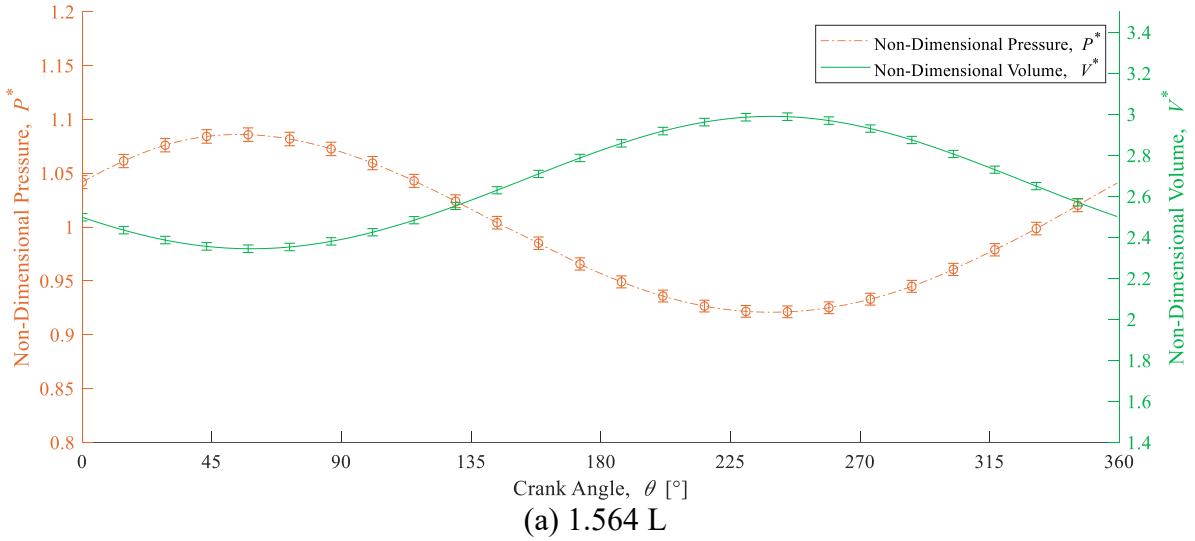
(b) 1.955 L

(c) 2.346 L

Figure 5-7: Baseline Pressure and Volume Fluctuations for Phase Angle 120° and Swept Volume (a) 1.564 L, (b) 1.955 L, and (c) 2.346 L at 60 rpm (Every 20th Data Marker Plotted)

The non-dimensional pressure and volume were compared to see if there were any discrepancies or unexpected results. Figure 5-7 shows the non-dimensional pressure fluctuations compared to the non-dimensional volume at the phase angle of 120° for each engine swept volume. The non-dimensional volume was larger when there was more dead space in the engine, since it was non-dimensionalized with respect to engine swept volume. The pressure was highest when the volume was at a minimum, and lowest when the volume was at a maximum, for all three cases, as expected. The pressure amplitude was lowest for a swept volume of 1.564 L, with the amplitudes of the other two cases being within uncertainty. It can also be seen that the maximum pressure occurred earlier in the cycle for a swept volume of 1.955 L than the other cases. This was due to the maximum and minimum volume occurring earlier in the cycle as a result of the combination of differing stroke lengths, shown in Section 5.2.1. In general, the relationships between pressure and volume for the baseline experiments were as expected. Additional pressure fluctuation plots may be seen in Appendix K.

5.2.3 Torque Fluctuations – Baseline Experiment

The baseline torque fluctuations were used in the calculation of the average shaft power input required to drive the engine at specified phase angles, swept volumes, and speeds. By analyzing the torque fluctuations, it was possible to visualize the instances where either there was increased mechanical friction, or where the servo-motor compensated for the speed fluctuations around the set point by increasing or decreasing the applied torque. The servo-motor was capable of outputting 15.05 Nm of torque, so a limit on the torque output was specified below 150% of the torque transducer rating when the 1 Nm transducer was installed. If the motor could not drive the engine at this torque limit, the 10 Nm transducer was installed which allowed for torque greater than 1.5 Nm to be applied. Figure 5-8 shows the torque fluctuation curves for each engine speed and swept volume for a phase angle of 120°, overlaid with the non-dimensional pressure fluctuations to better visualize areas of compression and expansion. The pressure variation was plotted for the 60 rpm test, since the fluctuations at the other speeds are within uncertainty. The uncertainty bounds for the torque curve are not present as they fall within the data markers. The approximate region of the expansion process was labelled on each figure.

(a) 1.564 L
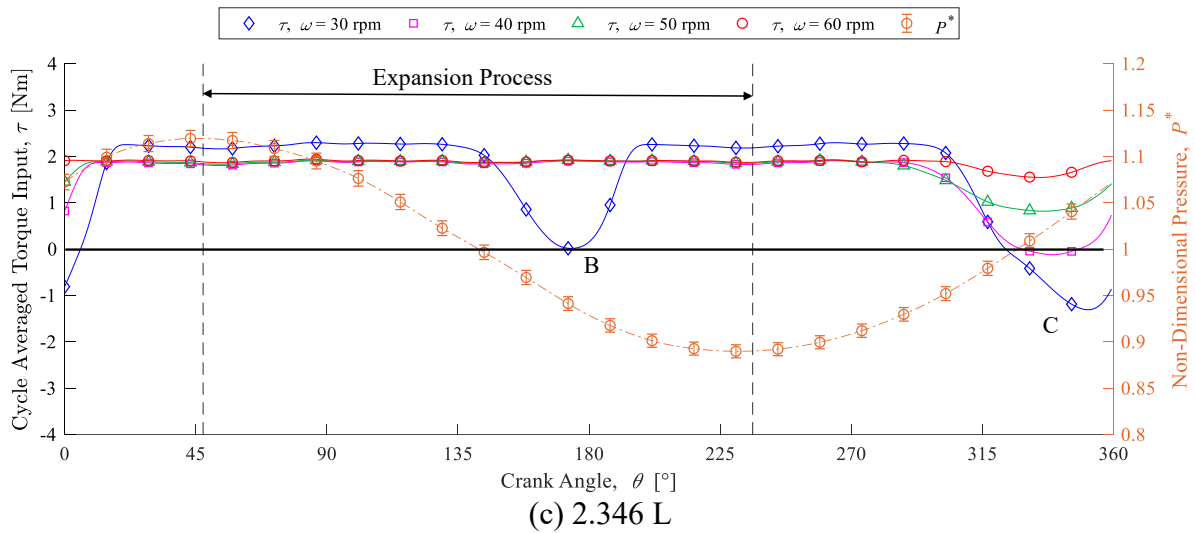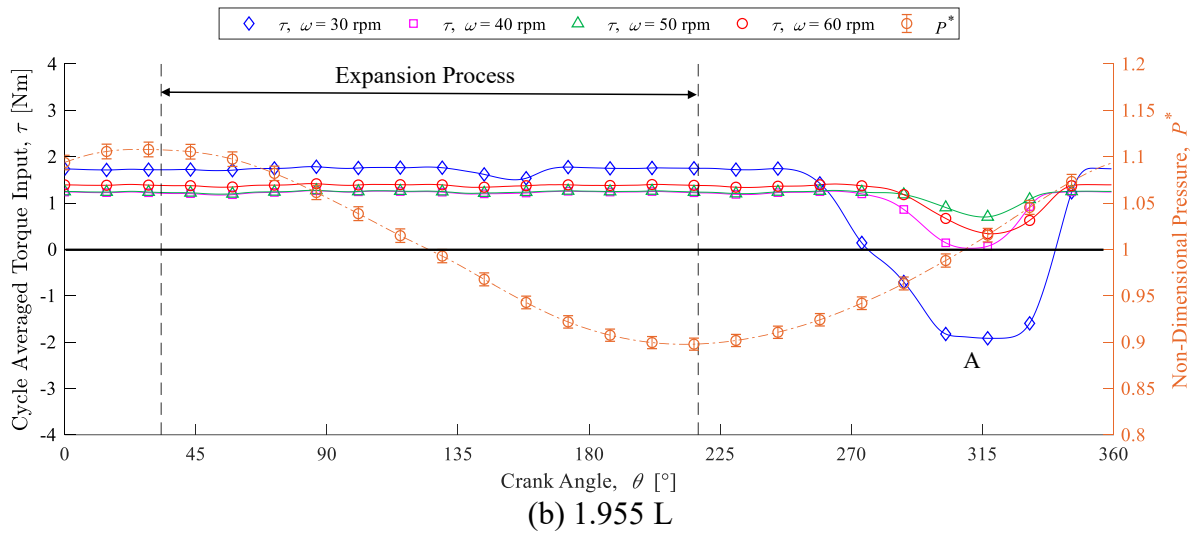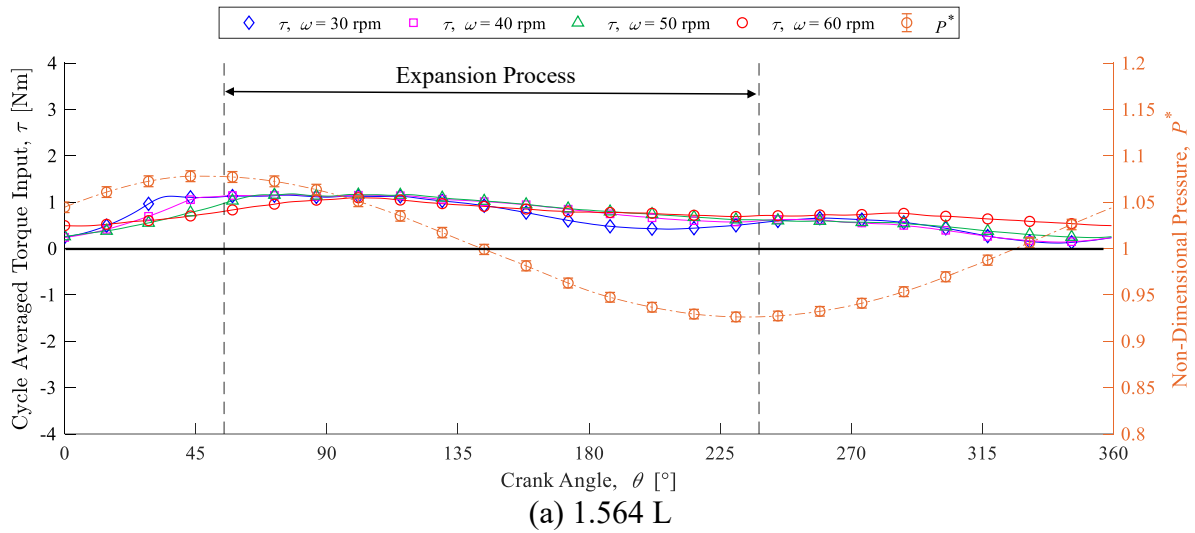
(b) 1.955 L

(c) 2.346 L

Figure 5-8: Baseline Cycle Averaged Smoothed Torque Curves and Non-Dimensional Pressure Fluctuations at Phase Angle of 120° and Swept Volume of (a) 1.564 L, (b) 1.955 L, and (c) 2.346 L (Every 20th Data Marker Plotted)

In Figure 5-8, the torque curves decreased between crank angles of 315° and 360°, which occurred before the maximum pressure during the compression process. This decrease was most apparent in Figure 5-8(b) and (c) at the labels "A" and "C", which increased in amplitude with decreasing speed. In addition, there was an initial reduction in torque near 180° crank angle, just before minimum pressure during expansion, labelled "B". This decrease was only present at 30 rpm. By viewing the additional plots for each swept volume and phase angle in Appendix L, the initial torque reduction at 30 rpm occurred at phase angles between 130° and 120°, which have significant compression. The sudden decrease in torque occurred at intermediate points close to the mean engine pressure. This may have been caused by the mechanism friction reducing during those sections of the cycle or backlash in the system since crank angles of 180° and 360° correspond to when the expansion space volume was maximized and minimized respectively.

In addition, the torque reduction was more apparent at slower speeds, where the flywheel would have a reduced angular momentum to overcome friction. The angular speed was overlaid with the torque fluctuations in Figure 5-9 for a set speed of 30 rpm and 60 rpm. For the 30 rpm case, the speed fluctuations were more pronounced. The peak speeds occurred near the torque reductions, likely as a result of the velocity control system of the servo-motor. When the speed was above the set-point, the torque output of the motor was reduced in response. For 60 rpm, the speed did not fluctuate as much, since the angular momentum of the flywheel would be increased and would dampen the speed fluctuations more effectively [80]. Also, since torque limits were applied, there were locations where the torque was relatively constant. For this particular configuration, the 10 Nm transducer was used and the limit was set at about 2 Nm.
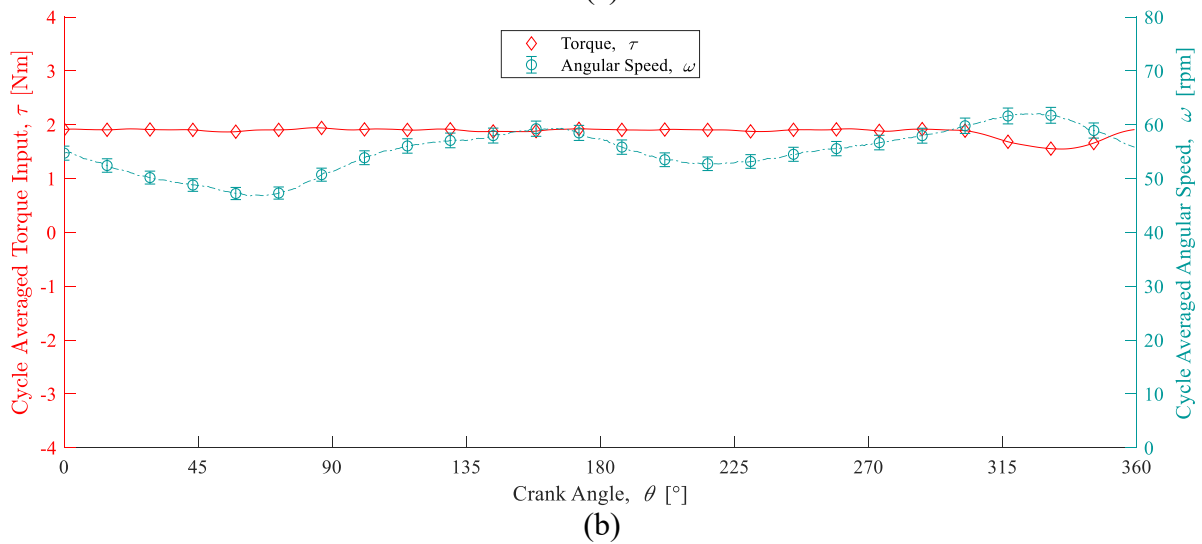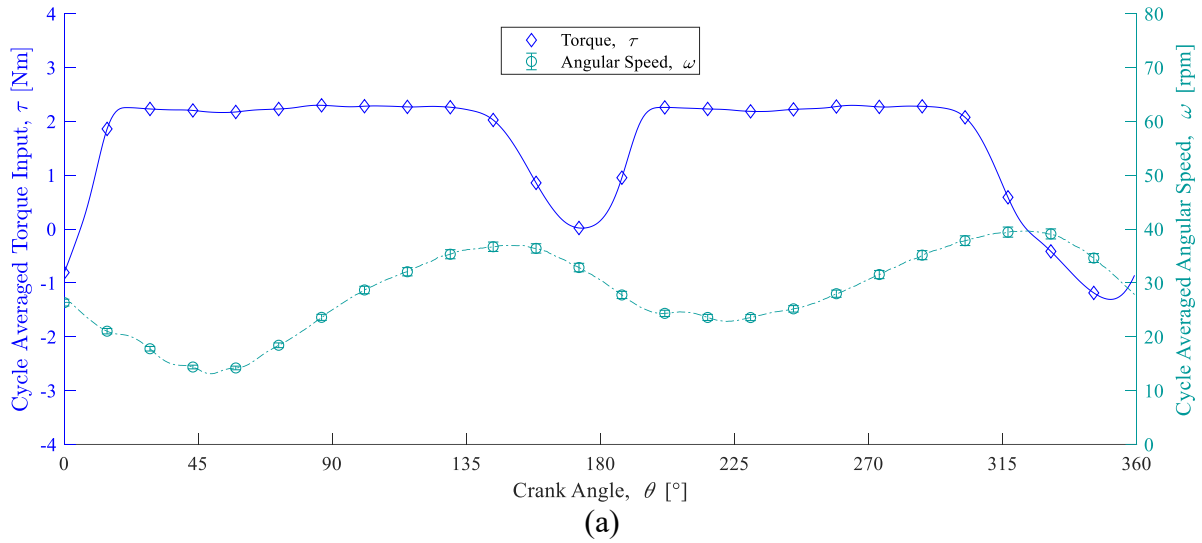
Figure 5-9: Cycle Averaged Smoothed Torque and Angular Speed Fluctuations at Phase Angle of 120° and Swept Volume of 2.346 L (a) 30 rpm (b) 60 rpm (Every 20th Data Marker Plotted)

It was also apparent that there were instances of consistent torque reversal, especially at lower engine speeds. Since no heat was being added or removed externally intentionally, this could be explained by the servo-motor control system. Throughout the cycle, the mechanism friction was not constant as a result of manufacturing and assembly tolerances, or backlash in the system. Since the speed of the servo-motor was being controlled, during the areas in which the mechanism friction was high, the motor applied a larger torque to attain the set speed. Once a point where the mechanism friction was low was reached, the motor applied a torque in the opposite direction, so that it did not go beyond the set speed. This became problematic, since the direction change in torque would result in underestimating the power input for the shaft power calculations.

To determine which configurations were affected by torque reversal, a ratio between minimum and maximum torque in the cycle, TR, was used, as shown in Equation 5-1, where τ_{min} was the minimum cycle averaged torque, and τ_{max} was the maximum cycle averaged torque.

$$TR = \frac{\tau_{min}}{\tau_{max}} \qquad\qquad 5\text{-}1$$

When the magnitude of the ratio was close to unity, the minimum value of torque approached the maximum value of torque, and the torque was relatively consistent. If the torque ratio was negative, then torque reversal occurred. It was also possible for the torque ratio magnitude to be greater than unity; however, this only occurred where the torque reversal magnitude was greater than the maximum torque magnitude. The torque ratios for engine speed of 30 rpm and 40 rpm are shown in Table 5-2, and the ratios for speeds of 50 rpm and 60 rpm are shown in Table 5-3. Cells were coded with green to show the cases without torque reversal, and with red to show cases with torque reversal.

Table 5-2: Baseline Torque Ratios for Engine Speeds of 30 rpm and 40 rpm

Phase Angle, α [°]	Torque Ratio, TR					
	Engine Speed, $\omega = 30$ [rpm]			Engine Speed, $\omega = 40$ [rpm]		
	$V_{sw} =1.564L$	$V_{sw} =1.955L$	$V_{sw} =2.346L$	$V_{sw} =1.564L$	$V_{sw} =1.955L$	$V_{sw} =2.346L$
180	-0.364	-0.185	-0.226	0.091	0.019	0.242
175	-0.513	-0.325	-0.317	0.075	0.003	0.217
170	-0.441	-0.245	-0.251	0.204	0.004	0.234
165	-0.397	-0.249	-0.228	0.217	-0.060	0.243
160	-0.368	-0.010	-0.002	0.247	0.142	0.414
155	-0.260	-0.117	0.434	0.179	0.121	0.501
150	-0.275	-0.100	0.493	0.033	0.259	0.690
145	-0.052	0.046	0.770	0.181	0.299	0.885
140	-0.039	0.159	-0.230	0.075	0.441	0.060
135	0.057	0.315	-0.169	0.085	0.550	0.037
130	-0.051	0.394	-0.220	0.061	0.605	0.431
125	0.008	-1.077	-0.582	0.015	0.088	0.039
120	0.104	-1.075	-0.569	0.120	0.018	-0.063

Table 5-3: Baseline Torque Ratios for Engine Speeds of 50 rpm and 60 rpm

Phase Angle, α [°]	Torque Ratio, TR					
	Engine Speed, $\omega = 50$ [rpm]			Engine Speed, $\omega = 60$ [rpm]		
	V_{sw} =1.564L	V_{sw} =1.955L	V_{sw} =2.346L	V_{sw} =1.564L	V_{sw} =1.955L	V_{sw} =2.346L
180	0.265	0.212	0.558	0.631	0.427	0.739
175	0.233	0.254	0.564	0.374	0.262	0.691
170	0.351	0.323	0.587	0.546	0.514	0.682
165	0.501	0.271	0.601	0.502	0.493	0.777
160	0.603	0.372	0.714	0.649	0.569	0.808
155	0.528	0.348	0.717	0.649	0.511	0.847
150	0.300	0.385	0.731	0.688	0.473	0.758
145	0.410	0.492	0.678	0.629	0.598	0.856
140	0.390	0.625	0.483	0.588	0.730	0.693
135	0.356	0.720	0.239	0.529	0.657	0.710
130	0.386	0.746	0.457	0.471	0.872	0.638
125	0.337	-0.090	0.644	0.463	0.140	0.651
120	0.201	0.548	0.425	0.445	0.237	0.797

From Table 5-2 and Table 5-3, the majority of the torque reversal instances occurred at the speed of 30 rpm, at various phase angles and swept volumes. Although, there were a few instances that occurred at higher compression phase angles of 125°.and 120° at higher speeds. Instances of the magnitude of the ratio above unity occurred at lower phase angles at a swept volume of 1.955 L.

5.2.4 Temperature Measurements – Baseline Experiment

Gas temperature measurements during the baseline experiments were used to aid in quantifying the compressive heating and expansion cooling effects. Since the water in the heat exchangers was not flowing and was at ambient temperature, the observed gas temperature change was attributed to compression and expansion effects. It should be noted that a cycle averaged gas temperature was calculated for each thermocouple, since the response time of the thermocouples were slow compared to the frequency of the engine. Figure 5-10 shows the mean temperature measurements for each phase angle. The scale of 0 °C to 100 °C was used to be consistent with the axis range of the thermal experiments.
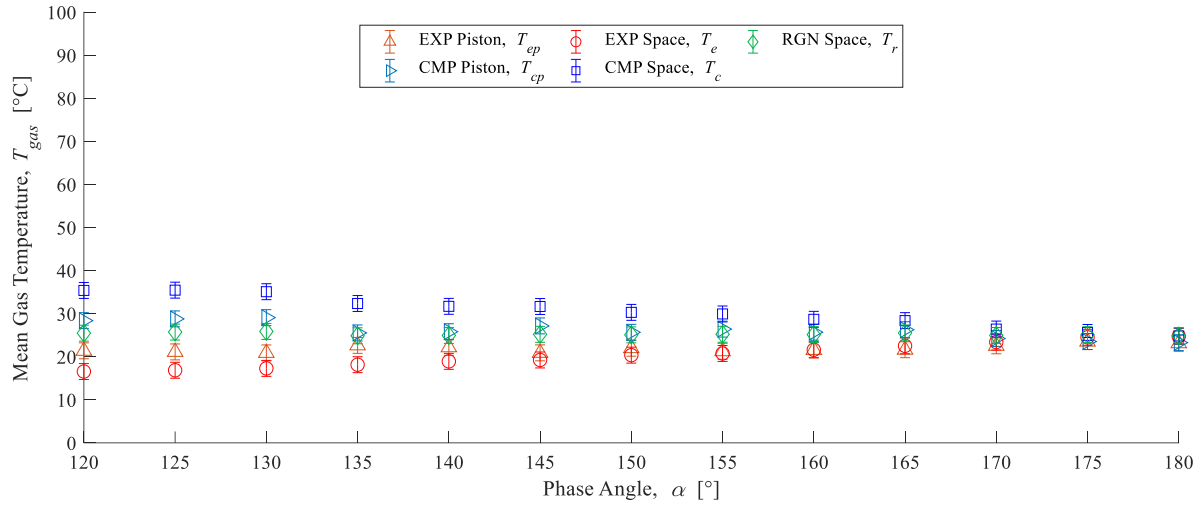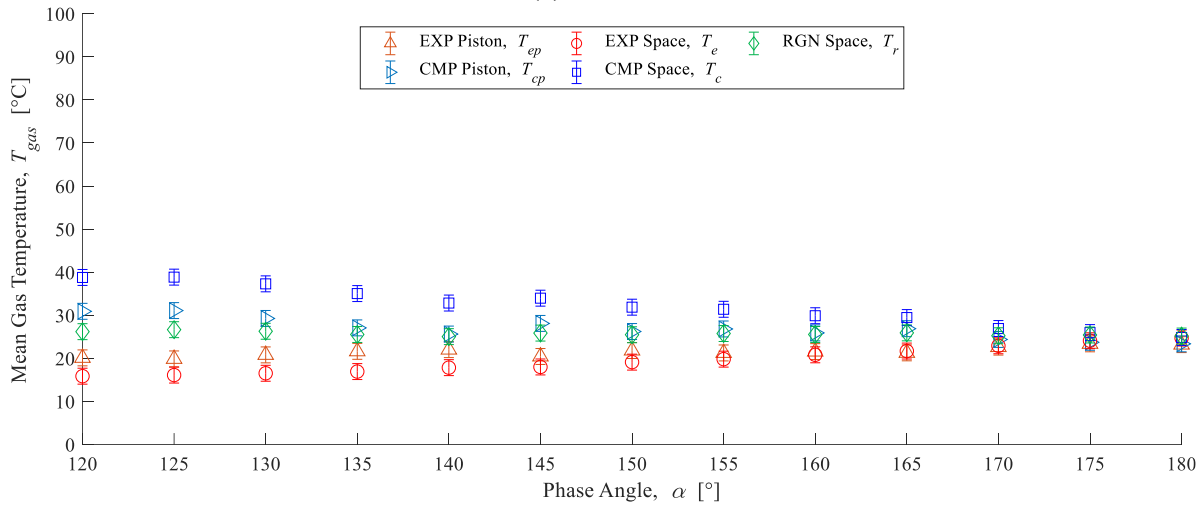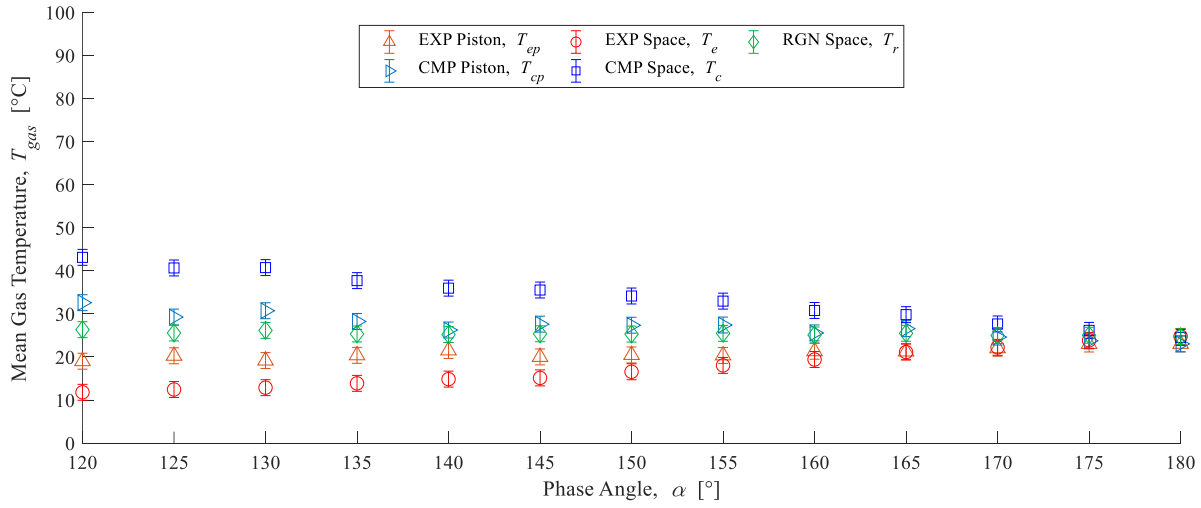
Figure 5-10: Mean Gas Temperature Measurements as a Function of Phase Angle for Baseline Experiments at a Swept Volume (a) 1.564 L, (b) 1.955 L, and (c) 2.346 L at 60 rpm

It can be seen that independent of the swept volume, the trend remained the same: as the phase angle decreased, the thermocouples within the compression space measured an increase in gas temperature, whereas those in the expansion space measured a decrease in temperature. The temperature in the regenerator space remained nearly constant. As the swept volume increased, the spread between temperature measurements also increased due to increasing compression ratios. It was also apparent that the thermocouples within the piston faces did not attain the same temperature reading as those that were within the workspace. The measured temperature in the regenerator space remained slightly above ambient temperature, at 25 °C. At a phase angle of 120°, the compression space temperature rose to a maximum average temperature of approximately 43 °C, and the expansion space decreased to a minimum average temperature of approximately 12 °C. The plots for the remaining speeds tested are shown in Appendix M.

5.2.5 Engine Indicator Diagrams – Baseline Experiment

The indicator diagrams for the baseline cases were plotted for later comparison with the thermal experiment indicator diagrams. Non-dimensional variables were used to make differences between data sets more apparent. Since the non-dimensional pressure was defined with respect to the mean pressure, a value of 1 was equivalent to the mean pressure for each cycle. By using non-dimensional volume with respect to swept volume, the amount of dead volume in each configuration could be visualized, as the indicator diagrams increased in dead volume from left to right. The leftmost indicator diagram corresponds to the configuration with the expansion and compression piston strokes at 76.2 mm (V_{sw}=2.346 L), which had the least amount of dead volume. The middle diagram corresponds to the 50.8 mm compression stroke and 76.2 mm expansion stroke (V_{sw}=1.955 L), which had more dead volume in the compression space than the expansion space. Lastly, the right-most diagram had the 50.8 mm stroke length for both pistons (V_{sw}=1.564 L), which had the most dead volume, but it was equally distributed. Therefore, as shown in Section 5.2.1, the swept volume configuration order from left to right was 2.346 L, 1.955 L, and then 1.564 L. Also, only the 60 rpm experiments will be shown, since the effect of speed on the pressure fluctuations could not be differentiated due to the uncertainty in the measurement, as shown in Section 5.2.2.
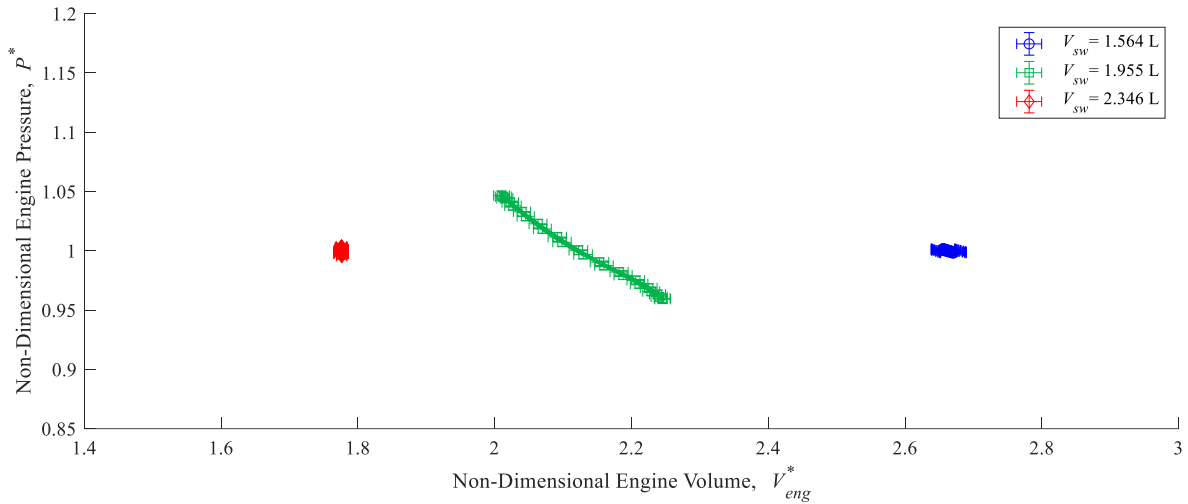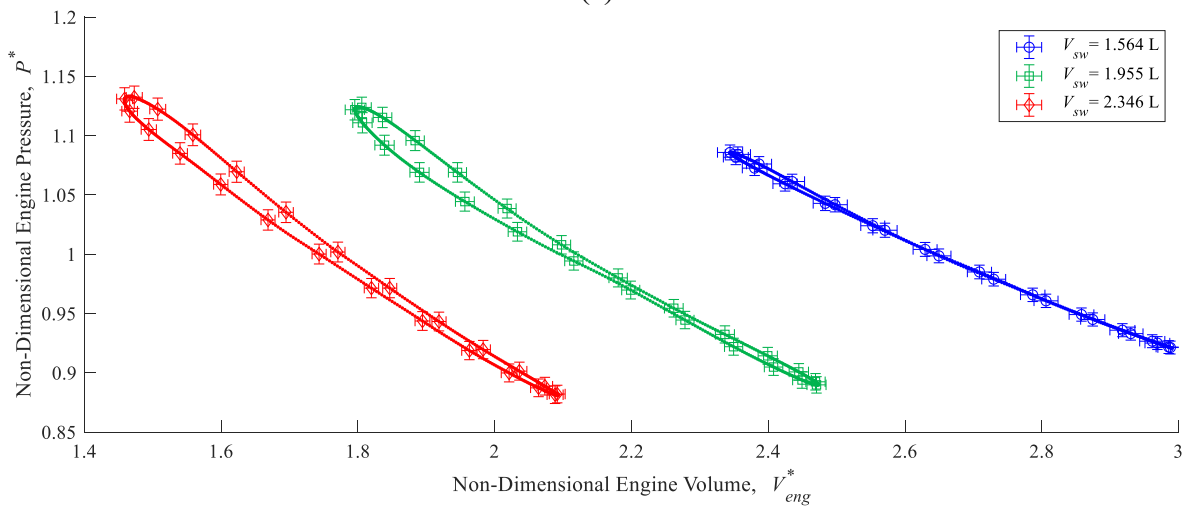
Figure 5-11:Baseline Experiment Non-Dimensional Indicator Diagrams at 60 rpm for (a) 180° (b) 120° Phase Angles (Every 20th Data Marker Plotted)

Figure 5-11 (a) and (b) show the non-dimensional indicator diagrams for a phase angle of 180° and 120°. For swept volumes of 1.564 L and 2.346 L and a phase angle of 180°, the indicator diagram was collapsed, as expected since there was no volume change to incite a pressure change. Contrarily, there were pressure and volume fluctuations for the 1.955 L swept volume configuration with a phase angle of 180°, which was expected from the findings in Section 5.2.1. As the phase angles decreased from 180° to 120°, the indicator diagrams elongated as the pressure ratio increased with compression ratio. Also, the diagram began to widen, but it was difficult to quantify because of the calculated uncertainty bounds. The remaining baseline indicator diagrams can be seen in Appendix N.

5.2.6 Shaft Power Consumption Measurements – Baseline Experiment

Along with understanding the trends in volume, pressure, torque, and temperature, one of the major goals of the baseline experiments was to determine the amount of power required to drive the engine at the specified speeds and stroke combinations. By calculating the cycle averaged power consumption, then taking the mean value of the power consumption, the relationship between speed, phase angle, swept volume, and shaft power could be observed. Recall that in Section 5.2.3 there were instances where the torque reversed direction, which would underestimate the measured mean power consumption. This occurred mostly during the 30 rpm experiments, with a few other instances at higher speeds. Table 5-2 and Table 5-3 may be referred to for the specific cases where torque reversal was present.

The mean shaft power input as a function of phase angle for each swept volume and speed tested can be seen in Figure 5-12. It should be noted that the majority of the uncertainty bounds fell within the data markers, so only the data with uncertainty beyond the markers have the uncertainty bars displayed. From the graphs, as the phase angle decreased, the power consumption tended to increase for all speed and stroke combinations. The compression ratio increased as well, so the mechanism forces and pressure were greater, and more compression work was required to complete the cycle. As a result, the servo-motor had to increase the torque applied to maintain the set velocity, as seen in the torque fluctuation plots in Appendix L. In general, the 2.346 L swept volume configurations required the most power, followed by the 1.955 L and 1.564 L configurations. Furthermore, as the engine speed was increased, so too did the power input. The work consumed during the cycle should be comparatively constant for a specific configuration for each speed; however, that amount of work would occur over a shorter period of time at higher speeds, which would increase the power consumption. There were some unexpected outcomes, such as at higher speeds the power consumption increased for the phase angle of 180° compared to between 175° to 165°. In addition, there were marked decreases in power input at the low phase angle high compression ratio for the 1.955 L swept volume cases. Without further repeats in the experiment, it is difficult to associate these abnormalities with an exact cause; however, it was likely due to the large torque fluctuations as can be seen by the low value of the torque ratios in Table 5-2 and Table 5-3. The values for the power consumption are tabulated in Table 5-4 for engine speeds of 30 rpm and 40 rpm, and in Table 5-5 for engine speeds of 50 rpm and 60 rpm.
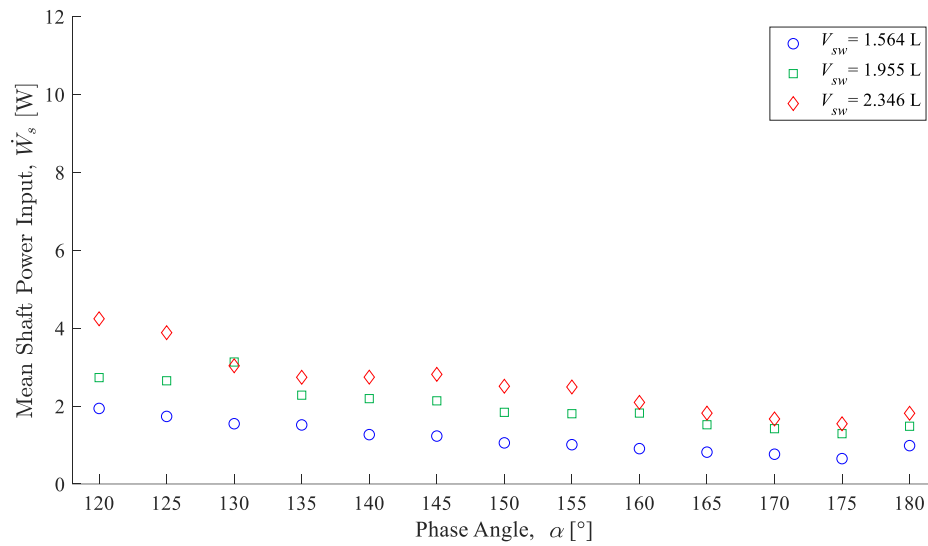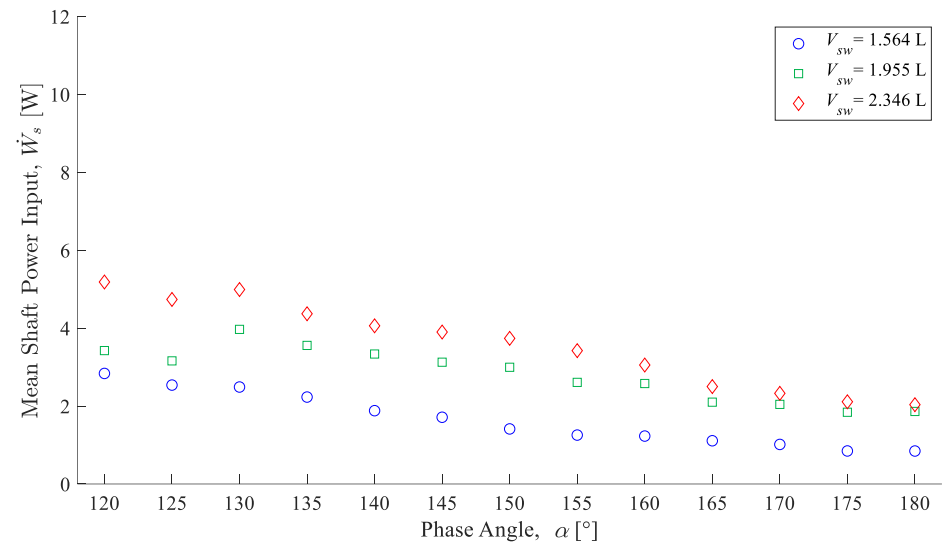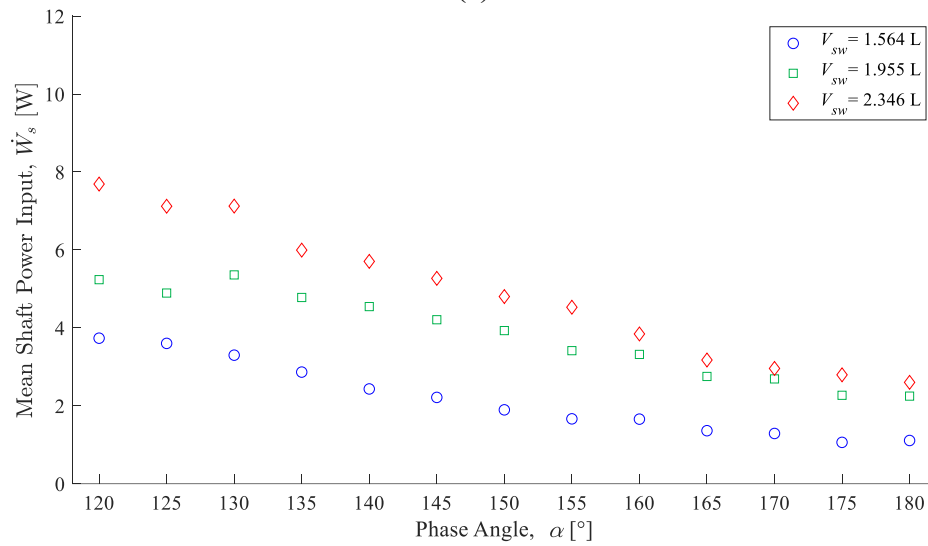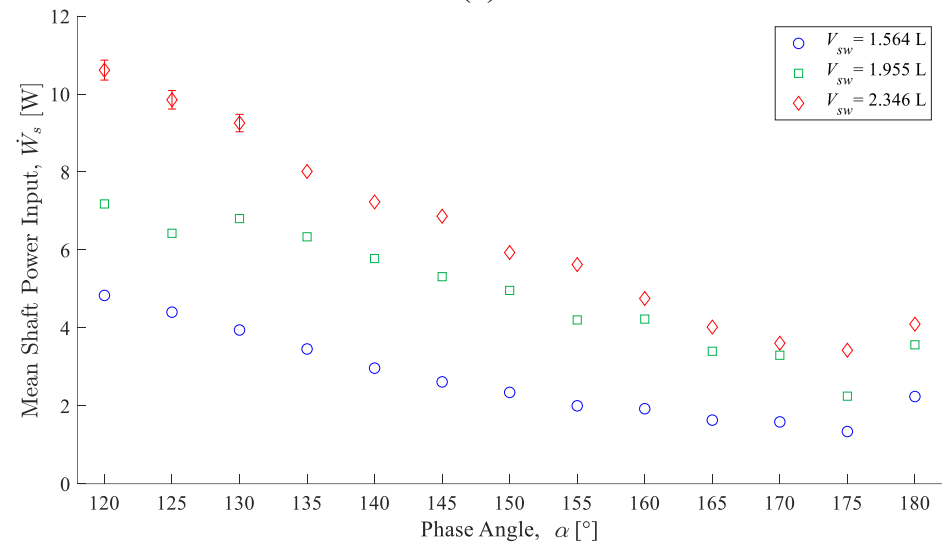
Figure 5-12:Mean Shaft Power Input as a Function of Phase Angle for Baseline Experiments Driven at Motor Speeds of (a) 30 rpm (b) 40 rpm (c) 50 rpm (d) 60 rpm

Table 5-4: Table of Mean Shaft Power Input for Engine Speeds of 30 rpm and 40 rpm for Baseline Experiments

Phase Angle, α [°]	Mean Shaft Power Input, $\dot{W}_s$ [W]					
	Engine Speed, $\omega = 30$ [rpm]			Engine Speed, $\omega = 40$ [rpm]		
	$V_{sw} =1.564$L	$V_{sw} =1.955$L	$V_{sw} =2.346$L	$V_{sw} =1.564$L	$V_{sw} =1.955$L	$V_{sw} =2.346$L
180	0.98	1.48	1.82	0.85	1.86	2.04
175	0.65	1.29	1.55	0.85	1.84	2.11
170	0.76	1.42	1.67	1.02	2.04	2.33
165	0.82	1.52	1.82	1.11	2.10	2.50
160	0.91	1.82	2.09	1.23	2.58	3.05
155	1.01	1.80	2.49	1.26	2.61	3.42
150	1.05	1.84	2.51	1.41	3.00	3.74
145	1.23	2.13	2.81	1.71	3.13	3.90
140	1.27	2.19	2.74	1.88	3.34	4.06
135	1.52	2.28	2.74	2.23	3.56	4.37
130	1.55	3.13	3.03	2.49	3.97	4.99
125	1.73	2.65	3.88	2.54	3.16	4.74
120	1.94	2.73	4.24	2.84	3.42	5.18

Table 5-5: Table of Mean Shaft Power Input for Engine Speeds of 50 rpm and 60 rpm for Baseline Experiments

Phase Angle, α [°]	Mean Shaft Power Input, $\dot{W}_s$ [W]					
	Engine Speed, $\omega = 50$ [rpm]			Engine Speed, $\omega = 60$ [rpm]		
	$V_{sw} =1.564$L	$V_{sw} =1.955$L	$V_{sw} =2.346$L	$V_{sw} =1.564$L	$V_{sw} =1.955$L	$V_{sw} =2.346$L
180	1.11	2.25	2.60	2.24	3.57	4.10
175	1.06	2.27	2.80	1.34	2.25	3.43
170	1.29	2.69	2.96	1.59	3.30	3.61
165	1.36	2.75	3.18	1.63	3.40	4.02
160	1.66	3.32	3.84	1.93	4.23	4.75
155	1.67	3.42	4.53	2.00	4.20	5.62
150	1.90	3.93	4.80	2.34	4.96	5.93
145	2.22	4.21	5.27	2.61	5.31	6.86
140	2.43	4.55	5.71	2.97	5.78	7.23
135	2.87	4.78	6.00	3.46	6.34	8.01
130	3.30	5.36	7.12	3.95	6.80	9.26
125	3.60	4.89	7.12	4.40	6.43	9.85
120	3.74	5.24	7.69	4.83	7.18	10.61

5.2.7 Baseline Experiments Summary

Many insightful outcomes about the performance of the engine were discovered by performing a set of baseline experiments without an active thermal source and sink, and will be useful in the analysis of the thermal experiment results.

Initially, the volume and pressure fluctuations were investigated. By looking at the change in volume throughout a cycle for each configuration, it was determined that the volume varied at a phase angle of 180° for the 1.955 L configuration. The compression ratios were calculated for each configuration, and were found to increase with decreasing phase angle, as expected, but the compression ratio was higher for the 1.955 L configuration compared to both 1.564 L and 2.346 L configurations between 180° and 150°. When analyzing the pressure fluctuations, a speed dependency could not be distinguished for the speeds tested.

The torque fluctuations were shown to have points of torque reversal, especially at lower engine speeds. They could be a result of varying mechanism friction or backlash in the system where the servo-motor would compensate for speed fluctuations. The reversals were reduced at higher speeds, where the angular momentum of the flywheel would be higher and the speed fluctuations would be dampened.

When focusing on the gas temperatures in the engine, compression heating and expansion cooling were significant as the phase angle was decreased. The effects were more apparent at larger swept volume configurations.

The indicator diagrams were created, and found to stretch as the pressure ratio increased with the compression ratio; however, the area within the diagrams was small because the thermal source and sink were inactive, so the gas was not heated during expansion or cooled during compression. The amount of power consumed to drive the engine at each configuration was determined, and it was found that as the phase angle decreased the power input increased. Furthermore, for larger swept volumes, more power was required to drive the engine.

5.3 Thermal Experiments

The thermal experiments were completed to determine the viability of a LTD alpha-type Stirling engine, and which of the tested configurations would result in the greatest performance. This section will follow a similar format to Section 5.2, so that a proper comparison between the baseline and thermal results may be provided. As mentioned, the engine did not produce a net positive amount of power, so a servo-motor was used to conduct these tests.

5.3.1 Pressure Fluctuations – Thermal Experiment

Throughout the cycle, the engine pressure fluctuated as a result of both thermal and volume fluctuations. With the addition of heat leading up to and during expansion, the expansion process should occur at higher pressures compared to the baseline experiments. Conversely, during compression, heat is removed such that the compression process occurs at lower pressures relative to the baseline experiment. For a given volume, if the higher pressures during expansion and lower pressures during compression are sustained, the indicator diagram will widen and increase in area, corresponding to an increase in indicated work for the thermal experiments.

The analysis for the baseline experiments showed that without thermal input, the pressure fluctuations were within uncertainty for all the speeds tested. The effect of engine speed on the pressure fluctuations was investigated again for the thermal experiments to see if the lower engine speeds would provide more time for heat transfer, hence distinguishing the separate pressure fluctuations for each speed. Also, to see if the increased time for heat transfer would create more sustained pressure peaks which would change the shape of the indicator diagram between speeds.
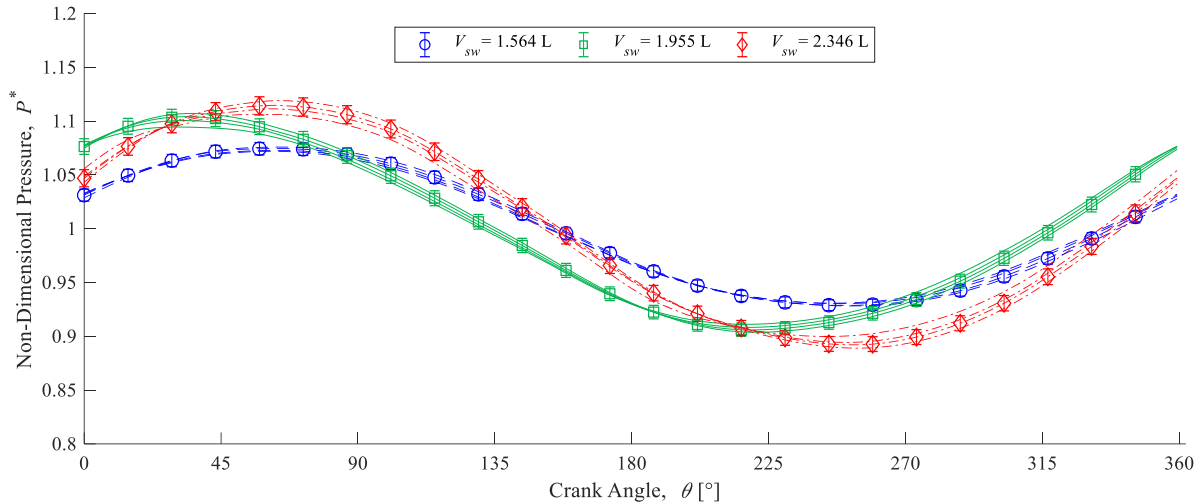
Figure 5-13: Pressure Fluctuation Speed Dependency for Thermal Experiment at 120°
(Every 20th Data Marker Plotted)

Figure 5-13 shows the non-dimensional pressure fluctuations as function of crank angle for all speeds and swept volumes tested. For each swept volume there are four lines representing each speed. Every 20th data point was plotted for the 50 rpm curve along with the uncertainty bounds. The uncertainty bounds for the crank angle are not shown, since they lie within the data markers. As with the baseline case, the uncertainty bounds for each curve would overlap, so the effect of speed on the pressure fluctuation could not be distinguished. If the dependency of pressure on speed and amount of time for heat transfer was to be analyzed further, a greater difference in engine speed would need to be investigated. As such, plots pertaining to pressure for the thermal experiments will be shown for the 60 rpm case unless otherwise specified. The remaining figures for the other phase angle configurations tested appear in Appendix O.

Upon examination of the 180° phase angle experiments, shown in Figure 5-14, it can be seen that pressure fluctuations occurred, which can be attributed to the thermal effects of heating and cooling the gas as it was shuttled without a volume change. In addition, the pressure fluctuation for a swept volume of 1.955 L at 180° was a result of both a volume variation and temperature variation, whereas the volume was constant in the cases with the same stroke length for both the expansion and compression pistons.
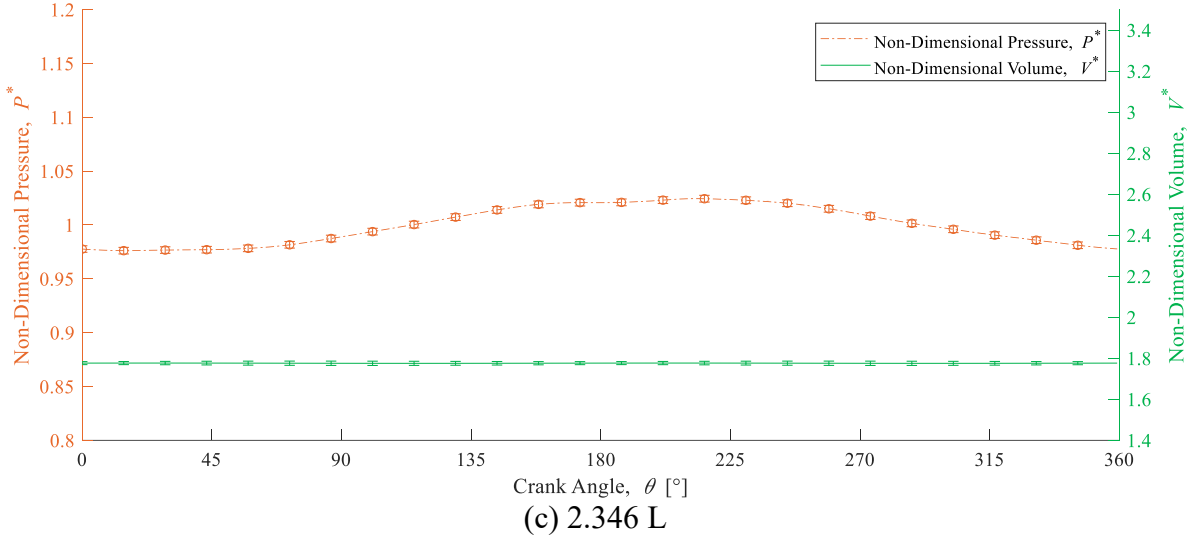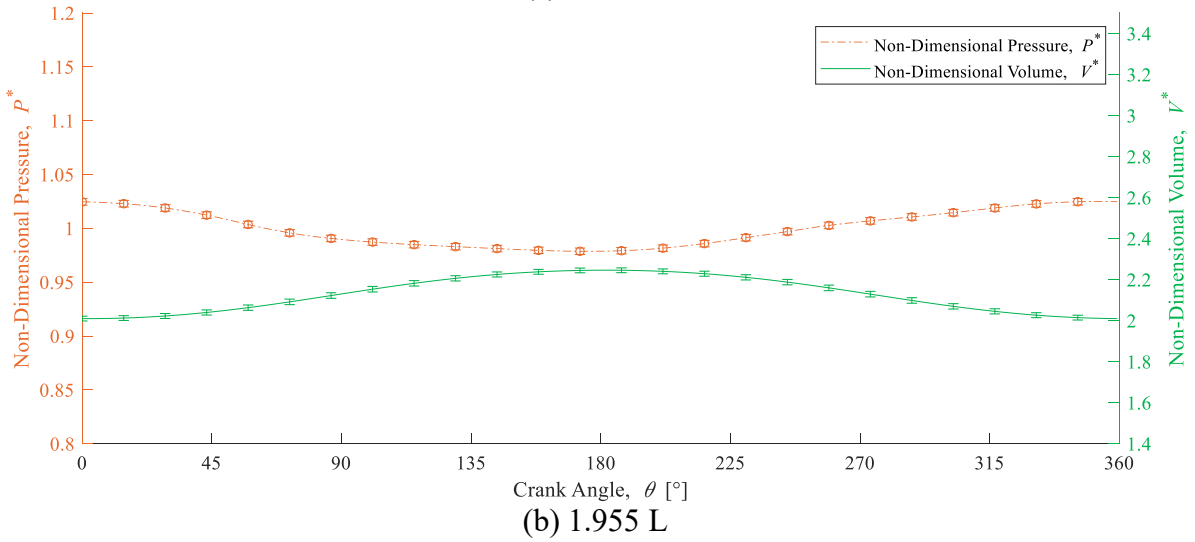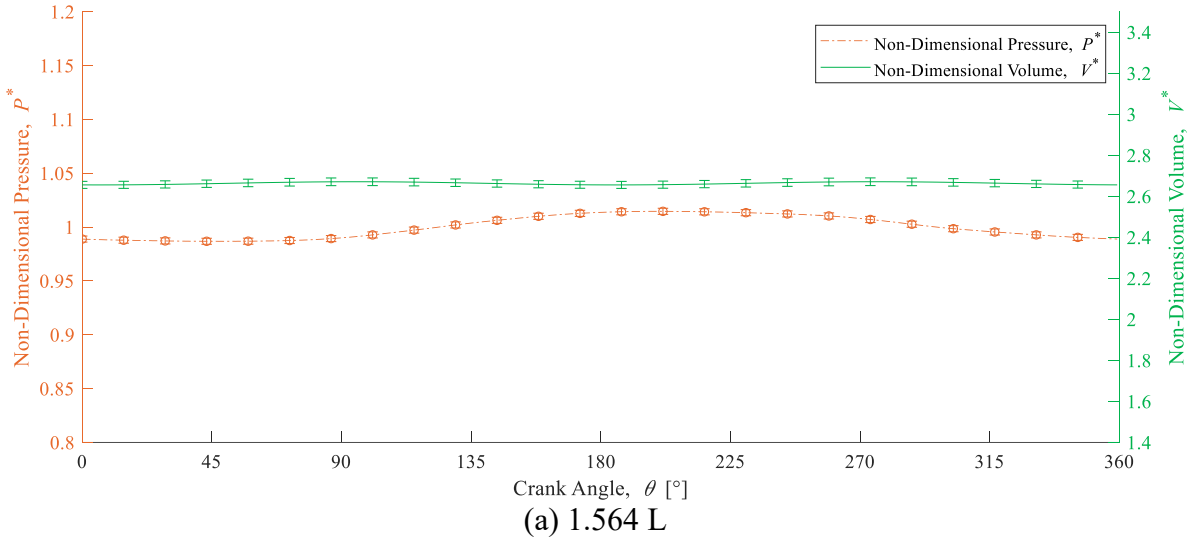
Figure 5-14: Thermal Pressure and Volume Fluctuations for Phase Angle 180° and Swept Volume (a) 1.564 L, (b) 1.955 L, and (c) 2.346 L at 60 rpm (Every 20th Data Marker Plotted)

(a) 1.564 L
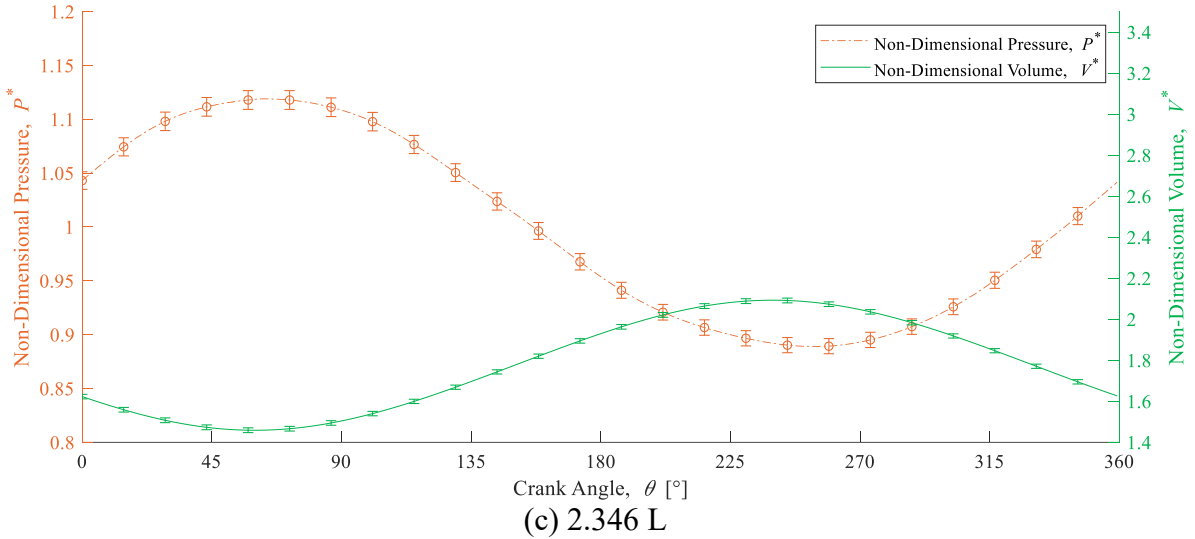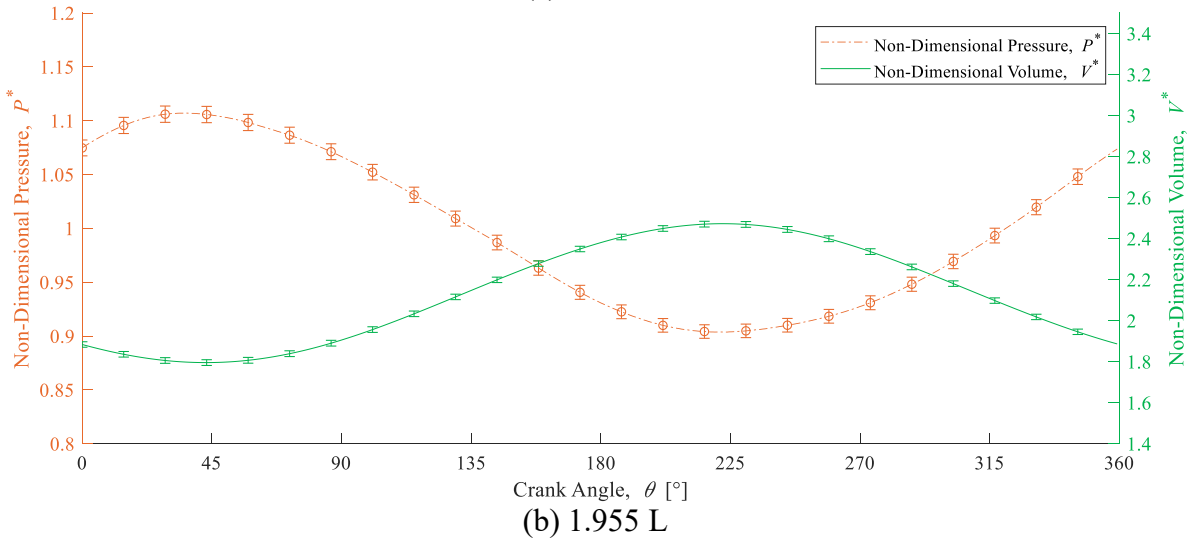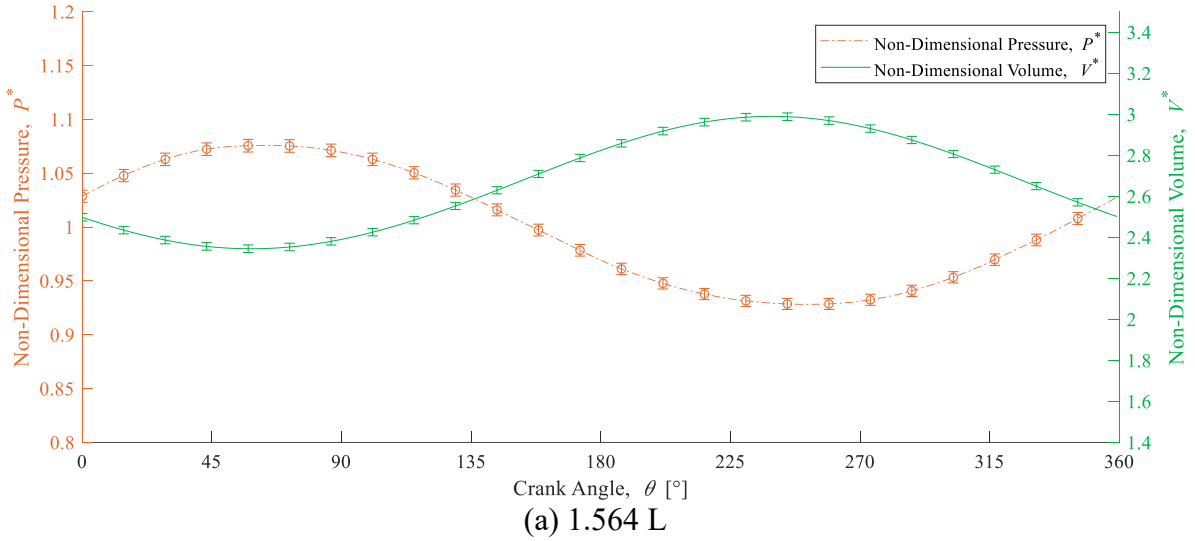
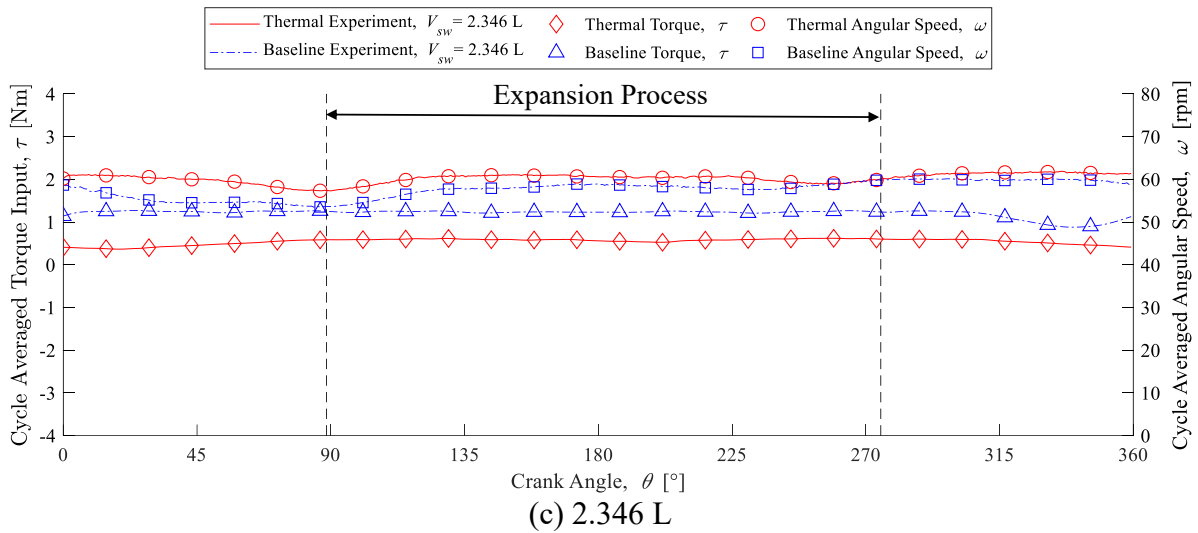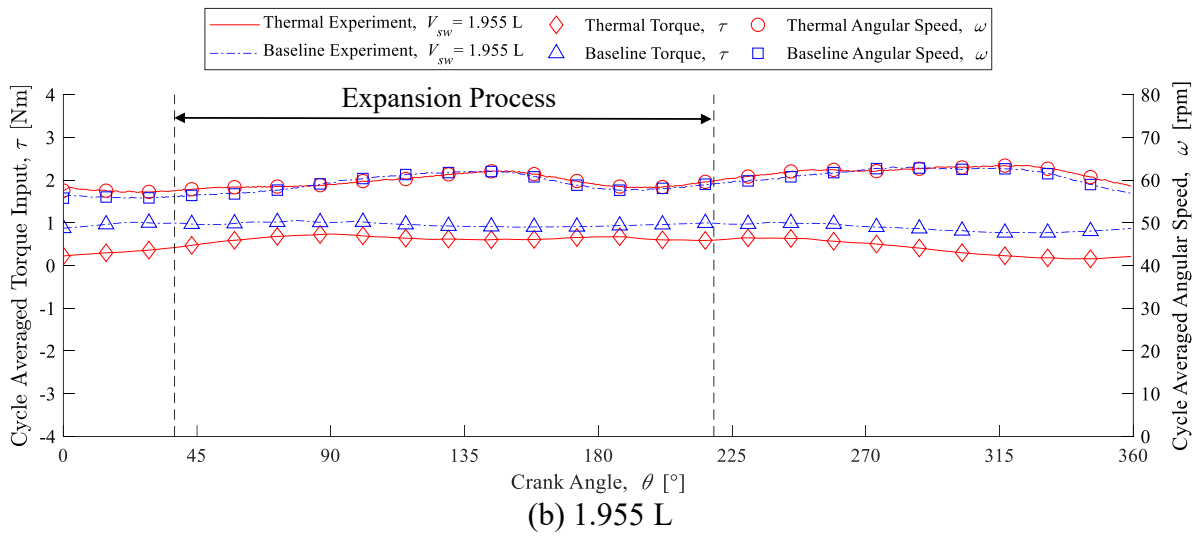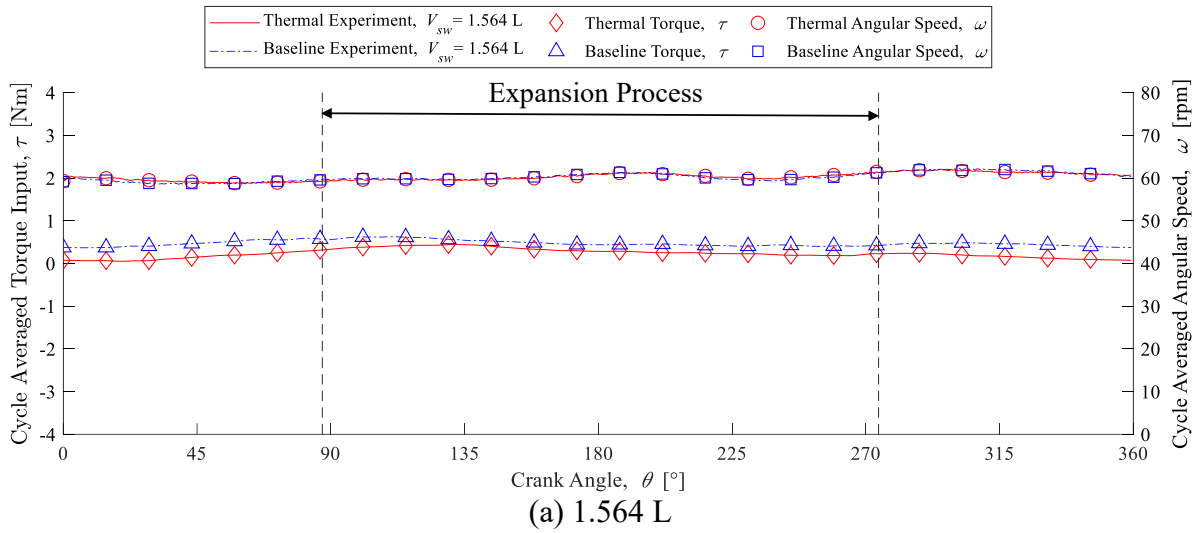(b) 1.955 L

(c) 2.346 L

Figure 5-15: Thermal Pressure and Volume Fluctuations for Phase Angle 120° and Swept Volume (a) 1.564 L, (b) 1.955 L, and (c) 2.346 L at 60 rpm (Every 20th Data Marker Plotted)

The non-dimensional pressure fluctuations for the thermal experiments at a phase angle of 120° is shown in Figure 5-15. The pressure was highest at the minimum engine volume and lowest at the maximum engine volume for all cases, which appears to indicate that the volume change had a greater influence on pressure than temperature in this engine. Similar to the baseline experiments, the pressure amplitudes were lowest for the 1.564 L swept volume configuration. Again, the pressure peak for the 1.955 L case occurred earlier in the cycle as can be seen from both Figure 5-13 and Figure 5-15 as a result of the altered point of maximum and minimum engine volume with differing stroke lengths. The remaining figures for the other phase angles can be seen in Appendix P.

5.3.2 Torque Fluctuations – Thermal Experiment

Similar to the baseline experiments, the torque fluctuations were investigated to see if the inclusion of a thermal source and sink would change the torque and speed in a significant manner. The torque curves for each speed and swept volume tested were plotted along with the pressure fluctuations for a phase angle of 120°, as shown in Figure 5-16. The approximate region of the expansion process was labelled on each figure. The fluctuations followed a similar trend at a swept volume of 1.564 L; however, at a swept volume of 1.955 L, the torque reversal no longer occurred at this phase angle, as it did in the baseline experiments. At a swept volume of 2.346 L, a significant torque reduction similar to the baseline experiment occurred at low speeds, with two instances, labelled "D" and "E" in Figure 5-16(c), at a speed of 30 rpm. These occurred near the same region as in the baseline case and was therefore likely a result of the servo-motor speed control algorithm correcting for mechanism friction or backlash in the system. The remaining figures comparing the torque fluctuations at different engine speeds can be seen in Appendix Q.
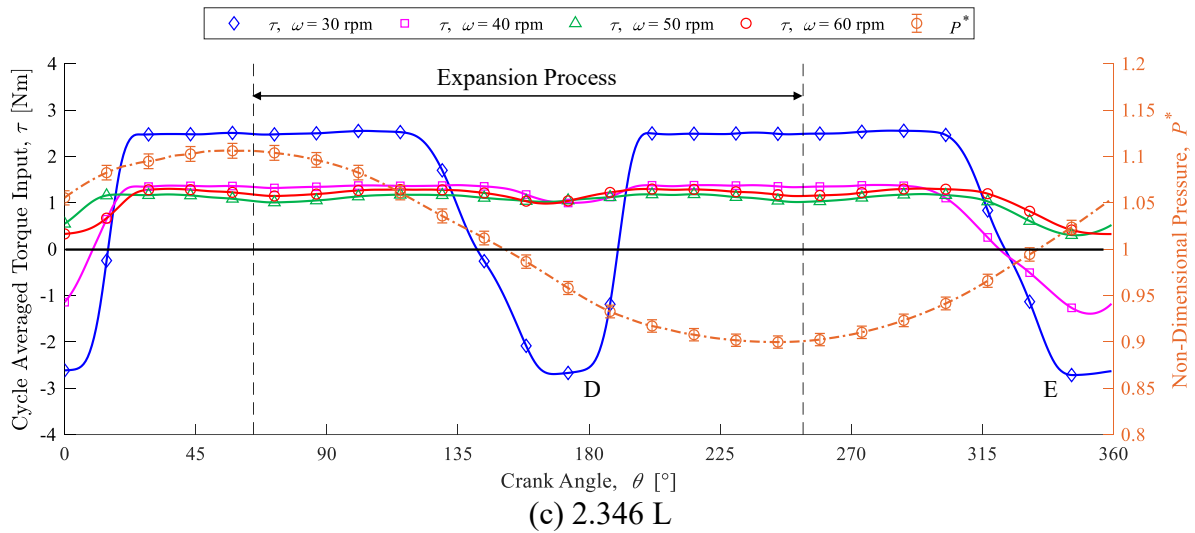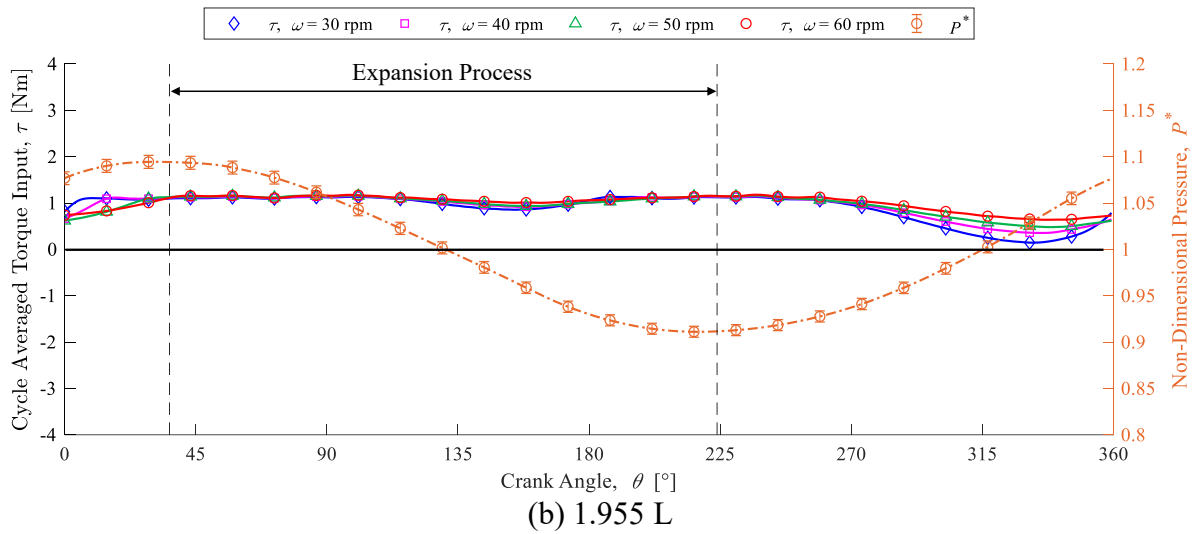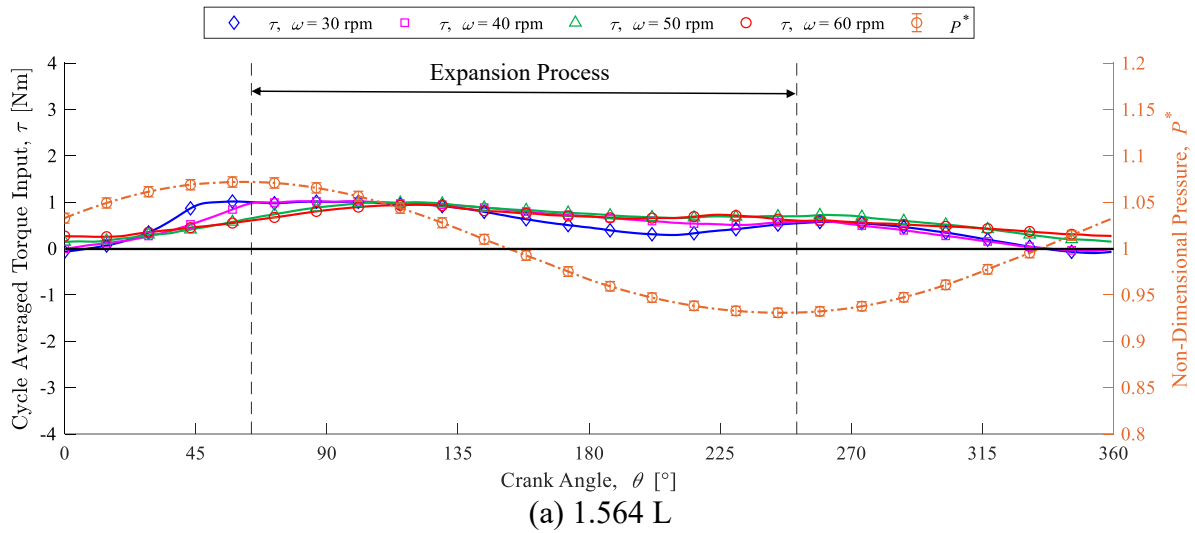
Figure 5-16: Thermal Experiment Cycle Averaged Smoothed Torque Curves and Non-Dimensional Pressure Fluctuations at Phase Angle of 120° and Swept Volume of (a) 1.564 L, (b) 1.955 L, and (c) 2.346 L (Every 20th Data Marker Plotted)

For thermal experiments, when power was produced, it was expected that the servo-motor would apply less torque to maintain the set speed compared to the baseline experiments. Therefore, the torque and speed fluctuations for the thermal experiment were compared to the baseline to determine if this was the case. Figure 5-17 shows the torque and pressure fluctuations at a phase angle of 140° and a 30 rpm engine speed set point for each swept volume configuration. A phase angle of 140° was chosen rather than 120°, since 120° had large torque reversals at 30 rpm which were likely a result of the mechanism and backlash rather than the inclusion of a thermal source and sink. Figure 5-18 shows the same comparison for an engine set speed of 60 rpm. For both the torque and speed, the uncertainty was within the data markers and was not plotted. The approximate region of the expansion process was labelled on each figure.

In Figure 5-17 (a), (b), and (c), the torque input was decreased during the expansion process, yet the speed fluctuation was stable. During the compression process, the speed reduced from compressing the gas, and the torque input was increased in response. The torque input during the thermal experiments was lower than the baseline experiments, and the speed fluctuations were more stable. For the 60 rpm engine speed in Figure 5-18, the torque and speed fluctuations were much more stable, yet the thermal experiments still required less torque input to maintain the set engine speed. The speed fluctuations were comparable for both experiments, which was dampened by the increased angular momentum of the flywheel compared to the lower speeds.
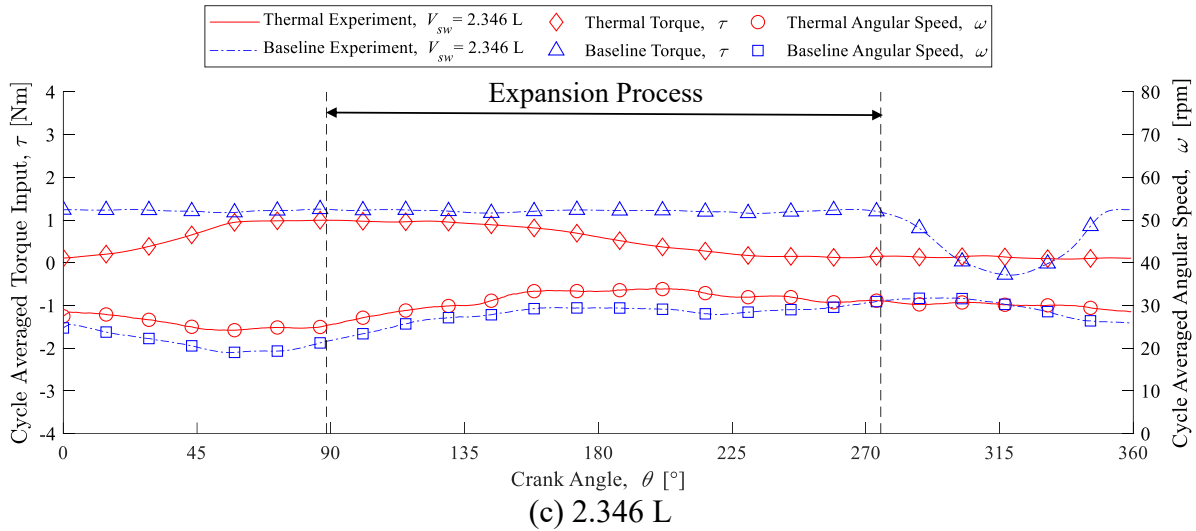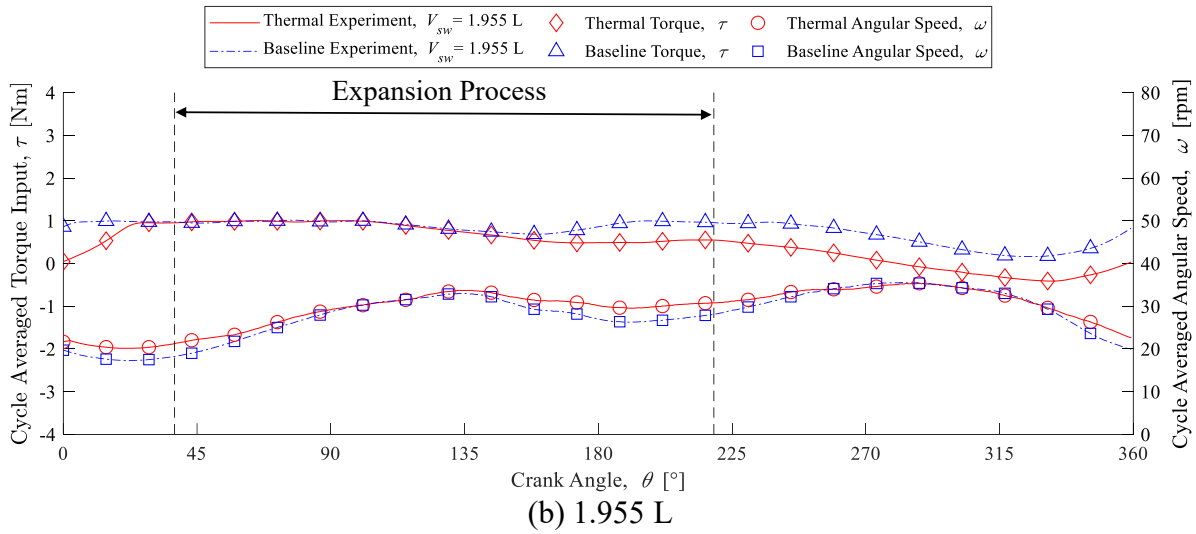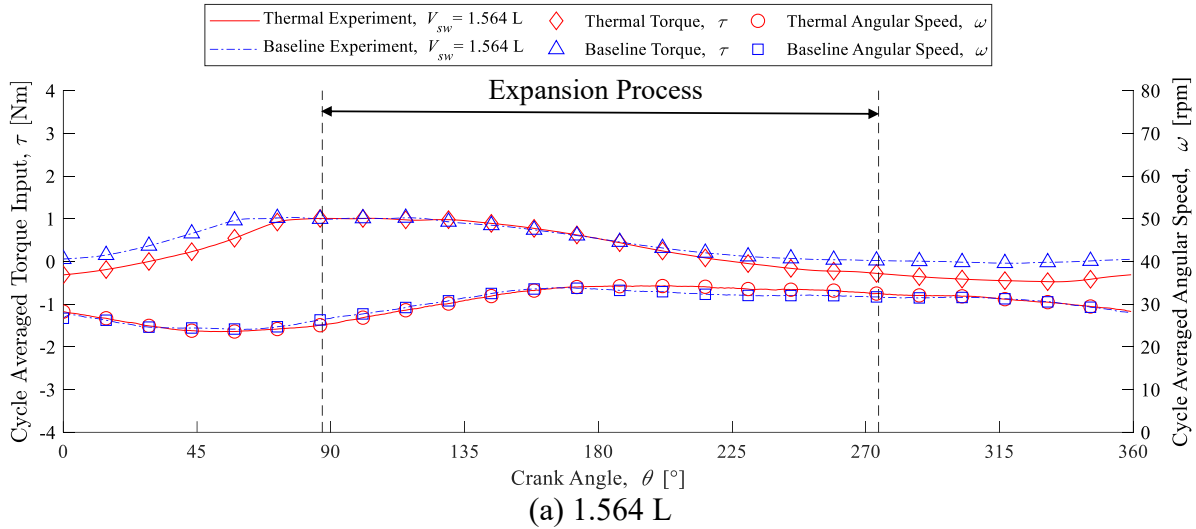
Figure 5-17: Torque and Speed Fluctuations at Phase Angle of 140° and Swept Volume of (a) 1.564 L, (b) 1.955 L, and (c) 2.346 L at a 30 rpm set point
(Every 20th Data Marker Plotted)

Figure 5-18: Torque and Speed Fluctuations at Phase Angle of 140° and Swept Volume of
(a) 1.564 L, (b) 1.955 L, and (c) 2.346 L at a 60 rpm set point
(Every 20th Data Marker Plotted)

As demonstrated with the baseline experiments, areas of torque reversal were present, which were a result of the combination of mechanism friction, backlash, and the servo-motor speed controller. It was shown that the torque input was decreased for the thermal experiments, so an additional cause for torque reversal could be due to a power producing section of the cycle. Tables documenting the torque ratios for each test were created for the thermal experiments, and are shown in Table 5-6 and Table 5-7. Cells were coded with green to show the cases without torque reversal, and with red to show cases with torque reversal.

Table 5-6:Thermal Experiment Torque Ratios for Engine Speeds of 30 rpm and 40 rpm

Phase Angle, α [°]	Torque Ratio, TR					
	Engine Speed, $\omega = 30$ [rpm]			Engine Speed, $\omega = 40$ [rpm]		
	$V_{sw} = 1.564$L	$V_{sw} = 1.955$L	$V_{sw} = 2.346$L	$V_{sw} = 1.564$L	$V_{sw} = 1.955$L	$V_{sw} = 2.346$L
180	-0.364	-0.233	-0.446	0.053	-0.082	0.028
175	-0.422	-0.503	-0.565	0.118	-0.128	0.118
170	-0.722	-0.655	-0.668	-0.265	-0.238	-0.069
165	-0.687	-0.414	-0.536	-0.035	-0.113	-0.025
160	-0.604	-0.487	-0.514	-0.222	-0.163	0.232
155	-0.386	-0.270	-0.083	-0.078	-0.075	0.108
150	-0.502	-0.381	-0.214	-0.071	-0.201	0.211
145	-0.384	-0.253	0.064	0.036	-0.237	0.366
140	-0.471	-0.411	0.086	-0.214	-0.293	0.079
135	-0.270	-0.350	0.243	-0.084	-0.081	0.183
130	-0.054	-0.263	0.226	-0.090	-0.031	0.376
125	-0.028	0.072	0.278	-0.023	0.258	0.350
120	-0.095	0.128	-1.062	-0.049	0.308	-1.005

Table 5-7: Thermal Experiment Torque Ratios for Engine Speeds of 50 rpm and 60 rpm

Phase Angle, α [°]	Torque Ratio, TR					
	Engine Speed, $\omega = 50$ [rpm]			Engine Speed, $\omega = 60$ [rpm]		
	$V_{sw} = 1.564$L	$V_{sw} = 1.955$L	$V_{sw} = 2.346$L	$V_{sw} = 1.564$L	$V_{sw} = 1.955$L	$V_{sw} = 2.346$L
180	0.227	0.165	0.286	0.364	0.336	0.485
175	0.272	0.255	0.417	0.587	0.449	0.641
170	-0.040	0.052	0.169	0.190	0.234	0.292
165	0.118	0.177	0.279	0.338	0.358	0.533
160	-0.140	0.099	0.478	0.029	0.346	0.569
155	0.176	0.215	0.388	0.311	0.501	0.473
150	0.551	0.050	0.512	0.565	0.284	0.507
145	0.196	0.108	0.578	0.368	0.295	0.699
140	-0.005	-0.005	0.442	0.117	0.212	0.589
135	0.114	0.177	0.428	0.335	0.357	0.421
130	0.234	0.124	0.472	0.420	0.309	0.720
125	0.109	0.449	0.458	0.326	0.593	0.632
120	0.144	0.413	0.253	0.268	0.542	0.249

When comparing the baseline torque ratios with the thermal torque ratios, the number of torque reversal cases almost doubled from 32 to 60 when a thermal source and sink were present. The mechanism remained the same between experiments, so the increased number in torque reversal cases are likely attributed to power production during expansion reducing the torque input and affecting the engine speed. In the 40 rpm experiments alone, torque reversal increased by 22 cases. Although, any power producing sections were not enough to overcome the required power for compression, because the engine did not run during the manual tests.

5.3.3 Temperature Measurements – Thermal Experiment

As discussed in Section 1.4.2.1, the temperature difference is one of the most important parameters for the operation of a Stirling engine. As a result of losses, the thermal sink and source temperatures are not equivalent to the actual gas temperature inside the engine. Therefore, RTD probes were used to measure water temperatures of the heat exchangers, and thermocouples were used to measure the mean gas temperature inside the engine. Figure 5-19 shows the mean RTD inlet and outlet measurements for the heat exchangers at each swept volume and at a speed of 60 rpm. Only the 60 rpm tests are shown because the measured water temperature was within uncertainty when comparing across the speeds tested. The uncertainty was also within the data markers, so the uncertainty bounds were not shown. From the figure, the difference between cooler inlet and outlet water temperature was within uncertainty for all phase angles. The same was true for the heater, except at 120° and 140° at a swept volume of 1.955 L. The larger difference in temperature at 120° could be a result of the hot water bath not being able to keep up with the heat transfer into the engine. The reason for the significant difference at 140° at a swept volume of 1.955 L was attributed to a drop in the water level in the hot water bath during this specific test, caused by of evaporation. Although the water baths were filled each day the experiment was performed, it was noted on the next day that a significant drop in the water level occurred during the collection of the 1.955 L tests at 140°. This was the only test affected.
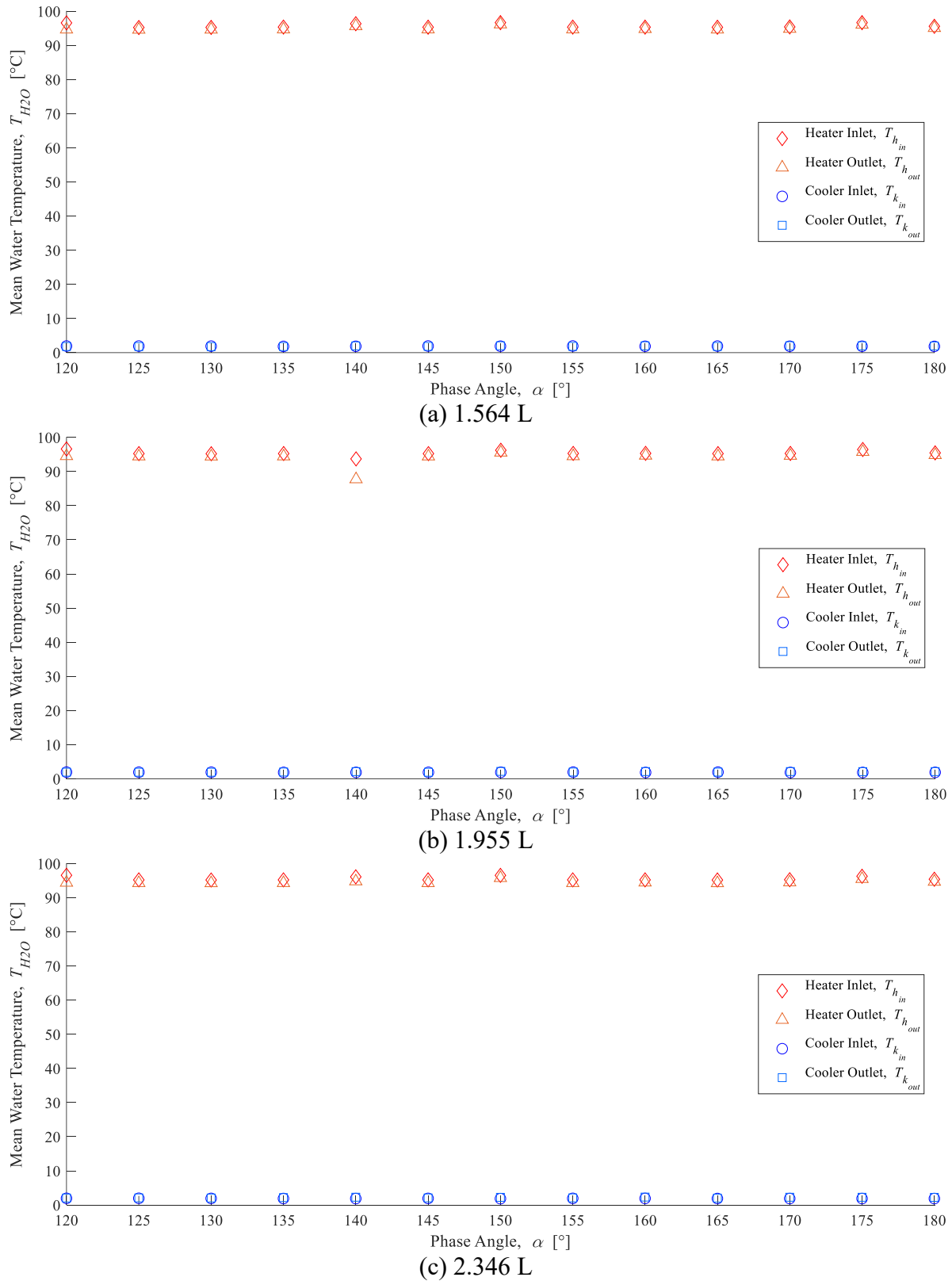
Figure 5-19: Mean Inlet and Outlet Radiator Temperatures as a Function of Phase Angle for Thermal Experiments at a Swept Volume (a) 1.564 L, (b) 1.955 L, and (c) 2.346 L at 60 rpm
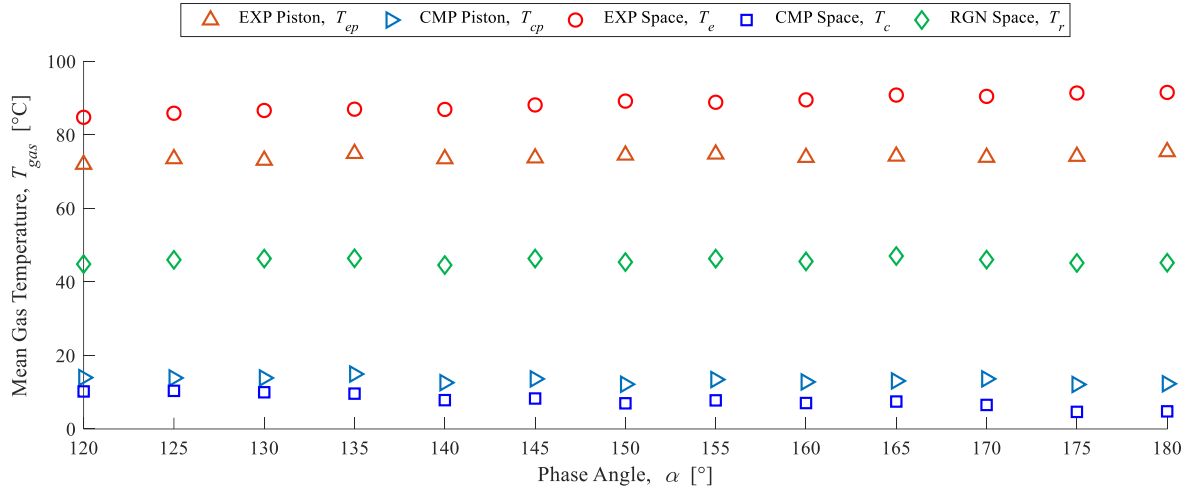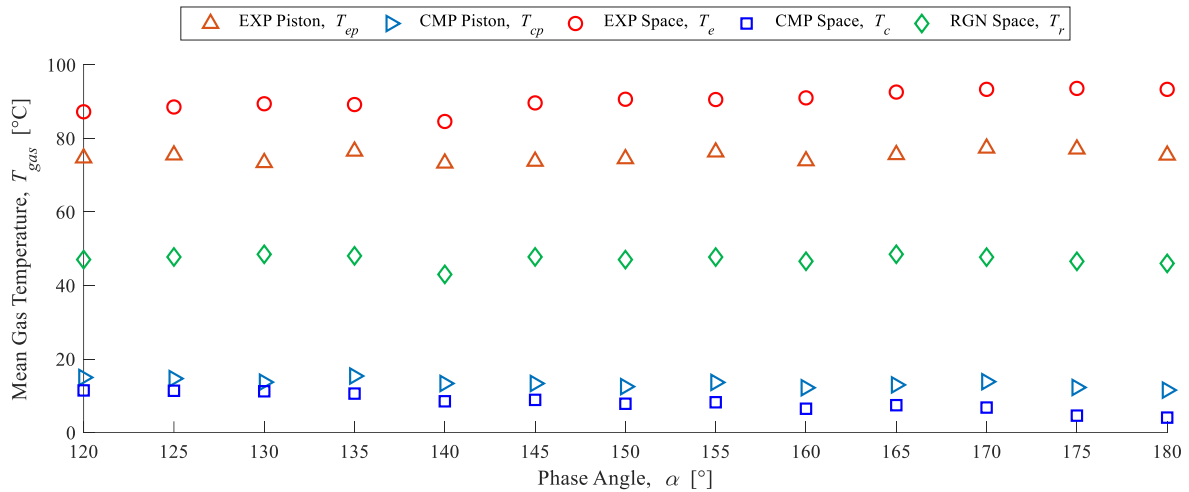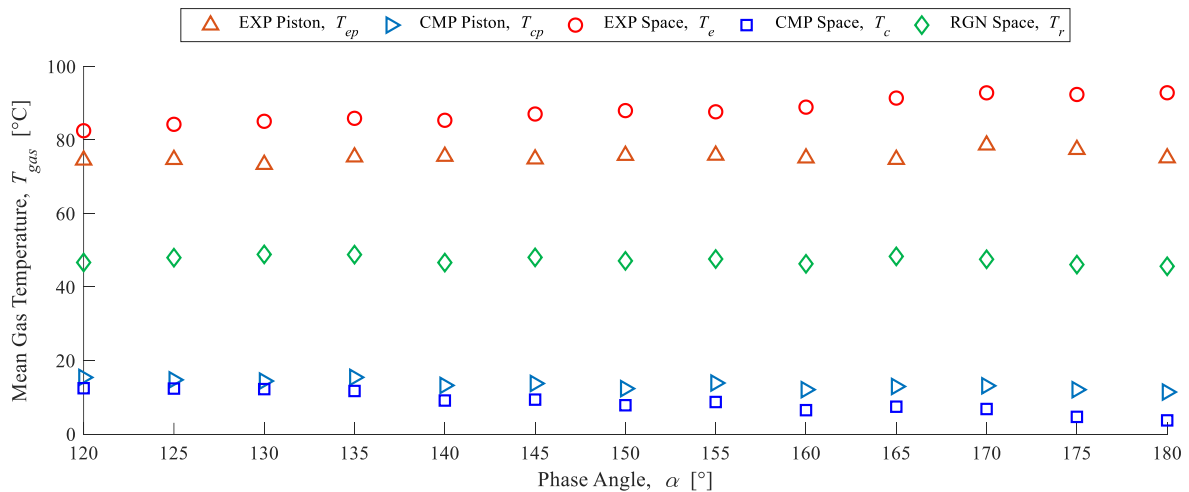
Figure 5-20: Mean Gas Temperature Measurements as a Function of Phase Angle for Thermal Experiments at a Swept Volume (a) 1.564 L, (b) 1.955 L, and (c) 2.346 L at 60 rpm

156

The mean thermocouple measurements of gas temperature are plotted in Figure 5-20 for each phase angle and swept volume tested at 60 rpm. Again, when comparing across speeds, the measurements were within uncertainty. For the figures, the regenerator space temperature was relatively constant, along with the embedded thermocouples on both the expansion and compression piston. Since the embedded thermocouples were moving with the piston, the values represent the mean amplitude measured in the path, and neither the maximum nor minimum temperature in the workspace. The stationary thermocouples near the radiators exhibited a trend where the hot side temperature decreased, and the cold side temperature increased, likely due to expansion cooling and compression heating shown in the baseline experiments.

5.3.4 Individual Workspace Indicator Diagrams – Thermal Experiment

The indicator diagrams for the expansion and compressions spaces were investigated for the thermal experiments to determine the total indicated work for each configuration. A midpoint Riemann sum was used to approximate the areas of efficacious and forced work using the engine pressure and workspace volume variations. Equations 5-2 and 5-3 were used to determine the total expansion space and compression space indicated work.

$$W_e = W_{eff,1} - W_{f,1} \qquad\qquad 5\text{-}2$$

$$W_c = W_{eff,2} - W_{f,2} \qquad\qquad 5\text{-}3$$
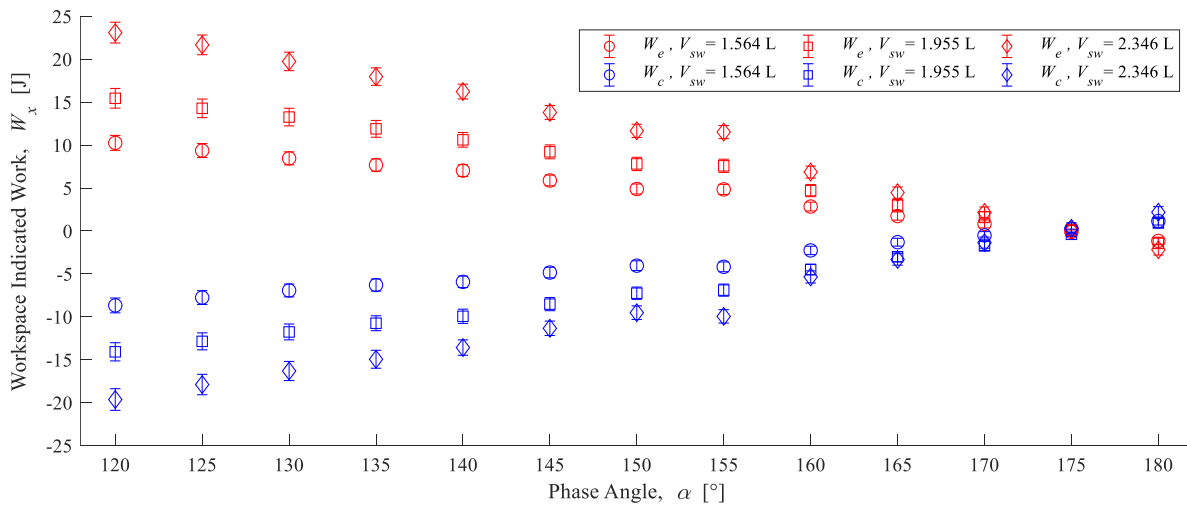
Figure 5-21: Indicated Expansion (W_e) and Compression (W_c) Work for Each Phase Angle and Swept Volume at 60 rpm

Figure 5-21 presents the values for the indicated expansion and compression space work, for each swept volume, as a function of phase angle. The positive and negative signs were included to illustrate the direction of the cycle. The expansion space indicated work should be positive because it was producing work, and the compression space indicated work should be negative, because it was consuming work. The negative values of the expansion work, and positive values of compression work, indicate that the thermodynamic cycle was in the reverse direction and functioning as a heat pump. This was occurring at high phase angles with little to no volume change, so the total indicated work would be near zero regardless. The higher swept volume configurations had larger areas of indicated work, which increased with decreasing phase angles. The calculated expansion and compression work are tabulated in Table 5-8.

Table 5-8: Indicated Expansion and Compression Work for Each Configuration

Phase Angle, α [°]	Indicated Expansion Work, W_e [J]			Indicated Compression Work, W_c [J]		
	V_{sw} =1.564L	V_{sw} =1.955L	V_{sw} =2.346L	V_{sw} =1.564L	V_{sw} =1.955L	V_{sw} =2.346L
180	-1.16	-1.43	-2.18	1.16	0.93	2.18
175	-0.11	0.08	0.11	0.26	-0.39	0.32
170	0.82	1.63	2.16	-0.51	-1.74	-1.36
165	1.74	3.00	4.47	-1.31	-3.00	-3.31
160	2.85	4.70	6.86	-2.26	-4.49	-5.35
155	4.84	7.59	11.52	-4.17	-6.89	-9.94
150	4.89	7.81	11.66	-4.04	-7.25	-9.52
145	5.88	9.22	13.80	-4.84	-8.52	-11.33
140	7.04	10.61	16.24	-5.92	-9.93	-13.58
135	7.68	11.90	17.98	-6.29	-10.74	-14.94
130	8.46	13.27	19.75	-6.93	-11.76	-16.30
125	9.37	14.29	21.68	-7.75	-12.85	-17.88
120	10.26	15.46	23.10	-8.67	-14.07	-19.63

Example plots of the expansion and compression indicator diagrams are shown in Figure 5-22 for a phase angle of 120°. Note that the non-dimensional indicator diagrams are shown for ease of comparison, but the values for indicated, efficacious, and forced work were calculated with dimensional parameters. For the 1.564 L and 2.346 L configurations, the expansion and compression space indicator diagrams had a similar shape, and the expansion space had more dead volume than the compression space, due to the engine assembly. Contrarily, the 1.955 L configuration had indicator diagrams with significantly different shapes, where the shifted compression space diagram indicates increased dead volume in the compression space. The calculated efficacious and forced work, and remaining indicator diagrams appear in Appendix R.
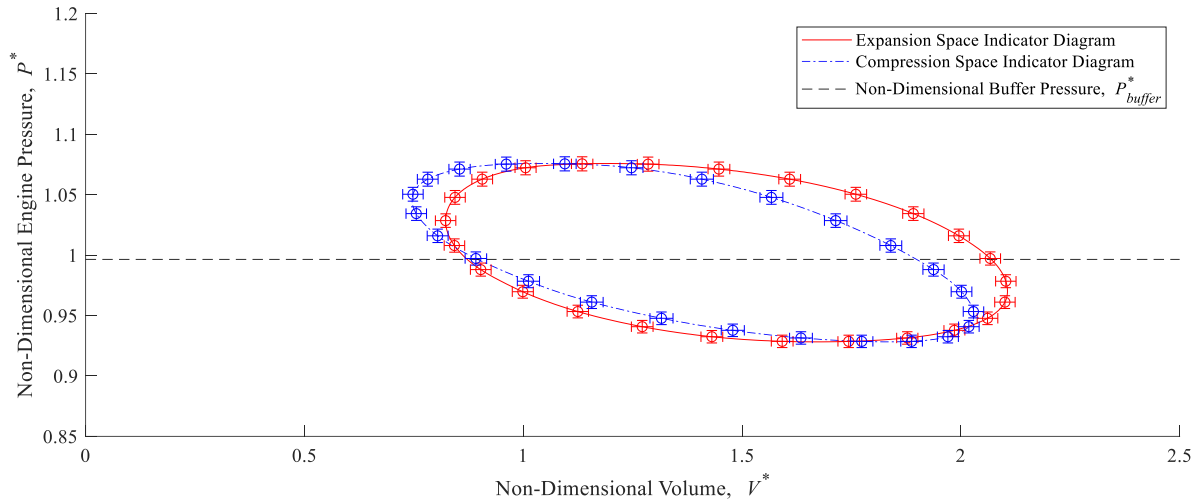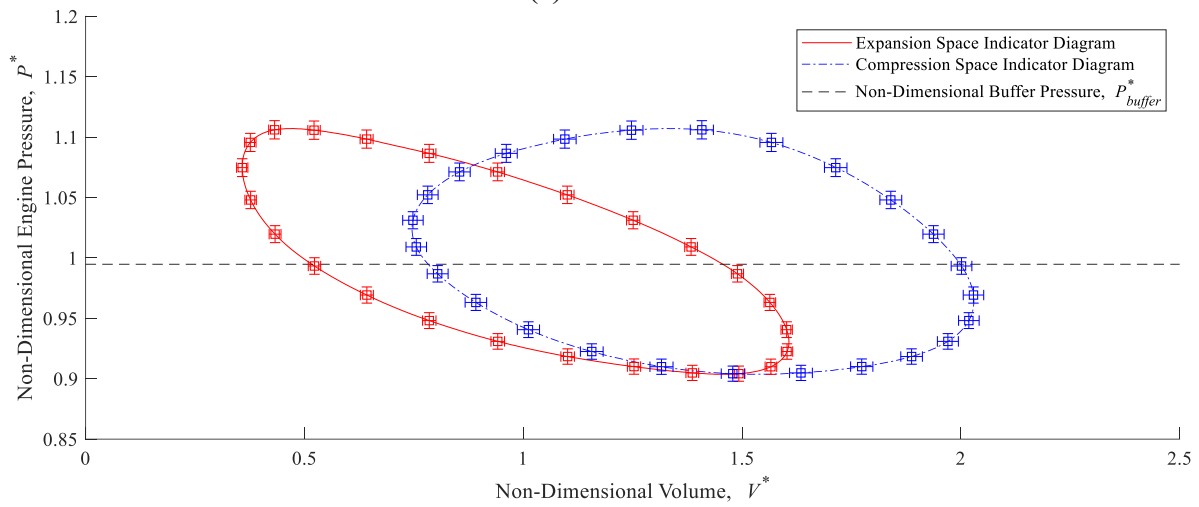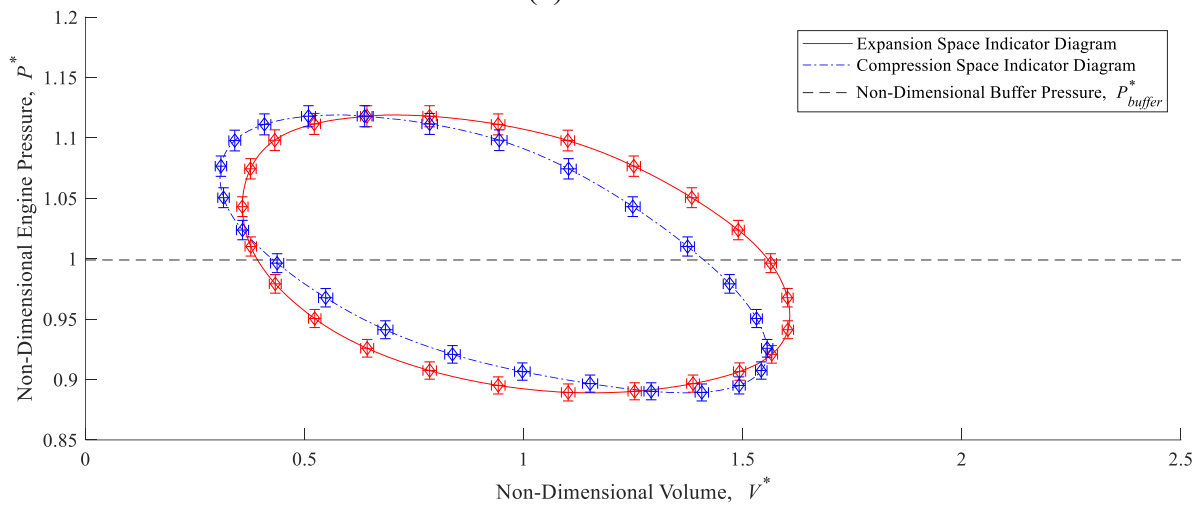
Figure 5-22: Expansion and Compression Space Indicator Diagrams at 120° and 60 rpm for a Swept Volume of (a) 1.564 L, (b) 1.955 L, and (c) 2.346 L (Every 20th Data Marker Plotted)

5.3.5 Engine Indicator Diagrams – Thermal Experiment

The total engine indicator diagrams for the thermal experiments were created to see the change in indicated work and cycle shape for different stroke length combinations and phase angles, as well as to compare the indicated work with the measured shaft work. Figure 5-23 displays the non-dimensional indicator diagrams for phase angles of 180° and 120° at a speed of 60 rpm. The complete set of indicator diagrams are shown in Appendix S.

(a)

(b)
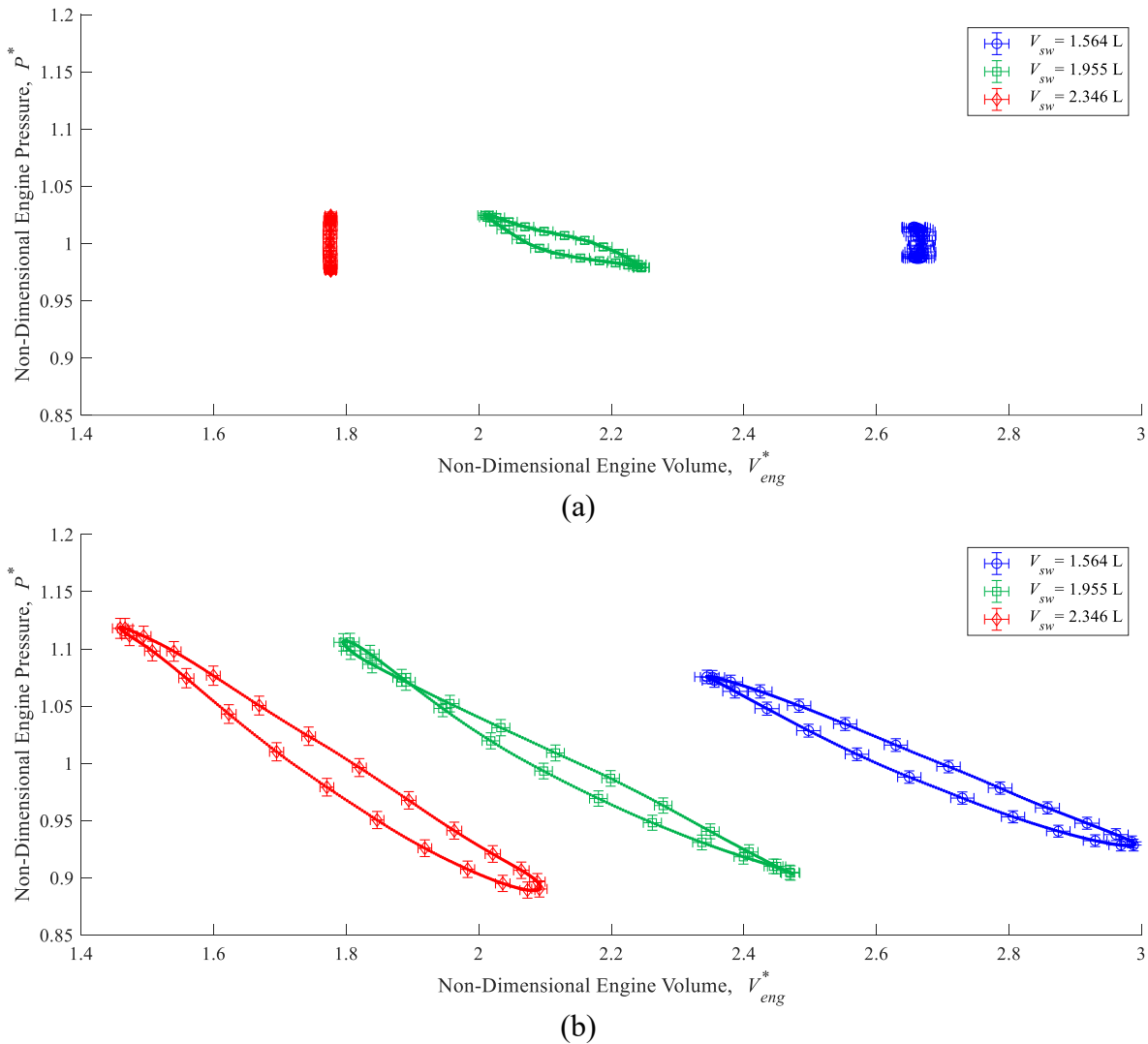
Figure 5-23: Thermal Experiment Non-Dimensional Indicator Diagram at 60 rpm for (a) 180° (b) 120° Phase Angles (Every 20th Data Marker Plotted)

On the non-dimensional indicator diagrams, as with the baseline experiments, the amount of dead volume increases from left to right, so the swept volume configuration order from left to right was 2.346 L, 1.955 L, and then 1.564 L. At a phase angle of 180°, the 1.564 L configuration had an unexpected shape resembling a "figure eight" where the cycle crossed. Although, the uncertainty bounds in volume prevents any conclusions to be made on the shape. The pressure variation due to temperature creates a vertical line without a volume change for the 2.346 L configuration. As the phase angle was decreased to 120°, the compression ratio was increased, so the non-dimensional pressure fluctuations increased as well, which stretched the indicator diagrams. Comparing the thermal experiments to the baseline experiments, the indicator diagrams contain more area as a result of heating during expansion and cooling during compression. This corresponds to a greater amount of indicated work being produced, which would decrease the amount of power required to drive the engine.

The 1.955 L configuration also yielded unexpected results. Starting with the 180° phase angle experiment, a volume change was expected because the stroke lengths were different, so the pressure fluctuation would vary with the volume change and temperature difference. Although, upon further inspection, the thermodynamic cycle was reversed, such that expansion occurred at lower pressures than compression, which suggested that it was consuming power and functioning as a heat pump rather than a heat engine. This was alluded to in the individual workspace indicator diagrams, since at 180° the expansion and compression diagrams were reversed. The other configurations were performing as heat engines, and the direction of the servo-motor was not altered, so this suggested that the temperature during expansion was somehow lower than during compression, and compression would consume more work than was extracted by expansion.

Several potential explanations exist for this behavior; however, an exact cause is not known. An explanation could be that since there was more dead volume in the compression space, the gas that remained in the cold space would reduce the overall temperature during the expansion process which reduced the pressure during expansion below the pressure during compression. The current experiment could not verify this, but if additional DVRCs were created to reduce the dead volume in the compression space, this could be further investigated. Another cause could be the bellows convolutions expanding during the expansion process, where the change in volume would decrease the pressure.
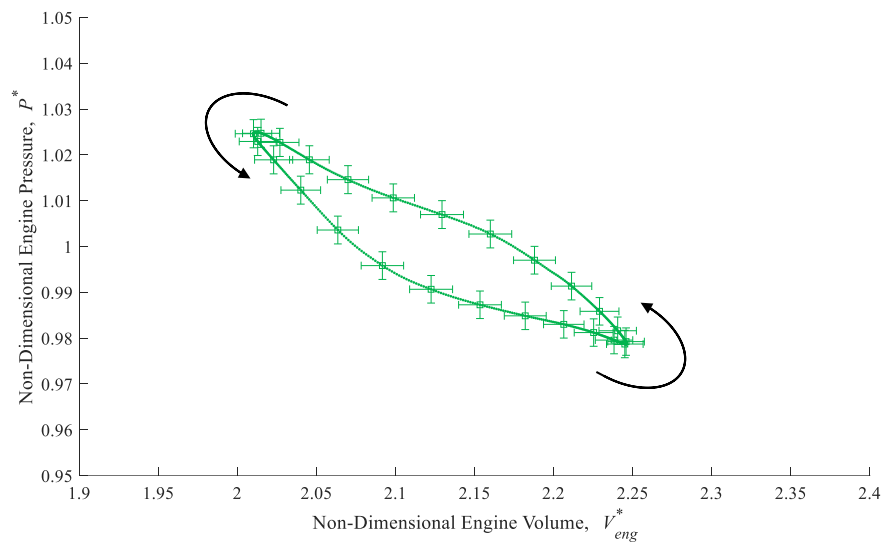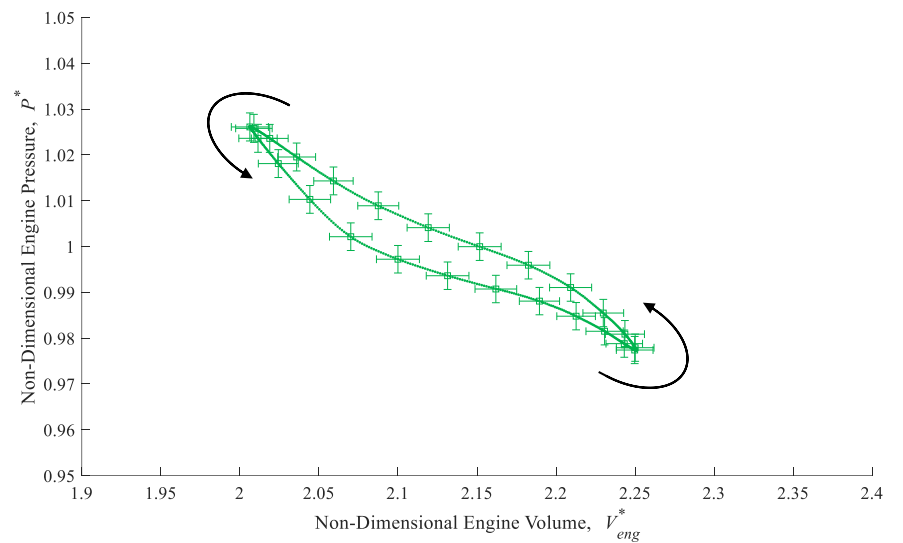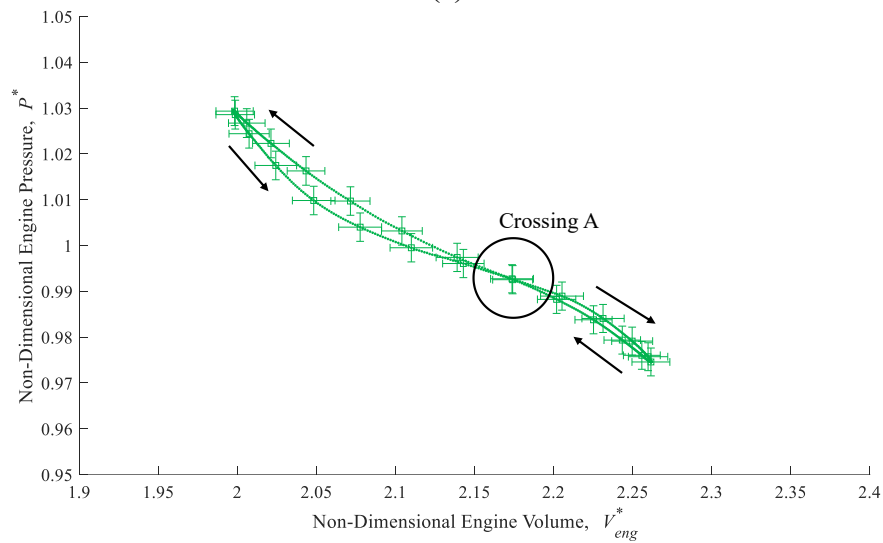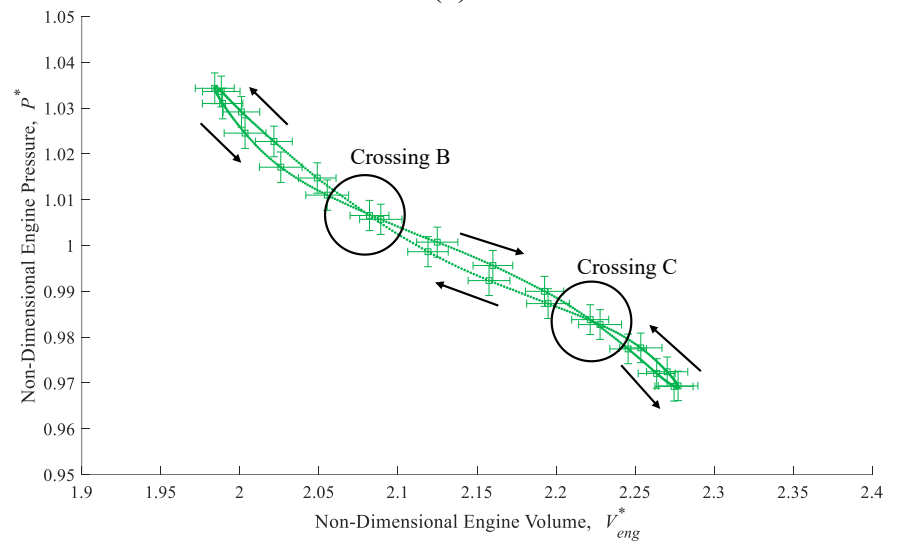
Figure 5-24: Annotated Plots of the 1.955 L Swept Volume Configuration at (a) 180° (b) 175° (c) 170° (d) 165° Phase Angles (Every 20th Data Marker Plotted)

A fully reversed indicator diagram occurred only at phase angles of 180° and 175°. As the phase angle was decreased, the diagram crossed such that it was acting partially as a heat engine during the cycle and partially as a heat pump during other portions. Figure 5-24 focuses on the 1.955 L configuration to show the evolution of the indicator diagram as the phase angle was decreased from 180° to 165° with the aid of annotations. As mentioned, Figure 5-24(a) and (b) show the fully reversed indicator diagrams. As the phase angle was decreased, the diagram collapsed until a crossing point, labelled "A", was present in Figure 5-24(c). Two crossing points, "B" and "C", appeared at 165° in Figure 5-24(d), and were present for the rest of the phase angles tested. This was a consistent result; however, the uncertainty in the measurements prevents a definitive conclusion as to the cause of the crossovers. The current experiment was not able to fully resolve this question, so further experiments looking into the effect of excess dead volume in the compression space, or comparing heat pump and engine configurations for this setup, would need to be performed.

The indicated work was calculated by taking the difference between the efficacious and forced work of the expansion and compression space indicator diagrams, and is shown in Table 5-9. This was compared to the indicated work calculated using *polyarea* in MATLAB, and was found to be the same, except the direction of energy transfer was captured by calculating the total indicated work using Equations 2-13, 2-14, and 2-15. It can be seen that at 1.955 L, the engine was consuming work until a phase angle of 160°, despite the crossing of the total indicator diagram.

Table 5-9: Cycle Averaged Indicated Work at 60 rpm

Phase Angle, α [°]	Indicated Work, W_{ind} [J]		
	V_{sw} =1.564 L	V_{sw} =1.955 L	V_{sw} =2.346 L
180	0.00	-0.50	0.00
175	0.15	-0.31	0.42
170	0.31	-0.11	0.80
165	0.44	-0.01	1.15
160	0.58	0.21	1.51
155	0.67	0.70	1.58
150	0.85	0.57	2.15
145	1.05	0.70	2.47
140	1.11	0.68	2.66
135	1.39	1.15	3.04
130	1.54	1.51	3.45
125	1.62	1.43	3.80
120	1.59	1.38	3.47

The mean shaft work input from the servo-motor for each configuration was measured using the torque transducer, and is tabulated in Table 5-10. Comparing the measured shaft work to the indicated work, there was a significant decrease. Because the indicated work would include flow and heat transfer losses, the reduction in shaft work was attributed to mechanical losses. As a result, the engine was unable to turn the crankshaft in any configuration.

Table 5-10: Mean Shaft Work for Each Configuration at 60 rpm

Phase Angle, α [°]	Shaft Work, W_s [J]		
	V_{sw} =1.564 L	V_{sw} =1.955 L	V_{sw} =2.346 L
180	-1.50	-2.83	-3.38
175	-1.58	-2.46	-2.88
170	-1.16	-2.23	-2.54
165	-1.71	-3.14	-2.85
160	-0.92	-2.31	-2.17
155	-1.94	-3.54	-3.57
150	-1.08	-2.73	-2.74
145	-1.79	-2.92	-3.59
140	-1.46	-3.17	-3.42
135	-2.27	-4.15	-4.44
130	-2.85	-4.35	-6.02
125	-3.17	-5.53	-6.29
120	-3.77	-6.32	-7.01

With the engine indicated work for each configuration known, as well as the forced work present in each cycle and the measured shaft work, it was possible to calculate the mechanism effectiveness using Equation 2-17. The mechanism effectiveness was plotted for each phase angle and swept volume tested at 60 rpm in Figure 5-25.
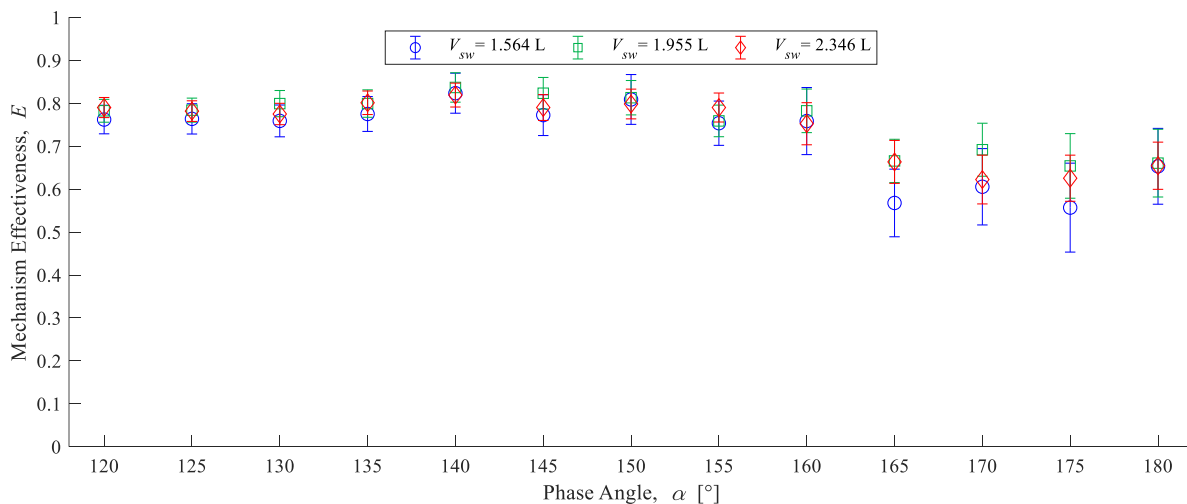
Figure 5-25: Average Mechanism Effectiveness for Each Phase Angle and Swept Volume

With the calculated uncertainty bounds, there was little distinction between the mechanism effectiveness for each swept volume. It appears that the mechanism effectiveness was slightly lower between phase angles of 165° to 180°, with the effectiveness being within uncertainty for all the phase angles below 165°. The average mechanism effectiveness values for each configuration is tabulated in Table 5-11.

Table 5-11: Average Mechanism Effectiveness for Each Configuration

Phase Angle, α [°]	Mechanism Effectiveness, E		
	$V_{sw} = 1.564$ L	$V_{sw} = 1.955$ L	$V_{sw} = 2.346$ L
180	0.65 ± 0.09	0.66 ± 0.08	0.65 ± 0.05
175	0.56 ± 0.10	0.65 ± 0.08	0.63 ± 0.05
170	0.61 ± 0.09	0.69 ± 0.06	0.62 ± 0.06
165	0.57 ± 0.08	0.67 ± 0.05	0.66 ± 0.05
160	0.76 ± 0.08	0.78 ± 0.05	0.75 ± 0.05
155	0.75 ± 0.05	0.76 ± 0.04	0.79 ± 0.03
150	0.81 ± 0.06	0.81 ± 0.04	0.80 ± 0.03
145	0.77 ± 0.05	0.82 ± 0.04	0.79 ± 0.03
140	0.82 ± 0.05	0.84 ± 0.03	0.82 ± 0.03
135	0.78 ± 0.04	0.80 ± 0.03	0.80 ± 0.03
130	0.76 ± 0.04	0.80 ± 0.03	0.78 ± 0.02
125	0.76 ± 0.04	0.78 ± 0.03	0.78 ± 0.02
120	0.76 ± 0.03	0.78 ± 0.03	0.79 ± 0.02

The mechanism effectiveness changes throughout the configurations because the amount of efficacious and forced work varies for each configuration. With the knowledge of the approximate mechanism effectiveness for each configuration, it was decided to determine a threshold value for the mechanism effectiveness that would be required to produce a net positive amount of work for the engine as built. Equation 2-16 was used with varying input for the mechanism effectiveness to calculate the resulting shaft work using the experiment values for indicated and forced work. It was found that with a mechanism effectiveness of at least 0.9, some configurations would start to produce a net positive amount of shaft work. At this value, only configurations with equal expansion and compression piston stroke lengths would produce work at phase angles between 160° and 170°; however, if the mechanism effectiveness was increased even higher, the 1.955 L configuration would also start to produce work. Therefore, the mechanism had a significant contribution to the engine not working, and a more effective mechanism could allow the engine to run.

5.3.6 Shaft Power Consumption Measurements – Thermal Experiment

The amount of power required to drive the engine with the servo-motor during the thermal experiments was calculated. The mean shaft power input as a function of phase angle was plotted for each speed and swept volume considered, and is shown in Figure 5-26. The majority of the uncertainty bounds fell within the data markers, so only the data with uncertainty beyond the markers have the uncertainty bars displayed. Also, it should be noted that since the engine was being driven, a lower shaft power input value is desired.

The 1.564 L tests required less power to motor, whereas the 1.955 L and 2.346 L tests were comparable, with the 2.346 L tests on average requiring more power. It also appears that the range of phase angles tested would contain the optimum phase angle for an alpha-type Stirling engine with comparable gas temperatures, heat exchangers, and engine speeds. Of the configurations tested, the phase angle that required the least amount of power to drive was at approximately 160°. This result was suggested by Hoegel [89], who concluded through an optimized Sage simulation (Sage, Gedeon Associates) for an alpha-type engine with a temperature difference of 120 °C and helium as a working fluid, that 160° was the optimum phase angle. As pointed out by Iwabuchi et al. [51] and Hoegel [89], this could be the optimum phase angle because the heat transfer coefficient may be larger at phase angles closer to 180°. An unexpected result was that the odd integer phase angles tested between 140° and 170° required more power than the even integer phase angles within that range. The mechanism effectiveness was shown to be lower for the phase angle of 165°, but between 140° and 160° the effectiveness was within the same range. The indicator diagrams also showed an increasing amount of indicated work, which should decrease the power consumption. An exact cause for this is unknown, and more repeats would be required to determine if this behavior was consistent. Also, at speeds of 30 and 40 rpm, the power input at 120° was significantly reduced. This can be attributed to the large negative torque ratio, which reduced the calculated shaft power input. Configurations with 180° phase angles also required more power, which could be due to the configuration behaving as a heat pump. The measured values of the shaft power input are shown in Table 5-12 and Table 5-13.
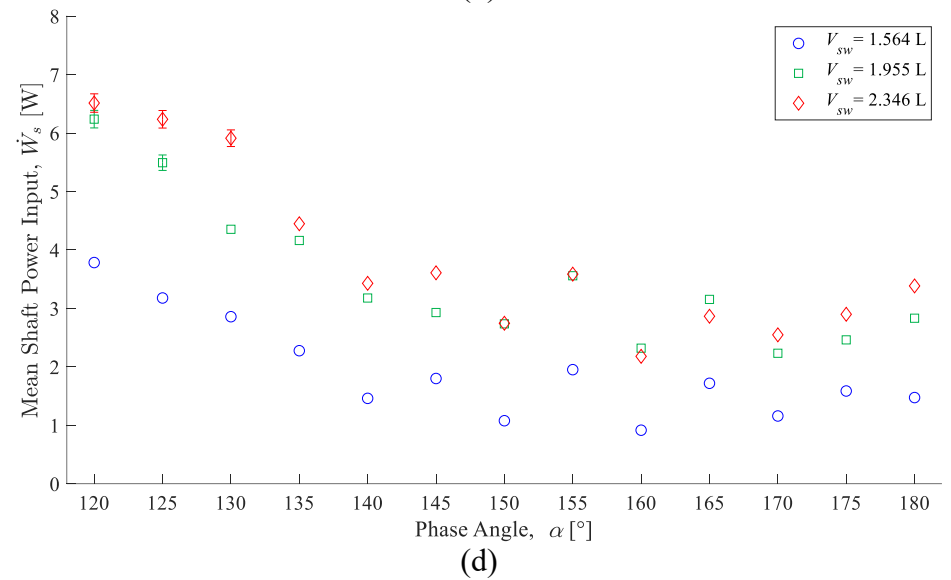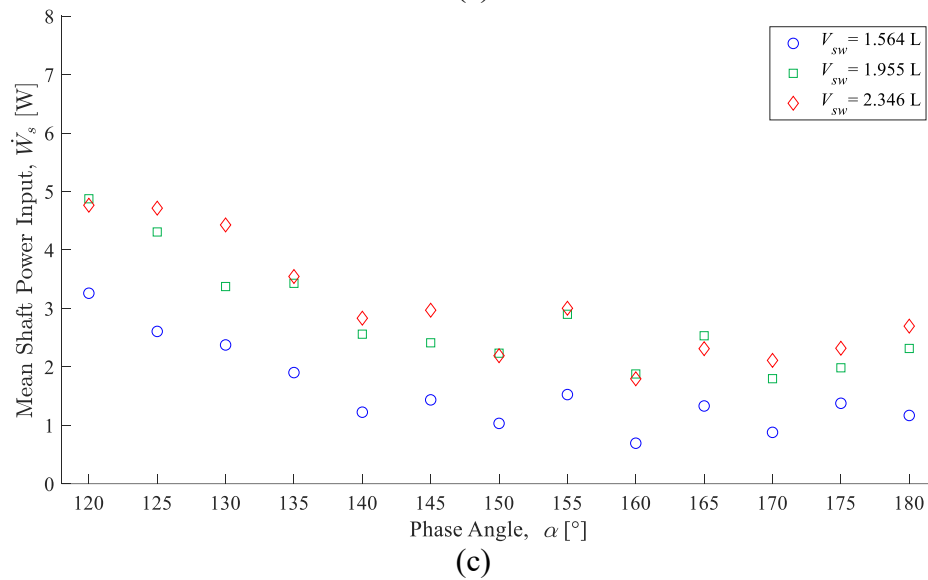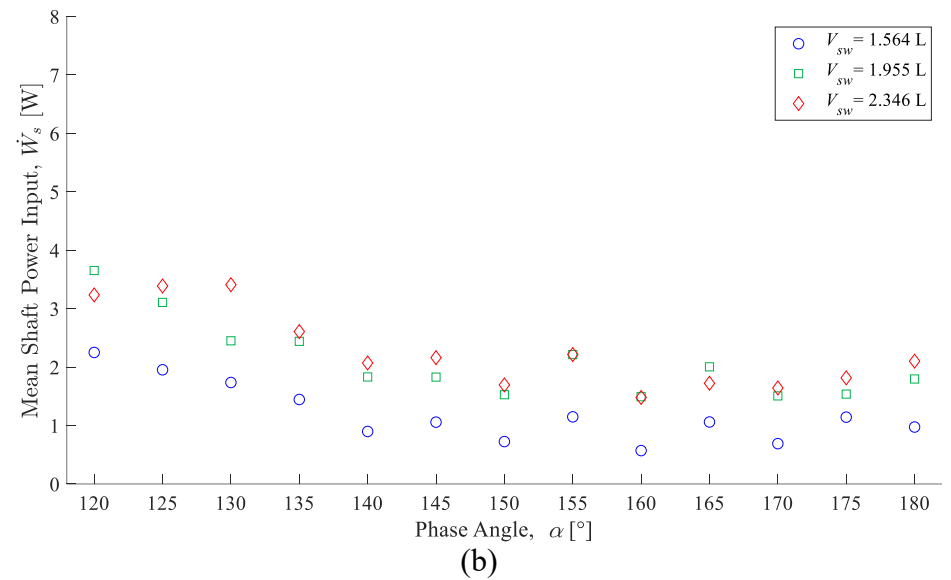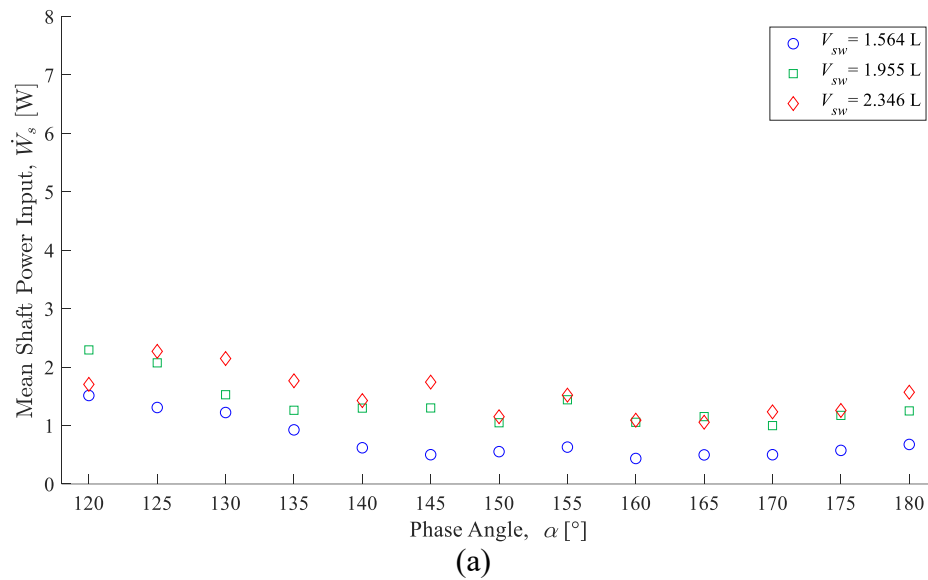
Figure 5-26: Mean Shaft Power Input as a Function of Phase Angle for Thermal Experiments Driven at Motor Speeds of (a) 30 rpm (b) 40 rpm (c) 50 rpm (d) 60 rpm

Table 5-12: Table of Mean Shaft Power Input for Engine Speeds of 30 rpm and 40 rpm for Thermal Experiments

| Phase Angle [°] | Mean Shaft Power Input, $\dot{W}_s$ [W] | | | | | |
| | Engine Speed, $\omega = 30$ [rpm] | | | Engine Speed, $\omega = 40$ [rpm] | | |
	$V_{sw} = 1.564L$	$V_{sw} = 1.955L$	$V_{sw} = 2.346L$	$V_{sw} = 1.564L$	$V_{sw} = 1.955L$	$V_{sw} = 2.346L$
180	0.68	1.25	1.57	0.97	1.80	2.10
175	0.57	1.17	1.26	1.14	1.54	1.82
170	0.50	1.00	1.23	0.69	1.51	1.64
165	0.50	1.15	1.06	1.06	2.00	1.72
160	0.44	1.06	1.09	0.57	1.49	1.48
155	0.63	1.44	1.52	1.15	2.21	2.21
150	0.55	1.05	1.15	0.73	1.53	1.69
145	0.50	1.30	1.74	1.06	1.83	2.16
140	0.62	1.30	1.43	0.90	1.83	2.07
135	0.93	1.26	1.77	1.45	2.44	2.61
130	1.22	1.53	2.15	1.74	2.45	3.41
125	1.31	2.07	2.27	1.95	3.11	3.39
120	1.51	2.29	1.70	2.25	3.65	3.23

Table 5-13: Table of Mean Shaft Power Input for Engine Speeds of 50 rpm and 60 rpm for Thermal Experiments

| Phase Angle [°] | Mean Shaft Power Input, $\dot{W}_s$ [W] | | | | | |
| | Engine Speed, $\omega = 50$ [rpm] | | | Engine Speed, $\omega = 60$ [rpm] | | |
	$V_{sw} = 1.564L$	$V_{sw} = 1.955L$	$V_{sw} = 2.346L$	$V_{sw} = 1.564L$	$V_{sw} = 1.955L$	$V_{sw} = 2.346L$
180	1.17	2.31	2.70	1.47	2.83	3.38
175	1.38	1.98	2.32	1.59	2.46	2.90
170	0.88	1.80	2.11	1.16	2.23	2.55
165	1.33	2.53	2.31	1.72	3.15	2.87
160	0.69	1.88	1.80	0.92	2.32	2.18
155	1.53	2.90	3.00	1.95	3.56	3.59
150	1.03	2.23	2.19	1.08	2.74	2.75
145	1.44	2.41	2.97	1.80	2.93	3.61
140	1.22	2.56	2.83	1.46	3.18	3.43
135	1.90	3.43	3.55	2.28	4.16	4.45
130	2.37	3.37	4.43	2.86	4.35	5.91
125	2.61	4.31	4.71	3.18	5.49	6.23
120	3.26	4.88	4.76	3.78	6.24	6.51

5.3.7 Thermal Experiments Summary

The thermal experiments provided an understanding into the performance of the current engine at varying configurations. With the addition of a thermal source and sink, the dependence of pressure on the engine speed could still not be distinguished, but at high phase angles the effect of temperature on the pressure fluctuations was apparent. As the phase angle decreased, the effect of temperature on the pressure fluctuations was less visible.

The torque fluctuations were analyzed again, since with the addition of a source and sink, the amount of torque required to drive the engine was expected to decrease. It was possible to see that the torque input decreased during the expansion process, likely from the work produced. In general, it was found that the torque decreased compared to the baseline experiments, and the speed fluctuations were more stable. There were still instances of torque reversal, which may also be caused from work produced by the engine, because the mechanism stayed the same.

When inspecting the gas temperatures, it was found that as the phase angle decreased, the gas temperatures near the radiators decreased as well, which was assumed to be a result of the compression heating and expansion cooling shown in the baseline experiments.

The individual indicator diagrams were used to calculate the total indicated work using the efficacious and forced work of the expansion and compression indicator diagrams. It was confirmed that as swept volume increased and phase angle decreased, the indicated work increased. The shapes of the expansion and compression indicator diagrams for 1.564 L and 2.346 L configurations were similar, but at 1.955 L they were significantly different. It was also found that the thermodynamic cycle was reversed at a phase angle of 180°.

The total engine indicator diagrams were then examined, and it was found that 1.955 L configurations were reversed at phase angles of 180° and 175°, and as the phase angle decreased, the indicator diagram crossed and eventually began to produce work. The mechanism effectiveness was then calculated, and found to lower between 180° to 165° than between 160° to 120°, where it was within uncertainty. It was concluded that for the current engine setup, the mechanism effectiveness would need to be above 0.9 to produce a net positive amount of work. In terms of power consumption, it was found that configurations with a phase angle of 160° consumed the least amount of power.

5.4 Baseline and Thermal Experiment Comparison

This section will provide a direct comparison between the baseline and thermal experiments. Specifically, the pressure fluctuations will be compared, and the difference in shaft power input will be examined. Also, the relationship between pressure ratio, compression ratio, and temperature difference will be more closely investigated. There may be some findings within Sections 5.2 and 5.3 that are reiterated within this section for discussion purposes.

5.4.1 Pressure Fluctuations Comparison

The non-dimensional pressure fluctuations for both the baseline and thermal experiments were directly compared, shown in Figure 5-27. The figure compares the curves for a phase angle of 120° at an engine speed of 60 rpm, for each swept volume combination. The solid curves represent the thermal experiments, and the dashed curves represent the baseline experiments.
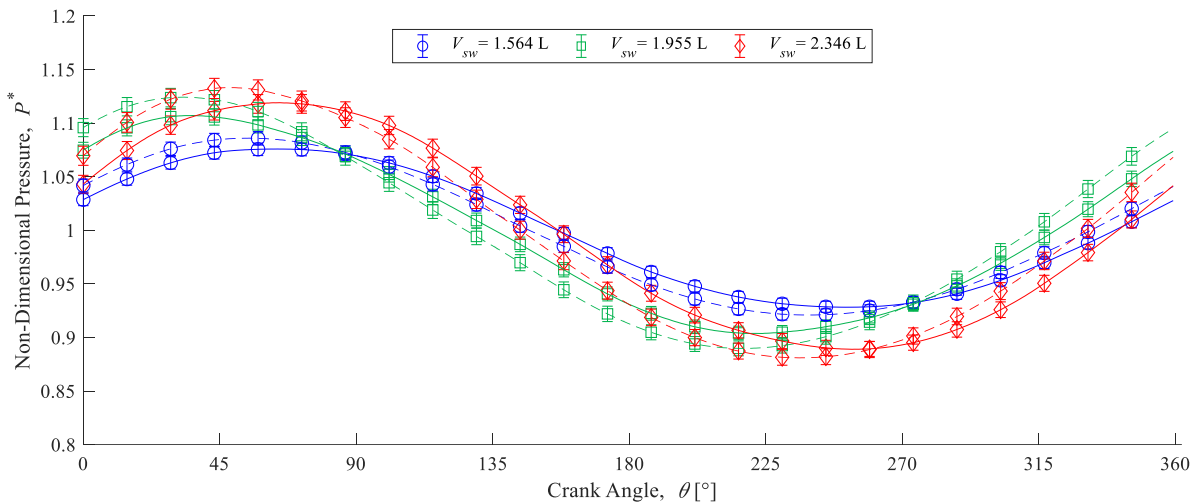
Figure 5-27: Pressure Fluctuation Comparison for Each Swept Volume at 60 rpm and a 120° Phase Angle (Every 20th Data Marker Plotted, Solid Curves for Thermal Experiments, Dashed Curves for Baseline Experiments).

When focusing on the pressure amplitude, the maximum pressure was higher and the minimum pressure was lower for the baseline experiment. The maximum and minimum pressures were not significantly different; however, they were outside the uncertainty bounds of the other experiment. This may be attributed to compressive heating and expansion cooling during the baseline experiments, with no thermal source or sink for offset. With compression space at a higher temperature in the baseline experiment compared to the thermal experiment, the peak pressure

would be higher. Conversely, with the expansion space at a lower temperature during the baseline experiment, the minimum pressure would be lower. Another cause could be a volume change from the expansion of the bellows which would dampen the pressure fluctuations.

In addition, for all swept volumes, the pressure during the expansion process for the thermal experiment was higher than it was during the baseline experiment, and it was lower during the compression process. This clearly illustrates why the indicator diagram area was larger for the thermal experiments, as mentioned to in Section 5.3.5. With a thermal source and sink, the expansion process occurred at higher temperatures than the baseline, where the pressure would be elevated and would decrease more slowly. The reverse happened during compression, where the temperature was lower, so the pressure was reduced and would increase at a slower rate. The remaining figures for the other phase angles can be seen in Appendix T.

5.4.2   Relationship between Pressure Ratio and Compression Ratio

The effect of volume and temperature change on the pressure ratio for each configuration was of interest. In Section 4.5.4, pressure ratio was defined as the ratio of the maximum pressure to the minimum pressure, and the compression ratio was the ratio of maximum volume to minimum volume. The pressure ratios for the baseline and thermal experiments were plotted on a 3D graph, for visualization, as a function of phase angle and swept volume, seen in Figure 5-28.
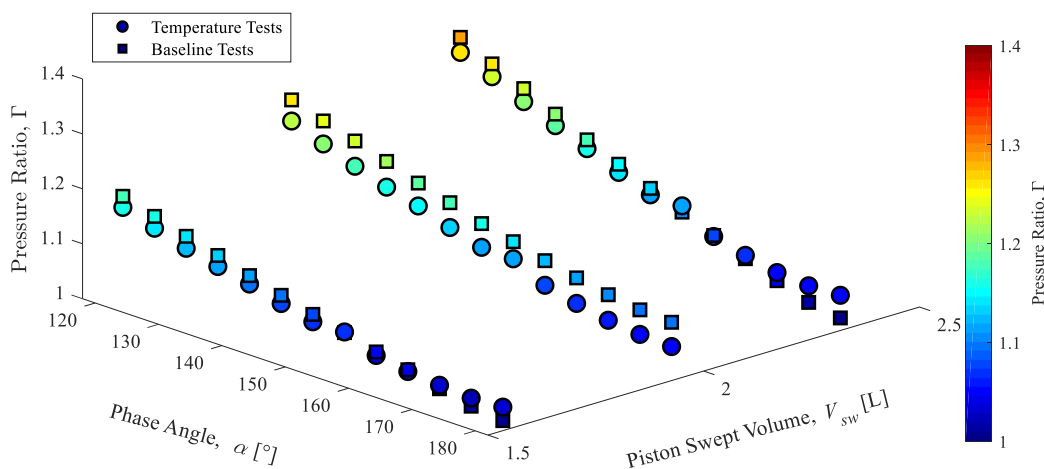
Figure 5-28: 3D Plot of the Pressure Ratio as a Function of Phase Angle and Swept Volume for the Baseline and Thermal Experiments at 60 rpm

For the majority of configurations, the pressure ratio was higher for the baseline experiments than the thermal experiments, as expected from the previous section. At higher phase angles, the pressure ratio for the thermal experiments were above the baseline, for equal stroke length configurations.

Figure 5-29 compares the pressure ratio and compression ratio as a function of phase angle to better illustrate their relationship. Figure 5-29(a) shows the baseline results, and Figure 5-29(b) shows the thermal results. It should be noted that the data points were connected to easily visualize the location of the data. Also, the uncertainty bounds for the pressure ratio are not displayed because they were within the data markers.
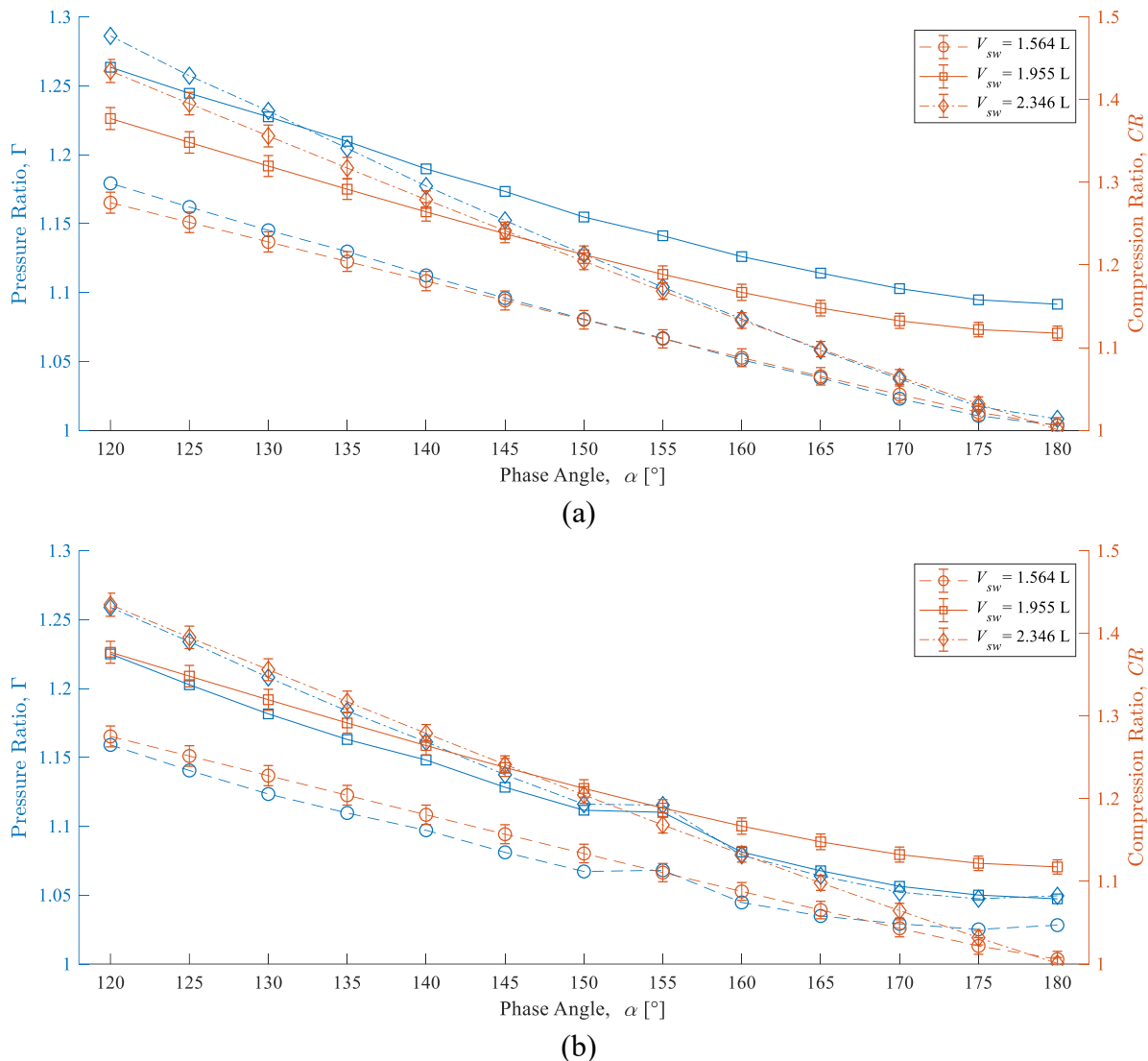
Figure 5-29: Pressure Ratio and Compression Ratio as a Function of Phase Angle at 60 rpm for (a) Baseline Experiment and (b) Thermal Experiment

172

In Figure 5-29(a), at swept volumes of 1.564 L and 2.346 L, both the pressure ratio and compression ratio were close to unity at a phase angle of 180°, and both increased with decreasing phase angle in a linear manner. At a swept volume of 1.955 L, neither the pressure ratio nor the compression ratio were close to unity, which was expected due to the volume change in that configuration; however, they did increase together proportionally with decreasing phase angle.

In Figure 5-29(b), the pressure ratio was dependent on the temperature, while the compression ratio remained the same. At higher phase angles with low compression ratios, the pressure ratio was higher for the thermal experiments, as was shown in Figure 5-28, suggesting that the gas temperature had more of an effect than the volume change for these phase angles. For the 2.346 L configuration, this occurred at phase angles between 165° to 180°. Similarly, for the 1.564 L configuration, this occurred between 170° to 180°.

To determine if the measured pressure ratios were as expected for the gas temperatures measured, the pressure ratio was calculated using the ideal gas law in Equation 1-2 at a phase angle of 180°, which would imply no volume change. This was done for the 2.346 L swept volume configuration, taking the ratio between the maximum and minimum temperatures measured by the thermocouples near the radiators and between the piston faces. The ideal pressure ratio was calculated to be 1.32 using the temperatures measure by the thermocouples near the radiators and 1.22 using the temperatures measured by the piston face thermocouples. These values are larger than the measured pressure ratio of 1.05 in this configuration. This suggests that either the bellows changed volume and dampened the pressure, or that the heat exchangers were not sufficiently changing the workspace temperatures. As seen in the radiator testing system in Section 3.5.1.1, the temperature measurements were not uniform within a plane of thermocouples. It was thought that this was due to the large dead volumes and insufficient flushing through the radiators, as well as the effect of temperature on fluid density. It was expected that with the new engine design this would have been minimized with the reduction in dead volume in the 2.346 L configuration, but the thermocouples may have been measuring hotspots that are not indicative of the entire workspace temperature. Therefore, the expansion space temperature may be lower and the compression space temperature may be higher than expected.

The 1.955 L configuration had a lower pressure ratio at all phase angles for the thermal experiments, suggesting that the initial volume change had a greater effect on the pressure ratio than the gas temperature. The compression ratio was greater for 1.955 L than the other swept volumes up until a phase angle of 150°, shown in Table 5-1. The pressure ratio was also reduced more for the thermal experiments at this configuration than the other swept volumes. This may be another indication that the overall temperature in the engine was lower. The additional cold gas in the compression space clearance volume would reduce the temperature that expansion occurs at and would increase the minimum pressure further, hence reducing the pressure ratio.

In addition, a notable increase in pressure ratio occurred at a phase angle of 155°. The cause for this is unknown, but would explain why the power consumption at 155° was higher than at 150° and 160°, which was noted in Section 5.3.6. This higher pressure ratio would be more difficult to overcome while driving the engine compared to the lower pressure ratios experienced in the 150° and 160° configurations, increasing the power input required. The pressure ratio then dropped for all configurations below 155°, continuing the trend.

5.4.3   Relationship between Pressure Ratio and Temperature Difference

The pressure ratio was also plotted against the average gas temperature difference measured from the stationary thermocouples in the expansion and compression spaces at 60 rpm, as seen in Figure 5-30. It should be noted that the data points were connected to easily visualize the location of the data. Also, only mean temperature values near the radiators were for the calculation of the average temperature difference, so it is not representative of the overall gas temperature in the engine when the majority of the gas was in either workspace; however, these measurements did provide insight into the performance of the radiators.
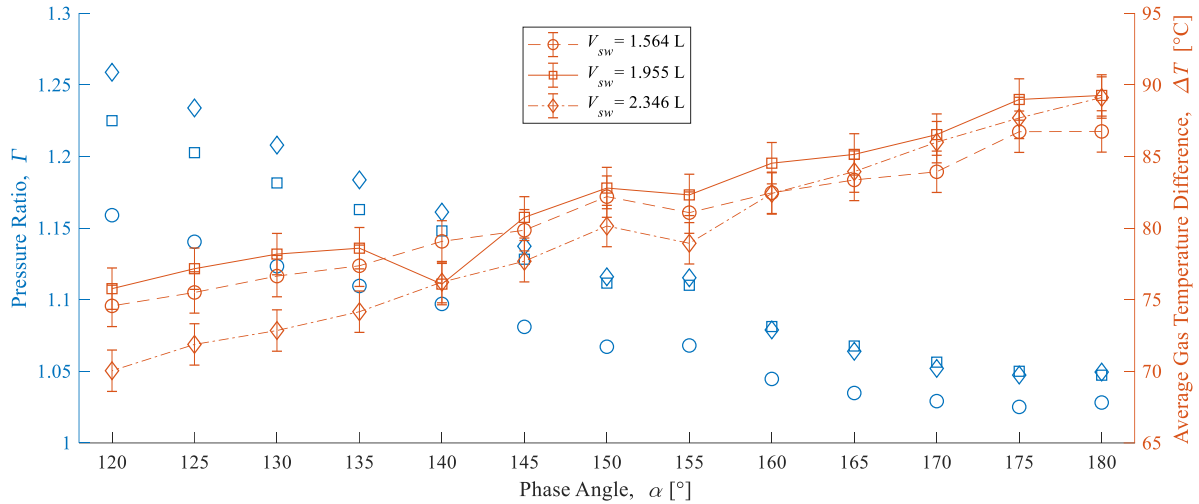
Figure 5-30: Pressure Ratio and Average Workspace Gas Temperature Difference as a Function of Phase Angle at 60 rpm

For all configurations, the temperature difference decreased with decreasing phase angle, which was originally expected to stay relatively constant. This indicated that the heater and cooler were not sufficiently sized to minimize the effect of compressive heating and expansion cooling throughout the cycle. The effect was more significant for decreased phase angles, as shown in the baseline experiment in Section 5.2.4. The heat transfer rate of the heat exchangers could not be determined, since the flow characteristics inside a Stirling engine for oscillating flow were not well defined and the convective heat transfer coefficient was unknown. In effect, this limited the amount of work that could be extracted from the cycle. The sudden reduction at 140° for the 1.955 L configuration was due to the low water bath levels explained in Section 5.3.3. The uncertainty bounds prevent a conclusion on which configuration maintained the largest average temperature difference. Although, the gas temperature difference seemed to decrease the most for the 2.346 L configuration once the phase angle was below 140°.
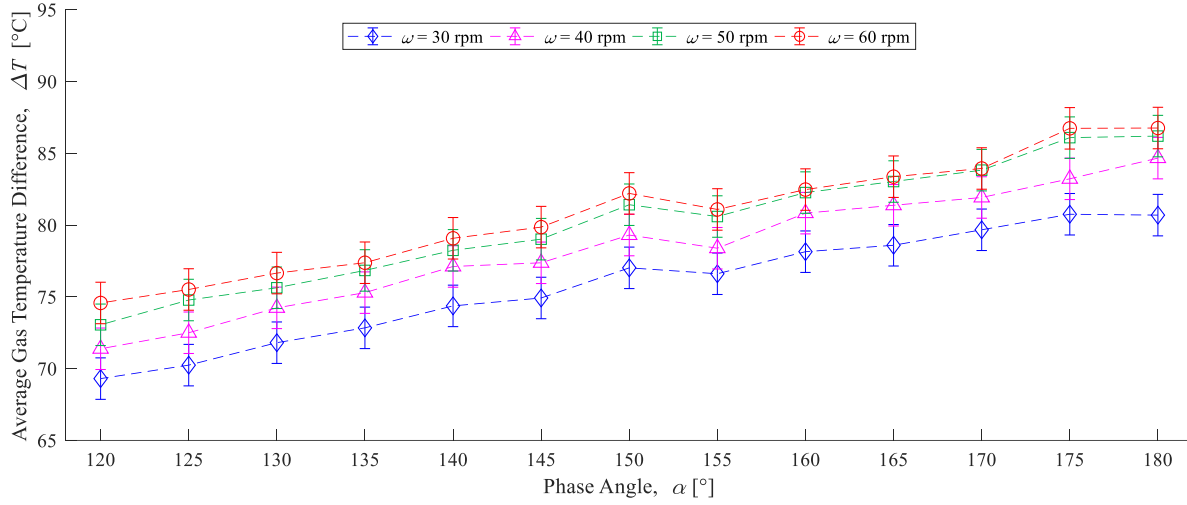
(a) 1.564 L
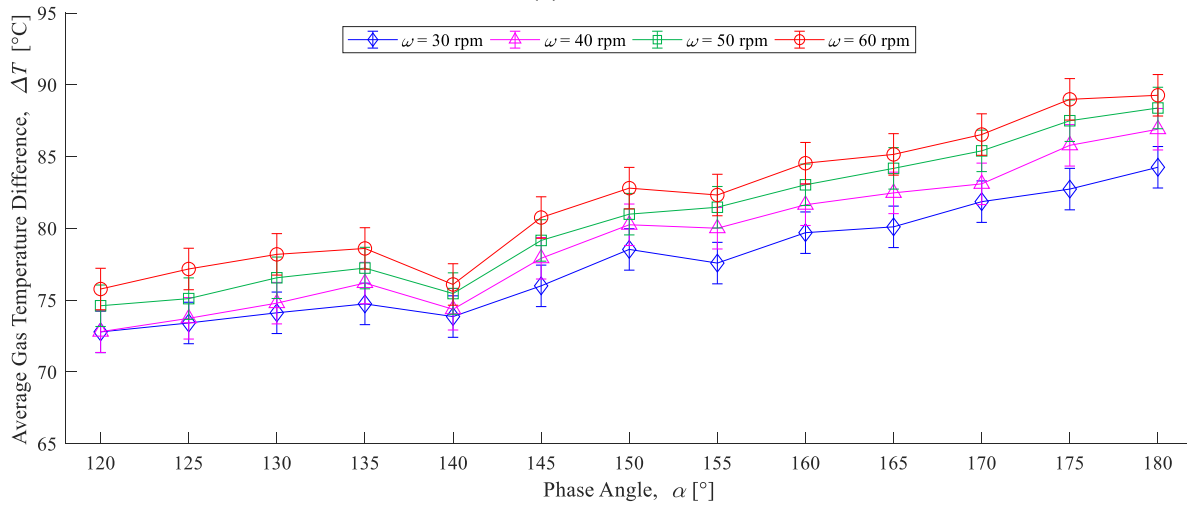
(b) 1.955 L
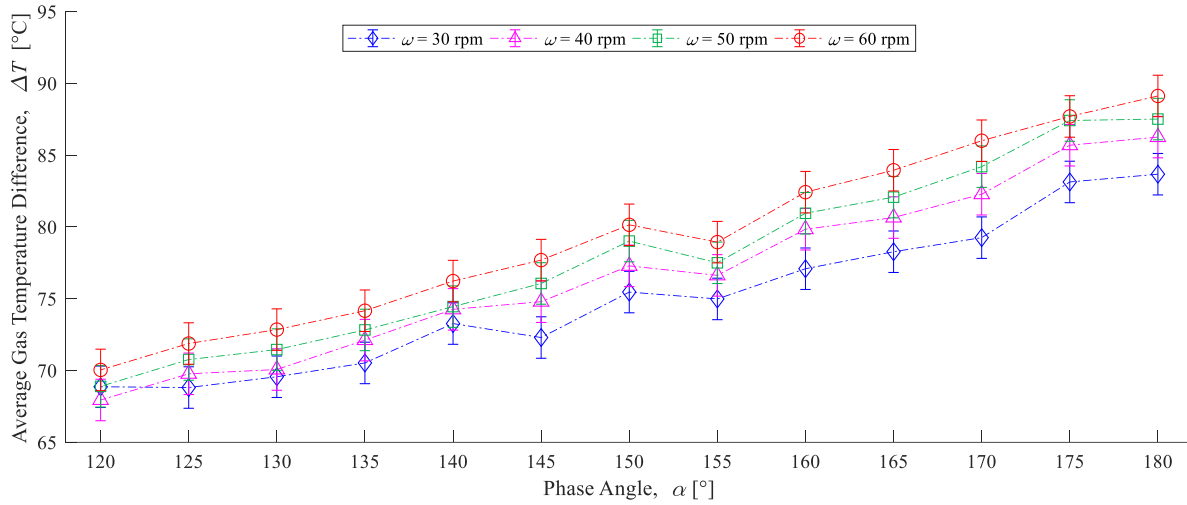
(c) 2.346 L

Figure 5-31: Average Workspace Gas Temperature Difference as a Function of Phase Angle at Each Speed for a Swept Volume of (a) 1.564 L, (b) 1.955 L, and (c) 2.346 L

The effect of engine speed on the average temperature difference was also investigated, with plots for each speed tested shown separately for each swept volume configuration, shown in Figure 5-31. Again, the uncertainty bounds were overlapping for each speed, but consistently for each plot 60 rpm had the largest temperature difference, followed by 50 rpm, 40 rpm, and 30 rpm respectively. In order to properly determine the effect of engine speed, higher speeds would need to be tested to perhaps obtain results beyond the uncertainty bounds of the other speeds.

5.4.4 Shaft Power Consumption Comparison

By comparing the shaft power input requirements of the baseline and thermal experiments, it was possible to see which engine configurations performed best out of those tested. Figure 5-32 shows a 3D plot for visualizing the baseline and thermal experiment measurements of shaft power input as a function of phase angle and swept volume, for each speed tested.

In general, save for a few cases, the thermal experiments had a reduced shaft power input. When the phase angle was decreased, the power input required increased for both the baseline and thermal experiments. This can be attributed to the increase in compression ratio with the decrease in phase angle, which would require more work transferred to the engine during compression. The reduced power input for the thermal experiments indicates that the work producing portions of the cycle did assist in reducing the load on the servo-motor, which was hypothesized in Section 5.3.2.

When comparing the effect of engine speed on shaft power input, the slower speeds required less power; however, for both the baseline and thermal experiments, torque reversal occurred at these lower speeds, which would underestimate the power. For the thermal experiments, the exact cause of the torque reversal could not be fully explained, yet the power requirements were still reduced when both baseline and thermal experiments experienced torque reversal.
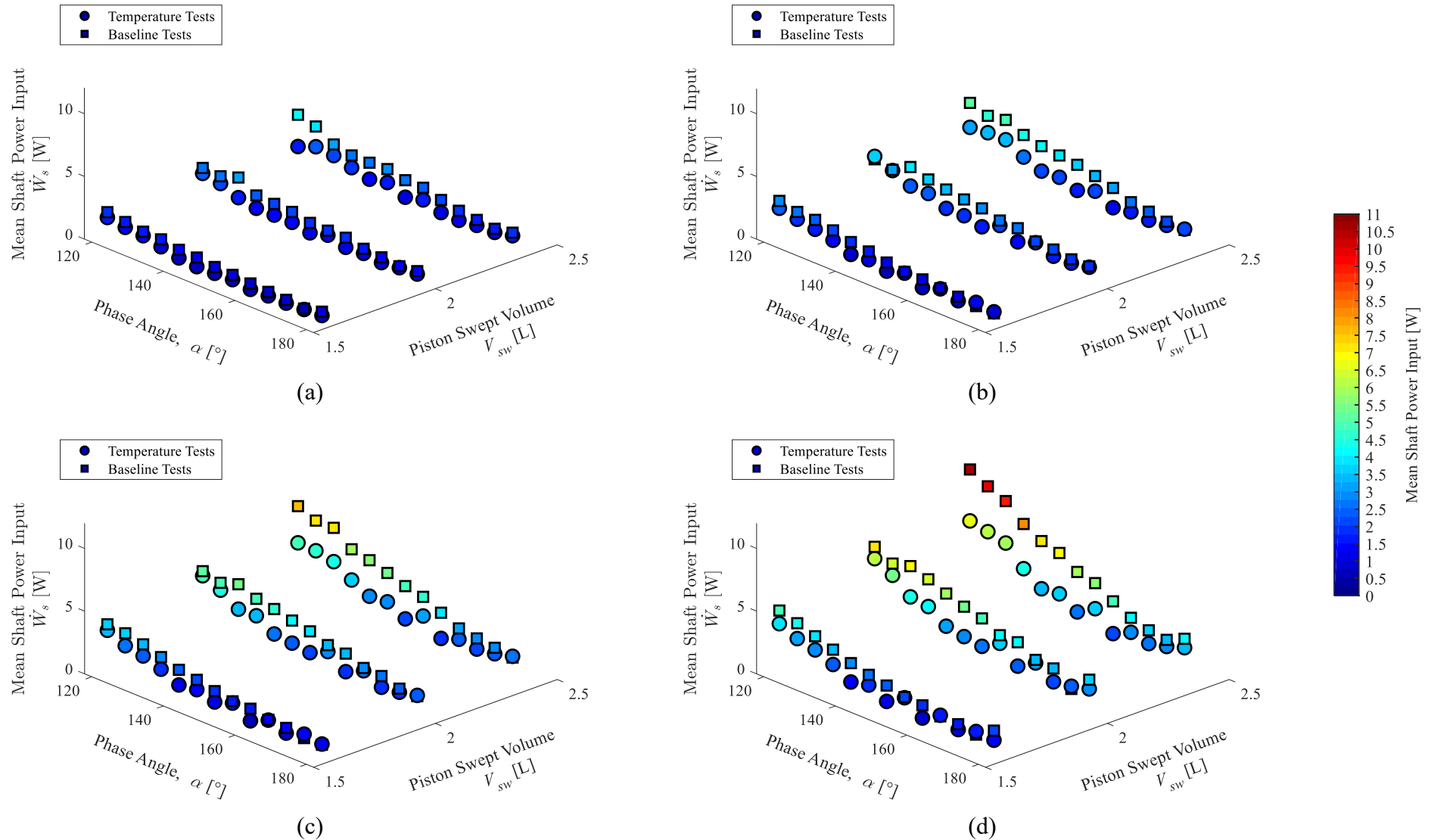
Figure 5-32: 3D Scatter Plot of the Relationship Between Shaft Power Input, Phase Angle, and Piston Swept Volume for both Temperature and Baseline Experiments Driven at a Motor Speed of (a) 30 rpm (b) 40 rpm (c) 50 rpm (d) 60 rpm
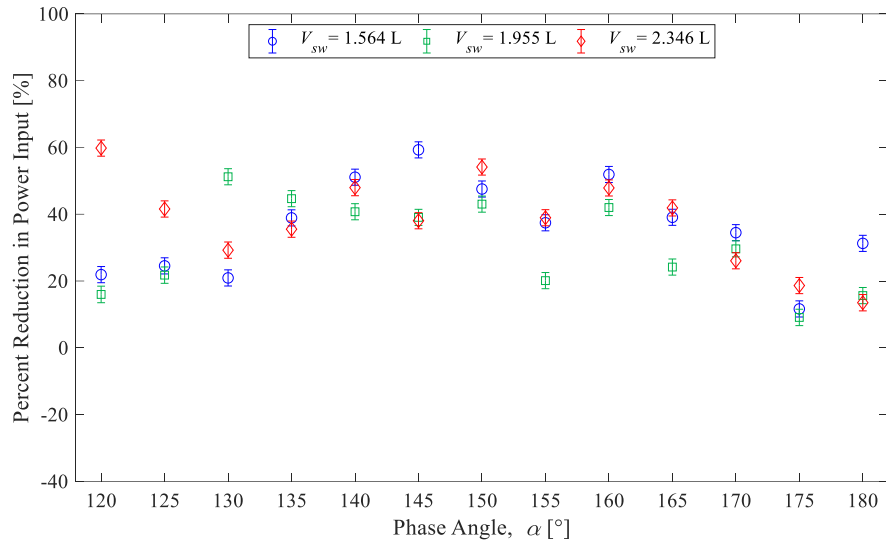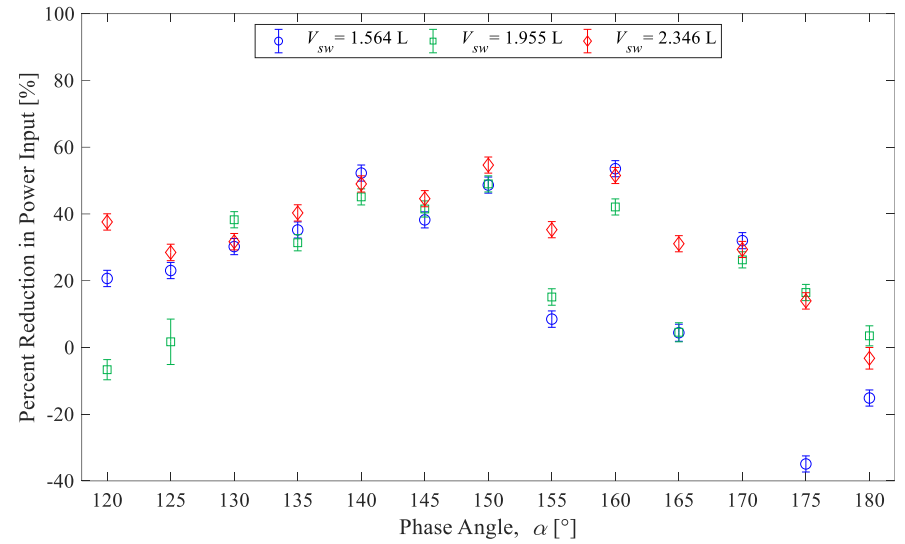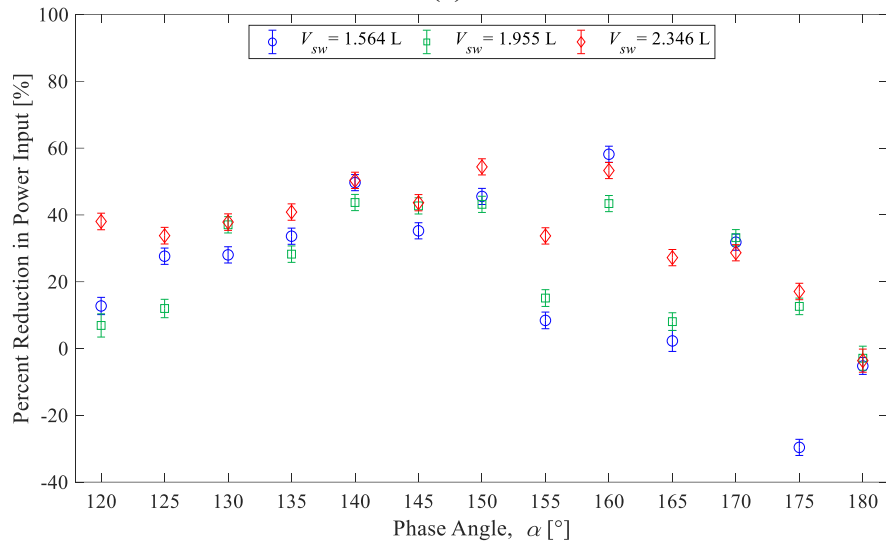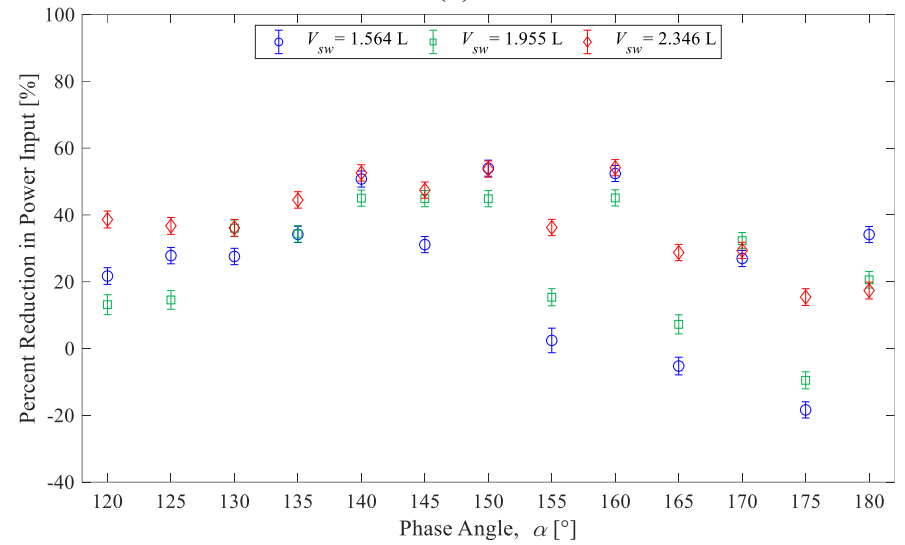
Figure 5-33: Percent Reduction in Shaft Power Input Driven at Speeds of (a) 30 rpm (b) 40 rpm (c) 50 rpm (d) 60 rpm as a Function of Phase Angle

179

A more instructive plot to show the reduction in the shaft power input between the baseline and thermal experiments is shown in Figure 5-33, where the calculated percent reduction in shaft power input was plotted against phase angle for each speed tested. A higher value of the percent reduction in shaft power input indicates which configuration was producing more power, and a value above 100% would indicate a power output from the engine. A negative value indicates that the thermal experiment was consuming more power than the baseline experiment did. The percent reduction in shaft power, $\dot{W}_\%$, was calculated using Equation 5-4, where the difference between the baseline shaft power, $\dot{W}_{base}$, and the thermal shaft power, $\dot{W}_{temp}$, was divided by the baseline shaft power.

$$\dot{W}_\% = \frac{\dot{W}_{base} - \dot{W}_{temp}}{\dot{W}_{base}} \times 100\% \qquad\qquad 5\text{-}4$$

Recall that in Section 5.3.6 the phase angle that resulted in the lowest shaft power input for the majority of the configurations tested was 160°. For speeds of 30 rpm and 40 rpm at a swept volume of 2.346 L, recall that there were large negative torque ratios at 120°, so the large shaft power reduction should be discounted at this configuration. After examining Figure 5-33, the phase angle that reduced the shaft power input the most was not specific to a single value. It appears that the optimal phase angle for this engine would lie within the range of 140° to 160°, with 150° and 160° being the most common phase angles with the largest reduction in power input. Phase angles at 155° and 165° did not reduce the shaft power as much as 150° and 160°. The lower reduction in power at 155° was associated with an abnormal increase in pressure ratio at this configuration, shown in Section 5.4.2, but the cause at 165° was unknown. The data point in Figure 5-33(b) at 125° and 1.955 L has larger uncertainty bounds. This is a result of the 10 Nm torque transducer being during the baseline experiment at this configuration, and the 1 Nm transducer during the thermal experiment. The optimal phase angles for each configuration are summarized in Table 5-14, where there were four instances of 160° and five instances of 150°. In general, at higher speeds, swept volumes with the same stroke length performed well compared to when the stroke lengths were different. In this particular experiment, the swept volume of 2.346 L reduced the shaft power input the most frequently in each configuration.

Table 5-14: Optimal Phase Angle for Each Swept Volume and Speed Configuration

Swept Volume, V_{sw} [L]	Engine Speed, ω [rpm]	Optimal Phase Angle, α [°]	Power Reduction, $\dot{W}_\%$ [%]	Compression Ratio, CR
1.564	30	145	59.3	1.157
	40	160	53.6	1.088
	50	160	58.2	1.088
	60	150	54.0	1.134
1.955	30	130	51.2	1.320
	40	150	49.0	1.212
	50	140	43.7	1.264
	60	160	54.0	1.167
2.346	30	150	54.1	1.204
	40	150	54.6	1.204
	50	150	54.4	1.204
	60	160	54.2	1.133

Taking the mean percent power reduction for each swept volume configuration gave 56.3 ± 3.8 %, 49.5 ± 5.0 %, and 54.3 ± 2.4 % for 1.564 L, 1.955 L, and 2.346 L respectively. Therefore, there was no clear distinction between which swept volume configuration produced the greatest reduction in shaft power input at their respective optimal phase angle. The mean optimal compression ratios were found to be 1.116 ± 0.02, 1.241 ± 0.03, and 1.186 ± 0.02 for swept volumes of 1.564 L, 1.955 L, and 2.346 L respectively. Using Stumpf's [48] expression for the optimal compression ratio, for the given temperature difference it was calculated to be approximately 1.211. This estimate was a close approximation to the mean compression ratios obtained, despite the expression not considering any low temperature alpha engines, and the amount of experimental data used to obtain the correlation was limited.

5.4.5 Baseline and Thermal Experiment Comparison Summary

By comparing the baseline and thermal experiments, an understanding into which configurations performed the best and why the engine did not function was possible. By comparing the pressure fluctuations directly, it was apparent that the maximum pressure was lower and the minimum pressure was higher for the thermal experiments. This was likely caused by the compression heating and expansion cooling reducing the effect of the heat exchangers. Although, with a thermal source and sink in the system, the pressure during expansion was higher and during compression was lower for the thermal experiment, which increased the amount of work produced.

The pressure ratio was compared between experiments, and was found to be higher for the thermal experiments at high phase angles between 165° and 180° for 1.546 L and 2.346 L configurations. This indicates that the temperature had a greater effect than the compression ratio. This was not the case at 1.955 L, where the compression ratio was the largest in comparison. The estimated pressure ratio using measured temperatures and the ideal gas law was greater than what was measured by the pressure transducer for the 180° phase angle and 2.346 L swept volume configuration. This indicates that the measured temperatures were not indicative of the entire workspace temperatures, and that the heat exchangers were not sufficiently changing the workspace temperatures.

With many results being attributed to the compression heating and expansion cooling of the gas, as well as to a lower pressure ratio than expected, the performance of the radiators came into question. The pressure ratio was compared to the average temperature difference and found that the temperature difference decreased with increasing pressure ratio. It was concluded that the heat exchanges could not overcome the compression heating and expansion cooling.

Comparing the shaft power input between experiments, it was found to be lower for the thermal experiments. Looking at the percent of shaft power reduction in the thermal experiments, it was found that the range of optimal phase angles for this engine was within the range of 140° to 160°. Phase angles of 150° and 160° seemed to reduce the power consumption the most frequently across configurations. The stroke combinations with equal expansion and compression piston strokes performed better in general than the differing stroke combination. A range that would contain the optimal compression ratio was calculated to be between 1.12 and 1.24.

Chapter 6   Thesis Conclusions and Future Work

A review of the literature identified a gap in the knowledge of low temperature difference alpha-type Stirling engines, especially those with a temperature difference less than 100 °C, using air as the working fluid, and a mean pressure close to atmospheric pressure. The primary objective of this thesis was to investigate the viability and experimentally evaluate the performance of such an engine that could rotate a crankshaft on its own accord. Several prototypes were designed and tested, yet none of them would function at these conditions. As a result, the objective shifted to determining what caused the engine to not function, so that anyone attempting to design a similar engine can address the issues identified. In addition, an evaluation on different configurations of stroke length and phase angles would be provided by experimentally driving the engine to determine which combination of parameters would increase the likelihood of a functioning engine by minimizing the power input required to rotate the engine, which is analogous to a configuration that would produce the maximum shaft power for a similar alpha-type Stirling engine.

The engine failed to run as a result of multiple factors that together prevented the production of a net positive amount of power. These factors were identified to be primarily insufficient heat transfer, as well as an insufficient mechanism effectiveness. One of the first indications of insufficient heat transfer was the measured pressure ratio. By comparing the ideal pressure ratio without compression using the measured temperatures to the measured pressure ratio, it was found to be significantly lower. This result brought into question whether the heat exchangers were effectively transferring heat such that the gas temperature was uniform in the workspace. In addition, the rather large effect that compressive heating and expansion cooling had on the engine at higher compression ratios alluded to insufficient heat exchangers as well. The measured temperature difference decreased as the phase angle decreased, indicating that the heat exchangers could not sufficiently offset the compressive heating and expansion cooling shown to occur in the baseline experiments. The insufficient heat transfer would decrease the temperature difference, and would in turn reduce the pressure fluctuations in the engine and reduce the indicated work. Without the wide indicator diagrams from sustained pressure during the expansion and compression processes, the forced work would increase. If the area of forced work increases more than the area of efficacious work, the indicated work will be reduced.

The effectiveness of the mechanism also contributed to the engine not functioning. Being an alpha-type Stirling engine, the two piston seals required for the configuration was an immediate disadvantage during the design of a mechanism with as low friction as possible. The triple Scotch yoke mechanism was promising; however, the mechanism effectiveness was found to vary between 0.57 and 0.81 depending on the configuration. At phase angles below 165° the mechanism effectiveness did not fall below 0.7. A higher mechanism effectiveness would be required, so that the work input required to overcome forced work is not greater than the work output of the engine after passing through the mechanism. By using the measured shaft work, a mechanism effectiveness above 0.9 would be required for net positive work to appear in the range of 170° to 160° with the current heat exchangers. This illustrates the interdependence between the mechanism and the heat exchangers; if the heat exchangers performance was increased, the mechanism effectiveness required to allow for a running engine would decrease due to an increase in available indicated work and potential decrease in forced work.

To determine the optimal configuration for minimum shaft power input for an LTD alpha-type Stirling engine using air with a mean pressure close to atmospheric pressure, the engine was tested at three different stroke combinations, at 13 different phase angles, and at four different driving speeds, for a total of 156 configurations. Two separate experiments were performed: a baseline experiment with an inactive thermal source and sink, and a thermal experiment with an active thermal source and sink. The stroke length combinations varied the swept volume, dead volume, and compression ratio, whereas the phase angle changed the compression ratio further. Speed tests were performed primarily to determine if the increased time for heat transfer at slower speeds had a noticeable impact on performance; however, such a relationship could not be confirmed at the speeds tested. The range of phase angles that likely contain the optimal phase angle was determined to be between 140° and 160°, with phase angles of 150° and 160° reducing the power input the most frequently across configurations. The optimal swept volume and phase angle combination tested that resulted in the greatest reduction in shaft power input could not be concluded, as the reduction in power input for all the swept volume configurations at their respective optimal phase angle were within uncertainty; however, the mean compression ratios that resulted in the greatest shaft power input reduction for each swept volume configuration were 1.116 ± 0.02, 1.241 ± 0.03, and 1.186 ± 0.02 for swept volumes of 1.564 L, 1.955 L, and 2.346 L

respectively. Therefore, an optimal compression ratio should lie within the range of approximately 1.12 to 1.24 for a similar sized engine at similar operating conditions.

Future work with the engine testing system could attempt the following:

- Determine if a regenerator would remove some of the heat transfer load from the heat exchangers, and increase the temperature difference and workspace temperature uniformity.
- Investigate the effect of dead volume more thoroughly. This could be completed by 3D printing more DVRCs to dictate more precisely where dead volume is located.
- Complete more experiments investigating the temperature distribution inside the engine.
- Perform further experiments to improve heat transfer and implement better heat exchangers.
- Potentially couple a second engine onto the same mechanism to see if the engines could rotate a crankshaft without being driven by a servo-motor.

List of References

[1]   Natural Resources Canada, "Renewable Energy Facts," 2019. [Online]. Available: https://www.nrcan.gc.ca/science-data/data-analysis/energy-data-analysis/energy-facts/renewable-energy-facts/20069#:~:targetText=Canadian production,-The primary source&targetText=In 2017%2C hydro accounted for,%25%2C solar at 0.6%25. [Accessed: 05-Dec-2019].

[2]   Natural Resources Canada, "FEED Study: Williston Basin Low Temperature Geothermal Demonstration," 2018. [Online]. Available: https://www.nrcan.gc.ca/science-and-data/funding-partnerships/funding-opportunities/current-investments/front-end-engineering-design-feed-study-williston-basin-low-temperature-geothermal-demonstration/16150. [Accessed: 05-Dec-2019].

[3]   Natural Resources Canada, "Eavor-Loop Demonstration Project," 2019. [Online]. Available: https://www.nrcan.gc.ca/science-and-data/funding-partnerships/funding-opportunities/current-investments/eavor-loop-demonstration-project/21896. [Accessed: 05-Dec-2019].

[4]   Natural Resources Canada, "Geothermal Energy Co-production from an Active Oil and Gas Operation," 2019. [Online]. Available: https://www.nrcan.gc.ca/science-and-data/funding-partnerships/funding-opportunities/current-investments/geothermal-energy-co-production-active-oil-and-gas-operation/22151. [Accessed: 05-Dec-2019].

[5]   S. E. Grasby, D. M. Allen, S. Bell, Z. Chen, G. Ferguson, A. Jessop, M. Kelman, M. Ko, J. Majorowicz, M. Moore, J. Raymond, and R. Therrien, "Geothermal energy resource potential of Canada," 2012.

[6]   S. Weides and J. Majorowicz, "Implications of Spatial Variability in Heat Flow for Geothermal Resource Evaluation in Large Foreland Basins: The Case of the Western Canada Sedimentary Basin," *Energies*, vol. 7, no. 4, pp. 2573–2594, 2014.

[7]   J. Banks and N. B. Harris, "Geothermal Potential of Foreland Basins: A Case Study from the Western Canadian Sedimentary Basin," *Geothermics*, vol. 76, no. May, pp. 74–92, 2018.

[8]   Government of Alberta, "Upstream oil and gas liability and orphan well inventory," 2019. [Online]. Available: https://www.alberta.ca/upstream-oil-and-gas-liability-and-orphan-well-inventory.aspx. [Accessed: 05-Dec-2019].

[9]   Orphan Well Association, "Orphan Wells To be Abandoned," 2019.

[10]   CMC, AITF, and AIHA, "Community Integrated Energy Mapping Feasibility Study In Alberta's Industrial Heartland And Strathcona Industrial Area," no. November, 2014.

[11]   C. E. C. Rodriguez, J. C. E. Palacio, O. J. Venturini, E. E. S. Lora, V. M. Cobas, D. M. Santos, F. R. L. Dotto, and V. Gialluca, "Exergetic and Economic Comparison of ORC and Kalina Cycle for Low Temperature Enhanced Geothermal System in Brazil," *Appl. Therm. Eng.*, 2013.

[12]   H. D. Madhawa Hettiarachchi, M. Golubovic, W. M. Worek, and Y. Ikegami, "Optimum Design Criteria for an Organic Rankine Cycle Using Low-Temperature Geothermal Heat Sources," *Energy*, vol. 32, no. 9, pp. 1698–1706, 2007.

[13]   Natural Resources Canada, "Clean Power by Waste Heat Recovery from Reciprocating Engines," 2018. [Online]. Available: https://www.nrcan.gc.ca/science-and-data/funding-partnerships/funding-opportunities/current-investments/clean-power-waste-heat-recovery-reciprocating-engines/4961. [Accessed: 05-Dec-2019].

[14]   G. Walker, *Stirling-cycle Machines*. Oxford University Press, 1973.

[15]   I. Kolin, "Low Temperature Difference Stirling Engine," in *19th Intersociety Energy Conversion Engineering Conference*, 1984.

[16]   I. Kolin, S. Koscak-kolin, and M. Golub, "Geothermal Electricity Production By Means Of the Low Temperature Difference Stirling Engine," *World Geotherm. Congr. 2000*, pp. 3199–3203, 2000.

[17]   Cool Energy Inc., "25 kW Low-Temperature Stirling Engine for Heat Recovery, Solar, and Biomass Applications."

[18]   Y. A. Çengel and M. A. Boles, *Thermodynamics An Engineering Approach*, Eighth. Mc Graw Hill, 2015.

[19]   G. T. Reader and C. Hooper, *Stirling Engines*. E. & F. N. Spon, 1983.

[20]   I. Urieli and D. M. Berchowitz, *Stirling Cycle Engine Analysis*. Bristol: Adam Hilger Ltd, 1984.

[21]   G. Walker, *Stirling Engines*. Oxford University Press, 1980.

[22]   J. R. Senft, "Mechanical Efficiency of Kinematic Heat Engines," *J. Franklin Inst.*, pp. 273–290, 1987.

[23]   C. D. West, *Principles and Applications of Stirling Engines*. New York: Van Nostrand Reinhold Company, 1986.

[24]   W. R. Martini, "Stirling Engine Design Manual," 1978.

[25]   C. P. Speer, "Modifications to Reduce the Minimum Thermal Source Temperature of the ST05G-CNC Stirling Engine," University of Alberta, 2018.

[26]   D. A. Miller, "Experimental Investigation of Stirling Engine Modelling Techniques at Reduced Source Temperatures," 2019.

[27]   G. Walker, R. Fauvel, R. Gustafson, and J. van Bentham, "Stirling Engine Heat Pumps," *Int. J. Refrig.*, vol. 5, no. 2, pp. 91–97, 1982.

[28]   G. Walker and J. R. Senft, *Free Piston Stiling Engines*. Springer-Verlag, 1985.

[29]   A. Ross, *Making Stirling Engines*. 1997.

[30]   E. W. Kitzner, "Automotive Stirling Engine Development Program," 1980.

[31]   N. Kagawa, "An Experimental Study of a 3-kW Stirling Engine," *AIAA*, 2000.

[32]   C. Çınar, F. Aksoy, H. Solmaz, E. Yılmaz, and A. Uyumaz, "Manufacturing and Testing of an A-type Stirling Engine," *Appl. Therm. Eng.*, vol. 130, pp. 1373–1379, 2018.

[33]   H. Karabulut, H. S. Yücesu, and A. Koca, "Manufacturing and Testing of a V-type Stirling Engine," *Turkish J. Eng. Environ. Sci.*, vol. 24, no. 2, pp. 71–80, 2000.

[34]   A. Matsuguchi and N. Kagawa, "Measurement of Characteristics of a 1-kW Stirling Engine for Renewable Energy," in *ISEC International Stirling Engine Conference*, 2018.

[35]   F. Toda and M. Matsubara, "Development of 1kW Low-Temperature Difference Stirling Engine," in *ISEC International Stirling Engine Conference*, 2018.

[36]   T. Tveit, A. Høeg, T. Asphjell, S. P. As, and N.- Limingen, "A Prototype α -Type Stirling Engine for Low Temperature Heat Recovery Power Generation," in *ISEC International Stirling Engine Conference*, 2007, no. 7898, pp. 0–3.

[37]   K. M. Bataineh, "Numerical Thermodynamic Model of Alpha-Type Stirling Engine," *Case Stud. Therm. Eng.*, vol. 12, March, pp. 104–116, 2018.

[38]   M. Altin, M. Okur, D. Ipci, S. Halis, and H. Karabulut, "Thermodynamic and Dynamic Analysis of an Alpha Type Stirling Engine and Numerical Treatment," *Energy*, vol. 169, pp. 34–44, 2018.

[39]   H. Karabulut, M. Okur, S. Halis, and M. Altin, "Thermodynamic, Dynamic and Flow Friction Analysis of a Stirling Engine with Scotch Yoke Piston Driving Mechanism," *Energy*, 2018.

[40]   A. K. Almajri, S. Mahmoud, and R. Al-Dadah, "Modelling and Parametric Study of an Efficient Alpha Type Stirling Engine Performance Based on 3D CFD Analysis," *Energy Convers. Manag.*, vol. 145, pp. 93–106, 2017.

[41]   I. Tlili and S. A. Musmar, "Thermodynamic Evaluation of a Second Order Simulation for Yoke Ross Stirling Engine," *Energy Convers. Manag.*, vol. 68, pp. 149–160, 2013.

[42]   D. Ipci and H. Karabulut, "Thermodynamic and Dynamic Analysis of an Alpha Type Stirling Engine and Numerical Treatment," *Energy Convers. Manag.*, vol. 169, December 2017, pp. 34–44, 2018.

[43]   B. Hoegel, D. Pons, M. Gschwendtner, and A. Tucker, "Theoretical Investigation of the Performance of an Alpha Stirling Engine for Low Temperature Applications," *ISEC Int. Stirling Engine Comm.*, January, 2012.

[44]   B. Hoegel, D. Pons, M. Gschwendtner, A. Tucker, and M. Sellier, "Thermodynamic Peculiarities of Alpha-Type Stirling Engines for Low-Temperature Difference Power Generation: Optimisation of Operating Parameters and Heat Exchangers Using a Third-Order Model," *Proc. Inst. Mech. Eng. Part C J. Mech. Eng. Sci.*, vol. 228, no. 11, pp. 1936–1947, 2014.

[45]   L. Bauwens, "Adiabatic Losses in Stirling Refrigerators," *J. Energy Resour. Technol. Trans. ASME*, vol. 118, no. 2, pp. 120–127, 1996.

[46]   M. Gschwendtner and G. Bell, "The Myth About Dead Volume in Stirling Engines," *Proc. Inst. Mech. Eng. Part C J. Mech. Eng. Sci.*, vol. 231, no. 19, pp. 3665–3675, 2017.

[47]   J. Egas and D. M. Clucas, "Stirling Engine Configuration Selection," *Energies*, vol. 11, no. 3, pp. 1–22, 2018.

[48]   C. J. A. Stumpf, "Parameter Optimization of a Low Temperature Difference Gamma-Type Stirling Engine to Maximize Shaft Power," University of Alberta, 2019.

[49]   I. Kolin, *Stirling Motor: History - Theory - Practice*. 1991.

[50]   A. A. El-Ehwany, G. M. Hennes, E. I. Eid, and E. A. El-Kenany, "Development of the Performance of an Alpha-Type Heat Engine by Using Elbow-Bend Transposed-Fluids Heat Exchanger as a Heater and a Cooler," *Energy Convers. Manag.*, vol. 52, no. 2, pp. 1010–1019, 2011.

[51]   M. Iwabuchi and M. Kanzaka, "Experimetal Investigation Into Heat Transfer Under the Periodically Reversing Flow Condition in Heated Tube," in *Stirling Engines - Progress Towards Reality*, IMechE, 1982.

[52]   V. M. Homutescu and D. Balanescu, "Optimization of Diameter Ratio for Alpha-Type Stirling Engines."

[53]   J. R. Senft, *Mechanical Efficiency of Heat Engines*. New York: Cambridge University Press, 2007.

[54]   J. R. Senft, "Extended Mechanical Efficiency Theorems for Engines and Heat Pumps," *Int. J. Energy Res.*, vol. 24, no. 8, pp. 679–693, 2000.

[55]   C. H. Cheng and H. S. Yang, "Optimization of Geometrical Parameters for Stirling Engines Based on Theoretical Analysis," *Appl. Energy*, vol. 92, pp. 395–405, 2012.

[56]   Government of Canada, "Canadian Climate Normals 1981-2010 Station Data," 2019. [Online]. Available:
http://climate.weather.gc.ca/climate_normals/results_1981_2010_e.html?searchType=stnName&txtStationName=Edmonton&searchMethod=contains&txtCentralLatMin=0&txtCentralLatSec=0&txtCentralLongMin=0&txtCentralLongSec=0&stnID=1865&dispBack=0.

[57]   B. Redwood, F. Schoffer, and B. Garret, *The 3D Printing Handbook: Technologies, Design and Applications*. 2017.

[58]   MatWeb LLC., "Overview of materials for Acrylonitrile Butadiene Styrene (ABS), Extruded." [Online]. Available: http://www.matweb.com/search/DataSheet.aspx?MatGUID=3a8afcddac864d4b8f58d40570d2e5aa&ckck=1. [Accessed: 28-Nov-2019].

[59]   Ultimaker BV, "PLA Technical Data Sheet." pp. 1–3, 2018.

[60]   Ultimaker BV, "Ultimaker 2 Fact Sheet." .

[61]   Ultimaker BV, "Ultimaker 2+ Specification sheet." .

[62]   Ultimaker BV, "Ultimaker 3 Product Data Sheet." .

[63]   Formlabs, "Form 2 Manual." .

[64]   Formlabs, "Material Data Sheet Standard." pp. 4–6.

[65]   Formlabs, "Material Data Sheet High Temp Resin." .

[66]   Formlabs, "Material Data Sheet Tough Resin." .

[67]   H. Gao, D. V. Kaweesa, J. Moore, and N. A. Meisel, "Investigating the Impact of Acetone Vapor Smoothing on the Strength and Elongation of Printed ABS Parts," *JOM*, vol. 69, no. 3, pp. 580–585, 2017.

[68]   G. B. P. Salata, "Post Finishing Techniques to Improve the Functionality of 3D Printed Parts," University of Alberta, 2019.

[69]   D. Clucas and S. Gutschmidt, "3D Printed Stirling Engines for Education of Machine Design and Analysis," 2016.

[70]   J. P. Michaud, C. P. Speer, D. A. Miller, and D. S. Nobes, "Empirical Heat Transfer Correlations of Finned - Tube Heat Exchangers in Pulsatile Flow," in *International Conference on Fluid Mechanics and Engineering*, 2017.

[71]   J. Michaud, D. Miller, C. Speer, and D. S. Nobes, "Dimensionless Heat Transfer Correlations of Finned-Tube Radiators in Fully Reversed Oscillating Flow," in *Okanagan Fluid Dynamics Meeting*, 2017.

[72]   McMaster-Carr, "Clear Scratch- and UV-Resistant Cast Acrylic Sheet." [Online]. Available: https://www.mcmaster.com/8560k355. [Accessed: 09-Dec-2019].

[73]   Omega Engineering Inc., "Thermocouple Response Time," 2019. [Online]. Available: https://www.omega.ca/en/resources/thermocouples-response-time. [Accessed: 09-Dec-2019].

[74]   B. Doyle, "Rolling Diaphram Seals Stay Strong Under Pressure," *Machine Design*, Oct-1999.

[75]   Bellofram Corp., "Bellofram Rolling Diaphragm Design Manual," 1998.

[76]   Freudenberg and NOK Group, "Diaphragm Design Manual." 2009.

[77]   M. A. White, S. G. Emigh, and P. Riggle, "Practical Bellows Seals for Stirling Engines," *SAE Trans.*, 1987.

[78]   S. Isshiki, A. Sakano, I. Ushiyama, and N. Isshiki, "Studies on Flow Resistance and Heat Transfer of Regenerator Wire Meshes of Stirling Engine in Oscillatory Flow," *JSME Int. J.*, vol. 40, 1997.

[79]   TheRubberStore.com, "Model # BC-2100 Nitrile Convoluted Rubber Bellow." [Online]. Available: http://www.rubberstore.com/catalog/nitrile-multi-convoluted-rubber-bellow-120mm-19mm-connector-140mm-p-9063.html.

[80]   W. L. Cleghorn and N. Dechev, *Mechanics of Machines*, Second. Oxford University Press, 2015.

[81]   A. J. Organ, *Stirling Cylce Engines: Inner Workings and Design*. John Wiley & Sons, Inc., 2014.

[82]   MasterFlex, "Operating Manual : L/S ® Pump Drives." 2008.

[83]   A. J. Wheeler and A. R. Ganji, *Introduction to Engineering Experimentation*, Third. Prentice Hall, 2010.

[84]   G. W. Burns and M. G. Scroger, "The Calibration of Thermocouples and Thermocouple Materials," U.S Government Printing Office, 1989.

[85]   National Instruments, "NI 9217 Data Sheet." 2016.

[86]   Futek Advanced Sensor Technology Inc., "Rotary Torque Sensor – Non-Contact Shaft-to-Shaft Model TRS600 - Specfication Sheet." 2014.

[87] Validyne Engineering, "Simple Manometer Calibrates Pressure Transducers." [Online]. Available: http://www.validyne.com/blog/simple-manometer-calibrates-pressure-sensors/. [Accessed: 15-Oct-2019].

[88] Meriam Instrument, "Using Manometers to Precisely Measure Pressure, Flow and Level." .

[89] B. Hoegel, "Thermodynamics Based Design of Stirling Engines for Low-Temperature Heat Sources," University of Canterbury, 2014.

[90] Alberta Health Services, "Thermometer Calibration," 2011.

[91] D. Montgomery, *Design and Analysis of Experiments*, Eighth. John Wiley & Sons, Inc., 2008.

[92] MathWorks Inc., "Zero-phase Digital Filtering." [Online]. Available: https://www.mathworks.com/help/signal/ref/filtfilt.html?s_tid=doc_ta#d117e61080. [Accessed: 08-Oct-2019].

[93] S. W. Smith, "Moving Average Filters," in *The Scientist and Engineer's Guide to Digital Signal Processing*, 1st ed., California Technical Publishing, 1997.

[94] H. W. Coleman and W. G. Steele, *Experimentation, Validation, and Uncertainty Analysis for Engineers*, 4th ed. John Wiley & Sons, Inc., 2018.

[95] Validyne Engineering, "DP15 Differential Pressure Transducer Specification Sheet." .

[96] Validyne Engineering, "CD280 Carrier Demodulator Specification Sheet." .

[97] National Instruments, "USB-6211 Specification Sheet." 2017.

[98] Wolfram Alpha LLC., "Local Acceleration of Gravity," 2019. [Online]. Available: https://www.wolframalpha.com/widgets/view.jsp?id=e856809e0d522d3153e2e7e8ec263bf2. [Accessed: 17-Oct-2019].

[99] Encoder Products Company, "Model 15S - Incremental Shaft Encoder - Specfication Sheet." 2014.

[100] D. J. King and Omega Engineering Inc., "Resistance Elements and RTD 's."

[101]   Omega Engineering Inc., "Wire Color Codes and Limits of Error." [Online]. Available: www.omega.com/temperature/pdf/tc_colorcodes.pdf%0Ahttp://www.omega.com/techref/colorcodes.html. [Accessed: 20-Sep-2008].

[102]   National Instruments, "BNC/TC-2095 Rack-Mount Adapter Installation Guide," no. September. p. 16, 1997.

[103]   National Instruments, "SCXI-1600 User Manual." 2004.

[104]   Omega Engineering Inc., "Type-T Thermocouple Reference Tables." 2011.

Appendix A   Calibration Certificates

FUTEK
ADVANCED SENSOR TECHNOLOGY, INC.

10 Thomas, Irvine, CA 92618 USA
Tel: (949) 465-0900
Fax: (949) 465-0905

Certificate of Calibration

Certificate Number: 1804130015

Sensor Info:

S/N: 761303   Model: TRS600
Item #: FSH01994   Capacity: 1 N-m

Description: TRS600, 1 N-m, Non-Contact Shaft to Shaft Rotary Torque Sensor, 10mm Shaft, 12 Pin Binder Receptacle, 09-0331-90-12

Notes: Zero Offset = 0.006 Vdc.

Calibration Procedure OP1000

CALIBRATION EQUIPMENT USED

Digital Multimeter:
HP Model: 34401A, S/N: MY53003258

Dead Weight(s):
0.2 #0oz. Traceability No: 679505

Torque Equipment:
Model: 2500-5-0-(2.5 in), S/N: 1323, Traceability No: 1603229

This certifies that the following sensor has been calibrated using equipment traceable to NIST. Supporting documentation relative to traceability is on file and is available for examination upon request. This certificate shall not be reproduced except in full, without the written approval of FUTEK.

Calibration Technician: *Jordan Jimenez*
Issue Date: 4/13/2018   Re-Calibration Date: One Year After Issue Date

Sensor Solution Source
Load · Torque · Pressure · Multi Axis · Calibration · Instruments · Software

www.futek.com

Page 1 of 3

ISO 9001   U.S. Manufacturer

Certificate Number: 1804130015

Single Channel Item

CALIBRATION DATA

Test Temp: 70 °F (21 °C)   Relative Humidity: 51 %   Excitation: 20.01 Vdc

TorqueCW

Load (N-m)	Output (Vdc)	Non-Lin. Error (% R.O.)
0.0000	0.000	0.000
0.1412	0.703	-0.052
0.2825	1.410	-0.033
0.4237	2.116	-0.025
0.5649	2.821	-0.036
1.0010	5.002	0.000
0.0000	0.001	

TorqueCCW

Load (N-m)	Output (Vdc)	Non-Lin. Error (% R.O.)
0.0000	0.000	0.000
0.1412	-0.706	-0.006
0.2825	-1.411	-0.041
0.4237	-2.117	-0.047
0.5649	-2.824	-0.033
1.0010	-5.007	0.000
0.0000	-0.008	

ADVANCED SENSOR TECHNOLOGY, INC.

10 Thomas, Irvine, CA 92618 USA
Tel: (949) 465-0900
Fax: (949) 465-0905

Certificate Number: 1804130015

Single Channel Item

SHUNT CALIBRATION

Direction	Shunt Value (KΩ)	Shunt Connection	Output Value (Vdc)	Equivalent Load (N·m)
TorqueCW	Internal	Pin A to K	5.003	1.0012
TorqueCCW	Internal	Pin A to K	5.003	1.0002

Sensor Solution Source
Load · Torque · Pressure · Multi Axis · Calibration · Instruments · Software

www.futek.com

ISO 9001

U.S. Manufacturer

197

FUTEK
ADVANCED SENSOR TECHNOLOGY, INC.

Certificate of Calibration

Certificate Number: 1702020098

Sensor Info:

S/N: 706341

Item #: FSH01907

Model: TRS600

Capacity: 10 N-m

Description: TRS600, 10 N-m, Non-Contact Shaft to Shaft Rotary Torque Sensor, 10mm Shaft, 12 Pin Binder Receptacle, 09-0331-90-12

Calibration Procedure OP1000

CALIBRATION EQUIPMENT USED

Digital Multimeter:

HP Model: 34401A, S/N: MY53003258

Dead Weight(s):

0.2 80oz, Traceability No: 679505

1-50 lb, Traceability No: 679504

Torque Equipment:

Model: 2500-5-0-(2.5 in), S/N: 1323, Traceability No: 1603229

This certifies that the following sensor has been calibrated using equipment traceable to NIST. Supporting documentation relative to traceability is on file and is available for examination upon request. This certificate shall not be reproduced except in full, without the written approval of FUTEK.

Calibration Technician: *Edgar Jimenez*

Issue Date: 2/2/2017

Re-Calibration Date: One Year After Issue Date

Page 1 of 3

Sensor Solution Source
Load · Torque · Pressure · Multi Axis · Calibration · Instruments · Software

www.futek.com

ISO 9001

U.S. Manufacturer

FUTEK
ADVANCED SENSOR TECHNOLOGY, INC.

10 Thomas, Irvine, CA 92618 USA
Tel: (949) 465-0900
Fax: (949) 465-0905

Certificate Number: **1702020098**

Single Channel Item

CALIBRATION DATA

Test Temp: 73 °F (23 °C)　　　　Relative Humidity: 41%　　　　Excitation: 20.00 Vdc

TorqueCW

Load (N-m)	Output (Vdc)	Non-Lin. Error (% R.O.)
0.000	0.000	0.000
1.695	0.846	-0.035
3.389	1.698	0.060
5.084	2.543	0.005
6.779	3.391	0.010
8.474	4.238	-0.005
9.999	5.001	0.000
0.000	0.013	

TorqueCCW

Load (N-m)	Output (Vdc)	Non-Lin. Error (% R.O.)
0.000	0.000	0.000
1.695	-0.846	-0.011
3.389	-1.691	-0.033
5.084	-2.536	-0.064
6.779	-3.383	-0.055
8.474	-4.231	-0.027
9.999	-4.994	0.000
0.000	0.001	

Page 2 of 3

Sensor Solution Source
Load · Torque · Pressure · Multi Axis · Calibration · Instruments · Software

www.futek.com

ISO 9001　　　U.S. Manufacturer

199

Certificate Number: 1702020098

Single Channel Item

SHUNT CALIBRATION

Direction	Shunt Value (KΩ)	Shunt Connection	Output Value (Vdo)	Equivalent Load (N-m)
TorqueCW	Internal	Pin A to K	4.998	9.993
TorqueCCW	Internal	Pin A to K	4.998	10.007

Appendix B   Experiment Plans

This Appendix provides the baseline and thermal experiment plans. The "run" column shows the order in which the configurations were tested, which are not in sequential order since they were randomized. The expansion and compression piston stroke lengths are shown in inches to be concise. The 2 in stroke (50.8 mm) cells are coded in blue, and the 3 in (76.2 mm) stroke cells are coded in red. The phase angles are also not in sequential order due to randomization, and their cell values were given a gradient between green and red, depending on the relative amount of compression. The speed cells were given arbitrary cell colors.

B.1 Baseline Experiment Plan

Run #	Phase Angle [°]	Expansion Stroke [in]	Compression Stroke [in]	Speed [rpm]
6	180	2	2	30
23	180	2	2	40
24	180	2	2	50
5	180	2	2	60
1	180	3	3	30
21	180	3	3	40
22	180	3	3	50
2	180	3	3	60
3	180	3	2	30
19	180	3	2	40
20	180	3	2	50
4	180	3	2	60
8	150	2	2	30
10	150	2	2	40
9	150	2	2	50
7	150	2	2	60
16	150	3	3	30
15	150	3	3	40
17	150	3	3	50
18	150	3	3	60
13	150	3	2	30
11	150	3	2	40
14	150	3	2	50
12	150	3	2	60
25	175	2	2	30
26	175	2	2	40
28	175	2	2	50
27	175	2	2	60

35	175	3	3	30
36	175	3	3	40
34	175	3	3	50
33	175	3	3	60
31	175	3	2	30
29	175	3	2	40
32	175	3	2	50
30	175	3	2	60
42	140	2	2	30
41	140	2	2	40
44	140	2	2	50
43	140	2	2	60
130	140	3	3	30
132	140	3	3	40
131	140	3	3	50
129	140	3	3	60
39	140	3	2	30
40	140	3	2	40
38	140	3	2	50
37	140	3	2	60
56	160	2	2	30
55	160	2	2	40
53	160	2	2	50
54	160	2	2	60
48	160	3	3	30
45	160	3	3	40
46	160	3	3	50
47	160	3	3	60
51	160	3	2	30
52	160	3	2	40
50	160	3	2	50
49	160	3	2	60
57	170	2	2	30
59	170	2	2	40
58	170	2	2	50
60	170	2	2	60
65	170	3	3	30
67	170	3	3	40
66	170	3	3	50
68	170	3	3	60
64	170	3	2	30
63	170	3	2	40
62	170	3	2	50

61	170	3	2	60
79	145	2	2	30
78	145	2	2	40
77	145	2	2	50
80	145	2	2	60
69	145	3	3	30
70	145	3	3	40
71	145	3	3	50
72	145	3	3	60
74	145	3	2	30
75	145	3	2	40
73	145	3	2	50
76	145	3	2	60
81	155	2	2	30
84	155	2	2	40
82	155	2	2	50
83	155	2	2	60
89	155	3	3	30
91	155	3	3	40
90	155	3	3	50
92	155	3	3	60
85	155	3	2	30
88	155	3	2	40
86	155	3	2	50
87	155	3	2	60
103	165	2	2	30
104	165	2	2	40
101	165	2	2	50
102	165	2	2	60
98	165	3	3	30
99	165	3	3	40
100	165	3	3	50
97	165	3	3	60
94	165	3	2	30
96	165	3	2	40
95	165	3	2	50
93	165	3	2	60
106	135	2	2	30
107	135	2	2	40
105	135	2	2	50
108	135	2	2	60
136	135	3	3	30
134	135	3	3	40

135	135	3	3	50
133	135	3	3	60
109	135	3	2	30
112	135	3	2	40
111	135	3	2	50
110	135	3	2	60
120	130	2	2	30
119	130	2	2	40
117	130	2	2	50
118	130	2	2	60
140	130	3	3	30
139	130	3	3	40
137	130	3	3	50
138	130	3	3	60
116	130	3	2	30
113	130	3	2	40
114	130	3	2	50
115	130	3	2	60
122	125	2	2	30
124	125	2	2	40
121	125	2	2	50
123	125	2	2	60
144	125	3	3	30
141	125	3	3	40
143	125	3	3	50
142	125	3	3	60
146	125	3	2	30
148	125	3	2	40
145	125	3	2	50
147	125	3	2	60
128	120	2	2	30
126	120	2	2	40
127	120	2	2	50
125	120	2	2	60
156	120	3	3	30
155	120	3	3	40
154	120	3	3	50
153	120	3	3	60
149	120	3	2	30
151	120	3	2	40
152	120	3	2	50
150	120	3	2	60

B.2 Thermal Experiment Plan

Run #	Phase Angle [°]	Expansion Stroke [in]	Compression Stroke [in]	Speed [rpm]
10	180	2	2	30
12	180	2	2	40
9	180	2	2	50
11	180	2	2	60
4	180	3	3	30
2	180	3	3	40
1	180	3	3	50
3	180	3	3	60
6	180	3	2	30
8	180	3	2	40
7	180	3	2	50
5	180	3	2	60
24	150	2	2	30
23	150	2	2	40
21	150	2	2	50
22	150	2	2	60
17	150	3	3	30
18	150	3	3	40
20	150	3	3	50
19	150	3	3	60
15	150	3	2	30
16	150	3	2	40
13	150	3	2	50
14	150	3	2	60
28	175	2	2	30
25	175	2	2	40
26	175	2	2	50
27	175	2	2	60
35	175	3	3	30
34	175	3	3	40
36	175	3	3	50
33	175	3	3	60
29	175	3	2	30
30	175	3	2	40
31	175	3	2	50
32	175	3	2	60
39	140	2	2	30
40	140	2	2	40

37	140	2	2	50
38	140	2	2	60
44	140	3	3	30
43	140	3	3	40
41	140	3	3	50
42	140	3	3	60
45	140	3	2	30
47	140	3	2	40
46	140	3	2	50
48	140	3	2	60
57	160	2	2	30
59	160	2	2	40
60	160	2	2	50
58	160	2	2	60
53	160	3	3	30
56	160	3	3	40
54	160	3	3	50
55	160	3	3	60
51	160	3	2	30
50	160	3	2	40
49	160	3	2	50
52	160	3	2	60
64	170	2	2	30
63	170	2	2	40
62	170	2	2	50
61	170	2	2	60
69	170	3	3	30
70	170	3	3	40
71	170	3	3	50
72	170	3	3	60
68	170	3	2	30
65	170	3	2	40
67	170	3	2	50
66	170	3	2	60
81	145	2	2	30
83	145	2	2	40
84	145	2	2	50
82	145	2	2	60
77	145	3	3	30
80	145	3	3	40
78	145	3	3	50

79	145	3	3	60
76	145	3	2	30
75	145	3	2	40
73	145	3	2	50
74	145	3	2	60
96	155	2	2	30
93	155	2	2	40
94	155	2	2	50
95	155	2	2	60
87	155	3	3	30
88	155	3	3	40
85	155	3	3	50
86	155	3	3	60
92	155	3	2	30
91	155	3	2	40
90	155	3	2	50
89	155	3	2	60
106	165	2	2	30
107	165	2	2	40
108	165	2	2	50
105	165	2	2	60
100	165	3	3	30
98	165	3	3	40
97	165	3	3	50
99	165	3	3	60
101	165	3	2	30
102	165	3	2	40
104	165	3	2	50
103	165	3	2	60
119	135	2	2	30
117	135	2	2	40
120	135	2	2	50
118	135	2	2	60
110	135	3	3	30
112	135	3	3	40
109	135	3	3	50
111	135	3	3	60
114	135	3	2	30
113	135	3	2	40
115	135	3	2	50
116	135	3	2	60

132	130	2	2	30
131	130	2	2	40
129	130	2	2	50
130	130	2	2	60
128	130	3	3	30
126	130	3	3	40
127	130	3	3	50
125	130	3	3	60
121	130	3	2	30
123	130	3	2	40
124	130	3	2	50
122	130	3	2	60
136	125	2	2	30
133	125	2	2	40
134	125	2	2	50
135	125	2	2	60
142	125	3	3	30
144	125	3	3	40
143	125	3	3	50
141	125	3	3	60
137	125	3	2	30
138	125	3	2	40
140	125	3	2	50
139	125	3	2	60
147	120	2	2	30
148	120	2	2	40
145	120	2	2	50
146	120	2	2	60
156	120	3	3	30
155	120	3	3	40
154	120	3	3	50
153	120	3	3	60
150	120	3	2	30
149	120	3	2	40
151	120	3	2	50
152	120	3	2	60

Appendix C   Steady State Justification

This section will present some additional figures pertaining to the justification of the cyclic steady-state period. The figures presented in this appendix are for after the warm-up period, with a phase angle of 150°, and a speed of 60 rpm. Figure C–1 shows the additional gas temperature measurements for each swept volume configuration. Figure C–2 shows the final 60 s of the test for the gage pressure, which shows that the pressure fluctuations have reached a steady state for each swept volume configuration. Figure C–3 shows the measured torque voltage during the final 60 s to show that the torque fluctuations have also reached steady state for each swept volume configuration.
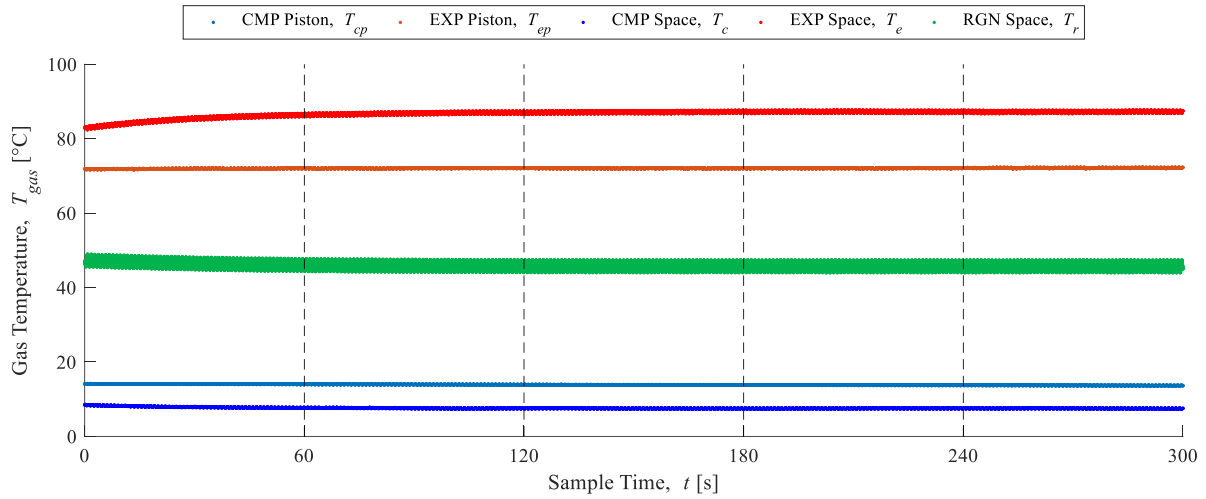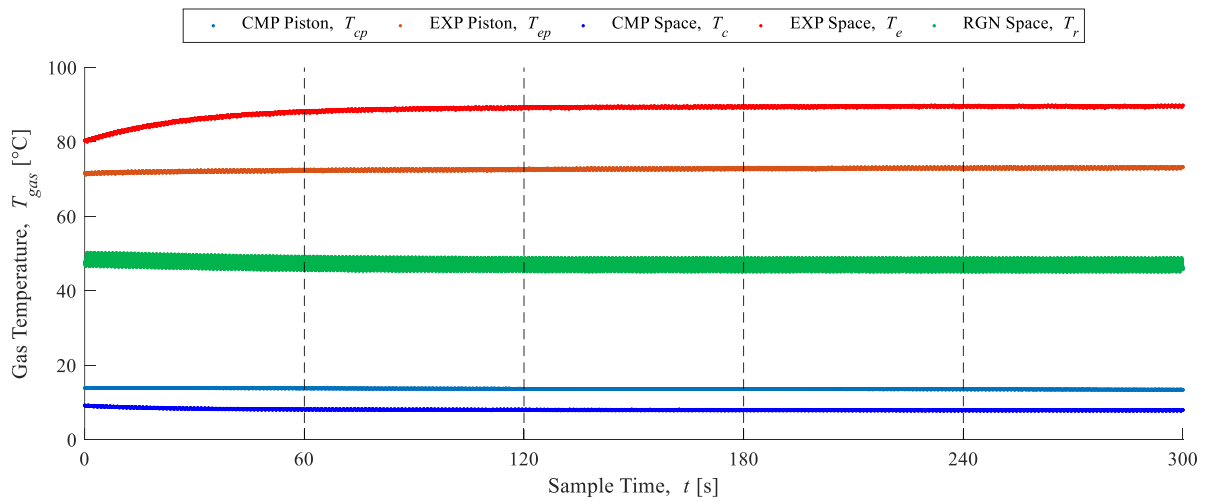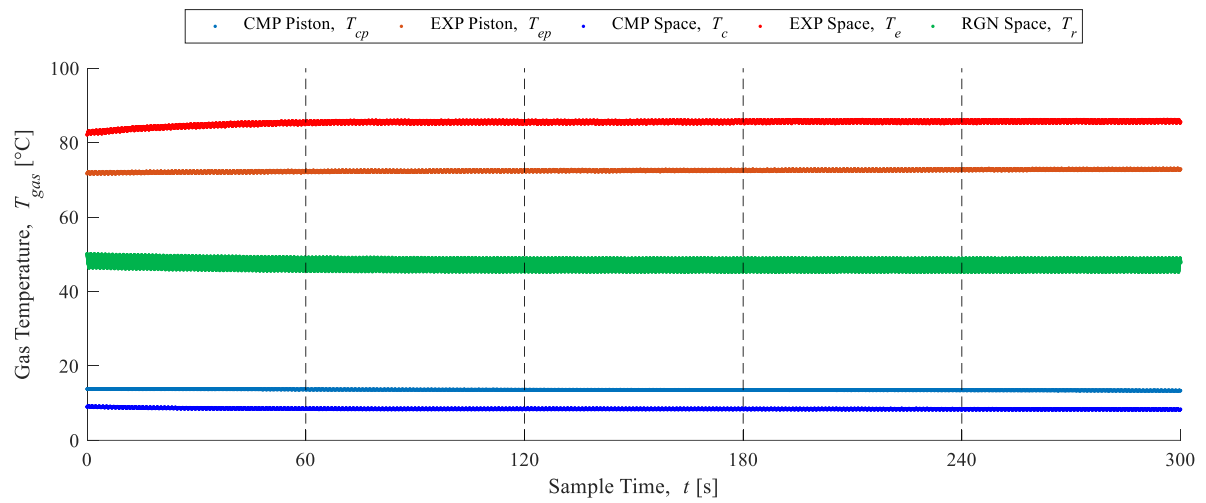
Figure C–1: Steady State Thermocouple Gas Temperature Readings (a) 1.564 L, (b) 1.955 L, and (c) 2.346 L at 60 rpm After Warm-Up
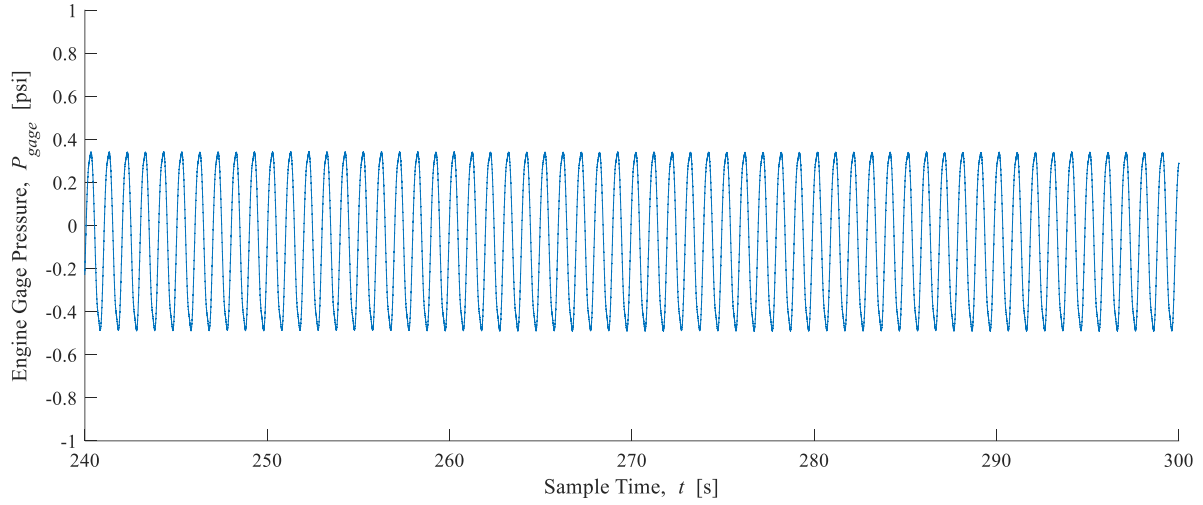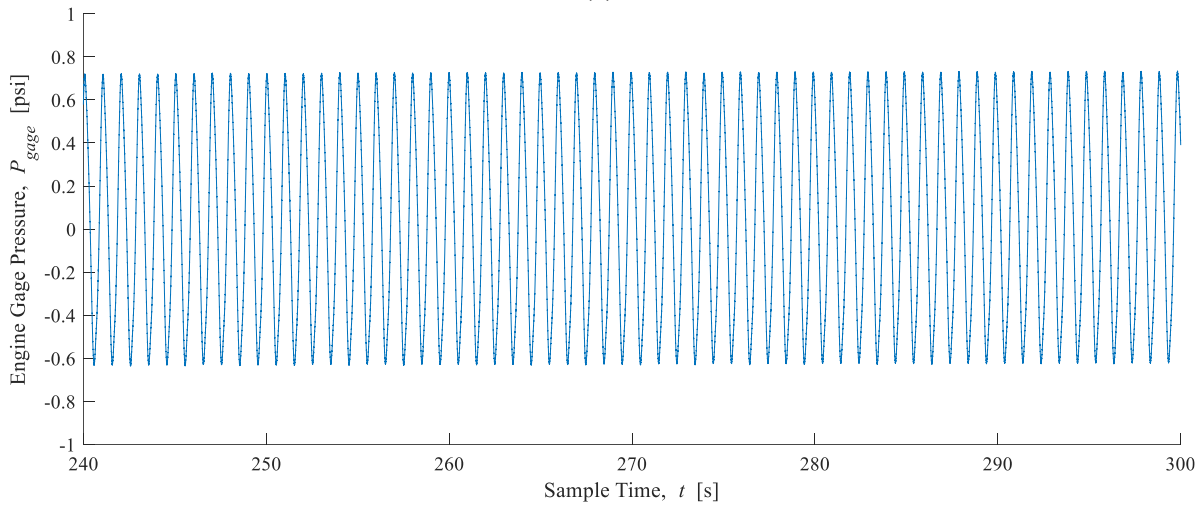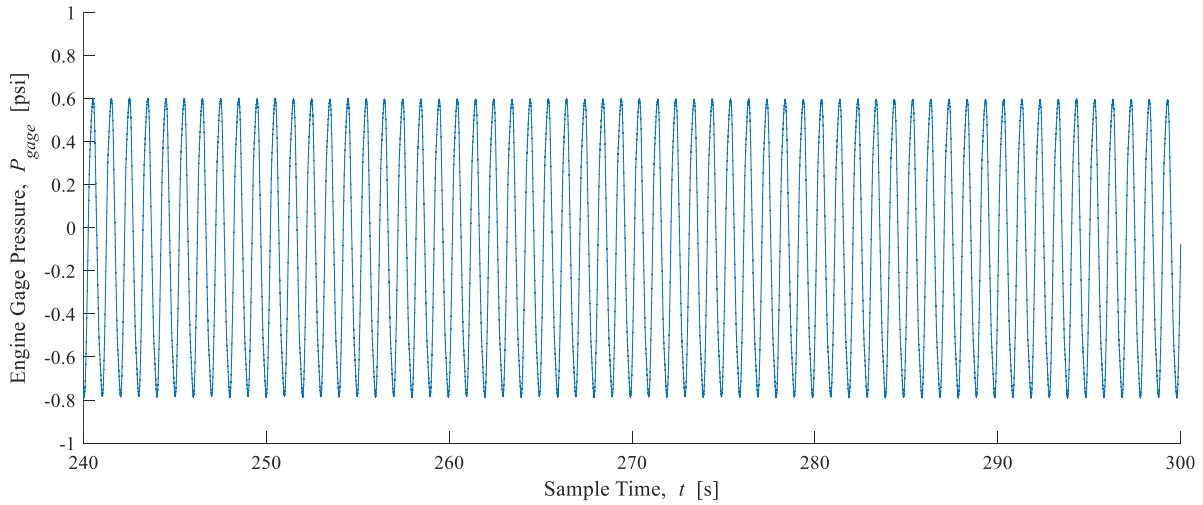
Figure C–2: Steady State Gage Pressure Readings (a) 1.564 L, (b) 1.955 L, and (c) 2.346 L at 60 rpm After Warm-Up
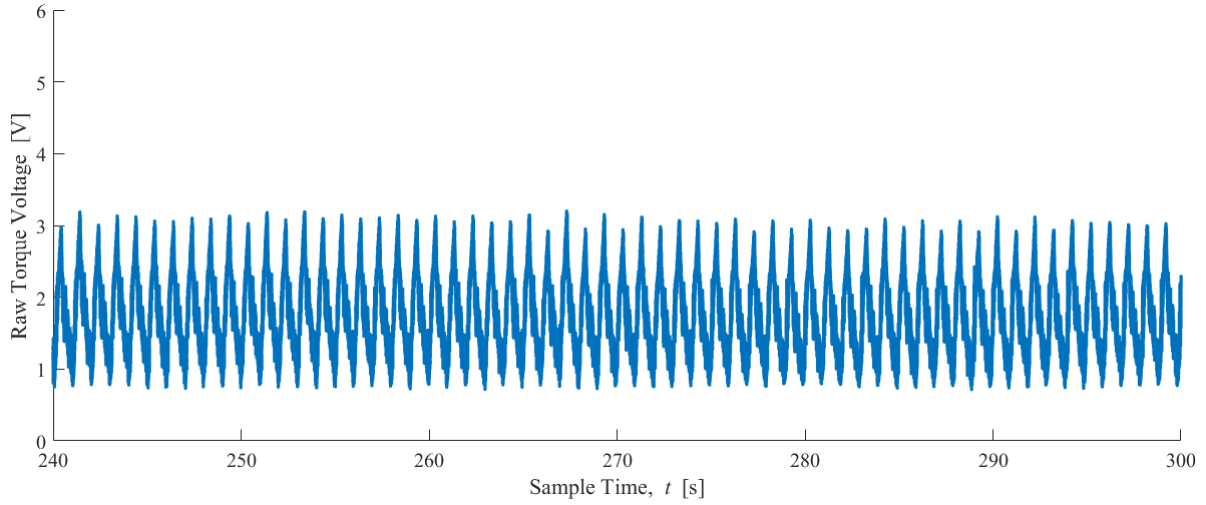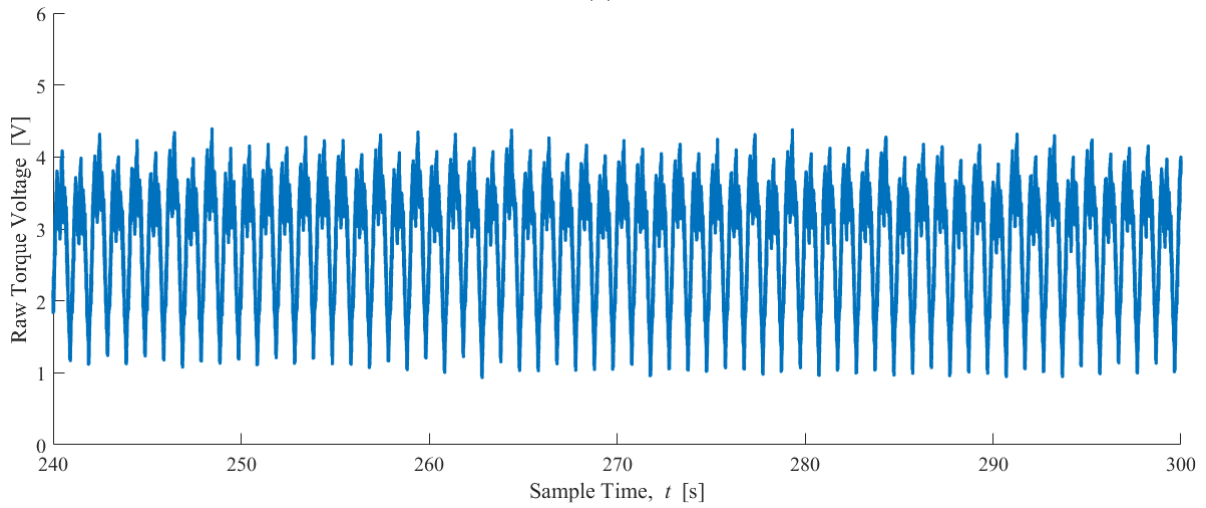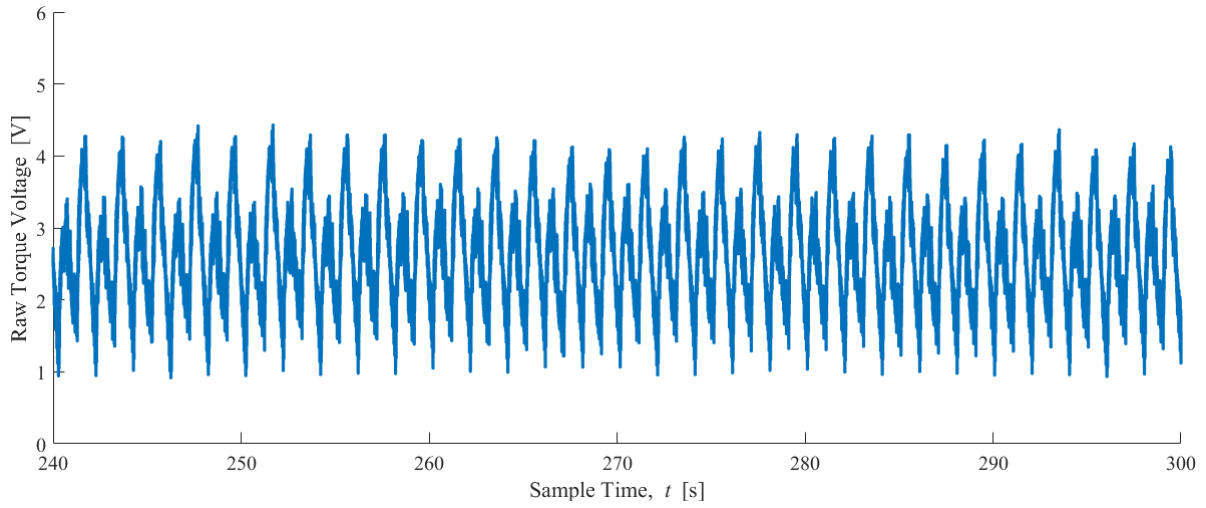
Figure C–3: Steady State Torque Voltage Readings (a) 1.564 L, (b) 1.955 L, and (c) 2.346 L at 60 rpm After Warm-Up

Appendix D   Scotch Yoke with Opposed Pistons Volume Variation Derivation

The volume variation for a Scotch yoke mechanism may be determined analytically by first determining the equation for the horizontal position of the yoke roller [80]. The position of the yoke roller can be described using the crank arm length, r_2. Since the crank arm length is known, at any crank angle, θ, the horizontal displacement of the piston may be calculated. For reference, a crank angle of 0° was arbitrarily chosen to be when the expansion space was at the minimum volume, since the Scotch yoke controlling the expansion piston was directly connected to the rotary encoder. A schematic of the mechanism used for defining the equations for volume variation in an opposed piston alpha engine with a Scotch yoke mechanism is shown in Figure A–1
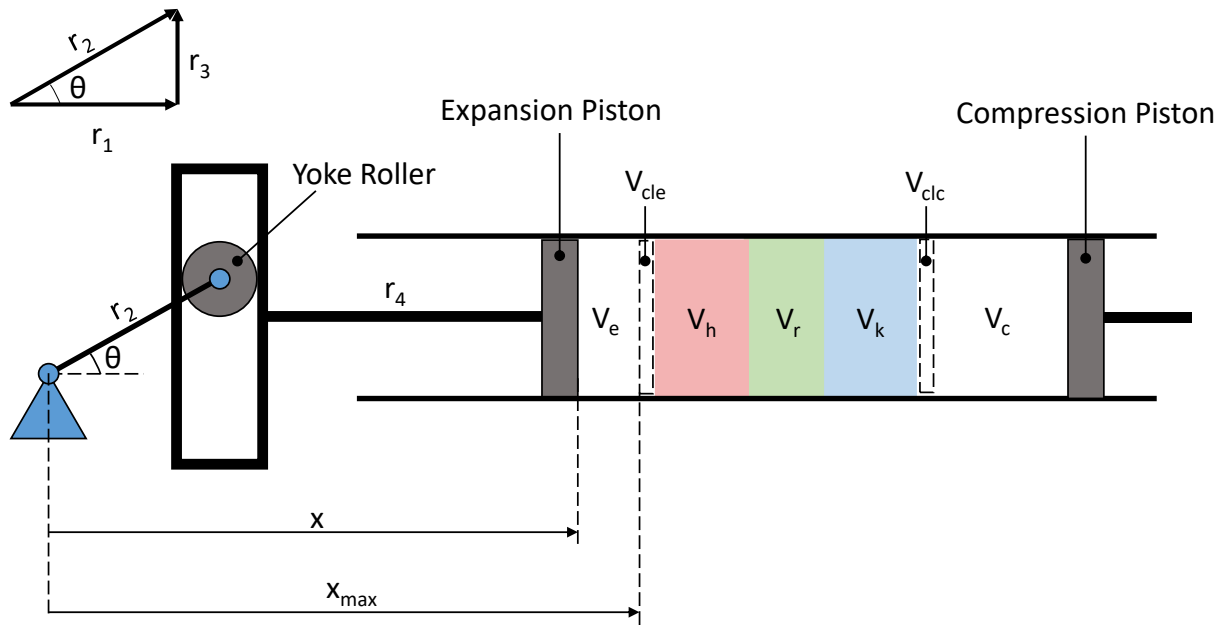
Figure A–1: Schematic of the Scotch Yoke Mechanism in the Opposed Piston Alpha Engine

Knowing the crank arm length, basic trigonometry shown in Equation A–1 was used to determine the horizontal piston displacement, r_1, as a function of crank angle in Equation A–2.

$$\cos \theta = \frac{r_1}{r_2}$$

A–1

$$r_1 = r_2 \cos \theta \qquad\qquad \text{A–2}$$

The swept volume, V_{sw}, was the volume displaced by the piston over the stroke length, L_s, multiplied by the frontal piston area, A_p, as shown:

$$V_{sw} = A_p * L_s \qquad\qquad \text{A–3}$$

The stroke length was two times the crank arm length, therefore Equation A–3 was expressed as:

$$V_{sw} = A_p * 2r_2 \qquad\qquad \text{A–4}$$

Considering the piston in the expansion space, the expansion space volume, V_e, was expressed as the sum of the expansion clearance space volume, V_{cle}, and volume between the piston face and the radiator, as shown in Equation A–5. Selecting a datum at the axis of rotation of rotation of the output shaft, the max piston face position, x_{max}, was expressed in Equation A–6, and the current position of the piston face, x, was expressed in Equation A–7, where r_4 was the connecting rod length.

$$V_e = V_{cle} + A_p * (x_{max} - x) \qquad\qquad \text{A–5}$$

$$x_{max} = r_2 + r_4 \qquad\qquad \text{A–6}$$

$$x = r_1 + r_4 = r_2 \cos \theta + r_4 \qquad\qquad \text{A–7}$$

Substituting Equations A–5 and A–6 into Equation A–7 yields:

$$V_e = V_{cle} + A_p * (r_2 + r_4 - (r_2 \cos \theta + r_4)) \qquad\qquad \text{A–8}$$

After simplifying Equation A–8 into Equation A–9, and substituting A_p into Equation A–9, the final expression for the expansion space volume variation in Equation A–10 was obtained.

$$V_e = V_{cle} + A_p * r_2(1 - \cos \theta) \qquad\qquad \text{A–9}$$

$$V_e = V_{cle} + \frac{1}{2}V_{swe}(1 - \cos\theta) \qquad\qquad \text{A–10}$$

For the compression space, the same derivation was performed with the exception that the expansion space volume change lead the compression space volume change by a chosen phase angle, α. Therefore, the crank angle was subtracted by the phase angle, as shown:

$$V_c = V_{clc} + \frac{1}{2}V_{swc}(1 - \cos(\theta - \alpha)) \qquad\qquad \text{A–11}$$

Appendix E   Bellows Measurements

This section presents the tabulated measurements used for estimating the bellows convolution volume variation. Table E–1 shows the measurements for a 50.8 mm stroke length, and Table E–2 shows the measurements for a 76.2 mm stroke length. These measurements were then used to create a solid model of the bellows at different crank angle positions, with the bellows solid model volume and convolution volume tabulated in Table E–3 and Table E–4.

Table E–1: Averaged Measurements of Bellows at Different Crank Angles with a
50.8 mm Stroke

Teknic Counts	Crank Angle [°]	Average Distance Peak to Peak [mm]	Average Distance Trough to Trough [mm]
0	0.00	36.06	48.01
34	15.30	37.75	49.33
67	30.15	40.31	52.42
100	45.00	44.05	56.47
134	60.30	49.28	61.70
167	75.15	54.02	68.12
200	90.00	59.85	75.08
234	105.30	65.58	81.33
267	120.15	70.08	87.46
300	135.00	74.26	91.75
334	150.30	77.21	96.26
367	165.15	78.44	98.30
400	180.00	79.29	98.95
433	194.85	77.61	96.77
467	210.15	75.41	93.38
500	225.00	72.29	90.04
533	239.85	68.26	84.55
567	255.15	62.94	78.03
600	270.00	56.84	71.15
633	284.85	51.71	65.46
667	300.15	46.41	60.11
700	315.00	41.85	54.71
733	329.85	38.58	51.22
767	345.15	36.36	48.78
800	360.00	36.06	48.01

Table E–2: Averaged Measurements of Bellows at Different Crank Angles with a
76.2 mm Stroke

Teknic Counts	Crank Angle [°]	Average Distance Peak to Peak [mm]	Average Distance Trough to Trough [mm]
0	0.00	24.60	36.63
34	15.30	25.65	38.71
67	30.15	28.95	41.76
100	45.00	34.53	46.92
134	60.30	41.88	54.90
167	75.15	49.54	62.66
200	90.00	57.42	71.83
234	105.30	65.89	84.49
267	120.15	72.55	90.17
300	135.00	78.65	99.04
334	150.30	83.77	104.41
367	165.15	86.69	109.51
400	180.00	87.70	110.57
433	194.85	86.70	108.24
467	210.15	84.95	105.13
500	225.00	79.62	99.83
533	239.85	73.57	93.32
567	255.15	67.30	83.15
600	270.00	59.78	72.93
633	284.85	49.99	63.84
667	300.15	40.71	54.02
700	315.00	35.60	46.81
733	329.85	29.71	43.20
767	345.15	26.00	39.37
800	360.00	24.60	36.63

Table E–3: Solid Model Bellows Convolution Volume Estimations for a 50.8 mm Stroke Length (Obtained from SolidWorks)

	Crank Angle [°]	Bellow Volume [m3]	Bellow Volume with rings[m³]	Convolution Volume [m³]	Convolution Volume With Rings [m³]	Percent of Volume [%]	Convolution Volume With Rings [mL]	Bellow Volume [mL]
Compressed	0	0.00087296	0.00084181	0.00013393	0.00010278	12.21%	102.78	841.81
	15	0.0009004	0.00086925	0.00014102	0.00010987	12.64%	109.87	869.25
	30	0.00096174	0.00093059	0.00015480	0.00012365	13.29%	123.65	930.59
	45	0.00104401	0.00101286	0.00017477	0.00014362	14.18%	143.62	1012.86
	60	0.00114989	0.00111874	0.00020010	0.00016895	15.10%	168.95	1118.74
	75	0.00127925	0.00124810	0.00023057	0.00019942	15.98%	199.42	1248.1
Mid Stroke	90	0.00142652	0.00139537	0.00027076	0.00023961	17.17%	239.61	1395.37
	105	0.00154375	0.00151260	0.00029172	0.00026057	17.23%	260.57	1512.6
	120	0.00166415	0.00163300	0.00031781	0.00028666	17.55%	286.66	1633
	135	0.00174616	0.00171501	0.00033383	0.00030268	17.65%	302.68	1715.01
	150	0.00174616	0.00171501	0.00034983	0.00031868	18.58%	318.68	1715.01
	165	0.00187028	0.00183913	0.00035701	0.00032586	17.72%	325.86	1839.13
Extended	180	0.00188271	0.00185156	0.00035955	0.0003284	17.74%	328.4	1851.56
	195	0.00184128	0.00181013	0.00035167	0.00032052	17.71%	320.52	1810.13
	210	0.0017772	0.00174605	0.00033968	0.00030853	17.67%	308.53	1746.05
	225	0.00171339	0.00168224	0.00032728	0.00029613	17.60%	296.13	1682.24
	240	0.00160902	0.00157787	0.00030752	0.00027637	17.52%	276.37	1577.87
	255	0.00148106	0.00144991	0.00027988	0.00024873	17.15%	248.73	1449.91
Mid Stroke	270	0.0013466	0.00131545	0.00025133	0.00022018	16.74%	220.18	1315.45
	285	0.00122921	0.00119806	0.00022148	0.00019033	15.89%	190.33	1198.06
	300	0.00111976	0.00108861	0.00019439	0.00016324	15.00%	163.24	1088.61
	315	0.00101139	0.00098024	0.00016915	0.000138	14.08%	138	980.24
	330	0.00093969	0.00090854	0.00015117	0.00012002	13.21%	120.02	908.54
	345	0.00089037	0.00085922	0.00013940	0.00010825	12.60%	108.25	859.22
Compressed	360	0.00087296	0.00084181	0.00013393	0.00010278	12.21%	102.78	841.81

Table E–4: Solid Model Bellows Convolution Volume Estimations for a 76.2 mm Stroke Length (Obtained from SolidWorks)

	Crank Angle [°]	Bellow Volume [m3]	Bellow Volume with rings[m^3]	Convolution Volume [m^3]	Convolution Volume With Rings [m^3]	Percent of Volume [%]	Convolution Volume With Rings [mL]	Bellow Volume [mL]
Compressed	0	0.00066606	0.00063491	0.00010219	0.00007104	11.19%	71.04	634.91
	15	0.00070633	0.00067518	0.00011043	0.00007928	11.74%	79.28	675.18
	30	0.0007658	0.00073465	0.00012295	0.0000918	12.50%	91.8	734.65
	45	0.00086703	0.00083588	0.00014475	0.0001136	13.59%	113.6	835.88
	60	0.00102247	0.00099132	0.00017735	0.0001462	14.75%	146.2	991.32
	75	0.00117659	0.00114544	0.00021201	0.00018086	15.79%	180.86	1145.44
Mid Stroke	90	0.00136487	0.00133372	0.00025913	0.00022798	17.09%	227.98	1333.72
	105	0.00160234	0.00157119	0.00030172	0.00027057	17.22%	270.57	1571.19
	120	0.00171589	0.00168474	0.00032783	0.00029668	17.61%	296.68	1684.74
	135	0.00188407	0.00185292	0.00035947	0.00032832	17.72%	328.32	1852.92
	150	0.00198673	0.00195558	0.00037946	0.00034831	17.81%	348.31	1955.58
	165	0.00208308	0.00205193	0.00039731	0.00036616	17.84%	366.16	2051.93
Extended	180	0.00210335	0.00207220	0.00040125	0.0003701	17.86%	370.1	2072.2
	195	0.00205952	0.00202837	0.00039330	0.00036215	17.85%	362.15	2028.37
	210	0.00200079	0.00196964	0.00038244	0.00035129	17.84%	351.29	1969.64
	225	0.0018993	0.00186815	0.00036254	0.00033139	17.74%	331.39	1868.15
	240	0.00177494	0.00174379	0.00033839	0.00030724	17.62%	307.24	1743.79
	255	0.00157838	0.00154723	0.00029839	0.00026724	17.27%	267.24	1547.23
Mid Stroke	270	0.00138118	0.00135003	0.00025851	0.00022736	16.84%	227.36	1350.03
	285	0.00119852	0.00116737	0.00021578	0.00018463	15.82%	184.63	1167.37
	300	0.00100591	0.00097476	0.00017433	0.00014318	14.69%	143.18	974.76
	315	0.00086525	0.00083410	0.00014467	0.00011352	13.61%	113.52	834.1
	330	0.00079217	0.00076102	0.00012716	0.00009601	12.62%	96.01	761.02
	345	0.00071836	0.00068721	0.00011231	0.00008116	11.81%	81.16	687.21
Compressed	360	0.00066606	0.00063491	0.00010219	0.00007104	11.19%	71.04	634.91

Appendix F   Detailed Uncertainty Analysis

This Appendix will present a detailed uncertainty analysis for the measured variables as well as the procedure for propagating the uncertainty for calculated output variables.

F.1 Measured Pressure Uncertainty

This section provides a sample of the calculation for the uncertainty in measured pressure. Table F–1 shows the elemental uncertainty sources for the pressure measurements. The pressures were reported in units of psi, so the pressure was converted to SI units from the imperial units to calculate the uncertainty.

Table F–1: Elemental Uncertainty Sources for Pressure Measurements

Uncertainty Category	Instrumentation	Elemental Error	Uncertainty Type	Uncertainty Value	Notes
Instrument	Validyne DP15 3-36	Manufacturer Accuracy	Systematic & Random	± 0.025 psi	±0.5% FS [95]
Calibration	Manometer	Readability	Systematic	± 0.0005 m	Half the Smallest division
	Ertco 1005-3S	Readability	Systematic	± 0.05 °C	Half the Smallest division
Data Acquisition	CD 280 Demodulator	Linearity	Systematic	± 0.0025 psi	± 0.05% FS [96]. (0.005V)*(5 psi/10V)
		Temperature Shift Zero	Random	Measurement Specific	± 0.005 % RO per °F (Assume RO = FS) [96] Assume temperature may vary by ± 2 °C or ± 3.6°F.
		Temperature Shift Span	Random	Measurement Specific	± 0.01 % RO per °F (Assume RO = FS) [96] Assume temperature may vary by ± 2 °C or ± 3.6°F.
	NI 6211 Multifunction I/O Device	Manufacturer Accuracy	Systematic & Random	± 0.001345 psi	Analog Input Absolute Accuracy 0.002690 V at ± 10 V [97] (0.00269V)*(5 psi/10V)

Sample Calculation:

The governing equation for determining the uncertainty in the pressure measurement using elemental uncertainty sources was:

$$u_{P_{eng}} = \sqrt{B_{P_{eng}}^2 + \left(2 \times S_{P_{eng}}\right)^2} \qquad\qquad \text{F–1}$$

The equation for the systematic uncertainty was defined by:

$$B_{P_{eng}}^2 = b_{DP15}^2 + b_{mano}^2 + b_{CD280}^2 + b_{NI6211}^2 \qquad \text{F–2}$$

The equation for the random uncertainty was defined by:

$$S_{P_{eng}}^2 = \left(\frac{\mathcal{P}_{zero}}{2}\right)^2 + \left(\frac{\mathcal{P}_{span}}{2}\right)^2 \qquad \text{F–3}$$

A summary of the uncertainty values is shown in Table F–2.

Table F–2: Measured Pressure Elemental Uncertainty Variables

Elemental Variable	Uncertainty Value	Units	Notes
b_{DP15}	$\pm\, 0.025$	psi	-
b_{mano}	$\pm\, 0.0013$	psi	Maximum Value
b_{CD280}	$\pm\, 0.0025$	psi	-
b_{NI6211}	$\pm\, 0.001345$	psi	-
$\mathcal{P}_{zero}$	$P_{eng} \times 1.8 \times 10^{-4}$	psi	Measurement Specific
$\mathcal{P}_{span}$	$P_{eng} \times 3.6 \times 10^{-4}$	psi	Measurement Specific
$u_{P_{eng}}$	$\pm 0.0252 \leq u_{P_{eng}} \leq 0.0254$	psi	Measurement Specific

For cycle average pressure uncertainties, $S_{P_{eng}}$ in Equation F–1 was replaced with the following:

$$S_{\bar{P}_{cycle}} = \frac{S_{P_{eng}}}{\sqrt{N_{cycle}}} \qquad \text{F–4}$$

where N_{cycle} is the number of cycles being used for cycle averaging. The engine pressure used to calculate P_{zero} and P_{span} would be cycle averaged as well.

Manometer Calibration Uncertainty:

The uncertainty in the manometer calibration was calculated using propagation of uncertainty on the governing equation:

$$\Delta P_{mano} = \rho_o g_o h_o \qquad \text{F–5}$$

where the uncertainty in the density of water and gravitational acceleration at standard conditions were assumed negligible. The corrected water column height at standard conditions is defined as:

$$h_o = \frac{\rho_l g_l h_l}{\rho_o g_o} \qquad \text{F–6}$$

Propagating the uncertainty in the above equations yielded Equations F–7 and F–8, where the variable values are summarized in Table F–3.

$$u_{h_o} = \left[\left(u_{h_l} \frac{\partial h_o}{\partial h_l} \right)^2 + \left(u_{\rho_l} \frac{\partial h_o}{\partial \rho_l} \right)^2 \right]^{\frac{1}{2}} \qquad \text{F–7}$$

$$u_{\Delta P_{mano}} = \left[\left(u_{h_o} \frac{\partial \Delta P_{mano}}{\partial h_o} \right)^2 \right]^{\frac{1}{2}} = b_{mano} \qquad \text{F–8}$$

Table F–3: Manometer Calibration Propagation of Uncertainty Variables

Variable	Value	Uncertainty Variable	Uncertainty Value	Units	Notes
ρ_l	997.8	u_{ρ_l}	0.227	kg/m^3	[88]
g_l	9.84	-	Negligible	m/s^2	[98]
h_l	Variable	u_{h_l}	0.0005	m	-
ρ_o	1000	-	Negligible	kg/m^3	-
g_o	9.81	-	Negligible	m/s^2	-
h_o	Variable	u_{h_o}	0.000945	m	Max Value

F.2 Measured Torque Uncertainty

This section provides a sample of the calculation for the uncertainty in measured torque. Table F–4 shows the elemental uncertainty sources for the torque measurements.

Table F–4: Elemental Uncertainty Sources for Torque Measurements

Uncertainty Category	Instrumentation	Elemental Error	Uncertainty Type	Uncertainty Value	Notes
Instrument	Futek TRS600	Non-Linearity	Systematic	Measurement Specific	± 0.2 % RO [86]
		Hysteresis	Systematic	Measurement Specific	± 0.1 % RO [86]
		Non-Repeatability	Random	Measurement Specific	± 0.2 % RO [86]
		Temperature Shift Zero	Random	Measurement Specific	± 0.02 % RO per °C [86] Assume temperature may vary by ± 2 °C.
		Temperature Shift Span	Random	Measurement Specific	± 0.02 % RO per °C [86] Assume temperature may vary by ± 2 °C.
Data Acquisition	NI 6211 Multifunction I/O Device	Manufacturer Accuracy	Systematic & Random	± 0.000269 Nm or ± 0.00269 Nm	Analog Input Absolute Accuracy 0.002690 V at ± 10 V [97] 1 Nm/10 V or 10 Nm/10V

Sample Calculation:

The governing equation for determining the uncertainty in the torque measurement using elemental uncertainty sources was:

$$u_\tau = \sqrt{B_\tau^2 + (2 \times S_\tau)^2}$$

F–9

The equation for the systematic uncertainty was defined by:

$$B_\tau^2 = b_{linearity}^2 + b_{hysteresis}^2 + b_{NI6211}^2$$

F–10

where the elemental systematic uncertainty values are shown in Table F–5. The equation for the random uncertainty was defined by:

$$S_\tau^2 = \left(\frac{\mathcal{P}_{repeat}}{2}\right)^2 + \left(\frac{\mathcal{P}_{zero}}{2}\right)^2 + \left(\frac{\mathcal{P}_{span}}{2}\right)^2$$

F–11

where the elemental random uncertainty values are also shown in Table F–5.

Table F–5: Measured Torque Elemental Uncertainty Variables

Elemental Variable	Uncertainty Value	Units	Notes
$b_{linearity}$	$\pm\,\tau\,\times 0.002$	Nm	Measurement Specific
$b_{hysteresis}$	$\pm\,\tau\,\times 0.001$	Nm	Measurement Specific
b_{NI6211}	$\pm\,0.000269$ or 0.00269	Nm	If 1 Nm or 10 Nm
$\mathcal{P}_{repeat}$	$\pm\,\tau\,\times 0.002$	Nm	Measurement Specific
$\mathcal{P}_{zero}$	$\pm\,\tau\,\times 0.0004$	Nm	Measurement Specific
$\mathcal{P}_{span}$	$\pm\,\tau\,\times 0.0004$	Nm	Measurement Specific
u_{τ}	$\pm 2.69 \times 10^{-4} \leq u_{\tau} \leq 7.23 \times 10^{-3}$	Nm	Measurement Specific

For cycle average pressure uncertainties, S_{τ} in Equation F–9 was replaced with the following:

$$S_{\bar{\tau}} = \frac{S_{\tau}}{\sqrt{N}} \qquad\qquad \text{F–12}$$

where N is the number of cycles being used for cycle averaging. The torque used to calculate the measurement dependent elemental uncertainties would be cycle averaged as well.

F.3 Measured Angular Position Uncertainty

This section provides a sample of the calculation for the uncertainty in measured angular position. Table F–6 summarizes the elemental sources of uncertainty when measuring with the rotary encoder.

Table F–6: Elemental Uncertainty Sources for Angular Position Measurements

Uncertainty Category	Instrumentation	Elemental Error	Uncertainty Type	Uncertainty Value	Notes
Instrument	500 Pulse Rotary Encoder	Manufacturer Accuracy	Systematic	± 0.017 °	Mechanical alignment from true position [99]
Methods	-	Encoder Alignment	Systematic	± 1.0°	When aligning the encoder with the engine's selected zero degree crank angle position.
Data Acquisition	NI 6211 Multifunction I/O Device	Manufacturer Accuracy	Systematic & Random	-	AI Absolute Accuracy 0.001410 V at ± 5 V [97] negligible since the uncertainty does not exceed the 2.5 V threshold

Sample Calculation:

The governing equation for determining the uncertainty in the angular position using elemental uncertainty sources was:

$$u_\omega = \sqrt{B_\omega^2 + (2 \times S_\omega)^2}$$
F–13

The equation for the systematic uncertainty was defined by:

$$B_\omega^2 = b_{encoder}^2 + b_{align}^2$$
F–14

The random uncertainty was grouped with the systematic uncertainty provided by the manufacturer, therefore S_ω in Equation F–13 was equal to zero. The uncertainty from the NI-6211 was also assumed to be negligible. The values of the elemental uncertainties are summarized in Table F–7.

Table F–7: Measured Angular Position Elemental Uncertainty Variables

Elemental Variable	Uncertainty Value	Units	Notes
$b_{encoder}$	± 0.017	°	-
b_{align}	± 1.0	°	-
u_ω	± 1.00	°	-

F.4 RTD Temperature Measurement Uncertainty

This section provides a sample of the calculation for the uncertainty in water temperature measured by the RTDs. Table F–8 summarizes the elemental sources of uncertainty.

Table F–8: Elemental Uncertainty Sources for RTD Temperature Measurements

Uncertainty Category	Instrumentation	Elemental Error	Uncertainty Type	Uncertainty Value	Notes
Instrument	RTD-810	Manufacturer Accuracy	Systematic & Random	±0.35 °C	[100]
Calibration	Ertco 1005-3S	Readability	Systematic	± 0.05 °C	Half the Smallest division
Data Acquisition	NI 9217 RTD DAQ	Manufacturer Accuracy	Systematic & Random	±0.5 °C	Maximum (-40 to 70 °C) between -200 to 150 °C [85] Including Noise

Sample Calculation:

The governing equation for determining the uncertainty in the RTD temperature measurements using elemental uncertainty sources was:

$$u_{T_{H2O}} = \sqrt{B_{T_{H2O}}^2 + \left(2 \times S_{T_{H2O}}\right)^2} \qquad \text{F–15}$$

The equation for the systematic uncertainty was defined by:

$$B_{T_{H2O}}^2 = b_{RTD}^2 + b_{ertco}^2 + b_{NI9217}^2 \qquad \text{F–16}$$

The random uncertainty was grouped with the systematic uncertainty provided by the manufacturer, therefore $S_{T_{H2O}}$ in Equation F–15 was equal to zero. The values of the elemental uncertainties are summarized in Table F–9.

Table F–9: Measured RTD Temperature Elemental Uncertainty Variables

Elemental Variable	Uncertainty Value	Units	Notes
b_{RTD}	± 0.35	°C	-
b_{ertco}	± 0.05	°C	-
b_{NI9217}	± 0.5	°C	-
$u_{T_{H2O}}$	± 0.61	°C	-

F.5 Thermocouple Temperature Measurement Uncertainty

This section provides a sample of the calculation for the uncertainty in gas temperature measured by the thermocouples. Table F–10 summarizes the elemental sources of uncertainty.

Table F–10: Elemental Uncertainty Sources for Thermocouple Gas Temperature Measurements

Uncertainty Category	Instrumentation	Elemental Error	Uncertainty Type	Uncertainty Value	Notes
Instrument	TTSS-116E-6 Type T Thermocouple	Manufacturer Accuracy	Systematic & Random	± 1 °C	±1 °C or 0.75% above 0 °C [101]
Calibration	Ertco 1005-3S	Readability	Systematic	± 0.05 °C	Half the Smallest division
Data Acquisition	TC 2095 Rack Mount Adapter	Cold-junction sensor Accuracy	Systematic	± 0.65 °C	From temperature range 15 to 35 °C [102]
		Cold-junction sensor Repeatability	Random	± 0.35 °C	From temperature range 15 to 35 °C [102]
	SCXI-1600 Data Acquisition Module	Manufacturer Accuracy	Systematic & Random	± 1.409 °C	Absolute accuracy 0.061 mV at a full scale of 5 mV [103]. From [104]: (0.061mV) (350 °C/15.153mV)
		Noise	Random	-	Included

Sample Calculation:

The governing equation for determining the uncertainty in the gas temperature measurements using elemental uncertainty sources was:

$$u_{T_{gas}} = \sqrt{B_{T_{gas}}^2 + \left(2 \times S_{T_{gas}}\right)^2} \qquad \text{F–17}$$

The equation for the systematic uncertainty was defined by:

$$B_{T_{gas}}^2 = b_{TTSS}^2 + b_{ertco}^2 + b_{TC2095}^2 + b_{SCXI}^2 \qquad \text{F–18}$$

The equation for the random uncertainty was defined by:

$$S_{T_{gas}}^2 = \left(\frac{\mathcal{P}_{TC2095}}{2}\right)^2 \qquad \text{F–19}$$

The values of the elemental uncertainties are summarized in Table F–11.

Table F–11: Measured Thermocouple Gas Temperature Elemental Uncertainty Variables

Elemental Variable	Uncertainty Value	Units	Notes
b_{TTSS}	$\pm\,1.00$	°C	-
b_{ertco}	$\pm\,0.05$	°C	-
b_{TC2095}	$\pm\,0.65$	°C	-
b_{SCXI}	$\pm\,1.41$	°C	-
$b_{T_{gas}}$	$\pm\,1.85$	°C	-
$\mathcal{P}_{TC2095}$	$\pm\,0.35$	°C	-
$u_{T_{gas}}$	$\pm\,1.85$	°C	-

F.6 Engine Volume Propagation of Uncertainty

The uncertainty in total engine volume, $u_{V_{eng}}$, was calculated using propagation of uncertainty on the governing equation:

$$V_{eng} = V_e + V_c + V_h + V_r + V_k \tag{F–20}$$

The uncertainties in expansion space volume, V_e, compression space volume, V_c, heater volume, V_h, regenerator space volume, V_r, and cooler volume, V_k, were determined using propagation of uncertainty as well. This section will present the analysis for the propagation of uncertainty in each volume.

Regenerator Volume Uncertainty:

Since the regenerator was not inserted in the engine, the regenerator volume was only a function of the length, L_{regen}, width, W_{regen}, and height, H_{regen}, of the 3D printed space as shown:

$$V_r = L_{regen} \times W_{regen} \times H_{regen} \tag{F–21}$$

With the governing equation being a produce of variables, the propagation of uncertainty simplification in Equation 4-29 was used:

$$\frac{u_{V_r}}{V_r} = \left[\left(\frac{u_{L_{regen}}}{L_{regen}} \right)^2 + \left(\frac{u_{W_{regen}}}{W_{regen}} \right)^2 + \left(\frac{u_{H_{regen}}}{H_{regen}} \right)^2 \right]^{\frac{1}{2}} \tag{F–22}$$

The uncertainty in all dimensions of the 3D printed component was $\pm$ 0.2 mm. Table F–12 summarizes the values of the uncertainty for variables in Equation F–22.

Table F–12: Regenerator Volume Propagation of Uncertainty Parameters

Variable	Value	Uncertainty Variable	Uncertainty Value	Units	Notes
L_{regen}	0.12	$u_{L_{regen}}$	$\pm$ 0.0002	m	-
W_{regen}	0.125	$u_{W_{regen}}$	$\pm$ 0.0002	m	-
H_{regen}	0.01245	$u_{H_{regen}}$	$\pm$ 0.0002	m	-
V_r	0.000187	u_{V_r}	$\pm$ 3.03×10⁻⁶	m³	-

<u>Heater and Cooler Volume Uncertainty:</u>

The heater and cooler were the same, and the air void volume, V_{HEX}, was determined subtracting the 3D printed heat exchanger housing volume, V_{house}, by the measured solid volume, V_{solid}, of the heat exchanger:

$$V_h = V_k = V_{HEX} = V_{house} - V_{solid} \qquad \text{F–23}$$

The uncertainty in the air void volume was:

$$u_{V_{HEX}} = \left[\left(u_{V_{house}} \right)^2 + \left(-u_{V_{solid}} \right)^2 \right]^{\frac{1}{2}} \qquad \text{F–24}$$

The heat exchanger housing volume was not rectangular, but will be approximated as rectangular as it is a conservative estimate. The governing equation for the housing volume was:

$$V_{house} = L_{house} \times W_{house} \times H_{house} \qquad \text{F–25}$$

The uncertainty in all dimensions of the 3D printed component was ± 0.2 mm, and the uncertainty propagation equation became:

$$\frac{u_{V_{house}}}{V_{house}} = \left[\left(\frac{u_{L_{house}}}{L_{house}} \right)^2 + \left(\frac{u_{W_{house}}}{W_{house}} \right)^2 + \left(\frac{u_{H_{house}}}{H_{house}} \right)^2 \right]^{\frac{1}{2}} \qquad \text{F–26}$$

The solid volume of the heat exchanger was determined from inserting the heat exchanger in a known amount of water in a tank with known dimensions, and measuring the change in volume, as shown:

$$V_{solid} = L_{tank} \times W_{tank} \times \left(H_{H2O_f} - H_{H2O_i} \right) = L_{tank} \times W_{tank} \times H_{H2O} \qquad \text{F–27}$$

The tank dimensions were measured with a large Vernier caliper with a reading uncertainty of ± 0.05 mm, and the water height was measured with another Vernier caliper with a reading uncertainty of ± 0.01 mm. The total uncertainty in the water height difference was calculated as:

$$u_{H_{H2O}} = \left[\left(u_{H_{H2O_f}} \right)^2 + \left(-u_{H_{H2O_i}} \right)^2 \right]^{\frac{1}{2}} \qquad \text{F–28}$$

The uncertainty in the heat exchanger solid volume is shown:

$$u_{V_{solid}} = \left[\left(u_{L_{tank}} \times W_{tank} \times H_{H2O}\right)^2 + \left(u_{W_{tank}} \times L_{tank} \times H_{H2O}\right)^2 \right.$$
$$\left. + \left(u_{H_{H2O}} \times L_{tank} \times W_{tank}\right)^2\right]^{\frac{1}{2}} \qquad \text{F–29}$$

Substituting the calculated uncertainties from Equations F–26 and F–29 into Equation F–24 yielded the uncertainty in heat exchanger void volume. Table F–13 summarizes the calculated uncertainty values.

Table F–13: Heat Exchanger Volume Propagation of Uncertainty Parameters

Variable	Value	Uncertainty Variable	Uncertainty Value	Units	Notes
L_{house}	0.1584	$u_{L_{house}}$	± 0.0002	m	-
W_{house}	0.1284	$u_{W_{house}}$	± 0.0002	m	-
H_{house}	0.06	$u_{H_{house}}$	± 0.0002	m	-
V_{house}	0.0012	$u_{V_{house}}$	$\pm 4.63 \times 10^{-6}$	m^3	-
L_{tank}	0.301	$u_{L_{tank}}$	± 0.00005	m	-
W_{tank}	0.146	$u_{W_{tank}}$	± 0.00005	m	-
H_{H2O_f}	0.0751	$u_{H_{H2O_f}}$	± 0.00001	m	-
H_{H2O_i}	0.0678	$u_{H_{H2O_i}}$	± 0.00001	m	-
H_{H2O}	0.0073	$u_{H_{H2O}}$	$\pm 1.41 \times 10^{-5}$	m	-
V_{solid}	3.23×10^{-4}	$u_{V_{solid}}$	$\pm 6.34 \times 10^{-7}$	m^3	-
V_{HEX}	8.68×10^{-4}	u_{HEX}	$\pm 4.68 \times 10^{-6}$	m^3	-

<u>Expansion Space Volume Uncertainty:</u>

Variables within the expansion space volume variation equation include the expansion space clearance volume, V_{cle}, the expansion piston swept volume V_{swe}, the bellows convolution volume, $V_{bellows}$, and the crank angle, θ. The method for determining the uncertainty in the bellows convolution volume has been detailed in Section 4.6.5, and will not be repeated here. The governing equation for the volume variation in the expansion space was:

$$V_e = V_{cle} + \frac{1}{2}V_{swe}(1 - \cos(\theta)) + V_{bellows} \qquad \text{F–30}$$

By using the by using propagation of uncertainty on Equation F–30, the following expression for the uncertainty in the expansion space volume, u_{V_e}, was obtained:

$$u_{V_e} = \left[\left(u_{V_{cle}} \frac{\partial V_e}{\partial V_{cle}} \right)^2 + \left(u_{V_{swe}} \frac{\partial V_e}{\partial V_{swe}} \right)^2 + \left(u_{\theta} \frac{\partial V_e}{\partial \theta} \right)^2 + \left(u_{V_{bellows}} \frac{\partial V_e}{\partial V_{bellows}} \right)^2 \right]^{\frac{1}{2}} \qquad \text{F–31}$$

The uncertainties $u_{V_{cle}}$ and $u_{V_{swe}}$ were determined from propagation of uncertainty within their respective governing equations. The uncertainty in crank angle was shown in Appendix F.3, and was calculated to be $\pm 1.00°$, or ± 0.0175 rad. The clearance volume was determined by separating the volume into three simple geometries: a rectangular volume in the heat exchanger cavity, a 130 mm diameter cylindrical volume inside the 3D printed expansion cylinder, and a 140 mm diameter cylindrical volume of the inner bellows, as shown in Figure F–1.
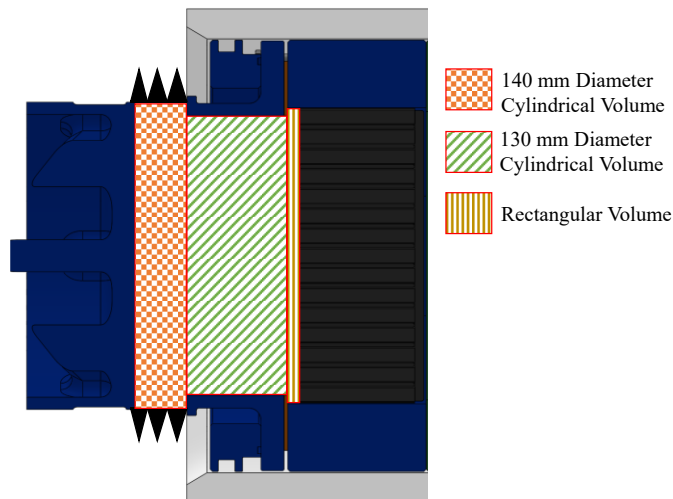
Figure F–1: Schematic of the Initial Clearance Volume Without DVRCs

This initial clearance volume was then subtracted by the solid volume of the DVRC for a 76.2 mm stroke. The governing and uncertainty equations for the clearance volume are shown in Equations F–32 and F–33. A detailed analysis into the propagation of uncertainty into geometric volumes will not be provided, but the parameters used are summarized in Table F–14.

$$V_{cle} = V_{cle_o} - V_{DVRC} \qquad \text{F–32}$$

$$u_{V_{cle}} = \left[\left(u_{V_{cle_o}}\right)^2 + \left(-u_{V_{DVRC}}\right)^2\right]^{\frac{1}{2}} \qquad \text{F–33}$$

Table F–14: Expansion Clearance Volume Propagation of Uncertainty Parameters

Variable	Value	Uncertainty Variable	Uncertainty Value	Units	Notes
L_{rect}	0.1584	$u_{L_{rect}}$	± 0.0002	m	-
W_{rect}	0.1284	$u_{W_{rect}}$	± 0.0002	m	-
H_{rect}	0.005	$u_{H_{rect}}$	± 0.0002	m	-
V_{rect}	1.01×10^{-4}	$u_{V_{rect}}$	$\pm 4.07\times10^{-6}$	m^3	-
D_{130}	0.13	$u_{D_{130}}$	± 0.0002	m	-
H_{130}	0.0436	$u_{H_{130}}$	± 0.0002	m	-
V_{130}	5.79×10^{-4}	$u_{V_{130}}$	$\pm 3.20\times10^{-6}$	m^3	-
D_{140}	0.14	$u_{D_{140}}$	± 0.0002	m	-
H_{140}	0.0264	$u_{H_{140}}$	± 0.0005	m	-
V_{140}	4.06×10^{-4}	$u_{V_{140}}$	$\pm 8.37\times10^{-6}$	m^3	-
V_{cle_o}	0.0011	$u_{V_{cle_o}}$	$\pm 9.84\times10^{-6}$	m^3	-
V_{DVRC}	9.86×10^{-5}	$u_{V_{DVRC}}$	$\pm 1.10\times10^{-6}$	m^3	-
V_{cle}	Variable	$u_{V_{cle}}$	$\pm 9.90\times10^{-6}$	m^3	-

For the swept volume, the governing equation was a function of bellows inner diameter, $d_{i,bellows}$, and stroke length, L_{stroke}, which was variable in the experiment, as shown:

$$V_{swe} = \frac{\pi}{4} d^2_{i,bellows} \times L_{stroke} \qquad \text{F–34}$$

The equation for the uncertainty in swept volume was then:

$$\frac{u_{V_{swe}}}{V_{swe}} = \left[\left(\frac{2 \times u_{d_{i,bellows}}}{d_{i,bellows}}\right)^2 + \left(\frac{u_{L_{stroke}}}{L_{stroke}}\right)^2\right]^{\frac{1}{2}} \qquad \text{F–35}$$

The uncertainty in the stroke length was assumed to be equal to the ± 0.01 mm linear tolerance given to the machinist that manufactured the crank arms, and the uncertainty in the bellows inner diameter was assumed negligible. The uncertainty for the expansion piston swept volume was found to be 1.54×10^{-7} m^3, with a negligible difference between a 50.8 mm and 76.2 mm stroke length.

Equation F–31 simplified into Equation F–36. Many of the parameters used in Equation F–36 were dependent on the configuration and crank angle position, so the uncertainty varied between ± 11.0 mL and ± 19.5 mL.

$$u_{V_e} = \left[\left(u_{V_{cle}}\right)^2 + \left(\frac{u_{V_{swe}}}{2} \times (1 - \cos(\theta))\right)^2 + \left(\frac{u_\theta}{2} \times V_{swe} \sin(\theta)\right)^2 + \left(u_{V_{bellows}}\right)^2 \right]^{\frac{1}{2}} \quad \text{F–36}$$

Table F–15 summarizes the values of the uncertainties used in Equation F–36.

Table F–15: Expansion Space Volume Uncertainty Parameters

Uncertainty Variable	Uncertainty Value	Units	Notes
$u_{V_{cle}}$	± 9.90×10^{-6}	m^3	Negligible Change With Stroke
$u_{V_{swe}}$	± 1.54×10^{-7}	m^3	Negligible Change With Stroke
u_θ	± 0.0175	rad	Same as Rotary Encoder
$u_{V_{bellows}}$	Variable	m^3	-
u_{V_e}	$\pm 11.0 \times 10^{-6} \leq u_{V_e} \leq 19.5 \times 10^{-6}$	m^3	Range depending on configuration

Compression Space Volume Uncertainty:

A similar procedure was followed for determining the uncertainty in the compression space volume variation; however, the compression space volume lagged the expansion space volume by a phase angle, α, as shown in the governing equation:

$$V_c = V_{clc} + \frac{1}{2}V_{swc}(1 - \cos(\theta - \alpha)) + V_{bellows} \qquad \text{F--37}$$

By propagating the uncertainty in Equation F–37, the following expression for the uncertainty in the compression space volume, u_{V_c}, was obtained:

$$u_{V_c} = \left[\left(u_{V_{clc}}\right)^2 + \left(\frac{u_{V_{swc}}}{2} \times (1 - \cos(\theta - \alpha))\right)^2 + \left(\frac{u_\theta}{2} \times V_{swc}\sin(\theta - \alpha)\right)^2 \right.$$
$$\left. + \left(\frac{-u_\alpha}{2} \times V_{swc}\sin(\theta - \alpha)\right)^2 + \left(u_{V_{bellows}}\right)^2 \right]^{\frac{1}{2}} \qquad \text{F--38}$$

The uncertainty in the phase angle, u_α, was assumed to be 1°, and the uncertainty in the compression clearance space, $u_{V_{clc}}$, and the compression piston swept volume, $u_{V_{swc}}$, were calculated in the same manner as the expansion space equivalents, but with slightly different values for the geometric shape heights due to assembly tolerances. The uncertainty range was between ± 11.1 mL and ± 21.0 mL depending on the configuration, with a summary of the uncertainties shown in Table F–16.

Table F–16: Compression Space Volume Uncertainty Parameters

Uncertainty Variable	Uncertainty Value	Units	Notes
$u_{V_{clc}}$	$\pm 9.97 \times 10^{-6}$	m^3	Negligible Change With Stroke
$u_{V_{swc}}$	$\pm 1.54 \times 10^{-7}$	m^3	Negligible Change With Stroke
u_θ	± 0.0175	rad	Same as Rotary Encoder
u_α	± 0.0175	rad	Assumed
$u_{V_{bellows}}$	Variable	m^3	-
u_{V_c}	$\pm 11.1 \times 10^{-6} \leq u_{V_e} \leq 21.0 \times 10^{-6}$	m^3	Range depending on configuration

<u>Total engine volume uncertainty</u>:

After propagating the uncertainty in the governing equation in Equation F–20, the following equation was obtained:

$$u_{V_{eng}} = \left[\left(u_{V_e} \right)^2 + \left(u_{V_c} \right)^2 + \left(u_{V_h} \right)^2 + \left(u_{V_r} \right)^2 + \left(u_{V_k} \right)^2 \right]^{\frac{1}{2}} \qquad \text{F–39}$$

A summary of the uncertainties is shown in Table F–17, where the units of volume was converted from m^3 to mL for clarity.

Table F–17: Summary of Total Engine Volume Uncertainty Parameters

Uncertainty Variable	Uncertainty Value	Units	Notes
u_{V_e}	$\pm 11.0 \leq u_{V_e} \leq 19.5$	mL	Range depending on configuration
u_{V_c}	$\pm 11.1 \leq u_{V_e} \leq 21.0$	mL	Range depending on configuration
u_{V_h}	± 4.68	mL	-
u_{V_r}	± 3.03	mL	-
u_{V_k}	± 4.68	mL	-
$u_{V_{eng}}$	$\pm 17.3 \leq u_{V_{eng}} \leq 29.3$	mL	Range depending on configuration

F.7 Non-Dimensional Volume Uncertainty

The governing equation for the non-dimensional engine volume, V_{eng}^*, is shown in Equation F–40, and the equation used to calculate the uncertainty, $u_{V_{eng}^*}$, is shown in Equation F–41. The uncertainty varied depending on the configuration and crank angle, and the calculated uncertainty range in engine volume, $u_{V_{eng}}$, is shown in Table F–17.

$$V_{eng}^* = \frac{V_{eng}}{V_{sw_{eng}}} \qquad\qquad \text{F–40}$$

$$\frac{u_{V_{eng}^*}}{V_{eng}^*} = \left[\left(\frac{u_{V_{eng}}}{V_{eng}}\right)^2 + \left(\frac{-u_{V_{sw_{eng}}}}{V_{sw_{eng}}}\right)^2 \right]^{\frac{1}{2}} \qquad\qquad \text{F–41}$$

The engine swept volume uncertainty, $u_{V_{sw_{eng}}}$, was also calculated by propagating the uncertainty into the summation of the expansion and compression space swept volumes, as shown:

$$u_{V_{sw_{eng}}} = \left[\left(u_{V_{swe}}\right)^2 + \left(u_{V_{swc}}\right)^2 \right]^{\frac{1}{2}} \qquad\qquad \text{F–42}$$

To determine the uncertainty in the non-dimensional expansion and compression space volume, a similar procedure was followed for the governing equations shown in Section 4.5.4. The equations for the uncertainty in non-dimensional expansion and compression space volume are shown in Equations F–43 and F–44 respectively. Table F–18 summarizes the uncertainty values.

$$\frac{u_{V_e^*}}{V_e^*} = \left[\left(\frac{u_{V_e}}{V_e}\right)^2 + \left(\frac{-u_{V_{swe}}}{V_{swe}}\right)^2 \right]^{\frac{1}{2}} \qquad\qquad \text{F–43}$$

$$\frac{u_{V_c^*}}{V_c^*} = \left[\left(\frac{u_{V_c}}{V_c}\right)^2 + \left(\frac{-u_{V_{swc}}}{V_{swc}}\right)^2 \right]^{\frac{1}{2}} \qquad\qquad \text{F–44}$$

Table F–18: Summary of Non-dimensional Volume Uncertainty Parameters

Uncertainty Variable	Uncertainty Value	Units	Notes
$u_{V_{sw_{eng}}}$	$\pm\, 0.218$	mL	-
$u_{V_e^*}$	$\pm 0.0094 \leq u_{V_e^*} \leq 0.0249$	-	-
$u_{V_c^*}$	$\pm 0.0095 \leq u_{V_c^*} \leq 0.0264$	-	-
$u_{V_{eng}^*}$	$\pm 0.0074 \leq u_{V_{eng}^*} \leq 0.0187$	-	-

F.8 Non-Dimensional Pressure Uncertainty

The governing equation for the non-dimensional engine pressure, P^*, was:

$$P^* = \frac{P_{eng}}{P_{mean}}$$

F–45

The equation used to calculate the uncertainty, u_{P^*}, was:

$$\frac{u_{P^*}}{P^*} = \left[\left(\frac{u_{P_{eng}}}{P_{eng}}\right)^2 + \left(\frac{-u_{P_{mean}}}{P_{mean}}\right)^2\right]^{\frac{1}{2}}$$

F–46

The process for calculating $u_{P_{eng}}$ was demonstrated in Appendix F.1, but the calculation of the mean pressure uncertainty was not shown. The uncertainty of the mean cycle pressure was:

$$u_{P_{mean}} = \sqrt{B_{P_{eng}}^2 + \left(2 \times S_{\bar{P}_{eng}}\right)^2}$$

F–47

where $B_{P_{eng}}$ was derived in Appendix F.1, and $S_{\bar{P}_{eng}}$ was defined as:

$$S_{\bar{P}_{eng}} = \frac{S_P}{\sqrt{N}}$$

F–48

The standard deviation in the pressure, S_P, was calculated directly from the data set, and N was the number of data points in the data set. Table F–19 summarizes the ranges of uncertainties to calculate the non-dimensional pressure uncertainty. The uncertainties were measurement specific, so a maximum and minimum value are provided.

Table F–19: Summary of Non-dimensional Pressure Uncertainty Parameters

Uncertainty Variable	Uncertainty Value	Units	Notes
$u_{P_{eng}}$	$\pm 0.0252 \leq u_{P_{eng}} \leq 0.0254$	psi	-
$u_{P_{mean}}$	$\pm 0.027 \leq u_{P_{mean}} \leq 0.102$	psi	-
u_{P^*}	$\pm 0.0027 \leq u_{P^*} \leq 0.0087$	-	-

F.9 Compression Ratio Uncertainty

The compression ratio was defined in Section 4.5.4, with the governing equation shown in Equation F–49, and the uncertainty in compression ratio shown in Equation F–50.

$$CR = \frac{V_{max}}{V_{min}} \qquad\qquad \text{F–49}$$

$$\frac{u_{CR}}{CR} = \left[\left(\frac{u_{V_{max}}}{V_{max}}\right)^2 + \left(\frac{-u_{V_{min}}}{V_{min}}\right)^2\right]^{\frac{1}{2}} \qquad\qquad \text{F–50}$$

The values for the maximum and minimum volume uncertainty were dependent on the engine configuration, so the range of calculated uncertainties in compression ratio are shown in Table F–20.

Table F–20: Summary of Non-dimensional Pressure Uncertainty Parameters

Uncertainty Variable	Uncertainty Value	Units	Notes
$u_{V_{max}}$	$\pm 18.85 \leq u_{V_{max}} \leq 29.29$	mL	-
$u_{V_{min}}$	$\pm 22.56 \leq u_{V_{min}} \leq 29.26$	mL	-
u_{CR}	$\pm 0.0073 \leq u_{CR} \leq 0.0140$	-	-

F.10 Pressure Ratio Uncertainty

The pressure ratio was defined in Section 4.5.4, with the governing equation:

$$\Gamma = \frac{P_{max}}{P_{min}} \qquad \text{F--51}$$

The uncertainty in compression ratio shown in Equation F–52, with the systematic and standard deviation terms defined in Equations F–53 and F–54. Correlation terms were accounted for in the systematic uncertainty because the same transducer was used for both pressure measurements, and there was a common calibration uncertainty, C_{calib}, and transducer uncertainty, C_{trans}. Other systematic uncertainty correlations were neglected, as they were an order of magnitude smaller than the ones considered.

$$u_\Gamma = [(B_\Gamma)^2 + (2 \times S_\Gamma)^2]^{\frac{1}{2}} \qquad \text{F--52}$$

$$B_\Gamma = \left[\left(b_{P_{max}} \times \frac{1}{P_{min}} \right)^2 + \left(b_{P_{min}} \times \frac{-P_{max}}{P_{min}^2} \right)^2 + C_{calib} + C_{trans} \right]^{\frac{1}{2}} \qquad \text{F--53}$$

$$S_\Gamma = \left[\left(S_{P_{max}} \times \frac{1}{P_{min}} \right)^2 + \left(S_{P_{min}} \times \frac{-P_{max}}{P_{min}^2} \right)^2 \right]^{\frac{1}{2}} \qquad \text{F--54}$$

The correlation terms were defined as follows:

$$C_{calib} = 2 \times \left(\frac{1}{P_{min}} \right) \times \left(\frac{-P_{max}}{P_{min}^2} \right) \times b_{mano} \times b_{mano} \qquad \text{F--55}$$

$$C_{trans} = 2 \times \left(\frac{1}{P_{min}} \right) \times \left(\frac{-P_{max}}{P_{min}^2} \right) \times b_{DP15} \times b_{DP15} \qquad \text{F--56}$$

By considering the correlation effects for a measurement made from the same transducer with the same calibration standard, the uncertainty in the pressure ratio, u_Γ, was reduced. The uncertainty range was calculated to be:

$$\pm\, 0.00066 \le u_\Gamma \le 0.00098 \qquad \text{F--57}$$

F.11 Gas Temperature Difference Uncertainty

The governing equation for the gas temperature difference, ΔT_{gas}, was defined as the difference between the temperature measured by the expansion space thermocouple, T_e, and the compression space thermocouple, T_c, as shown:

$$\Delta T_{gas} = T_e - T_c \qquad \text{F–58}$$

The equation for the uncertainty in gas temperature difference, $u_{\Delta T_{gas}}$, is shown in Equation F–59. Correlated uncertainties between the two thermocouples included the common calibration standard uncertainty, C_{calib}, and the uncertainties in the DAQ devices, C_{TC2095} and C_{SCXI}.

$$u_{\Delta T_{gas}} = \left[\left(B_{\Delta T_{gas}} \right)^2 + \left(2 \times S_{\Delta T_{gas}} \right)^2 \right]^{\frac{1}{2}} \qquad \text{F–59}$$

$$B_{\Delta T_{gas}} = \left[\left(b_{T_e} \right)^2 + \left(-b_{T_c} \right)^2 + C_{calib} + C_{TC2095} + C_{SCXI} \right]^{\frac{1}{2}} \qquad \text{F–60}$$

$$S_{\Delta T_{gas}} = \left[\left(S_{T_e} \right)^2 + \left(-S_{T_c} \right)^2 \right]^{\frac{1}{2}} \qquad \text{F–61}$$

The systematic and standard deviations were the same for both thermocouples, and were defined in Appendix F.5. The expressions for the correlation terms are shown in Equations F–62 to F–64.

$$C_{calib} = 2 \times (1) \times (-1) \times 0.05\ ^\circ C \times 0.05\ ^\circ C \qquad \text{F–62}$$

$$C_{TC2095} = 2 \times (1) \times (-1) \times 1.409\ ^\circ C \times 1.409\ ^\circ C \qquad \text{F–63}$$

$$C_{SCXI} = 2 \times (1) \times (-1) \times 0.65\ ^\circ C \times 0.65\ ^\circ C \qquad \text{F–64}$$

By considering the correlation effects the uncertainty in the gas temperature difference was reduced to:

$$u_{\Delta T_{gas}} = \pm 1.45\ ^\circ\text{C} \qquad \text{F–65}$$

F.12 Shaft Power Uncertainty

The shaft power, $\dot{W}_s$, was calculated from the measurements of torque, τ, and the angular velocity, ω, provided by the rotary encoder, as shown:

$$\dot{W}_s = \tau \times \omega \tag{F–66}$$

The uncertainty in shaft power was expressed as:

$$\frac{u_{\dot{W}_s}}{\dot{W}_s} = \left[\left(\frac{u_\tau}{\tau}\right)^2 + \left(\frac{u_\omega}{\omega}\right)^2\right]^{\frac{1}{2}} \tag{F–67}$$

The uncertainty in torque, u_τ, was derived in Appendix F.2, but to determine the uncertainty in angular velocity, u_ω, propagation of uncertainty was performed in the governing equation:

$$\omega = \frac{d\theta}{dt} = \frac{\Delta\theta}{\Delta t} \tag{F–68}$$

where $\Delta\theta$ is the change in crank angle position between samples, and Δt is the time step between samples. The uncertainty equation was therefore:

$$\frac{u_\omega}{\omega} = \left[\left(\frac{u_{\Delta\theta}}{\Delta\theta}\right)^2 + \left(\frac{-u_{\Delta t}}{\Delta t}\right)^2\right]^{\frac{1}{2}} \tag{F–69}$$

The change in crank angle position was 0.72° or 0.0126 rad, and because the voltage was sampled at 10,000 Hz the time step was 0.0001 s. The mechanical alignment from the true position of the rotary encoder was ± 0.0003 rad, and the timing resolution of the NI 6211 device was ± 50 ns. The uncertainty parameters for calculating shaft power uncertainty are summarized in Table F–21.

Table F–21: Summary of Shaft Power Uncertainty Parameters

Uncertainty Variable	Uncertainty Value	Units	Notes
$u_{\Delta\theta}$	± 0.0003	rad	[99]
$u_{\Delta t}$	$\pm 50 \times 10^{-9}$	s	[97]
$\dfrac{u_\omega}{\omega}$	± 0.0239	-	-
$u_{\dot{W}_s}$	$\pm 7.11 \times 10^{-4} \leq u_{\dot{W}_s} \leq 0.28$	W	-

Appendix G   Bellows Convolution Volume Uncertainty

Section 4.6.5 presented the process to determine the difference in area of a pressurized bellows relative to the area of an unpressurized bellows to estimate the uncertainty in the bellows convolution volume. This section provides the tabulated values for the uncertainty in the bellows convolution volume. The green cells indicate the chosen uncertainty intervals.

Table G–1: Bellows Convolution Volume Uncertainty Estimation for 50.8 mm Stroke

Pressure [psi]	Difference in Area Ratio	Difference in Area [%]	Convolution Volume Difference [m³]	Half Convolution Volume Uncertainty [mL]	Total Bellows Convolution Uncertainty [mL]	Uncertainty Intervals [± mL]
0.00	0.00	0.00	0.00	0.00	0.00	0.00
0.25	-0.0473	-4.73	-0.00000122	-1.22	-12.22	15.3
0.50	-0.0591	-5.91	-0.00000153	-1.53	-15.29	15.3
0.75	-0.0316	-3.16	-0.00000082	-0.812	-8.18	15.3
1.00	-0.0390	-3.90	-0.00000101	-1.01	-10.08	15.3
1.25	-0.0567	-5.67	-0.00000147	-1.47	-14.66	15.3
1.50	-0.0234	-2.34	-0.00000060	-0.60	-6.04	15.3
1.75	-0.0161	-1.61	-0.00000042	-0.42	-4.16	15.3
2.00	0.0233	2.33	0.00000060	0.60	6.04	15.3
2.00						31.8
2.25	0.0164	1.64	0.00000042	0.42	4.24	31.8
2.50	0.0933	9.33	0.00000241	2.41	24.12	31.8
2.75	0.1231	12.31	0.00000318	3.18	31.82	31.8
3.00	0.1127	11.27	0.00000292	2.92	29.15	31.8
3.00						54.6
3.25	0.1570	15.70	0.00000406	4.06	40.60	54.6
3.50	0.1784	17.84	0.00000461	4.61	46.14	54.6
3.75	0.1857	18.57	0.00000480	4.80	48.03	54.6
4.00	0.2110	21.10	0.00000546	5.46	54.57	54.6

Table G–2: Bellows Convolution Volume Uncertainty Estimation for 76.2 mm Stroke

Pressure [psi]	Difference in Area Ratio	Difference in Area [%]	Convolution Volume Difference [m³]	Half Convolution Volume Uncertainty [mL]	Total Bellows Convolution Uncertainty [mL]	Uncertainty Intervals [± mL]
0	0.00	0.00	0.00	0.00	0.00	0.00
0.25	-0.017	-1.70	-0.00000049	-0.49	-4.92	4.9
0.50	-0.0048	-0.48	-0.00000014	-0.14	-1.40	4.9
0.75	0.0058	0.58	0.00000017	0.17	1.67	4.9
1.00	-0.0153	-1.53	-0.00000044	-0.44	-4.43	4.9
1.00						11.4
1.25	0.0119	1.19	0.00000034	0.34	3.44	11.4
1.50	0.0144	1.44	0.00000042	0.42	4.16	11.4
1.75	0.0184	1.84	0.00000053	0.53	5.33	11.4
2.00	0.0395	3.95	0.00000114	1.14	11.42	11.4
2.00						26.9
2.25	0.0438	4.38	0.00000127	1.27	12.66	26.9
2.50	0.0886	8.86	0.00000256	2.56	25.63	26.9
2.75	0.0619	6.19	0.00000179	1.79	17.91	26.9
3.00	0.0930	9.30	0.00000269	2.69	26.89	26.9
3.00						47.4
3.25	0.0931	9.31	0.00000269	2.69	26.92	47.4
3.50	0.1107	11.07	0.00000320	3.20	32.0	47.4
3.75	0.1328	13.28	0.00000384	3.84	38.39	47.4
4.00	0.1638	16.38	0.00000474	4.74	47.37	47.4

Appendix H   Indicated Work Uncertainties

This section shows the tabulated uncertainties for efficacious and forced expansion work in Table H–1 and Table H–2, efficacious and forced compression work in Table H–3 and Table H–4, the indicated expansion and compression work in Table H–5 and Table H–6, engine efficacious work in Table H–7, and engine forced work for each configuration in Table H–8.

Table H–1: Efficacious Expansion Work Uncertainty

Phase Angle, α [°]	Efficacious Expansion Work Uncertainty, $u_{W_{eff,1}}$ [±J]		
	V_{sw} =1.564 L	V_{sw} =1.955 L	V_{sw} =2.346 L
180	0.17	0.25	0.24
175	0.28	0.37	0.37
170	0.35	0.49	0.49
165	0.43	0.56	0.59
160	0.50	0.62	0.68
155	0.59	0.71	0.76
150	0.59	0.71	0.77
145	0.63	0.75	0.81
140	0.68	0.79	0.86
135	0.71	0.92	1.01
130	0.75	0.97	1.07
125	0.80	1.02	1.14
120	0.86	1.08	1.19

Table H–2: Forced Expansion Work Uncertainty

Phase Angle, α [°]	Forced Expansion Work Uncertainty, $u_{W_{f,1}}$ [±J]		
	V_{sw} =1.564 L	V_{sw} =1.955 L	V_{sw} =2.346 L
180	0.27	0.36	0.38
175	0.17	0.27	0.26
170	0.11	0.16	0.16
165	0.05	0.12	0.08
160	0.01	0.08	0.02
155	0.00	0.06	0.00
150	0.00	0.06	0.00
145	0.00	0.06	0.00
140	0.00	0.06	0.00
135	0.00	0.06	0.00
130	0.00	0.06	0.01
125	0.01	0.06	0.01
120	0.01	0.07	0.02

Table H–3: Efficacious Compression Work Uncertainty

Phase Angle, α [°]	Efficacious Compression Work Uncertainty, $u_{W_{eff,2}}$ [±J]		
	V_{sw} =1.564 L	V_{sw} =1.955 L	V_{sw} =2.346 L
180	0.38	0.42	0.50
175	0.29	0.33	0.40
170	0.23	0.25	0.31
165	0.19	0.23	0.24
160	0.16	0.23	0.19
155	0.20	0.28	0.21
150	0.21	0.28	0.22
145	0.24	0.31	0.25
140	0.28	0.36	0.28
135	0.31	0.39	0.41
130	0.35	0.43	0.46
125	0.39	0.48	0.51
120	0.44	0.54	0.56

Table H–4: Forced Compression Work Uncertainty

Phase Angle, α [°]	Forced Compression Work Uncertainty, $u_{W_{f,2}}$ [±J]		
	V_{sw} =1.564 L	V_{sw} =1.955 L	V_{sw} =2.346 L
180	0.08	0.11	0.16
175	0.14	0.19	0.24
170	0.21	0.29	0.34
165	0.26	0.35	0.43
160	0.33	0.39	0.52
155	0.37	0.43	0.58
150	0.36	0.44	0.57
145	0.37	0.45	0.59
140	0.39	0.47	0.61
135	0.39	0.48	0.64
130	0.40	0.49	0.65
125	0.41	0.50	0.67
120	0.43	0.52	0.70

Table H–5: Indicated Expansion Work Uncertainty

Phase Angle, α [°]	Indicated Expansion Work Uncertainty, u_{W_e} [±J]		
	V_{sw} =1.564 L	V_{sw} =1.955 L	V_{sw} =2.346 L
180	0.43	0.62	0.62
175	0.23	0.64	0.64
170	0.46	0.65	0.64
165	0.48	0.68	0.66
160	0.51	0.71	0.69
155	0.59	0.77	0.77
150	0.59	0.77	0.77
145	0.63	0.81	0.81
140	0.68	0.85	0.86
135	0.72	0.98	1.02
130	0.76	1.03	1.08
125	0.81	1.08	1.15
120	0.87	1.15	1.21

Table H–6: Indicated Compression Work Uncertainty

Phase Angle, α [°]	Indicated Compression Work Uncertainty, u_{W_c} [±J]		
	V_{sw} =1.564 L	V_{sw} =1.955 L	V_{sw} =2.346 L
180	0.46	0.53	0.66
175	0.43	0.26	0.64
170	0.44	0.54	0.65
165	0.46	0.57	0.67
160	0.49	0.62	0.71
155	0.57	0.71	0.78
150	0.57	0.71	0.79
145	0.61	0.76	0.84
140	0.67	0.83	0.90
135	0.70	0.87	1.05
130	0.75	0.92	1.11
125	0.80	0.99	1.19
120	0.87	1.06	1.26

Table H–7: Engine Efficacious Work Uncertainty

Phase Angle, α [°]	Engine Efficacious Work Uncertainty, $u_{W_{eff}}$ [±J]		
	V_{sw} =1.564 L	V_{sw} =1.955 L	V_{sw} =2.346 L
180	0.42	0.49	0.55
175	0.40	0.49	0.55
170	0.42	0.55	0.58
165	0.47	0.60	0.63
160	0.53	0.66	0.70
155	0.62	0.76	0.79
150	0.62	0.76	0.80
145	0.67	0.81	0.85
140	0.74	0.87	0.90
135	0.78	1.00	1.09
130	0.83	1.06	1.16
125	0.89	1.13	1.25
120	0.97	1.21	1.32

Table H–8: Engine Forced Work Uncertainty

Phase Angle, α [°]	Engine Forced Work Uncertainty, u_{W_f} [±J]		
	V_{sw} =1.564 L	V_{sw} =1.955 L	V_{sw} =2.346 L
180	0.28	0.38	0.41
175	0.22	0.33	0.36
170	0.24	0.33	0.37
165	0.27	0.36	0.44
160	0.33	0.40	0.52
155	0.37	0.43	0.58
150	0.36	0.44	0.57
145	0.37	0.46	0.59
140	0.39	0.47	0.61
135	0.39	0.48	0.64
130	0.40	0.49	0.65
125	0.41	0.51	0.67
120	0.43	0.52	0.70

Appendix I   Engine and Workspace Volume Variations

This section presents the remaining figures for the workspace and engine volume variations for each swept volume and phase angle. Figures for the 120° phase angle are not reproduced.

I.1 Swept Volume of 1.564 L

(a) 180°

(b) 175°

(c) 170°

(d) 165°

(e) 160°

(f) 155°

(g) 150°

(h) 145°

(i) 140°

(j) 135°

(k) 130°
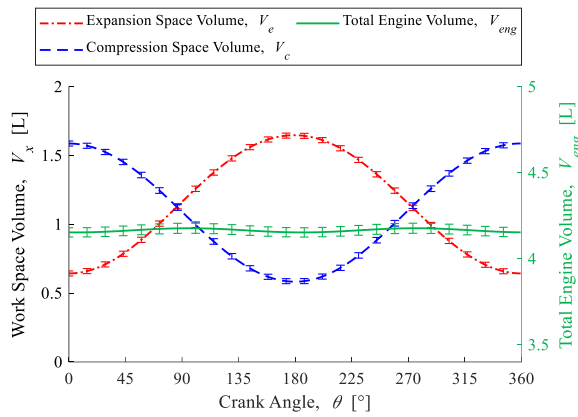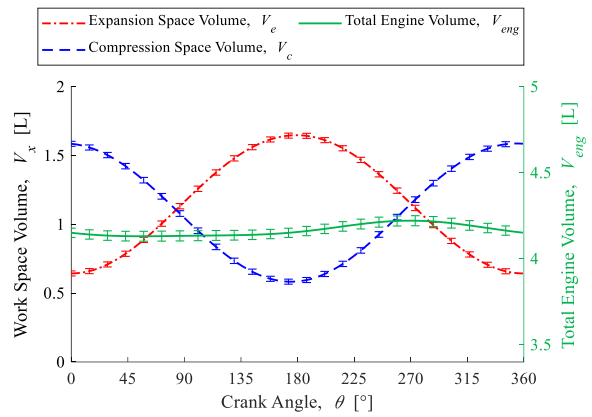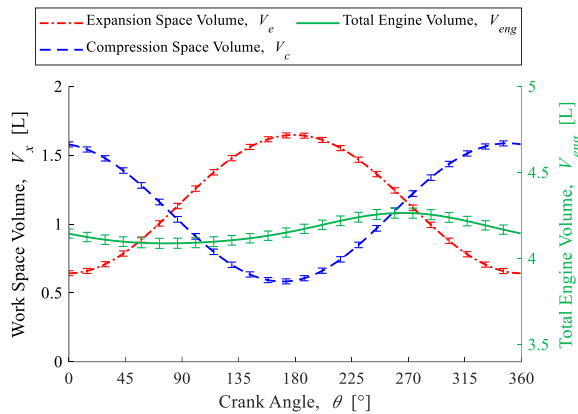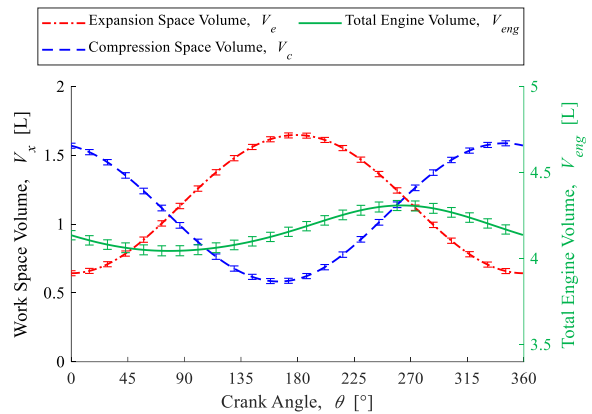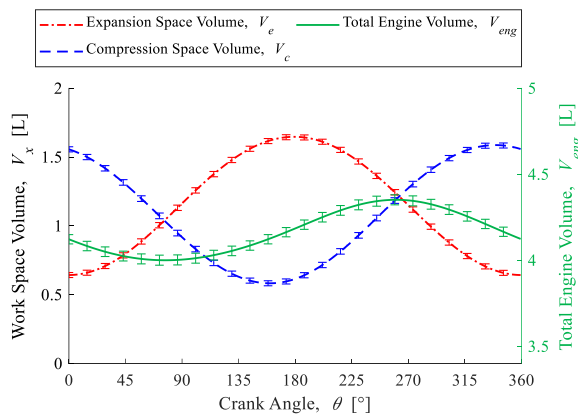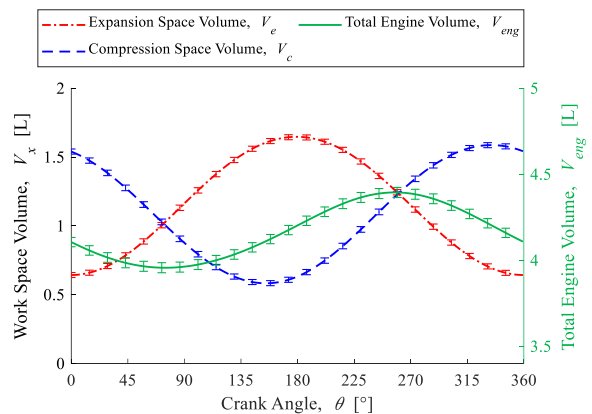
(l) 125°
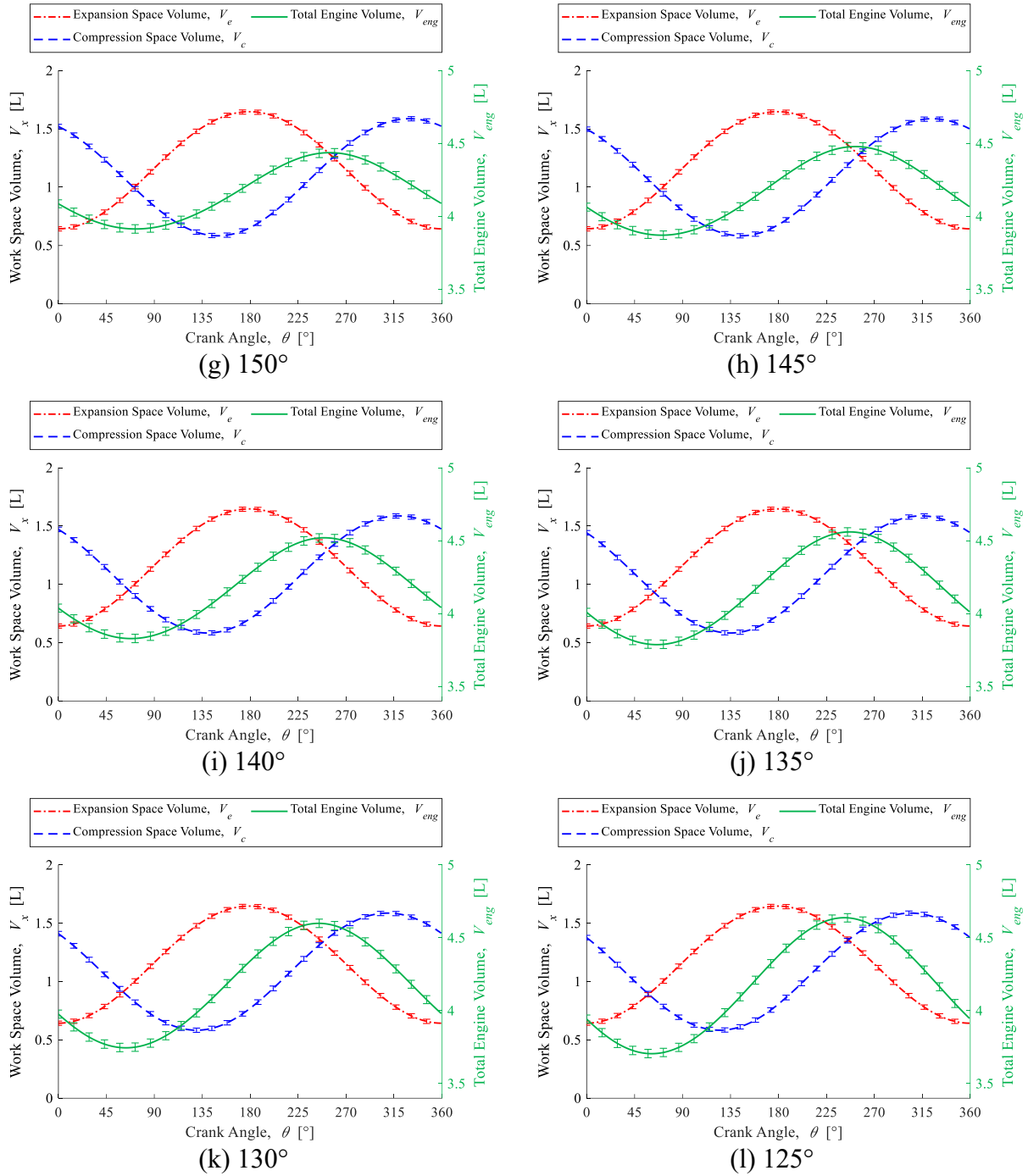
Figure I–1: Workspace and Engine Volume Variations for Swept Volume of 1.564 L for Phase Angles Between 125° and 180°

I.2 Swept Volume of 1.955 L

(a) 180°

(b) 175°

(c) 170°

(d) 165°

(e) 160°

(f) 155°
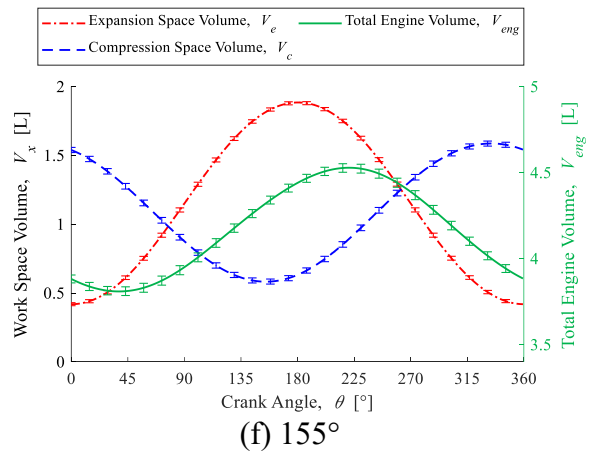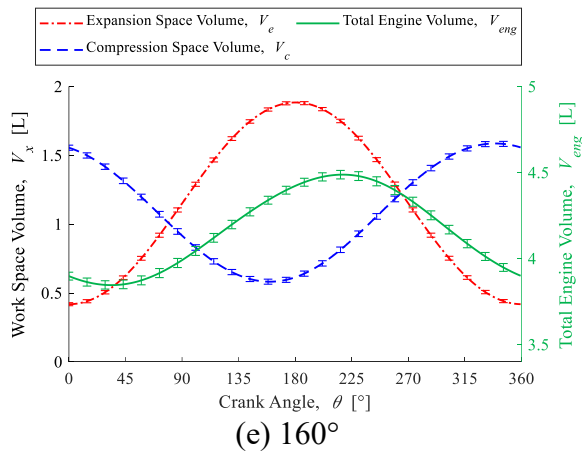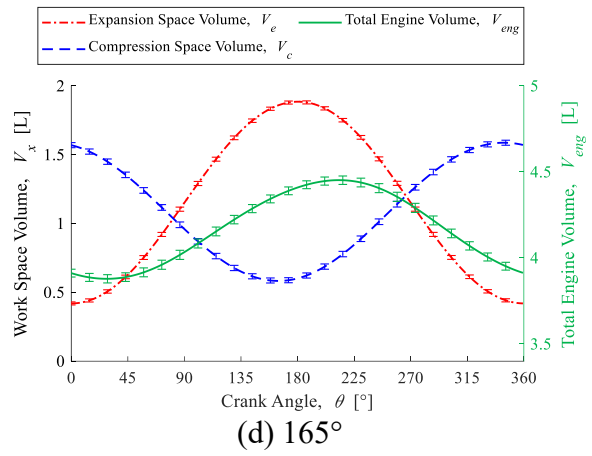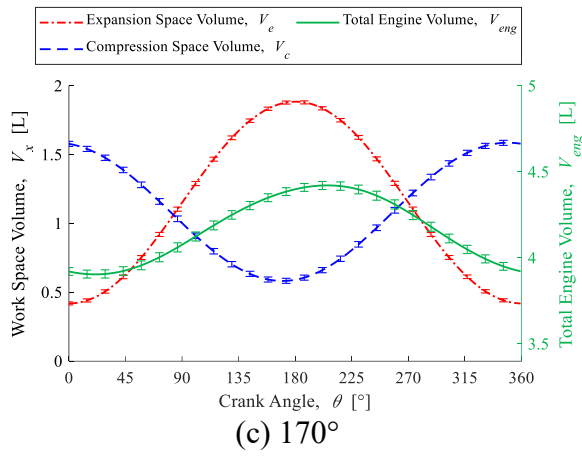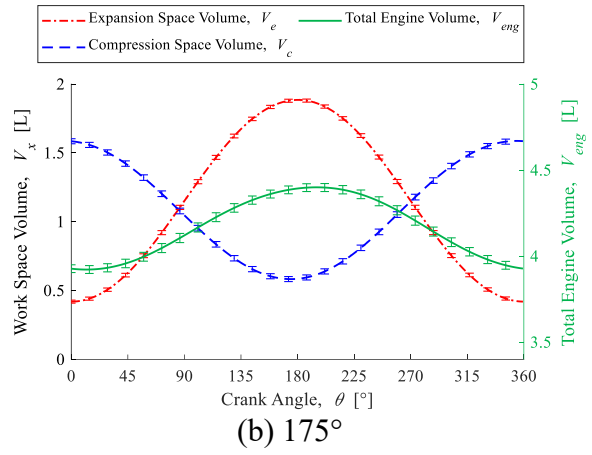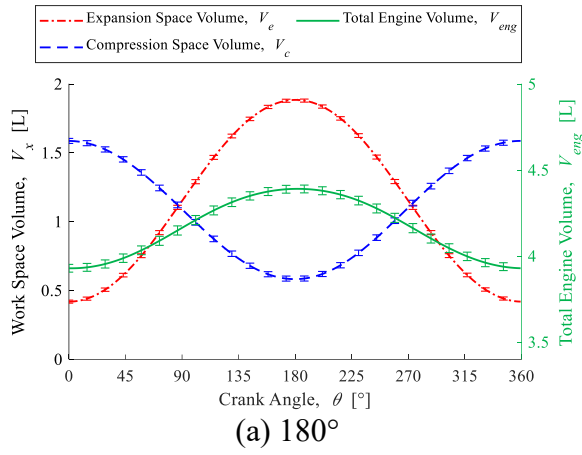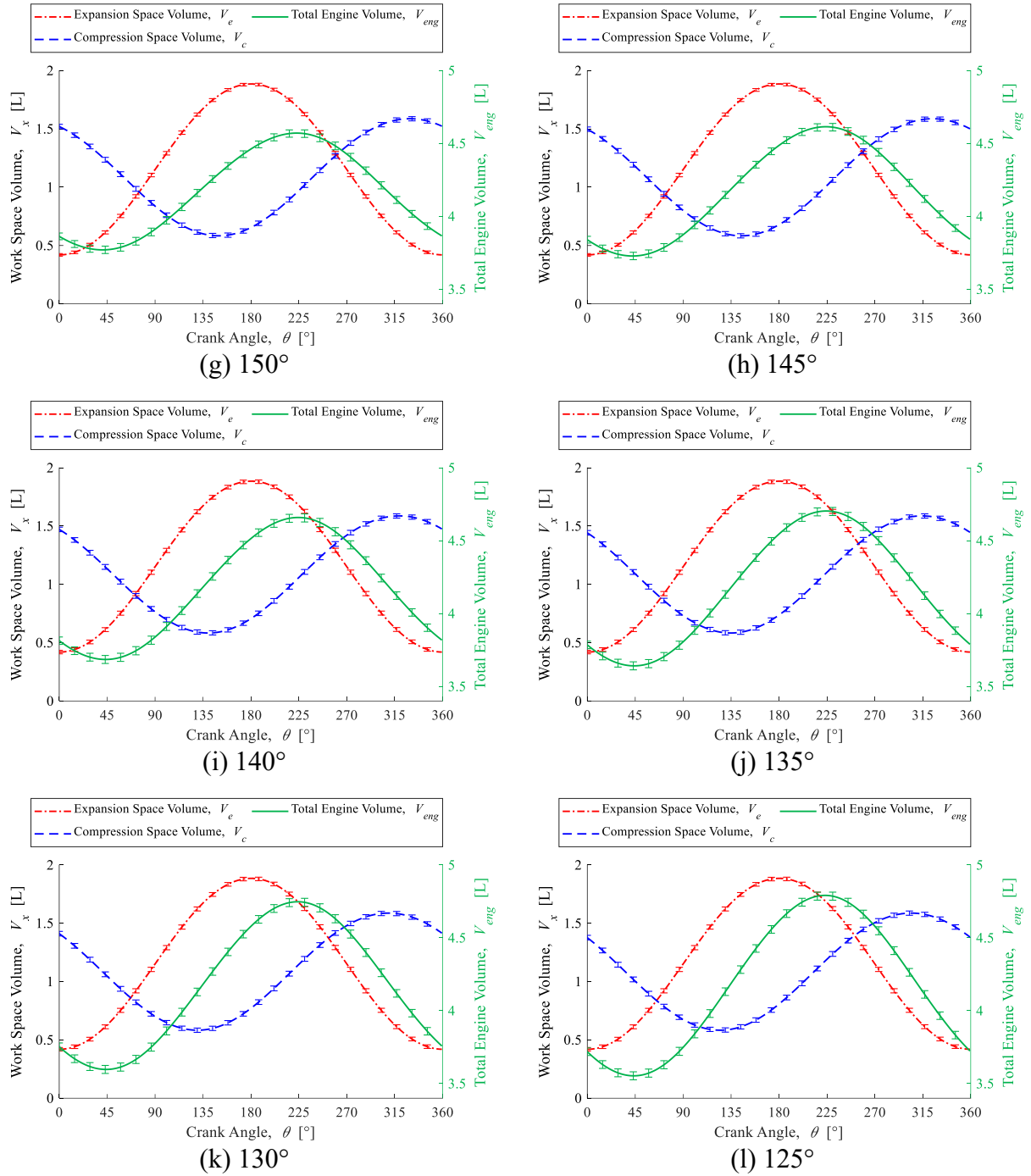
Figure I–2: Workspace and Engine Volume Variations for Swept Volume of 1.955 L for Phase Angles Between 125° and 180°

I.3 Swept Volume of 2.346 L

(a) 180°

(b) 175°

(c) 170°

(d) 165°

(e) 160°

(f) 155°

(g) 150°

(h) 145°

(i) 140°

(j) 135°

(k) 130°

(l) 125°
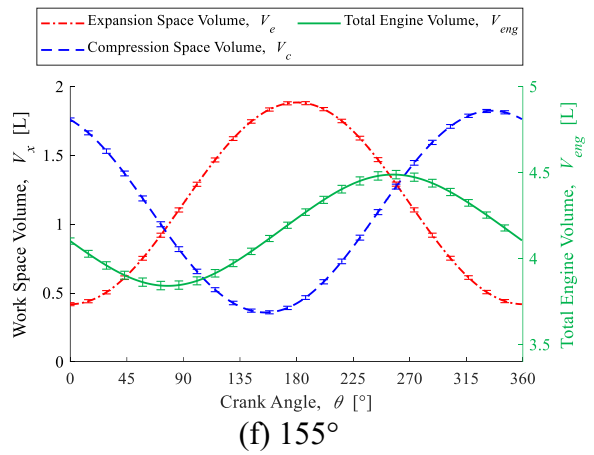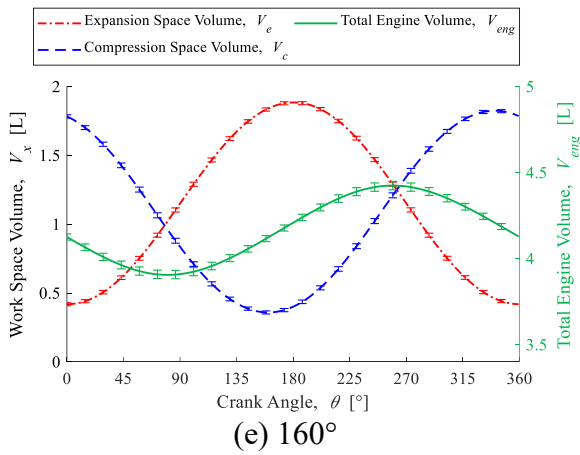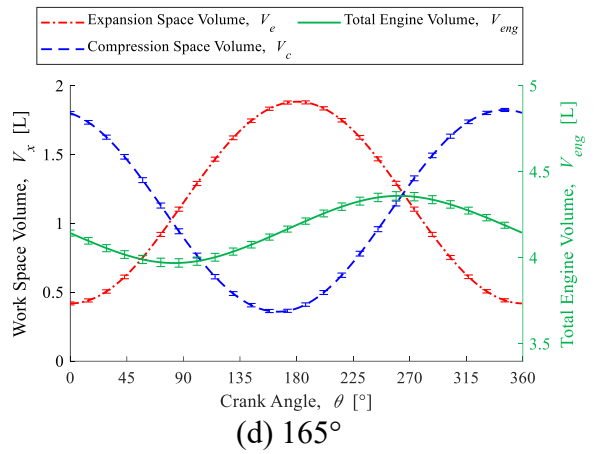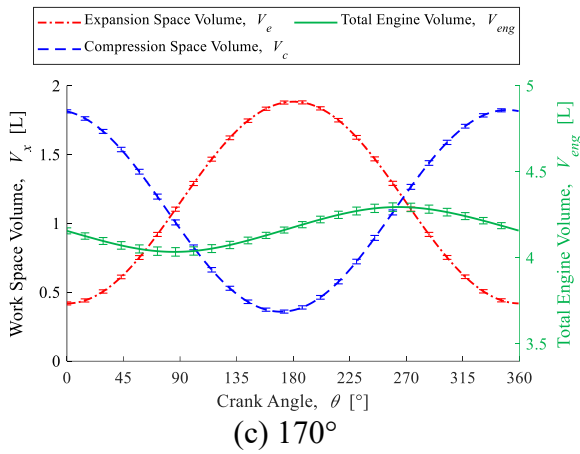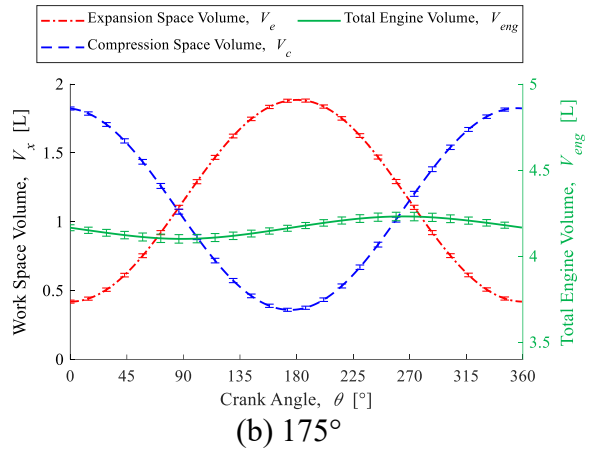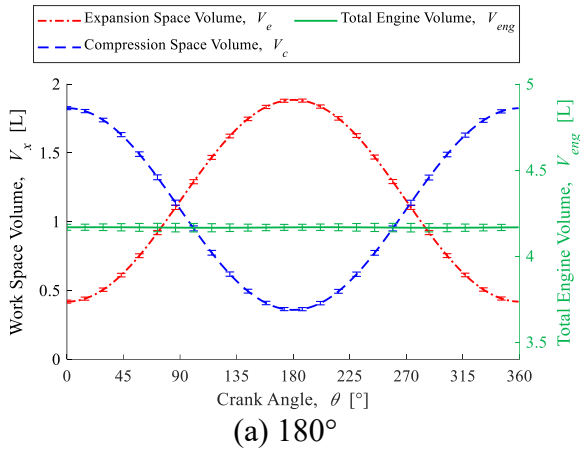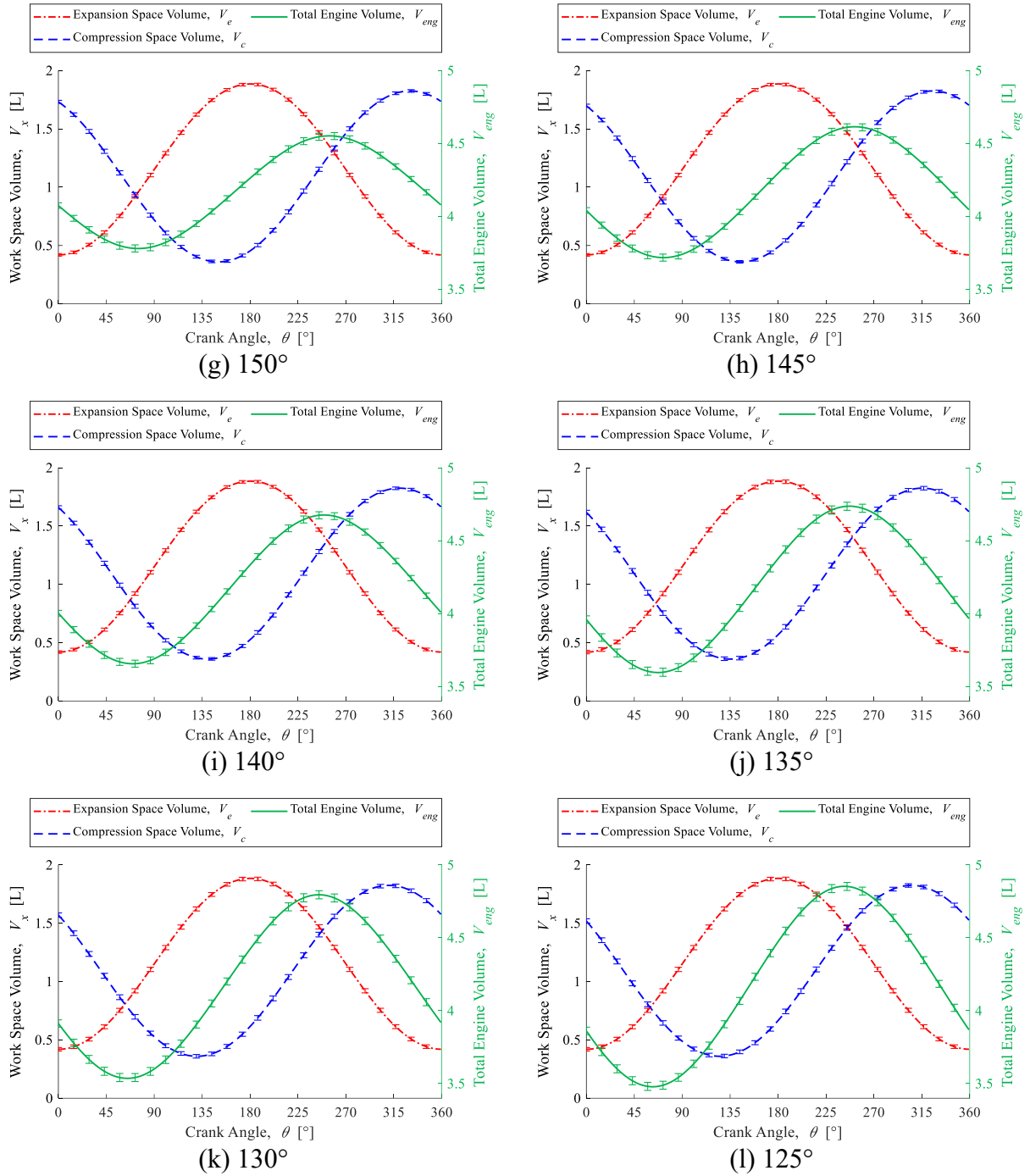
Figure I–3: Workspace and Engine Volume Variations for Swept Volume of 2.346 L for Phase Angles Between 125° and 180°

Appendix J Baseline Pressure Fluctuations for Each Speed

This section presents the remaining set of baseline experiment pressure fluctuation figures for each swept volume, speed, and phase angle. Figures for a 120° phase angle are not reproduced.

(a) 180°

(b) 175°

(c) 170°

(d) 165°

(e) 160°

(f) 155°

(g) 150°

(h) 145°

(i) 140°

(j) 135°

(k) 130°

(l) 125°
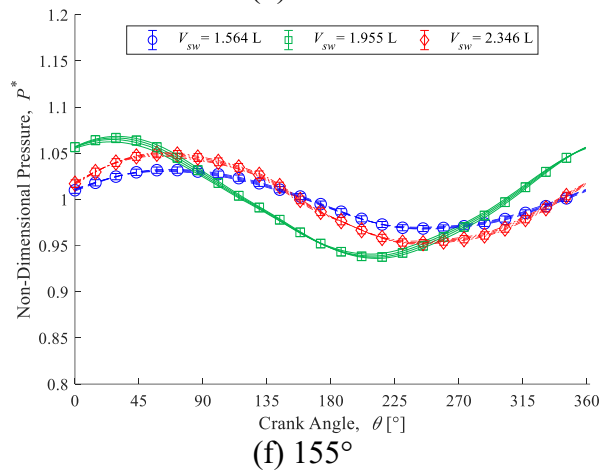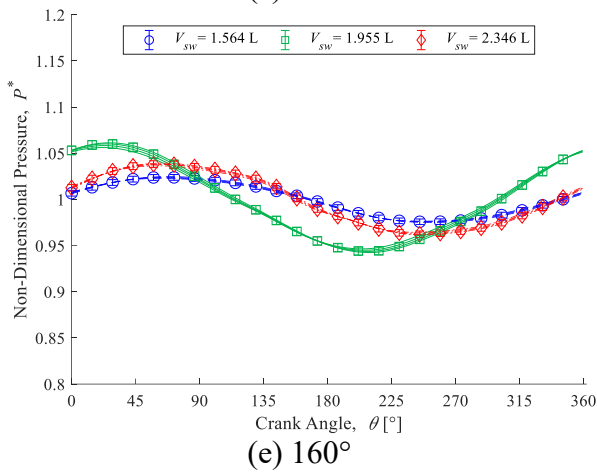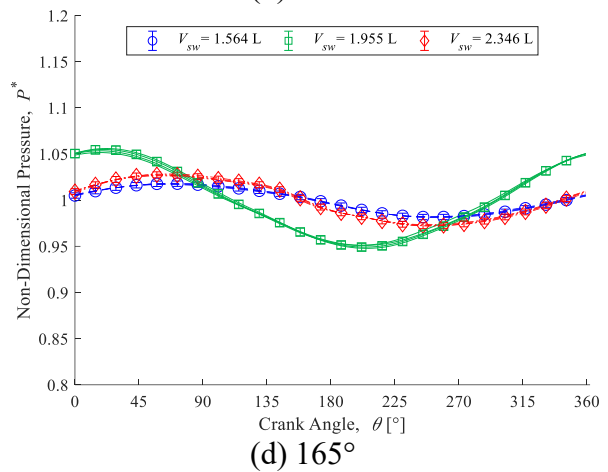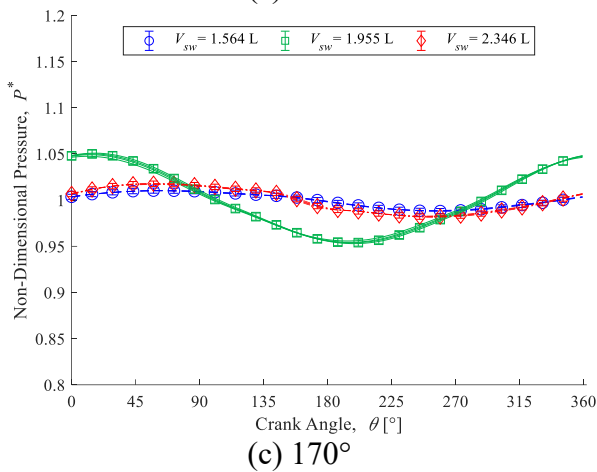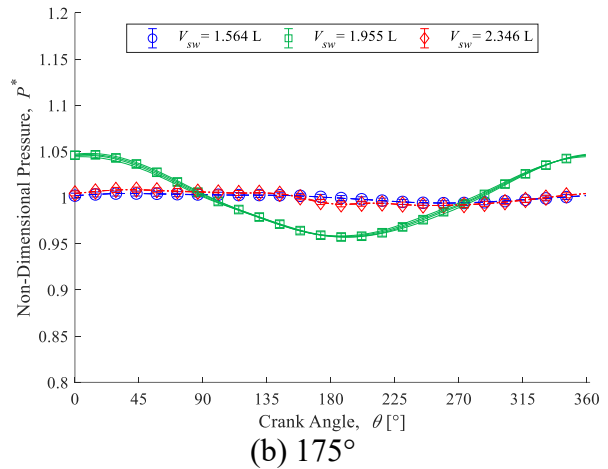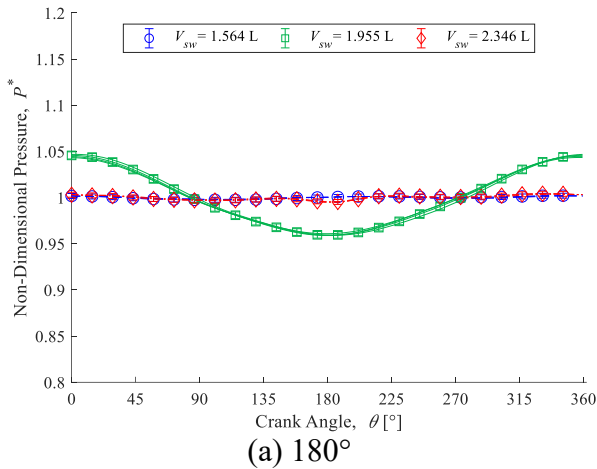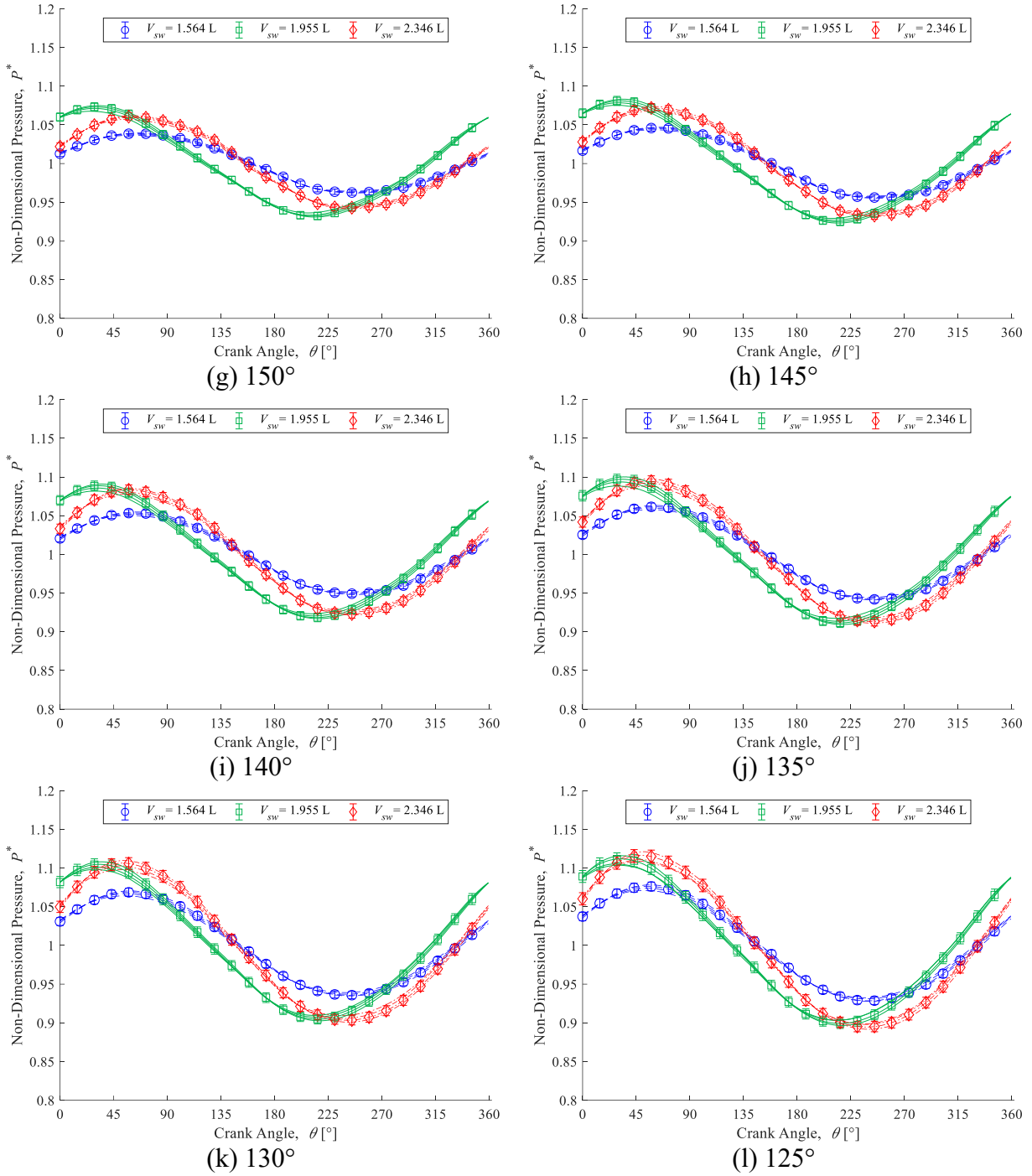
Figure J–1: Baseline Experiment Non-Dimensional Pressure Fluctuation for Each Swept
Volume and Engine Speed for Phase Angles Between 125° and 180°

Appendix K   Baseline Non-Dimensional Pressure Fluctuations

This section presents the remaining figures for the baseline experiment non-dimensional pressure fluctuations at 60 rpm. Figures for a 120° phase angle are not reproduced.
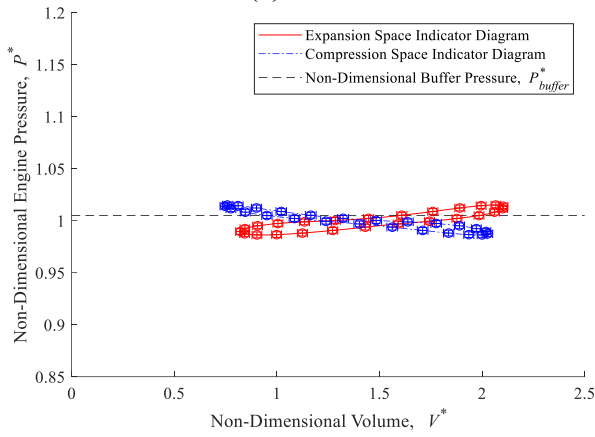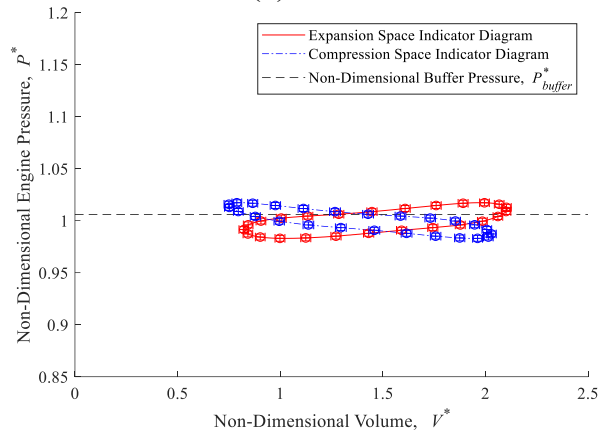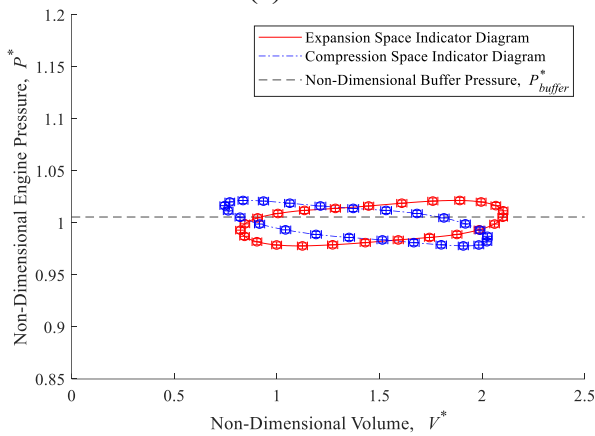
K.1 Swept Volume of 1.564 L

(a) 180°

(b) 175°

(c) 170°

(d) 165°

(e) 160°

(f) 155°

(g) 150°

(h) 145°

(i) 140°

(j) 135°

(k) 130°

(l) 125°
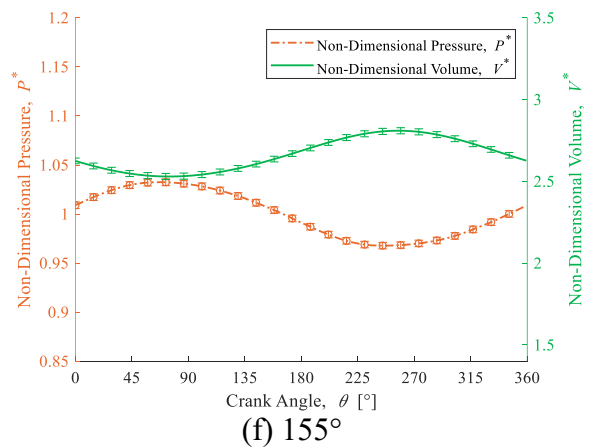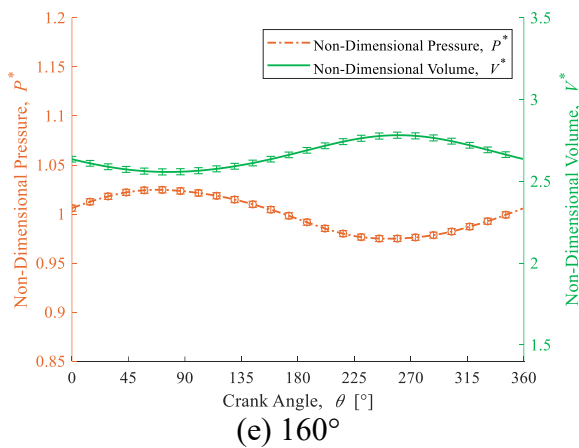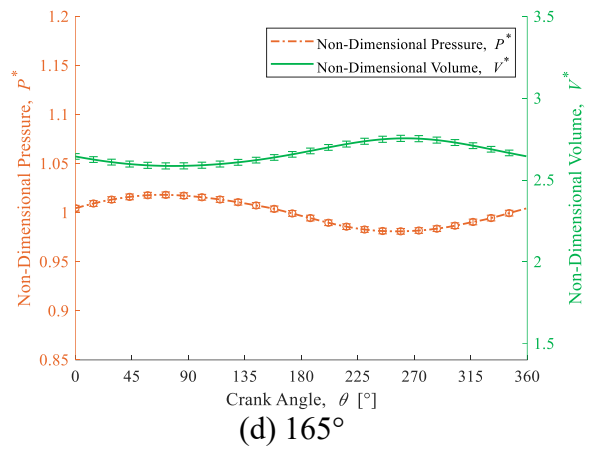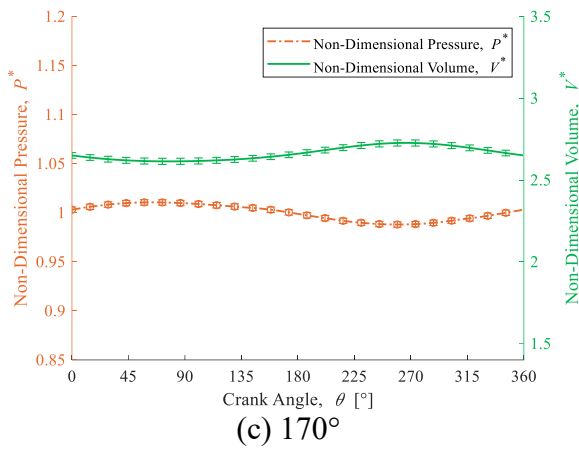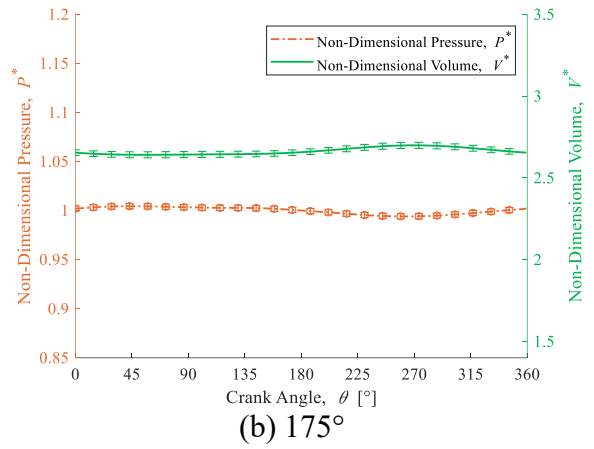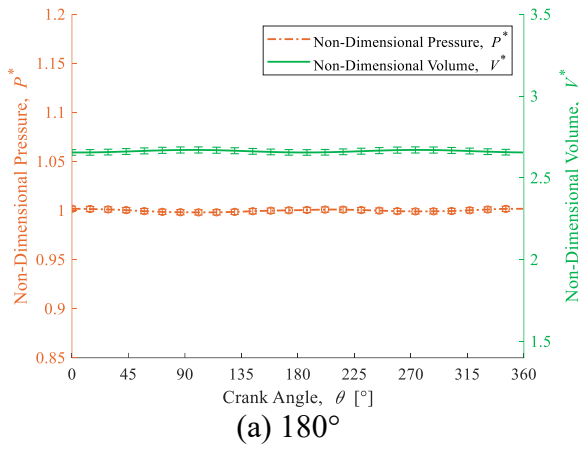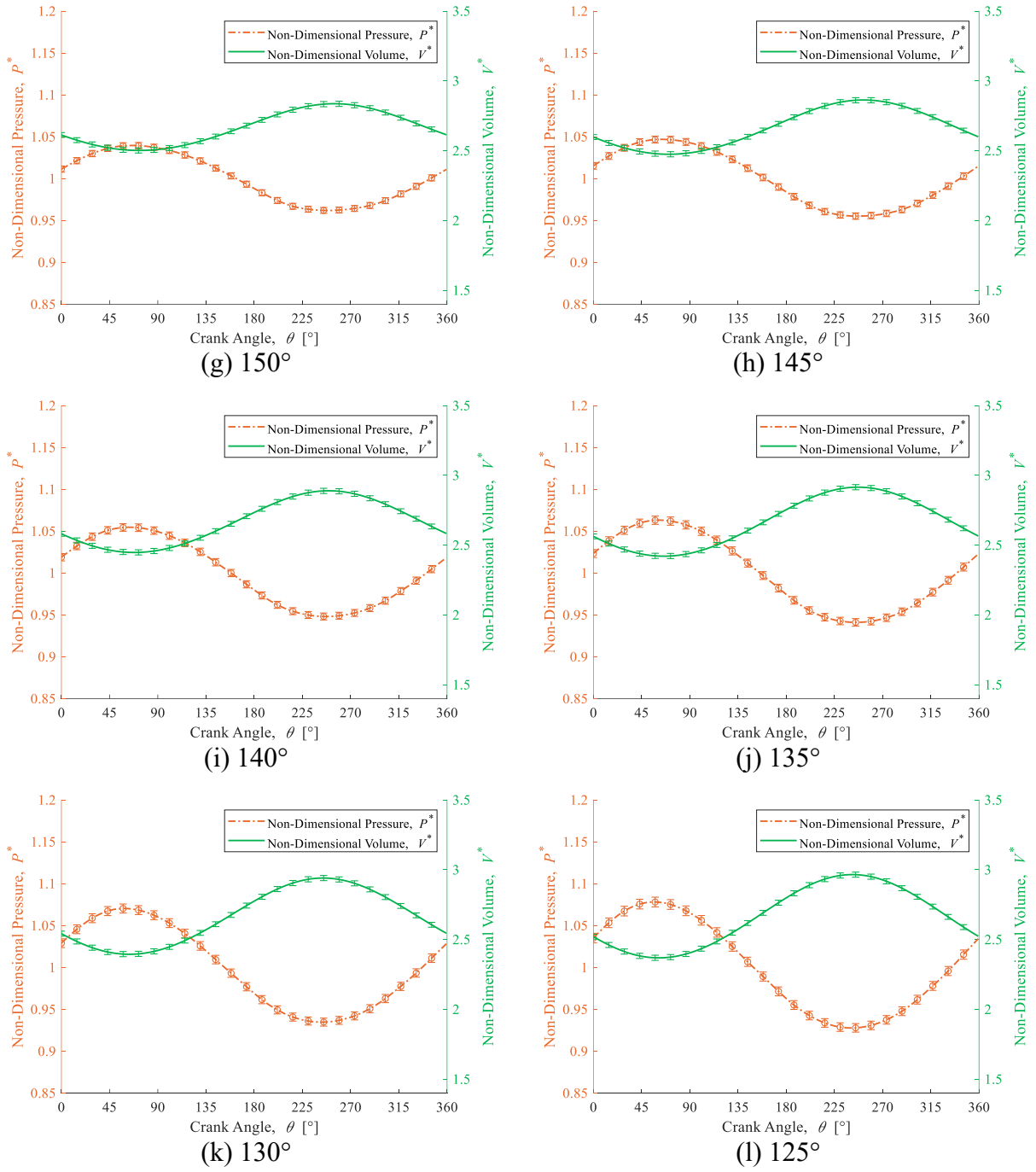
Figure K–1: Baseline Experiment Non-Dimensional Pressure and Engine Volume Fluctuations for a Swept Volume of 1.564 L at 60 rpm for Phase Angles Between 125° and 180°

K.2 Swept Volume of 1.955 L

(a) 180°

(b) 175°

(c) 170°

(d) 165°

(e) 160°

(f) 155°

(g) 150°

(h) 145°
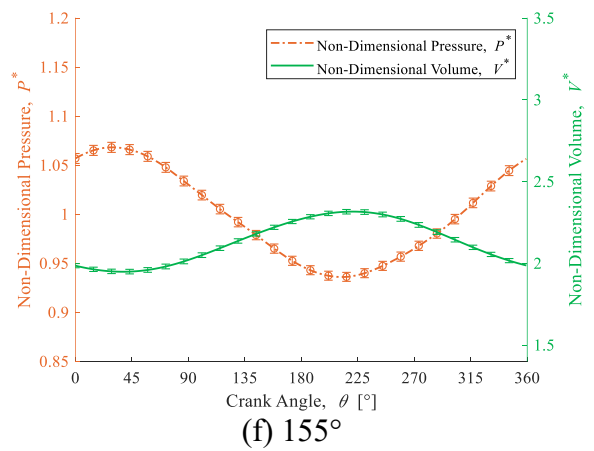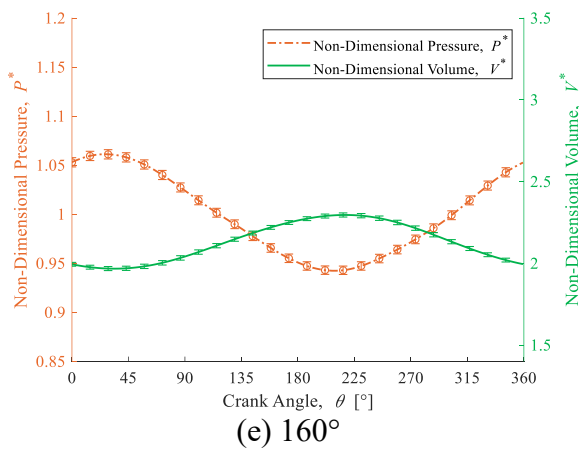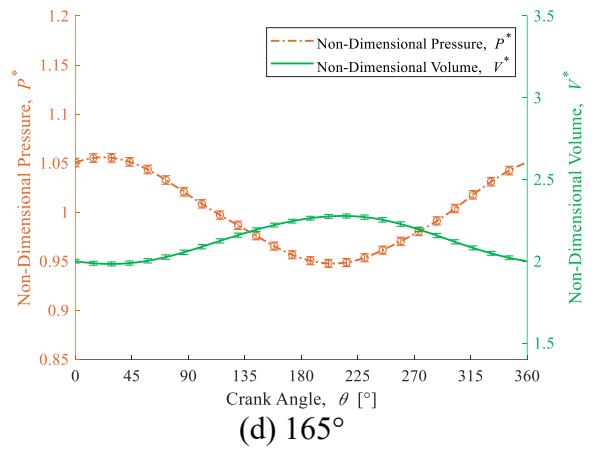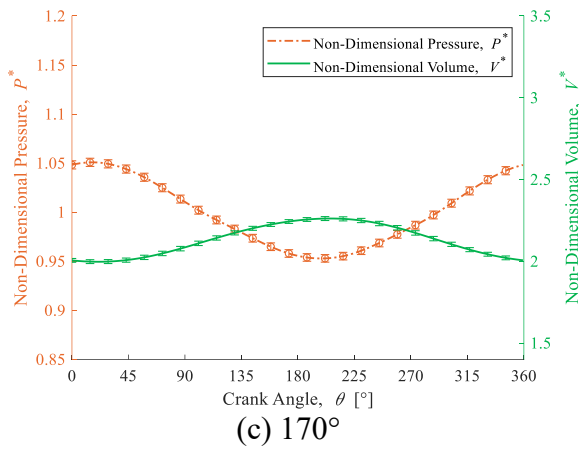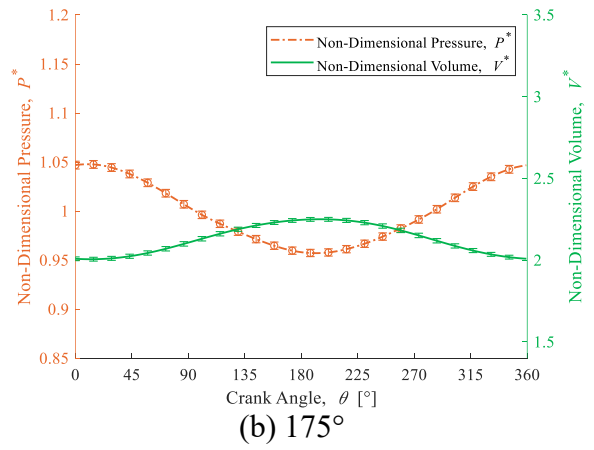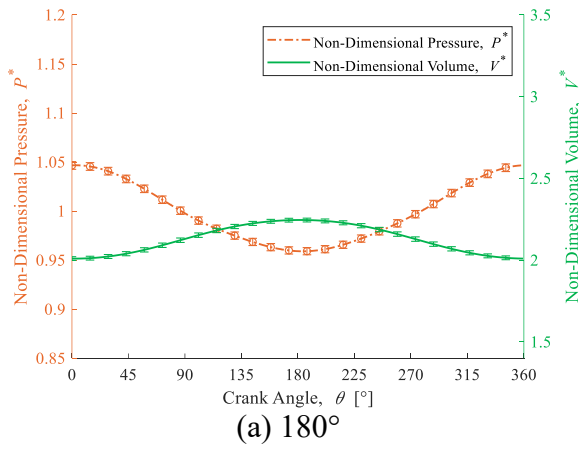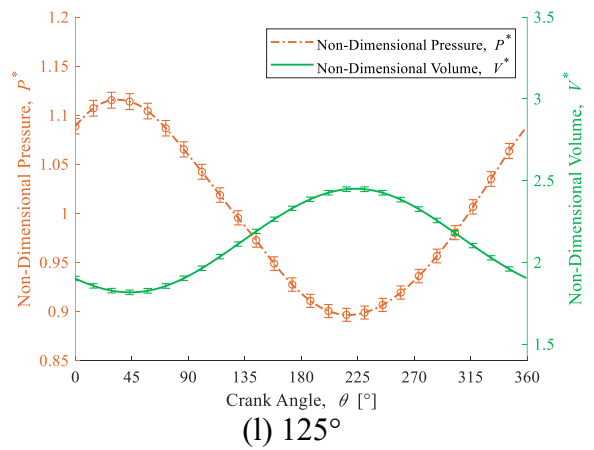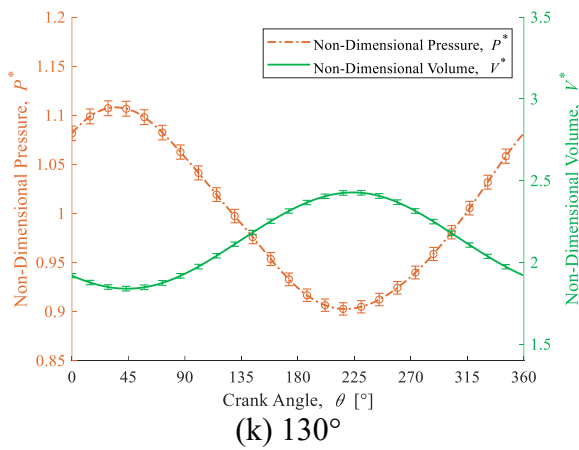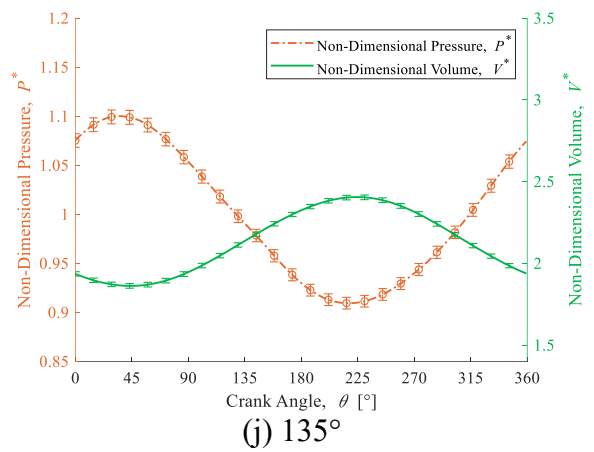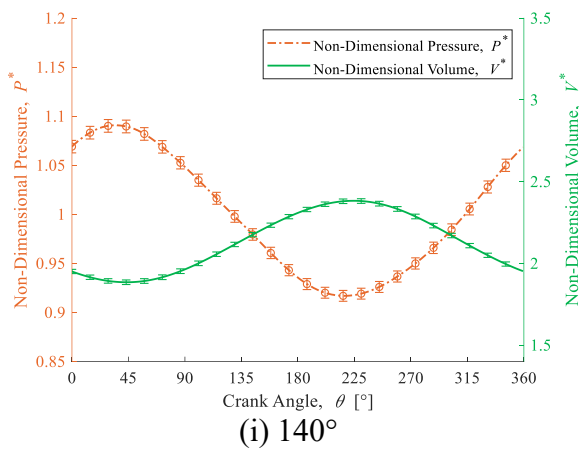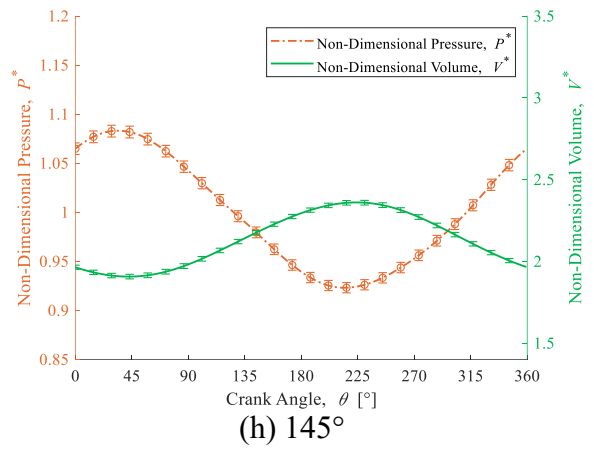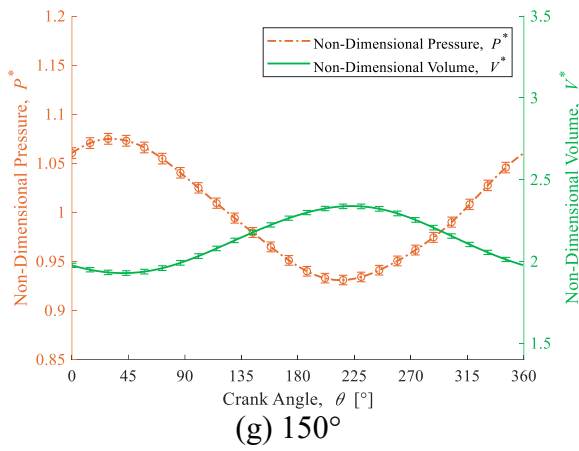
(i) 140°

(j) 135°

(k) 130°

(l) 125°

Figure K–2: Baseline Experiment Non-Dimensional Pressure and Engine Volume Fluctuations for a Swept Volume of 1.955 L at 60 rpm for Phase Angles Between 125° and 180°

K.3 Swept Volume of 2.346 L
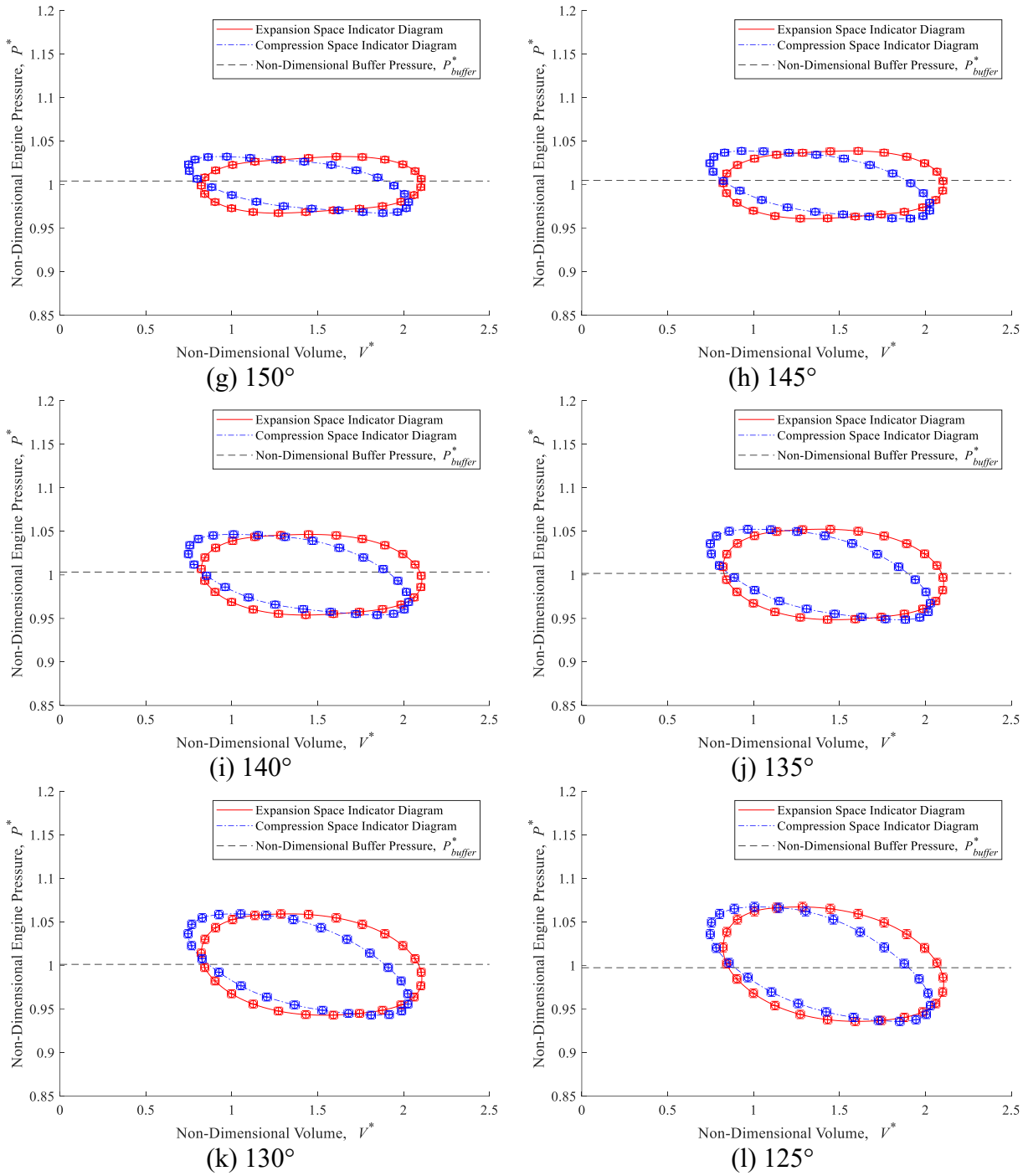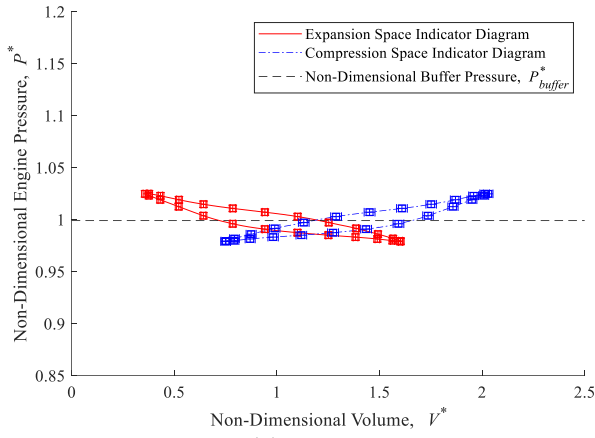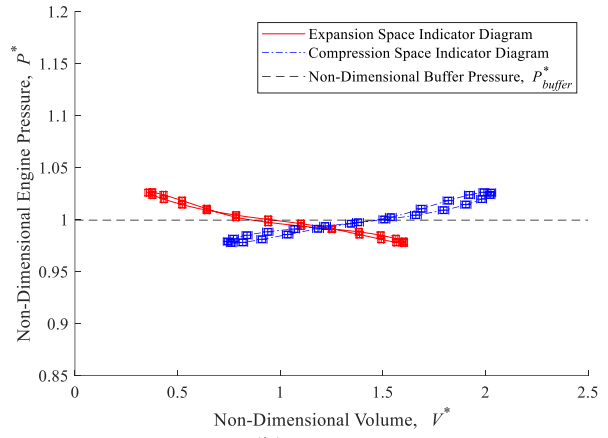

(a) 180°

(b) 175°

(c) 170°

(d) 165°

(e) 160°

(f) 155°
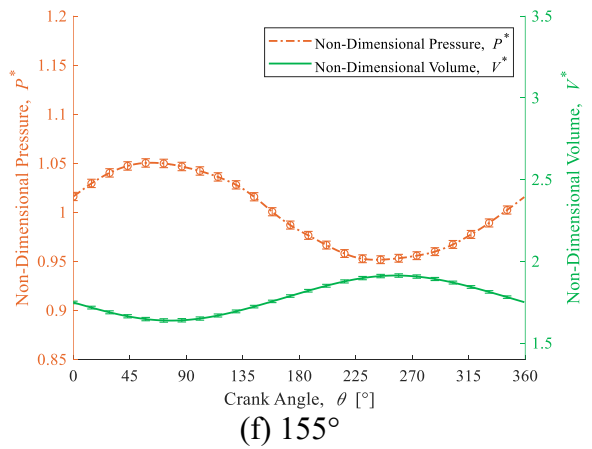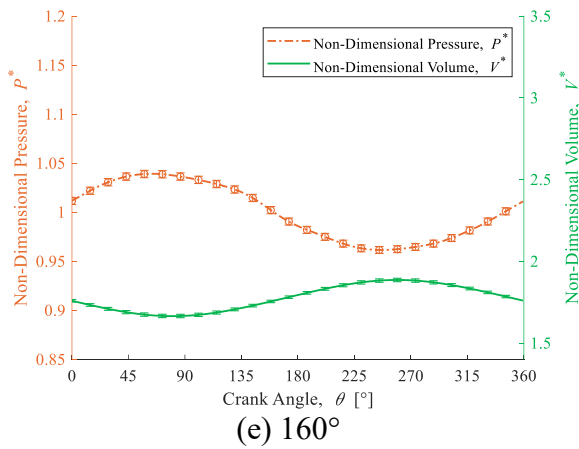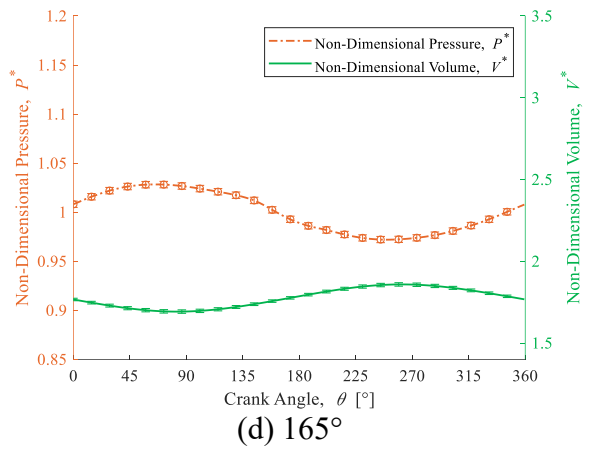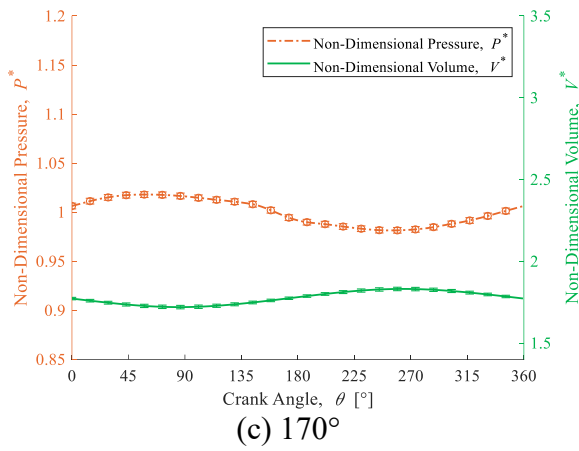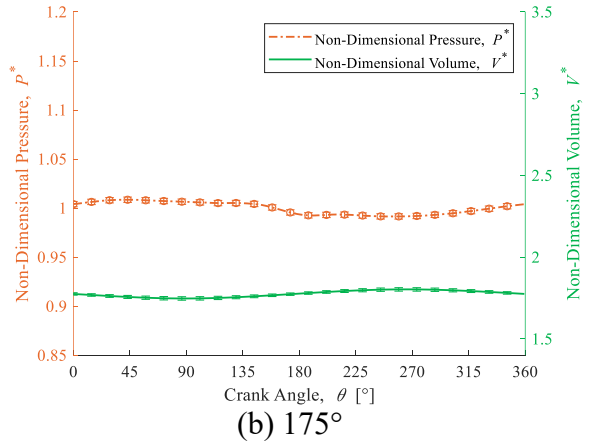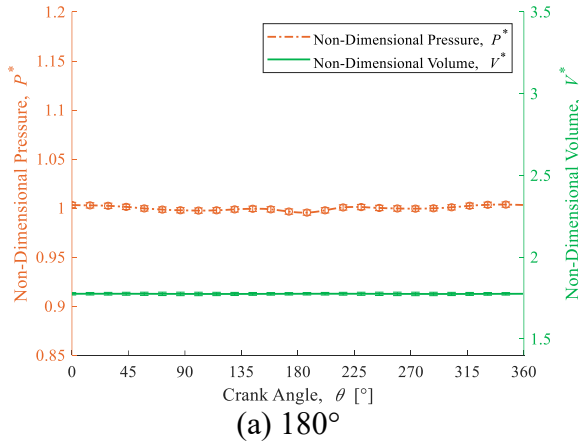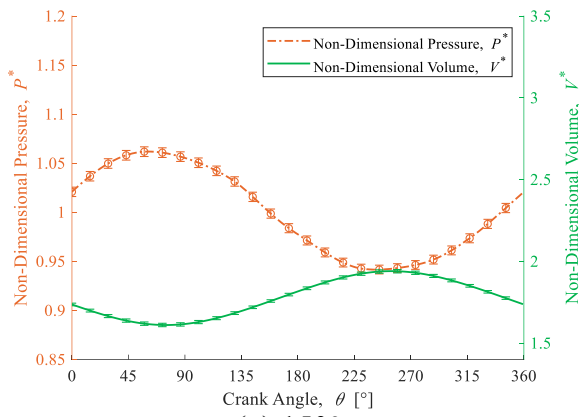
(g) 150°
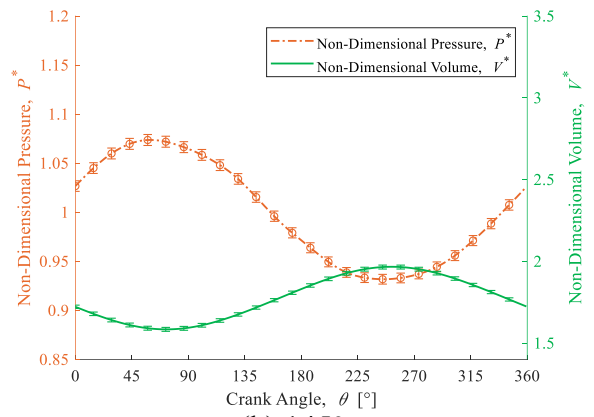
(h) 145°
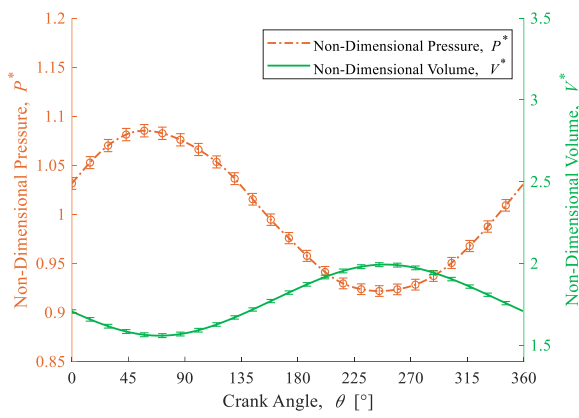
(i) 140°
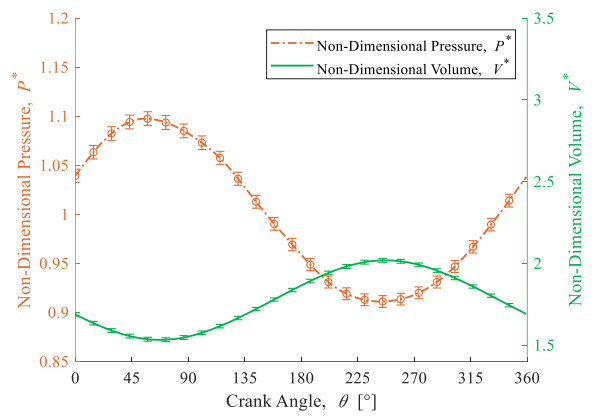
(j) 135°
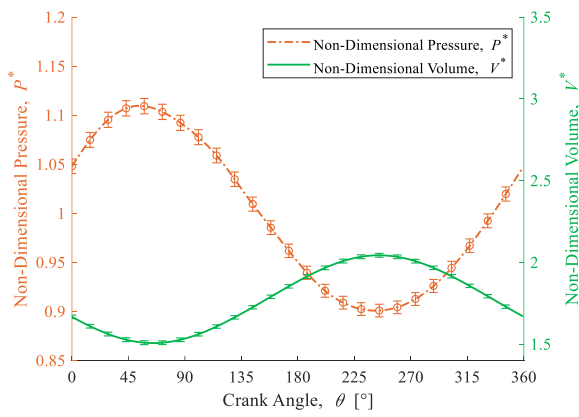
(k) 130°
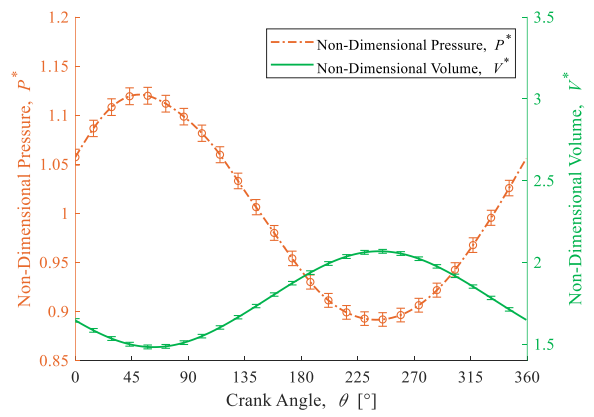
(l) 125°

Figure K–3: Baseline Experiment Non-Dimensional Pressure and Engine Volume Fluctuations for a Swept Volume of 2.346 L at 60 rpm for Phase Angles Between 125° and 180°

Appendix L   Baseline Experiment Torque Fluctuations

This section presents the remaining figures for the torque and non-dimensional pressure fluctuations for the baseline experiments. Figures for a 120° phase angle are not reproduced.

L.1 Swept Volume of 1.564 L
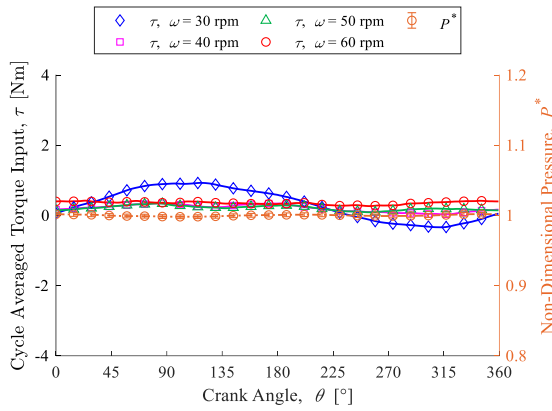
(a) 180°
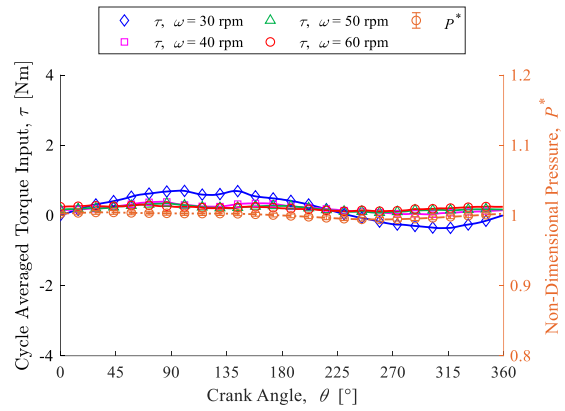
(b) 175°
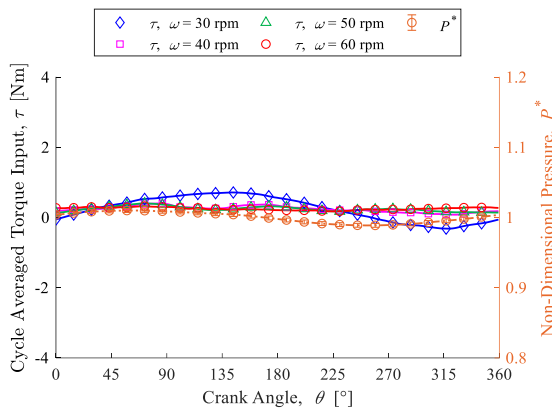
(c) 170°
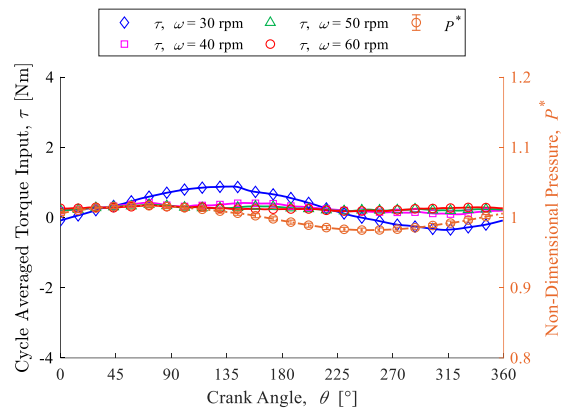
(d) 165°
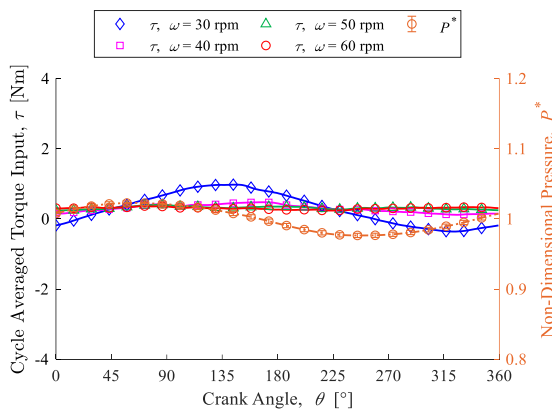
(e) 160°
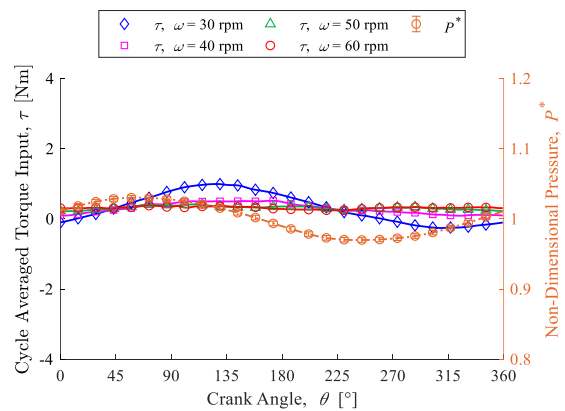
(f) 155°
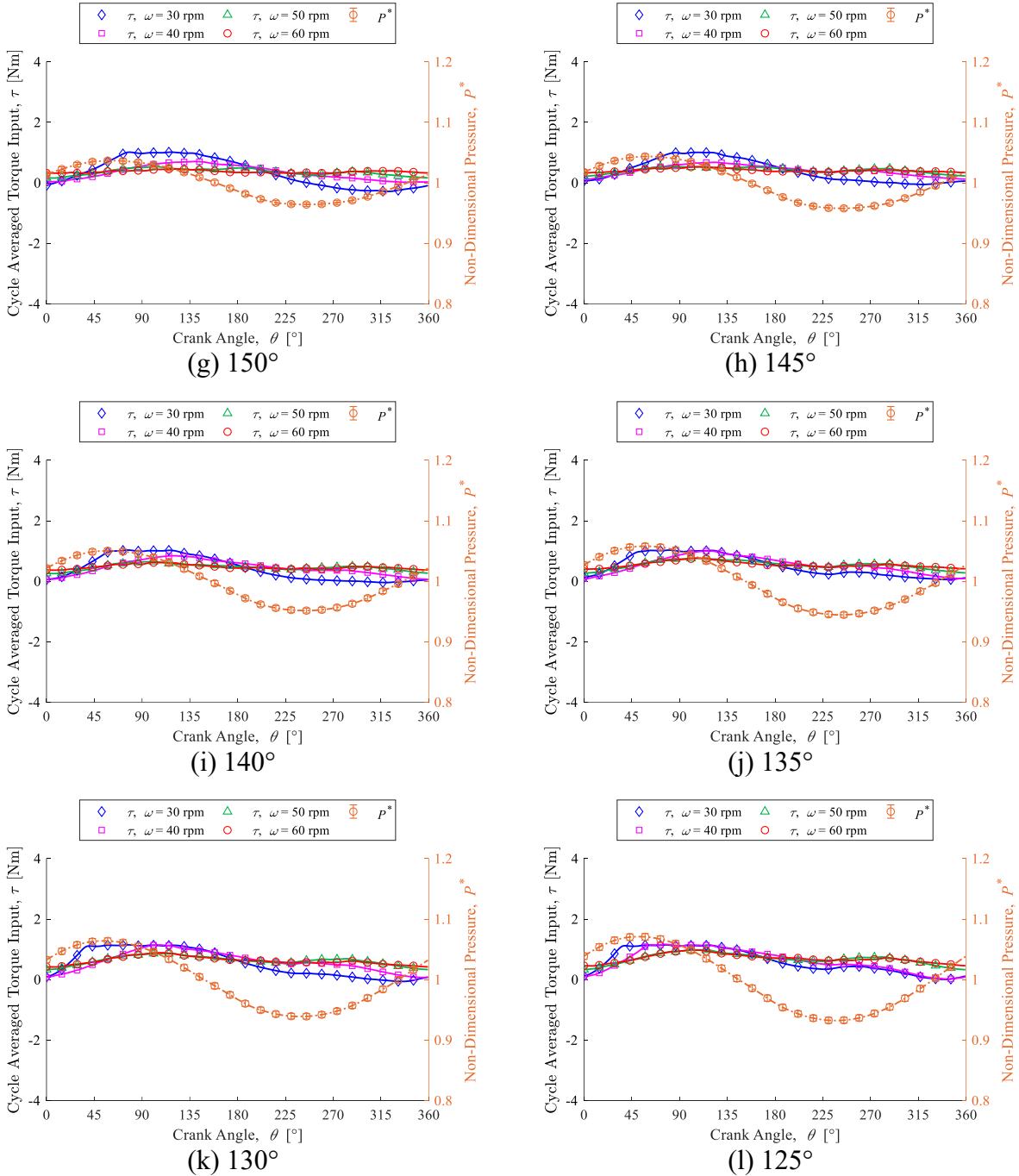
Figure L–1: Baseline Experiment Torque and Non-Dimensional Pressure for a Swept Volume of 1.564 L for Phase Angles Between 125° and 180°
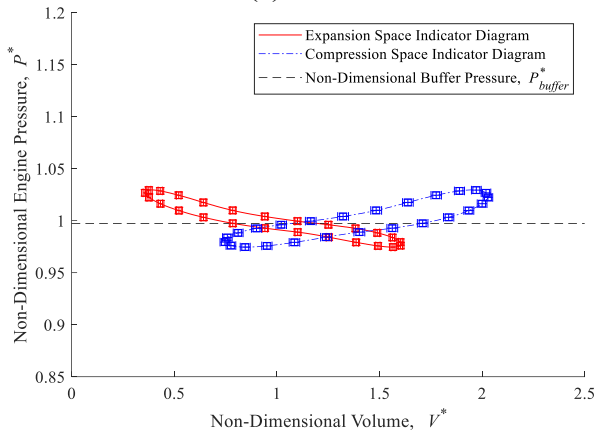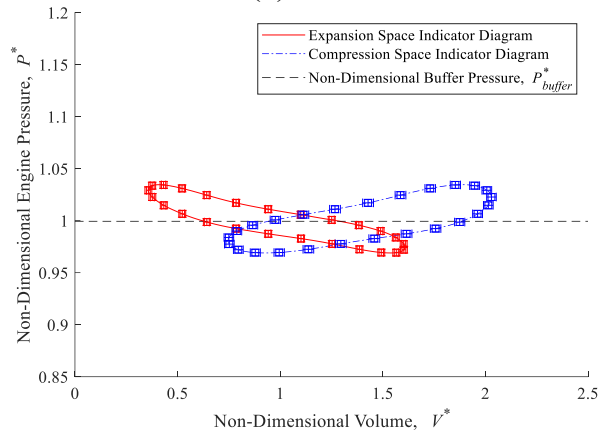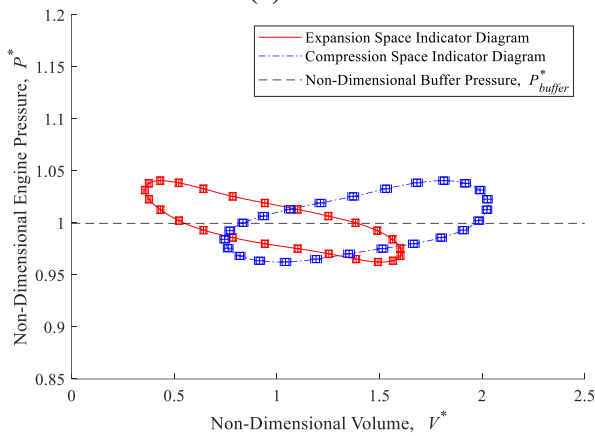
L.2 Swept Volume of 1.955 L

(a) 180°

(b) 175°
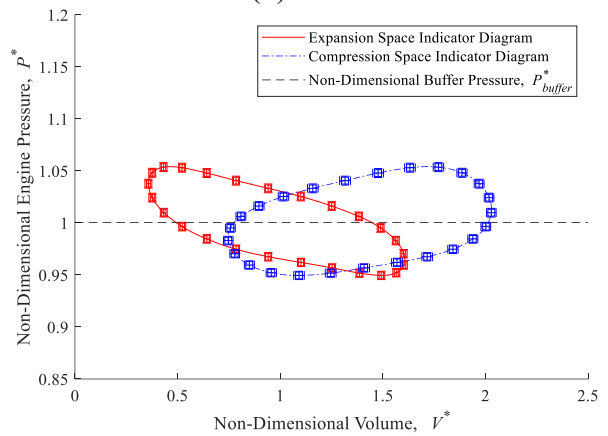

(c) 170°

(d) 165°

(e) 160°

(f) 155°

(g) 150°

(h) 145°

(i) 140°

(j) 135°

(k) 130°

(l) 125°
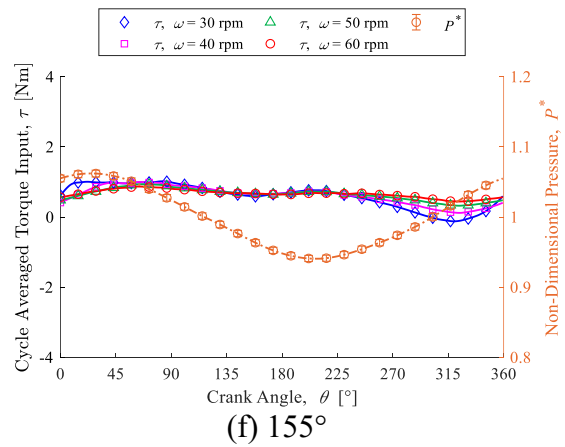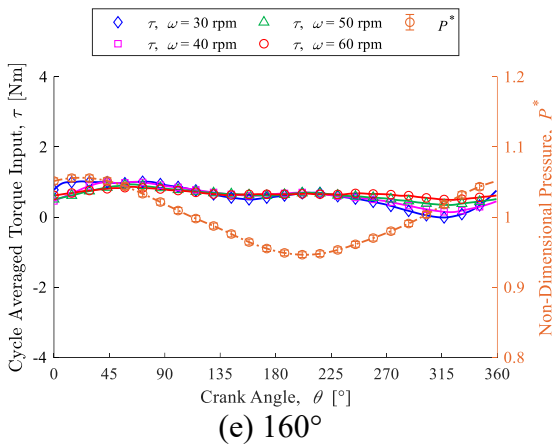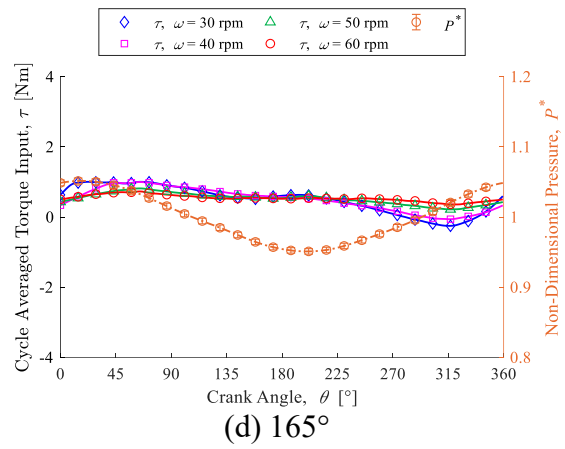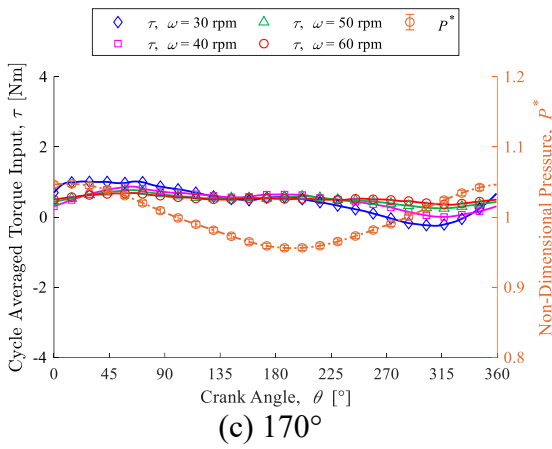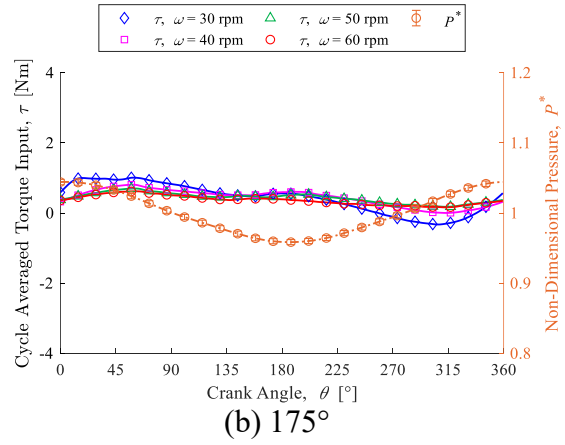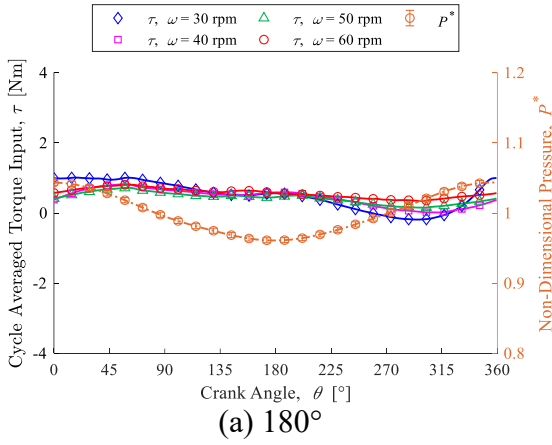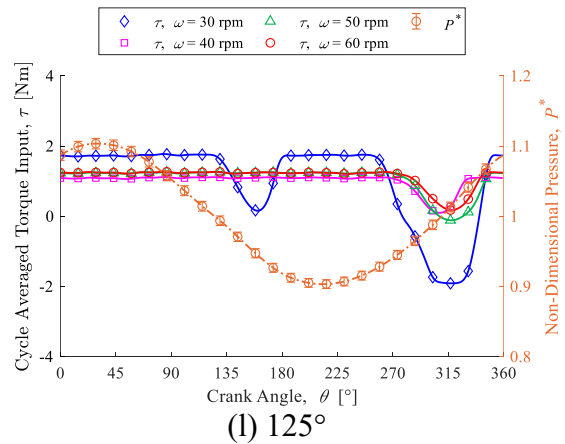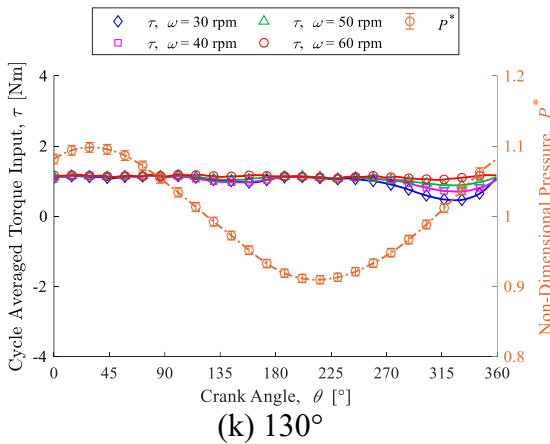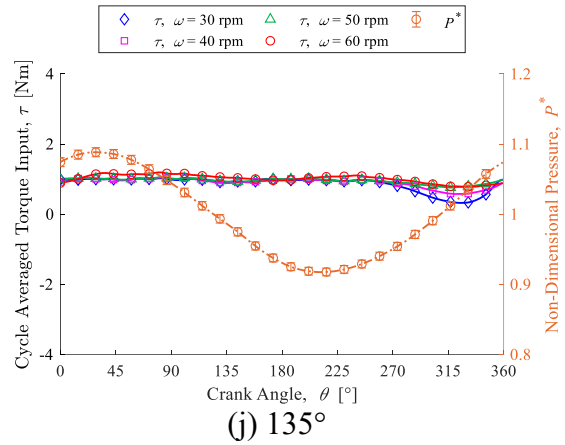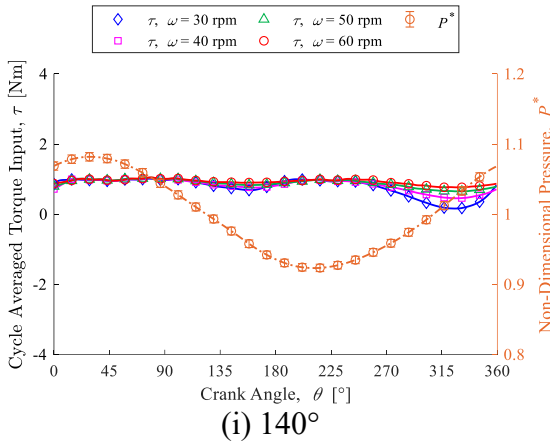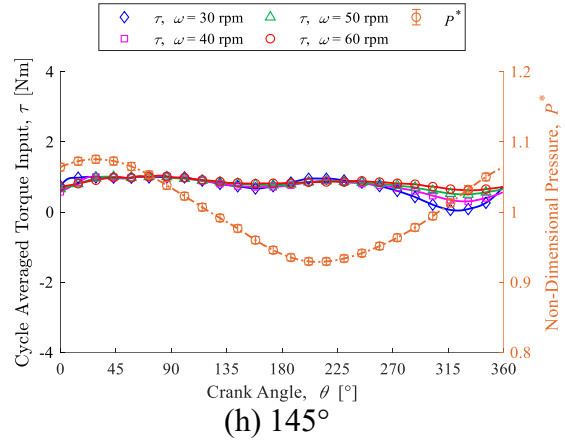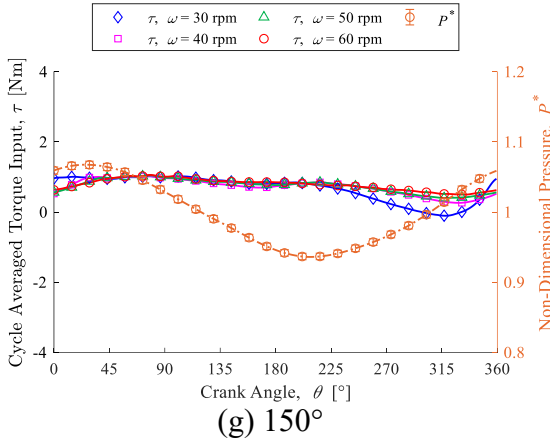
Figure L–2: Baseline Experiment Torque and Non-Dimensional Pressure for a Swept Volume of 1.955 L for Phase Angles Between 125° and 180°

L.3 Swept Volume of 2.346 L
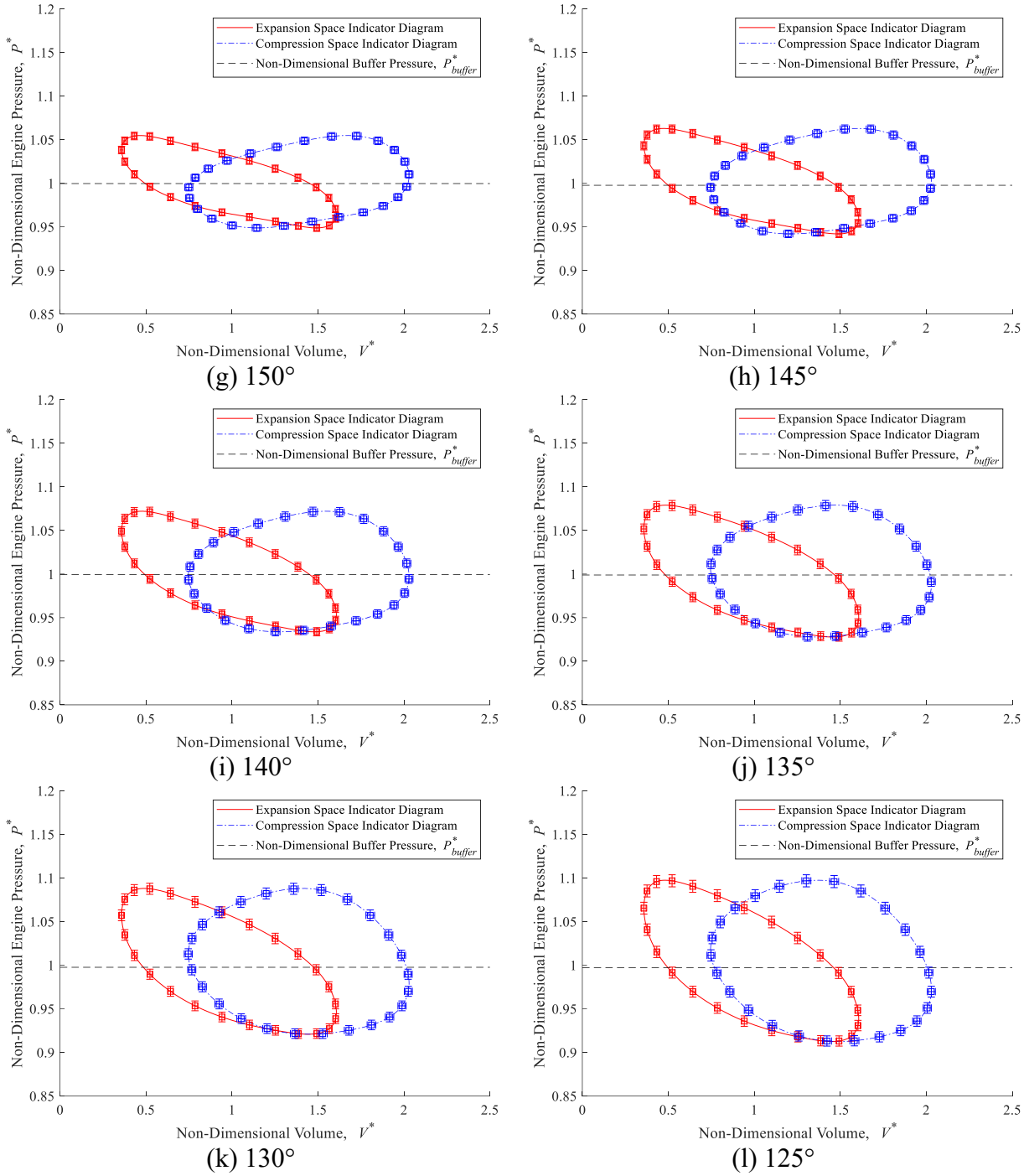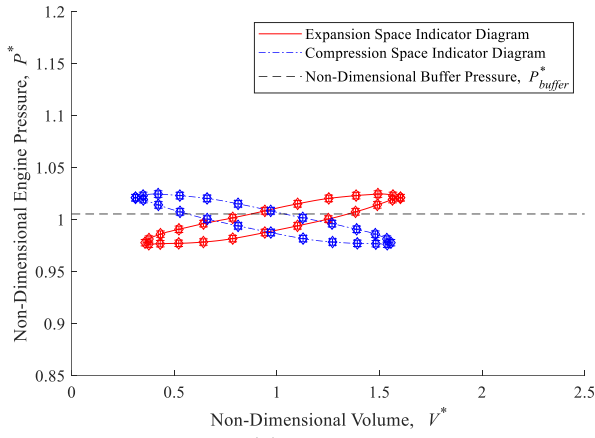

(a) 180°

(b) 175°

(c) 170°

(d) 165°

(e) 160°

(f) 155°
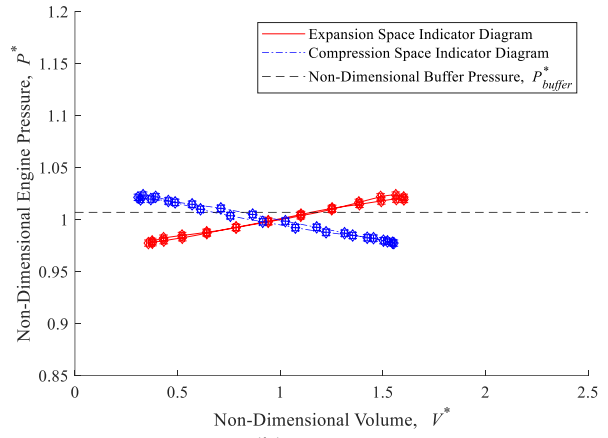
(g) 150°

(h) 145°

(i) 140°

(j) 135°

(k) 130°

(l) 125°
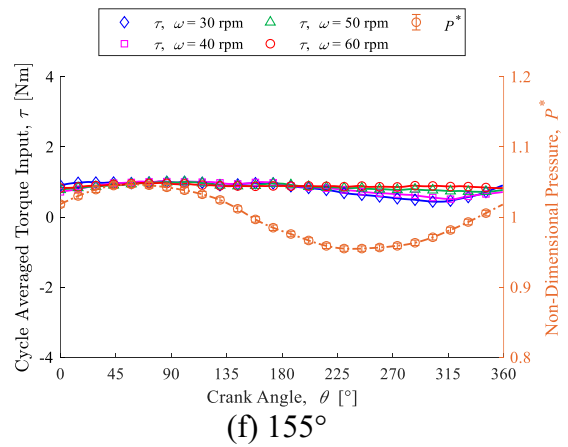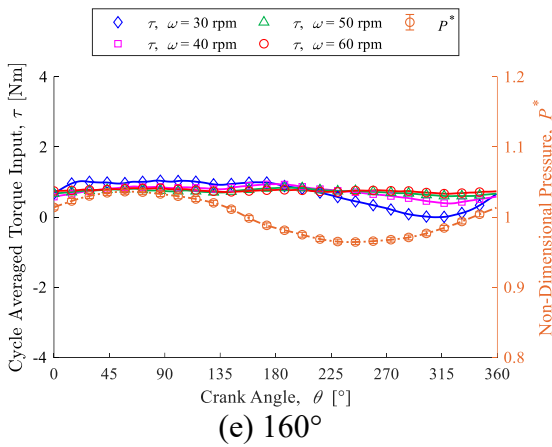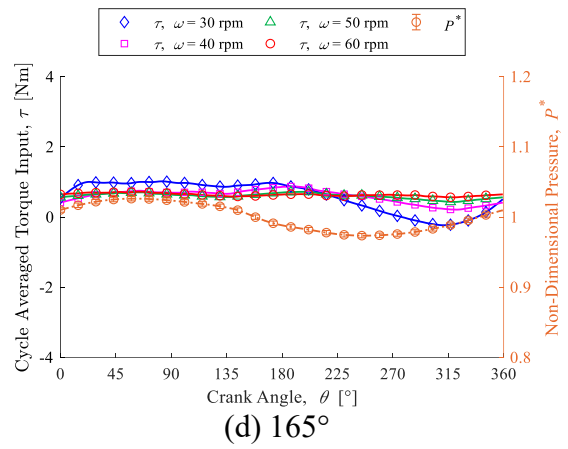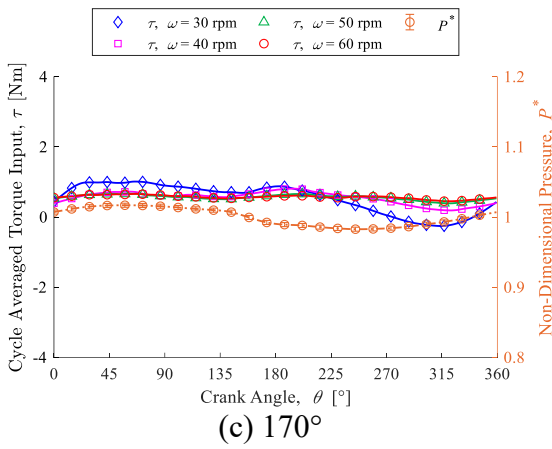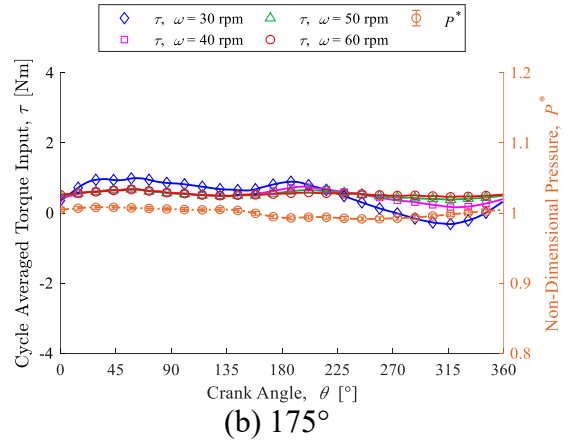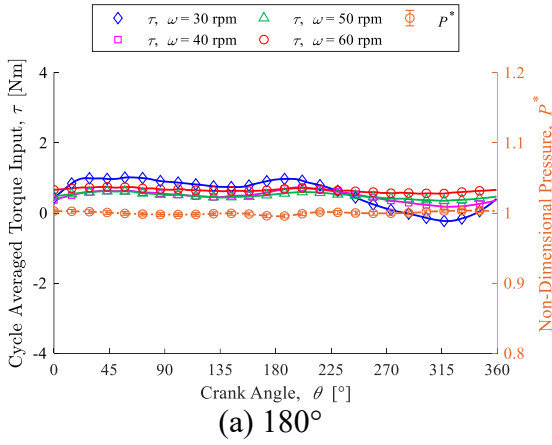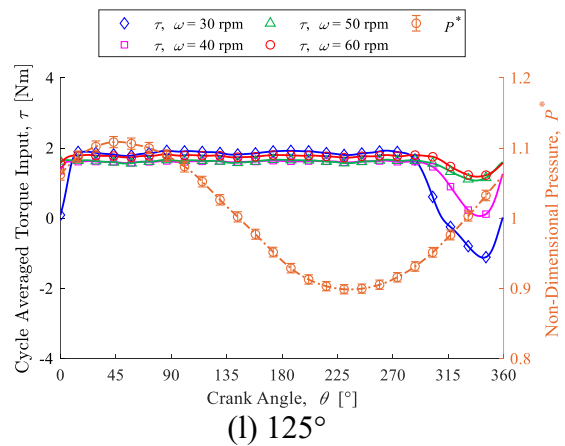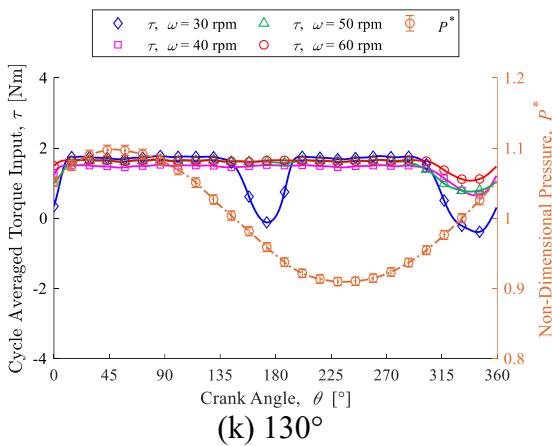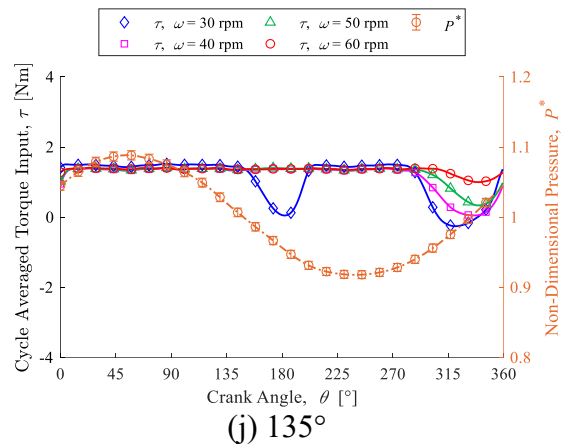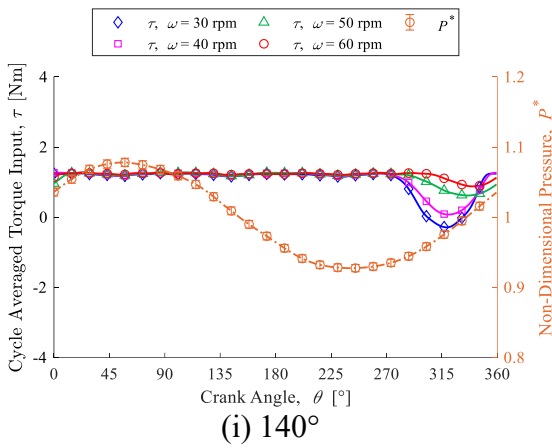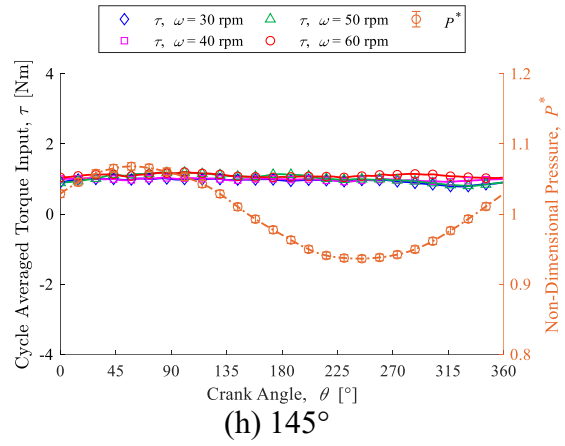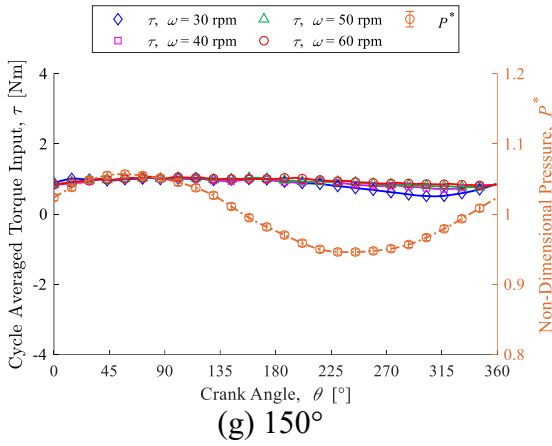
Figure L–3: Baseline Experiment Torque and Non-Dimensional Pressure for a Swept Volume of 2.346 L for Phase Angles Between 125° and 180°

Appendix M   Baseline Mean Temperature Measurements

This section presents the remaining figures for the mean gas temperature for the baseline experiments. Figures for a servo-motor speed of 60 rpm are not reproduced.

M.1 Servo-Motor Speed of 30 rpm
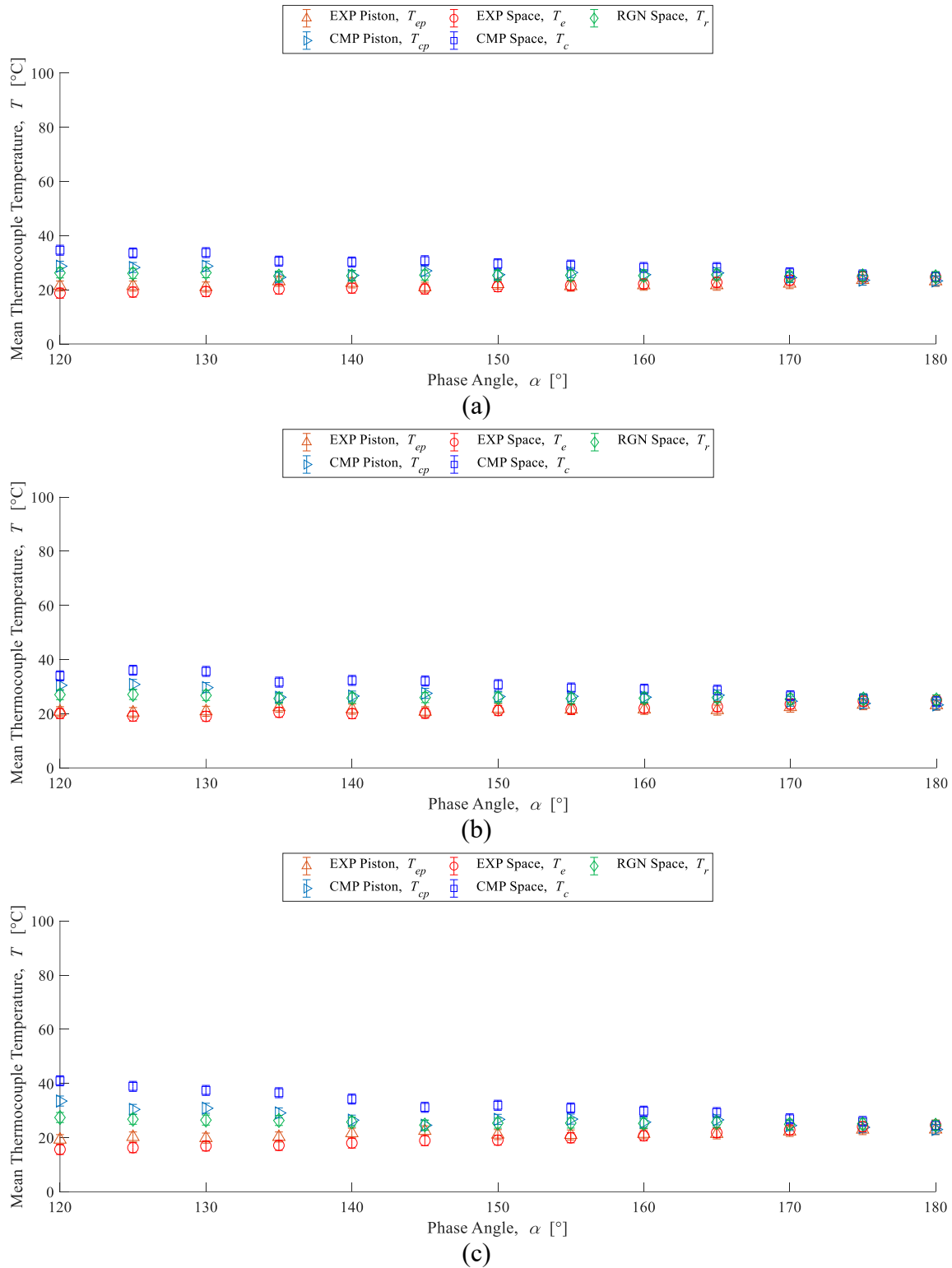
Figure M–1: Mean Gas Temperature Measurements as a Function of Phase Angle for Baseline Experiments at a Swept Volume (a) 1.564 L, (b) 1.955 L, and (c) 2.346 L at 30 rpm

M.1 Servo-Motor Speed of 40 rpm
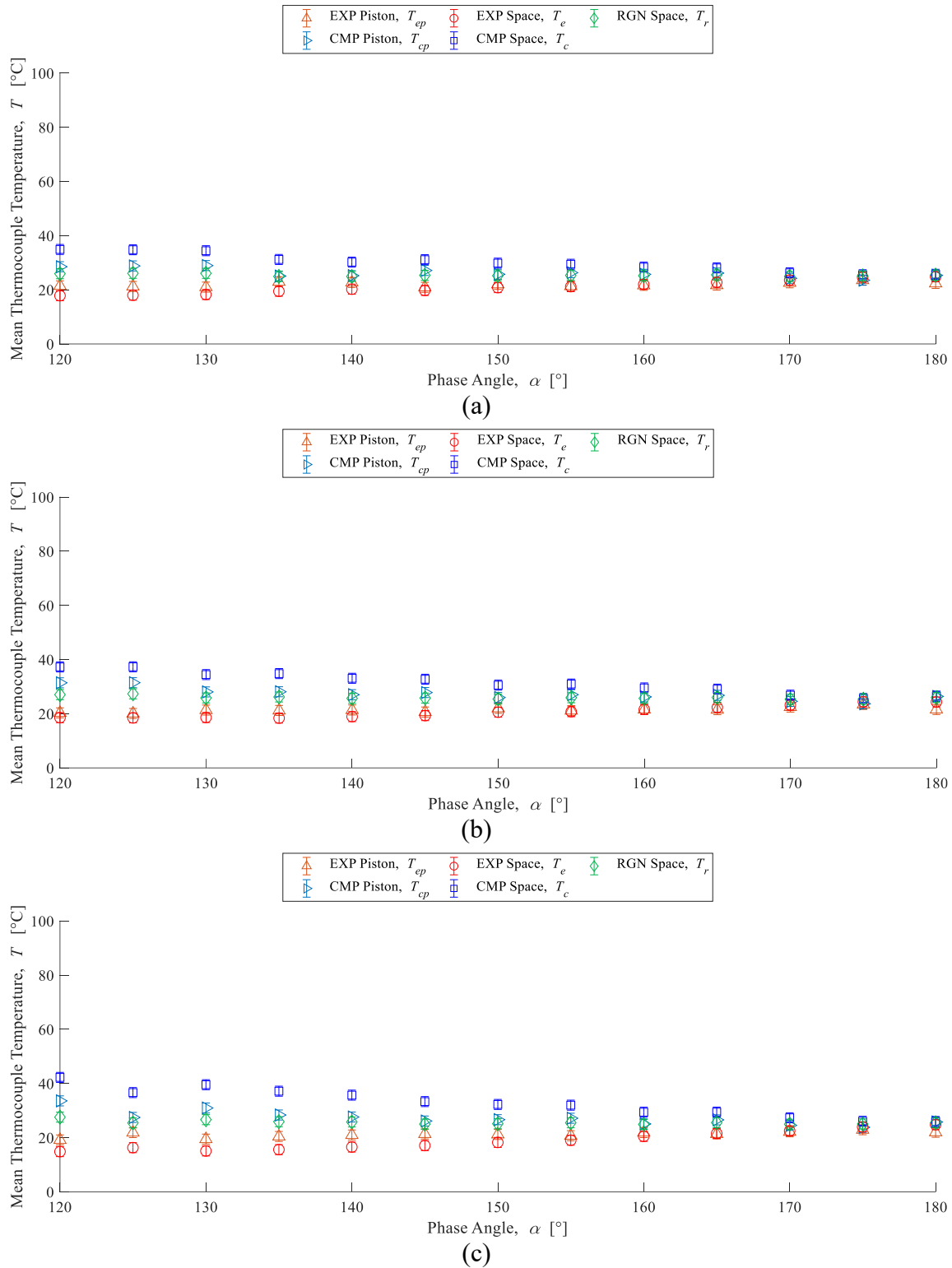
Figure M–2: Mean Gas Temperature Measurements as a Function of Phase Angle for Baseline Experiments at a Swept Volume (a) 1.564 L, (b) 1.955 L, and (c) 2.346 L at 40 rpm

M.1 Servo-Motor Speed of 50 rpm
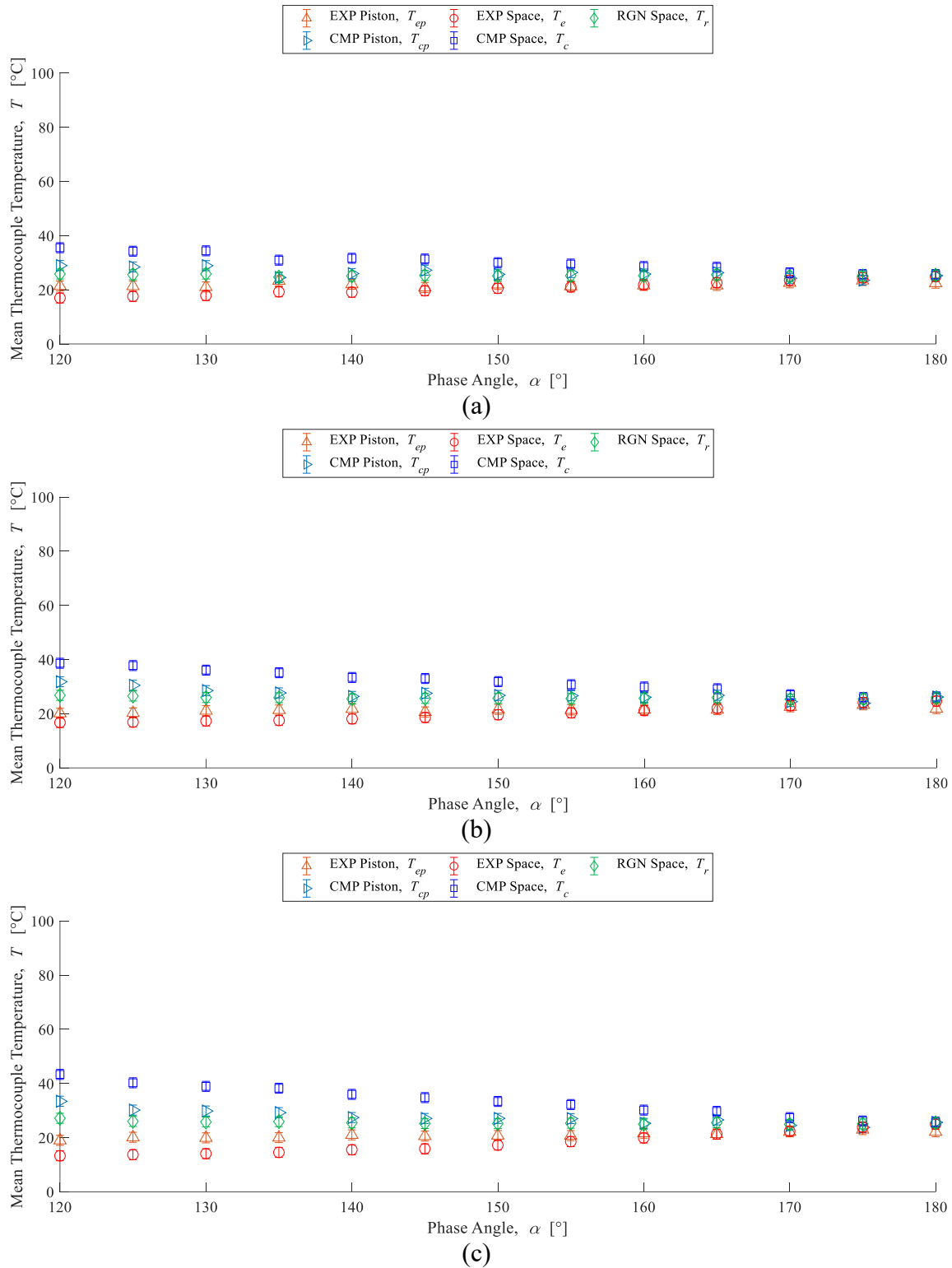
Figure M–3: Mean Gas Temperature Measurements as a Function of Phase Angle for Baseline Experiments at a Swept Volume (a) 1.564 L, (b) 1.955 L, and (c) 2.346 L at 50 rpm

Appendix N   Baseline Non-Dimensional Indicator Diagrams

This section presents the remaining figures for the non-dimensional indicator diagrams for the baseline experiments at 60 rpm. Figures pertaining to a 120° phase angle are not reproduced.
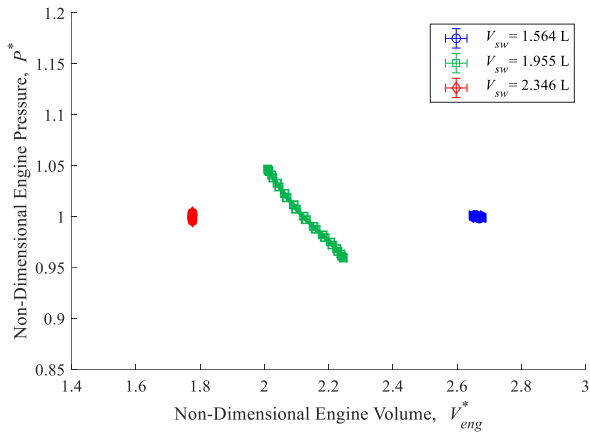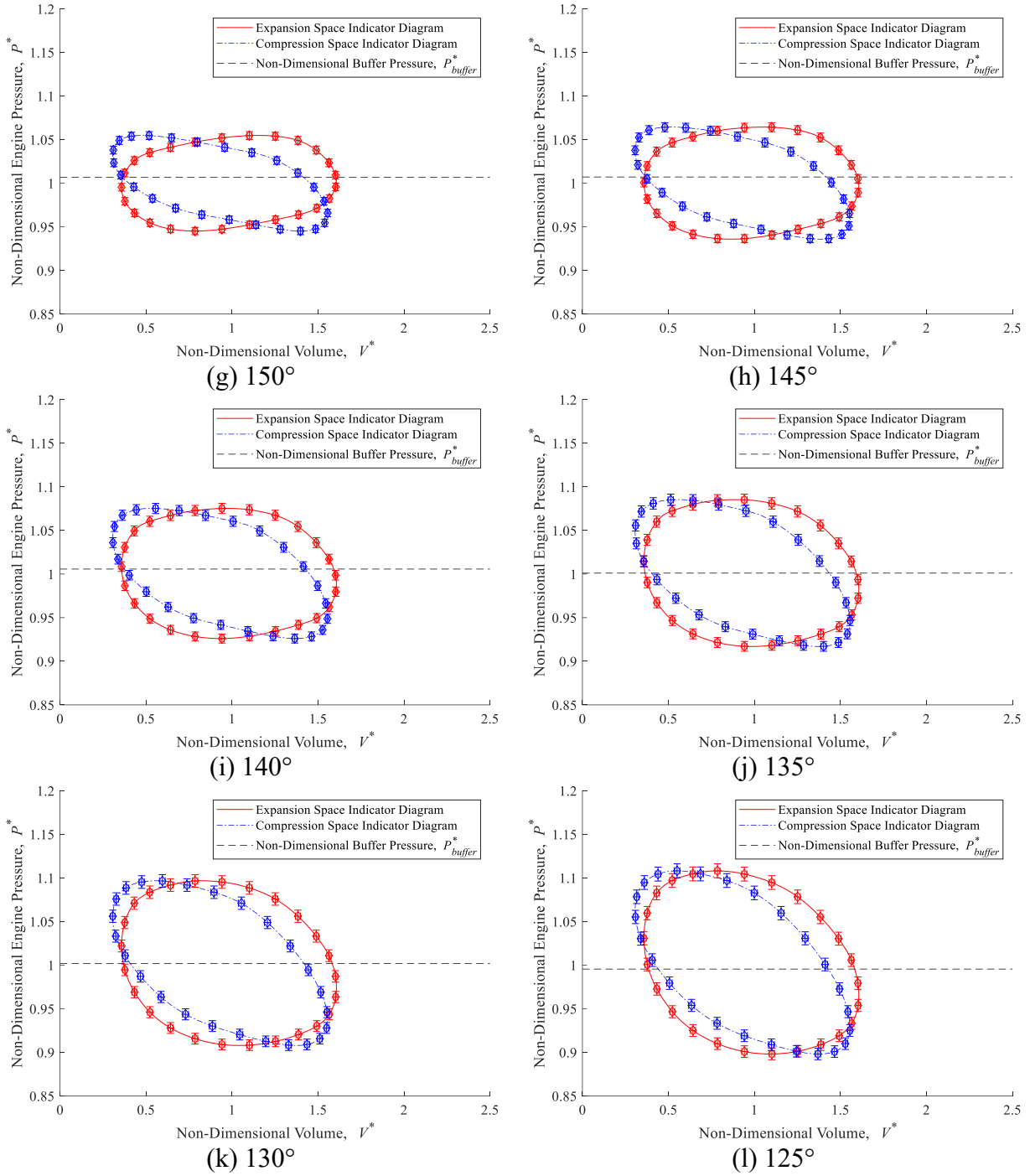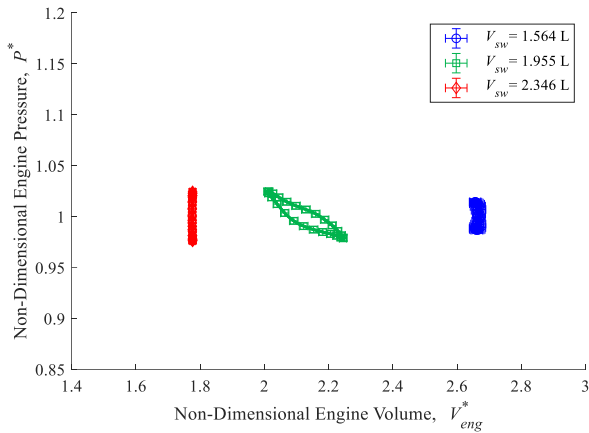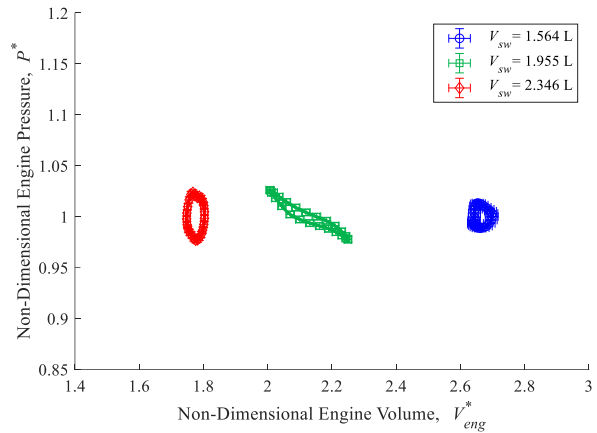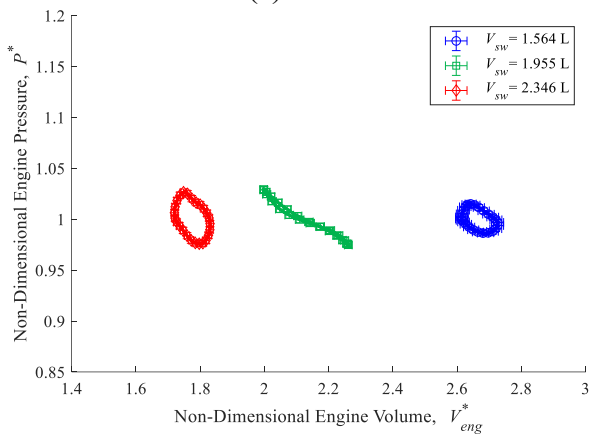

(a) 180°
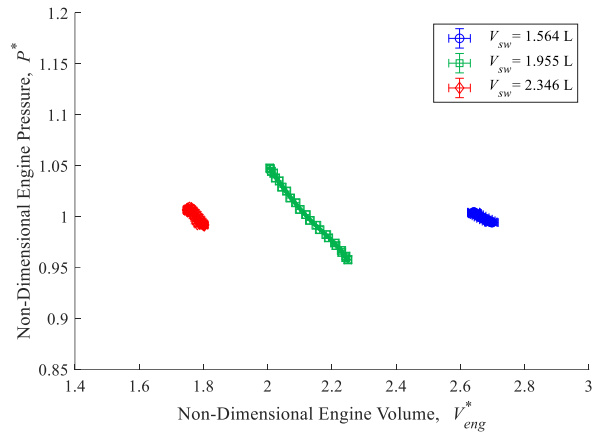
(b) 175°
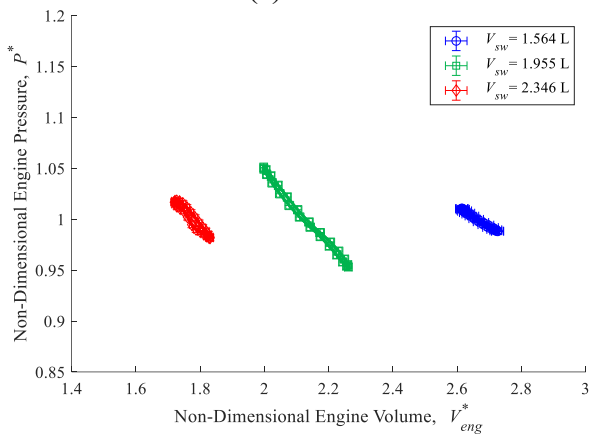
(c) 170°
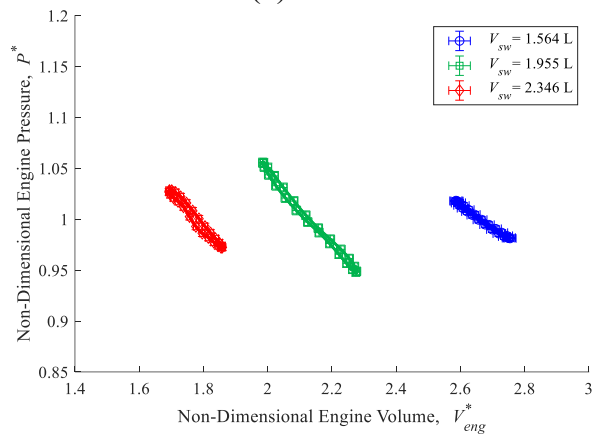
(d) 165°
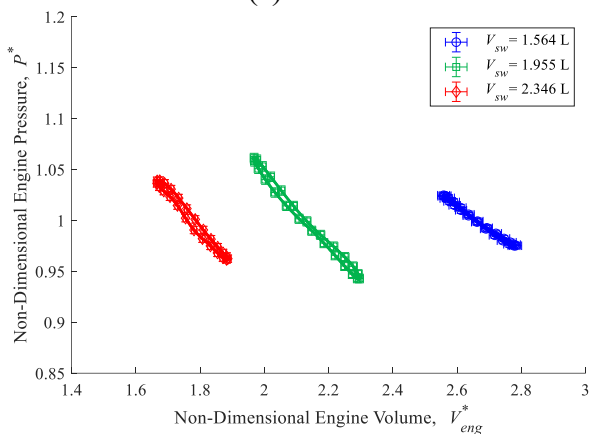
(e) 160°
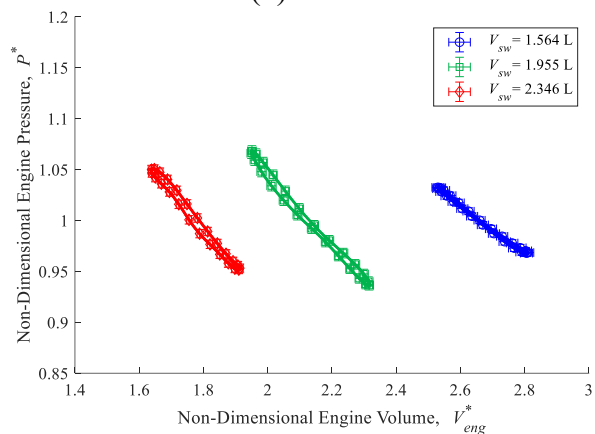
(f) 155°
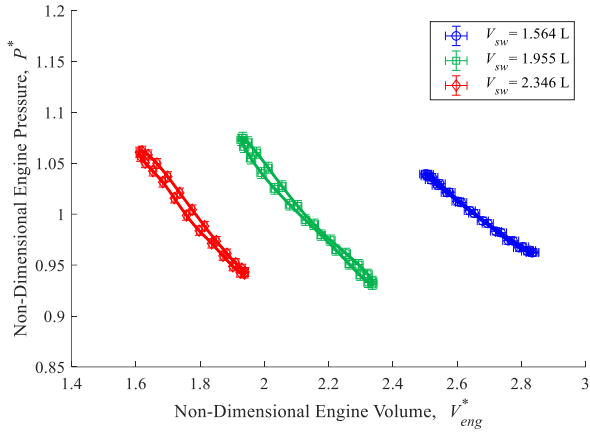
(g) 150°
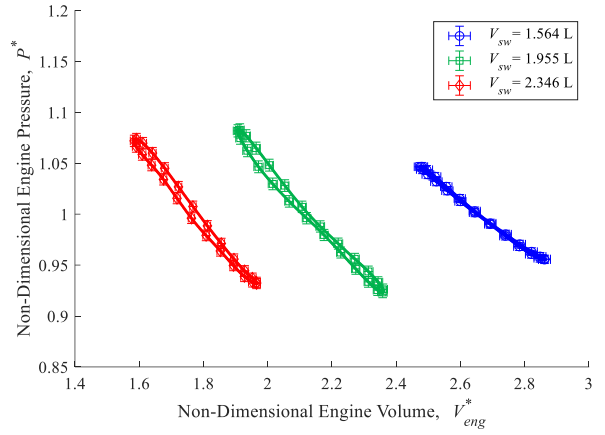
(h) 145°
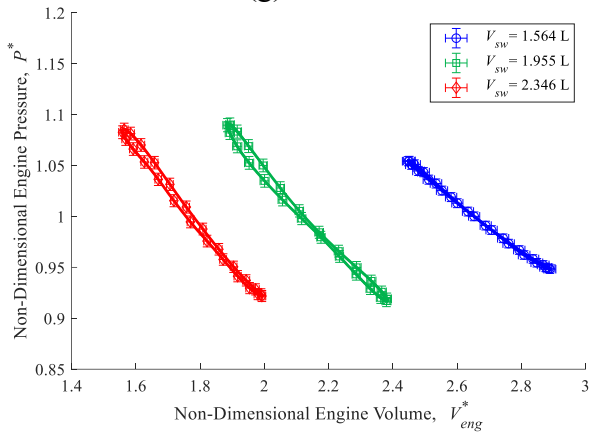
(i) 140°
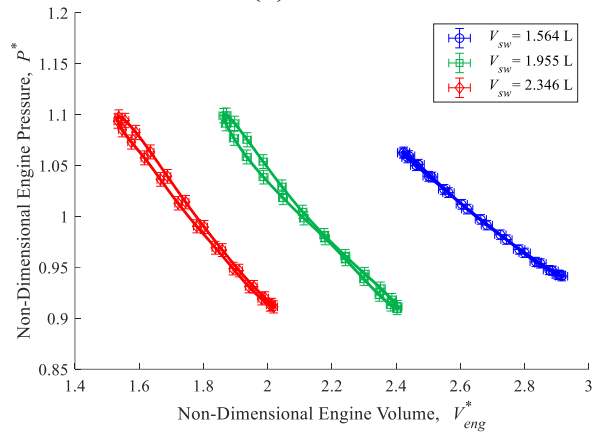
(j) 135°
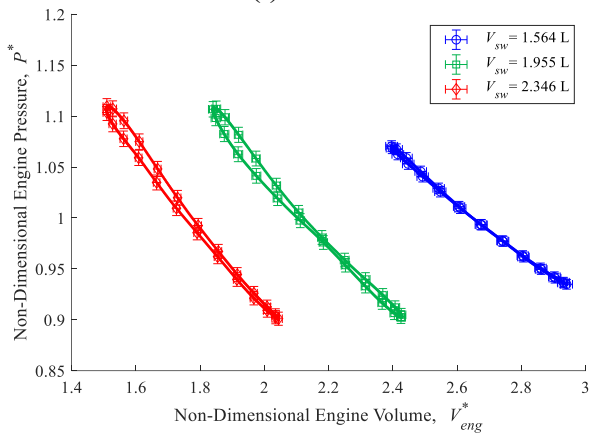
(k) 130°
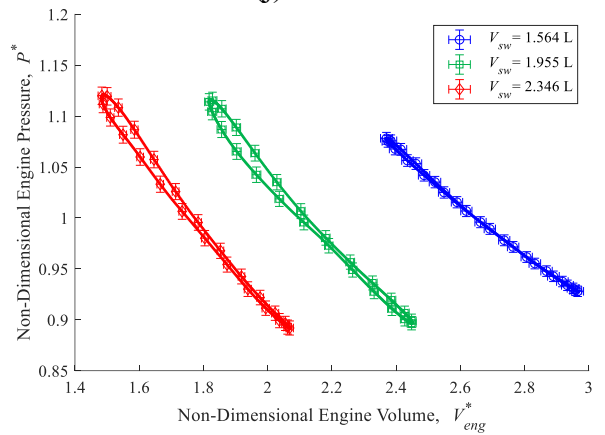
(l) 125°

Figure N–1: Baseline Experiment Non-Dimensional Indicator Diagrams at 60 rpm for Phase Angles Between 125° and 180°

Appendix O   Thermal Pressure Fluctuations for Each Speed

This section presents the remaining figures for the non-dimensional pressure fluctuations at each speed for the thermal experiments. Figures for a 120° phase angle are not reproduced.

(a) 180°

(b) 175°

(c) 170°

(d) 165°

(e) 160°

(f) 155°

(g) 150°

(h) 145°

(i) 140°

(j) 135°

(k) 130°

(l) 125°
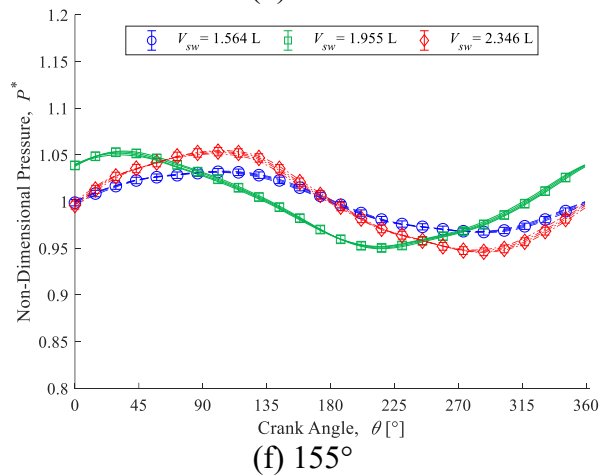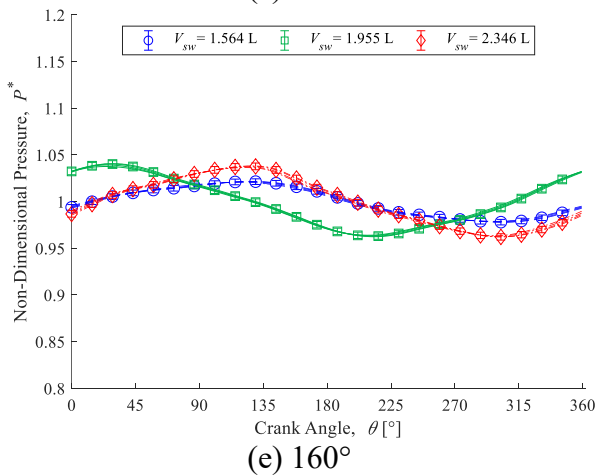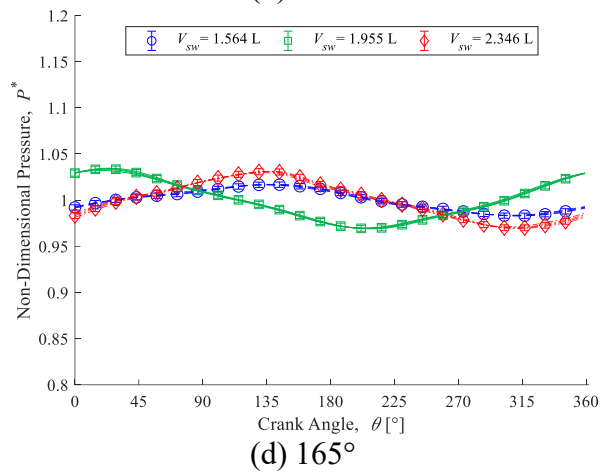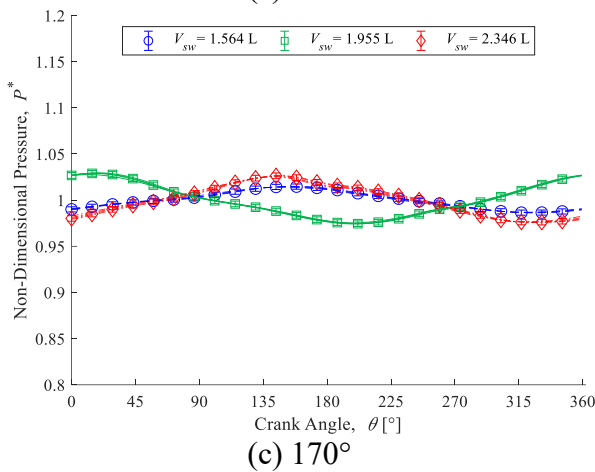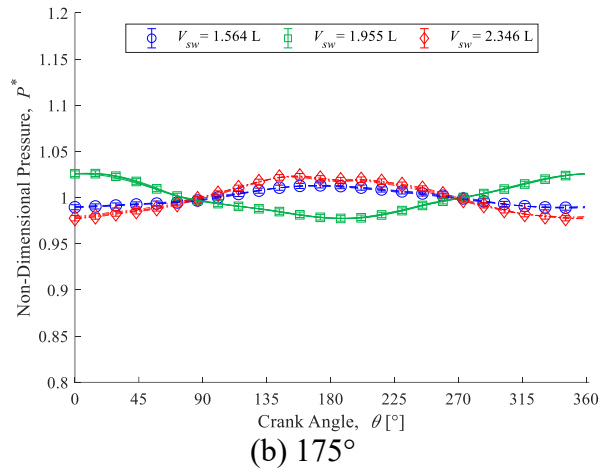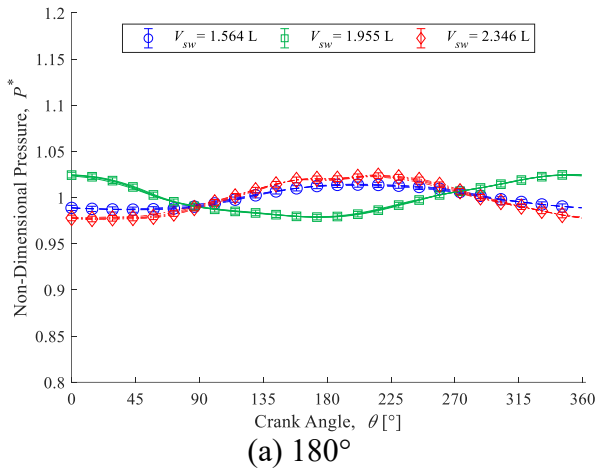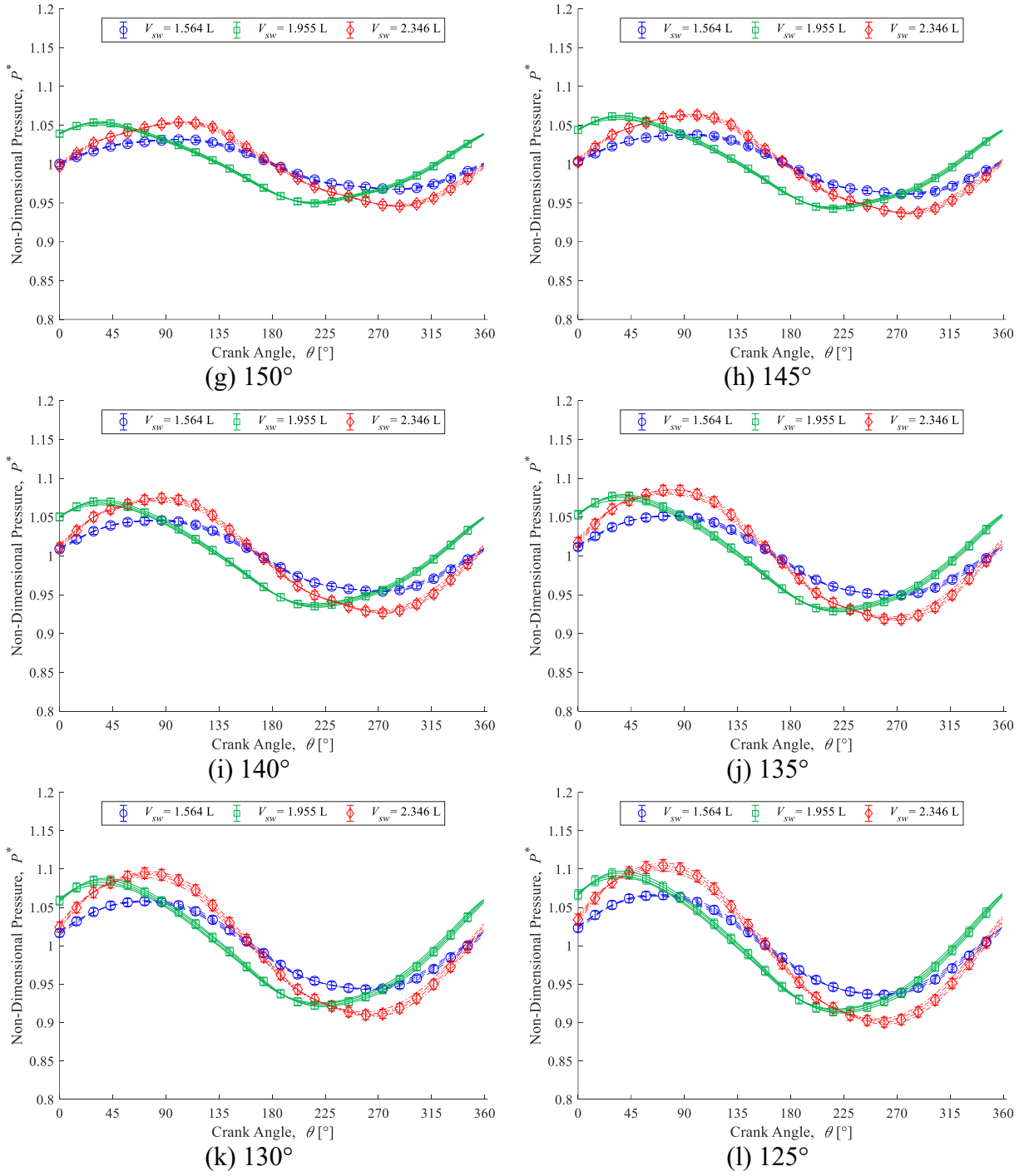
Figure O–1: Thermal Experiment Non-Dimensional Pressure Fluctuation for Each Swept Volume and Engine Speed for Phase Angles Between 125° and 180°

Appendix P   Thermal Non-Dimensional Pressure Fluctuations

This section presents the remaining figures for the thermal experiment non-dimensional pressure fluctuations at 60 rpm. Figures for a 120° phase angle are not reproduced.

P.1 Swept Volume of 1.564 L

(a) 180°

(b) 175°

(c) 170°

(d) 165°

(e) 160°
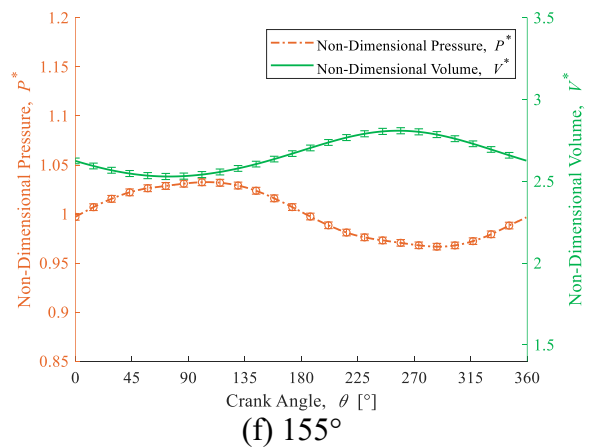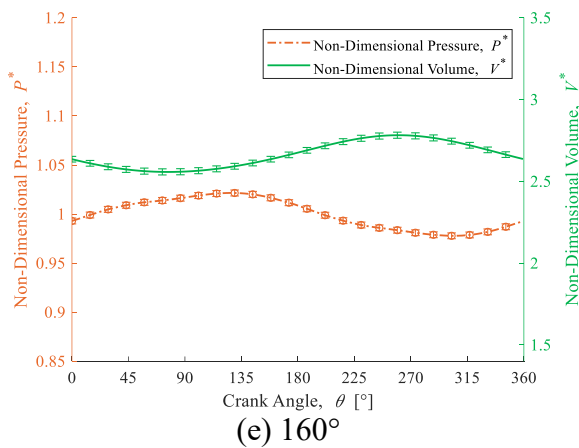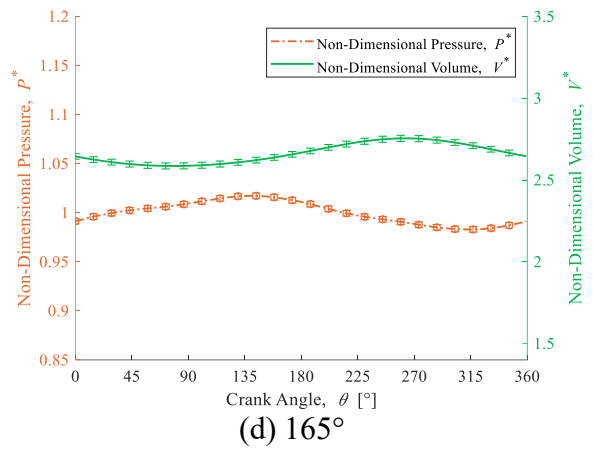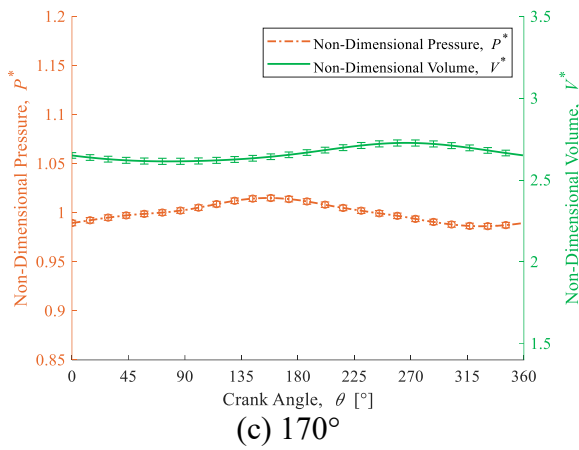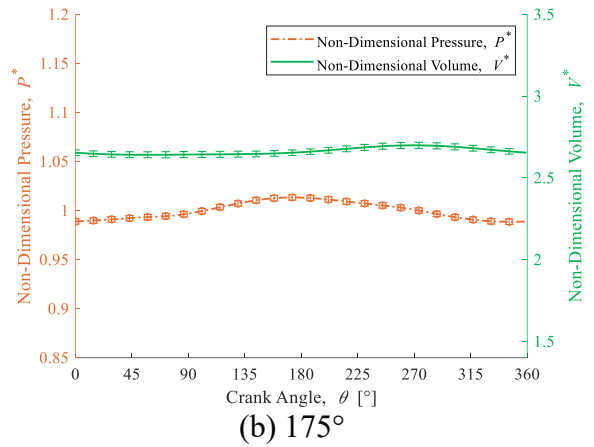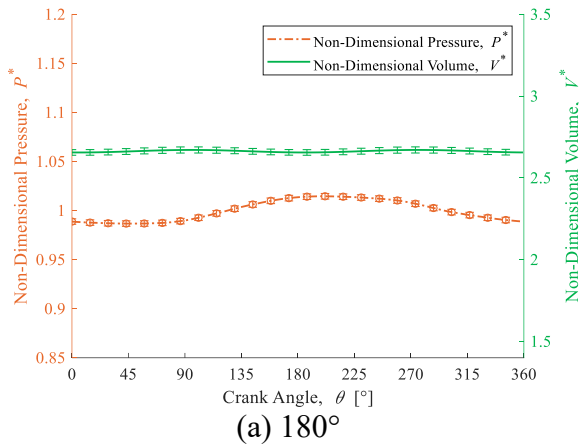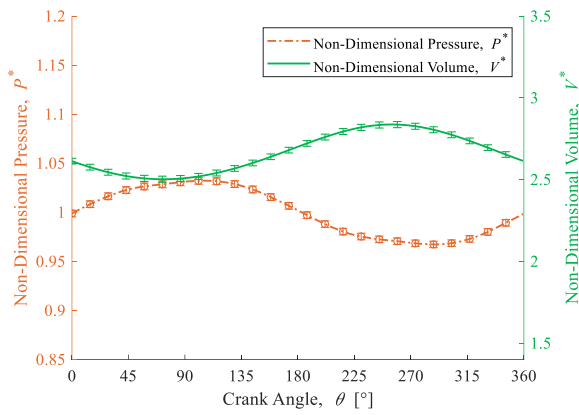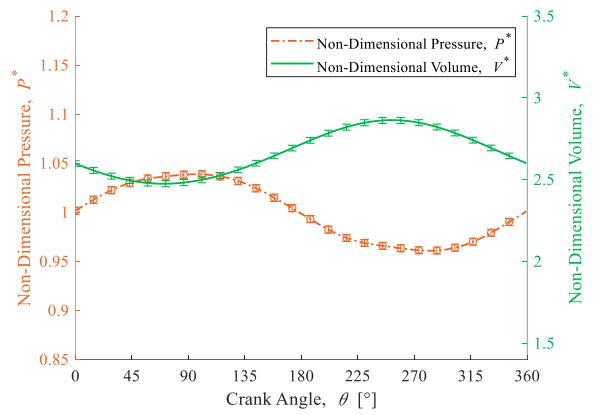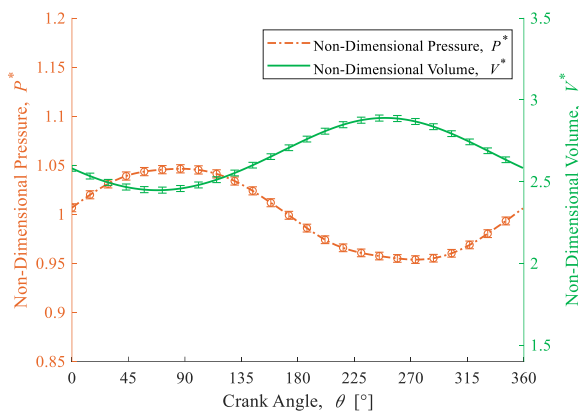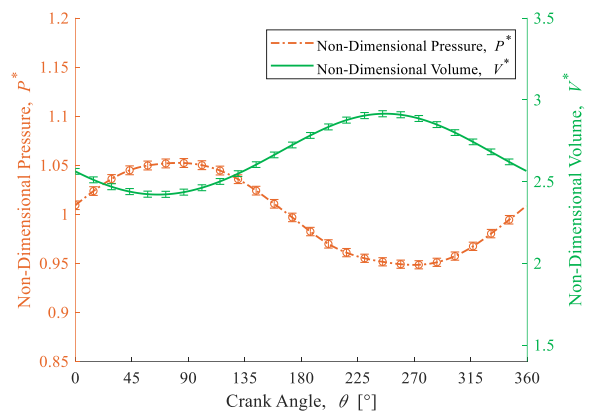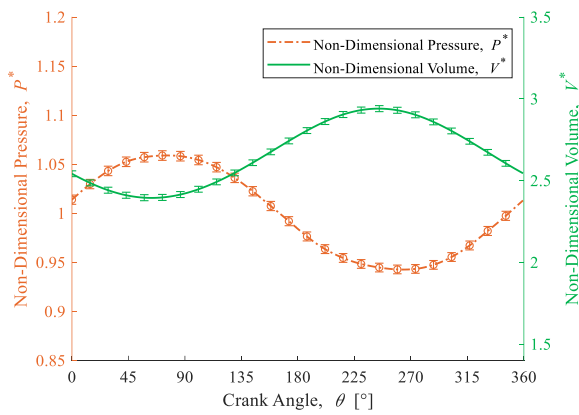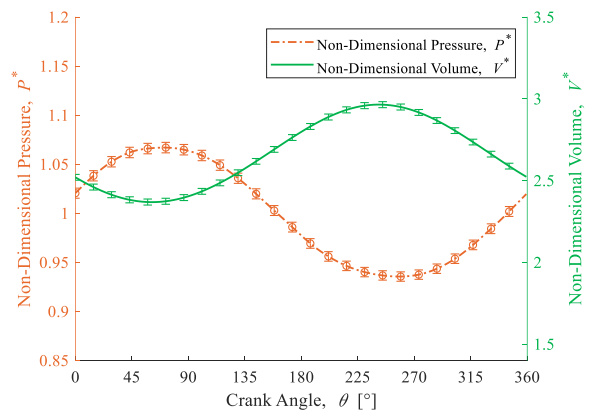
(f) 155°

Figure P–1: Thermal Experiment Non-Dimensional Pressure and Engine Volume Fluctuations for a Swept Volume of 1.564 L at 60 rpm for Phase Angles Between 125° and 180°
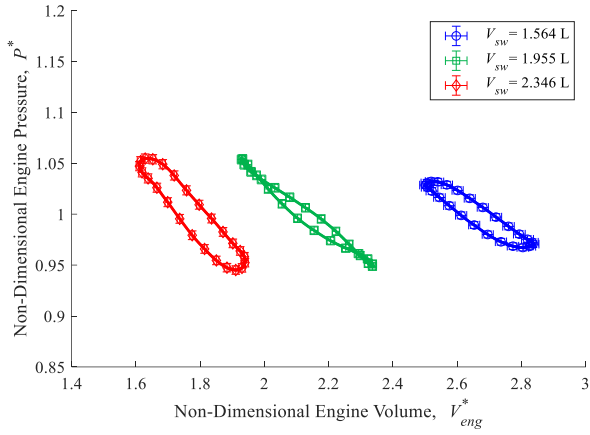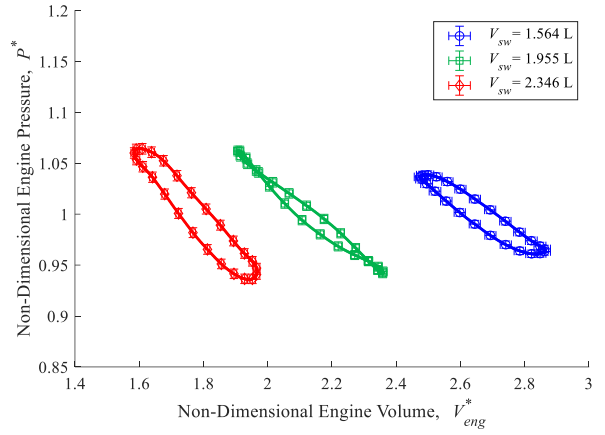
P.2 Swept Volume of 1.955 L

(a) 180°

(b) 175°

(c) 170°

(d) 165°

(e) 160°

(f) 155°

(g) 150°

(h) 145°

(i) 140°

(j) 135°

(k) 130°

(l) 125°
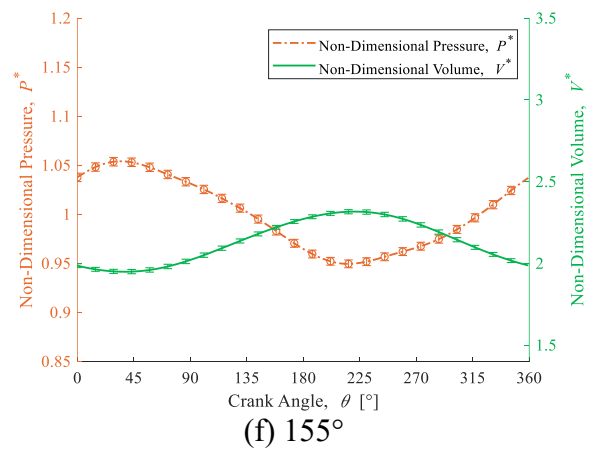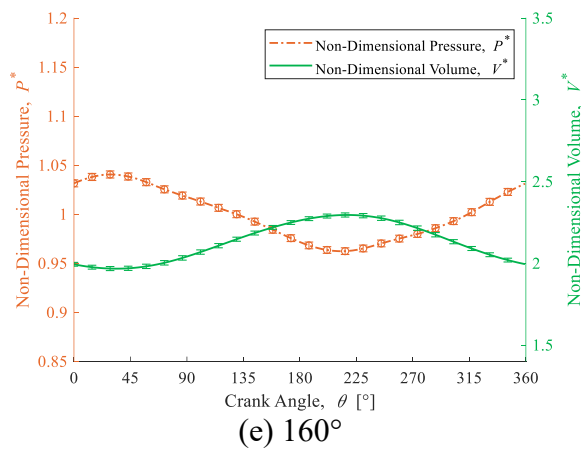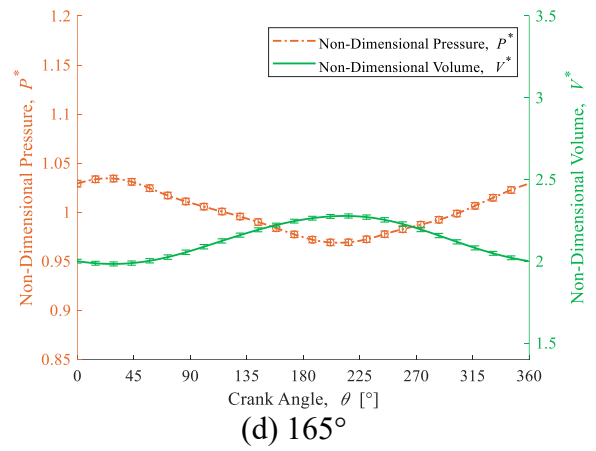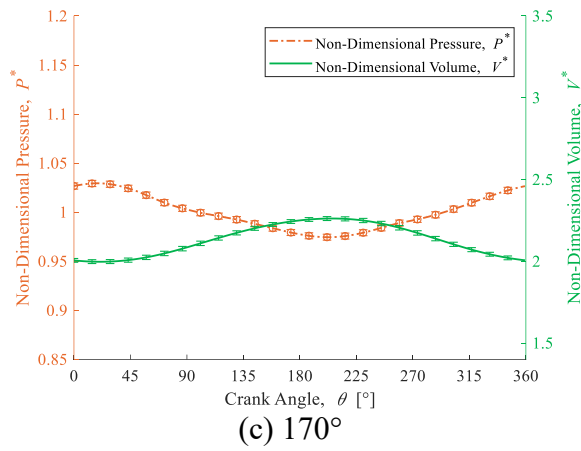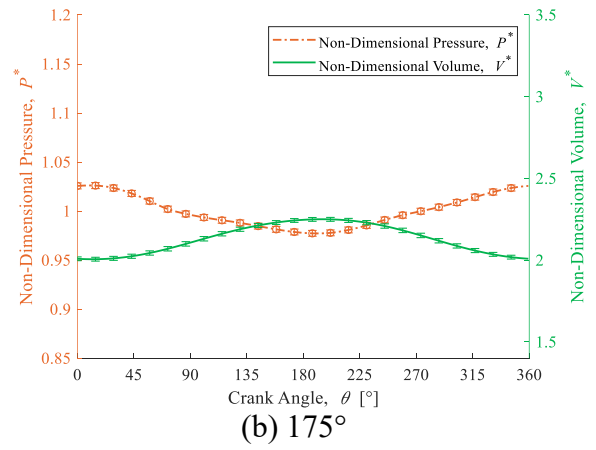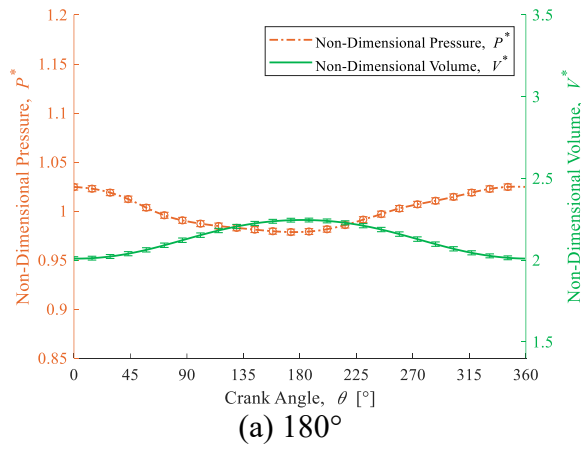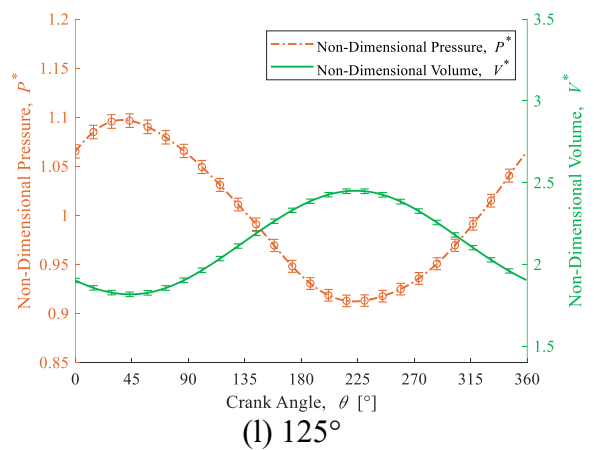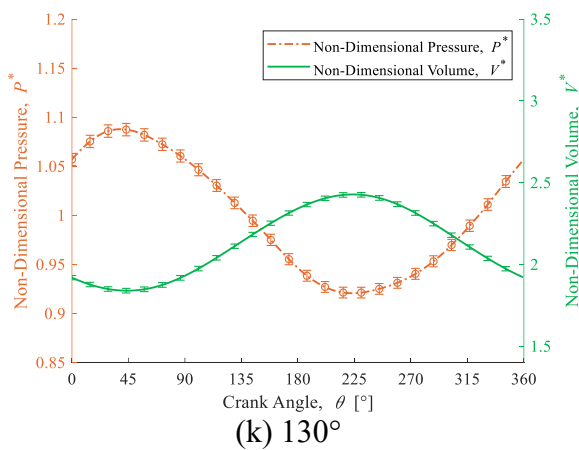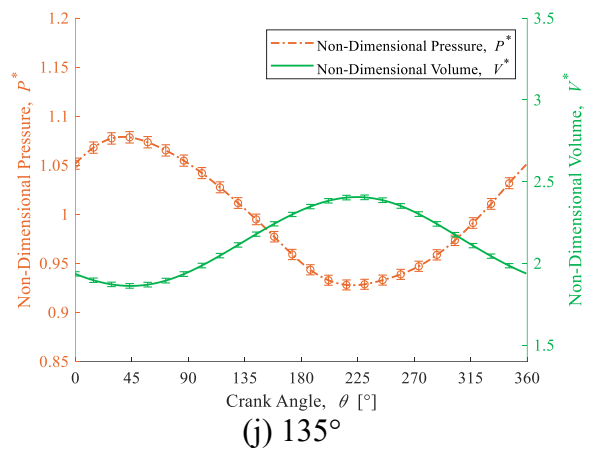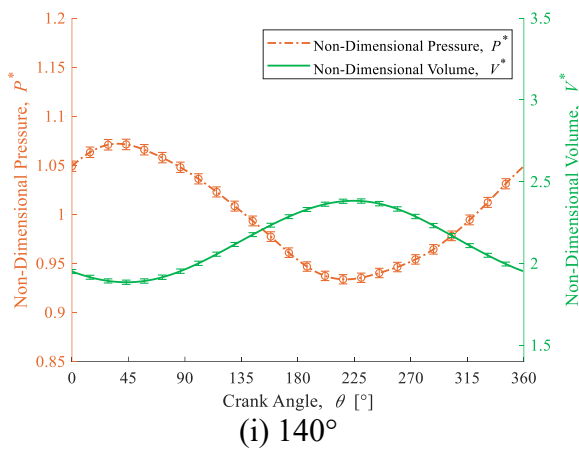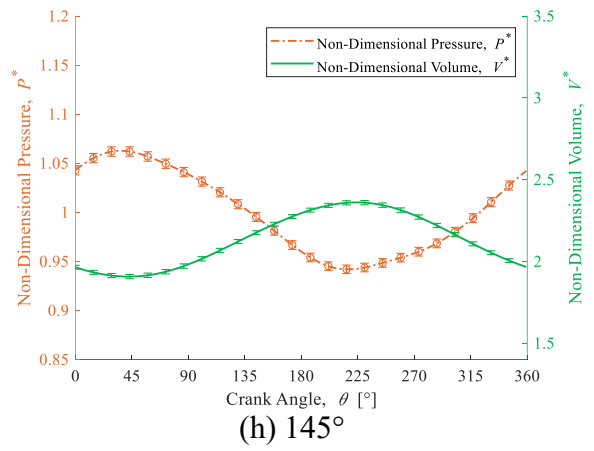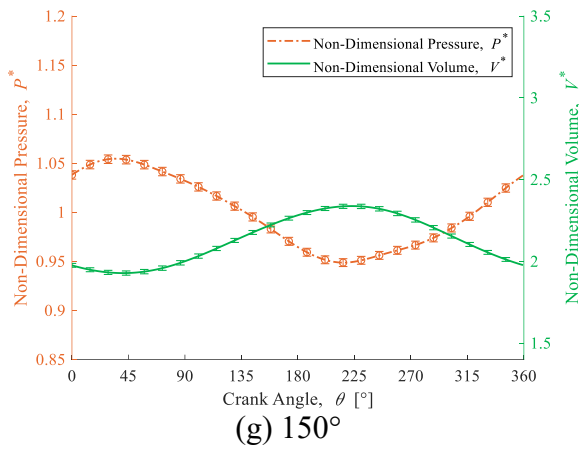
Figure P–2: Thermal Experiment Non-Dimensional Pressure and Engine Volume Fluctuations for a Swept Volume of 1.955 L at 60 rpm for Phase Angles Between 125° and 180°

P.3 Swept Volume of 2.346 L

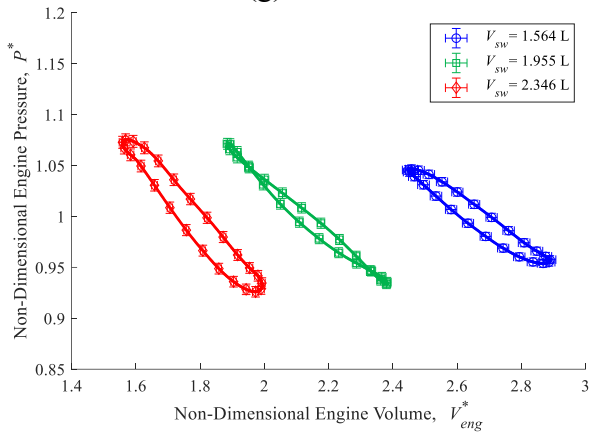(a) 180°

(b) 175°

(c) 170°

(d) 165°

(e) 160°

(f) 155°

(g) 150°

(h) 145°

(i) 140°

(j) 135°

(k) 130°

(l) 125°
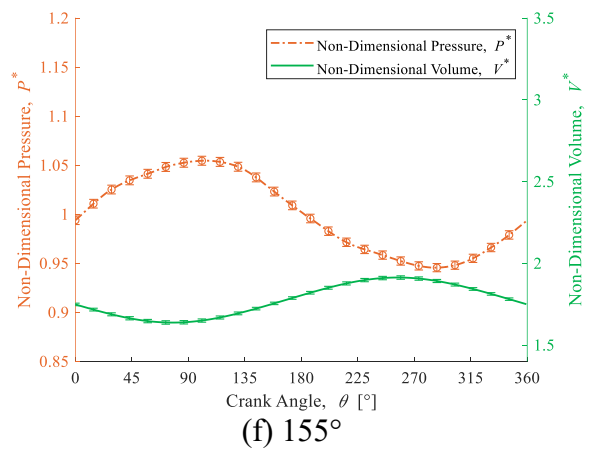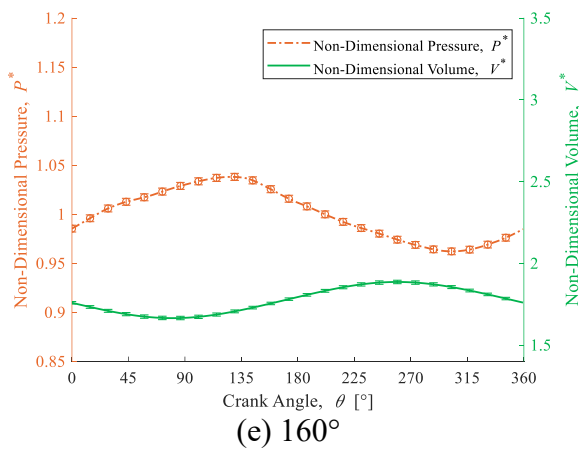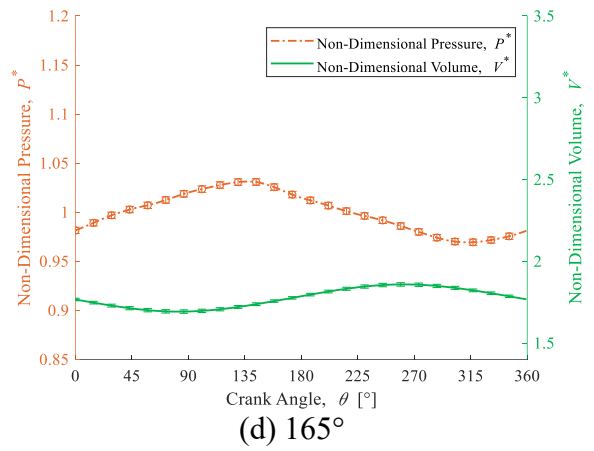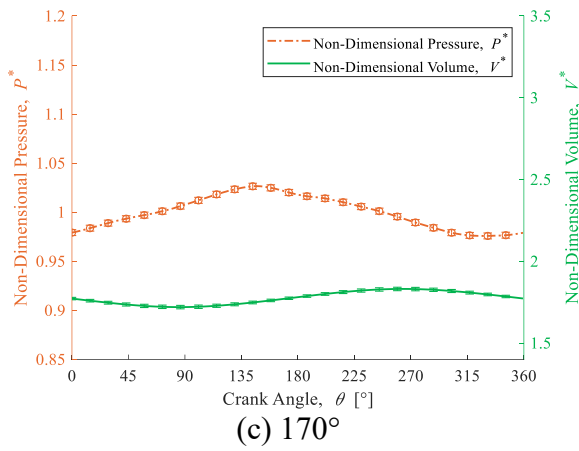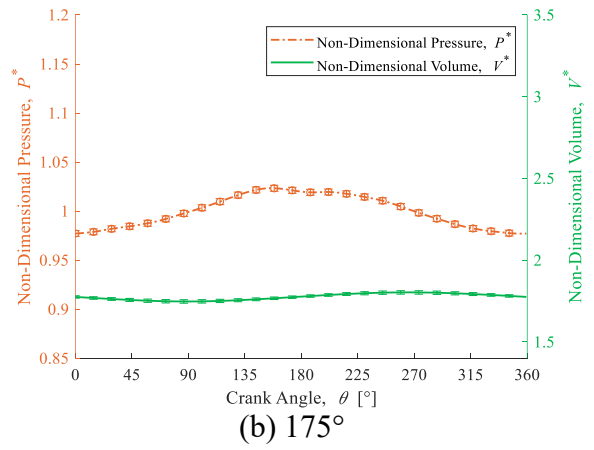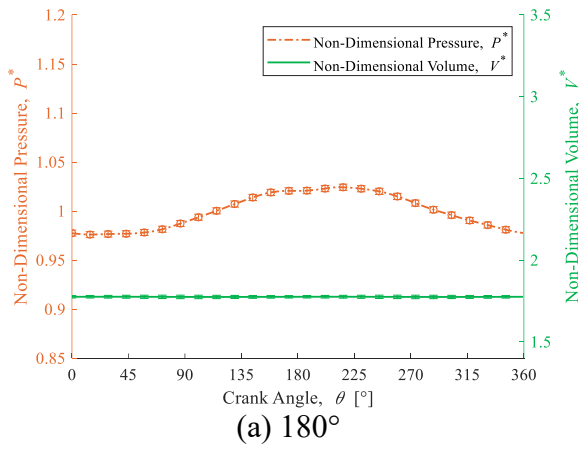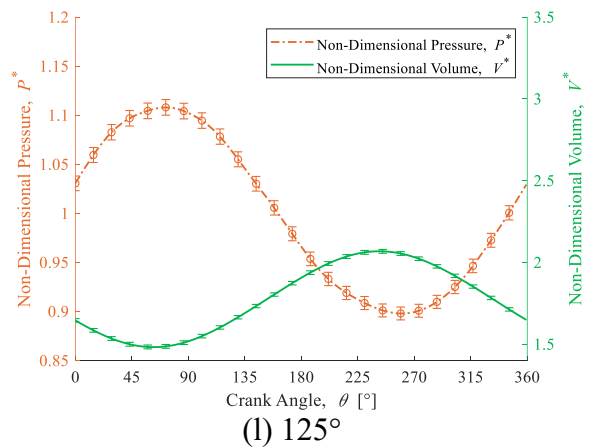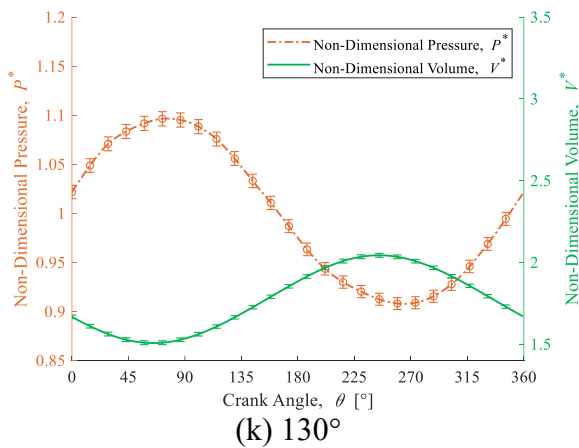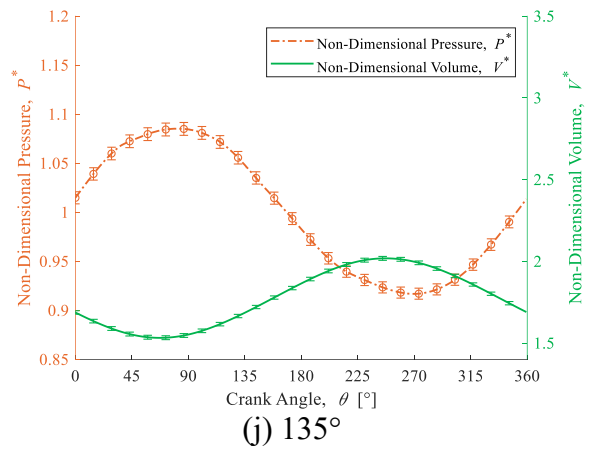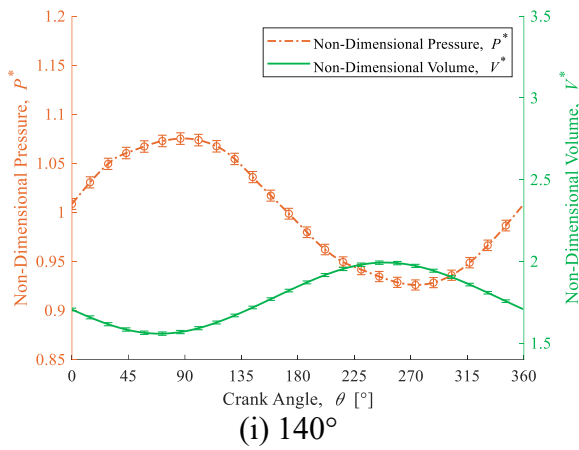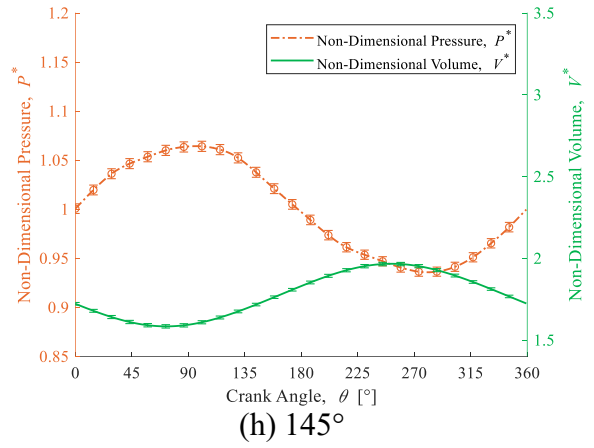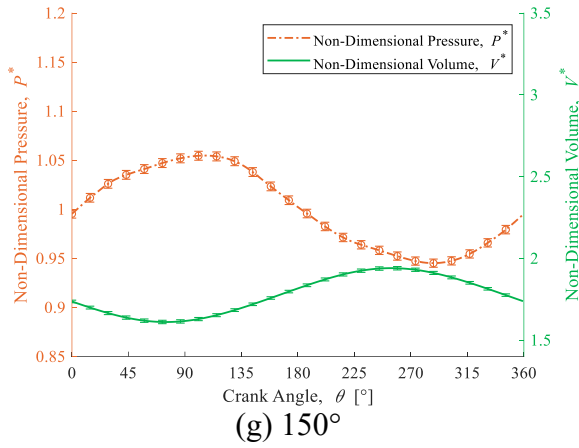
Figure P–3: Thermal Experiment Non-Dimensional Pressure and Engine Volume Fluctuations for a Swept Volume of 2.346 L at 60 rpm for Phase Angles Between 125° and 180°

Appendix Q   Thermal Experiment Torque Fluctuations

       This section presents the remaining figures for the torque and non-dimensional pressure fluctuations for the thermal experiments. Figures for a 120° phase angle are not reproduced.

Q.1 Swept Volume of 1.564 L

(a) 180°

(b) 175°

(c) 170°

(d) 165°

(e) 160°

(f) 155°

(g) 150°

(h) 145°

(i) 140°

(j) 135°

(k) 130°
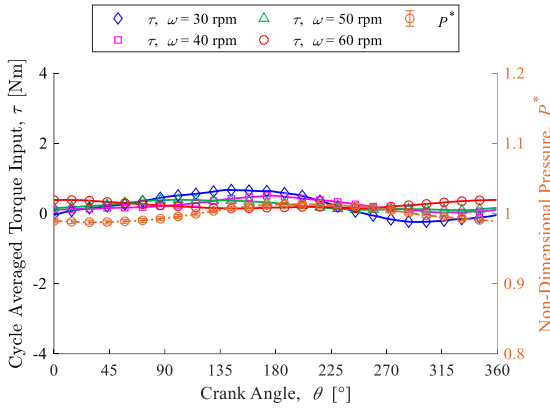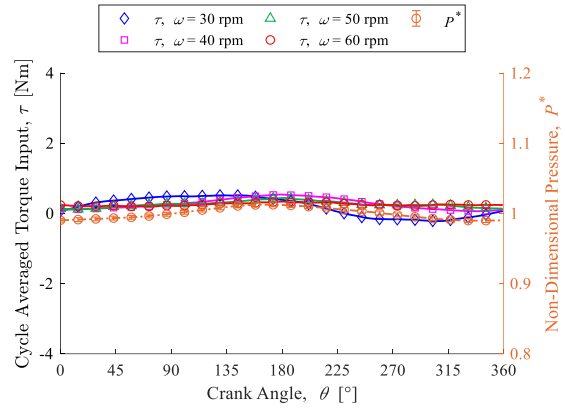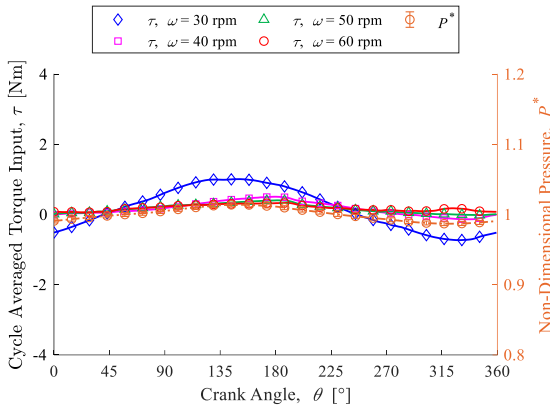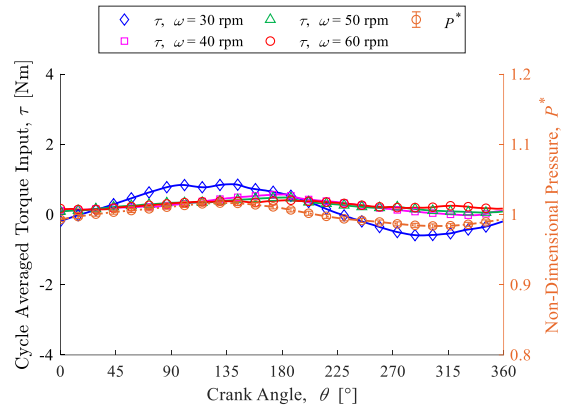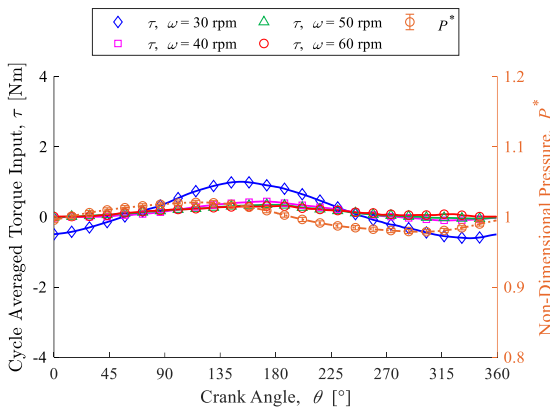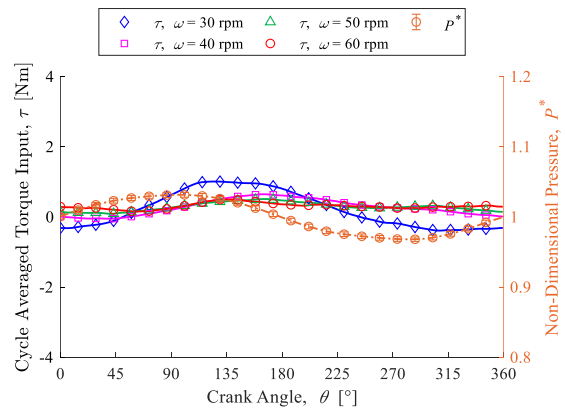
(l) 125°
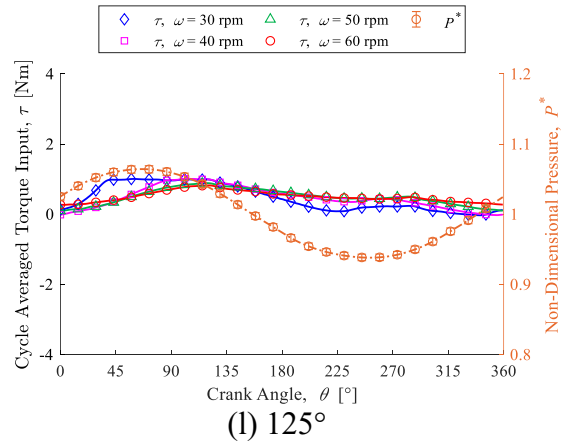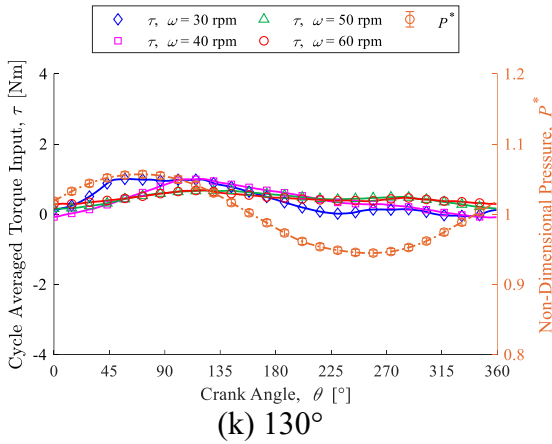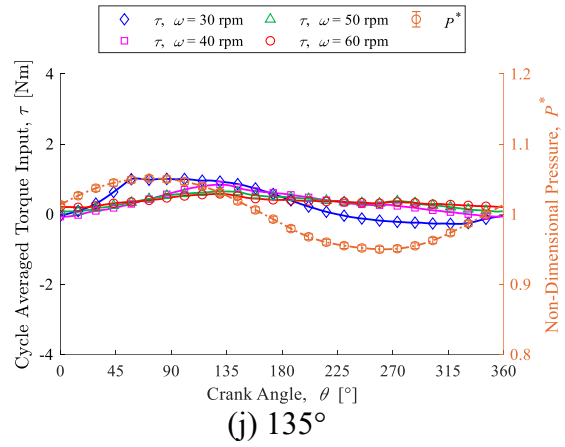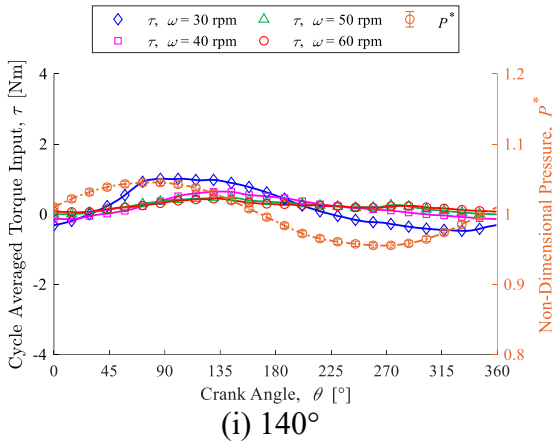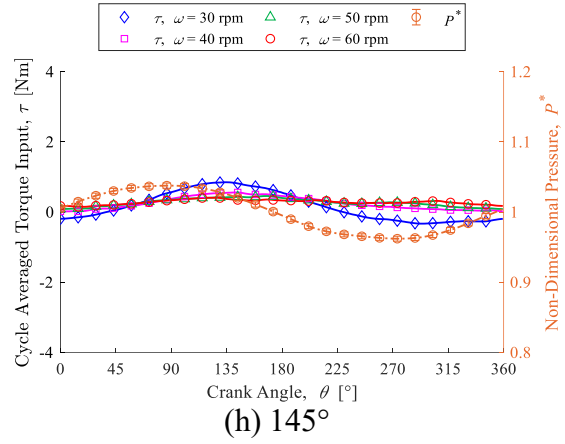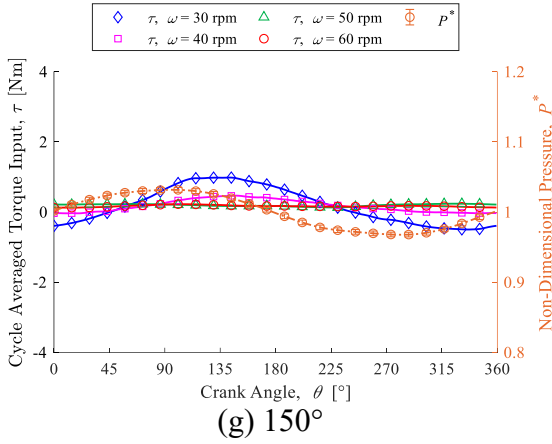
Figure Q–1: Thermal Experiment Torque and Non-Dimensional Pressure for a Swept Volume of 1.564 L for Phase Angles Between 125° and 180°

Q.2 Swept Volume of 1.955 L

(a) 180°

(b) 175°

(c) 170°

(d) 165°

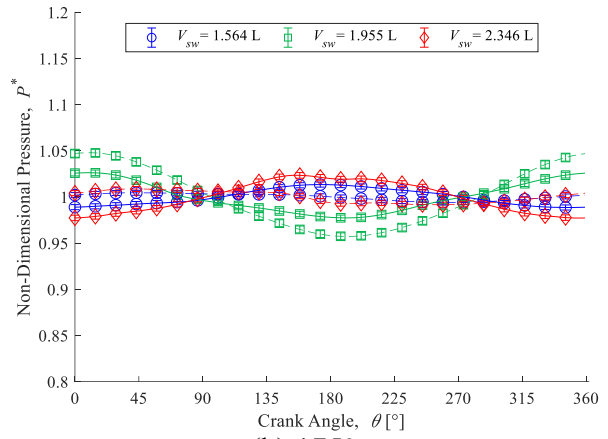(e) 160°

(f) 155°

(g) 150°

(h) 145°

(i) 140°

(j) 135°

(k) 130°

(l) 125°
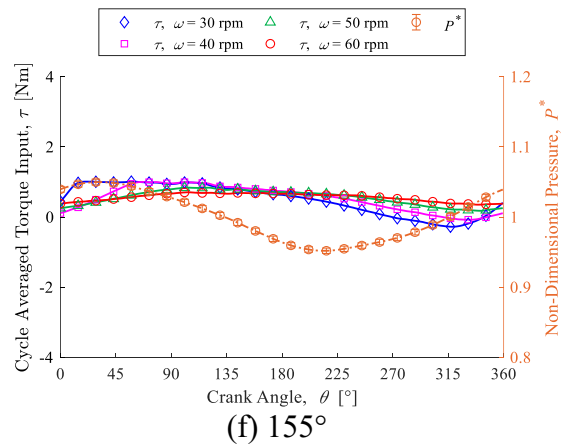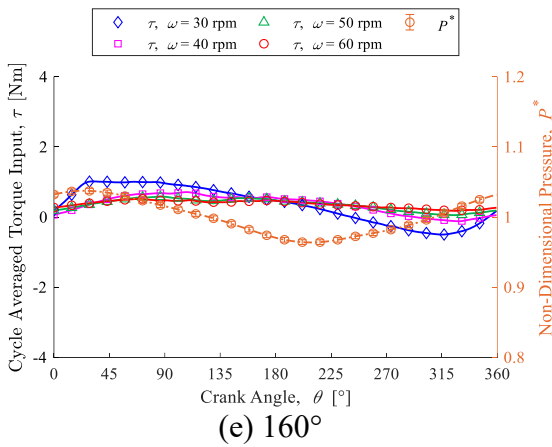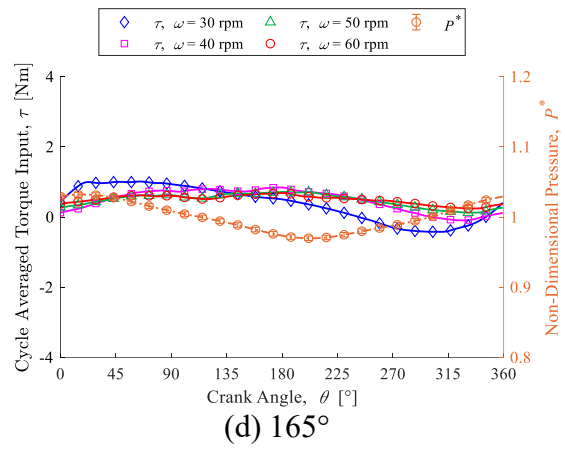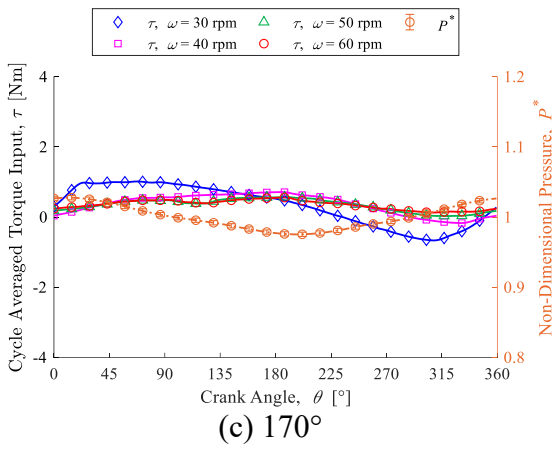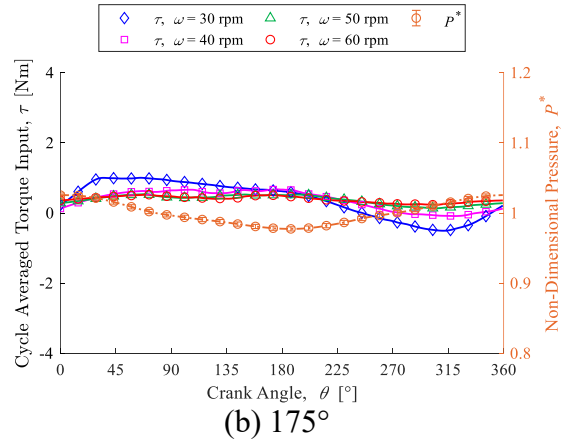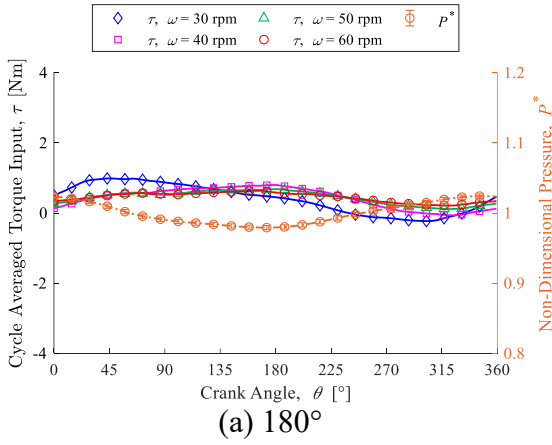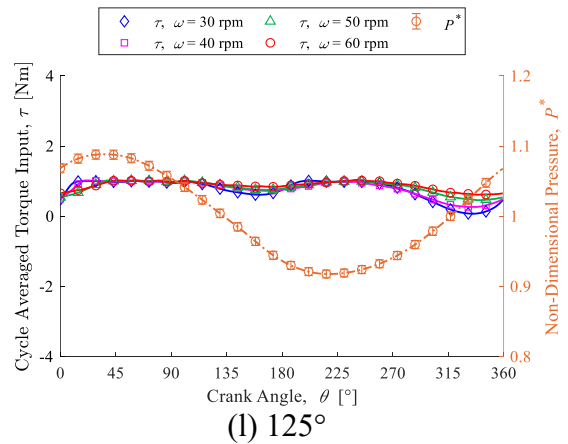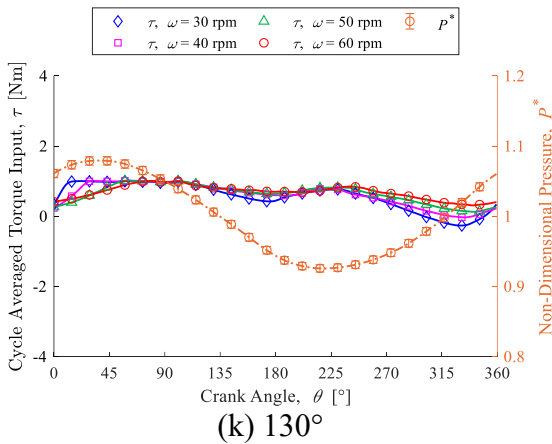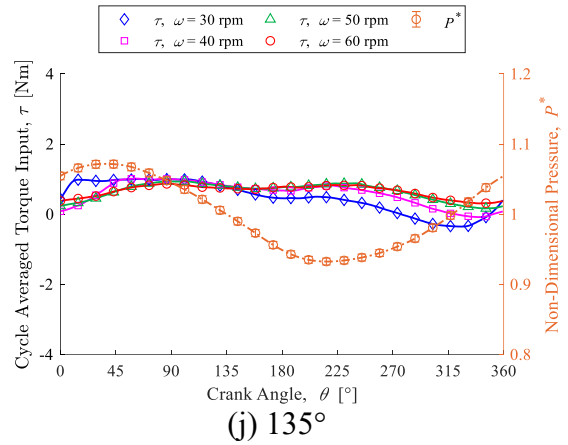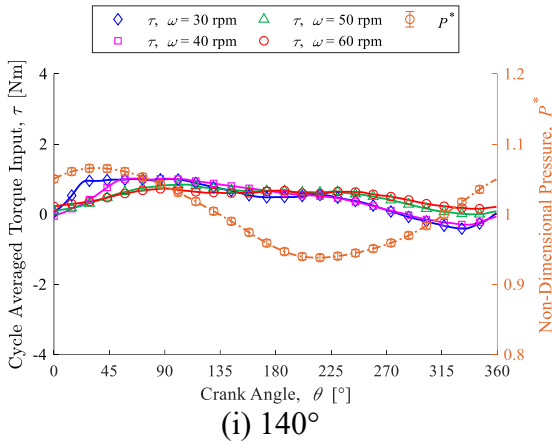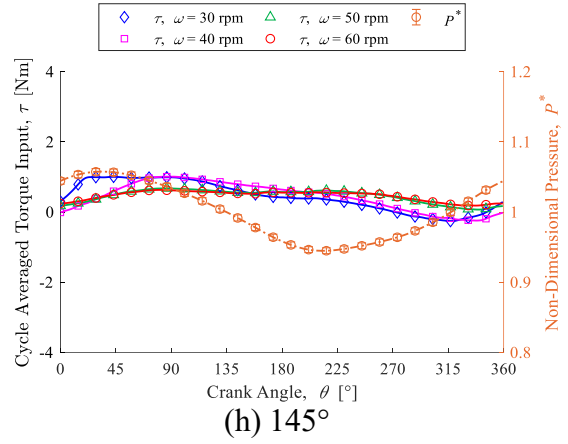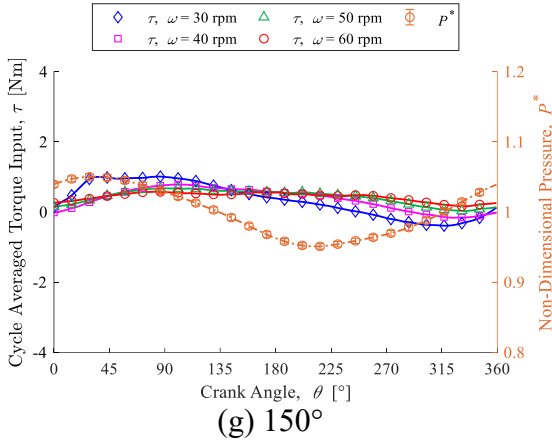
Figure Q–2: Thermal Experiment Torque and Non-Dimensional Pressure for a Swept Volume of 1.955 L for Phase Angles Between 125° and 180°

Q.3 Swept Volume of 2.346 L

(a) 180°

(b) 175°

(c) 170°

(d) 165°

(e) 160°

(f) 155°

(g) 150°

(h) 145°

(i) 140°

(j) 135°

(k) 130°

(l) 125°
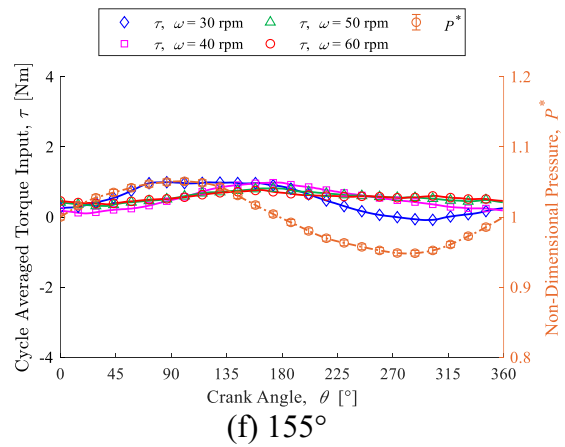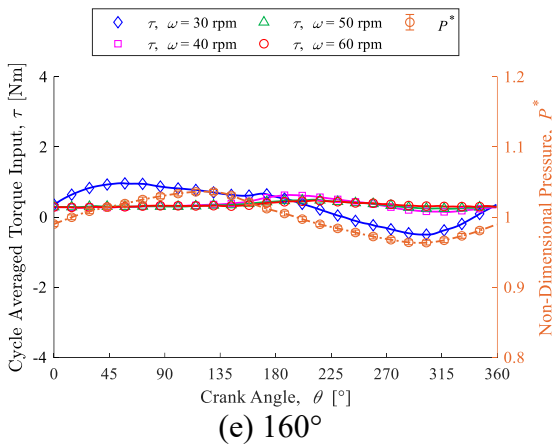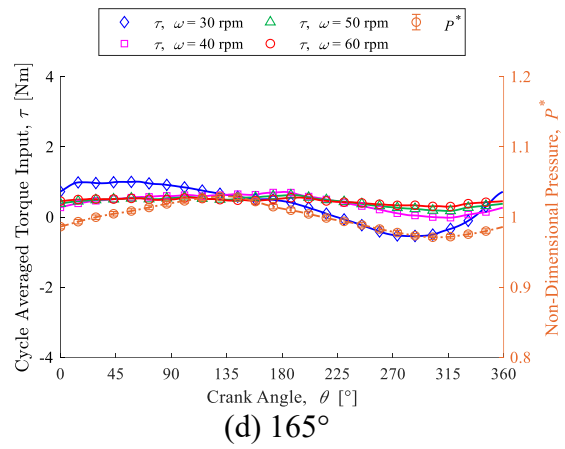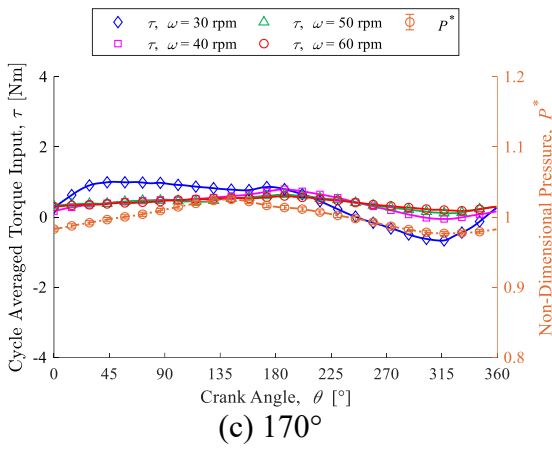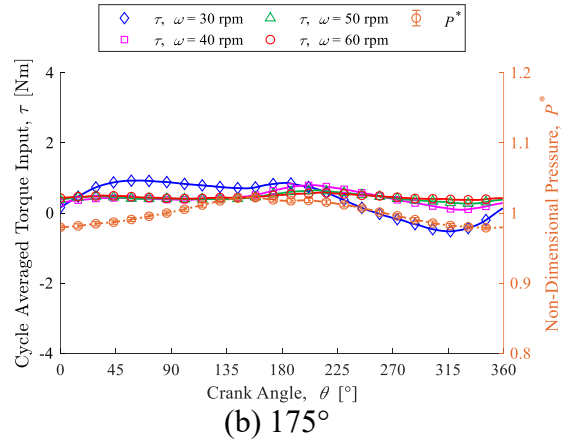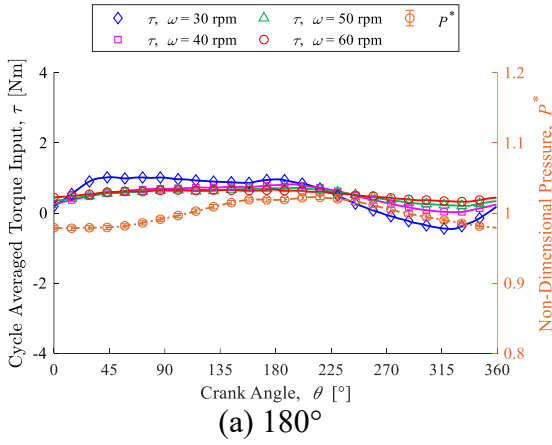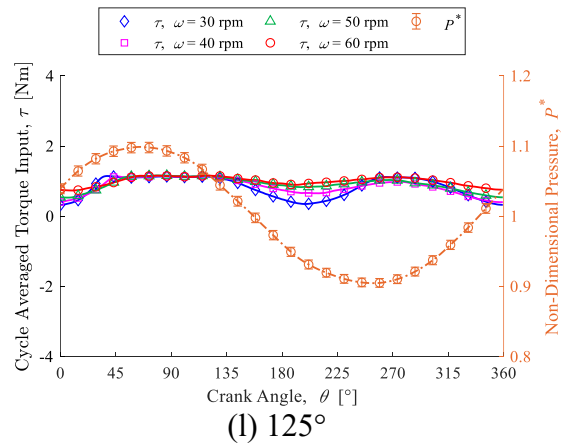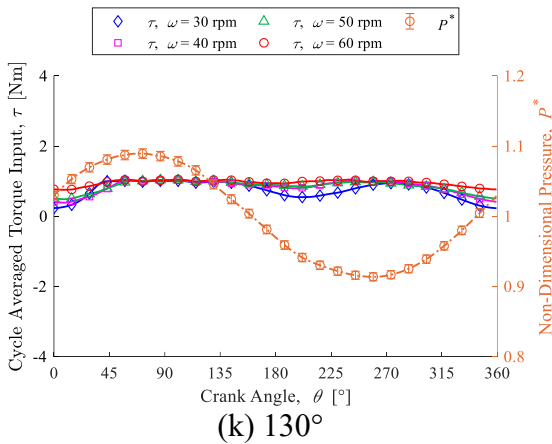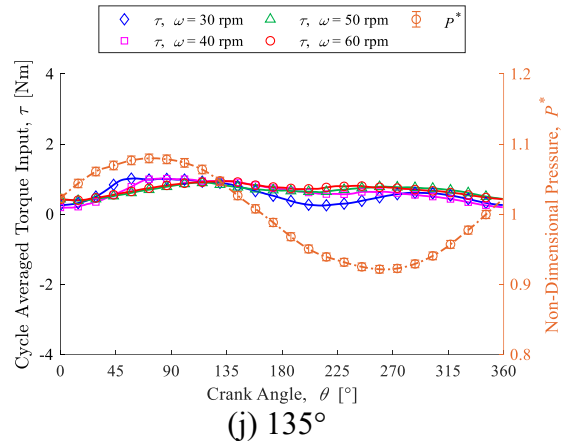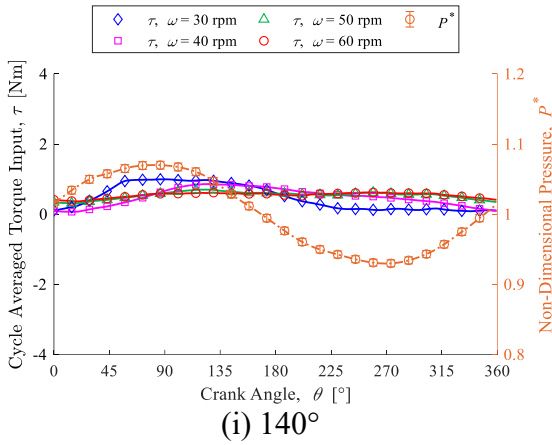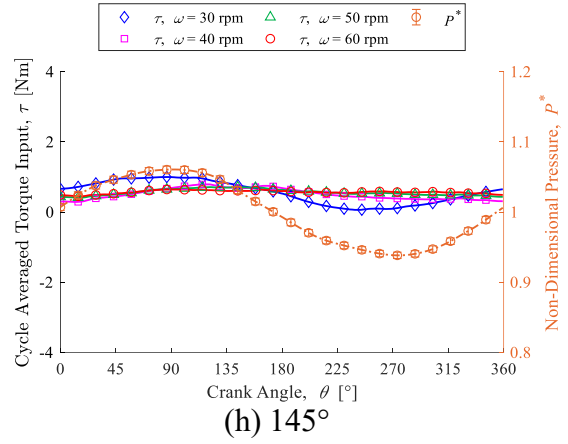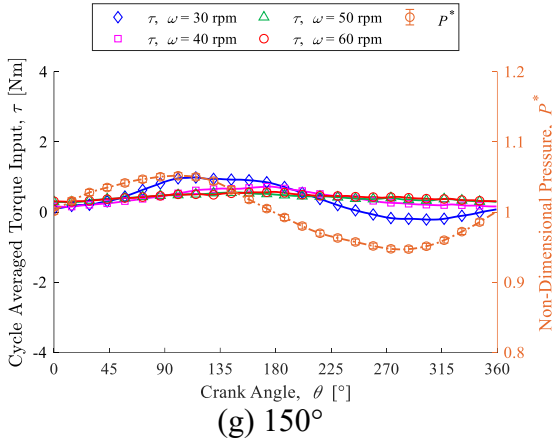
Figure Q–3: Thermal Experiment Torque and Non-Dimensional Pressure for a Swept Volume of 2.346 L for Phase Angles Between 125° and 180°

Appendix R   Thermal Experiment Individual Workspace Indicator Diagrams

This section first presents the calculated values of the indicated efficacious and forced work from the expansion space indicator diagrams in Table R–1, then presents the indicated efficacious and forced work from the compression space indicator diagrams in Table R–2. The individual expansion and compression space indicator diagrams will then be presented for each swept volume at 60 rpm, where the diagrams for a phase angle of 120° will not be reproduced here.

Table R–1: Calculated Expansion Space Indicated Efficacious and Forced Work

Phase Angle, α [°]	Efficacious Expansion Work, $W_{eff,1}$ [J]			Forced Expansion Work, $W_{f,1}$ [J]		
	V_{sw} =1.564L	V_{sw} =1.955L	V_{sw} =2.346L	V_{sw} =1.564L	V_{sw} =1.955L	V_{sw} =2.346L
180	0.28	0.88	0.84	1.44	2.30	3.02
175	0.67	1.46	1.78	0.78	1.38	1.67
170	1.16	2.42	2.88	0.34	0.79	0.72
165	1.86	3.59	4.80	0.12	0.59	0.33
160	2.88	5.16	6.92	0.03	0.45	0.06
155	4.85	7.99	11.53	0.00	0.40	0.01
150	4.89	8.21	11.67	0.00	0.40	0.00
145	5.88	9.64	13.81	0.00	0.43	0.00
140	7.04	11.13	16.25	0.00	0.52	0.01
135	7.69	12.38	17.99	0.00	0.49	0.01
130	8.47	13.79	19.78	0.01	0.52	0.03
125	9.40	14.95	21.74	0.03	0.66	0.06
120	10.32	16.29	23.24	0.06	0.83	0.14

Table R–2: Calculated Compression Space Indicated Efficacious and Forced Work

| Phase Angle, α [°]	Efficacious Compression Work, $W_{eff,2}$ [J]			Forced Compression Work, $W_{f,1}$ [J]		
	V_{sw} =1.564L	V_{sw} =1.955L	V_{sw} =2.346L	V_{sw} =1.564L	V_{sw} =1.955L	V_{sw} =2.346L
180	1.43	1.55	3.02	0.27	0.62	0.85
175	0.83	0.80	1.88	0.57	1.19	1.56
170	0.43	0.34	1.01	0.95	2.07	2.36
165	0.22	0.16	0.64	1.53	3.16	3.96
160	0.14	0.06	0.32	2.40	4.55	5.67
155	0.09	0.01	0.19	4.27	6.90	10.13
150	0.11	0.00	0.28	4.15	7.25	9.80
145	0.14	0.00	0.32	4.98	8.52	11.66
140	0.15	0.00	0.35	6.07	9.93	13.93
135	0.20	0.00	0.42	6.50	10.75	15.36
130	0.25	0.01	0.54	7.17	11.77	16.85
125	0.29	0.03	0.66	8.05	12.88	18.54
120	0.34	0.05	0.75	9.01	14.12	20.37

R.1 Swept Volume of 1.564 L
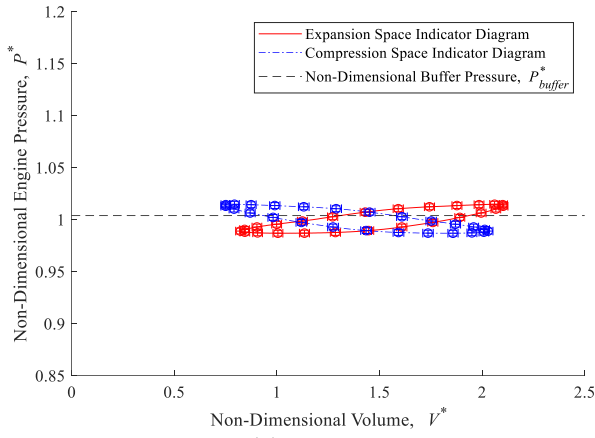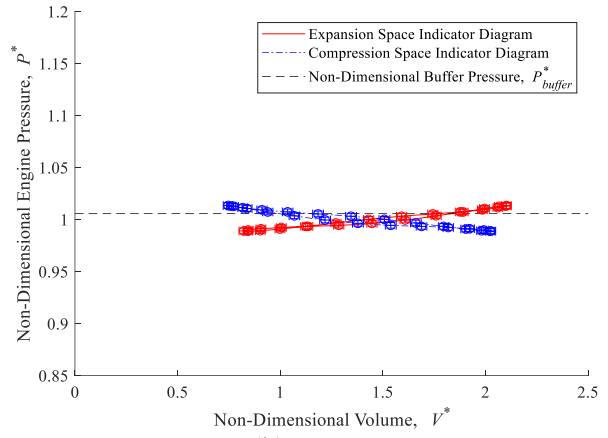
(a) 180°
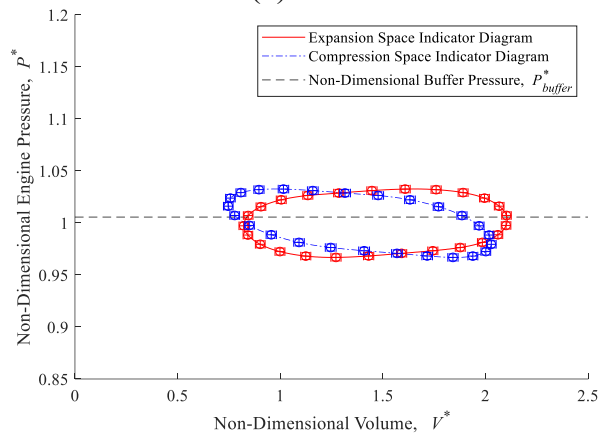
(b) 175°

(c) 170°

(d) 165°

(e) 160°

(f) 155°

Figure R–1: Expansion and Compression Space Indicator Diagrams for a Swept Volume of 1.546 L and Phase Angles Between 125° and 180° at 60 rpm

R.2 Swept Volume of 1.955 L

(a) 180°

(b) 175°

(c) 170°

(d) 165°

(e) 160°

(f) 155°

(g) 150°

(h) 145°

(i) 140°

(j) 135°

(k) 130°

(l) 125°

Figure R–2: Expansion and Compression Space Indicator Diagrams for a Swept Volume of 1.955 L and Phase Angles Between 125° and 180° at 60 rpm

293

R.3 Swept Volume of 2.346 L

(a) 180°

(b) 175°

(c) 170°

(d) 165°

(e) 160°

(f) 155°

(g) 150°

(h) 145°

(i) 140°

(j) 135°

(k) 130°
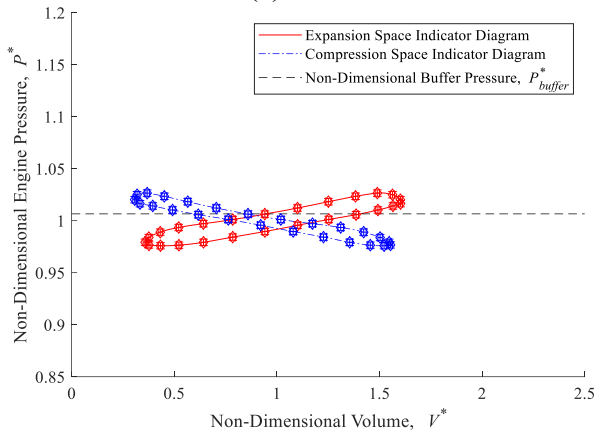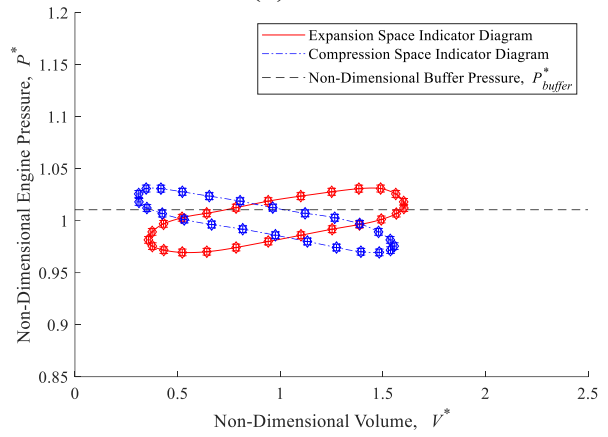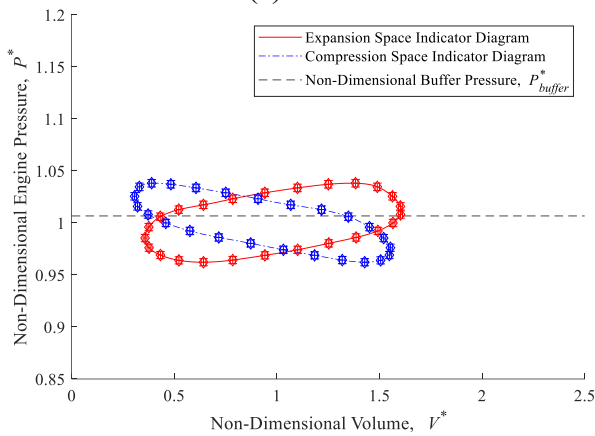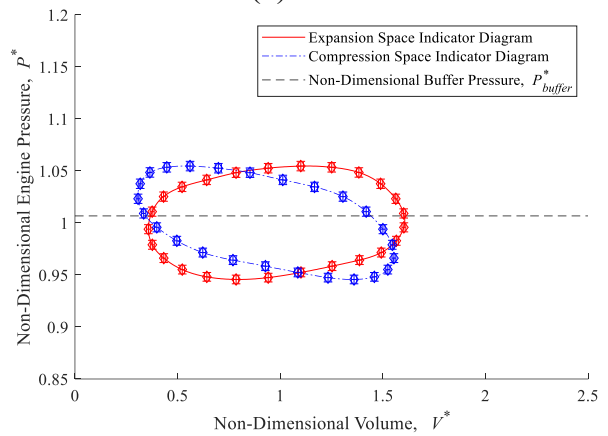
(l) 125°

Figure R–3: Expansion and Compression Space Indicator Diagrams for a Swept Volume of 2.346 L and Phase Angles Between 125° and 180° at 60 rpm

Appendix S   Thermal Non-Dimensional Indicator Diagrams

This section presents the remaining figures for the non-dimensional indicator diagrams for the thermal experiments at 60 rpm. Figures pertaining to a 120° phase angle are not reproduced.

(a) 180°

(b) 175°

(c) 170°
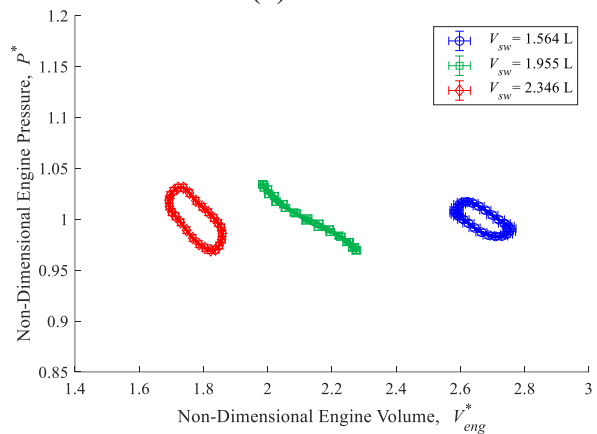
(d) 165°
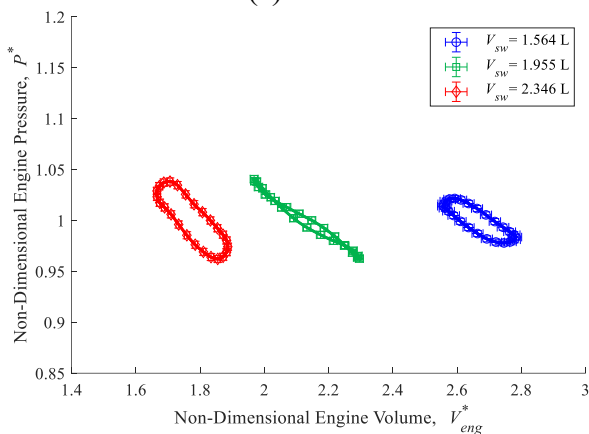
(e) 160°
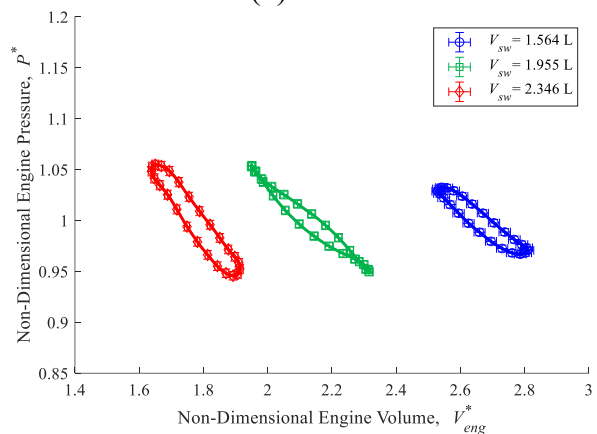
(f) 155°

(g) 150°

(h) 145°

(i) 140°
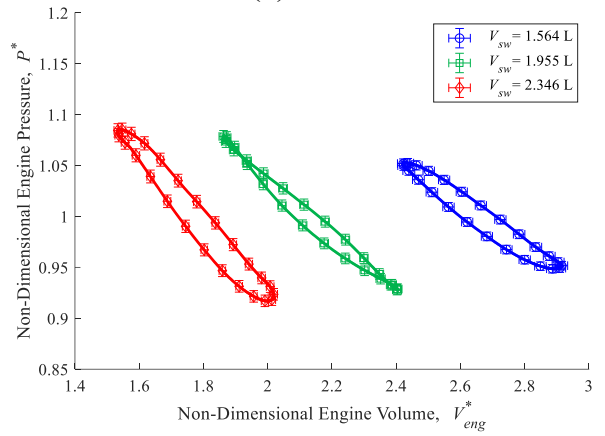
(j) 135°
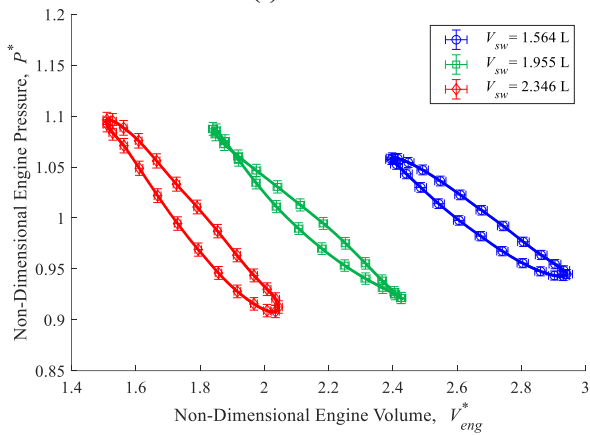
(k) 130°
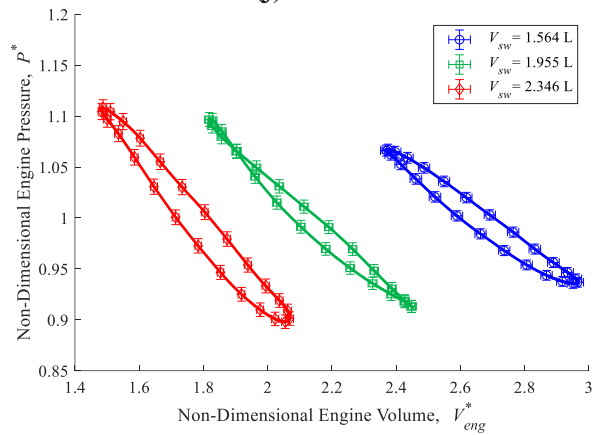
(l) 125°

Figure S–1: Thermal Experiment Non-Dimensional Indicator Diagrams at 60 rpm for Phase Angles Between 125° and 180°

Appendix T   Baseline and Thermal Experiment Pressure Fluctuation Comparison

This section presents the remaining figures for the baseline and thermal experiment comparison of pressure fluctuation. Figures pertaining to a 120° phase angle are not reproduced.

(a) 180°

(b) 175°

(c) 170°

(d) 165°

(e) 160°

(f) 155°

(g) 150°

(h) 145°

(i) 140°

(j) 135°

(k) 130°
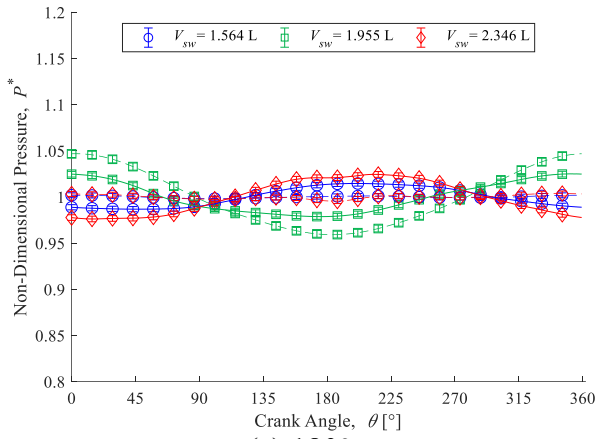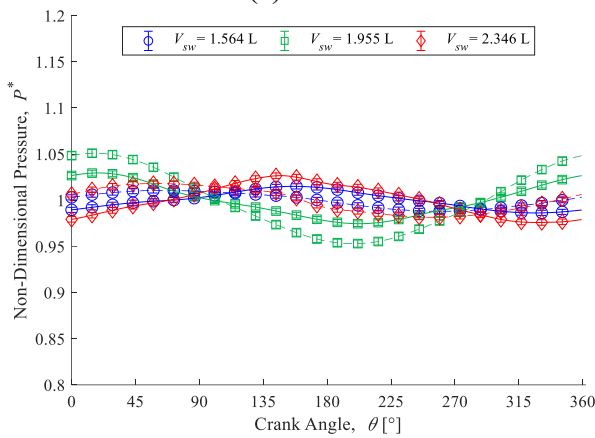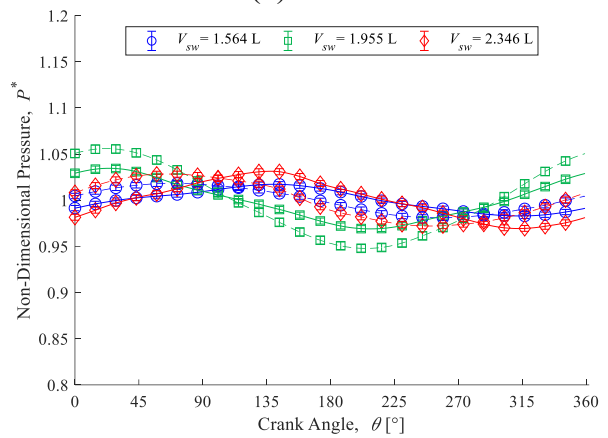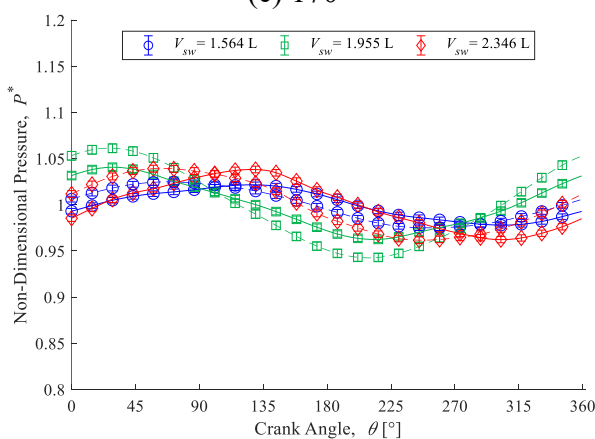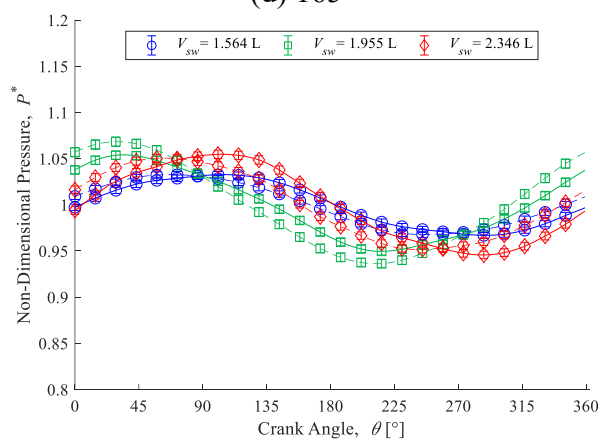
(l) 125°
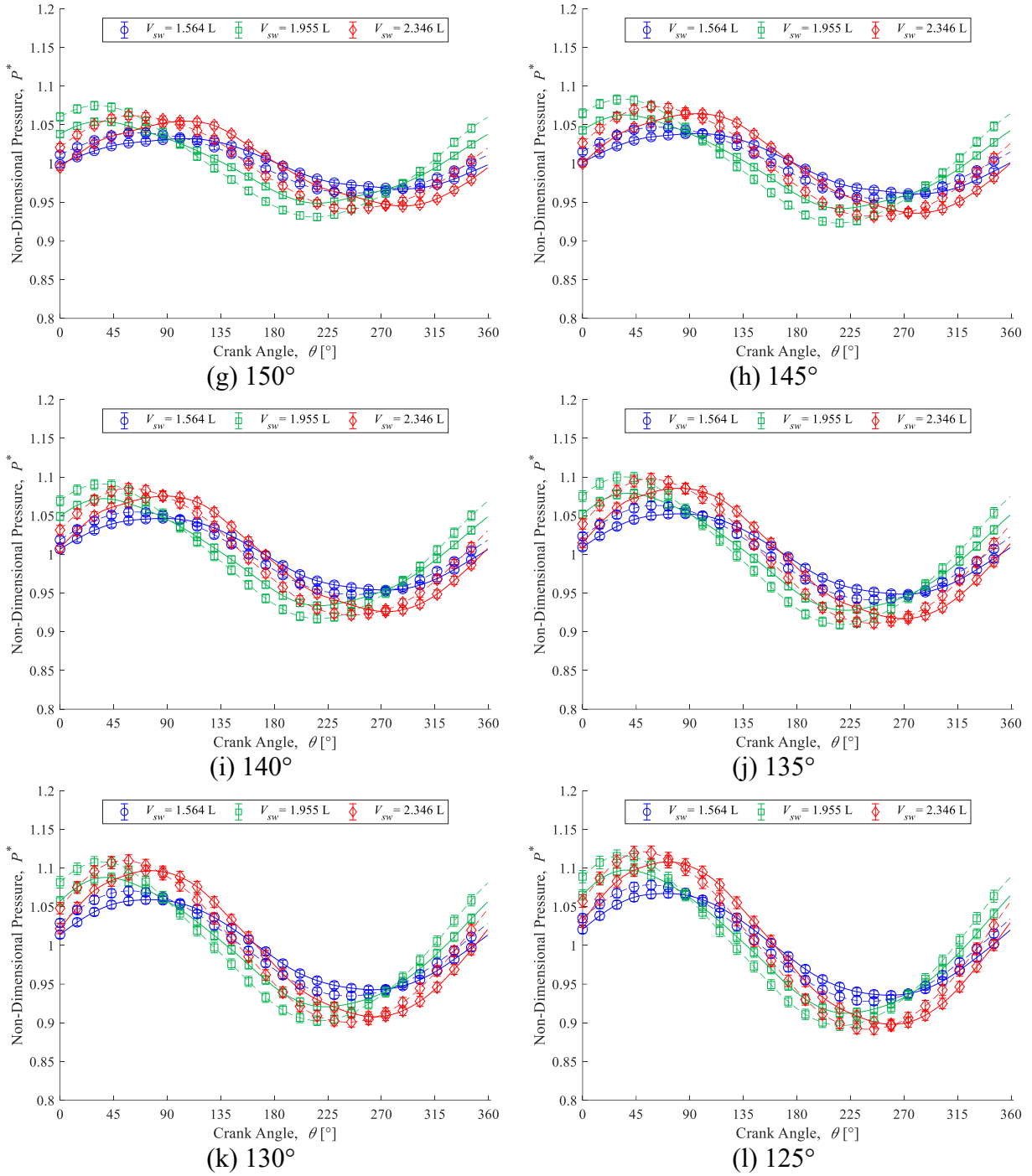
Figure T–1: Pressure Fluctuation Comparison for Each Swept Volume at 60 rpm Between Phase Angles of 125° and 180° (Solid Curves for Thermal Experiments, Dashed Curves for Baseline Experiments).

Appendix U Drawing Package

This section will present the CAD drawing package of the OPA MK III, which includes drawings with overall dimensions for the OPA MK III assembly, sub-assemblies, and important parts.

Notes:
Most fastners are omitted from drawing.
Bellows seals are not shown.
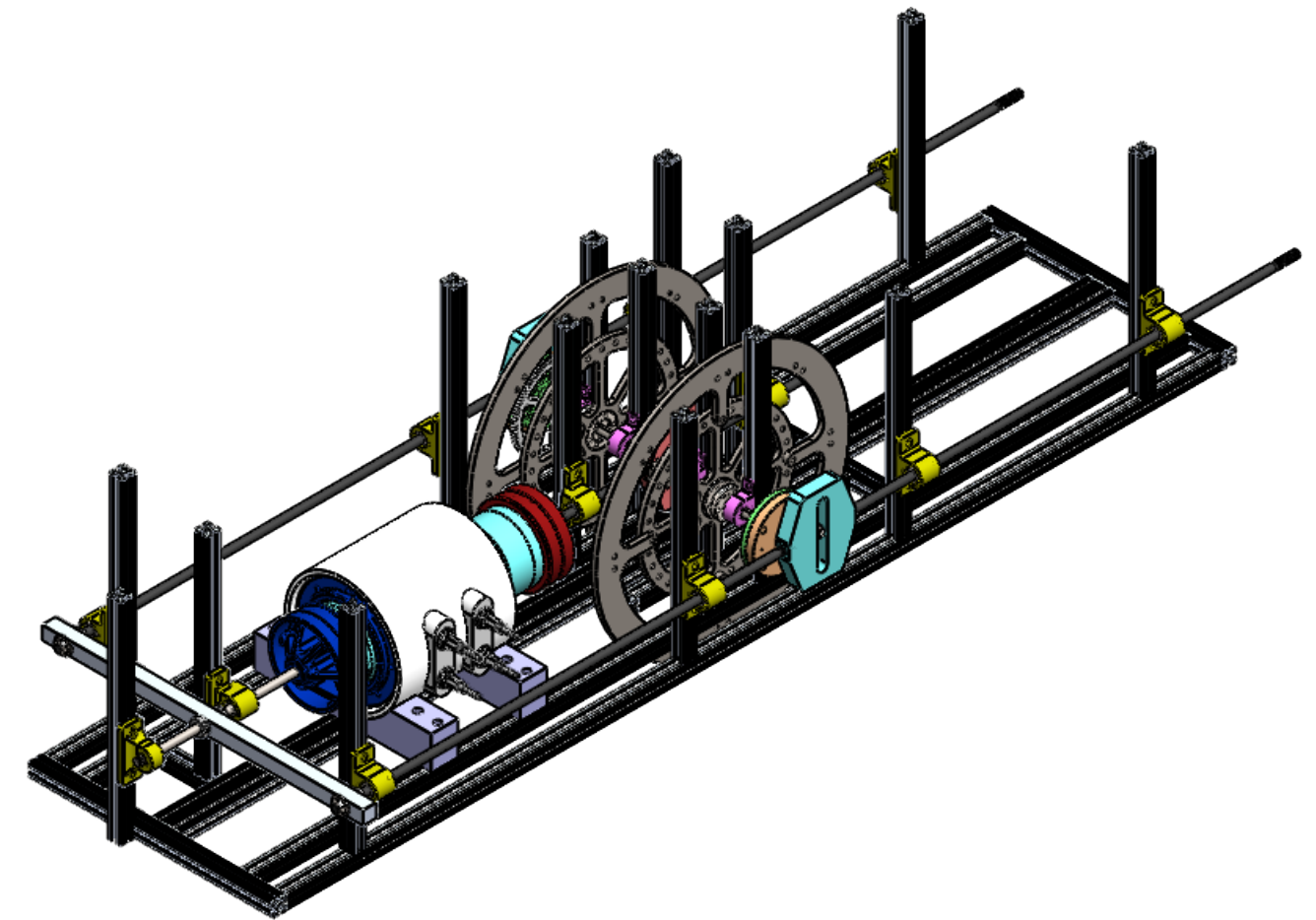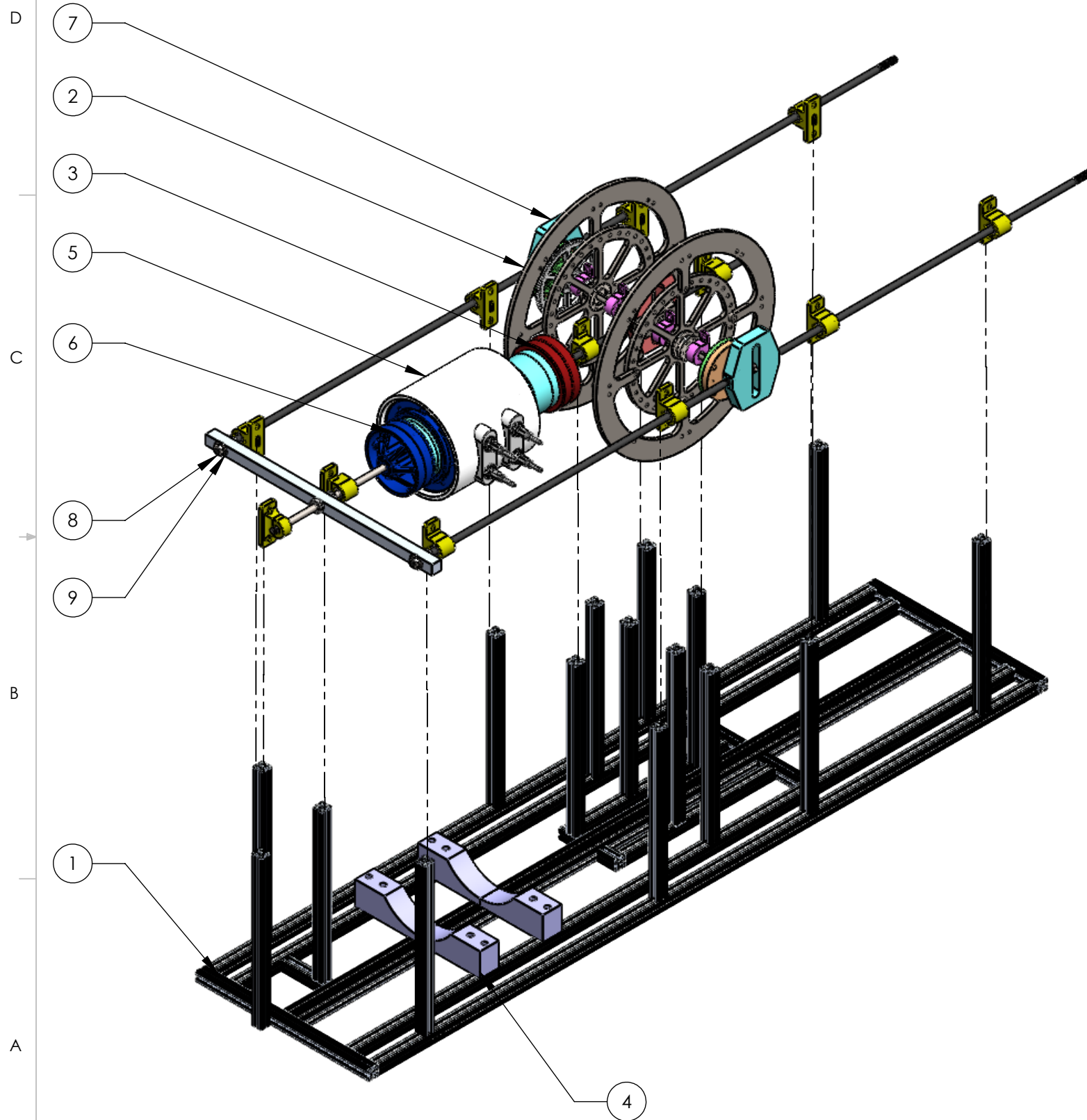
ITEM NO.	DESCRIPTION	Material	Frame/QTY.
1	Frame Assembly	N/A	1
2	Mechanism Assembly	N/A	1
3	Expansion Piston Assembly	N/A	1
4	Engine Body Cradle Assembly	N/A	2
5	Engine Body Assembly	N/A	1
6	Compression Piston Assembly	N/A	1
7	Compression Piston Yoke Mechanism Assembly	N/A	2
8	1/2"-13 Hex Nut	Stainless Steel	4
9	1/2" Washer	Stainless Steel	4

UNLESS OTHERWISE SPECIFIED:		NAME	The Department of Mechanical Engineering
DIMENSIONS ARE IN MM			UNIVERSITY OF ALBERTA
TOLERANCES: ANGULAR: ± 0.5°	DRAWN BY	Jason Michaud	
.X = ± 0.25	MODEL BY	Jason Michaud	TITLE:
.XX = ± 0.05	CHECKED BY		OPA MK III Assembly
SURFACE FINISH 0.6 μm	Comments:		
MATERIAL: N/A			

SIZE **B**	Project: **OPA MK III**	REV **B**

DO NOT SCALE DRAWING

December 11, 2019 7:59:59 PM
December 17, 2019 8:38:43 PM

SCALE: 1:10   Mass: 58955.58   Page: 301

A

A

SECTION A-A

Ø480

[16.75]
425.40

[15.75]
400

104.54

[73.00]
1854.20

[18.25]
463.55

[24.00]
609.60

UNLESS OTHERWISE SPECIFIED:		NAME	The Department of Mechanical Engineering UNIVERSITY OF ALBERTA
DIMENSIONS ARE IN MM TOLERANCES: ANGULAR: ± 0.5° .X = ± 0.25 .XX = ± 0.05	DRAWN BY	Jason Michaud	
	MODEL BY	Jason Michaud	TITLE:
	CHECKED BY		OPA MK III Assembly
SURFACE FINISH 0.6 μm	Comments:		
MATERIAL: N/A			

				SIZE **B**	Project: **OPA MK III**	REV **B**
DO NOT SCALE DRAWING		December 11, 2019 7:59:59 PM				
		December 17, 2019 8:38:43 PM		SCALE: 1:8	Mass: 58955.58	Page: 302

8 7 6 5 4 3 2 1

D C B A

Notes:
Most fastners are omitted from drawing.
Bellows seals are not shown.

ITEM NO.	DESCRIPTION	Material	No Frame/QTY.
1	Mechanism Assembly	N/A	1
2	Expansion Piston Assembly	N/A	1
3	Engine Body Assembly	N/A	1
4	Compression Piston Assembly	N/A	1
5	Compression Piston Yoke Mechanism Assembly	N/A	2
6	1/2"-13 Hex Nut	Stainless Steel	4
7	1/2" Washer	Stainless Steel	4

UNLESS OTHERWISE SPECIFIED:		NAME		The Department of Mechanical Engineering UNIVERSITY OF ALBERTA
DIMENSIONS ARE IN MM TOLERANCES: ANGULAR: ± 0.5° .X = ± 0.25 .XX = ± 0.05	DRAWN BY	Jason Michaud		
	MODEL BY	Jason Michaud		TITLE:
	CHECKED BY			OPA MK III Assembly
SURFACE FINISH 0.6 μm	Comments:			
MATERIAL: N/A				

SURFACE FINISH 0.6 μm

MATERIAL: N/A

DO NOT SCALE DRAWING

December 11, 2019 7:59:59 PM
December 17, 2019 8:38:43 PM

SIZE **B**

Project: **OPA MK III**

REV **B**

SCALE: 1:8   Mass: 39206.88   Page: 303

B

B

SECTION B-B

74.27   1.97

C

C

SECTION C-C

1.93   78.17

UNLESS OTHERWISE SPECIFIED:		NAME	The Department of Mechanical Engineering
DIMENSIONS ARE IN MM			UNIVERSITY OF ALBERTA
TOLERANCES:	DRAWN BY	Jason Michaud	
ANGULAR: ± 0.5°	MODEL BY	Jason Michaud	TITLE:
.X = ± 0.25			Swept Volume 1.564L
.XX = ± 0.05	CHECKED BY		180° Phase Angle Clearance
SURFACE FINISH 0.6 μm	Comments:		Volumes
MATERIAL:	Section B-B: Minimum Expansion Space Volume		
N/A	Section C-C: Maximum Expansion Space Volume		

SURFACE FINISH 0.6 μm

MATERIAL: N/A

Comments:
Section B-B: Minimum Expansion Space Volume
Section C-C: Maximum Expansion Space Volume

DO NOT SCALE DRAWING

January 18, 2018 10:22:50 AM
December 17, 2019 9:31:53 PM

TITLE:
Swept Volume 1.564L
180° Phase Angle Clearance
Volumes

SIZE	Project:	REV
B	OPA MK III	B

SCALE: 1:8   Mass: 59705.65   Page: 304

SECTION D-D

61.57   14.67

SECTION E-E

10.77   65.47

UNLESS OTHERWISE SPECIFIED:		NAME		The Department of Mechanical Engineering
DIMENSIONS ARE IN MM TOLERANCES: ANGULAR: ± 0.5° .X = ± 0.25 .XX = ± 0.05	DRAWN BY	Jason Michaud		UNIVERSITY OF ALBERTA
	MODEL BY	Jason Michaud		TITLE: Swept Volume 2.346L 180° Phase Angle Clearance Volumes
	CHECKED BY			
SURFACE FINISH 0.6 μm	Comments: Section D-D: Minimum Expansion Space Volume Section E-E: Maximum Expansion Space Volume			
MATERIAL: N/A				SIZE **B**	Project: **OPA MK III**	REV **B**
DO NOT SCALE DRAWING	January 18, 2018 10:22:50 AM December 17, 2019 9:31:53 PM			
			SCALE: 1:8	Mass: 59705.65	Page: 305

SECTION F-F

61.57   1.97

SECTION G-G

10.77   78.17

UNLESS OTHERWISE SPECIFIED:		NAME	The Department of Mechanical Engineering UNIVERSITY OF ALBERTA		
DIMENSIONS ARE IN MM TOLERANCES: ANGULAR: ± 0.5° .X = ± 0.25 .XX = ± 0.05	DRAWN BY	Jason Michaud	TITLE: Swept Volume 1.955L 180° Phase Angle Clearance Volumes		
	MODEL BY	Jason Michaud			
	CHECKED BY				
SURFACE FINISH 0.6 μm MATERIAL: N/A	Comments: Section F-F: Minimum Expansion Space Volume Section G-G: Maximum Expansion Space Volume		SIZE B	Project: OPA MK III	REV B
DO NOT SCALE DRAWING	January 18, 2018 10:22:50 AM December 17, 2019 9:31:53 PM		SCALE: 1:8	Mass: 59705.65	Page: 306

Notes:

Most fastners are omitted from drawing.

Bellows seals are not shown.

ITEM NO.	DESCRIPTION	Material	QTY.
1	CPVC Size 8 Pipe	CPVC	1
2	Heat Exchanger Housing	ABS	2
3	Heat Exchanger - Heater	N/A	1
4	Workspace Cylinder	ABS	2
5	1/8" NPT Threaded Pipe, 2" Length	Copper	4
6	1/4" Hose Barbed Fitting to 1/8" NPT Female Thread	Steel	4
7	Silicone Thermocouple Spacing Gasket	Silicone	2
8	Heat Exchanger - Cooler	N/A	1
9	Regenerator Housing	ABS	1
10	Workspace Outer Sealing Cap	ABS	2
11	Heat Exchanger Inlet/Outlet Port	Clear Resin	2
12	Inlet/Outlet Port Sealing Cap	Clear Resin	4

UNLESS OTHERWISE SPECIFIED:

DIMENSIONS ARE IN MM
TOLERANCES:
ANGULAR: ± 0.5°
.X = ± 0.25
.XX = ± 0.05

SURFACE FINISH 0.6 μm

MATERIAL:
N/A

DO NOT SCALE DRAWING

	NAME	
DRAWN BY	Jason Michaud	
MODEL BY	Jason Michaud	
CHECKED BY		

Comments:

January 5, 2018 3:27:44 PM
December 16, 2019 3:45:25 PM

The Department of Mechanical Engineering
UNIVERSITY OF ALBERTA

TITLE:
Engine Body Assembly

SIZE **B**

Project: **OPA MK III**

REV **B**

SCALE: 1:8   Mass: 11722.43   Page: 307

SECTION H-H

H

H

Ø193.68
Ø219.08
Ø130

116.23
103.78
43.78
42.19
32.19

A

119.54
68.11

A

55.08
93.18
127.18
220

UNLESS OTHERWISE SPECIFIED:		NAME	The Department of Mechanical Engineering UNIVERSITY OF ALBERTA		
DIMENSIONS ARE IN MM TOLERANCES: ANGULAR: ± 0.5° .X = ± 0.25 .XX = ± 0.05	DRAWN BY	Jason Michaud	TITLE: Engine Body Assembly		
	MODEL BY	Jason Michaud			
	CHECKED BY				
SURFACE FINISH 0.6 µm	Comments:		SIZE B	Project: OPA MK III	REV B
MATERIAL: N/A					
DO NOT SCALE DRAWING	January 5, 2018 3:27:44 PM December 16, 2019 3:45:25 PM		SCALE: 1:3	Mass: 11722.43	Page: 308

Notes:
Most fastners are omitted from drawing.
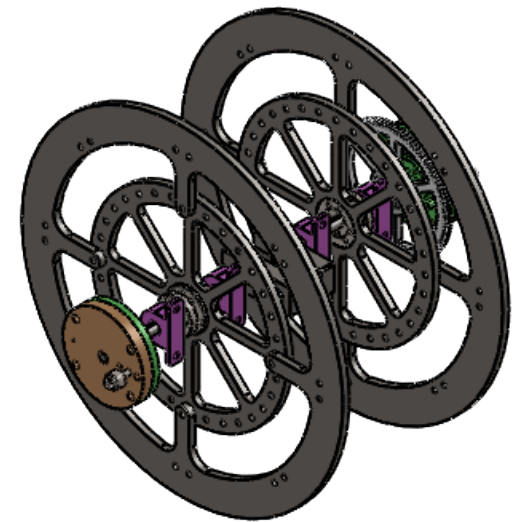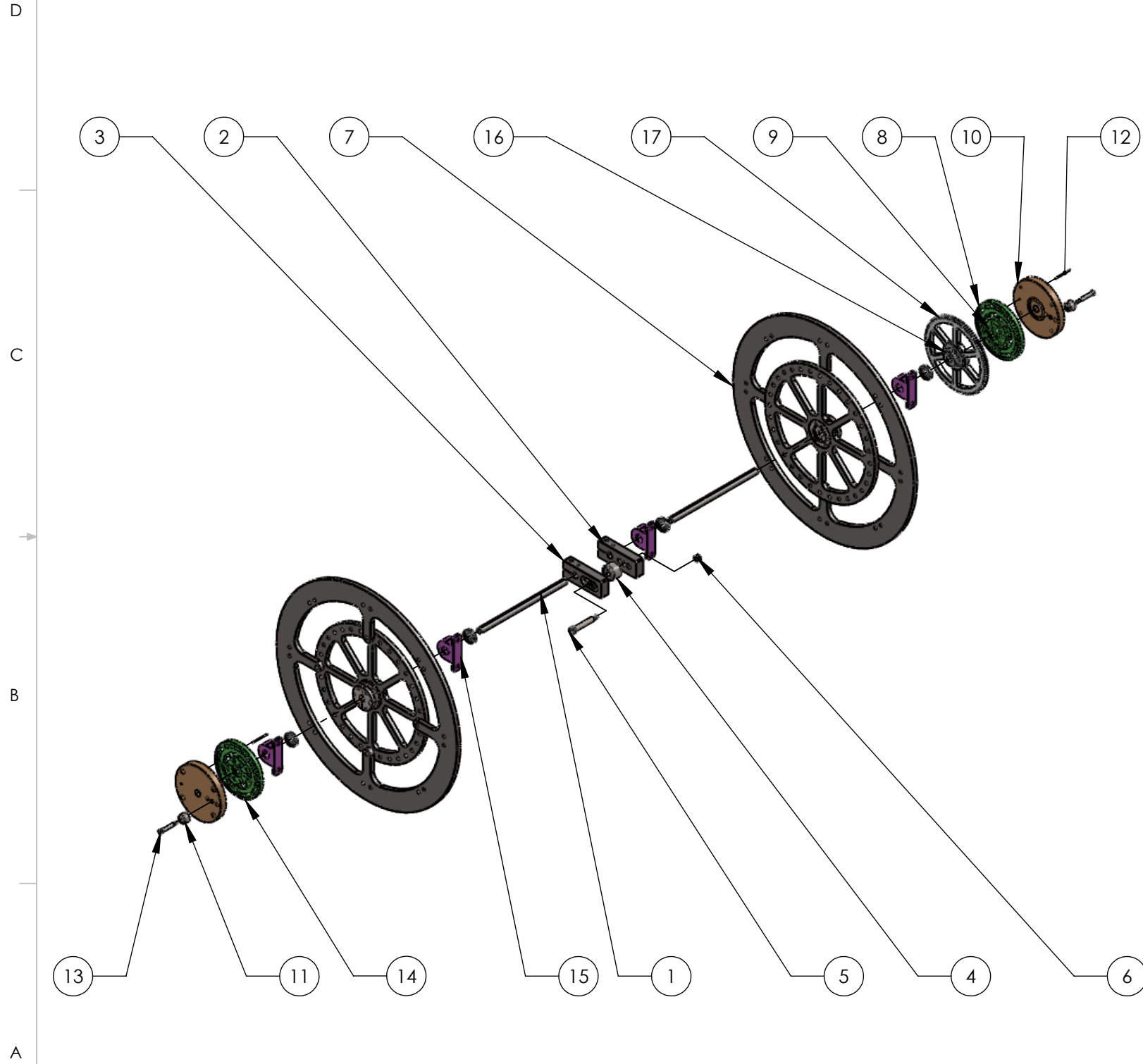
ITEM NO.	DESCRIPTION	Material	QTY.
1	1/2" Crank Shaft	AISI 1045 Steel, cold drawn	2
2	Expansion Piston Crank Arm#1	AISI 1020 Steel, Cold Rolled	1
3	Expansion Piston Crank Arm #2	AISI 1020 Steel, Cold Rolled	1
4	1.25" Diameter Track Roller Bearing, 3/8" Shaft	Alloy Steel	1
5	3/8" Diameter Shoulder Screw	Alloy Steel	1
6	5/16-18" Hex Nut	Alloy Steel (SS)	1
7	Flywheel Assembly	N/A	2
8	Compression Piston Variable Phase Angle Wheel #1	ABS	1
9	Phase Angle Wheel Hub	CLEAR RESIN (POSTCURED)	2
10	Compression Piston Variable Stroke Crank	ABS	2
11	3/4" Diameter Track Roller Bearing, 1/4" Shaft	Alloy Steel	2
12	2 mm Dowel Pin	Alloy Steel (SS)	2
13	1/4" Diameter Shoulder Screw	Alloy Steel	2
14	Compression Piston Variable Phase Angle Wheel #2	ABS	1
15	Ball Bearing Assembly	N/A	4
16	Spur Gear Hub	CLEAR RESIN (POSTCURED)	1
17	100 Tooth Spur Gear	ABS	1

UNLESS OTHERWISE SPECIFIED:		NAME	The Department of Mechanical Engineering
DIMENSIONS ARE IN MM			UNIVERSITY OF ALBERTA
TOLERANCES:	DRAWN BY	Jason Michaud	
ANGULAR: ± 0.5°	MODEL BY	Jason Michaud	TITLE:
.X = ± 0.25			Mechanism Assembly
.XX = ± 0.05	CHECKED BY		
SURFACE FINISH 0.6 μm	Comments:		
MATERIAL: N/A			

SIZE **B** Project: **OPA MK III** REV B

SCALE: 1:10   Mass: 17801.06   Page: 309

January 18, 2018 3:48:49 PM
December 17, 2019 8:36:12 PM

DO NOT SCALE DRAWING

Notes:
Most fastners are omitted from drawing.

[9.00]
228.60

168.57

106.36

97.49

76.49

24.03

⌀292.10

⌀480

27.9

43.50

485.14

548.21

UNLESS OTHERWISE SPECIFIED:		NAME	The Department of Mechanical Engineering UNIVERSITY OF ALBERTA
DIMENSIONS ARE IN MM TOLERANCES: ANGULAR: ± 0.5° .X = ± 0.25 .XX = ± 0.05	DRAWN BY	Jason Michaud	TITLE: Mechanism Assembly
	MODEL BY	Jason Michaud	
	CHECKED BY		
SURFACE FINISH 0.6 μm	Comments:		
MATERIAL: N/A			
DO NOT SCALE DRAWING			SIZE **B** · Project: **OPA MK III** · REV **B**
	January 18, 2018 3:48:49 PM December 17, 2019 8:36:12 PM		SCALE: 1:4 · Mass: 17801.06 · Page: 310

ITEM NO.	DESCRIPTION	Material	QTY.
1	Weld-on Bushing	Alloy Steel	1
2	1/2" Shaft Coupling	Alloy Steel	1
3	Flyhweel Assembly	ASTM A36 Steel	1

UNLESS OTHERWISE SPECIFIED:		NAME	The Department of Mechanical Engineering
DIMENSIONS ARE IN MM			UNIVERSITY OF ALBERTA
TOLERANCES:	DRAWN BY	Jason Michaud	
ANGULAR: ± 0.5°	MODEL BY	Jason Michaud	TITLE:
.X = ± 0.25			
.XX = ± 0.05	CHECKED BY		Flyhweel Assembly

SURFACE FINISH 0.6 µm

MATERIAL: N/A

Comments:

DO NOT SCALE DRAWING

June 5, 2017 9:18:01 AM
December 16, 2019 7:26:18 PM

SIZE	Project:	REV
B	OPA MK III	B

SCALE: 1:3   Mass: 7718.27   Page: 311

Ø 6.15 X 20 THRU
Ø 480
Ø 292.10
R195
R121.05
Ø 6.60 X 32 THRU
Ø 57.15

[0.375]
9.53
[0.375]
9.53
31
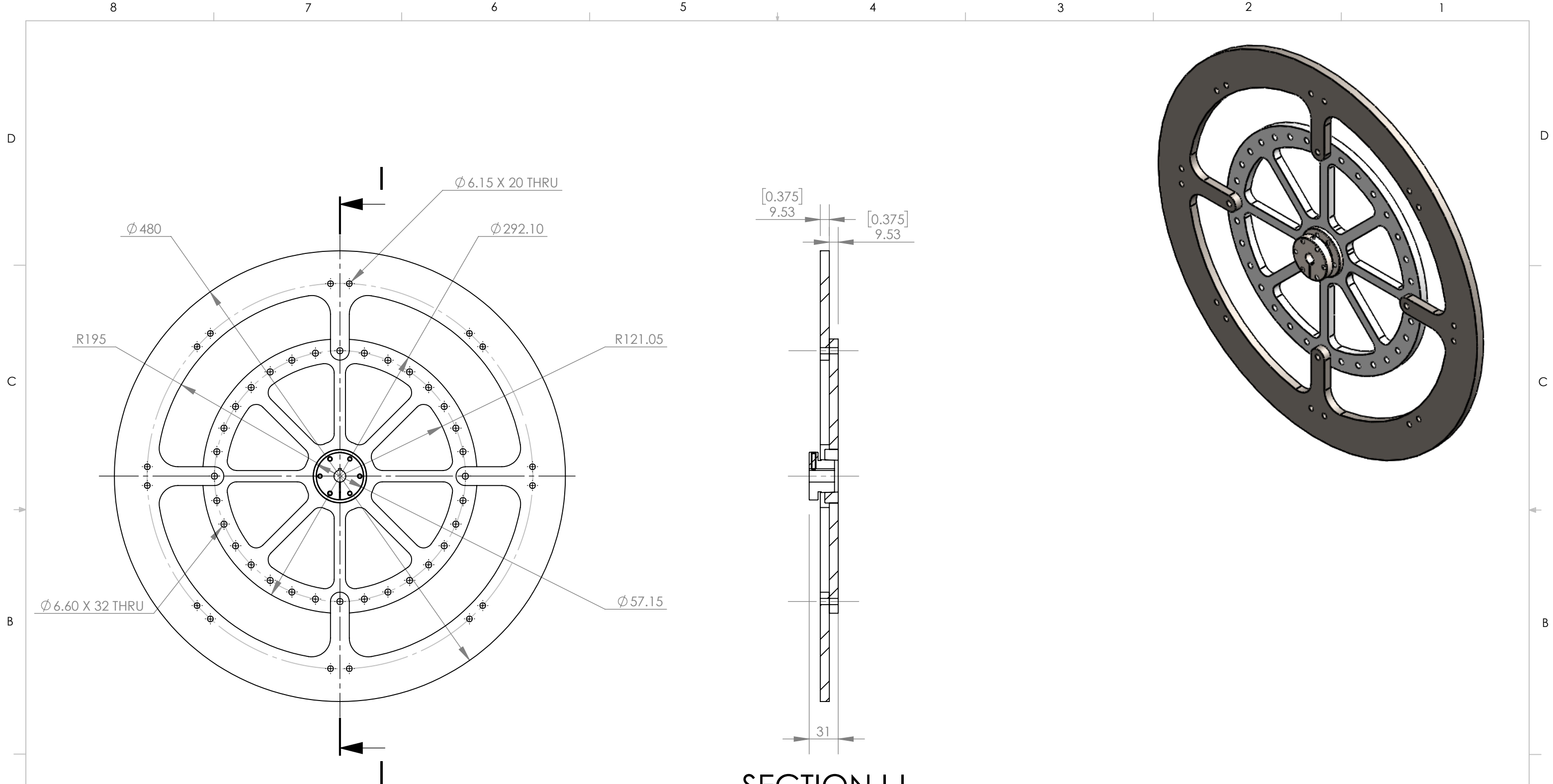
SECTION I-I

UNLESS OTHERWISE SPECIFIED:		NAME	The Department of Mechanical Engineering
DIMENSIONS ARE IN MM			UNIVERSITY OF ALBERTA
TOLERANCES: ANGULAR: ± 0.5°	DRAWN BY	Jason Michaud	
.X = ± 0.25	MODEL BY	Jason Michaud	TITLE:
.XX = ± 0.05	CHECKED BY		Flyhweel Assembly
SURFACE FINISH 0.6 μm	Comments:		
MATERIAL: N/A			

SURFACE FINISH 0.6 μm

MATERIAL: N/A

DO NOT SCALE DRAWING

June 5, 2017 9:18:01 AM
December 16, 2019 7:26:18 PM

SIZE	Project:		REV
B	OPA MK III		B

SCALE: 1:4 | Mass: 7718.27 | Page: 312

Ø 120

Ø 4.50 THRU
⌴ Ø 9 ▽ 10

Ø 2.38 THRU

Ø 120

Ø 13

[2.00]
Ø 50.80

[3.00]
Ø 76.20

[4.00]
Ø 101.60

Ø 88.90

Ø 6.76 X 3 THRU

J

J

14.50

SECTION J-J

3.90

8.90

K

5°

⌀120

Ø 2.40 X 19 THRU

7.50 ⊻ 3

⌀ 24.80

R47.42

R3.38 THRU

Ø 4.50 X 6 THRU

164°

37°

K

9.53

SECTION K-K

UNLESS OTHERWISE SPECIFIED:		NAME	The Department of Mechanical Engineering UNIVERSITY OF ALBERTA
DIMENSIONS ARE IN MM TOLERANCES: ANGULAR: ± 0.5° .X = ± 0.25 .XX = ± 0.05	DRAWN BY	Jason Michaud	TITLE: Variable Phase Angle Wheel
	MODEL BY	Jason Michaud	
	CHECKED BY		
SURFACE FINISH 0.6 μm	Comments:		
MATERIAL: ABS			

DO NOT SCALE DRAWING

January 18, 2018 11:47:16 AM
December 17, 2019 8:48:46 PM

SIZE
B

Project:
OPA MK III

REV
B

SCALE: 1:1   Mass: 66.17   Page: 314
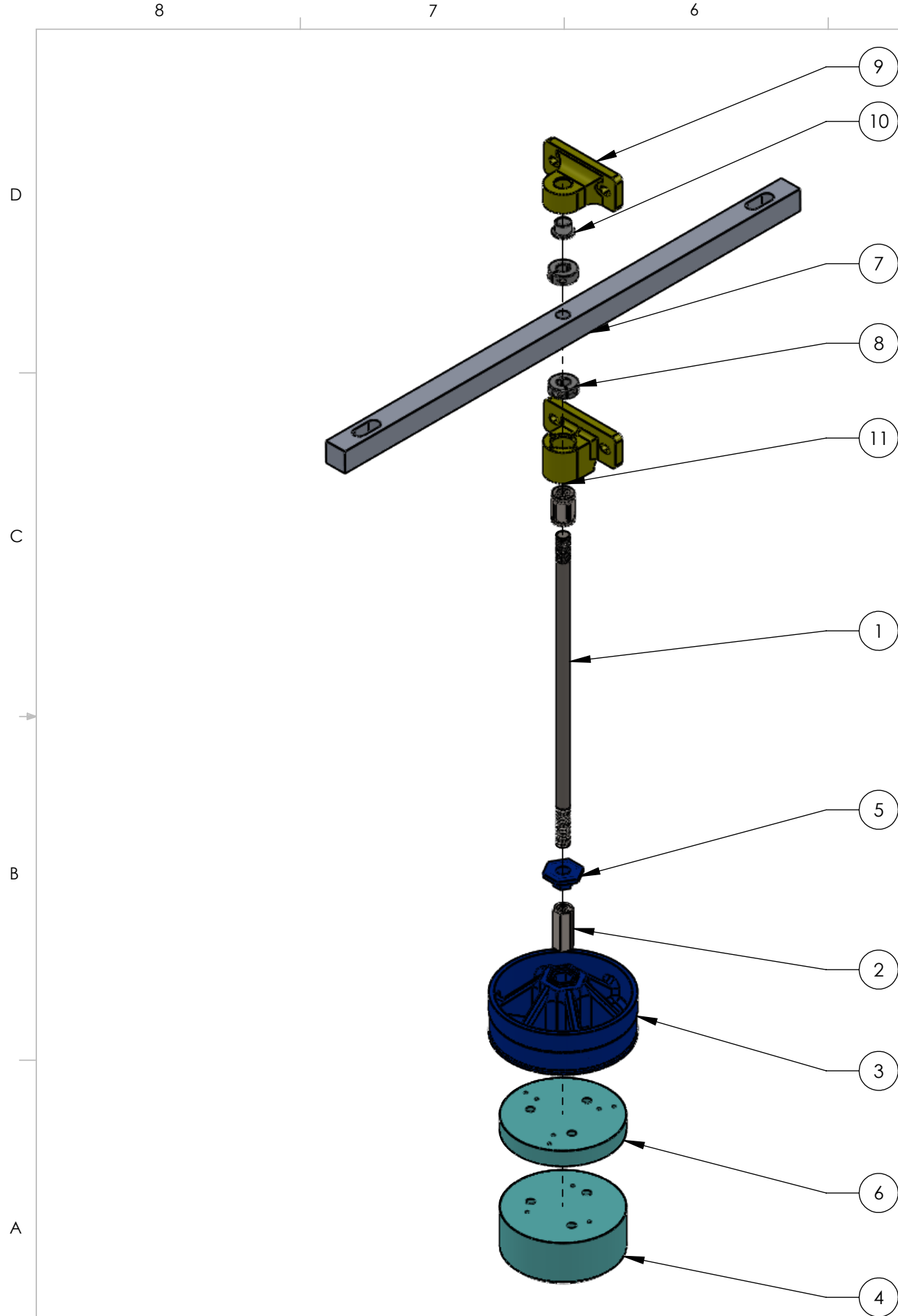
ITEM NO.	DESCRIPTION	Material	QTY.
1	1/2"-13 Double Threaded Piston Rod	Alloy Steel (SS)	1
2	1/2"-13 Coupling Nut	Alloy Steel	1
3	Compression Piston	CLEAR RESIN (POSTCURED)	1
4	Dead Volume Reducing Component - 50 mm Thick	ABS	1
5	Coupling Nut Cap	CLEAR RESIN (POSTCURED)	1
6	Dead Volume Reducing Component - 18 mm Thick	ABS	1
7	Compression Piston to Scotch Yoke Mechanism Connecting Bar	6061 Alloy	1
8	1/2" Collar	0.08	2
9	Linear Sleeve Bearing Mount	CLEAR RESIN (POSTCURED)	1
10	1/2" Linear Sleeve Bearing	N/A	1
11	1/2" Linear Ball Bearing Assembly	N/A	1

UNLESS OTHERWISE SPECIFIED:

DIMENSIONS ARE IN MM
TOLERANCES:
ANGULAR: ± 0.5°
.X = ± 0.25
.XX = ± 0.05

SURFACE FINISH 0.6
μm

MATERIAL:
N/A

DO NOT SCALE DRAWING

NAME

DRAWN BY Jason Michaud

MODEL BY Jason Michaud

CHECKED BY

Comments:

February 13, 2017 1:54:13 PM
December 17, 2019 8:13:13 PM

The Department of Mechanical Engineering
UNIVERSITY OF ALBERTA

TITLE:
Compression Piston Assembly

SIZE **B**

Project: **OPA MK III**

REV **B**

SCALE: 1:5   Mass: 2898.51   Page: 315

[1.00]
25.40

Ø141

[24.00]
609.60

37.75

[1.00]
25.40

128.35

50.75

436.65

136

115

68

50

A

DETAIL A
SCALE 2 : 1

R2 ALL ROUND

1

R1 ALL ROUND

UNLESS OTHERWISE SPECIFIED:		NAME	The Department of Mechanical Engineering
DIMENSIONS ARE IN MM			UNIVERSITY OF ALBERTA
TOLERANCES: ANGULAR: ± 0.5°	DRAWN BY	Jason Michaud	TITLE:
.X = ± 0.25	MODEL BY	Jason Michaud	Compression Piston
.XX = ± 0.05	CHECKED BY		Assembly
SURFACE FINISH 0.6 μm	Comments:		

MATERIAL: N/A		
DO NOT SCALE DRAWING	February 13, 2017 1:54:13 PM	SIZE **B**	Project: **OPA MK III**	REV **B**
	December 17, 2019 8:13:13 PM			
		SCALE: 1:5	Mass: 2898.51	Page: 316

ITEM NO.	DESCRIPTION	Material	QTY.
1	Compression Piston Yoke	6061 Alloy	1
2	1/2"-13 DoubleThreaded Linear Shaft	6061 Alloy	2
3	Linear Bearing Mount	CLEAR RESIN (POSTCURED)	4
4	Linear Ball Bearing	Alloy Steel	4

UNLESS OTHERWISE SPECIFIED:

DIMENSIONS ARE IN MM
TOLERANCES:
ANGULAR: ± 0.5°
.X = ± 0.25
.XX = ± 0.05

SURFACE FINISH 0.6 μm

MATERIAL:
N/A

DO NOT SCALE DRAWING

	NAME
DRAWN BY	Jason Michaud
MODEL BY	Jason Michaud
CHECKED BY	

Comments:

December 11, 2019 12:34:37 PM
December 17, 2019 7:31:20 PM

The Department of Mechanical Engineering
UNIVERSITY OF ALBERTA

TITLE:

Compression Yoke
Assembly

SIZE **B**

Project:
OPA MK III

REV B

SCALE: 1:6   Mass: 2059.13   Page: 317

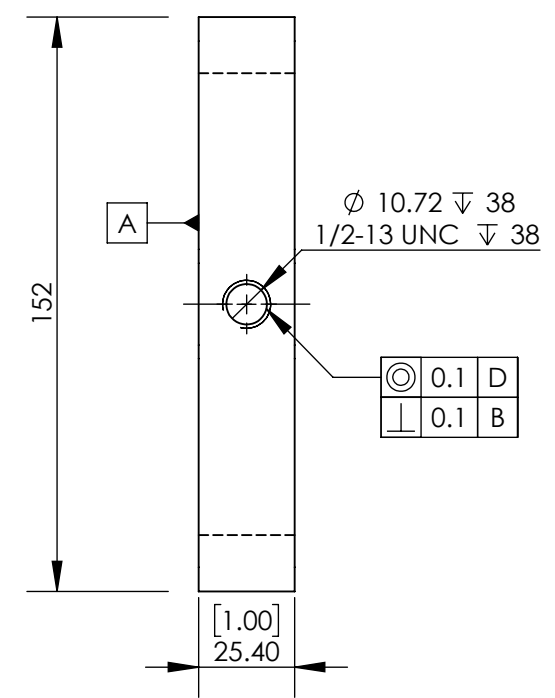Note: Bearing housing locations not dimensioned because assembly moves.

1828

44.13

152

[1.00]
25.40

UNLESS OTHERWISE SPECIFIED:		NAME	The Department of Mechanical Engineering
DIMENSIONS ARE IN MM			UNIVERSITY OF ALBERTA
TOLERANCES: ANGULAR: ± 0.5°	DRAWN BY	Jason Michaud	
.X = ± 0.25	MODEL BY	Jason Michaud	TITLE:
.XX = ± 0.05	CHECKED BY		Compression Yoke
SURFACE FINISH 0.6 μm	Comments:		Assembly
MATERIAL: N/A			

SURFACE FINISH 0.6 μm

MATERIAL: N/A

DO NOT SCALE DRAWING

December 11, 2019 12:34:37 PM
December 17, 2019 7:31:20 PM

SIZE **B**

Project: **OPA MK III**

REV B

SCALE: 1:6   Mass: 2059.13   Page: 318

126

63

R10 X 8

⌒ 0.01
⊕ 0.01 | A | B | C
BOUNDARY

// 0.1 | B

122.20

B

D

⊥ 0.1 | B
⊕ 0.1 | A | C

[0.50]
12.70

19.20

C

2X R

68.92°

76

A

Ø 10.72 ▽ 38
1/2-13 UNC ▽ 38

152

◎ 0.1 | D
⊥ 0.1 | B

[1.00]
25.40

ITEM NO.	DESCRIPTION	Material	QTY.
1	1/2"-13 Double Threaded Linear Shaft	6061 Alloy	2
2	1/2"-13 Coupling Nut	Alloy Steel	1
3	Expansion Piston Scotch Yoke	6061 Alloy	1
4	Expansion Piston	CLEAR RESIN (POSTCURED)	1
5	Dead Volume Reducing Component - 50 mm Thick	ABS	1
6	Dead Volume Reducing Component - 18 mm Thick	ABS	1
7	Coupling Nut Cap	CLEAR RESIN (POSTCURED)	1
8	Linear Bearing Mount	CLEAR RESIN (POSTCURED)	2
9	Linear Ball Bearing	Alloy Steel	2

UNLESS OTHERWISE SPECIFIED:

DIMENSIONS ARE IN MM
TOLERANCES:
ANGULAR: ± 0.5°
.X = ± 0.25
.XX = ± 0.05

SURFACE FINISH 0.6
μm

MATERIAL:
N/A

DO NOT SCALE DRAWING

NAME

DRAWN BY   Jason Michaud

MODEL BY   Jason Michaud

CHECKED BY

Comments:

February 13, 2017 1:54:13 PM
December 17, 2019 8:01:45 PM

The Department of Mechanical Engineering
UNIVERSITY OF ALBERTA

TITLE:

Expansion Piston
Assembly

SIZE
B

Project:
OPA MK III

REV
B

SCALE: 1:5   Mass: 2574.37   Page: 320

Ø141

152
95.73

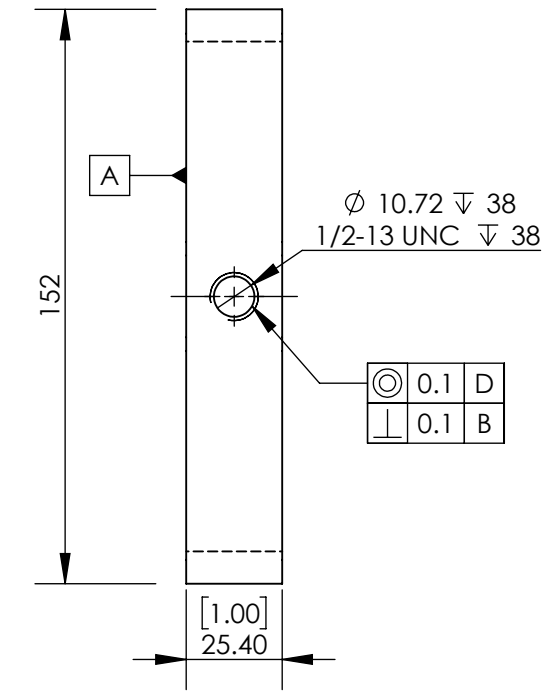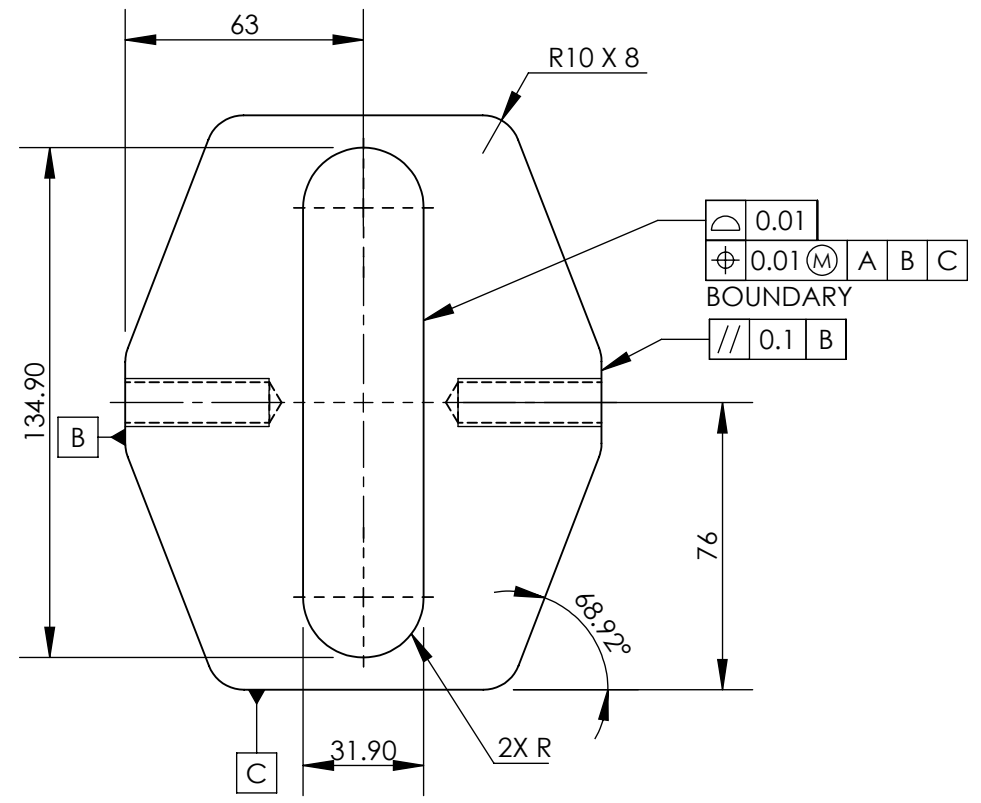663.20
444.15
318.15
154
115
68
50

35.75

A

UNLESS OTHERWISE SPECIFIED:		NAME		The Department of Mechanical Engineering
DIMENSIONS ARE IN MM				UNIVERSITY OF ALBERTA
TOLERANCES: ANGULAR: ± 0.5° .X = ± 0.25 .XX = ± 0.05	DRAWN BY	Jason Michaud		TITLE:
	MODEL BY	Jason Michaud		Expansion Piston Assembly
	CHECKED BY			
SURFACE FINISH 0.6 μm	Comments:			
MATERIAL: N/A				
DO NOT SCALE DRAWING		February 13, 2017 1:54:13 PM		SIZE **B**	Project: **OPA MK III**	REV B
		December 17, 2019 8:01:45 PM				

SCALE: 1:4   Mass: 2574.37   Page: 321

126

63

R10 X 8

⌓ 0.01
⌖ 0.01 Ⓜ A B C
BOUNDARY

// 0.1 B

134.90

B

76

68.92°

31.90

2X R

C

D

⊥ 0.1 B
⌖ 0.1 A C

[0.50]
12.70

A

152

∅ 10.72 ▽ 38
1/2-13 UNC ▽ 38

◎ 0.1 D
⊥ 0.1 B

[1.00]
25.40

The Department of Mechanical Engineering
UNIVERSITY OF ALBERTA

TITLE:
Expansion Piston Scotch
Yoke

SIZE   Project: REV
B   OPA MK III   B

SCALE: 1:2   Mass: 799.15   Page: 322